The genesis and evolution of lode gold mineralization and mafic host lithologies in the late-Archean Norseman Terrane, Yilgarn Block, Western Australia

A thesis submitted to the College of Graduate Studies and Research in partial fulfillment of the requirements for the degree of Doctor of Philosophy in the Department of Geological Sciences, University of Saskatchewan, Saskatoon, Saskatchewan.

by

Thompson Campbell McCuaig

Spring, 1997

UNIVERSITY OF SASKATCHEWAN

College of Graduate Studies and Research

SUMMARY OF DISSERTATION

Submitted in partial fulfillment of the requirements for the

DEGREE OF DOCTOR OF PHILOSOPHY

by

Thompson Campbell McCuaig

Department of Geological Sciences

University of Saskatchewan

Spring 1997

Examining Committee:

Dr. D.H. de Boer	~~Dean~~/~~Associate Dean~~/Dean's Designate, Chair College of Graduate Studies & Research
Dr. R. Kerrich	Supervisor, Department of Geological Sciences
Dr. M. Stauffer	Department of Geological Sciences
Dr. K. Ansdell	Department of Geological Sciences
Dr. D. Stead	Department of Geological Sciences
Dr. Y. Pan	Department of Geological Sciences
Dr. R. Verrall	Department of Chemistry

External Examiner:

Dr. W.S. Fyfe

Earth Sciences

University of Toronto

London, Ontario N6A 5B7

Abstract

Six distinct types of mafic igneous rocks are present within the ca. 2714-2690 Ma Woolyeenyer Formation of the Norseman Terrane, East Central Yilgarn Superterrane (ECYS), Yilgarn Block, Western Australia. (1) Tholeiitic basalts and gabbros comprise the bulk of the formation, and are characterized by flat to slightly depleted mantle-normalized incompatible element patterns, and ε_{Nd} values of +2 to +3. (2) High-MgO tholeiite dykes (HMT) with normalized REE and multielement patterns like those of tholeiites, albeit at slightly lower abundances. (3) Enriched high-MgO tholeiite dikes (EHMT) with MgO, Cr similar to HMT but with extreme Al-depletion, enrichment in incompatible elements and HREE depletion, and ε_{Nd} values of -2.0 to -1.2. (4) High-MgO tholeiites with characteristics transitional to HMT and EHMT (THMT). Incompatible element enriched tholeiites transitional between HMT, HMT and tholeiite, subdivided into (5) ET1, characterized by enrichment in incompatible elements and LREE, with relatively flat HREE patterns and ε_{Nd} values ranging from -0.1 to 1.0, and (6) ET2, characterized by Al-depletion and pronounced HREE depletion.

The HMT and tholeiites are comagmatic, and positive ε_{Nd} values and comparable normalized trace element patterns suggest derivation of these rocks from a similar depleted source. Conversely, detailed modelling demonstrates that EHMT compositions cannot be generated by alteration or crustal contamination of HMT, Al-undepleted or Al-depleted komatiitic magmas, and require a source (1) that was enriched in incompatible elements by small volume partial melts prior to melting, and (2) where garnet was retained during melting. The distinctive garnet geochemical signature of Al-depletion, HREE fractionation, negative P anomalies, variably negative Zr, Hf anomalies, and no marked Nb, Ti anomalies, is also present in most early-Archean, many late-Archean, and (rarely) younger Al-depleted komatiites. Mantle phase relations and density considerations suggest that this signature can only develop in melts from mantle plumes in which melting commenced between 8-24 GPa, where pyrope-majorite garnet is expected to be a residual phase. These requisite conditions may explain the restriction of this distinctive geochemical signature to the Archean, where mantle sources melted at deeper levels in a hotter mantle. Furthermore, this study demonstrates that the magnitude of the negative Zr, Hf, and P anomalies increase with increasing depth of melting.

Generation of the above mafic lithologies require that incompatible element enriched and depleted sources existed at 2.7 Ga in the Norseman Terrane. The EHMT are the first report of such severely Al-depleted 2.7 Ga rocks from the Norseman-Wiluna belt. Negative ε_{Nd} values for these rocks may require a long-term enriched source: the first evidence for preservation of an incompatible element enriched source in the hot Archean aesthenosphere or mantle-lithosphere. Modern examples of coeval operation of diverse mantle magma sources occur in within-plate settings, accordingly, the Norseman mafic rocks may have been formed in an OIB-like setting.

The Archean lode-gold deposits at Norseman, Western Australia, consist of auriferous quartz veins in dextral-reverse ductile shear zones within tholeiitic metabasalts of upper-greenschist to amphibolite facies metamorphic grade. Three types of deposits (northern, central, southern) are delineated on the basis of their spatial distribution, veining style, alteration mineralogy and metamorphic grade of host rocks. Northern deposits, hosted in upper-greenschist to lower-amphibolite facies rocks, comprise massive to laminated quartz veins with selvedges of quartz-chlorite-calcite-biotite-plagioclase. Central deposits, hosted in lower-amphibolite facies rocks, consist of laminated to massive quartz veins with selvedges of quartz-actinolite-biotite-plagioclase-calcite. Southern deposits, hosted in middle-amphibolite facies metabasalts, consist of banded quartz-diopside-calcite-microcline-zoisite veins.

All deposits exhibit variable ductile deformation of veins and contiguous alteration haloes, implying a syn-deformational genesis at high temperatures. From Northern to Southern deposits, the alteration assemblages are indicative of higher temperatures, and there are progressively greater degrees of dynamically recovered textures in quartz. These observations imply that a thermal variation of gold-related hydrothermal alteration exists within the Norseman Terrane over a distance of 40 km, with $T_{Northern} < T_{Central} < T_{Southern}$. This thermal zonation is corroborated by arsenopyrite and O-isotope mineral-pair geothermometry, and T-X_{CO2} phase relations between vein selvedge assemblages, which signify temperatures of approximately 420°-475°C, 450°-495°C and 500°-600°C for Northern, Central and Southern deposits, respectively. The sum of structural, petrographic and mineral chemistry data indicates that the alteration assemblages formed in high-temperature, open hydrothermal systems and have not been subsequently metamorphosed as previously believed. The three groups of deposits are interpreted as having formed at progressively deeper crustal levels from north to south, and may then represent a crustal continuum of gold deposition from upper greenschist to amphibolite facies, now exposed in an oblique section through the Archean crust at Norseman.

Initial Pb isotope compositions of galena and altaite from lode gold deposits of the Norseman Terrane yield the most variable initial Pb-isotopic compositions for these minerals of any Archean lode gold deposit. Interpreted initial Pb isotope compositions of galena and altaite are systematically more radiogenic with increasing proximity to felsic intrusive rocks and older crust. This variation reflects mixing of Pb from four potential Pb reservoirs: (1) mafic greenstone lithologies, (2) older felsic basement, (3) felsic intrusive rocks derived from this basement, and a high Th/U source, perhaps depleted lower crustal granulites. Felsic sources dominate the Pb isotopic signature as they contain higher Pb abundances than the greenstones.

The Pb isotope data require that the plumbing architecture of the lode gold systems is crustal in scale, and that ore fluids are produced at depths external to the greenstones, and advect into the greenstone terranes where they partially equilibrate with greenstone lithologies and greenstone-derived fluids. The initial Pb isotope composition of the Norseman ore fluids is much more radiogenic than any gold deposits of similar age elsewhere in the ECYS. These extremely radiogenic initial Pb compositions suggest that the substrate to the Norseman greenstones may be older than that below adjacent greenstone terranes.

Gold mineralization occurred ca. 2630 Ma as determined from ^{40}Ar-^{39}Ar and Sm-Nd isochron ages on gold-related hydrothermal minerals and felsic dykes that crosscut mineralization. Yet, in these same deposits, alteration minerals can yield variable ^{40}Ar-^{39}Ar ages of ca. 2400-1000 Ma. Furthermore, Pb isotope data from galena and altaite in these deposits locally preserve paleoisochrons indicating at least two periods of galena growth/resetting ca. 1950 Ma and an indeterminate later event. The younger ages correspond to metamorphic/magmatic events recorded in Proterozoic orogens bounding the Yilgarn Craton. Thus, there has been cryptic fluid movement through this Archean craton at multiple times during the Proterozoic, with fluid activity is driven by orogenic events in bounding terranes.

BIOGRAPHICAL

Born: December 8, 1965 in Fort William, Ontario, Canada

Hons. B.Sc. Geology and Energy and Fuel Science (1988)
Lakehead University, Thunder Bay, Ontario

AWARDS

September 1992 - August 1994	University of Saskatchewan Postgraduate Scholarship
September 1988 - August 1992	NSERC Postgraduate Scholarship
September 1986 - May 1987	Lakehead University In-course Scholarship
September 1985 - May 1988	J.P. Bickell Foundation Scholarship
September 1984 - May 1988	Lakehead University Alumni Association Award
September 1984 - May 1987	Lakehead University Entrance Award
September 1984 - May 1985	Bora Laskin Memorial Scholarship

PUBLICATIONS

McCuaig, T.C and Kissin, S.A. The Port Coldwell Veins, Northern Ontario: Pb-Zn-Ag Deposits in a rift setting. Proceedings of the 10th Annual International Conference on Basement Tectonics, Duluth, Minnesota. *Geological Society of America Special Paper*, in press.

Groves, D.I., Ridley, J.R., Bloem, M.J., Gebre-Mariam, M., Hagemann, S.G., Hronsky, J.M.A., Knight, J.T., McNaughton, N.J., Ojala, J., Vielreicher, R.M., McCuaig, T.C., and Holyland, P.W. (1995) Lode-gold deposits of the Yilgarn Block: products of late-Archaean crustal-scale overpressured hydrothermal systems. In: Coward, M.P. and Ries, A.C. (Eds.) Early Precambrian Processes. Geological Society Special Publication 95.

Xie, Q., McCuaig, T.C., and Kerrich, R., 1995. HFSE and REE systematics of Archean Al-depleted komatiites and high-Mg tholeiites from Canada and Western Australia: implications for source compositions and melting depths of mantle plumes. *Chemical Geology* special volume on Mafic Magmatism through Time.

McCuaig, T.C. and Kerrich, R., 1994, P-T-t-deformation-fluid characteristics of lode gold deposits: evidence from alteration systematics. **in** Lentz, D.R., ed., Alteration and Alteration Processes Associated with Ore-forming Systems: *Geological Association of Canada, Short Course Notes*, v. 11, p. 339-379.

McCuaig, T.C., Kerrich, R. and Xie, Q., 1994. Phosphorus anomalies in Archean high-magnesian magmas as possible indicators of source mineralogy and depth. *Earth and Planetary Science Letters*, v. 124, p. 221-239.

Permission to Use

In presenting this thesis in partial fulfillment of the requirements for a Doctor of Philosophy degree from the University of Saskatchewan, I agree that the libraries of this university may make it freely available for inspection. I further agree that permission for copying of this thesis in any manner, in whole or in part, for scholarly purposes may be granted by my supervisor Dr. R. Kerrich or, in his absence, by the head of the Department of Geological Sciences or Dean of Arts and Science. It is understood that any copying of this thesis, or parts thereof, shall not be allowed without my written permission. It is also understood that due recognition shall be given to me and the University of Saskatchewan in any scholarly use which may be made of any material in this thesis.

Requests for permission to copy or make other use of material in this thesis, in whole or in part, should be addressed to:

Head of the Department of Geological Sciences
114 Science Place, University of Saskatchewan
Saskatoon, Saskatchewan, S7N 5E2.

Abstract

Six distinct types of mafic igneous rocks are present within the ca. 2714-2690 Ma Woolyeenyer Formation of the Norseman Terrane, East Central Yilgarn Superterrane (ECYS), Yilgarn Block, Western Australia. (1) Tholeiitic basalts and gabbros comprise the bulk of the formation, and are characterized by flat to slightly depleted mantle-normalized incompatible element patterns, and ε_{Nd} values of +2 to +3. (2) High-MgO tholeiite dykes (HMT) with normalized REE and multielement patterns like those of tholeiites, albeit at slightly lower abundances. (3) Enriched high-MgO tholeiite dikes (EHMT) with MgO, Cr similar to HMT but with extreme Al-depletion, enrichment in incompatible elements and HREE depletion, and ε_{Nd} values of -2.0 to -1.2. (4) High-MgO tholeiites with characteristics transitional to HMT and EHMT (THMT). Incompatible element enriched tholeiites transitional between HMT, HMT and tholeiite, subdivided into (5) ET1, characterized by enrichment in incompatible elements and LREE, with relatively flat HREE patterns and ε_{Nd} values ranging from -0.1 to 1.0, and (6) ET2, characterized by Al-depletion and pronounced HREE depletion.

The HMT and tholeiites are comagmatic, and positive ε_{Nd} values and comparable normalized trace element patterns suggest derivation of these rocks from a similar depleted source. Conversely, detailed modelling demonstrates that EHMT compositions cannot be generated by alteration or crustal contamination of HMT, Al-undepleted or Al-depleted komatiitic magmas, and require a source (1) that was enriched in incompatible elements by small volume partial melts prior to melting, and (2) where garnet was retained during melting. The distinctive garnet geochemical signature of Al-depletion, HREE fractionation, negative P anomalies, variably negative Zr, Hf anomalies, and no marked Nb, Ti anomalies, is also present in most early-Archean, many late-Archean, and (rarely) younger Al-depleted komatiites. Mantle phase relations and density considerations suggest that this signature can only develop in melts from mantle plumes in which melting commenced between 8-24 GPa, where pyrope-majorite garnet is expected to be a residual phase. These requisite conditions may explain the restriction of this distinctive geochemical signature to the Archean, where mantle sources melted at deeper levels in a hotter mantle. Furthermore, this study demonstrates that the magnitude of the negative Zr, Hf, and P anomalies increase with increasing depth of melting.

Generation of the above mafic lithologies require that incompatible element enriched and depleted sources existed at 2.7 Ga in the Norseman Terrane. The EHMT are the first report of such severely Al-depleted 2.7 Ga rocks from ECYS. Negative ε_{Nd} values for these rocks may require a long-term enriched source: the first evidence for

preservation of an incompatible element enriched source in the hot Archean asthenosphere or mantle-lithosphere. Modern examples of coeval operation of diverse mantle magma sources occur in within-plate settings, accordingly, the Norseman mafic rocks may have been formed in an ocean-island-basalt-like setting.

The Archean lode-gold deposits at Norseman, Western Australia, consist of auriferous quartz veins in dextral-reverse ductile shear zones within tholeiitic metabasalts of upper-greenschist to amphibolite facies metamorphic grade. Three types of deposits (northern, central, southern) are delineated on the basis of their spatial distribution, veining style, alteration mineralogy and metamorphic grade of host rocks. Northern deposits, hosted in upper-greenschist to lower-amphibolite facies rocks, comprise massive to laminated quartz veins with selvedges of quartz-chlorite-calcite-biotite-plagioclase. Central deposits, hosted in lower-amphibolite facies rocks, consist of laminated to massive quartz veins with selvedges of quartz-actinolite-biotite-plagioclase-calcite. Southern deposits, hosted in middle-amphibolite facies metabasalts, consist of banded quartz-diopside-calcite-microcline-zoisite veins.

All deposits exhibit variable ductile deformation of veins and contiguous alteration haloes, implying a syn-deformational genesis at high temperatures. From Northern to Southern deposits, the alteration assemblages are indicative of higher temperatures, and there are progressively greater degrees of dynamically recovered textures in quartz. These observations imply that a thermal variation of gold-related hydrothermal alteration exists within the Norseman Terrane over a distance of 40 km, with $T_{Northern} < T_{Central} < T_{Southern}$. This thermal zonation is corroborated by arsenopyrite and O-isotope mineral-pair geothermometry, and T-X_{CO2} phase relations between vein selvedge assemblages, which signify temperatures of approximately 420°-475°C, 450°-495°C and 500°-600°C for Northern, Central and Southern deposits, respectively. The sum of structural, petrographic and mineral chemistry data indicates that the alteration assemblages formed in high-temperature, open hydrothermal systems and have not been subsequently metamorphosed as previously believed. The three groups of deposits are interpreted as having formed at progressively deeper crustal levels from north to south, and may then represent a crustal continuum of gold deposition from upper greenschist to amphibolite facies, now exposed in an oblique section through the Archean crust at Norseman.

Initial Pb isotope compositions of galena and altaite from lode gold deposits of the Norseman Terrane yield the most variable initial Pb-isotopic compositions for these minerals of any Archean lode gold deposit. Interpreted initial Pb isotope compositions of galena and altaite are systematically more radiogenic with increasing proximity to felsic

intrusive rocks and older crust. This variation reflects mixing of Pb from four potential Pb reservoirs: (1) mafic greenstone lithologies, (2) older felsic basement, (3) felsic intrusive rocks derived from this basement, and (4) a high Th/U source, perhaps depleted lower crustal granulites. Felsic sources dominate the Pb isotopic signature as they contain higher Pb abundances than the greenstones.

The Pb isotope data require that the plumbing architecture of the lode gold systems is crustal in scale, and that ore fluids are produced at depths external to the greenstones, and advect into the greenstone terranes where they partially equilibrate with greenstone lithologies and greenstone-derived fluids. The initial Pb isotope composition of the Norseman ore fluids is much more radiogenic than any gold deposits of similar age elsewhere in the ECYS. These extremely radiogenic initial Pb compositions suggest that the substrate to the Norseman greenstones may be older than that below adjacent greenstone terranes.

Gold mineralization occurred at ca. 2630 Ma as determined from ^{40}Ar-^{39}Ar and Sm-Nd isochron ages on gold-related hydrothermal minerals and felsic dykes that crosscut mineralization. Yet, in these same deposits, alteration minerals can yield variable ^{40}Ar-^{39}Ar ages of ca. 2400-1000 Ma. Furthermore, Pb isotope data from galena and altaite in these deposits locally preserve paleoisochrons indicating at least two periods of galena growth/resetting ca. 1950 Ma and an indeterminate later event. The younger ages correspond to metamorphic/magmatic events recorded in Proterozoic orogens bounding the Yilgarn Craton. Thus, there has been cryptic fluid movement through this Archean craton at multiple times during the Proterozoic, with fluid activity driven by orogenic events in bounding terranes.

Acknowledgements

Firstly I graciously acknowledge the financial and technical support of my advisor Rob Kerrich, who continually challenged and expanded my scientific boundaries, and allowed my Ph.D. experience to be an intellectual adventure. I also acknowledge the support of my cosupervisor David Groves at the University of Western Australia, who was instrumental in organizing my project, provided logistical and financial support during my work at the Key Centre for Strategic Mineral Deposits, University of Western Australia, and has significantly influenced my views on the genesis of ore deposits. During the course of my studies, I received NSERC and University of Saskatchewan Postgraduate Scholarships.

This study would not have been possible without the support of Central Norseman Gold Corporation and Western Mining Corporation, who allowed access to mines, logistical support during field work, and financial support for sample shipment and geochemical analyses. I am indebted to the many CNGC and WMC geologists with whom I had detailed geological discussions, including N. Archer, P. Bird, J. Chapman, G. Hopkins, J. Hronsky, K. Johnson, D. Kelly, D. Miller, L. Offe, S. Peters, M. Ritchie, B. Turner, and R. Waugh. Without the support of these individuals, my present understanding of the geology of the Norseman Terrane would be incomplete.

I have benefitted from abundant technical assistance in acquiring geochemical data for this thesis, for which the following people are duly acknowledged: Pb-isotopes - N.J. McNaughton; ICP-MS - J. Fan, J. Jain, L. Song; Microprobe - T. Bonli, R. George; Thin Sections - B. Novakovski; Stable isotopes - K. Durocher, S. Hagemann, D. Pezderic; ^{40}Ar-^{39}Ar analyses - K. Durocher, J. Fedorowich; Nd isotopes - H. Kagami; photo digitizing - M. Reeves.

P. Morris is especially thanked for supplying samples and a partial geochemical database for the EHMT, and for numerous discussions on basalt geochemistry which are reflected in this thesis. Other scientists who have greatly contributed to my geological knowledge during my studies, through numerous discussions or by reviewing parts of this thesis, include: K. Ansdell, K.F. Cassidy, K. Durocher, J. Fan, P. Field, M. Fayek, S. Hagemann, F. Hrdy, B. Janser, A.J.R. Kent, C. MacPherson, N.J. McNaughton, E. Mikucki, J. Ridley, D. Schultz, M. Skwarnecki, D. Wyman, Q. Xie.

I whole-heartedly thank my parents Tom and Marilyn McCuaig, and my sister Katie, for their support, patience and encouragement throughout the years of my study.

Finally, I acknowledge my wife Val, who brightened the final years of my study, and who inspired me to finish so that I could begin the rest of my life with her.

Dedication

This thesis is dedicated to my mother,

Marilyn Gail McCuaig

who inspired me to pursue my Ph.D.

Table of Contents

List of Tables

List of Figures

CHAPTER 1

INTRODUCTION AND SCOPE

1.1 Background

Late Archean terranes formed ca. 3000-2500 Ma are richly endowed with varied mineral resources including syngenetic Cu-Ni massive sulphide and epigenetic gold deposits. Historically, Archean terranes have accounted for approximately 50% of total gold production worldwide (Woodall, 1988). This enormous metal inventory has served as an impetus for voluminous research into the genesis and metallogeny of these terranes and their deposits. In addition, numerous studies have investigated these terranes in an effort to constrain the evolution of the young earth (Nisbet, 1987; Glover and Ho, 1990; Percival and Ludden, 1995).

Despite this enormous body of research on Archean terranes, from many disciplines within the earth sciences, numerous questions regarding the evolution and metallogeny of late Archean terranes remain unresolved. Of particular interest are the evolution of the mafic-ultramafic volcanic sequences that characterize Archean 'greenstone' belts. Issues that are currently the focus of research on these lithologies include the mineralogical, geochemical, and thermal nature of the mantle sources from which their parental magmas were ultimately derived; the mechanisms by which the magmas were generated and separated from their mantle sources; the mechanisms and effects of magma-lithosphere interaction during ascent, and the tectonic settings in which these magmas were generated and emplaced into or onto the crust (Sun and Nesbitt, 1978; Arndt and Nisbet, 1982; Huppert and Sparkes, 1985; Arndt and Jenner, 1986; Xie et al., 1993; 1995; McCuaig et al., 1994; Herzberg, 1995).

The genesis of Archean gold deposits also remains controversial. Sharp rises in gold prices during the 1970's fueled a concomitant increase in research into the genesis of these deposits, which has continued into the 1990's. From this research, there has arisen a general consensus of an epigenetic origin for Archean gold deposits, which share many common features with Proterozoic and Phanerozoic mesothermal counterparts (cf. Kerrich, 1993; McCuaig and Kerrich, 1994). Notwithstanding three decades of intensive

research, several important aspects of Archean lode gold genesis remain unresolved. Fluid and solute sources and fluid production mechanisms remain largely unconstrained: included are devolatization of host greenstones; granulitization of the lower crust; fluids expelled during the crystallization of granitoid plutons; deep circulation of meteoric waters, or devolatization of subcreted material (e.g. Groves and Phillips, 1987; Burrows and Spooner, 1987; Cameron, 1988; Wyman and Kerrich, 1988; Nesbitt and Muelenbachs, 1989). Controls on orebody location and gold deposition mechanisms, from the scale of individual deposits to entire terranes, are inadequately understood in most Archean deposits. The timing of gold introduction remains fiercely contested, and ranges from pre-metamorphic to >100 Ma post-peak metamorphic (e.g. Phillips and de Nooy, 1988; Hanes et al., 1992; Kerrich and Cassidy, 1994). Furthermore, the post-mineralization deformation-fluid history of the host terranes, the resultant modification of orebody location and geometry, and the effects on the interpretation of radiometric dating techniques has only recently been addressed (Guha and Kanwar, 1987; Kerrich and Cassidy, 1994; Powell et al., 1995; Kent and McCuaig, submitted).

1.2 Scope of the thesis

In an attempt to constrain the unresolved issues outlined above, a multidisciplinary study of the evolution and metallogeny of the late Archean Norseman Terrane, Western Australia was undertaken. The Norseman Terrane is an appropriate study area for the following reasons. (1) The terrane contains an extensive mafic volcanic rock sequence, on which many petrographic studies have been performed, but only a limited and incomplete geochemical database exists, and the petrogenesis of the sequence is largely unconstrained. (2) These mafic lithologies host extensively developed lode gold mineralization, the genesis of which remains controversial. Previous research has postulated genetic origins ranging from pre-peak metamorphism to post-peak metamorphism, and from late-volcanic modified seawater fluid sources to magmatic ± metamorphic fluids expelled during the emplacement of regional batholiths (Golding, 1982; Keele, 1984; Mueller, 1992; McCuaig et al., 1993).

This study employs multidisciplinary research techniques to resolve these issues. New ICP-MS technology is utilized to obtain precise low-level trace element geochemical data on the mafic host rocks. A comprehensive geochemical database has been aquired on these lithologies, and is used to make inferences as to the nature of the Archean mantle and magma-mantle-crust interactions during the petrogenesis of these rock types, to constrain the tectonic setting in which the mafic volcanic sequence was

formed, and to constrain element behaviour during hydrothermal processes. Gold mineralization throughout the Norseman terrane is also documented in detail. Orebody geometry, hydrothermal alteration assemblages and their distribution, mineral chemistry, phase equilibria, and stable and radiogenic isotope data are considered in combination in an attempt to constrain genetic models for gold mineralization within the Norseman Terrane.

1.3 Structure of the thesis

The thesis is organized as follows. The present understanding of the geological setting of the Norseman Terrane is outlined in Chapter 2. Chapter 3 describes in detail the mafic lithologies which host the lode gold deposits, and presents a comprehensive geochemical database for these lithologies. What was previously believed to be a monotonous sequence of tholeiitic mafic volcanics is shown to be a geochemically diverse lithological sequence. The effects of crustal contamination and hydrothermal alteration are systematically assessed from this geochemical database in an attempt to constrain the mineralogical and geochemical compositions of the mantle source, depths of magma genesis, and the tectonic setting in which the magmas were generated.

The rationale for studying lode gold deposits within the Norseman Terrane, and documentation of the macroscopic and mesoscopic geometry of the hydrothermal plumbing systems in which the gold deposits are sited, is presented in Chapter 4. Chapter 5 reports the distribution, petrography, mineral chemistry and calculated temperature ranges of metamorphic and hydrothermal alteration assemblages within the Norseman Terrane. The latter part of this chapter details the textural characteristics of the gold-related hydrothermal alteration assemblages, from which conclusions are drawn regarding the relative timing relationships of fluid flow and hydrothermal alteration to deformation and metamorphism in the Norseman Terrane.

In Chapter 6, all available geochronological data for the Norseman Terrane is compiled and new ^{40}Ar-^{39}Ar data is presented for hydrothermal and igneous minerals. This data is used to constrain the age of gold mineralization, the thermochronological evolution of the Norseman Terrane, and post-cratonization fluid resetting of the ^{40}Ar-^{39}Ar system in hydrothermal minerals. An extensive database of Pb isotope analyses of Pb-rich ore minerals is then presented. These data are interpreted in terms of Pb and fluid sources for primary gold mineralization, regional variation in the nature of the basement to the greenstone lithologies, and post-cratonization resetting of the Pb isotopic system by fluid movement during the Proterozoic.

The final Chapter 7 summarizes the major contributions of this study, and the implications of the results obtained, to the understanding of the genesis and evolution of Archean lode gold deposits and their host metamorphic terranes.

CHAPTER 2

REGIONAL GEOLOGICAL SETTING

2.1 Yilgarn Craton

This chapter outlines the geological setting of the Norseman Terrane within the Archean Yilgarn Craton of Western Australia. The Yilgarn Craton of Western Australia is one of the largest exposures (1.25 million km^2) of Archean crust globally, forming a major crustal block of the Australian continent (Fig. 2.1). The craton is tectonically bounded by Proterozoic orogens to the south and northwest, and is unconformably overlain by Proterozoic sedimentary rocks to the northeast, flat-lying Phanerozoic sedimentary rocks to the east, and the Darling fault and associated Phanerozoic sedimentary rocks to the west (Gee et al., 1981; Myers, 1993). The Yilgarn is an economically important craton in terms of lode gold and copper-nickel production (see Solomon and Groves, 1994, for a review).

The Yilgarn Craton is an amalgamation of several Archean volcano-sedimentary terranes ranging in age from 3730 to 2550 Ma, intruded by numerous generations of plutons. The craton was subdivided by previous workers into four major provinces: the Western Gneiss Terrane, the Murchison Province, the Southern Cross Province and the Eastern Goldfields (Gee et al., 1981). However, with the recent application of the terrane concept (cf. Irwin, 1973) to Archean cratons, allied with detailed mapping by the Geological Survey of Western Australia and the Australian Geological Survey Organisation, the Yilgarn Craton has been regrouped into numerous tectonostratigraphic terranes separated by major crustal lineaments (Fig. 2.1; Swager et al., 1992; Myers, 1993). The terrane nomenclature is followed in this thesis.

Individual terranes within the Yilgarn are grouped into four superterranes, the West Yilgarn, West Central Yilgarn, East Central Yilgarn, and East Yilgarn (Fig. 2.1; Myers, 1993). The West Yilgarn Superterrane comprises the Narryer, Murchison and Southwest Yilgarn Composite Terranes. The Narryer and Southwest Yilgarn Composite Terranes contain substantial portions of middle to early Archean crust (>3000 Ma), and consist of complexly deformed gneisses of upper amphibolite to granulite facies

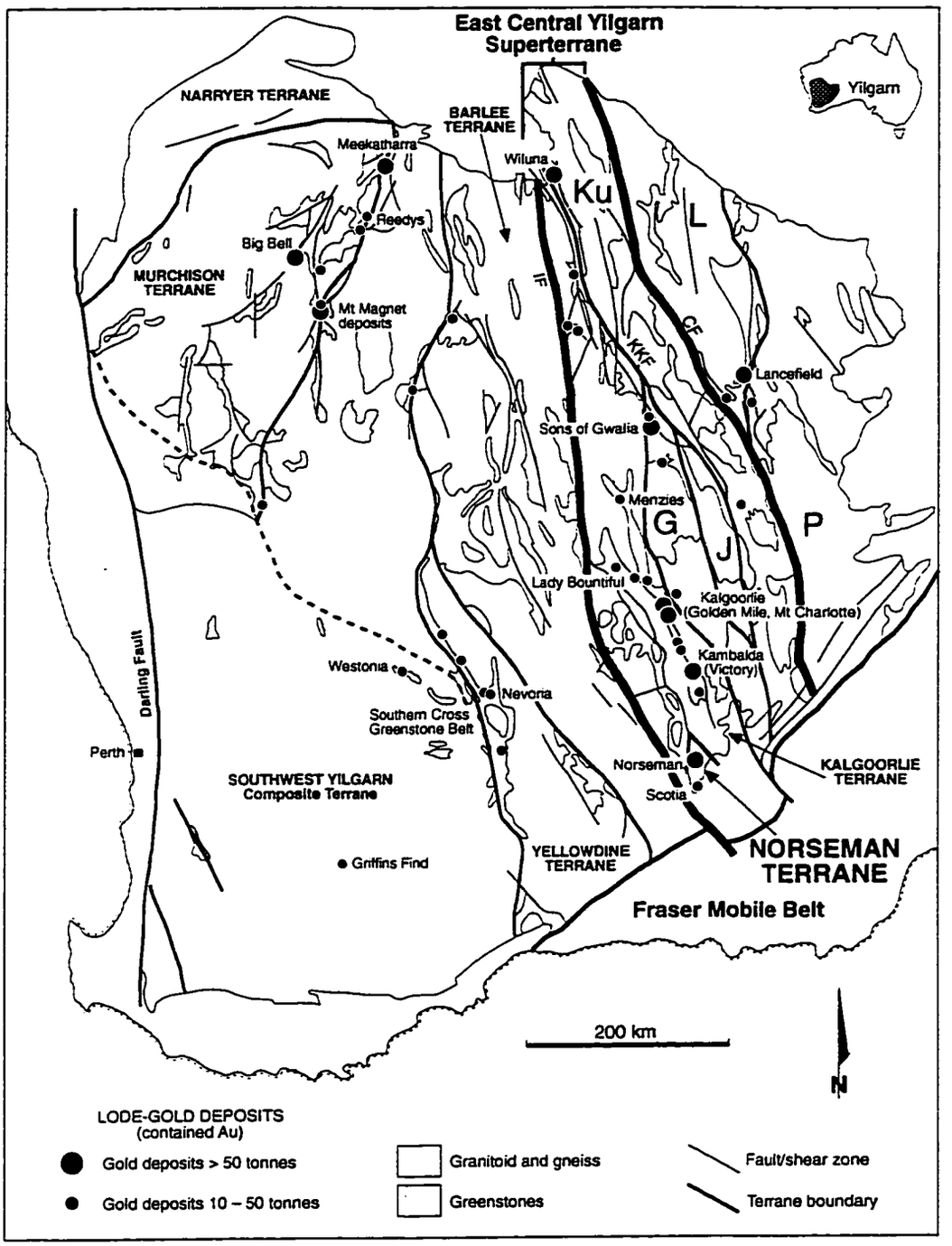

Figure 2.1. Simplified geological map of the Yilgarn Craton of Western Australia, highlighting terrane subdivisions and the location of the Norseman Terrane study area. Terrane abbreviations: Ku = Kurnalpi, L = Laverton, P = Pinjin, G = Gindalbee, J = Jubilee. Fault abbreviations: CF = Celia fault, KKF = Keith-Kilkenny fault, IF = Ida fault. The distribution of lode gold deposits is also shown, categorized by tonnes of produced gold. Map modified from Cassidy (1992), production data for gold deposits from Woodall (1990).

metamorphic grade. Periods of metamorphism and magmatism have been identified, with varying degrees of confidence, at 3600-3730 Ma, 3350-3310 Ma, 3100 Ma and 2780-2630 Ma in the Narryer Terrane, and 3180 Ma, 3000 Ma, 2860 Ma, 2780 Ma, 2680-2660 Ma and 2560-2500 Ma in the southwestern Yilgarn (McNaughton and Dahl, 1987; Myers, 1993 and references therein).

The Murchison Terrane is a granitoid-greenstone terrane, dominantly metamorphosed to greenschist facies, and comprises two major volcanosedimentary sequences (Myers, 1993, and references therein). The lower (ca. 3000 Ma) sequence consists dominantly of tholeiitic and high-Mg basaltic lavas, interlayered with silicic volcanic and volcaniclastic rocks at stratigraphically higher levels, overlain by banded iron formation (BIF). These rocks were intruded by granitoids ca. 2900 Ma, and the entire assemblage was intensely deformed. A younger volcano-sedimentary sequence (ca. 2800 Ma) unconformably overlies this sequence, and all rocks were intruded by granitoids at 2690-2680 Ma and subsequently deformed and juxtaposed with the Mt. Narryer Terrane ca. 2680-2640 Ma (compilation of Myers, 1993). The latest stages of ductile deformation formed regional north-south shear zones and were coeval with emplacement of granitoid plutons at 2630 Ma (Gee et al., 1981; Watkins and Hickman, 1990). The contact of the Narryer Terrane with the Murchison Terrane appears to be tectonic, whereas no tectonic contact has yet been identified between the Southwest Yilgarn Terrane and the Murchison Terrane. This southwestern margin of the Murchison Terrane may be gradational, representing a tilted section through the Archean crust (Gee et al., 1986).

The Yellowdine and Barlee Terranes constitute the West Central Yilgarn Superterrane. These terranes comprise two distinct volcano-sedimentary greenstone sequences, one ca. 3000-2900 Ma, the second ca. 2700 Ma. The earlier sequences comprise lower units consisting of tholeiites, magnesian basalts, komatiites and BIF overlain by dominantly terriginous sedimentary rocks with BIF. These are unconformably overlain by the younger sedimentary and volcanic sequences, that noteably lack BIF (Pidgeon, 1986; Barley et al., 1990). Collectively, these greenstone sequences were metamorphosed and deformed broadly coeval with granitoid intrusion at 2700-2650 Ma (Watkins and Hickman, 1988). Metamorphic grades in the greenstones range from prehnite-pumpellyite to upper amphibolite facies, and generally increase towards large granitoid batholiths and greenstone belt margins.

The Laverton and Pinjin Terranes that constitute the East Yilgarn Superterrane are less well-studied than other counterparts: they include high grade gneiss, granitoids, and 2800 and 2700 Ma greenstones, and strongly resemble counterparts of the Barlee, Yellowdine and Murchison Terranes (Myers, 1993).

2.2 East Central Yilgarn Superterrane (Norseman-Wiluna belt)

The north-northwest trending East Central Yilgarn Superterrane (ECYS, previously known as the Norseman-Wiluna belt, Gee et al., 1981) comprises the Gindalbie, Jubilee, Kurnalpi, Kalgoorlie, and Norseman Terranes. With dimensions up to 800 km long and 150 km wide, it is the largest Archean greenstone belt in Australia (Fig. 2.1). This superterrane is a repository for world class epigenetic lode, or mesothermal, gold and syngenetic copper-nickel sulphide deposits (Drew and Gole, 1994; Solomon and Groves, 1994), and is consequently one of the most extensively studied regions in the Yilgarn Craton. Outcrop is both extremely scarce and severely weathered throughout much of the Yilgarn, thus most of the stratigraphic correlations and regional structures have been determined principally by geophysical techniques, such as aeromagnetic mapping (Isles et al., 1989). As a result, there are many discrepancies in the literature between the location of major lineaments, terrane boundaries, and correlations of stratigraphic sequences between terranes, even in the most extensively studied areas (Libby et al., 1990; Swager et al., 1990; 1992; Swager, 1993; Myers, 1993; Rattenbury, 1993).

2.2.1 Stratigraphy

Two distinct volcano-sedimentary associations are recognized in the terranes (Barley et al., 1990; Barley and Groves, 1990). A magnesian basalt - komatiite - sulphidic shale association dominates in the western terranes of the ECYS, for example, the Kalgoorlie Terrane. Available geochronology constrains this subaqueous mafic volcanism, including intrusion of sills, to between ca. 2715 and 2690 Ma in the southern Kalgoorlie and Norseman Terranes, where it is best documented (Campbell and Hill, 1988; Claoué-Long et al., 1988; Pidgeon and Wilde, 1990; Hill et al., 1992), but may be older in the northern areas (e.g. > 2750 Ma at Wiluna, Kent, 1994). The second association comprises interlayered tholeiite, subaerial calc-alkaline volcanic rocks, ranging in composition from basalt to rhyolite, and feldspathic sedimentary rocks. This association is predominant in eastern terranes of the ECYS, such as the Kurnalpi Terrane. Felsic volcanic rocks of this association formed between 2705 and 2685 Ma, and are thus coeval with the Mg-basalt-komatiite-shale association. With the exception of the Norseman Terrane (Fig. 2.2), no evidence for an earlier volcano-sedimentary sequence, such as the ca. 3000-2900 Ma sequence observed in the other superterranes, has been observed.

Basement to the greenstones is not directly observed, but in the southern

Kalgoorlie and Norseman Terranes can be inferred to be older sialic crust from indirect evidence such as xenocrystic zircons, Sm-Nd ages older than contemporaneous volcanism, and trace element evidence for crustal contamination in ultramafic volcanics of the Kalgoorlie Terrane (Arndt and Jenner, 1986; Barley, 1986; Compston et al., 1986; Claoué-Long et al., 1988); xenocrystic zircons and radiogenic Pb isotope data from granitoids of the Kalgoorlie and Norseman Terranes (Oversby, 1975; Campbell and Hill, 1988). Geophysical data indicates that the supracrustal sequences are relatively thin and underlain by sialic crust (gravity, Drummond, 1988; seismic, Williams, 1993).

2.2.2 Granitoids

The above supracrustal sequences are intruded or bounded by numerous granitoid bodies. These granitoids were originally subdivided into internal and external varieties (Sofoulis, 1963), and this terminology has been adhered to by recent researchers (Bettenay, 1988; Campbell and Hill, 1988; Cassidy et al., 1991; Hill et al., 1992). External granitoids are those situated between the greenstone belts, and comprise complex masses of pre-, syn- and post-tectonic granitoids ranging from monzogranite to granodiorite in composition (Bettenay, 1988). Internal granitoids are those enclosed by, or marginal to, the supracrustal belts, and comprise large composite calc-alkaline bodies that formed coeval with felsic volcanism, and smaller calc-alkaline bodies transgressive to volcanic-plutonic sequences. Compositions range from syenogranite, through monzogranite to granodiorite, with rare syenite and quartz syenite (Cassidy et al., 1991). Minor felsic to intermediate intrusive suites are locally abundant (Perring et al., 1991). Within the southern Kalgoorlie and Norseman Terranes, voluminous granitoid emplacement occurred at 2690-2685 Ma and 2665-2660 Ma, with minor intrusive activity at 2630-2600 Ma (Campbell and Hill, 1988; Hill et al., 1992; Kent, 1994).

2.2.3 Deformation

One of the prominent features of the ECYS is the north to northwest trending crustal scale lineaments, some being traceable for up to 300 km, which both bound the belt and dissect it internally into its constituent terranes (Gee et al., 1981; Swager et al., 1992). The granitoid-greenstone terranes of the ECYS are also cut by structures that separate distinct tectonostratigraphic domains, although recent application of sequence stratigraphy to these ancient terranes has indicated that lithological sequences can be correlated across many of these structures, albeit with significant displacements (Rattenbury, 1993). The geometry and displacement vectors in these complex regional structures indicate protracted histories of episodic movement and reactivation, and are

poorly understood (Swager, 1993). The depth extent of these structures is also poorly constrained. Recent high-resolution seismic reflection studies in the Kalgoorlie Terrane image these high-strain zones as steeply dipping structures at shallow levels, that displace subhorizontal reflectors, and may become listric at depth (cf. Williams, 1993).

Outcrop is sparse, and structural interpretation is based largely on aeromagnetic data, as mentioned above. Accordingly, there is much debate to the actual form and style of structures and deformational events (Archibald et al., 1978; Hammond and Nisbet, 1992; Swager et al., 1992; Swager, 1993; Williams, 1993). The southern Kalgoorlie Terrane has been the focus of the most detailed structural studies, and there is general consensus that three main phases of deformation can be recognized: (1) low-angle shear zones, variously interpreted as thrusts or extensional zones, that cause repetition of stratigraphic units and recumbent folds in some sedimentary units (D1). (2) upright regional folding, associated axial planar fabrics, and regional shear zones related to ENE-WSW shortening (D2). (3) strike-slip fault systems with both sinistral and dextral displacements (D3).

However, recent studies have emphasized the potential extensional character of some structures (Hammond and Nisbet, 1992; Williams, 1993), including an extensional event preceeding D1 that caused rifting accompanied by deposition of the greenstones (D1e of Williams, 1993), and an extensional event following D1 but preceeding E-W shortening (D2), referred to as D2e and interpreted as representing extensional collapse of "overthickened" greenstones and exhumation of mid-crustal gneiss domes (Williams, 1993).

2.2.4 Metamorphism

Metamorphic grades of lithologies of the ECYS range from prehnite-pumpellyite to amphibolite facies. Individual terranes generally possess characteristic patterns of metamorphic isograds, in which metamorphic grade progressively increases towards adjacent granitoid-gneiss terranes, where middle-amphibolite to amphibolite-granulite transition facies prevails. These isograd patterns may be truncated against terrane- and domain-bounding faults (Binns et al., 1976; Witt, 1991; Ridley, 1993). The net result of these patterns is greenstone belts with centres at low metamorphic grade, and margins at higher-grades. This pattern is distinct from that observed in most Phanerozoic orogens, which generally possess higher metamorphic grades in the orogen core (Ridley, 1993). Metamorphism is generally of the low-pressure, moderate- to high-temperature type, with calculated maximum pressures rarely surpassing that of the Al_2SiO_5 triple point, and there no evidence for increasing pressure accompanying increasing temperature (Binns et

al., 1976; Ridley, 1993). These observations are consistent with the primary control on metamorphic grade being distance from granitoid batholiths (cf. Binns et al., 1976), with metamorphism occurring in response to heat advection by granitoid intrusion. Conversely, areas of low metamorphic grade, at or below lower greenschist facies, may instead reflect seafloor or burial metamorphism effects during formation of the primary stratigraphic sequences (e.g. Barley and Groves, 1987).

The timing of metamorphism is poorly constrained. At Kambalda, a syn-metamorphic granodiorite has a U-Pb_{zircon} age of 2662 ± 4 Ma (Hill and Compston, 1986). At Kalgoorlie, peak metamorphism is constrained by non-metamorphosed felsic dykes to > 2674 ± 6 Ma (Kent, 1994). Swager et al. (1992) estimate that peak metamorphism occurred in the southern Kalgoorlie Terrane at ca. 2660 Ma based on correlations between metamorphism, granitoid intrusion and deformation events. However, if metamorphism corresponded to the timing of granitoid intrusion, it is possible that three metamorphic events have occurred at ca. 2690, 2660 and 2630 Ma, respectively, all superimposed upon any original seafloor or burial metamorphism. Therefore, the timing of peak metamorphism in any given area would be dependent upon the relative volume of melts intruded into that area at these times, and the peak of metamorphism may have occurred at different times in separate areas within a single terrane.

2.3 Geology of the Norseman Terrane

The Norseman Terrane is situated at the southernmost end of the ECYS (Figs. 2.1, 2.2). This terrane is bounded by large granitoid complexes to the southeast and southwest, and by major regional shear zones to the northwest (Mission Shear Zone) and northeast (Zuleika Shear Zone). The Mission and Zuleika Shear Zones separate the Norseman Terrane from the Kalgoorlie Terrane (Swager et al. 1992).

2.3.1 Stratigraphy

All Archean rock types in the Norseman Terrane have been variably metamorphosed to greenschist through amphibolite facies; therefore, the prefix meta is implicit in all descriptions below. The strata (terminology after Doepel, 1973) consist of two distinct greenstone sequences. The Penneshaw Formation, on the eastern edge of the greenstone belt, is poorly exposed, with outcrops limited to scattered low-lying exposures on the edges of salt lakes, and thus the complete nature of the formation is not well understood. Poor outcrop is reflected in the range of thicknesses quoted for this

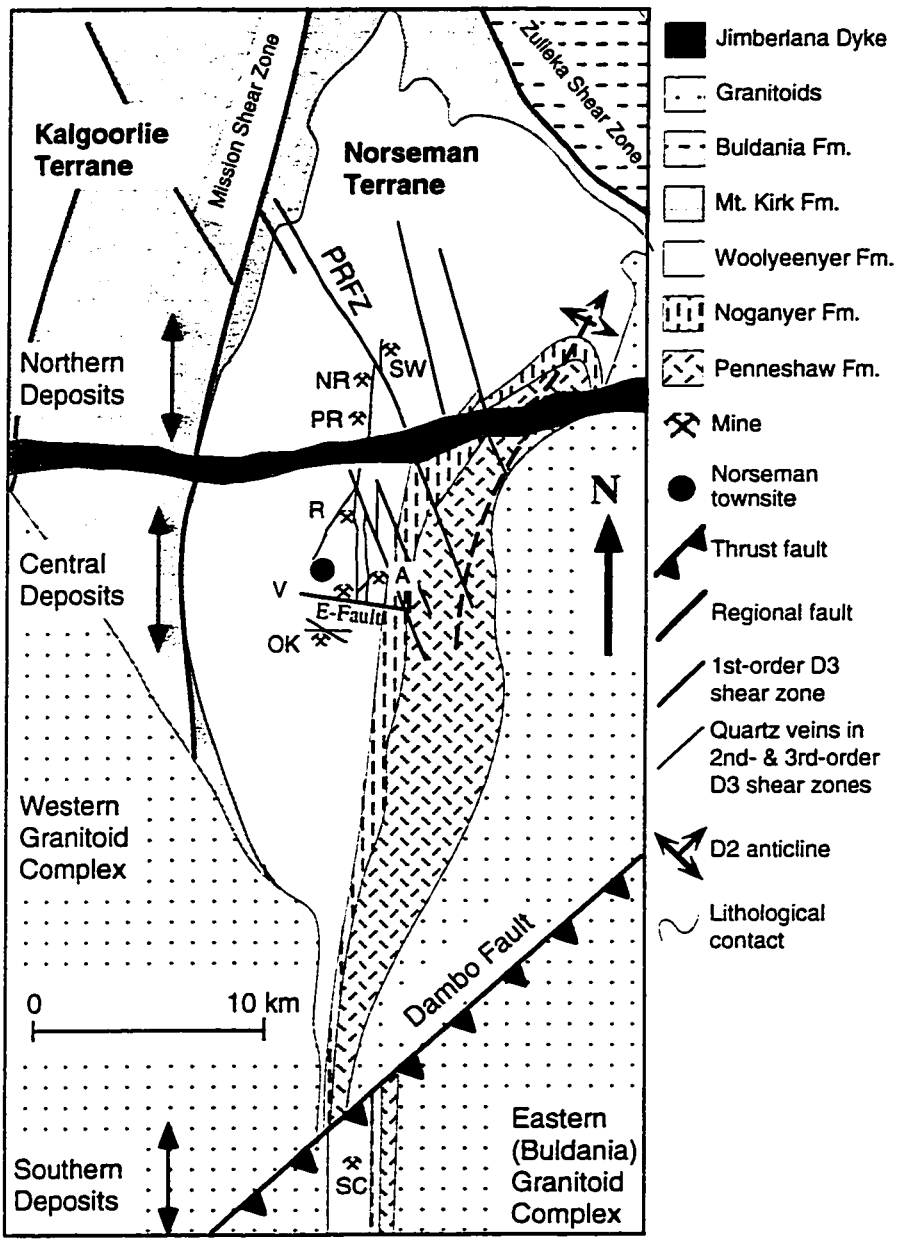

Figure 2.2. Simplified geological map of the Norseman Terrane, Western Australia. Adapted from Johnson (1988) and Swager et al. (1990). First-order structures = NNW striking faults; second-order structures = N-striking quartz veins and host shear zones; third-order structures = NE-striking veins. PRFZ = Princess Royal Fault Zone. Deposits: SW = Surface Winze, NR = North Royal, PR = Princess Royal, R = Regent, A = Ajax, V = Viking Decline, OK = Okay, SC = Scotia.

formation, which range from 3 km (Hall and Bekker, 1965; Spray, 1985) to 6 km (Doepel, 1973; Keele, 1984). Similarily, the constituent lithologies are variably quoted as dominantly mafic (Doepel, 1973; Spray, 1985), or dominantly sedimentary rocks (Hallberg, 1970); to dominantly felsic volcanics and related volcanogenic sedimentary rocks (Campbell and Hill, 1988). According to McGoldrick (1993) the bulk of the eastern half of the sequence appears to consist of predominantly mafic rocks, whereas sedimentary and felsic rocks are more common towards its western contact with the Noganyer Formation. Many of the mafic lithologies preserve pillow structures, although deformed, indicating a subaqueous depositional environment. Definite younging directions have been reliably determined in the Penneshaw. It has been assumed that the sequence faces west due to the consistent west-facing nature of the Woolyeenyer Formation (Doepel, 1973), although there are no data confirming this. The entire formation is intensely tectonized, and is interleaved with granitoid, with the ratio of granitoid to supracrustal rocks increasing towards the margin of the Eastern Granitoid Complex (Keele, 1984; Spray, 1985). These granitoid sheets are commonly, but not ubiquitously, gneissose in texture, and may represent tectonically interleaved basement slices as well as deformed sills or dykes.

A felsic unit in an upper member of the Penneshaw Formation has been dated at 2938 ± 10 Ma ($U\text{-}Pb_{zircon}$, Campbell and Hill, 1988; Hill et al. 1992). However, the origin of this felsic unit is uncertain. The sample is from drill core: the host felsic unit is interleaved with biotite-garnet and amphibole schists, is not unambiguously recognizable as pyroclastic, and contains inherited zircons as old as 3100 Ma. It may, therefore, be a tectonically interleaved slice of sialic basement. Nevertheless, this is the only available age constraint, and is taken as the maximum age for the Penneshaw Formation.

To the west, the Penneshaw Formation is directly overlain by the Noganyer Formation. The latter comprises interlayered siliciclastic sedimentary rocks, including sandstone, siltstone, conglomerate, shale, pyroclastic rocks, and silicate facies banded iron formation (BIF), that form resistant topographic ridges and act as regional stratigraphic marker horizons. The contact with the underlying Penneshaw Formation appears to be gradational, and the Penneshaw-Noganyer transition is defined by the first appearance of laterally continuous BIF (Hallberg, 1970; Doepel, 1973). The Noganyer Formation is intruded by mafic sills and dykes that are presumed to be equivalents of the overlying Woolyeenyer Formation. The sequence appears to young to the west overall, although reversals in younging direction indicate repetition of the Noganyer stratigraphy by folding (Keele, 1984).

Attempts to date a chert unit in the Noganyer Formation yielded two zircon

populations: one with ages 3670-3650 Ma, and a second population with ages of 2705 ± 5 Ma (Campbell and Hill, 1988). The first population is undoubtedly detrital, and yields the oldest ages of any inherited zircons yet recovered from rocks of the ECYS. The second population may represent either hydrothermal activity associated with chert deposition, or growth during contact metamorphism or hydrothermal activity associated with intrusion of a nearby mafic sill (Campbell and Hill, 1988). In light of the older age obtained for an intrusive dyke in the Woolyeenyer Formation, the latter interpretation is favoured. Thus the maximum age of the Noganyer remains unconstrained.

The Noganyer Formation is conformably overlain by the Woolyeenyer Formation, an 8000 m thick sequence of tholeiitic basalts, intruded by gabbroic dykes and sills, one of which has been dated at 2714 ± 5 Ma (U-Pb$_{baddellyite}$, Hill et al. 1992), and a suite of high-MgO tholeiitic dykes. The contact with the Noganyer Formation appears to be gradational and non-tectonized. Pillowed basalts are overlain by BIF near the base of the Woolyeenyer, consequently the commencement of Woolyeenyer Formation volcanism is thought to have closely followed deposition of the upper members of the Noganyer Formation (Thomas, 1990).

Interpreted gradational contacts between the Penneshaw - Noganyer - Woolyeenyer Formations, in concert with the available geochronology, present an apparent dichotomy. The data require (1) a ca. 200 Ma depositional history for the Noganyer Formation, considered an unlikely scenario given the nature of the Noganyer siliciclastic sedimentary rocks, or (2) incorrect interpretation of observations in various studies, or (3) that the age for the Penneshaw Formation is an inherited age. The present database is insufficient to distinguish between options (2) and (3). Numerous observations of younging directions from pillowed basalt flows indicate consistent westward facing, and no evidence has yet been discovered for structural repetition of the Woolyeenyer stratigraphy. Further details of the Woolyeenyer Formation are presented in Chapter 3.

The Mt Kirk Formation, on the westernmost flank of the greenstone belt, comprises a sequence of felsic volcanic, volcaniclastic and sedimentary rocks, intruded by two large layered mafic sills. The base of the formation is defined by a laterally continuous chert horizon, which can be traced throughout the terrane, and appears to conformably overlie the Woolyeenyer Formation lithologies (Fig 2.1). The Mission Fault dissects the Mt.Kirk Formation: rocks to the west dip steeply east, whereas those to the east dip moderately west. Rocks to the west of this fault have been redefined as part of the Coolgardie Domain of the Kalgoorlie Terrane (Swager et al. 1990). As the Mt Kirk Formation has not yet been reinterpreted into the terrane model of the ECYS, the

traditional classification of the formation is retained here (Doepel, 1973). Moreover, as the Mission Fault is generally accepted as the western margin of the Norseman Terrane, this interpretation results in the Mt. Kirk Formation straddling a terrane boundary (Fig. 2.2). A U-Pb_{zircon} date from a volcaniclastic unit near the base of the Mt. Kirk Formation yields an age of 2688 ± 8 Ma (Hill et al. 1992).

2.3.2 Granitoids

Felsic intrusive rocks in the region comprise: (1) the large (external) granitoid complexes that bound the greenstones to the southeast and southwest, (2) small (internal) granitoid bodies that intrude the greenstone sequence, and (3) three suites of fine-grained intermediate to felsic dykes and stocks (internal) that intrude the Woolyeenyer Formation (Perring 1990). The external batholithic complexes are variably deformed to undeformed rocks that are pre-, syn- and post-tectonic. The Eastern and Western Granitoid Complexes have been dated at 2686 ± 6 Ma and 2691 ± 8 Ma, respectively, whereas some small internal granitoid bodies are dated at 2665 ± 4 Ma (U-Pb_{zircon}, Hill et al. 1992). No radiogenic ages for the felsic dykes in the vicinity of the Norseman townsite have been obtained. In the Scotia mine, however, a pegmatite dyke that crosscuts earlier felsic dykes and gold mineralization yields a Sm-$Nd_{mineral\ isochron}$ age of 2622 ± 62 Ma and a $^{40}Ar/^{39}Ar$ muscovite plateau age of 2612 ± 12 Ma (Kent, 1994; Chapter 6).

The youngest Precambrian lithologies recognized in the area are those of the mafic Jimberlana Dyke Suite, dated at 2411 ± 38 Ma (Sm-$Nd_{mineral\ isochron}$, Fletcher et al. 1987). The available geochronology for the Norseman Terrane and the adjacent Proterozoic Fraser Mobile Belt is illustrated in Figure 2.3.

2.3.3 Regional structure of the Norseman Terrane

The structural architecture of the Norseman Terrane developed in a sequence of six principal stages (Archibald et al., 1978; Keele, 1984; Spray, 1985). D1 structures consist of (1) isoclinal folds in the Noganyer Formation, and (2) layer-parallel fabrics in the Penneshaw Formation and interleaved gneisses which represent the tectonic juxtaposition of the external gneisses and supracrustal sequence to the east of Norseman (Spray, 1985). Small WNW-striking faults within the Woolyeenyer Formation, which offset W-dipping stratigraphy, but are cut by later mafic and felsic dykes, are interpreted as listric normal faults formed during deposition of the volcanic stratigraphy. Although ascribed to D1, their timing with respect to D1 structures observed in the Penneshaw and Noganyer is unconstrained given the geochronological problems detailed above. Whereas D1 repetition of stratigraphy across layer-parallel shear zones occurred in the supracrustal

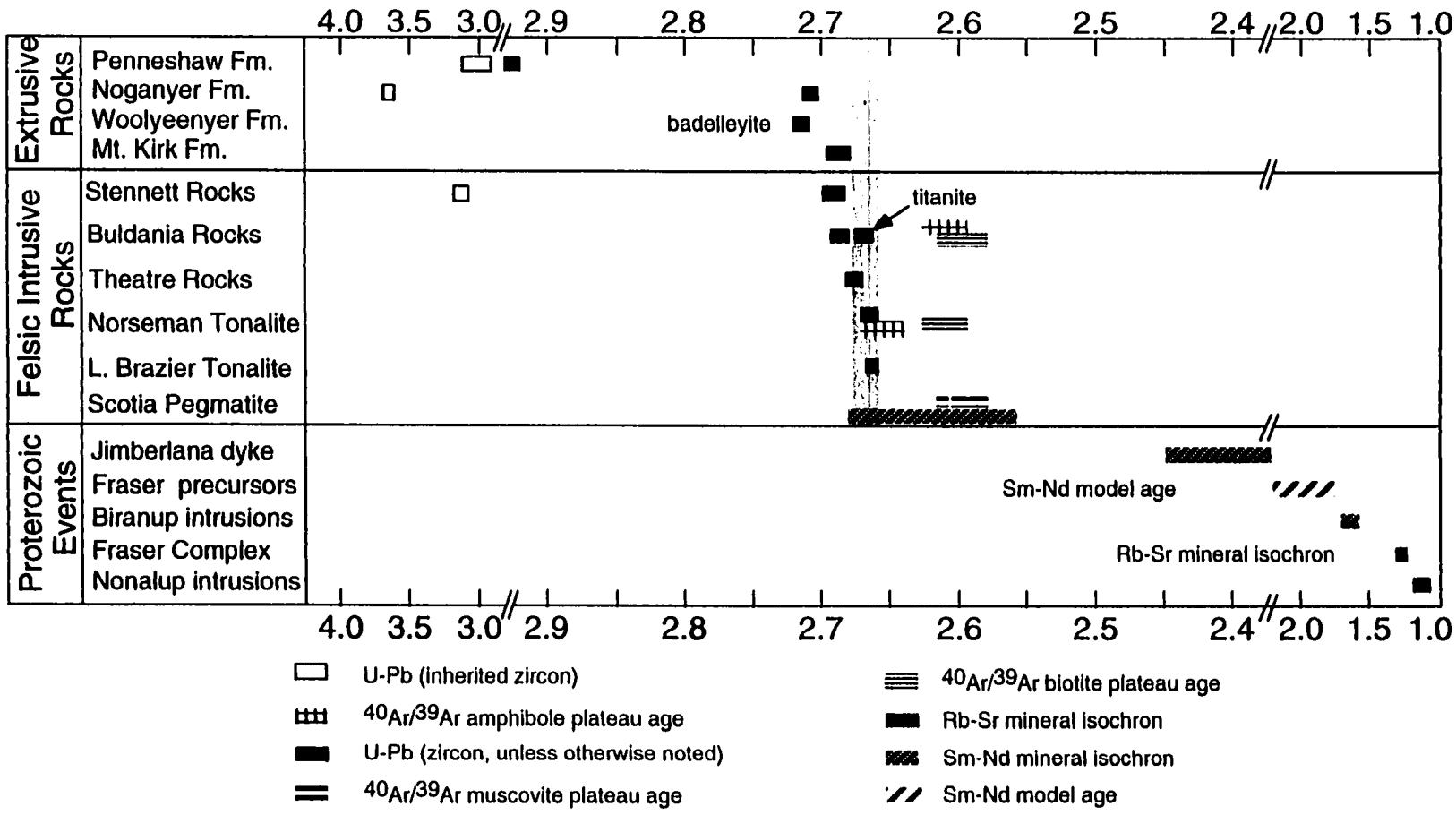

Figure 2.3. Compilation of available geochronological data for the Archean Norseman Terrane, and the Proterozoic Fraser orogen to the southeast of Norseman. All ages are in Ga. Data sources: Fletcher et al. (1987; 1991), Campbell and Hill (1988); Hill et al. (1989; 1992); Myers (1993); Kent (1994), Kent and McCuaig (submitted), this study (Chapter 6).

rocks of the Kalgoorlie Terrane (Clark et al., 1986; Swager et al., 1992), no such repetition of stratigraphy has yet been identified in the Norseman Terrane, with the exception of folding in the Noganyer sedimentary rocks..

The D2 through D4 events are considered as part of one continuous regional dynamothermal metamorphic event. D2 deformation involved approximately E-W compression, with the formation of shallowly N-plunging folds with a N-striking, subvertical axial planar cleavage in the sedimentary rocks of the Noganyer Formation. The Penneshaw, Noganyer and Woolyeenyer Formations are folded about the gently N-plunging D2 Penneshaw Anticline, imparting a N- to NE- strike and moderate westerly dip (55-65°) to the exposed greenstone sequence (Fig. 2.2). This event was closely followed by D3 deformation that involved folding and overprinting of the N-S striking D2 cleavage by a NNW-striking, steeply E-dipping cleavage (70-90°) in the vicinity of dextral-reverse shear zones of the same orientation (e.g. Princess Royal Fault Zone, Fig. 2.2). During these events, most strain was accommodated along discrete NNW and N-striking shear zones, with intervening low-strain zones without discernable metamorphic fabrics. Regional metamorphism appears to have reached its peak during or shortly after the D3 episode, and was accompanied by the intrusion of internal granitoids, which continued through the D4 event (Campbell and Hill, 1988). Gold mineralization appears to have formed during this D2-D3 event.

D4 structures comprise a WNW-striking fracture cleavage that crosscuts the auriferous veins and contains retrograde mineral assemblages. Emplacement of the early Proterozoic Jimberlana Dyke Suite along E-striking fractures is the D5 event. The latest (D6) structures identified in the terrane consist of ENE- to NE- striking Proterozoic brittle faults, probably related to the accretion of the Proterozoic Fraser Mobile Belt to the southeast (Fig. 2.1; Keele, 1984; Spray, 1985). Proterozoic events may also have reactivated some D1-D5 structures.

2.3.4 Metamorphism

Peak metamorphic conditions in the Norseman Terrane are poorly constrained due to the lack of widespread diagnostic mineral assemblages. However, recrystallization of supracrustal lithologies appears broadly synchronous with D3 deformation, and ranges from upper greenschist facies in the vicinity of the North Royal Mine (Golding, 1982; MacGeehan, 1983; Keele, 1984; Mueller, 1992) to amphibolite facies metamorphism at the southern tip of the terrane in the vicinity of the Scotia Mine based on assemblages in mafic lithologies (Binns et al., 1976; McCuaig et al., 1993; Chapter 5). The metamorphic grade of the greenstones also varies in an east-west direction, from upper greenschist in

the centre of the terrane to upper amphibolite facies at the greenstone margins (Binns et al., 1976; Keele, 1984).

The Penneshaw Formation is metamorphosed to amphibolite facies, from lower amphibolite at its contact with the Noganyer Formation to upper amphibolite at its transitional and highly tectonized basal contact with the Buldania Granitoid Complex. Peak pressures are limited to below the Al_2SiO_5 triple-point by the presence of andalusite and lack of kyanite in sedimentary rocks of the upper Penneshaw Formation (Keele, 1984). Metamorphic grades in the Woolyeenyer Formation are discussed in more detail in Chapter 5.

The timing of metamorphism within the Norseman Terrane is also poorly constrained, but is likely coeval with either the ca. 2690 Ma or ca. 2665 Ma felsic intrusive events. Independent cooling curves have been obtained for an internal granitoid with a crystallization age of 2665 Ma, and an external granitoid with a crystallization age of 2690 Ma (Fig. 2.4; Kent, 1994). These curves indicate that the supracrustal rocks immediately south of the Norseman Townsite had cooled through the 'conventional' closing temperature for Ar diffusion in amphibole at 2656 ± 15 Ma, which serves as a lower age limit for peak metamorphism (Norseman Tonalite sample, Kent, 1994). This age of metamorphism is consistent with findings in the Kalgoorlie Terrane supracrustal rocks. The Buldania Granitoid Complex, conversely, cooled through the conventional closing temperature for Ar in amphibole at ca. 2615 Ma. This could represent slower cooling of the external granitoids, which would be consistent with their higher pressure (and thus depth) of formation. Alternatively, the younger age may represent a second thermal event that did not effect the supracrustal rocks of the Norseman Terrane. The entire Norseman Terrane appears to have cooled through the closure temperature for Ar diffusion in biotite by 2600 Ma (Kent, 1994).

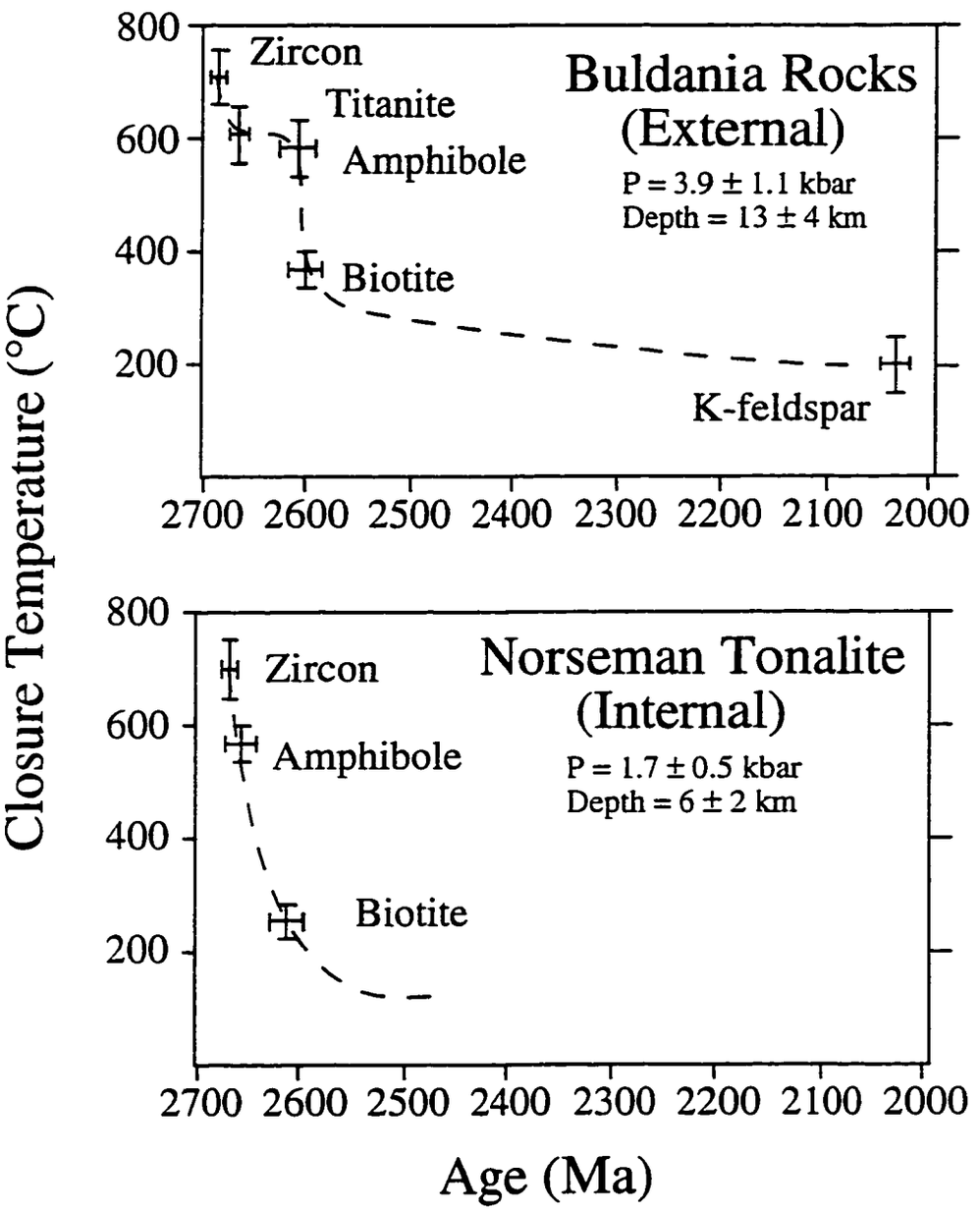

Figure 2.4. Estimated cooling curve for an external granitoid to the east of the Norseman Terrane, and for an internal granitoid immediately south of the OK mine. Estimated pressures and depths of crystallization are given for each sample, as calculated from hornblende geobarometry. All data, calculations of closure temperatures, and geobarometric calculations are from Kent (1994).

CHAPTER 3

GEOCHEMISTRY AND PETROGENESIS OF MAFIC LITHOLOGIES OF THE WOOLYEENYER FORMATION, NORSEMAN TERRANE

3.1 Introduction

Geochemical studies of mafic magmatic rocks of various ages have been increasingly successful in determining the evolution of mafic magma sources through time and the tectonic settings in which they were formed. These advances have stemmed from progressively more sophisticated analyses, combined with improved understanding of geodynamics (Zindler and Hart, 1986; Smith and Ludden, 1989; Sun and McDonough, 1989; Xie et al., 1995).

Archean terranes preserve an abundance of mafic lithologies, and are unique in that they are the major repository of komatiites; high-temperature ultramafic volcanic rocks with MgO contents > 18 wt.% (Arndt and Nisbet, 1982). These ultramafic lavas are subdivided into two broad groups: (1) Al-undepleted komatiites (AUK), characterized by chondritic Al_2O_3/TiO_2 ratios (≈ 20), flat to light rare-earth element (LREE)-depleted patterns ($La/Sm_n \leq 1$), and flat heavy-REE (HREE) patterns ($Gd/Yb_n \geq 1$), and (2) Al-depleted komatiites (ADK), with $Al_2O_3/TiO_2 < 10$, flat to depleted or enriched LREE patterns, and fractionated and depleted HREE patterns ($Gd/Yb_n > 1$) [Sun and Nesbitt, 1977, 1978; Jahn et al., 1982; Condie, 1990; Jochum et al., 1991].

These AUK and ADK both possess positive ε_{Nd} values, and they are interpreted as resulting from melting of variably incompatible-element-depleted mantle sources at different depths: AUK in upper mantle with olivine + spinel on the liquidus, and ADK from deeper mantle where garnet is a liquidus phase. Conventionally, ADK are considered as restricted to the early Archean, an observation supporting progressively shallower melting and decreasing mantle potential temperatures with time (Sun and Nesbitt, 1977, 1978; Ohtani et al., 1989; Smith and Ludden, 1989; Shirey, 1991; Herzberg, 1992; 1995; Xie et al., 1995), although late Archean examples have been identified (Newton Township, Ontario, Cattell and Arndt, 1987; Boston Township,

Ontario, Xie et al., 1993).

Archean terranes apparently lack volcanic rocks with the characteristics of Phanerozoic within-plate basalts from ocean islands (OIB), typified by the conjunction of enrichment in large-ion lithophile elements (LILE), LREE and high-field-strength elements (HFSE) Nb, Ti, Zr and Hf relative to other basalt types, and generally HREE depletion (Pearce, 1983; Condie, 1990). The rare occurrences of such rocks have been attributed to contamination of more typical komatiitic magmas by continental crust (Arndt and Jenner, 1986; Cattell and Arndt, 1987; Sun et al., 1989). Enrichment of some modern OIB magmas can be achieved by low degrees of partial melting of depleted mantle (cf. Hawaii, Clague, 1987). However, the majority of OIB's require that the mantle source itself is enriched in LREE and HFSE relative to primitive mantle, in some cases much prior to melt generation, as signified by the conjunction of radiogenic Sr but non-radiogenic Nd-isotope characteristics (e.g. enriched mantle (EM) OIB, Zindler and Hart, 1986; Sun and McDonough, 1989; Weaver, 1991).

The paucity of such EM-OIB in Archean terranes suggests either that enriched mantle sources were absent early in Earth history, were short-lived, or were sparsely preserved in the hotter convective Archean mantle. As it has been postulated that EM-OIB source regions result either from the recycling of subduction zone material into the deep mantle (cf. Ringwood, 1990 and references therein) or enrichment of mantle lithosphere by low-degree partial melts from the asthenosphere (cf. Menzies, 1990), the absence of EM-OIB in the Archean may place important constraints on Archean mantle lithosphere and aesthenosphere evolution, and tectonic processes.

This chapter reports the occurrence and geochemistry of mafic rocks of Archean age from the Norseman Terrane, Western Australia. Emphasis is placed on characteristics of, and differences between, Al-undepleted rocks that are typical of Archean greenstone terranes, and Al-depleted rocks that show EM-OIB characteristics. The latter are the first reported Al-depleted, high MgO rocks from the East Central Yilgarn Superterrane of the Yilgarn Craton. These LILE- and LREE-enriched rocks with fractionated and depleted HREE may be the first reported occurrence of such OIB-like rocks from the Archean (Morris, 1990). The data show that two distinct mantle sources operated coevally in the formation of these rocks: one with long-term depletion of incompatible elements, and one enriched in incompatible elements.

3.2 Stratigraphy of the Woolyeenyer Formation

The Woolyeenyer Formation, while poorly exposed, has been mapped in considerable detail on surface, in underground exposure, and in drill core in the environs of the Norseman lode gold deposits (Bekker, 1963; Thomas, 1990; Chapman and Offe, 1993). This formation is comprised predominantly of pillowed, commonly amygdaloidal, to massive basalts with minor amounts of interflow sediment. Numerous faults transect and offset the stratigraphy of this formation: however, no evidence has yet been found for structural repetition of stratigraphy within the Woolyeenyer Formation. This sequence of mafic volcanic rocks is intruded by several generations of mafic to ultramafic dykes, which crosscut the stratigraphic sequence at high angles, and can comprise as much as 40% of the entire Woolyeener Formation (Bekker, 1963).

Various workers have examined the volcanology and geochemistry of this formation in outcrop and drillcore (Bekker, 1963; Hallberg, 1972; Hallberg and Williams, 1972; Thomas 1990; Morris 1990, 1992; Chapman and Offe 1993; McCuaig et al. 1994). In this study, six mafic rock types have been identified on the basis of field relationships, petrography and geochemistry:

(1) tholeiitic basalts, and tholeiitic gabbro dykes and sills that predominate in the formation,
(2) high-MgO tholeiitic dykes (HMT),
(3) incompatible element enriched high-MgO tholeiitic dykes (EHMT),
(4) transitional high-MgO tholeiitic dykes (THMT), and
(5), (6) incompatible element enriched tholeiites (ET), which are further subdivided into ET1 and ET2 (section 3.4).

The high-MgO dyke suites intrude the volcanic sequence, but are crosscut by late gabbro dykes similar to those of group (1). Three suites of felsic dykes crosscut all of these mafic lithologies (Perring, 1990), and are thought to be broadly coeval with peak regional metamorphism. The stratigraphic relationships and relative timing of volcanic and intrusive events are illustrated in Figs. 3.1 and 3.2.

3.3 Petrography of mafic lithologies

Metamorphic grades of Archean lithologies within the Norseman Terrane vary north to south, from mid- to upper-greenschist facies north of the Jimberlana Dyke to lower-amphibolite facies at the southernmost end of the Terrane. Igneous textures are largely preserved in the basalts and dykes away from zones of deformation, and

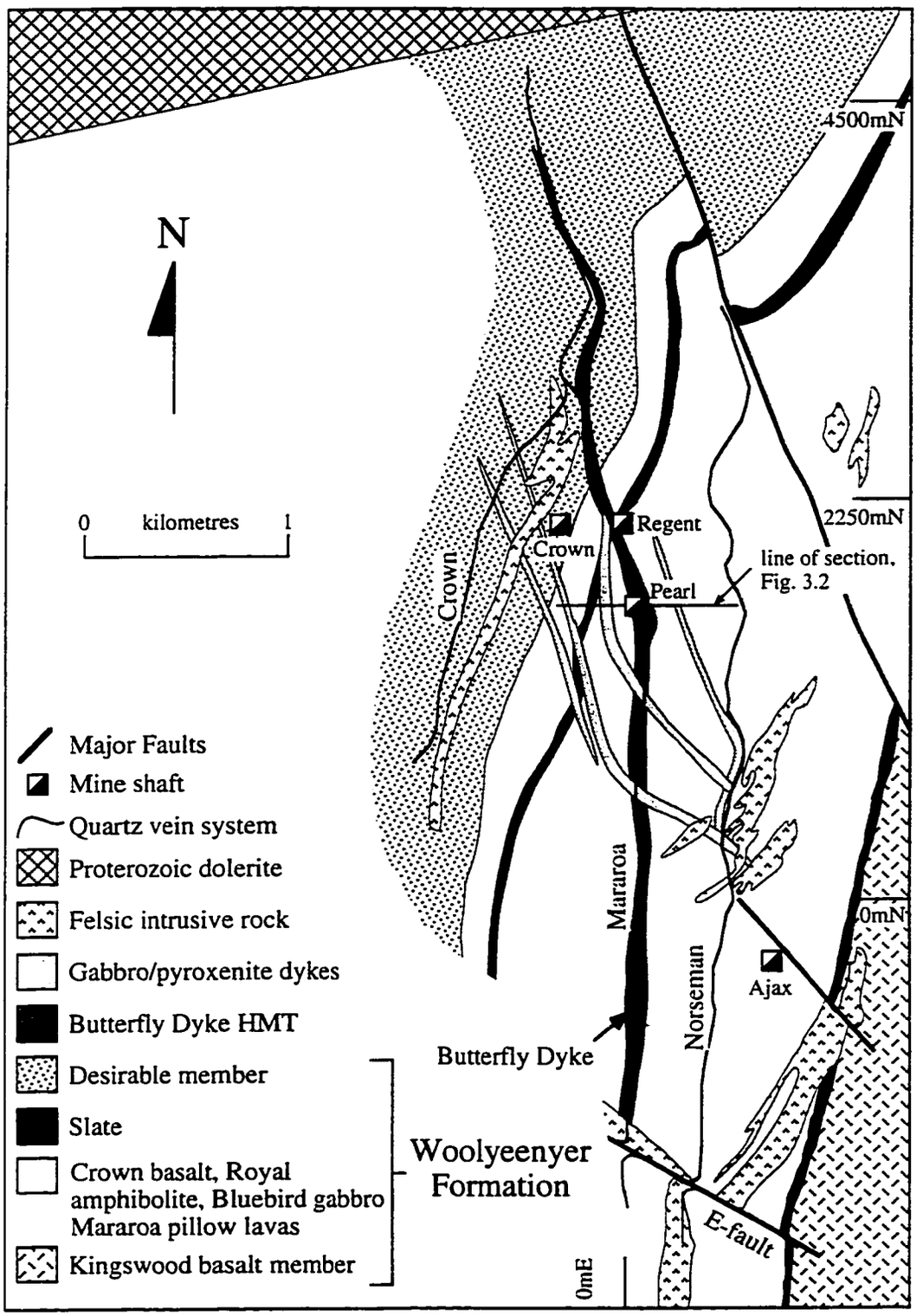

Figure 3.1. Geology of the Woolyeenyer Formation in the vicinity of the Central deposits. Modified from Chapman and Offe (1993). Mine (Pheonix) grid coordinates in metres.

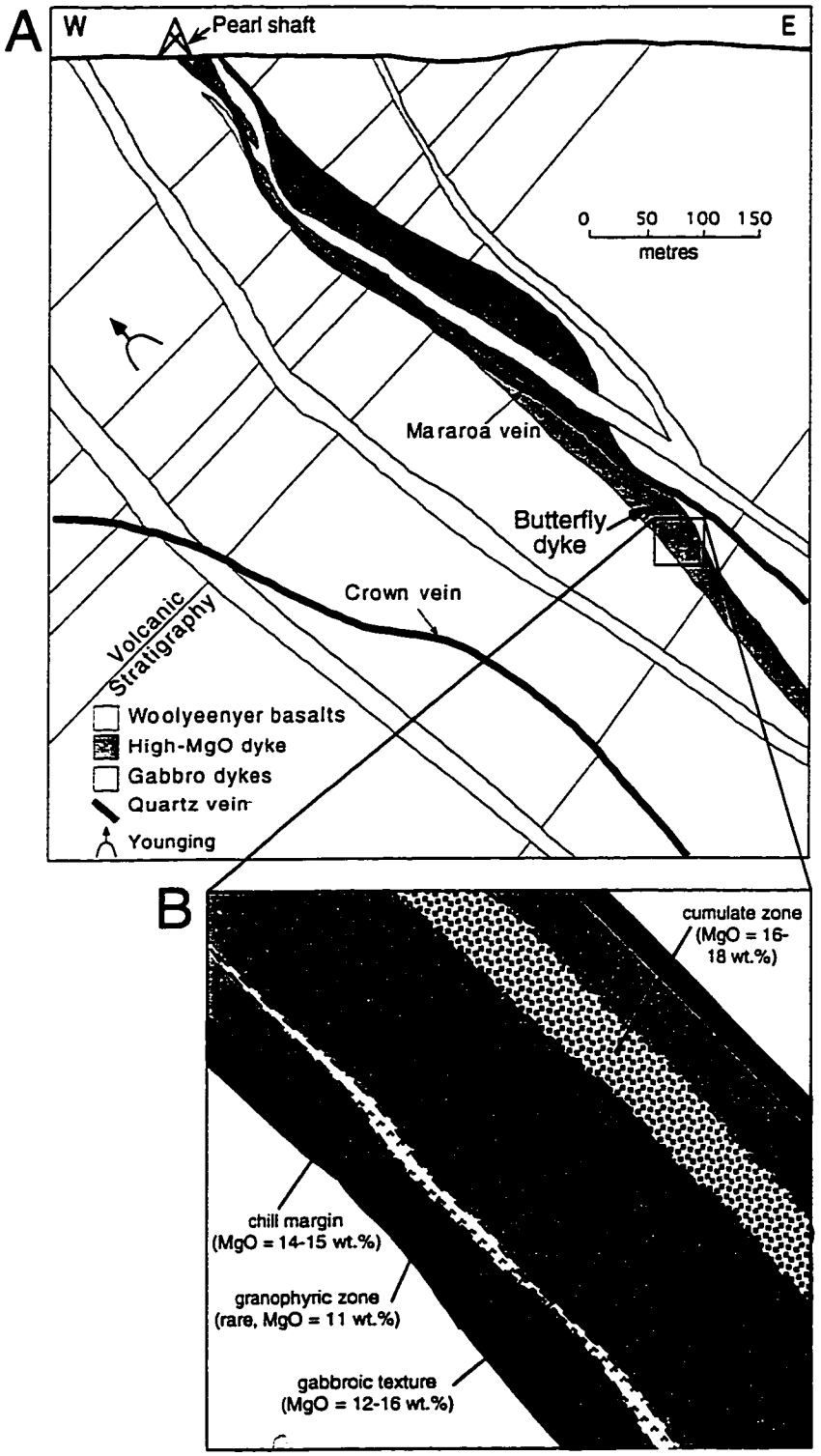

Figure 3.2. A. A cross section through the Woolyeenyer Formation in the vicinity of the Pearl Shaft (Fig. 3.1), after Thomas (1990) and Chapman and Offe (1993). Younging direction was determined from pillowed lavas. B. Schematic zonation of the Butterfly Dyke HMT.

primary mineralogy can still be discerned from the pseudomorphing metamorphic mineral assemblages (Hallberg, 1972; Hallberg and Williams, 1972; Binns et al. 1976).

3.3.1 Mafic volcanic rocks

The volcanic rocks are predominantly plagioclase-phyric, but rarely pyroxene-phyric, varying from flows with isolated, tabular plagioclase laths, through glomeroporphyritic flows to spectacular megacrystic counterparts, with plagioclase phenocrysts over 10 cm in diameter. Pyroxene-phyric flows are more abundant in the lower members of the Woolyeenyer Formation; plagioclase phyric flows occur throughout the volcanic sequence (Thomas, 1990). An increase in the abundance of amygdales with stratigraphic height has been noted in the lower members of the formation (Bekker, 1963), possibly indicating progressively shallower water depths of lava extrusion through time. Individual flows, particularily the distinct megacrystic flows, can be traced over a strike length of kilometres, although many generations of faults crosscut the stratigraphy, and these flows are used as stratigraphic marker horizons due to the lack of laterally continuous interbedded sedimentary horizons

Least-altered assemblages in tholeiitic basalts dominantly comprise actinolite-hornblende and plagioclase, in varying proportions, with minor quartz, epidote, chlorite, ilmenite and accessory apatite, titanite, leucoxene and biotite (Fig. 3.3A). A distinct paragenesis is evident in all samples. Metamorphic amphiboles (actinolite to actinolitic-hornblende) pseudomorph primary pyroxenes, with relict pyroxene cores rarely preserved. Finer-grained actinolitic-hornblende to Mg-hornblende forms fibrous rims around the pseudomorphous amphiboles and along plagioclase cleavage planes and grain boundaries.

Plagioclase comprises well-preserved laths and glomeroporphyritic to (rarely) megaphenocryst patches, lightly dusted by sausseritic alteration and exhibiting relict Carlsbad and albite twinning. Plagioclase compositions vary throughout mafic lithologies of the Norseman Terrane, from (An_{40-45}) in basalts north of the Jimberlana dyke, through (An_{40-65}) in basalts around the Norseman townsite, to (An_{48-52}) in the vicinity of the Scotia deposit (Appendix A). Minor quartz, ilmenite and accessory apatite are ubiquitous; ilmenite as skeletal grains up to 200 μm in diameter, and apatite as finer-grained inclusions in plagioclase. The changes in plagioclase composition correspond with a decrease in epidote and chlorite contents of mafic lithologies from north to south within the Norseman Terrane, and are collectively taken as reflecting an increase in metamorphic grade from north to south (McCuaig et al., 1993; Chapter 6).

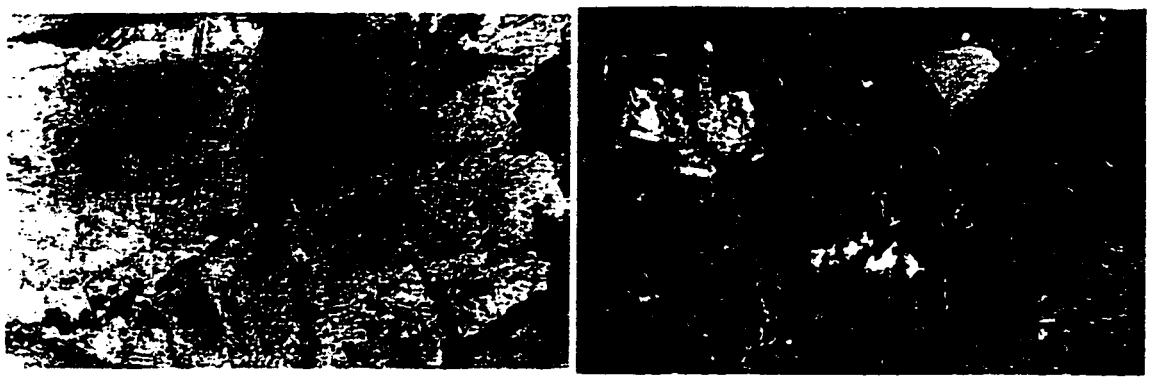

(a) (b)

Figure 3.3: Photomicrographs of least-altered metamorphic assemblages
(a) Least-altered tholeiite assemblage, from Central deposi area, comprising plagioclase and amphibole, with minor amounts of epidote (very fine-grained, high relief) and ilmenite (not shown). Plagioclase exhibits sausseritized cores and clear rims; hornblende overgrows actinolitic-hornblende cores. Sample S13A, Regent mine. (b) Cumulate zone of Butterfly Dyke, sample AB372686, Ajax mine. Note the amphibole pseudomorphs after pyroxene, coarse opaques, and interstitial plagioclase.

3.3.2 Mafic intrusive rocks

3.3.2.1 Tholeiitic gabbros

Mafic lithologies that are recognizably discordant to the north-striking, west-dipping volcanic stratigraphy are abundant at Norseman, comprising as much as 40% of the entire formation (Bekker, 1963). They mirror the compositional variety of the volcanic flows in that they are variably pyroxene- or plagioclase-phyric gabbros, now comprising hornblende-plagioclase-chlorite-ilmenite assemblages (Figs. 3.3B), and are likely co-magmatic feeder dykes to flows higher in the volcanic sequence.

3.3.2.2 Enriched tholeiites (ET)

Enriched tholeiites have been identified in drill core S657 through the OK mine orebodies, and all come from a gabbro sill that intrudes the volcanic stratigraphy. This rock type is petrographically indistinguishable from the tholeiitic basalts and gabbros described above.

3.3.3 High-MgO intrusive rocks

High-MgO intrusive rocks are recognized throughout the Woolyeenyer Formation, and are distinguished by their low felsic index (< 15 modal %) and their high chlorite content (25-55 modal % versus < 10 modal % for other mafic flows and intrusives). Although these high-MgO intrusive lithologies are common, no extrusive equivalent has yet been positively identified in the Norseman Terrane. As many occurrences of these lithologies have only been identified in drill core, their range of structural attitudes cannot be precisely determined: however, where they outcrop on surface or are well exposed in mine workings they range in strike from NW to NNE and dip 30-70°E.

Recognizing primary igneous textures in these lithologies proves to be a challenge, as their chlorite content causes them to be less competent than the surrounding volcanic sequence, and consequently a focus for the nucleation of regional shear zones. Nevertheless, igneous textures are preserved in instances where the dykes are not sheared, and primary mineralogy can be inferred.

3.3.3.1 High-MgO tholeiites (HMT)

The Butterfly Dyke is the largest, most compositionally complex, and most intensely studied high-MgO lithology yet identified in the Woolyeenyer Formation, and is representative of the HMT that have been identified throughout the Norseman Terrane. Although poorly exposed on surface, the dyke is known, through mine workings and drill intersections, to extend over a strike length of at least 5.6 km, from the Jimberlana Dyke

in the north, to E-fault in the south, where it is truncated by Proterozoic movement along this structure (Fig. 3.1). Striking approximately due north and dipping between 45° and 60°E, the dyke averages 50 m in thickness, and is known, from drilling, to extend at least 1300 m down dip. The Butterfly Dyke crosscuts W-dipping stratigraphy at a high angle, as well as intruding earlier mafic dykes and crosscutting early D1 block faults, and it is in turn crosscut by later mafic dykes, felsic dykes, and Proterozoic dolerite dykes (Figs. 3.1, 3.2).

Over its relatively consistent width, the dyke can display marked textural variation and differences in the modal proportions of mineral phases, comprising 45-75 % actinolitic hornblende (after primary pyroxene), 25-55 % chlorite, <15 % plagioclase/quartz, and trace skeletal ilmenite (after primary titanomagnetite or ulvospinel). Trace amounts of biotite, calcite and sericite may be present, increasing in abundance towards zones of gold-related hydrothermal alteration. Although HMT dykes have high MgO contents, pseudomorphs after olivine have never been observed. Therefore, these intrusives are pyroxenites or pyroxene gabbros.

Four primary igneous zones have been identified within the Butterfly Dyke. These are schematically presented in Figure 3.2B, and consist of (1) chill margins; (2) a pyroxene cumulate zone; (3) gabbroic-textured pyroxenite, and possibly (4) a rare granophyric zone (Chapman and Offe, 1993).

Chill margins are only rarely preserved, as dyke contacts are often sheared. Where identified, they are characterized by grain fining towards the dyke margins and randomly oriented acicular actinolite after chilled pyroxene (Chapman and Offe, 1993). Although grain fining occurs, no extremely fine-grained chill margins have been recognized, indicating that either grain size coarsening occurred during metamorphic recrystallization, or the Butterfly Dyke was intruded into a 'hot' volcanic sequence (i.e. the dyke is syn to late volcanic).

A cumulate zone has been identified both petrographically and geochemically (McCuaig, 1992; Chapman and Offe, 1993). Petrographically the cumulate zone is identified by the preservation of grain-supported textures, of amphibole after primary pyroxene, with skeletal ilmenite and intercumulus plagioclase (Fig. 3.3C). This texture is most prominent towards the hangingwall of the dyke, approximately 10 m from the contact. Geochemical analyses of samples taken across the dyke corroborate the petrographic evidence, showing that MgO contents are slightly higher towards the hangingwall, likely due to the accumulation of pyroxene (Fig. 3.2B). Semi-quantitative modal analyses by XRD corroborate these profiles, illustrating the compositional variation within the dyke, with chlorite most abundant in the more mafic portions of the

dyke (Chapman and Offe, 1993).

The remainder of the Butterfly Dyke comprises even-textured pyroxenite to gabbro. In one locality, a possible granophyric quartz + plagioclase + amphibole + chlorite + biotite zone has been identified: however, due to the proximity of this zone to a sheared and altered contact at the footwall of the dyke, it is possible that the zone is an altered gabbroic section of the dyke (Chapman and Offe, 1993).

3.3.3.2 Enriched high-MgO tholeiites (EHMT)

These lithologies have only been identified from one drill hole (S433; Morris, 1990), although similar lithologies have been identified by major element geochemistry surveys (Al-depletion, see below). The HMT and EHMT are mineralogically similar and can only be differentiated by geochemical analysis. As with the HMT, no evidence of pseudomorphs after primary olivine have been observed in EHMT.

3.3.3.3 Transitional high-MgO tholeiites (THMT)

Transitional high-MgO tholeiites have been identified at one location in the Regent Mine, and are petrographically indistinguishable from HMT and EHMT.

3.3.3.4 Age and proportion of high-MgO intrusions

The upper age of the high-MgO lithologies is constrained by U/Pb zircon SHRIMP dating of a tholeiitic dyke at 2714 ± 5 Ma (Hill et al., 1992), which the high-MgO dykes crosscut. A lower age limit is provided by the age of metamorphism and felsic porphyry dyke intrusion (ca. 2665 Ma, Chapter 2; Hill et al., 1992). As the high-MgO lithologies preferentially weather and erode, relative to the tholeiitic volcanic rocks they intrude, they rarely outcrop and, therefore, their areal extent is largely undetermined.

3.4 Geochemistry of the Woolyeenyer Formation

3.4.1 Terminology and presentation of whole-rock geochemical data

The abundance and behaviour elements in various geological environments and processes are detailed in numerous publications (see Faure, 1991 for an overview), and are only briefly addressed below. Traditionally, major elements refer to the most abundant elements in the earth's crust that constitute the common mineral phases, and are reported as weight percent (wt.%) of their oxide compound. Trace elements are those elements that are less common to rare, and substitute for major elements of similar ionic size and valence. Trace element concentrations are generally reported as parts per million

(ppm).

It is useful to subdivide the elements according to their general geochemical behaviour into large ion lithophile elements (LILE), rare earth elements (REE) and high field strength elements (HFSE). The LILE, such as K, Rb, Cs, and Ba are those elements which have large ionic radii coupled with low ionic charges, and are generally incompatible during mafic igneous processes. The lanthanide series of the periodic table (La-Lu) are the REE, which have comparable but smoothly differing geochemical behaviour in most geological processes due to the lanthanide contraction. The light-REE (LREE) have slightly larger ionic radii and are highly to moderately incompatible during mafic igneous processes, whereas the HREE have smaller radii and are generally weakly incompatible. The HFSE are those elements with high ionic charges (Z) compared to their ionic radii (r). These high Z/r minerals include Nb, Ta, Zr, Hf, Ti, V, Sc, and Al. These elements have variable incompatability during mafic igneous processes, from highly incompatible (Nb, Ta) through moderately incompatible (Zr, Hf, Ti) to highly compatible (Al, V, Sc; Figs. 3.4A,B).

Presentation of data is generally in two forms: as Cartesian plots of element abundances or ratios, or as multielement diagrams normalized to a common reference material. Multielement diagrams are extremely useful in that they allow examination of the interrelationships of many elements, including LILE, REE and HFSE, that may have widely differing absolute abundances, in a single diagram (Fig. 3.5). Standard presentation of elements on these diagrams involves normalizing the element abundances of a sample to the corresponding abundance in a standard reference material, and ordering the elements in a consistent manner; this allows rapid comparisons of geochemical data between different rock samples. The standard reference material used (primitive mantle), and the order of elements, are as defined by Sun and McDonough (1989). Elements are presented in order of increasing compatibility in spinel lherzolite, determined from experiment and observations on oceanic rocks. Positions of the LILE, REE and HFSE are shown on Figure 3.5.

The behaviour of the LILE, REE and HFSE in various igneous environments are extensively discussed in various publications (Henderson, 1984; Pearce, 1983; Taylor and McLennan, 1985; Wilson, 1989; Sun and McDonough, 1989; Weaver, 1991; Hawkesworth et al., 1993; Pearce and Peate, 1995), and are not presented in detail here. However, it is important to note that the LILE, REE and HFSE behave differently in many geochemical environments (eg. Fig. 3.4A,B) causing variation from the smooth patterns depicted in Figure 3.5, and are thus powerful indicators of petrogenetic processes.

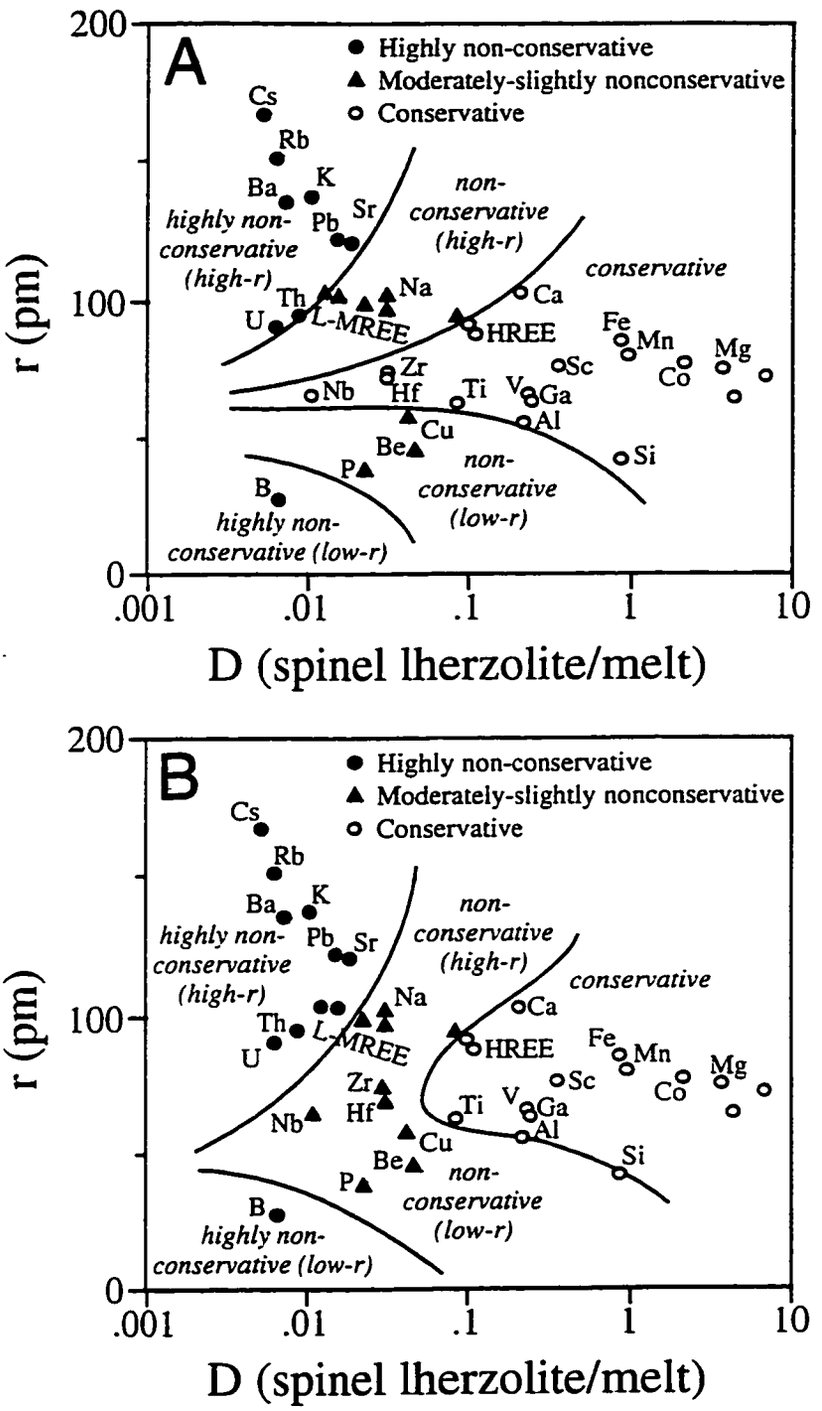

Figure 3.4. Element behaviour as a function of ionic radius and bulk distribution coefficient between mantle and melt for (A) hydrous fluids, and (B) siliceous melts, based on experiment and observation of subduction zone magmatism. From Pearce and Peate (1995).

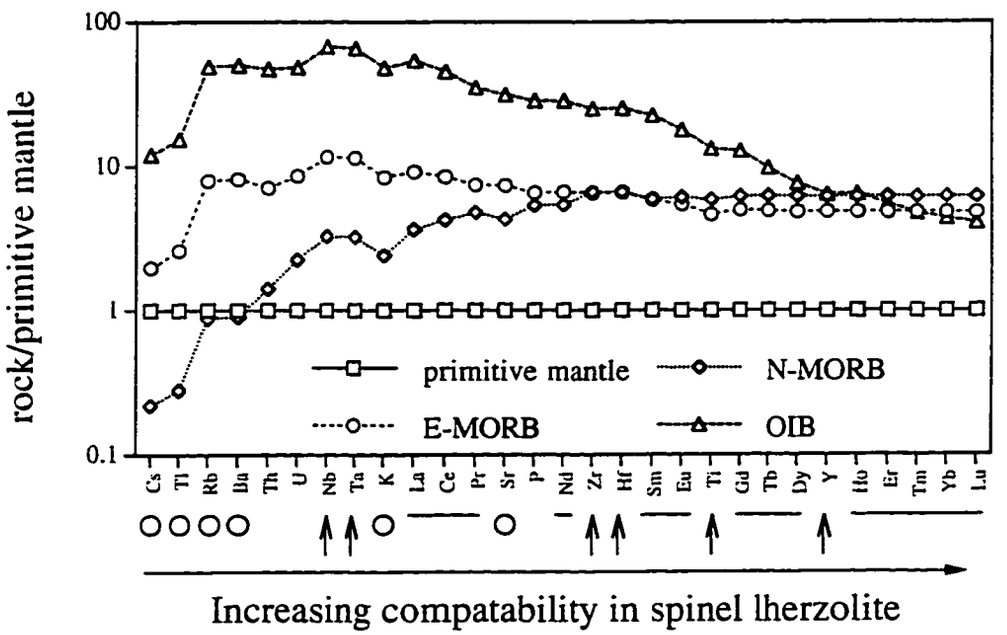

Figure 3.5. Primitive mantle-normalized multielement diagram highlighting the relative position of LILE (open circles), REE (horizontal bars) and HFSE (vertical arrows). Order of elements, compositions of N-MORB, E-MORB, OIB and primitive mantle from Sun and McDonough (1989).

Normalized ratios of the rare earths La/Ybn are a monitor of degree of deviation from flat patterns on Figure 3.5. Thus, rocks with $La/Yb_n < 1$ are considered to be "depleted" in incompatible elements (e.g. N-MORB), those with $La/Yb_n \approx 1$ are considered to be "undepleted" in incompatible elements (e.g. primitive mantle), and rocks with $La/Yb_n > 1$ are considered to be "enriched" in incompatible elements (e.g. OIB).

Deviations of elements from smooth patterns on Figure 3.5 are termed "anomalies" and are quantified by comparison to neighbouring REE. The HFSE anomalies are monitored in particular, and are quantified by the expression HFSE/HFSE*, which measures the magnitude of deviation of measured HFSE from the expected position of the HFSE in a smooth mantle-normalized pattern (e.g. Salters and Shimuzu, 1988). These ratios are calculated by a method similar to that given by Taylor and McLennan (1985) for calculating Eu/Eu*, with formulas for each (Nb/Nb*, Zr/Zr*, Hf/Hf*, Ti/Ti*) listed in the caption of Table 3.4. To facilitate analysis of normalized P anomalies, the expression P/P* is introduced as a measure of the magnitude of the P anomalies (Table 3.4, McCuaig et al., 1994). For comparison between datasets with limited REE data, the P/Nd ratio is also reported. Thus, a negative phosphorus anomaly is indicated by $P/P^* < 1.0$, or by $P/Nd < 70$ (primitive mantle value, Sun and McDonough, 1989).

3.4.2 Sample selection and analytical methods

Samples were carefully selected to (a) avoid areas of severe deformation and hydrothermal alteration, (b) provide broad areal coverage of lower members of the Woolyeenyer Formation both along and across strike, and (c) provide samples of the entire range of petrographic compositions of basalts, gabbros and high-MgO rocks. Sample locations are given in Appendix C.

XRD analyses to estimate modal mineralogy were performed at Western Mining Corporation (WMC) laboratories in Kalgoorlie, Western Australia. Mineral chemistry was determined at the University of Saskatchewan using a GXA JEOL 8600 Superprobe with wavelength-dispersive spectroscopy (WDS) and Tracor Northern automation for data reduction. Detection limits for all elements are 100 ppm (0.01%).

Whole-rock major elements and selected trace elements were determined by XRF independently by WMC labs in Kalgoorlie, Western Australia and X-Ray Assay Laboratories (XRAL), Mississauga, Ontario. Results were cross-checked for some samples by ICP-AES by XRAL, and INAA by Activation Laboratories. Major element and selected trace element data for GSWA samples were supplied by Paul Morris. Trace elements, including REE and HFSE, were analyzed simultaneously by ICP-MS at the

University of Saskatchewan, using the protocol of Jenner et al. (1990), using pure elemental standards for external calibration, standard additions and MRG-1, BHVO-1, and BIR-1 as reference materials. Detection limits in ppm for some critical elements are as follows: Nb (0.006), La (0.01), Ce (0.009), Nd (0.04), Zr (0.004), Hf (0.008), and Sm (0.03). Precision for most elements is between 2 to 4 % relative standard deviation (RSD), with the exception of Nb (6 % RSD). For BIR-1, different laboratories report closely comparable results for the REE, but Zr, Hf and Nb are systematically lower in some laboratories (Jochum et al., 1990) than others (Jenner et al., 1990). The values reported by Jenner et al. (1990), which are within error of those generated at the University of Saskatchewan, are adopted for this study (Xie et al., 1994). Laser ablation ICP-MS analysis of BIR-1 glass, prepared by fusion on a molybdenum strip under Ar atmosphere, yielded results for REE and HFSE within error of the results by solution mode ICP-MS (Fedorowich et al., 1993). Accordingly, instability of these elements in solution is not a problem in this study.

Whole-rock Nd and Sm isotope analyses were carried out by Hiroo Kagami at the Institute for Study of the Earth's Interior, Okayama University, Japan. Sample preparation, extraction, analytical, standardization and calibration procedures follow those described in Morris and Kagami (1989).

3.4.3 Whole-rock geochemistry results

Complete tables of geochemical data are given in 3.1 with selected interelement ratios, P/REE and HFSE/REE relationships. Plots of selected major elements and element ratios versus MgO show a considerable spread of data (Fig. 3.6). A distinct grouping by MgO content is apparent into high MgO (11.7-17.1 wt.% MgO) and low-MgO lithologies (5.0-9.1 wt.% MgO). MgO content effectively subdivides tholeiitic basalts and gabbros from high-MgO tholeiites (terminology after Arndt and Nisbet, 1982; Redman and Keays, 1985). A further grouping is noted within each of the high and low MgO groups into high TiO_2 (>1.2 wt.%) and low TiO_2 (<1.2 wt.%), effectively distinguishing tholeiites (low-MgO, low TiO_2) from enriched tholeiites (ET, low-MgO, high TiO2), and high MgO tholeiites (HMT, high MgO, low TiO_2) from enriched high MgO tholeiites (EHMT, high MgO, high TiO_2, Fig. 3.6A). The EHMT and ET are also characterized by low Al_2O_3/TiO_2 ratios of 4.0-4.7 and 7.8-8.4 respectively. In contrast, variable but higher Al_2O_3/TiO_2 ratios are observed in the HMT and tholeiites (Fig. 3.7). These geochemical groupings correspond to the petrographic subdivisions noted earlier (section 3.3).

Cr and Ni abundances covary with MgO contents, with ET having the lowest

Table 3.1 Geochemical analyses of mafic lithologies from the Norseman Terrane

	EHMT						HMT						
	GSWA 99934	GSWA 99938	GSWA 109064	GSWA 109065	GSWA 109066	GSWA 109068	AB 372679	AB 372682	AB 372683	AB 213759	AB 213763	AB 372685	AB 372686
SiO2 %	47.0	46.0	47.6	48.7	46.9	45.0	48.4	45.5	49.0	47.1	48.8	48.7	48.1
TiO2 %	1.49	1.69	1.63	1.27	1.78	1.90	0.54	0.56	0.53	0.49	0.67	0.48	0.43
Al2O3 %	6.1	7.8	6.5	5.9	7.4	8.4	11.7	12.1	10.1	14.7	11.6	10.2	9.6
Fe2O3 %	1.6	1.7	13.9	12.3	14.3	15.7	12.2	13.4	12.7	12.0	13.1	11.9	11.8
FeO %	9.6	11.8											
MnO %	0.20	0.23	0.23	0.21	0.23	0.25	0.21	0.23	0.22	0.21	0.21	0.18	0.20
MgO %	13.9	13.3	15.2	14.2	15.1	14.1	12.8	14.8	15.3	11.7	12.5	15.0	17.1
CaO %	13.3	11.5	11.1	13.0	10.6	10.9	8.2	7.8	7.9	8.8	8.2	7.8	7.2
Na2O %	0.42	0.54	0.66	0.70	0.68	0.64	0.81	1.06	0.68	1.09	1.46	0.45	0.57
K2O %	0.46	0.12	0.16	0.35	0.49	0.11	0.09	0.09	0.05	1.09	0.06	0.66	0.04
P2O5 %	0.13	0.12	0.13	0.10	0.14	0.16	0.05	0.05	0.06	0.05	0.07	0.05	0.05
LOI %	5.41	3.87	2.92	3.09	2.49	2.57	3.23	3.62	3.31	3.08	2.54	2.85	3.77
Total %	99.52	98.59	99.92	99.88	100.07	99.68	98.23	99.18	99.88	100.27	99.16	98.25	98.89
La	19.84	25.73	24.87	15.91	25.76	29.13	1.81	1.83	1.68	1.49	2.56	1.67	1.51
Ce	42.10	52.99	53.95	34.61	54.80	60.81	4.82	5.07	4.50	4.11	6.63	4.54	3.78
Pr	5.21	6.54	6.71	4.37	6.71	7.54	0.76	0.81	0.71	0.68	1.02	0.72	0.60
Nd	21.48	25.76	28.71	18.34	28.72	31.15	4.45	4.48	3.77	3.68	5.29	4.09	3.05
Sm	4.27	5.12	5.46	3.64	5.09	6.00	1.25	1.34	1.20	0.98	1.64	1.17	0.93
Eu	1.42	1.38	1.49	1.21	1.51	1.52	0.49	0.48	0.41	0.36	0.61	0.48	0.37
Gd	4.02	4.77	4.89	3.60	5.16	5.60	1.71	1.83	1.58	1.23	2.16	1.67	1.34
Tb	0.52	0.64	0.63	0.46	0.65	0.76	0.30	0.33	0.27	0.19	0.36	0.26	0.22
Dy	3.20	3.78	3.66	2.88	3.94	4.51	2.16	2.30	1.88	1.44	2.70	1.97	1.67
Ho	0.57	0.71	0.68	0.52	0.69	0.79	0.44	0.49	0.39	0.32	0.56	0.44	0.37
Er	1.63	1.92	1.76	1.36	1.95	2.10	1.39	1.46	1.25	0.99	1.82	1.31	1.16
Tm	0.22	0.27	0.24	0.18	0.28	0.30	0.21	0.23	0.19	0.16	0.26	0.20	0.17
Yb	1.39	1.55	1.56	1.17	1.75	1.85	1.39	1.44	1.23	0.91	1.69	1.31	1.09
Lu	0.20	0.22	0.21	0.18	0.24	0.26	0.21	0.22	0.21	0.15	0.26	0.21	0.18
Th	2.74	3.01	2.98	2.30	3.17	3.52	0.23	0.17	0.28	0.18	0.44	0.19	0.20
U	0.49	0.48	0.49	0.43	0.54	0.62	0.06	0.04	0.06	0.06	0.12	0.05	0.05
Cs	3.25	0.24	2.10	1.67	4.24	0.23	0.57	0.92	0.50	14.21	0.46	8.52	0.68
Rb	28.1	2.9	6.8	18.3	27.6	1.9	2.2	1.1	1.3	44.8	0.7	49.8	1.3
Sr	33	14	18	32	16	12	49	30	41	118	68	49	48
Ba	46	20	6	28	41	15	63	25	10	138	5	62	9
Nb	15.56	14.86	16.60	13.65	18.26	20.95	1.60	1.61	1.40	1.58	2.16	1.48	1.19
Ta	0.95	1.01	0.97	0.85	1.04	1.14	0.10	0.09	0.08	0.08	0.13	0.09	0.08
Zr	115	134	130	98	137	153	28	29	28	30	37	32	25
Hf	3.11	3.47	3.58	2.78	4.04	4.17	0.85	0.93	0.99	0.92	1.27	0.97	0.72
Y	14.5	16.8	16.4	12.7	17.1	19.2	11.2	12.1	10.5	8.0	13.8	10.7	9.0
V	191	235	213	176	241	260	205	241	198	200	237	190	166
Sc	22	27	24	20	26	29	38	47	34	37	39	36	29
Cr	936	1431	1325	1018	1245	1706	1280	1790	1880	962	1250	1690	1950
Co	-	-	-	-	-	-	-	-	-	-	-	-	-
Ni	781	1384	844	716	782	1081	-	-	-	-	-	-	-
Cu	35	358	44	43	74	290	-	-	-	-	-	-	-
Zn	128	125	103	170	149	107	-	-	-	-	-	-	-
Pb	2.05	2.04	1.29	1.76	1.64	1.96	1.07	0.93	1.39	7.96	2.73	2.63	1.14
Au (ppb)	18	17	-	-	-	-	-	-	-	-	-	-	-
Mg#	50	44	49	50	48	44	47	49	51	46	45	52	56
Al2O3/TiO2	4.1	4.6	4.0	4.7	4.2	4.4	21.5	21.5	18.9	29.9	17.4	21.3	22.4
CaO/Al2O3	2.18	1.48	1.70	2.18	1.43	1.31	0.70	0.64	0.79	0.60	0.70	0.76	0.75
Nb/Ta	16	15	17	16	18	18	15	17	17	19	16	17	15
Zr/Hf	37	39	36	35	34	37	33	31	29	32	29	33	32
Ti/Zr	78	76	75	77	78	74	115	115	113	100	108	91	92
Zr/La	5.8	5.2	5.2	6.2	5.3	5.2	15.7	16.1	16.8	19.8	14.5	19.0	18.6
P/Nd	26	20	20	24	21	22	49	49	70	59	58	53	72
Total REE	106	131	135	88	137	152	21	22	19	17	28	20	16
(La/Yb)cn	9.39	10.95	10.52	8.95	9.70	10.38	0.86	0.84	0.90	1.08	1.00	0.84	0.91
(La/Sm)cn	2.85	3.09	2.80	2.69	3.11	2.98	0.90	0.84	0.86	0.93	0.96	0.88	1.00
(Gd/Yb)cn	2.34	2.49	2.54	2.49	2.39	2.45	0.99	1.03	1.04	1.09	1.03	1.04	1.00
Nb/Nb*	0.62	0.44	0.54	0.70	0.56	0.56	0.87	0.91	0.83	1.09	0.82	0.90	0.74
P/P*	0.33	0.25	0.25	0.30	0.27	0.28	0.75	0.73	1.02	0.89	0.84	0.80	1.04
Zr/Zr*	0.83	0.81	0.72	0.83	0.79	0.77	0.84	0.83	0.92	1.08	0.87	1.00	1.15
Hf/Hf*	0.82	0.76	0.72	0.85	0.84	0.77	0.91	0.96	1.17	1.22	1.08	1.11	1.31
Ti/Ti*	0.93	0.89	0.83	0.90	0.88	0.85	0.88	0.85	0.92	1.08	0.85	0.80	0.90

Major element and select trace element analyses for GSWA samples supplied by P. A. Morris.
See text for analytical methods.

Table 3.1 (continued)

	HMT								THMT	ET1		ET2	
	AB 372688	PRS1177 -11	PRS1177 -12	PRS1177 -13	PRS1177 -14	PRS1177 -15	PRS1177 -17	PRS1177 -18	AB 213755	GSWA 99941	GSWA 99944	S657 -19	S657 -20
SiO2 %	49.8	48.4	44.2	47.5	45.5	45.7	45.1	47.3	49.8	53.6	50.4	49.80	49.80
TiO2 %	0.61	0.61	0.69	0.56	0.65	0.64	0.38	0.43	0.65	1.72	1.07	1.60	1.78
Al2O3 %	10.0	9.7	9.8	10.0	9.6	10.0	10.5	12.1	4.4	14.4	14.4	13.30	13.10
Fe2O3 %	13.5	12.4	12.3	12.6	12.8	12.8	10.7	11.0	12.8	2.0	1.75	14.60	15.40
FeO %										9.0	8.56		
MnO %	0.22	0.18	0.19	0.20	0.22	0.21	0.19	0.17	0.26	0.22	0.19	0.23	0.25
MgO %	14.3	15.8	14.3	16.0	15.4	14.8	14.2	13.8	14.2	5.0	7.31	6.07	5.86
CaO %	8.4	5.8	5.8	5.3	7.8	7.6	8.3	6.4	12.4	8.1	10.4	10.70	10.60
Na2O %	0.84	0.19	0.04	0.11	0.07	0.11	0.07	1.35	0.34	3.85	2.71	1.95	2.05
K2O %	0.16	0.10	0.73	0.61	0.06	0.10	0.02	0.04	0.09	0.08	0.17	0.34	0.37
P2O5 %	0.05	0.06	0.07	0.05	0.06	0.06	0.04	0.04	0.04	0.14	0.1	0.15	0.15
LOI %	2.23	6.16	12.30	6.31	7.93	7.93	9.85	7.08	2.77	1.68	2.54	0.62	0.54
Total %	100.12	99.34	100.39	99.23	100.03	99.94	99.31	99.70	97.76	99.66	99.6	99.36	99.90
La	1.73	2.10	2.12	1.71	1.83	1.85	1.13	1.29	4.59	6.80	6.37	9.84	10.48
Ce	4.52	5.83	5.56	4.51	4.92	4.68	3.01	3.33	12.58	17.85	15.57	25.54	26.62
Pr	0.72	0.92	0.83	0.74	0.80	0.70	0.48	0.55	1.92	2.82	2.06	3.44	3.58
Nd	4.05	4.42	4.32	3.80	4.52	4.03	2.31	3.07	9.20	13.53	9.75	15.85	17.53
Sm	1.33	1.34	1.37	1.13	1.26	1.24	0.74	0.84	2.40	4.03	2.64	4.41	4.54
Eu	0.44	0.52	0.41	0.46	0.45	0.38	0.45	0.41	1.32	1.32	0.80	1.51	1.47
Gd	1.76	1.82	1.71	1.45	1.77	1.68	1.01	1.16	2.76	5.35	3.12	4.95	5.13
Tb	0.30	0.30	0.30	0.25	0.30	0.28	0.17	0.21	0.40	0.86	0.47	0.72	0.77
Dy	2.14	2.20	2.02	1.86	2.16	2.09	1.38	1.55	2.55	6.18	3.24	4.66	4.79
Ho	0.46	0.48	0.43	0.39	0.43	0.41	0.29	0.32	0.52	1.30	0.67	0.88	0.90
Er	1.38	1.41	1.39	1.20	1.32	1.34	0.90	1.00	1.42	3.86	1.95	2.55	2.54
Tm	0.21	0.22	0.21	0.18	0.21	0.18	0.14	0.15	0.20	0.58	0.29	0.36	0.36
Yb	1.43	1.38	1.36	1.10	1.36	1.30	0.92	1.05	1.20	3.69	1.80	2.22	2.34
Lu	0.24	0.23	0.22	0.18	0.21	0.21	0.15	0.16	0.19	0.59	0.24	0.35	0.33
Th	0.23	0.21	0.64	0.74	0.49	0.49	0.34	0.22	0.52	0.59	0.73	1.14	1.14
U	0.07	0.05	0.06	0.04	0.04	0.04	0.03	0.03	0.22	0.18	0.12	0.21	0.21
Cs	1.45	0.94	6.16	6.37	0.66	0.94	0.25	0.19	0.75	0.01	0.28	0.26	0.14
Rb	11.3	3.8	35.4	29.9	2.5	4.1	0.4	0.5	1.6	1.3	4.23	11.0	9.6
Sr	57	23	54	21	22	23	35	30	42	129	105	163	155
Ba	12	9	94	71	6	10	1	8	2	77	177	70	63
Nb	1.62	1.66	1.92	1.46	1.77	1.69	0.86	1.00	4.99	5.55	6.14	9.82	10.00
Ta	0.09	0.10	0.14	0.13	0.11	0.11	0.07	0.08	0.23		-	0.51	0.52
Zr	28	36	36	29	33	32	20	21	64	113	72	112	113
Hf	0.88	1.13	1.12	0.99	1.04	0.93	0.56	0.62	1.70	3.24	-	2.91	3.01
Y	11.4	11.6	11.2	9.6	11.5	10.9	7.2	8.2	11.9	30.0	17.87	25.9	25.8
V	228	204	205	187	189	201	149	178	140	381	310.62	372	461
Sc	39	34	31	34	31	32	34	38	20	44	46.60	44	43
Cr	1340	1600	1500	1650	1490	1470	1310	1390	1180	71	181	90	62
Co	77	64	66	66	63	62	60	58	-	-	-	58	67
Ni	333	363	341	379	335	333	299	285	-	-	124	64	61
Cu	134	68	6	40	49	144	29	10	-	42	370	139	179
Zn	100	124	103	110	117	111	92	94	-	90	87	101	117
Pb	2.37	1.29	1.13	0.92	1.14	1.65	1.30	1.23	1.73	4.05	3.48	1.42	2.11
Au (ppb)	-	14	1	13	1	5	3	2	-	-	-	2	3
Mg#	48	52	50	52	51	50	53	52	49	27	36	26	25
Al2O3/TiO2	16.3	15.9	14.1	17.8	14.7	15.6	27.6	28.1	6.8	8.4	13.5	8.3	7.4
CaO/Al2O3	0.84	0.59	0.60	0.54	0.82	0.76	0.79	0.53	2.81	0.56	0.72	0.80	0.81
Nb/Ta	18	17	14	11	16	15	12	13	22		-	19	19
Zr/Hf	32	32	32	29	32	35	36	34	37	35	-	39	38
Ti/Zr	132	102	116	117	117	119	114	123	61	91	89	85	94
Zr/La	16.2	17.0	16.8	16.8	18.2	17.4	17.7	16.3	13.9	16.7	11.3	11.4	10.8
P/Nd	54	59	71	57	58	65	76	57	19	45	45	41	37
Total REE	21	23	22	19	22	20	13	15	41	69	49	77	81
(La/Yb)cn	0.80	1.00	1.03	1.03	0.89	0.94	0.81	0.81	2.52	1.22	2.34	2.92	2.95
(La/Sm)cn	0.80	0.96	0.95	0.93	0.89	0.92	0.94	0.94	1.17	1.04	1.48	1.37	1.42
(Gd/Yb)cn	1.00	1.07	1.02	1.07	1.05	1.05	0.89	0.90	1.86	1.18	1.41	1.81	1.78
Nb/Nb*	0.92	0.82	0.89	0.84	0.97	0.86	0.76	0.75	1.11	0.80	0.88	0.97	0.90
P/P*	0.81	0.84	1.02	0.85	0.88	0.97	1.08	0.86	0.27	0.64	0.60	0.55	0.51
Zr/Zr*	0.83	1.02	1.01	0.96	0.97	1.00	1.06	0.91	0.94	1.06	0.98	0.93	0.88
Hf/Hf*	0.95	1.17	1.16	1.20	1.09	1.05	1.08	0.97	0.91	1.10	-	0.87	0.85
Ti/Ti*	0.95	0.92	1.09	1.05	1.02	1.05	1.04	1.03	0.63	0.88	0.91	0.85	0.91

Table 3.1 (continued)

	ET2		Tholeiitic Basalts											
	S657 -23	S657 -27	GSWA 99787	GSWA 99912	GSWA 99932	GSWA 99937	GSWA 99955	CN 380911	AB 213797	S657 -17	S657 -18	S657 -28	S657 -29	SC 1484 -5
SiO2 %	46.00	49.80	50.6	48.5	51.2	50.4	48.9	50.7	52.0	51.80	52.70	50.70	51.10	49.6
TiO2 %	1.75	1.73	0.68	0.67	1.03	1.07	0.68	0.88	1.03	0.94	0.98	1.14	0.95	1.20
Al2O3 %	13.20	13.20	14.9	13.6	15.3	14.6	14.6	14.4	14.2	14.50	15.60	15.10	14.60	13.5
Fe2O3 %	12.90	15.20	1.36	1.9	1.72	1.75	1.88	11.7	12.5	11.70	11.40	12.30	11.90	14.2
FeO %			8.85	8.77	8.46	9.28	10							
MnO %	0.20	0.22	0.22	0.18	0.22	0.23	0.22	0.23	0.29	0.26	0.25	0.26	0.24	0.21
MgO %	4.80	5.81	7.41	9.05	6.13	7.13	8.38	7.3	6.2	6.52	4.93	6.19	6.66	6.6
CaO %	10.70	10.50	11.3	10.5	10.8	10.8	10.1	11.3	10.0	10.50	12.00	10.60	11.70	9.2
Na2O %	1.74	1.86	1.91	1.63	2.35	2.31	2.23	2.07	3.09	2.39	1.89	3.01	1.92	2.26
K2O %	1.33	0.41	0.13	1.05	0.12	0.14	0.35	0.15	0.20	0.30	0.16	0.28	0.14	0.44
P2O5 %	0.16	0.15	0.05	0.06	0.08	0.08	0.05	0.08	0.09	0.08	0.07	0.09	0.08	0.10
LOI %	6.54	0.62	2.06	3.44	2.18	2.12	2.4	0.54	0.77	0.47	0.47	0.31	0.47	1.00
Total %	99.32	99.50	99.47	99.35	99.59	99.91	99.79	99.35	100.39	99.46	100.45	99.98	99.76	98.32
La	11.16	10.73	1.82	2.08	2.93	2.87	2.02	2.33	2.89	2.25	2.54	4.16	2.79	3.92
Ce	27.99	26.78	5.25	5.33	8.19	8.14	4.83	6.45	7.94	6.70	7.37	11.31	7.75	10.52
Pr	3.79	3.59	0.76	0.79	1.19	1.23	0.73	1.07	1.30	1.02	1.13	1.61	1.18	1.65
Nd	18.15	17.39	4.64	4.24	6.60	6.54	4.01	6.17	7.33	5.48	6.16	8.36	6.83	8.79
Sm	4.92	4.71	1.58	1.49	2.20	2.23	1.38	2.21	2.39	2.09	2.14	2.64	2.34	2.71
Eu	1.35	1.56	0.55	0.58	0.81	0.86	0.45	0.87	0.85	0.62	0.85	1.01	0.85	0.99
Gd	5.09	5.02	2.18	2.19	3.33	3.15	1.85	3.41	3.20	2.99	3.04	3.69	3.20	3.56
Tb	0.74	0.74	0.37	0.33	0.57	0.52	0.33	0.57	0.53	0.51	0.55	0.61	0.55	0.60
Dy	4.55	4.61	2.60	2.39	3.92	3.81	2.32	4.24	4.09	3.61	3.79	4.29	3.94	4.39
Ho	0.90	0.91	0.56	0.52	0.87	0.83	0.51	0.89	0.86	0.78	0.81	0.92	0.85	0.90
Er	2.59	2.57	1.75	1.58	2.56	2.62	1.61	2.66	2.67	2.47	2.45	2.72	2.60	2.72
Tm	0.37	0.36	0.26	0.25	0.40	0.39	0.25	0.37	0.41	0.38	0.38	0.42	0.41	0.42
Yb	2.19	2.21	1.80	1.57	2.43	2.34	1.55	2.35	2.68	2.46	2.63	2.66	2.56	2.73
Lu	0.33	0.33	0.25	0.23	0.37	0.34	0.21	0.41	0.42	0.40	0.38	0.40	0.41	0.42
Th	1.22	1.17	0.23	0.25	0.30	0.32	0.21	0.18	0.29	0.27	0.24	0.42	0.27	0.53
U	0.21	0.21	0.03	0.12	0.05	0.04	0.15	0.05	0.06	0.04	0.05	0.09	0.05	0.36
Cs	5.79	0.33	0.47	0.88	0.05	0.13	0.36	0.06	0.88	0.74	0.04	0.11	-0.01	2.67
Rb	64.6	13.6	3.34	55.26	0.31	1.82	16.38	1.3	6.1	28.0	1.4	4.9	0.7	39.8
Sr	96	163	97	93	107	136	134	80	123	90	92	134	133	105
Ba	165	87	35	404	27	23	66	37	42	101	27	80	34	165
Nb	9.44	10.38	2.10	2.05	2.72	3.00	2.07	2.10	2.62	2.41	2.57	3.78	2.55	3.17
Ta	0.58	0.55	-	-	-	-	-	0.16	0.16	0.14	0.14	0.22	0.14	0.20
Zr	113	108	38	40	59	60	37	49	54	64	59	52	52	64
Hf	3.08	2.75	-	-	-	-	-	1.80	1.89	1.55	1.15	1.51	1.25	1.35
Y	23.2	26.5	14.19	13.49	22.98	22.75	15.24	19.1	21.4	22.7	23.2	24.8	23.8	23.4
V	422	458	285.26	234.63	351.68	366.68	268.82	289	307	327	347	417	405	341
Sc	41	43	50.61	38.75	54.52	53.29	48.39	44	44	51	44	53	53	44
Cr	60	63	308	283	234	241	313	273	278	206	219	207	215	144
Co	57	65	56.69	77.31	63.55	80.68	-	36	-	61	51	67	59	45
Ni	60	65	125	329	132	92	125	100	-	126	125	127	122	71
Cu	123	160	98	6	101	76	40	58	-	95	71	72	117	66
Zn	95	131	91	112	83	96	145	68	-	118	122	119	108	108
Pb	3.21	1.63	2.84	4.62	2.69	3.40	8.08	37.05	2.30	1.61	1.75	2.07	1.33	71.31
Au (ppb)	61	6	-	-	-	-	-	-	-	1	1	3	2	-
Mg#	24	25	36	40	32	34	36	35	30	32	27	30	33	29
Al2O3/TiO2	7.5	7.6	21.9	20.3	14.9	13.6	21.5	16.3	13.8	15.4	15.9	13.2	15.4	11.3
CaO/Al2O3	0.81	0.80	0.76	0.77	0.71	0.74	0.69	0.78	0.70	0.72	0.77	0.70	0.80	0.68
Nb/Ta	16	19	-	-	-	-	-	13	17	17	18	17	18	16
Zr/Hf	37	39	-	-	-	-	-	27	29	41	51	34	42	47
Ti/Zr	93	96	107	100	105	107	110	108	114	88	100	131	110	112
Zr/La	10.1	10.1	20.8	19.2	20.1	20.9	18.3	21.0	18.7	28.4	23.2	12.5	18.6	16.3
P/Nd	38	38	47	62	53	53	54	57	54	64	50	47	51	50
Total REE	84	82	24	24	36	36	22	34	38	32	34	45	36	44
(La/Yb)cn	3.36	3.20	0.67	0.87	0.80	0.81	0.86	0.65	0.71	0.60	0.64	1.03	0.72	0.95
(La/Sm)cn	1.39	1.40	0.71	0.86	0.82	0.79	0.90	0.65	0.74	0.66	0.73	0.97	0.73	0.89
(Gd/Yb)cn	1.88	1.84	0.98	1.13	1.11	1.09	0.97	1.18	0.97	0.99	0.94	1.12	1.01	1.06
Nb/Nb*	0.79	0.90	1.24	0.94	0.97	1.11	0.91	0.93	0.93	1.19	1.09	0.92	0.95	0.81
P/P*	0.52	0.51	0.71	0.90	0.77	0.77	0.80	0.87	0.81	0.93	0.73	0.66	0.77	0.73
Zr/Zr*	0.78	0.78	0.97	1.10	1.07	0.91	1.09	0.92	0.89	1.10	0.79	0.73	0.72	0.91
Hf/Hf*	0.82	0.76	-	-	-	-	-	1.22	1.14	1.15	0.80	0.81	0.79	0.69
Ti/Ti*	0.89	0.89	0.86	0.86	0.88	0.95	1.01	0.74	0.88	0.88	0.90	0.86	0.82	0.92

Table 3.1 (continued)

	Tholeiitic Basalts			Tholeiitic Gabbros										
	SC1484 -10	SC 358 -1	SC 358 -31	SC 1484 -3	SC 358 -2	SC 358 -3	S1113 B	S1113 C	S1113 D	S1113 W	S1113 Y	PRS1177 -19	PRS1177 -20	PRS1177 -21
SiO2 %	47.8	50.0	53.3	49.4	49.2	49.6	50.0	49.5	49.9	50.2	49.3	49.3	49.6	48.4
TiO2 %	1.01	0.92	1.20	1.23	0.90	0.91	0.88	0.98	0.95	0.86	0.95	0.65	1.15	0.75
Al2O3 %	14.9	15.4	14.5	13.7	14.9	14.9	16.4	15.4	15.4	14.4	15.7	15.2	13.5	15.8
Fe2O3 %	13.4	11.3	11.0	14.5	12.5	11.8	11.2	12.3	12.4	12.4	12.2	12.4	15.0	13.2
FeO %														
MnO %	0.17	0.24	0.23	0.23	0.23	0.24	0.18	0.19	0.20	0.19	0.19	0.22	0.26	0.22
MgO %	7.8	7.4	4.8	6.8	8.2	7.3	6.5	6.7	6.8	8.0	6.8	7.7	5.6	6.6
CaO %	9.2	9.1	8.2	9.4	9.1	9.2	12.1	11.1	11.3	10.7	11.7	10.4	9.3	11.6
Na2O %	2.27	2.33	4.47	2.32	2.19	2.43	1.96	1.91	1.85	2.30	1.80	2.02	3.40	1.98
K2O %	0.24	0.79	0.24	0.43	1.09	1.01	0.12	0.23	0.13	0.15	0.11	0.39	0.18	0.20
P2O5 %	0.09	0.08	0.10	0.11	0.08	0.08	0.08	0.09	0.08	0.07	0.09	0.06	0.10	0.06
LOI %	1.77	1.16	0.62	1.00	1.77	1.39	0.93	1.54	1.00	0.85	1.00	2.08	1.93	2.00
Total %	98.66	98.66	98.62	99.07	100.11	98.93	100.39	99.98	100.03	100.11	99.80	100.45	100.07	100.81
La	3.95	2.44	2.80	3.74	2.57	2.19	3.54	3.20	3.09	2.92	3.65	2.08	4.24	2.04
Ce	9.90	6.85	8.44	10.35	7.20	6.34	9.19	8.38	8.29	8.01	9.39	5.23	11.17	5.79
Pr	1.55	1.11	1.42	1.62	1.16	1.11	1.45	1.33	1.28	1.28	1.43	0.81	1.70	0.91
Nd	7.49	5.94	8.13	8.50	6.38	5.99	6.96	6.99	6.97	6.46	7.03	4.33	8.22	4.72
Sm	2.40	2.12	2.56	2.76	2.07	1.97	2.09	2.19	2.09	2.00	2.08	1.41	2.59	1.59
Eu	0.80	0.79	0.90	0.96	0.86	0.74	0.84	0.80	0.85	0.79	0.82	0.56	0.94	0.64
Gd	3.23	2.84	3.64	3.73	2.94	2.81	2.91	2.83	2.92	2.79	2.91	2.01	3.43	2.29
Tb	0.55	0.51	0.61	0.62	0.48	0.47	0.48	0.50	0.47	0.47	0.49	0.34	0.56	0.37
Dy	3.81	3.77	4.39	4.50	3.63	3.39	3.39	3.48	3.53	3.45	3.49	2.53	4.01	2.97
Ho	0.79	0.80	0.97	0.96	0.74	0.72	0.72	0.71	0.70	0.72	0.73	0.57	0.89	0.63
Er	2.55	2.45	2.85	2.76	2.29	2.17	2.05	2.08	2.06	2.15	2.29	1.75	2.67	1.94
Tm	0.38	0.38	0.44	0.42	0.36	0.32	0.33	0.31	0.32	0.33	0.34	0.27	0.42	0.31
Yb	2.33	2.40	2.85	2.83	2.15	2.10	2.09	2.09	1.93	2.16	2.29	1.79	2.73	2.00
Lu	0.37	0.35	0.42	0.42	0.31	0.31	0.32	0.29	0.29	0.33	0.34	0.27	0.43	0.32
Th	0.38	0.53	0.34	0.73	0.36	0.35	0.29	0.52	0.29	0.28	0.35	0.21	0.46	0.22
U	1.06	0.54	0.14	0.31	0.21	0.10	0.08	0.78	0.08	0.47	0.06	0.05	0.13	0.05
Cs	1.51	1.13	0.21	2.67	4.56	3.28	0.31	0.73	0.42	0.07	0.15	0.22	0.23	0.23
Rb	19.5	42.1	7.8	40.4	52.1	58.2	0.9	3.0	1.9	0.5	0.6	12.9	1.4	4.1
Sr	136	128	110	107	102	104	146	119	112	85	111	93	91	94
Ba	38	102	44	166	162	185	21	21	18	21	19	39	22	32
Nb	3.19	2.25	2.97	3.22	2.23	2.23	2.81	2.68	2.80	2.20	2.87	1.44	3.28	1.69
Ta	0.18	0.14	0.19	0.19	0.15	0.13	0.16	0.16	0.16	0.14	0.16	0.09	0.21	0.11
Zr	63	53	70	52	55	61	56	57	47	51	56	34	68	38
Hf	1.94	1.37	1.10	1.77	0.71	0.69	1.65	2.02	0.95	1.63	1.77	1.11	2.04	1.33
Y	20.0	19.5	23.4	23.4	18.1	17.7	17.2	16.3	16.2	17.6	18.2	13.3	20.4	14.6
V	306	303	351	345	274	267	238	275	277	298	245	219	301	235
Sc	41	45	47	45	39	39	36	38	39	46	37	40	40	38
Cr	276	295	163	165	246	301	235	274	272	322	268	256	112	185
Co	45	51	45	45	45	45	43	44	43	46	50	57	56	39
Ni	115	109	65	74	116	109	83	89	91	120	96	125	69	86
Cu	127	110	5	67	166	88	92	91	117	51	95	110	89	95
Zn	96	96	78	110	102	108	94	100	107	103	101	108	138	88
Pb	22.59	79.97	3.18	6.33	7.27	145.82	1.82	2.39	1.87	1.78	1.92	3.05	3.82	2.76
Au (ppb)	-	-	-	-	-	-	6	4	8	1	2	10	15	8
Mg#	34	36	27	29	36	35	33	32	32	36	32	35	24	30
Al2O3/TiO2	14.8	16.7	12.1	11.1	16.6	16.4	18.6	15.7	16.2	16.7	16.5	23.4	11.7	21.1
CaO/Al2O3	0.62	0.59	0.57	0.68	0.61	0.62	0.74	0.72	0.73	0.74	0.75	0.68	0.69	0.73
Nb/Ta	18	16	16	17	15	17	18	17	18	16	18	16	16	15
Zr/Hf	33	39	63	29	77	88	34	28	49	32	32	31	33	28
Ti/Zr	96	104	96	142	98	89	95	103	121	100	102	113	102	119
Zr/La	16.0	21.7	26.8	13.9	21.4	27.9	15.8	17.8	15.2	17.6	15.3	16.6	16.0	18.5
P/Nd	52	59	54	56	55	58	50	56	50	47	56	60	53	55
Total REE	40	33	40	44	33	31	36	35	35	34	37	24	44	27
(La/Yb)cn	1.12	0.67	0.65	0.87	0.79	0.69	1.12	1.01	1.06	0.89	1.05	0.77	1.02	0.67
(La/Sm)cn	1.01	0.71	0.67	0.83	0.76	0.68	1.04	0.90	0.91	0.90	1.08	0.91	1.01	0.79
(Gd/Yb)cn	1.12	0.96	1.04	1.07	1.11	1.08	1.13	1.10	1.23	1.05	1.03	0.91	1.02	0.93
Nb/Nb*	0.75	0.97	1.19	0.89	0.91	1.10	0.77	0.82	0.91	0.77	0.75	0.65	0.76	0.88
P/P*	0.75	0.88	0.83	0.83	0.82	0.89	0.71	0.83	0.74	0.69	0.79	0.89	0.75	0.81
Zr/Zr*	1.03	1.04	1.14	0.74	1.05	1.23	1.01	1.01	0.85	0.99	1.01	0.97	1.02	0.95
Hf/Hf*	1.15	0.97	0.61	0.92	0.49	0.50	1.09	1.30	0.63	1.14	1.16	1.13	1.11	1.22
Ti/Ti*	0.86	0.89	0.92	0.91	0.85	0.90	0.84	0.94	0.90	0.86	0.91	0.90	0.92	0.92

Table 3.1 (continued)

	Tholeiitic Gabbros							
	PRS1177 -22	PRS1177 -23	S657 -1	S657 -2	S657 -12	S657 -13	S657 -14	S657 -26
SiO2 %	45.8	44.2	50.5	49.8	50.2	48.5	50.0	48.50
TiO2 %	0.75	0.78	0.94	0.91	0.98	1.00	0.96	0.91
Al2O3 %	15.1	14.9	14.7	14.3	15.1	15.5	14.4	14.60
Fe2O3 %	13.2	17.6	12.5	11.7	11.8	11.4	12.6	11.60
FeO %								
MnO %	0.19	0.18	0.27	0.26	0.26	0.24	0.27	0.21
MgO %	7.8	7.6	5.8	6.7	6.4	5.4	6.5	7.55
CaO %	7.7	5.8	12.2	10.0	11.2	11.3	9.9	11.80
Na2O %	2.35	2.08	1.82	2.36	1.91	2.11	1.37	1.88
K2O %	0.88	0.28	0.19	1.19	0.69	0.82	0.88	0.74
P2O5 %	0.07	0.07	0.08	0.08	0.08	0.08	0.08	0.06
LOI %	7.00	5.16	0.77	1.77	1.31	1.85	2.62	1.47
Total %	100.76	98.63	99.76	99.03	99.93	98.21	99.58	99.32
La	2.38	2.39	2.84	2.54	2.70	2.92	2.67	2.07
Ce	6.35	6.41	7.40	6.87	7.24	7.58	7.36	5.46
Pr	1.03	0.98	1.21	1.13	1.18	1.22	1.18	0.81
Nd	5.16	5.16	6.49	6.26	6.31	6.36	6.61	4.31
Sm	1.69	1.80	2.20	2.04	2.11	2.20	2.21	1.43
Eu	0.40	0.53	0.76	0.90	0.81	0.90	0.82	0.60
Gd	2.31	2.52	3.30	2.94	3.03	3.29	3.20	1.91
Tb	0.40	0.44	0.56	0.51	0.50	0.55	0.56	0.35
Dy	3.15	3.13	4.15	3.75	3.69	4.16	3.95	2.31
Ho	0.65	0.67	0.89	0.79	0.76	0.89	0.90	0.51
Er	2.02	2.03	2.80	2.40	2.36	2.81	2.67	1.52
Tm	0.30	0.32	0.43	0.36	0.36	0.44	0.41	0.23
Yb	2.07	2.02	2.84	2.42	2.27	2.85	2.76	1.48
Lu	0.33	0.32	0.40	0.38	0.35	0.45	0.40	0.23
Th	0.28	0.51	0.65	0.28	0.24	0.56	0.26	0.18
U	0.05	0.06	0.08	0.05	0.07	0.10	0.06	0.03
Cs	2.98	0.70	0.03	0.71	1.24	2.02	1.76	0.95
Rb	37.0	10.0	0.9	50.3	30.0	41.3	43.5	38.9
Sr	65	64	80	75	93	75	65	116
Ba	108	38	30	157	51	63	288	178
Nb	1.95	2.02	2.30	2.06	2.29	2.42	2.25	1.79
Ta	0.12	0.11	0.13	0.14	0.14	0.14	0.13	0.10
Zr	41	39	62	38	47	53	44	32
Hf	1.01	1.44	1.57	1.16	1.38	1.83	1.27	0.97
Y	16.4	16.9	22.9	18.5	19.5	22.0	21.9	14.5
V	211	226	313	283	319	329	312	282
Sc	40	42	46	42	48	50	45	44
Cr	242	292	234	219	235	225	202	301
Co	42	79	56	57	54	46	43	50
Ni	105	143	99	101	106	99	92	122
Cu	143	546	35	18	14	384	143	30
Zn	100	109	154	127	139	124	133	113
Pb	2.82	3.80	3.87	3.25	3.60	4.37	2.63	2.07
Au (ppb)	2	11	5	7	2	66	17	5
Mg#	34	27	29	33	32	29	31	36
Al2O3/TiO2	20.1	19.1	15.6	15.7	15.4	15.5	15.0	16.0
CaO/Al2O3	0.51	0.39	0.83	0.70	0.74	0.73	0.69	0.81
Nb/Ta	16	18	18	15	16	17	17	18
Zr/Hf	41	27	39	33	34	29	35	33
Ti/Zr	110	118	91	144	126	114	129	170
Zr/La	17.2	16.5	21.8	15.0	17.2	18.1	16.7	15.5
P/Nd	59	59	54	56	55	55	53	61
Total REE	28	29	36	33	34	37	36	23
(La/Yb)cn	0.76	0.78	0.66	0.69	0.78	0.68	0.64	0.92
(La/Sm)cn	0.87	0.82	0.79	0.76	0.79	0.82	0.74	0.89
(Gd/Yb)cn	0.90	1.01	0.94	0.98	1.08	0.94	0.94	1.05
Nb/Nb*	0.82	0.85	0.79	0.82	0.85	0.80	0.87	0.85
P/P*	0.86	0.86	0.80	0.84	0.83	0.81	0.80	0.88
Zr/Zr*	0.96	0.90	1.14	0.74	0.88	0.98	0.81	0.90
Hf/Hf*	0.86	1.19	1.04	0.82	0.95	1.23	0.83	0.98
Ti/Ti*	0.90	0.86	0.80	0.87	0.90	0.86	0.84	1.31

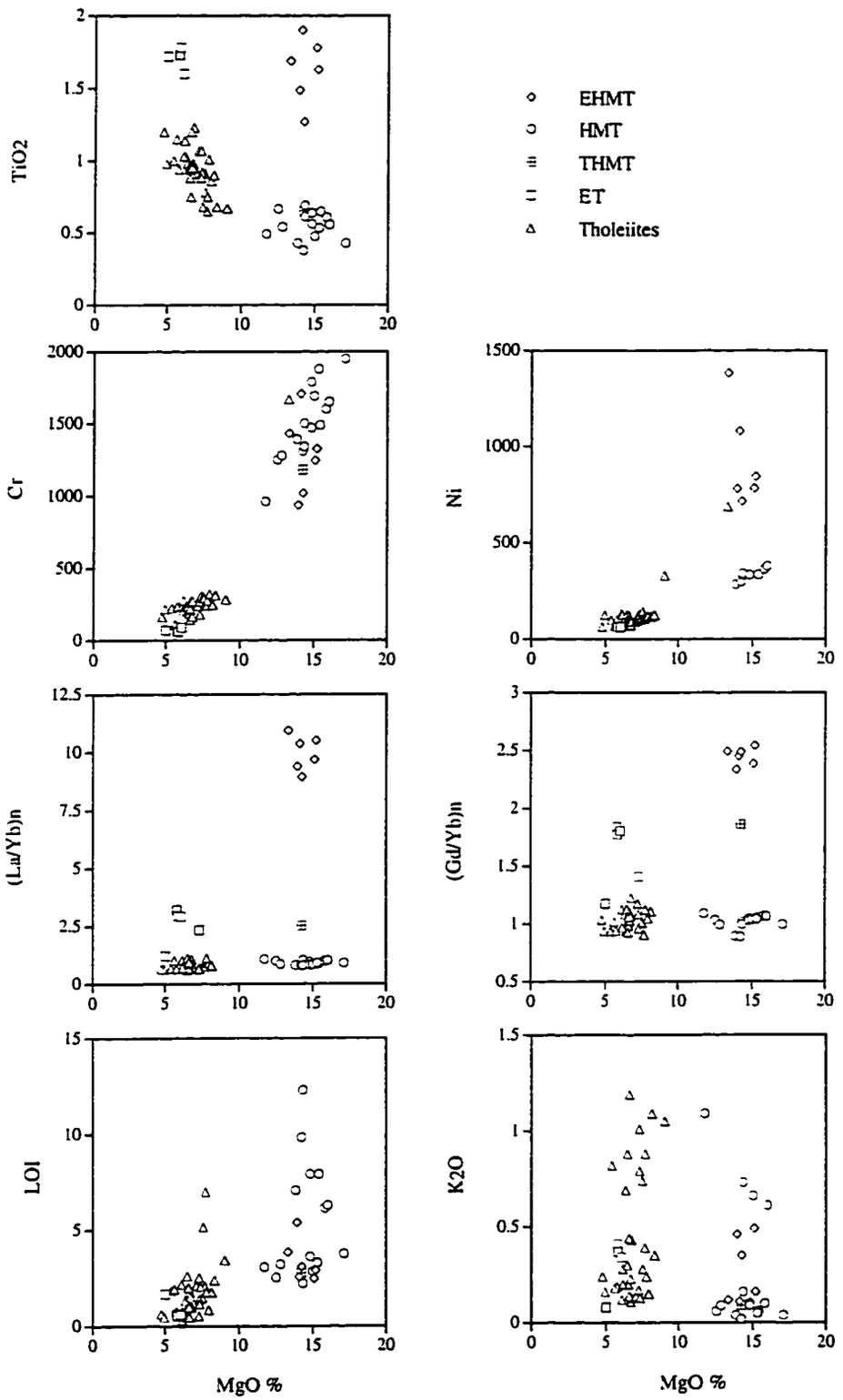

Figure 3.6. Plots of element concentrations and normalized REE ratios versus MgO content, highlighting the different types of mafic lithologies found within the Woolyeenyer Formation.

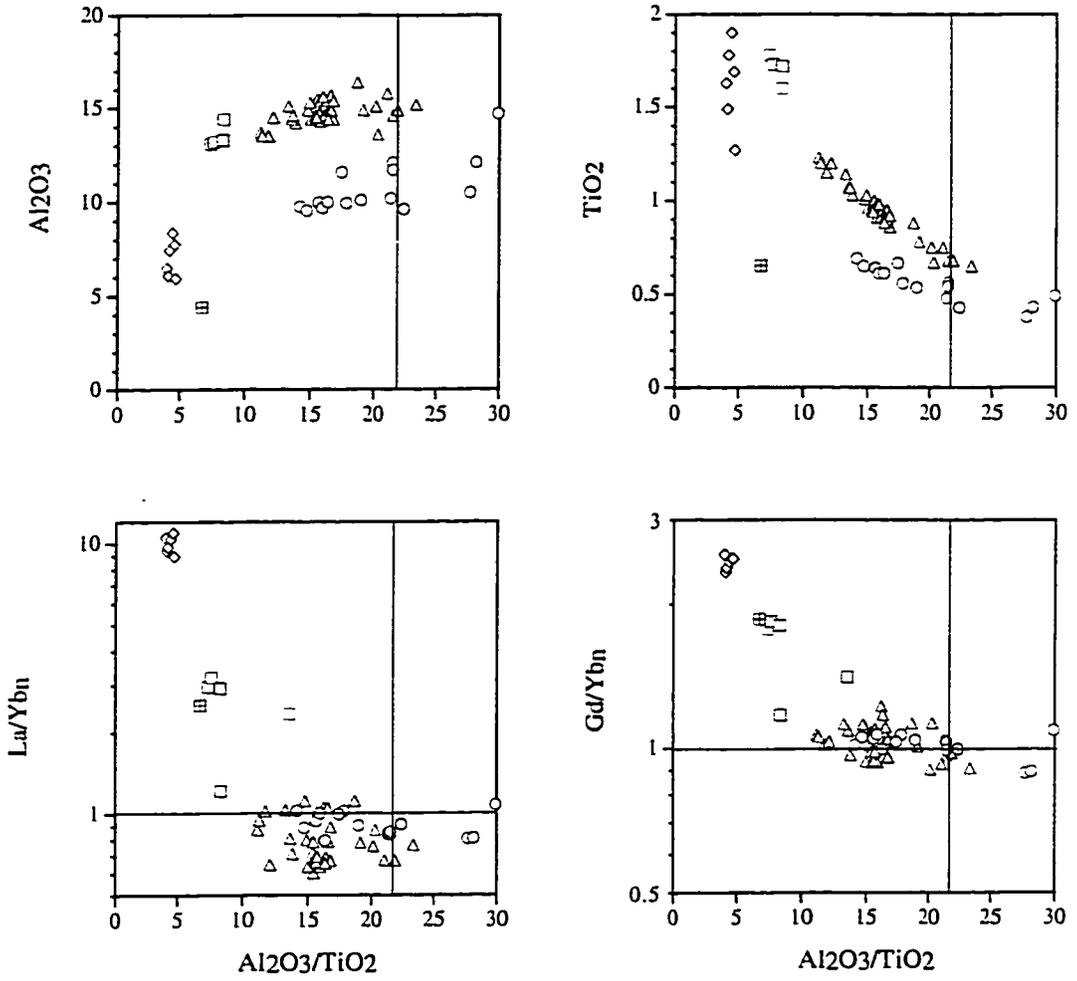

Figure 3.7. Plots of element concentrations and normalized REE ratios versus Al2O3/TiO2 ratio for mafic lithologies of the Woolyeenyer Formation. Symbols as for Figure 3.6. Chondritic ratios of 22 for Al2O3/TiO2, and 1 for normalized REE, are indicated for reference (Taylor and McLennan, 1984).

abundances (Cr = 60-90 ppm, Ni = 60-65 ppm), followed by tholeiites (Cr = 112-322 ppm, Ni = 69-329 ppm), HMT (Cr = 962-1950 ppm, Ni = 285-379 ppm), and EHMT (Cr = 936-1706 ppm, Ni = 716-1384 ppm) possessing the highest abundances (Figs. 3.6B,C). Although the EHMT and HMT have similar concentrations of Cr and MgO, Ni abundances are noteably higher in the EHMT. A fifth rock type, noted only in one sample, appears to be transitional between HMT and EHMT, with MgO = 14.2 wt.%, TiO_2 = 0.65 wt.%, Al_2O_3/TiO_2 = 6.8, Cr = 1180 ppm, and is termed transitional enriched high-MgO tholeiite (THMT).

Mantle normalized diagrams also effectively distinguish between tholeiites, ET, HMT, THMT and EHMT (Fig. 3.8A-N) Tholeiites are characterized by flat to slightly depleted mantle normalized patterns with flat HREE, variably depleted LREE, and no significant fractionation of HFSE from neighbouring REE. The HMT mimic these patterns, albeit at lower absolute abundances. In contrast, EHMT exhibit fractionated mantle normalized patterns with significant enrichment of incompatible elements, fractionated LREE and HREE, and pronounced P depletions relative to neighbouring REE (Fig. 3.8, Table 3.1). The ET samples show two distinct types of mantle normalized patterns. Two ET samples display relatively flat HREE patterns, similar to tholeiites, but at elevated absolute abundances, with enriched LREE (ET1). Three other ET samples display pronounced fractionation of all REE (ET2, Fig. 3.8E). Note that the degree of enrichment in incompatible elements broadly correlates with the fractionation of REE, and with consistently lower Al_2O_3/TiO_2 ratios (Fig. 3.7).

Reconnaisance Nd isotope data is listed and compared to that from the Kambalda Domain of the Kalgoorlie Terrane in Table 3.2 and Figure 3.9. The grouping of tholeiite data at more radiogenic compositions (i.e. higher $^{147}Sm/^{144}Nd$) is taken as representative of the magma source, and is comparable to the data for tholeiitic Footwall Basalts at Kambalda (Fig. 3.9A). An isochron constructed through the most radiogenic (most depleted) sample at 2.71 Ga, the approximate age of the lower Woolyeenyer Formation (Chapter 2), serves as a reference for the remaining data, which all fall below this isochron. The EHMT are extremely non-radiogenic compared to the tholeiites. Calculated ε_{Nd} values (at 2.7 Ga) for the samples range from +1.0 to +3.5 to for the tholeiites, -1.9 to -1.2 for EHMT, and -0.2 to +1.0 for ET1. No Nd isotope data has yet been obtained for HMT, THMT, or ET2.

From these results, six rock types identified in the Woolyeenyer Formation have distinct geochemical characteristics, and are best distinguished by a combination of major and trace elements (Table 3.3; Figs. 3.6, 3.7, 3.8).

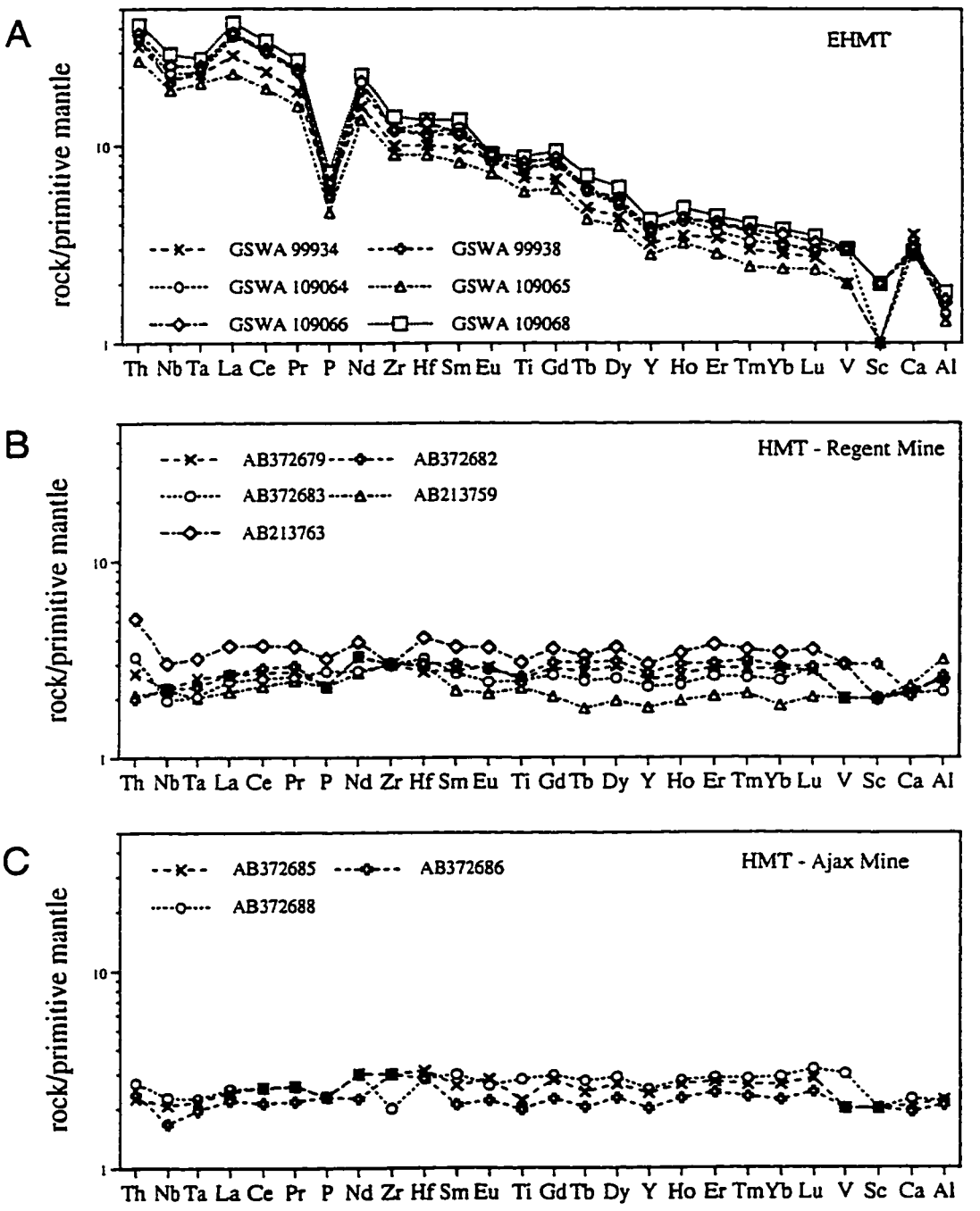

Figure 3.8. Primitive mantle-normalized multielement plots of mafic lithologies within the Woolyeenyer Formation. Data from Table 3.1, primitive mantle values from Sun and McDonough (1989) and Sun et al. (1989).

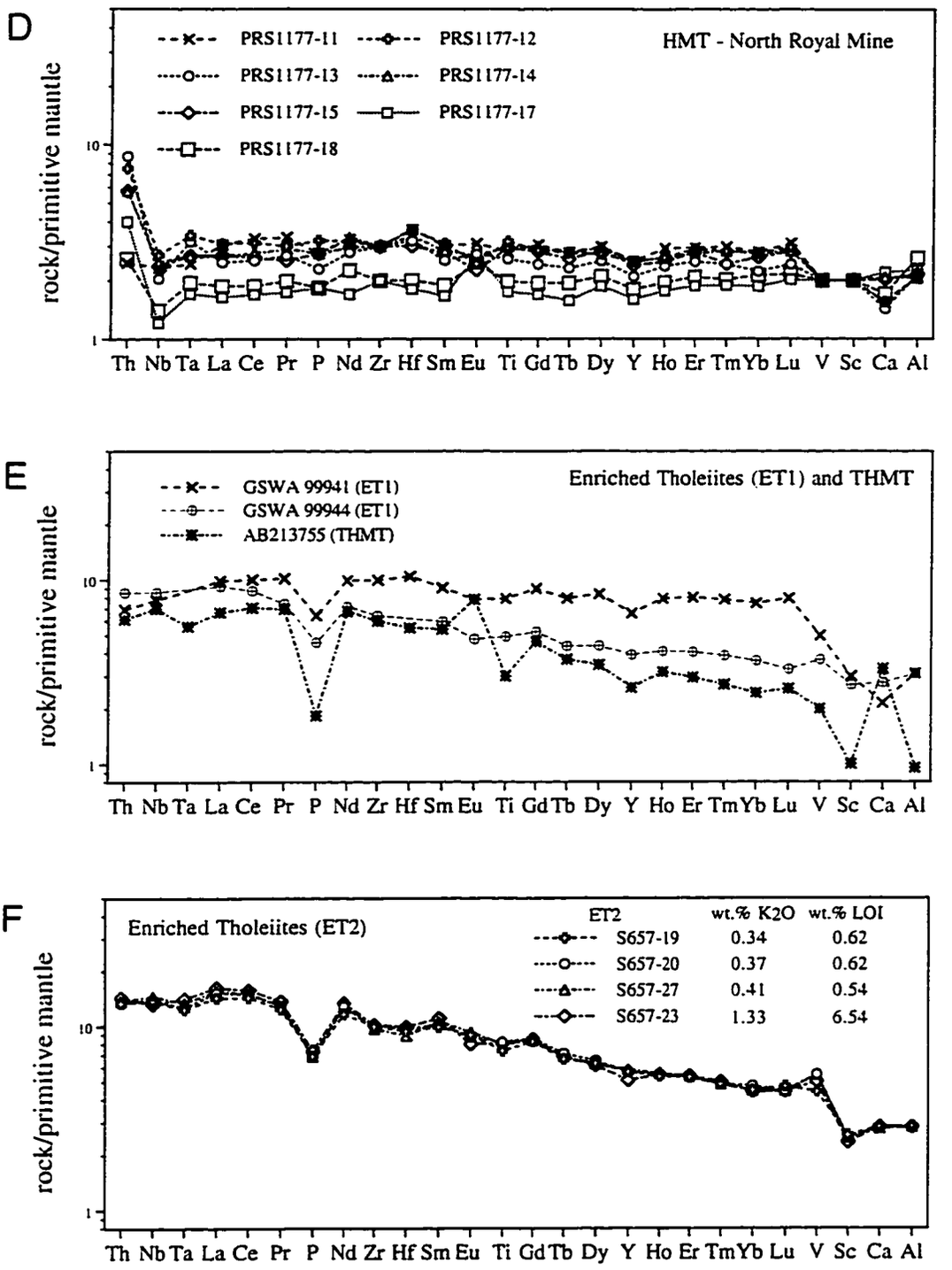

Figure 3.8 (continued).

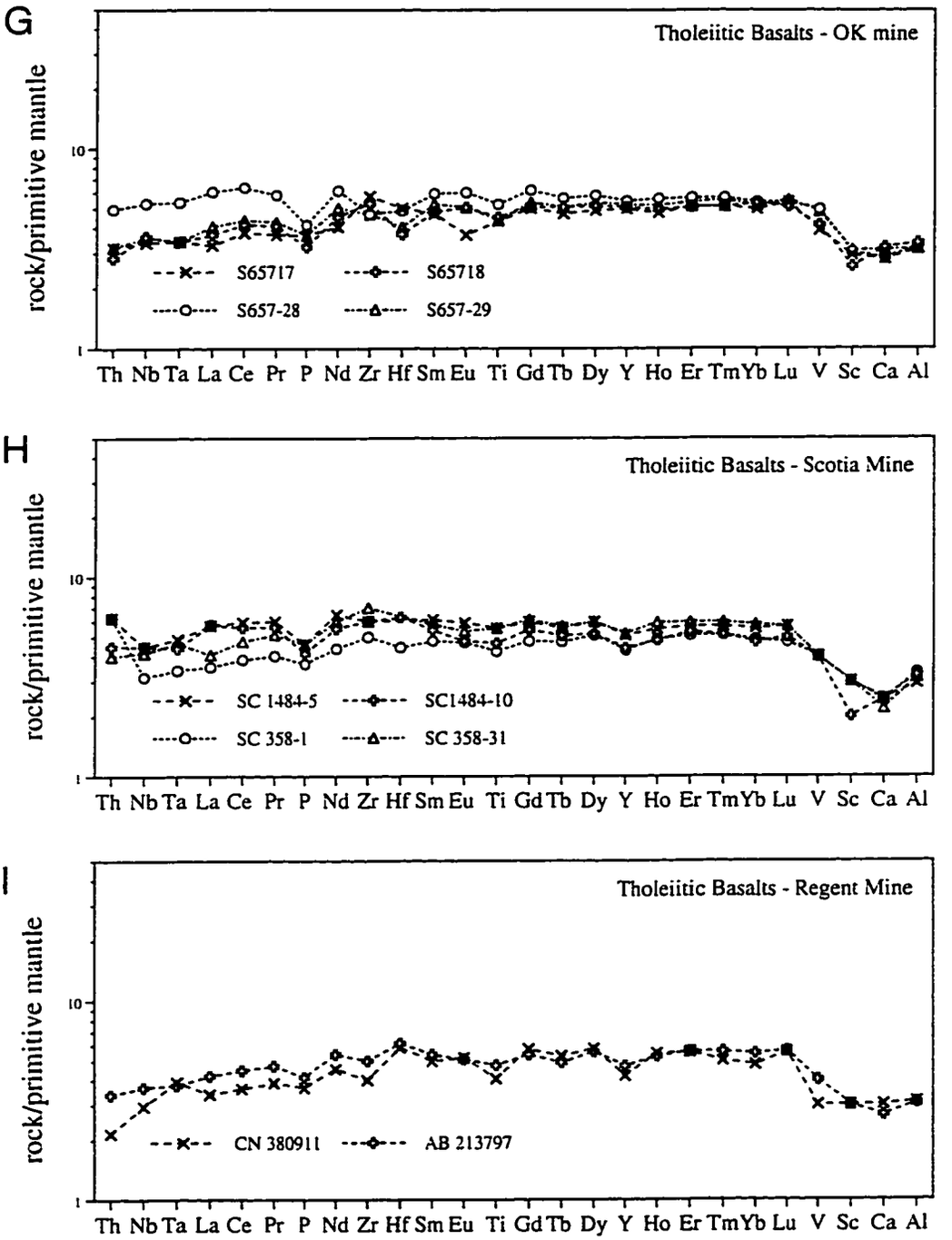

Figure 3.8 (continued)

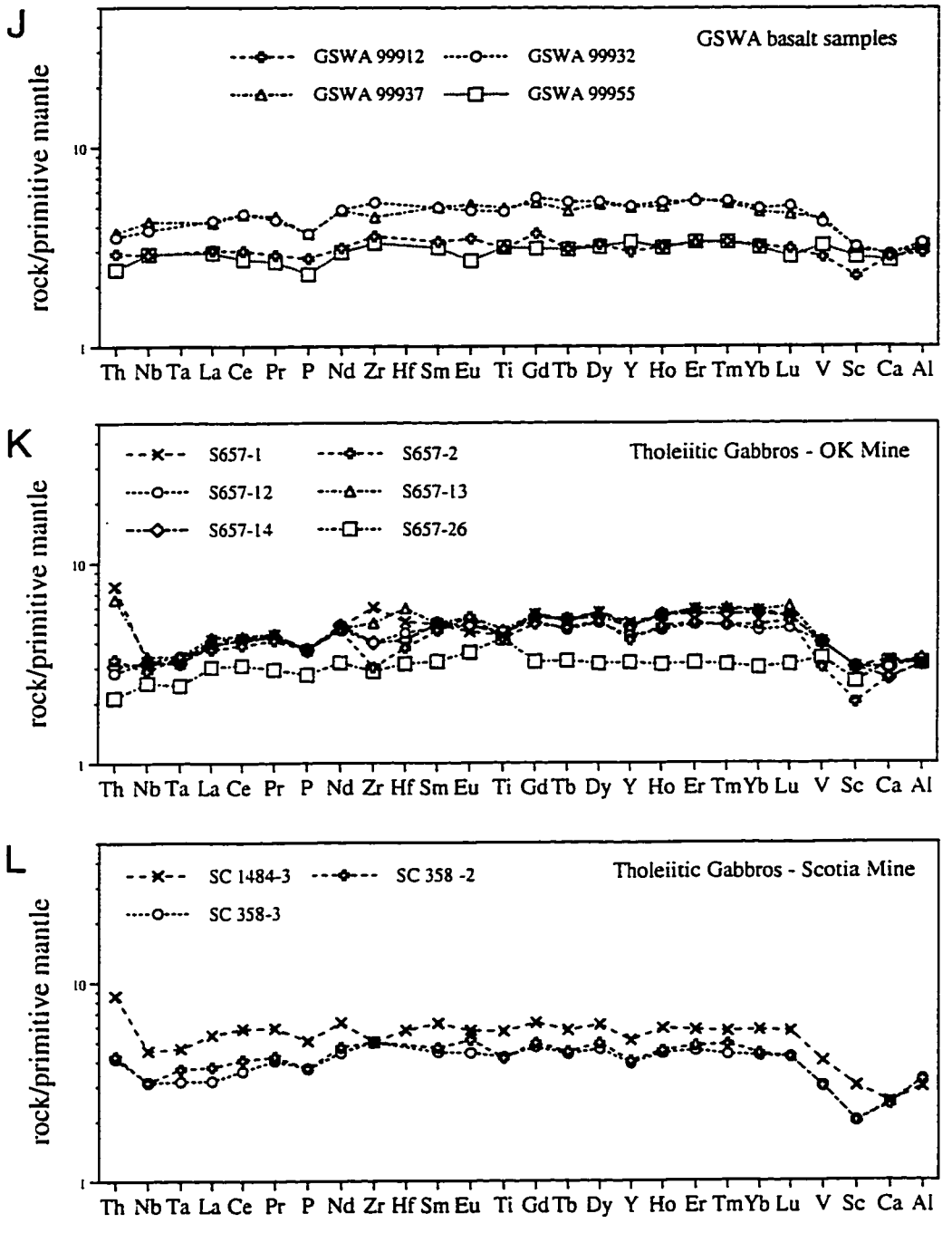

Figure 3.8 (Continued).

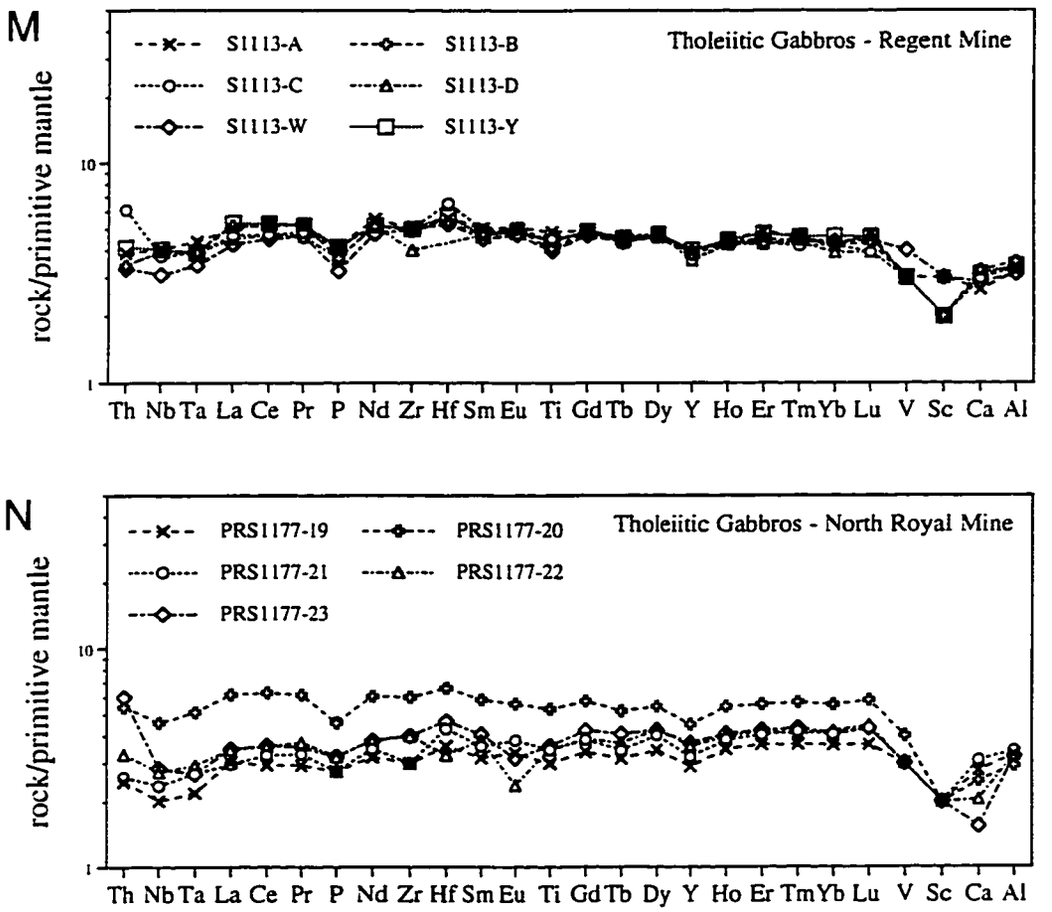

Figure 3.8 (continued)

Table 3.2 Sm-Nd isotope data and calculation of epsilon Nd values at 2.7 Ga

	Sample	rock type	location	Sm	Nd	147Sm/144Nd	143Nd/144Nd	error	Epsilon Nd	Reference
	upper cont. crust	granite		5	26	0.12	0.511158		-2.23	1
	KA12	sediment		2.54	12.17	0.1266	0.511368		-0.42	2
		CHUR		0.199	0.62	0.1967	0.512638		0.00	3
Norseman										
	99941	ETI	S207; 330.6m	4.09	13.41	0.18429	0.512467	27	0.98	4
	99944	ETI	S207; 282.7m	2.58	9.78	0.15949	0.511966	12	-0.18	5
	99912	tholeiite	C126; 1683'3"	1.41	4.26	0.20036	0.512856	34	3.00	5
	99955	tholeiite	S156; 220.5m	1.41	4.15	0.20479	0.512833	32	1.00	5
	99787	tholeiite	S169; 318m	1.39	4.09	0.20462	0.512865	22	1.69	5
	99932	tholeiite	S433; 166.7m	2.18	6.52	0.2024	0.512915	34	3.45	5
	99937	tholeiite	S433; 81.3m	4	12.76	0.18976	0.512631	25	2.29	5
	99934	EHMT	S433; 130.05m	3.82	19.07	0.12108	0.511193	27	-1.92	4
	99938	EHMT	S433; 61.3m	4.84	24.58	0.11899	0.51119	28	-1.25	4
Kambalda										
	1020A/158.2	HWB	in sample number	2.136	8.993	0.1436	0.51161	8	-1.61	6
	1020A/268.6	HWB	in sample number	1.816	6.089	0.1804	0.512413	8	1.28	6
	1020A/473.2	HWB	in sample number	3.069	12.203	0.152	0.511832	41	-0.19	6
	1020A/507.3	HWB	in sample number	2.229	7.007	0.1923	0.512634	12	1.46	6
	6033/479.7	komatiite	in sample number	0.826	2.125	0.2352	0.513601	34	5.44	6
	29/456.0	komatiite	in sample number	0.636	1.484	0.2592	0.51411	25	7.04	6
	29/501.5	komatiite	in sample number	1.164	3.462	0.2034	0.512997	14	4.71	6
	1025/624	FWB	in sample number	2.112	6.222	0.2053	0.512942	22	2.96	6
	1029/3366	FWB	in sample number	0.794	2.429	0.1976	0.512762	16	2.12	6
	1029/4780	FWB	in sample number	1.982	5.986	0.2002	0.512843	12	2.80	6
Bluebush										
	UMH62	basalt		0.756	2.563	0.1782	0.512594	32	5.61	6
	UMH72	basalt		2.557	8.055	0.192	0.512857	9	5.95	6
	UMH74	basalt		2.767	8.398	0.1993	0.512943	12	5.08	6
	UMH81	basalt		2.568	7.863	0.1975	0.512879	14	4.45	6
	UMH97	komatiite		0.859	2.221	0.234	0.513705	24	7.91	6
Kambalda										
	CD339W3/795.6	HWB	in sample number	2.679	11.38	0.1423	0.51155	21	-2.33	7
	CD339W3/1041.7	HWB	in sample number	1.829	6.135	0.1802	0.512433	25	1.75	7
	CD339W3/1041.7b	HWB	in sample number	1.794	6.012	0.1803	0.512461	15	2.26	7
	KD330/770'	HWB	in sample number	2.005	6.628	0.1829	0.512462	18	1.37	7
	CD339/256.6	HWB	in sample number	1.712	7.083	0.1461	0.51163	16	-2.09	7
	CD339/547.9	HWB	in sample number	2.479	10.478	0.1431	0.51158	20	-2.03	7
	CD339/591.8	HWB	in sample number	3.092	13.251	0.141	0.511564	11	-1.60	7
	KD330/1100.5'	komatiite	in sample number	0.718	1.87	0.232	0.513414	19	2.89	7
	KD330/1140.5'	komatiite	in sample number	0.549	1.483	0.2239	0.513323	17	3.94	7
	KA2	komatiite	in sample number	0.32	0.936	0.2069	0.513045	38	4.42	7
	KA1	FWB	in sample number	1.886	5.684	0.2024	0.51288	11	2.76	7
Ora Banda sill										
	OB1	WR		0.284	1.068	0.1608	0.511924	31	-1.46	7
	OB1	cpx		2.478	8.397	0.1784	0.512252	19	-1.18	7
	OB1	plag		0.32	2.432	0.0795	0.510446	18	-2.04	7
	OB1	opx		0.143	0.415	0.2075	0.51278	9	-0.99	7
	OB1	opx		0.143	0.415	0.2075	0.51278	9	-0.99	7

References: 1. Taylor and McLennan (1981); 2. Arndt and Jenner (1986); 3. Faure (1986); 4. Morris (1990); 5. This study; 6. Claoué-Long et al. (1984); 7. Chauvel et al. (1985).

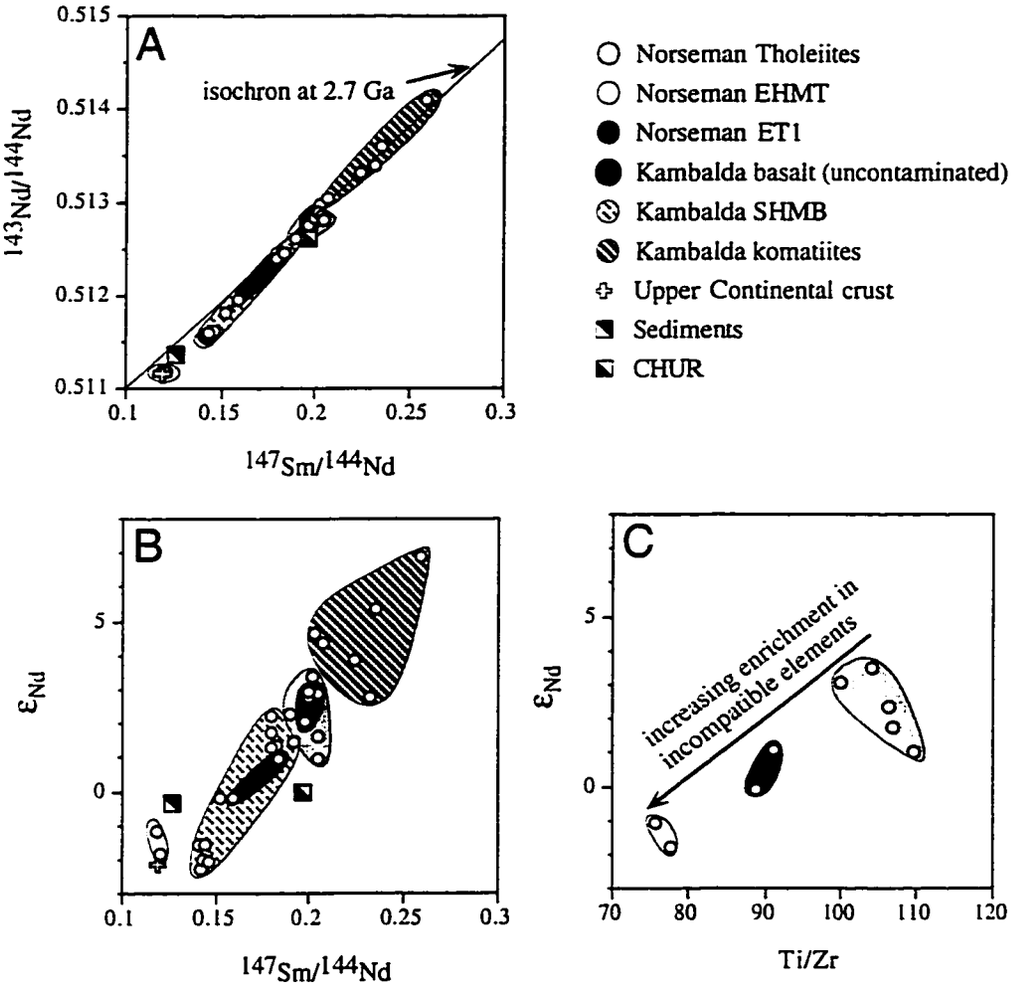

Figure 3.9. Plots of (A) $^{143}Nd/^{144}Nd$ versus $^{147}Sm/^{144}Nd$, (B) ε_{Nd} (at 2.7 Ga) versus $^{147}Sm/^{144}Nd$, and (C) ε_{Nd} versus Ti/Zr for mafic lithologies of the Woolyeenyer Formation. Data for komatiites, tholeiitic basalts, and crustally contaminated basalts and komatiitic basalts (SHMB) from the Kamblada Domain of the Kalgoorlie Terrane (Chapter 2) are shown for comparison. Data and sources are given in Table 3.2. Isochron is constructed through the most radiogenic Norseman tholeiite (sample with the highest $^{147}Sm/^{144}Nd$).

TABLE 3.3 Distinguishing Geochemical Characteristics of Norseman Mafic Lithologies

	HMT	EHMT	Tholeiites	ET1	ET2	THMT
SiO2 wt.%	45.5-49.8	45.0-48.7	47.8-53.3	50.4-53.6	49.8	49.8
TiO2 wt.%	0.43-0.67	1.27-1.90	0.68-1.23	1.07-1.72	1.60-1.78	0.65
Al2O3 wt.%	10.1-12.1	5.9-8.4	13.5-16.4	14.4	13.1-13.3	4.4
MgO wt.%	12.5-17.1	13.3-15.2	4.9-8.4	5.0-7.31	5.8-6.1	14.2
Cr ppm	1250-1950	936-1706	112-322	71-181	62-90	1180
Ni ppm	333-379	716-1384	65-132	124	61-65	-
Mg#	45-56	44-50	24-36	27-36	25-26	49
Al2O3/TiO2	14.7-22.4	4.0-4.7	11.1-23.4	8.4-13.5	7.4-8.3	6.8
CaO/Al2O3	0.54-0.84	1.3-2.2	0.57-0.83	0.56-0.72	0.80-0.81	2.8
total REE ppm	16-28	88-152	24-44	49-69	77-82	41
La/Ybcn	0.80-1.03	8.95-10.95	0.64-1.12	1.22-2.34	2.92-3.36	2.52
Gd/Ybcn	0.99-1.07	2.34-2.54	0.91-1.18	1.18-1.41	1.78-1.84	1.86
Nb/Nb*	0.74-0.97	0.44-0.70	0.65-1.19	0.80-0.88	.90-.97	1.11
P/P*	0.73-1.04	0.25-0.33	0.69-0.89	0.60-0.64	0.51-0.55	0.27
Zr/Zr*	0.83-1.15	0.72-0.83	0.74-1.23	0.98-1.06	0.78-0.93	0.94
Hf/Hf*	0.91-1.31	0.72-0.85	0.49-1.30	1.1	0.76-0.87	0.91
Ti/Ti*	0.80-1.05	0.83-0.90	0.74-0.94	0.88-0.91	0.85-0.89	0.63
Epsilon Nd	-	-1.9 to -1.2	+1.0 to +3.5	-0.2 to +1.0	-	-

(1) Tholeiitic basalts and gabbros that comprise the bulk of the formation are characterized by flat to slightly depleted mantle-normalized incompatible element patterns with no significant fractionation of HFSE from neighbouring REE, and ε_{Nd} values = +1.0 to +3.5.

(2) High-MgO tholeiite dikes (HMT) with normalized REE and multielement patterns like those of tholeiites, albeit at slightly lower abundances.

(3) Enriched high-MgO tholeiite dikes (EHMT) with MgO, SiO_2 and Cr contents similar to HMT but with higher Ni contents and extreme Al-depletion, significant enrichment in incompatible elements, fractionated and depleted HREE, moderate negative Nb anomalies and pronounced negative P anomalies, and with ε_{Nd} values of -1.9 to -1.2.

(4) The single THMT sample is transitional between HMT and EHMT, with depleted Al_2O_3, incompatible element enrichment and fractionated REE. This THMT sample also has pronounced negative P and moderately negative Ti anomalies.

Incompatible element enriched tholeiites (ET1) possess characteristics transitional between EHMT and tholeiites, showing Ti-enrichment, minor Al-depletion, moderate enrichment in incompatible elements and moderate negative P anomalies, and can be further subdivided into:

(5) ET1 with moderate LREE-enrichment, relatively flat HREE patterns, and ε_{Nd} values of -0.2 to +1.0, and

(6) ET2 with significant LREE-enrichment and fractionated HREE

3.4.4 Approach to interpretation of whole-rock geochemical data

There are many geological processes that have potentially acted in combination to produce the geochemical compositions of the mafic rocks at Norseman as determined at present. These include (1) the chemical composition of the source of the magma, which is in turn dependent on the history of the source, such as previous melt extraction or metasomatic processes, (2) the modal composition of the magma source, which is dependent upon source composition and depth (pressure), (3) the processes of magma production and separation from source rocks (e.g. equilibrium versus fractional melting), (4) processes that alter the magma chemistry during ascent through the lithosphere, including contamination by overlying lithosphere, or crystal fractionation at various crustal levels, and (5) post-magmatic processes that act upon the mafic rocks such as

seafloor metasomatism, regional metamorphism, syn-tectonic hydrothermal alteration, weathering, etc.

The approach taken in this study is to filter backwards through the effects of these processes. In other words, to filter out the geochemical effects of various postmagmatic processes, then determine the geochemical differentiation of the magma during its ascent, and finally to draw conclusions as to the nature of the mantle magma source. Comparison of these conclusions to geochemical databases of other mafic rocks of various geological ages allows inferences to be made regarding the evolution and tectonic setting of the mafic magmatism.

3.4.5 Introduction to P/REE and HFSE/REE systematics

Particular attention is directed towards P/REE and HFSE/REE systematics in the Norseman lithologies, with emphasis on genesis of the anomalous EHMT samples. Comparison is made to HFSE/REE relationships in other Archean lithologies, particularly in high-MgO lavas which show incompatible element enrichments and pronounced negative P anomalies that are comparable to those in the EHMT.

Due to its siderophile and moderately refractory nature, most of the phosphorus in the bulk earth fractionated into the core early in the earth's history (Sun, 1984). Nevertheless it remains an important minor element in most geological systems, comprising approximately 0.19 wt.% of the bulk continental crust and 0.02 wt.% of the primitive mantle (Weaver and Tarney, 1984; Sun and McDonough, 1989). This element has not been considered in some studies addressing the petrogenesis of mafic and ultramafic rocks, inasmuch as peridotites and high-MgO lavas have P contents close to the detection limit of 0.01 wt.% for XRF analyses (McCuaig et al., 1994).

Oceanic basalts (MORB, OIB) are characterized by smooth patterns through Pr-P-Nd on primitive-mantle-normalized diagrams (Fig. 3.5, Sun and McDonough, 1989; Langmuir et al., 1992). In addition, most oceanic basalts show no HFSE/REE fractionations, excepting positive Nb anomalies in some OIB (Fig. 3.5, Sun and McDonough, 1989; Weaver, 1991). Zero to positive normalised HFSE anomalies also characterize some uncontaminated Archean high-MgO rocks, although they have variable P/REE systematics (Sun and Nesbitt, 1978; Jahn et al., 1982; Arndt and Jenner, 1986; Cattell and Arndt, 1987; Sun et al., 1989; Jolly and Hallberg, 1990; Jochum et al., 1991; Xie et al., 1993). Archean Al-depleted komatiites, basaltic komatiites and high-MgO tholeiites ($Al_2O_3/TiO_2 < 18$) are characterized by variably negative P anomalies, as are Al-enriched Archean high-MgO rocks ($Al_2O_3/TiO_2 > 22$). Archean high-MgO rocks with approximately chondritic Al_2O_3/TiO_2 (18-22) possess variably negative, zero or

positive P anomalies, although the majority possess only minor P anomalies ($P/P^* = 0.7$-1.4, Fig. 3.10). Arc basalts, and alkaline mafic rocks from intracontinental settings, have more complex geochemical systematics, commonly including negative P anomalies. Arc basalts with negative P anomalies have pronounced normalized depletions of Nb and can have variable depletions of other HFSE relative to REE; alkaline intracontinental rocks with negative P anomalies also display variable depletions of some or all HFSE relative to REE (Cameron et al., 1983; Rock, 1989). Examples from selected suites of high-MgO basalts that display significant negative P anomalies are listed in Table 3.4 and shown in Fig. 3.11 (McCuaig et al., 1994).

3.4.6 Alteration Effects

Some element mobility is a possibility for Archean igneous rocks that have undergone seafloor hydrothermal alteration, polyphase deformation and greenschist-amphibolite facies metamorphism (cf., Seyfried et al., 1978; Ludden et al., 1982; Pearce, 1983; Marsh, 1991). Thus, particular attention is directed to assessing the effects of post-magmatic processes on the geochemistry of the Woolyeenyer mafic lithologies. Although rocks were petrographically screened to select least-altered samples, each sample has been metamorphosed, and many have been erupted subaqueously, therefore it is likely that each experienced some degree of hydrothermal alteration.

To examine the effects of alteration on the geochemistry of the rocks, some severely sheared and hydrothermally altered samples have been included in the database. McCuaig and Kerrich (1990) and McCuaig et al. (1993) discuss the petrographic and geochemical effects of gold-related hydrothermal alteration in mafic lithologies at Norseman (see Chapter 5) Such alteration is characterized by a systematic increase in volatiles (CO_2, H_2O, measured as loss on ignition (LOI)) and most LILE (K_2O, Rb, Ba, Cs) with increasing proximity to the quartz veins and their host shear zones. Thus, altered samples are easily identified by anomalously high LOI and K_2O contents (Fig. 3.6). It is crucial to note that, whereas some major and trace element chemistry is variably affected by these processes, Al_2O_3, TiO_2, MgO, discrimination ratios such as TiO_2/MgO and TiO_2 vs. Al_2O_3/TiO_2, HFSE, REE and primitive mantle normalized patterns using these elements remain relatively unchanged (Figs. 3.7, 3.8), with no fractionation of REE or HFSE, resulting in similar ratios of these elements within each of the distinct rock groups (Table 3.3; Lesher et al., 1991).

Thus, emphasis is placed on HFSE's and REE's. Evidence signifying limited mobility of the HFSE and REE include:

TABLE 3.4
Selected geochemical data for suites of mafic rocks that display significant negative normalized P anomalies.

Element/ ratio	Norseman EHMT	Boston Township komatiite+ferropicrite	Kambalda SHMB+tholeiite	Pechenga ferropicrites	SW Pacific boninite	Archean shoshonitic mafic lamprophyre	Al-depleted komatiite	Al-depleted Mg-tholeiite
SiO2 %	45.0 - 48.7	37.1 - 47.1	51.7 - 54.2	42.1 - 48.5	53.7 - 59.6	39.9 - 48.2	38.3 - 48.1	46.5 - 55.0
Al2O3 %	5.9 - 8.4	1.7 - 5.7	11.9 - 14.1	6.1 - 11.9	7.8 - 10.5	8.6 - 10.4	2.7 - 9.7	5.2 - 12.0
Fe2O3 %	1.6 - 1.7	14.8 - 17.8	11.0 - 12.1	1.5 - 1.7	1.3 - 2.4	8.9 - 9.9	12.3 - 15.4	11.1 - 13.1
FeO %	9.6 - 11.8			12.1 - 14.0	4.9 - 7.0			
MgO %	13.3 - 15.2	11.2 - 29.4	5.5 - 13.2	5.7 - 16.5	10.6 - 18.5	12.6 - 13.8	18.0 - 35.0	12.7 - 16.0
CaO %	10.6 - 13.3	2.43 - 14.3	7.9 - 10.7	6.9 - 11.2	3.6 - 4.6	6.5 - 11.1	1.7 - 11.4	10.5 - 15.0
Cr ppm	936 - 1706	194 - 3420	32 - 1460	11 - 1638	655 - 1930	798 - 915	2479 - 5200	1327 - 1340
Ni ppm	716 - 1384	203 - 1965	48 - 341	46 - 1046	194 - 540	199 - 368	727 - 2285	273 - 354
Nb ppm	13.7 - 20.9	3.1 - 9.5	2.8 - 5.1	16.8 - 37.0	1.5 - 2.0	5.0 - 13.0	0.1 - 1.9	1.3 - 3.0
La ppm	15.9 - 29.1	3.6 - 11.0	7.9 - 14.0	12.1 - 28.6	2.5 - 5.0	33.1 - 122	0.7 - 3.9	1.6 - 3.6
Ce ppm	34.6 - 60.8	8.1 - 24.3	16.6 - 25.5	30.9 - 62.0	5.5 - 11.9	68.0 - 227	2.6 - 6.2	4.6 - 10.2
P ppm	436 - 698	175 - 349	262 - 436	742 - 1266	131 - 218	1570 - 6283	44 - 305	175 - 349
Nd ppm	18.3 - 31.2	4.8 - 14.7	8.2 - 12.3	17.7 - 35.3	2.8 - 5.9	32.0 - 112	1.7 - 5.7	4.0 - 6.0
Zr ppm	98 - 153	17 - 67	57 - 89	111 - 200	30 - 78	91 - 295	11 - 33	34 - 45
Sm ppm	3.6 - 6.0	1.0 - 3.2	1.8 - 2.7	4.6 - 7.8	0.8 - 1.3	5.4 - 19.3	0.5 - 1.9	1.4 - 1.9
Eu ppm	1.2 - 1.5	0.3 - 1.2	0.5 - 0.9	1.3 - 2.4	0.2 - 0.5	1.4 - 4.3	0.2 - 0.6	0.5 - 0.7
Ti ppm	7612 - 11389	2338 - 6294	3536 - 5574	11149 - 19540	1259 - 1798	3357 - 8631	1439 - 4316	3057 - 4795
Gd ppm	3.6 - 5.6	1.0 - 3.3	2.1 - 2.3	-	0.7 - 1.6	0.8 - 1.7	0.6 - 2.7	1.5 - 2.4
Yb ppm	1.2 - 1.9	0.4 - 1.3	1.4 - 2.0	1.0 - 2.0	0.5 - 1.1	1.2 - 1.9	0.4 - 1.3	1.2 - 1.6
Al2O3/TiO2	4.0 - 4.7	4.4 - 5.4	15.1 - 20.5	3.2 - 4.4	34.9 - 81.3	6.0 - 17.8	10.5 - 15.2	10.1 - 15.7
(La/Yb)n	8.9 - 10.5	5.5 - 6.3	3.1 - 4.6	5.1 - 13.4	2.9 - 3.9	11.9 - 47.3	0.7 - 4.5	0.8 - 2.0
(Gd/Yb)n	2.3 - 2.5	2.0 - 2.2	1.2	2.0 - 2.5~	0.6 - 1.4		1.0 - 1.8	1.0 - 1.3
ΣREE	88 - 152	22 - 68	42 - 68	76 - 132	15 - 32	145 - 487	5 - 23	18 - 29
Nb/Nb*	0.54 - 0.70	0.76 - 0.78	0.25 - 0.39	0.56 - 1.05	0.31 - 0.53	0.03 - 0.34	0.36 - 0.92	0.66 - 1.06
P/P*	**0.24 - 0.33**	**0.31 - 0.48**	**0.39 - 0.46**	**0.33 - 0.56**	**0.31 - 0.58**	**0.40 - 0.69**	**0.36 - 1.40**	**0.45 - 0.97**
Zr/Zr*	0.72 - 0.83	0.39 - 0.52	1.02 - 1.08	0.76 - 1.01	1.67 - 1.84	0.15 - 0.61	0.64 - 1.16	0.77 - 1.14
Ti/Ti*	0.88 - 0.95	0.75 - 1.19	0.75 - 0.87	0.89 - 1.42	0.47 - 0.73	0.15 - 0.56	0.56 - 1.10	0.89 - 1.30
P/Nd	**19 - 26**	**24 - 37**	**31 - 41**	**31 - 49**	**24 - 46**	**32 - 56**	**25 - 126**	**32 - 66**

Data sources: Norseman enriched high-MgO basalts (EHMT) (this study); Boston Township (Xie et al., 1993); Kambalda SHMB (Arndt and Jenner, 1986; Sun et al., 1989; Jochum et al., 1991); boninites (Cameron et al., 1983); Superior Province shoshonites (Wyman and Kerrich, 1989); Al-depleted komatiites and Mg-tholeiites (basaltic komatiites) (Sun and Nesbitt, 1978; Jahn et al., 1982; Arndt and Jenner, 1986; Cattell and Arndt, 1987; Jolly and Hallberg, 1990; Jochum et al., 1991)5-8,11,10]. HFSE/HFSE* values are calculated by logarithmic rather than the traditional linear method (Salters and Shimuzu, 1988) as the former does not generate virtual anomalies in extremely LREE-enriched or -depleted rocks as the linearmethod does. Thus, Nb/Nb* = Nb/(La * (La/Ce)), P/P* = P/((Ce * Nd^2)^0.33), Zr/Zr* = Zr/((Nd * Sm)^0.5), Hf/Hf* = Hf/((Nd * Sm)^0.5), and Ti/Ti* = Ti/((Eu*) * Gd)^0.5), where all elemental values are normalized to primitive mantle. ~= calculated as (Tb/Yb)n.

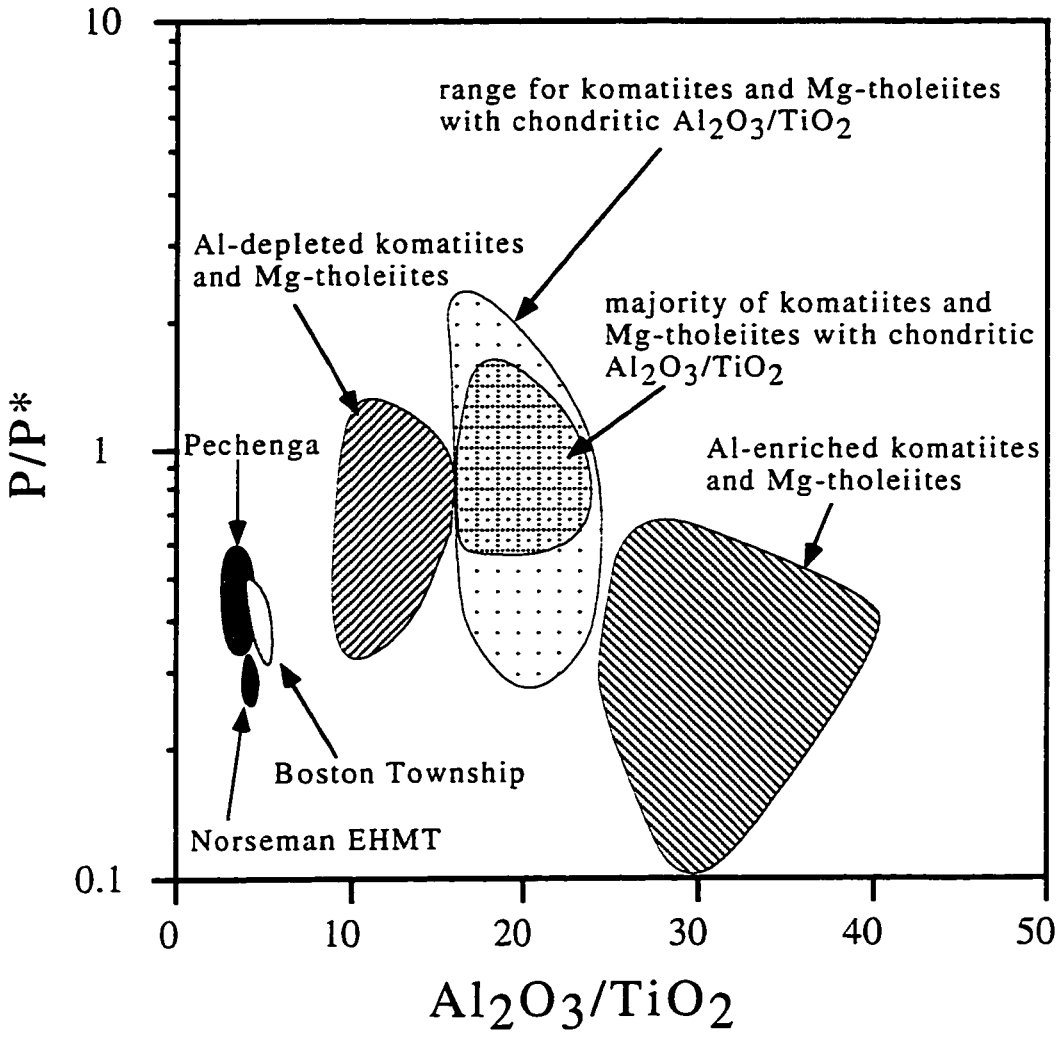

Figure 3.10. Plot of P/P* versus Al_2O_3/TiO_2 for komatiites and basaltic komatiites of various ages, Norseman EHMT, Boston Township ferropicrites and Pechenga ferropicrites. Data sources for Pechenga and Boston Township ferropicrites are given in Table 3.4. Other sources: Al-depleted lithologies - Sun and Nesbitt (1978), Jahn et al. (1982), Cattell and Arndt (1987), Jochum et al. (1991); Al-undepleted lithologies - Sun and Nesbitt (1978), Arndt and Jenner (1986), Cattell and Arndt (1987), Jochum et al. (1991); Al-enriched lithologies - Sun and Nesbitt (1978), Jahn et al. (1982).

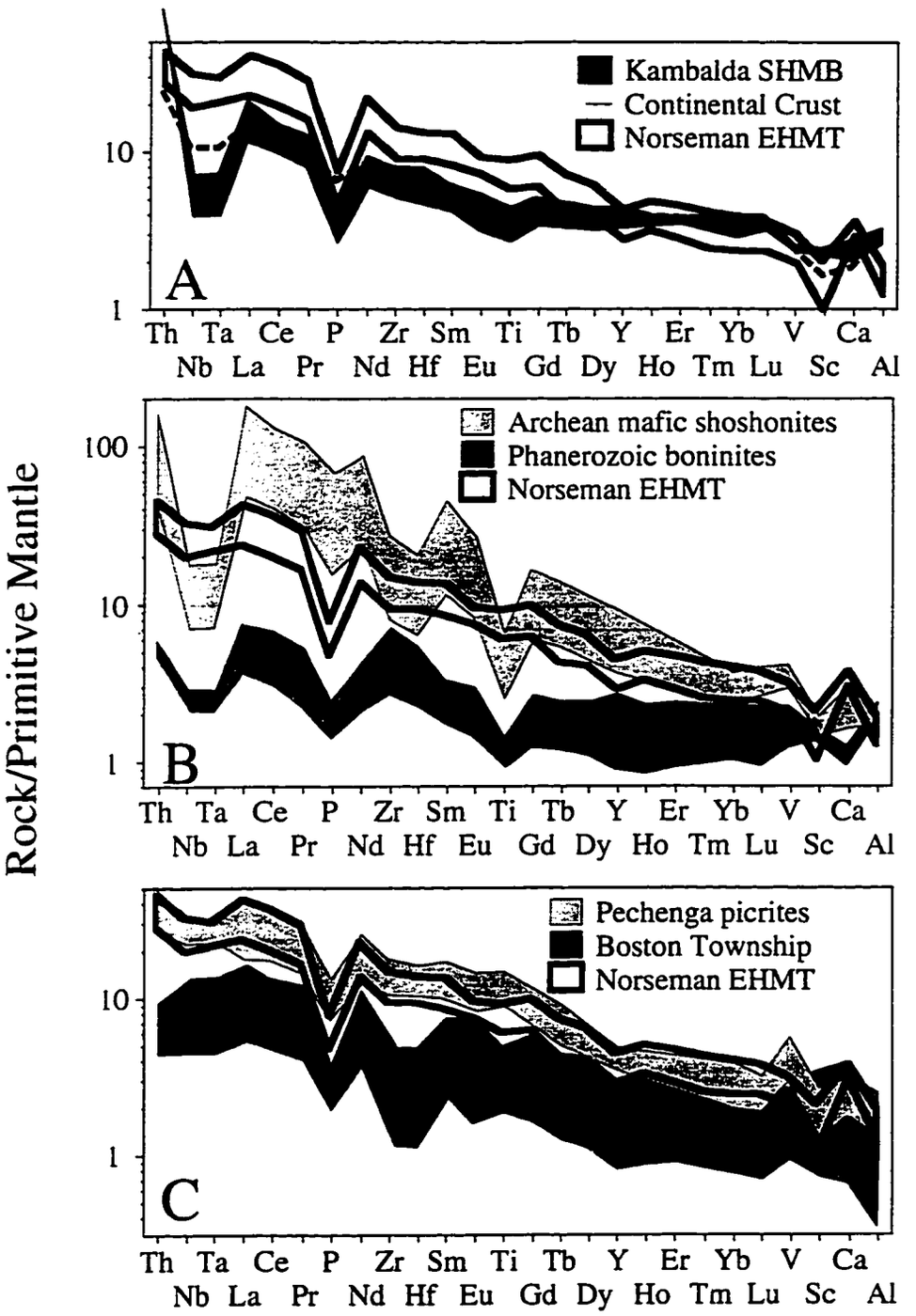

Figure 3.11. Primitive mantle-normalized multielement diagrams comparing selected high-MgO rock types, which display LREE enrichments and negative P anomalies, to Norseman EHMT. Data sources given in Table 3.4.

(1) igneous textures are identifiable,

(2) tholeiitic basalts show chondritic Ti-Zr relations (r=0.99, n=63, Morris, 1990; 1992), indicating that no fractionation between HFSE's has occurred,

(3) Zr/La ratios are consistent for a given rock type (Table 3.1), indicating no significant fractionation between the most mobile REE and relatively immobile HFSE,

(4) mantle-normalized diagrams of selected trace elements exhibit consistent patterns for HFSE and REE, whereas irregular REE (Ce, Eu) and HFSE/REE anomalies would be expected in severely altered samples (Michard and Albarède, 1986; Brookins, 1989; Michard, 1989; Greenough et al., 1990; Kuschel and Smith, 1992), and

(5) samples analyzed in this study have Nb/Ta and Zr/Hf ratios close to 17 and 36, respectively, that are typical of uncontaminated terrestrial, non-alkaline mafic volcanic rocks (Sun and McDonough, 1989).

The mantle-normalized diagrams of EHMT and ET dyke geochemistry display the pronounced chemical coherence of all samples, with systematic enrichments of LREE and HFSE and pronounced negative P anomalies (Fig. 3.8; Morris, 1990). Of particular interest is the diagram for the ET samples, which includes one intensely hydrothermally altered sample immediately adjacent to an auriferous quartz vein (S657-23, Fig. 3.8F). Note that the REE and HFSE abundances and interelement relationships of the sample are unaffected by the hydrothermal alteration. The results corroborate those of Lesher et al. (1991), who found no significant element mobility of REE, first row transition metals, and HFSE during gold-related hydrothermal alteration in metabasaltic host rocks of the Hunt Mine, Kambalda. These findings are consistent with empirical and experimental studies which indicate that extremely high fluid/rock ratios ($>10^5$), such as those found in alteration pipes underlying large volcanogenic massive sulphide deposits, are required to significantly mobilize the REE (Michard and Alberède, 1986; Michard, 1989; Bau, 1991; Lécuyer et al., 1994; Wood and William-Jones, 1994). Alternatively, extremely F or CO_2-rich fluids are required (Kerrich and Fryer, 1979; Wood, 1990a,b). Even higher water/rock ratios are required for significant mobilization of the HFSE (Ludden et al., 1982, Campbell et al., 1984, Pan et al., 1994)

Significantly, HMT that coexist with mineralogically identical EHMT are altered to similar degrees, have comparable SiO_2, MgO, and Cr abundances as EHMT, although the latter have higher CaO and Ni, but lower Al_2O_3 contents, and show no evidence of LREE or HFSE enrichments, with zero or minor P and HFSE anomalies. The EHMT are

also isotopically distinct from the coexisting tholeiites and HMT ($\varepsilon_{Nd} < 0$ versus $\varepsilon_{Nd} > 0$, respectively; Figure 3.9; Tables 3.2, 3.3; Morris, 1990). In an independent study of the Norseman volcanic rocks by Hallberg (1972), investigating major and trace element mobility between rims and cores of basalt pillows, it was found that all major elements, including P, behaved isochemically during seafloor alteration. Therefore, the incompatible element enrichments and negative P anomalies observed in EHMT, ET and THMT are not considered to stem from hydrothermal alteration or metamorphism.

These observations preclude the formation of the volumetrically smaller ET, THMT and EHMT from alteration of their non-enriched counterparts. For the remainder of this discussion, only the relatively unaltered rocks are discussed, taken as those with $K_2O < 0.5$ wt.%, and LOI < 3 wt.% for tholeiites and ET, and LOI < 4 wt.% for HMT and EHMT. The HMT and EHMT yield higher LOI values due to their relatively high chlorite abundances after clinopyroxene.

3.4.7 Crustal Contamination

3.4.7.1 Theory and Approach

High-MgO magmas, with concomitant high liquidus temperatures, are capable of thermally eroding and assimilating significant amounts of wallrock during their ascent (e.g. Huppert and Sparkes, 1985). For example, Archean high-MgO tholeiites with enriched LREE, and $\varepsilon_{Nd} < 0$ have been identified in the Kambalda Domain of the Kalgoorlie Terrane, approximately 100 km north of Norseman (Arndt and Jenner, 1986). These rocks have been termed siliceous high-Mg basalts (SHMB) by Redman and Keays (1985) due to their high SiO_2 contents relative to MgO contents. Sun et al. (1989) argued that the chemical and isotopic characteristics of the SHMB were consistent with assimilation of $\approx$ 14% felsic crust by an Al-undepleted komatiite magma (24 wt.% MgO), followed by $\approx$ 35% fractional crystallization. As EHMT and ET from Norseman have LREE enrichments and ε_{Nd} values similar to those of SHMB, it is imperative that the possibility of crustal contamination in their petrogenesis be investigated (Fig. 3.11A, Table 3.4).

Modelling of crustal contamination of high magnesian lavas by assimilation-fractionanal crystallization (AFC) processes was undertaken in an attempt to reproduce the geochemical characteristics of the EHMT (cf. DePaolo, 1981; Sun et al., 1989). Emphasis is placed on the EHMT because they are the most incompatible element enriched mafic rocks found in the Woolyeenyer Formation, they are very primitive in nature (high Ni, Cr, MgO), and they appear to have experienced a simple fractional crystallization history (clinopyroxene-only). Three different starting compositions were

selected to cover all likely possibilities for primary melt compositions, and these are listed in Table 3.5.

(1) Al-undepleted komatiite. These are the most common ultramafic volcanic rocks in late Archean terranes, and although not yet identified within the Norseman Terrane, are abundant in the Kambalda Domain of the Kalgoorlie Terrane to the north (Sun and Nesbitt, 1978; Arndt and Jenner, 1986; Condie 1990). The composition chosen is similar to that used in the modelling of Sun et al. (1989) for the Kambalda Domain SHMB.

(2) Al-depleted komatiite. These rock types are common in mid-Archean terranes, and much less common in late-Archean terranes. Such rocks have not yet been identified in the ECYS, but as the EHMT are very Al-depleted, it is essential that this melt composition be considered.

(3) HMT from Norseman. As these rocks coexist with EHMT, the possibility of derivation of the incompatible element enriched rocks from these HMT melts by assimilation of crust must be assessed.

Potential contaminants were selected to cover the broadest possible range of compositions, and are listed in Table 3.6. These include:

(1) typical tholeiitic basalt from the Norseman Terrane,

(2) various estimates of average Archean crustal compositions, and

(3) the average compositions of some granitoid rocks in the East Central Yilgarn Superterrane, which are the best estimates for felsic upper crustal compositions in the Norseman Terrane (Cassidy et al., 1991). These granitoids of the East Central Yilgarn Superterrane also represent partial melts of crust below the Norseman Terrane (Oversby, 1975; Bettenay, 1988; Cassidy et al., 1991), and are thus representative of partial melts that may have been incorporated into the mafic magmas during non-bulk assimilation of country rock.

The AFC modelling follows that of Sun et al. (1989) and employs two different approaches. The first is where bulk assimilation and fractional crystallization occur simultaneously (c.f. DePaolo, 1981). This approximates situations in magma chambers in the upper crust, where assimilation of cooler country rock requires heat from the magma, and is accommodated by crystallization of minerals from the magma. Behaviour of elements during this process is described by the relationship:

$$Cm_i = Co_i(F^{-z}) + rCa_i/(r+D_i+1)(1-F^{-z}) \qquad (3.1)$$

TABLE 3.5 Compositions of primary magmas used in modelling (Co)

	Starting Compositions			Target Compositions			
	AUK	ADK	HMT	EHMT	ET1	ET2	THMT
Nb	0.8	0.81	1.61	15.56	5.55	9.82	4.99
La	0.82	1.82	1.83	19.84	6.8	9.84	4.59
Ce	2.04	4	5.07	42.1	17.85	25.54	12.58
P	44	218	218	567	611	654	174
Nd	1.76	2.3	4.48	21.48	13.53	15.85	9.2
Zr	20	18.2	29	115	113	112	64
Hf	0.42	0.49	0.93	3.11	3.24	2.91	1.7
Sm	0.74	0.62	1.34	4.27	4.03	4.41	2.4
Eu	0.32	0.23	0.48	1.42	1.32	1.51	1.32
Ti	1978	1678	3375	8931	10310	9590	3896
Gd	1.03	0.78	1.83	4.02	5.35	4.95	2.76
Yb	0.79	0.43	1.44	1.39	3.69	2.22	1.2
Sc	28	nr	47	22	44	44	20
Cr	3113	5200	1790	936	71	90	1180
Ni	1267	1640	333	781	-	63	-
Epsilon Nd	+2, +5	+2, +5	+2, +5	-2	1	-	-

AUK = Al-undepleted komatiite, samples 31 and 33 of Arndt and Jenner (1986)
ADK = Al-depleted komatiite, sample 5019 of Jahn et al. (1982)
HMT = Norseman high-MgO basalt sample AB372682
EHMT = Norseman enriched high-MgO tholeiite, sample 99934
ET1 = Norseman Enriched tholeiite GSWA99941
ET2 = Norseman enriched tholeiite S657-19
THMT = Norseman transitional enriched high-MgO tholeiite AB 213755
nr = not reported

Table 3.6 Contaminant compositions used in modelling (Ca)

	Tholeiite	AGW	BCC	AUC	ATC	NWEG	NWCDG	GG	AG
Nb	2.1	6	11			9	2	5	6
La	2.33	17	16	20	15	56	13	22	36
Ce	6.45	33	33	42	31	96	29	44	69
P	349	218	829	nd	nd	393	393	786	611
Nd	6.17	17	16	20	16	47.6	nr	18.5	30
Zr	49	113	110	125	100	164	108	202	193
Hf	1.8	2.8	3	3	3	6.16	nr	3.6	3.8
Sm	2.21	3.1	3.5	4	3.4	6	nr	3.3	4.4
Eu	0.87	1.1	1.1	1.2	1.1	0.95	nr	1.18	1.09
Ti	5287	3117	5395	5000	6000	1439	1439	3237	2038
Gd	3.41	3.2	3.3	3.4	3.2	nr	nr	202	193
Yb	2.35	1.6	2.2	2	2.2	0.75	nr	1.2	0.76
Sc	44	16	30	14	30	3.25	nr	nr	nr
Cr	273	1	185	180	230	5	2	88	32
Ni	100	95	105	105	130	3	4	58	20
epsilon Nd	2	-2, -4	-2, -4	-2, -4	-2, -4	-2, -4	-2, -4	-2, -4	-2, -4

Tholeiite = Norseman tholeiite sample CN380911
AGW = Archean greywacke KH44 of Taylor and McLennan (1985)
BCC = Bulk continental crust of Taylor and McLennan (1985); P from Weaver and Tarney (1984)
AUC = Archean upper crust of Taylor and McLennan (1985)
ATC = Archean total crust of Taylor and McLennan (1985)
NWEG = average of 87 external granitoids from the Norseman-Wiluna belt, Cassidy et al. (1991). Nd, Sm, Eu, Yb, Hf, Sc from Watkins and Hickman (1990)
NWCDG = crustally-derived granitoid gneiss from the Norseman-Wiluna belt, Cassidy et al. (1991)
GG = Granulite gneiss of Weaver and Tarney (1981), approximates Archean lower crust
AG = amphibolite gneiss of Weaver and Tarney (1981)
nr = element not reported

where Cm_i = the concentration of element i in the melt, Co_i = the concentration of element i in the primary melt (starting composition), Ca_i = the concentration of element i in the assimilant, F = melt fraction = (mass of fractionated magma)/(mass of the primary magma), D_i = bulk distribution coefficient for element i between fractionating minerals and the melt, r = assimilation/crystallization ratio = (mass of assimilant added)/(mass of crystals removed), and z = (r+D-1)/(r-1) [DePaolo, 1981].

The second approach is where assimilation occurs deep in the crust, and is followed by fractional crystallization at shallower levels. In this scenario, wallrocks of the lower lithosphere may be very close to their fusion temperatures, in which case little heat from the magma is required for assimilation of material. Thus, significant assimilation could occur without concomitant fractional crystallization. Fractional crystallization would occur later, when the magma began to solidify at upper crustal conditions. This model theoretically allows for a greater proportion of assimilation than in the assimilation + simultaneous crystal fractionation model. The equation governing element behaviour in this situation is:

$$Cm_i = (Co_i(1-P) + Ca_i(P))F^{Di-1} \qquad (3.2)$$

where P = proportion of assimilation = (mass of assimilant added)/(mass of primary melt), and other variables are as previously defined. In this model, element concentration before the onset of crystallization is strictly a mass balance relationship between the primary melt, contaminant, and the proportion of assimilation. Therefore, this equation also describes the case of mixing of magmas (Sun et al., 1989).

Elements used in the modelling are shown in Tables 3.5-3.7, and were selected to represent the HFSE, REE and highly compatible trace elements (Cr, Ni) that have been established as relatively immobile through post-magmatic alteration and thus preserve magmatic interelement ratios.

Mineral phases considered are those that are most likely to dominate fractionation processes in high MgO magmas: olivine, orthopyroxene, clinopyroxene and spinel. Plagioclase was not considered, as the MgO contents of the komatiitic primary melts are too high, such that olivine or pyroxene crystallization is predominant. Partition coefficients of each element in these minerals is given in Table 3.7.

Proportions of fractionating mineral phases for komatiite starting compositions were taken as olivine:spinel = 95:05 (Takahashi and Scarfe, 1985), and for HMT starting

TABLE 3.7 Selected partition coefficients for mineral phases

Element	Perovskite		Garnet		Clinopyroxene[3]	Olivine[9]	Orthopyroxene[3]	Spinel[3]	Plagioclase[12]
	Ca[1]	Mg[1]	pyrope[3]	majorite[6]					
Nb	1.4	1	0.005[4]	0.1[1]	0.05	0.01[3]	0.01[4]	0.01[4]	0.01
La	3.8	0.1	0.01	0.09	0.054	0.005	0.002	0.01	0.1
Ce	4*	0.12*	0.02	0.095*	0.098	0.005	0.003	0.01	0.08
P	0.55[2]	0.55[2]	0.15[5]	0.53[2]	0.5[2]	0.03[10]	0.01[10]	0.11[2]	0.01
Nd	4.6	0.2*	0.08	0.16*	0.21	0.005	0.007[4]	0.01	0.07
Zr	5	9	0.25[4]	0.46	0.2[7]	0.005[4]	0.03[4]	0.05[4]	0.01
Hf	6	14	0.23	0.69	0.233	0.01	0.01	0.05~	0.01
Sm	5.5	0.3	0.22	0.2	0.26	0.005	0.01	0.01	0.06
Eu	4.5*	0.4*	0.32	0.2	0.31	0.007	0.013	0.01	1
Ti	4	3	0.1	0.4[11]	0.1	0.006[3]	0.1[11]	0.15	0.01
Gd	4*	0.6*	0.5	0.26	0.3	0.006	0.016	0.01	0.05
Yb	1.2	2	4.03	1.4[11]	0.28	0.002[3]	0.049	0.01	0.05
Sc					0.03[8]	0.36[8]	4[8]	1[8]	0.017[13]
Cr					15[8]	1.8[8]	2.8[8]	600[8]	0.05[14]
Ni					4[8]	13[8]	6.6[8]	16[8]	0.04[13]

* = REE D value logarithmically interpolated from neighbouring REE. ~ = Hf partition coefficient for spinel assumed equal to Zr partition coefficient. Phosphorus values for perovskite, majorite, clinopyroxene and spinel calculated as $P_{majorite}/P_{bulk\ rock}$ from data of Ringwood et al. (1992).

References: [1] Kato et al. (1988), [2] Ringwood et al. (1992), [3] compilation of McKenzie and O'Nions (1991), [4] compilation of Hawkesworth et al. (1993), [5] Thompson (1975), [6] Ohtani et al. (1989), [7] compilation of Kelemen et al. (1990), [8] compilation of Halleran and Russell (1990), [9] Fujimaki et al. (1984), [10] Anderson and Greenland (1969), [11] compilation of Woodhead et al (1993), [12] compilation of Arth (1976), [13] Lindstrom (1976), [14] D for Cr in plagioclase assumed = 0.05, consistent with value range reported in Ragland (1989).

compositions as entirely clinopyroxene, given the petrographic evidence for significant clinopyroxene fractionation in these rocks, and the lack of evidence for olivine crystallization (section 3.3.3.1). Values of r for each scenario were chosen as 0.01 (approximating pure crystal fractionation with minor assimilation), 0.10, 0.25, 0.50, and 0.98 (assimilant added = crystals removed). F values for each run were set at 0.98 (2% crystallization of the magma), 0.90, 0.80, 0.50, 0.20, 0.10, and 0.02 (98% crystallization of the magma). The entire range of values was considered, even though some combinations are unlikely to occur. Reasonable estimates of r values are ≈ 0.50 (cf. Sun et al., 1989), and reasonable F values are limited by the highly compatible elements Cr and Ni (discussed below).

Isotopes of Nd were also modelled for all permutations and combinations of the above parameters. For primary magmas, ε_{Nd} values of +5, the most primitive values of Al-undepleted komatiites of the Kambalda Domain, and +2 , the average value for tholeiite from Norseman, were used (as data for HMT are not yet available). For contaminants, ε_{Nd} values of -2 and -4 were assigned, and are reasonable values given the interpreted age of older felsic crust below the southern Kalgoorlie and Norseman Terranes (Oversby, 1975; Chauvel et al., 1985; Campbell and Hill, 1988; Claoué-Long et al. 1988; Sun et al., 1989). The equation governing the behaviour of isotopes during crustal contamination processes is different from trace elements and is given by:

$$Em = Eo + (Ea-Eo)[1-(Co/Cm)(F^{-z})] \qquad (3.3)$$

where Co, Cm, F, z are defined previously, Em = ε_{Nd} value of the melt, Eo = ε_{Nd} value of the primary melt (starting composition), and Ea = ε_{Nd} value of the assimilant (DePaolo, 1981).

3.4.7.2. Assimilation accompanied by fractional crystallization

Results of AFC modelling where assimilation is accompanied by fractional crystallization are illustrated in Figs. 3.12-3.15. Only partial results for the basalt, bulk continental crust, granulite gneiss (equivalent to lower crust) and Norseman-Wiluna granitoid (equivalent to partial melts) are presented, as they cover the extreme compositional range of possible contaminants. The results presented on these diagrams can be interpreted by monitoring four independent parameters:

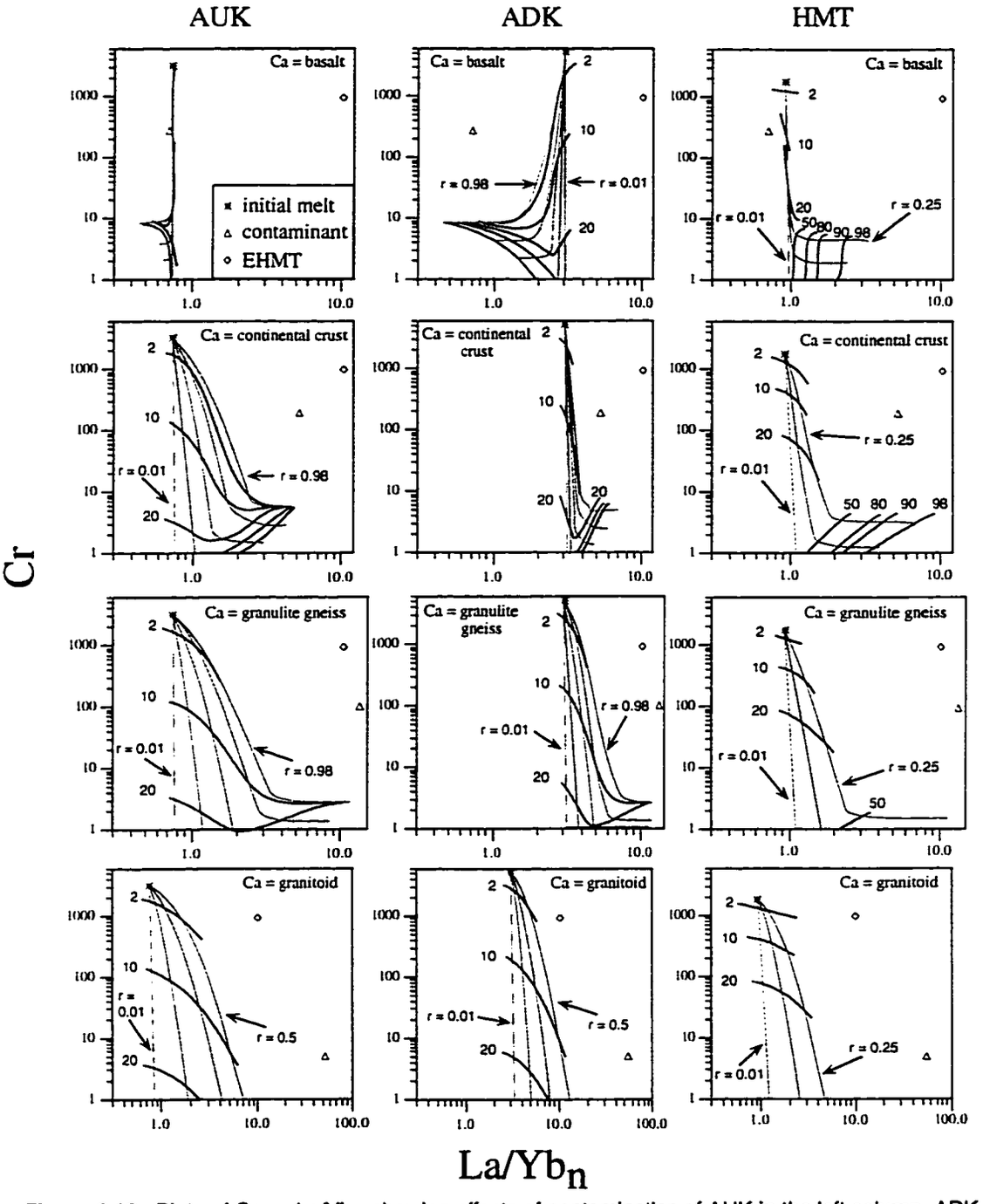

Figure 3.12. Plots of Cr vs. La/Yb_n showing effects of contamination of AUK in the left column, ADK in the centre column, and HMT in the right column. Contaminants are labelled from top row to bottom row. Modelling assumes assimilation with concomitant crystal fractionation (AFC) processes (equation 3.1). Data sources for initial melt and contaminant compositions are given in tables 3.5 and 3.6, respectively. EHMT GSWA 99934 is shown for comparison. Shaded areas represent compositional ranges achieved by model conditions (see text). Fine lines represent values of r ((mass of assimilant added)/(mass of crystals removed)), thick lines represent percentage of original magma mass removed by fractional crystallization. Fractionating phases = olivine and spinel in the ratio 95:05 for AUK and ADK runs, and = clinopyroxene only for HMT runs. See text for discussion.

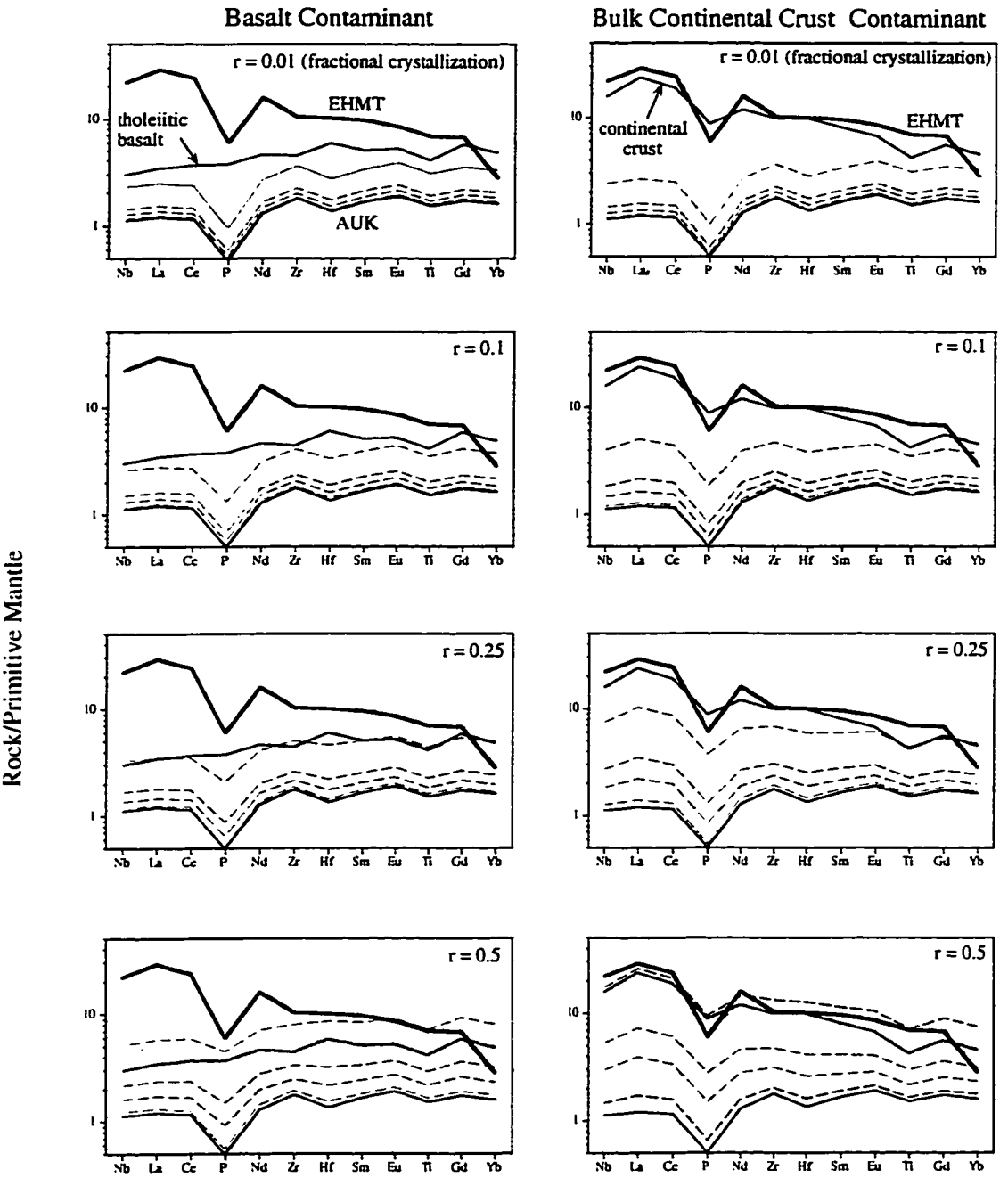

Figure 3.13. Abbreviated mantle-normalized diagrams illustrating results of contamination of AUK by AFC processes (equation 3.1), for r values of 0.01(approximating fractional crystallization only) to 0.5 (mass of assimilant = 1/2 mass of crystals removed). Shaded areas on diagrams represent range of compositions acheived by the modelling for F values of 0.98, 0.9, 0.8 and 0.5 (dashed lines, represents 2 - 50% crystallization of original magma mass. Fractionating phases as for Fig. 3.12.

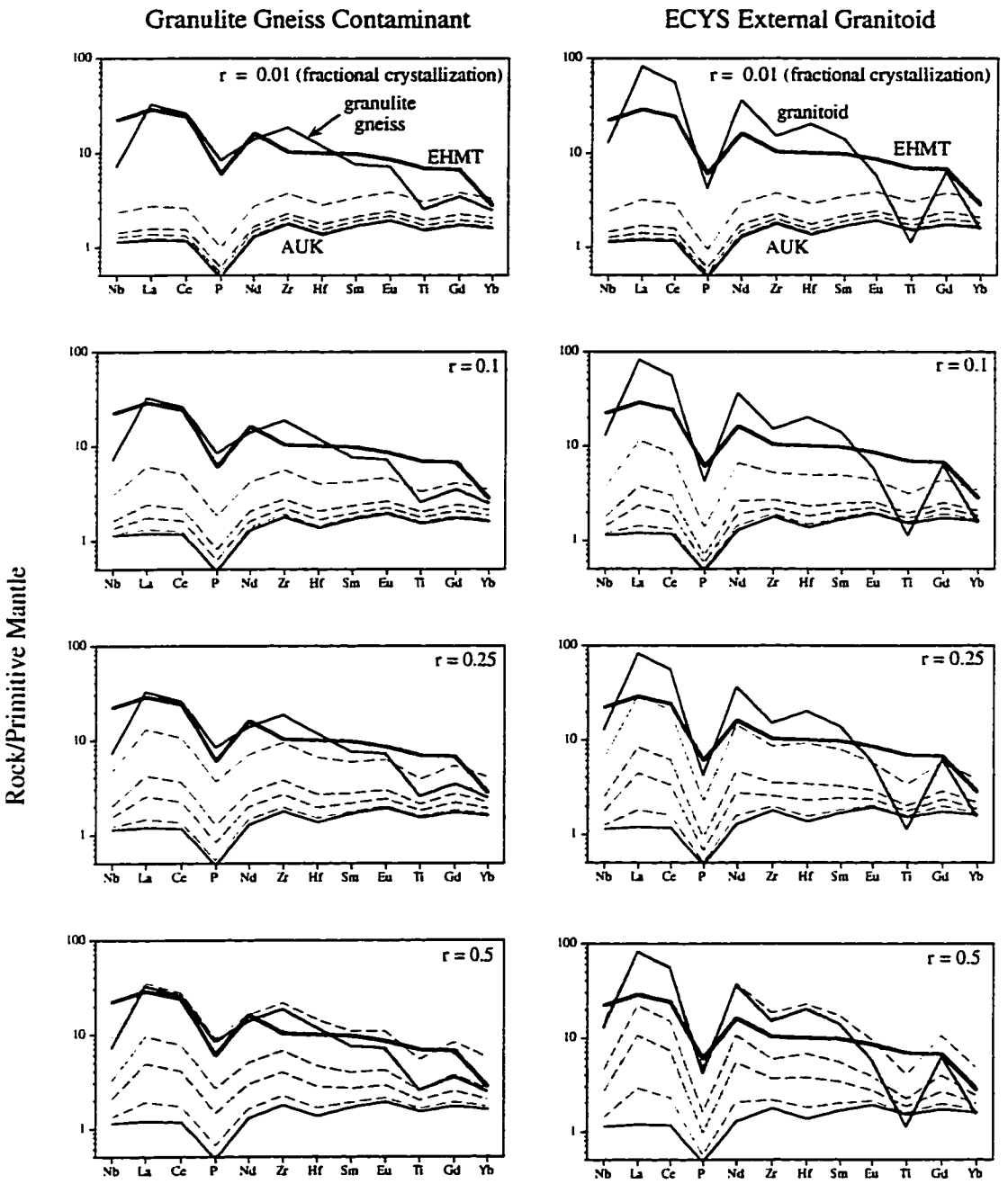

Figure 3.13. (continued)

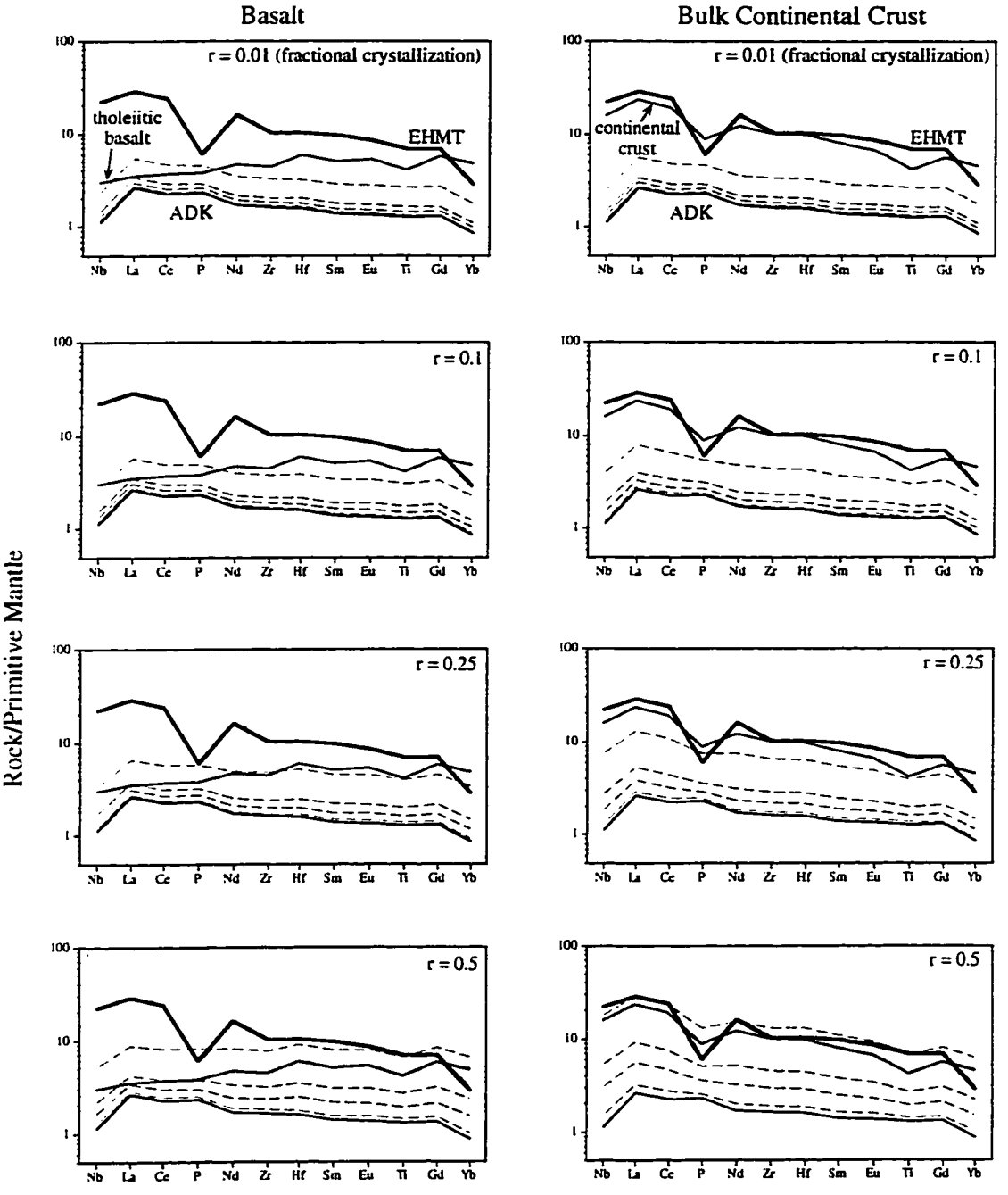

Figure 3.14. Mantle-normalized, in the style of Fig. 3.13, showing the results of modelling of AFC contamination of ADK (equation 3.1).

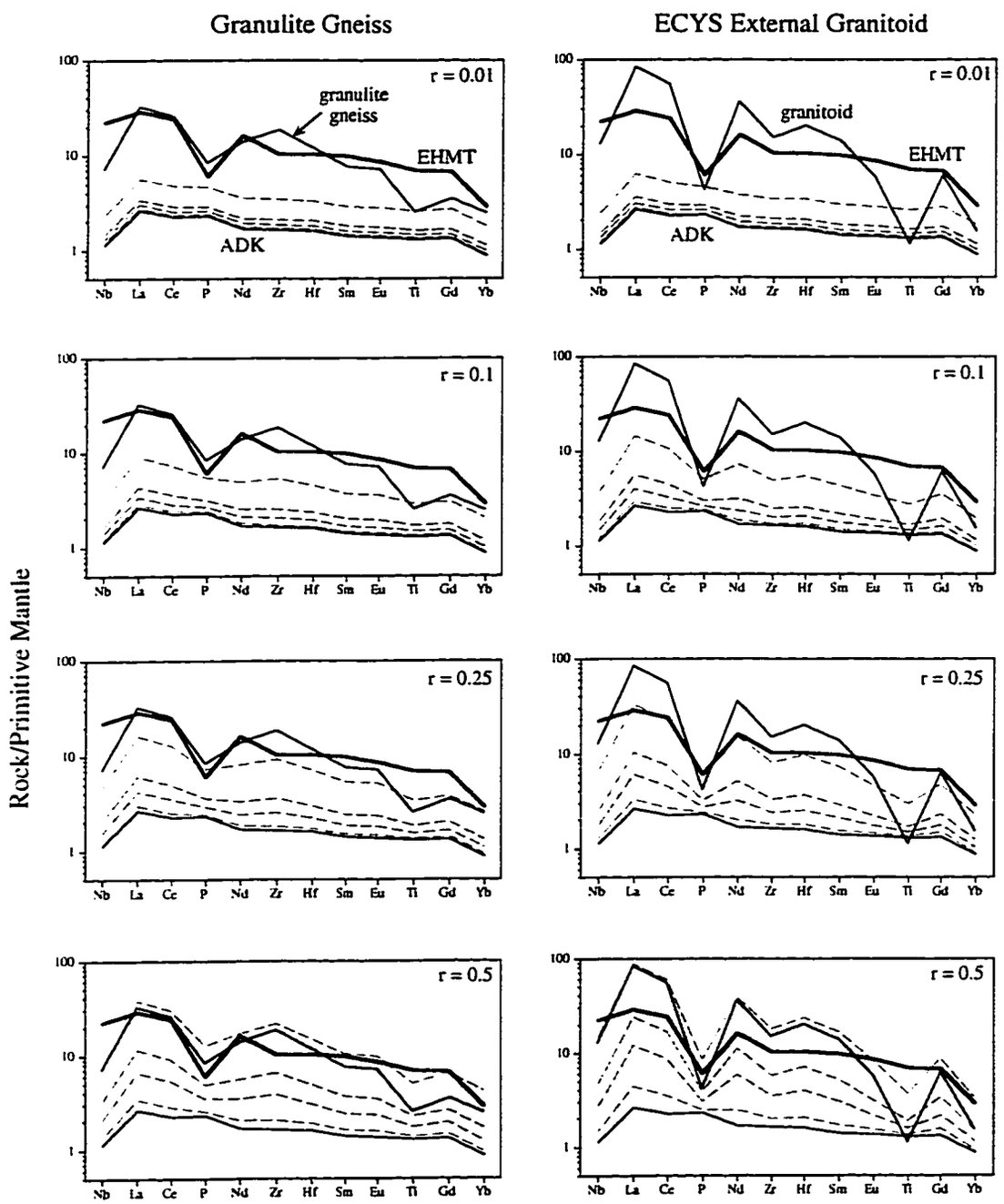

Figure 3.14. (continued).

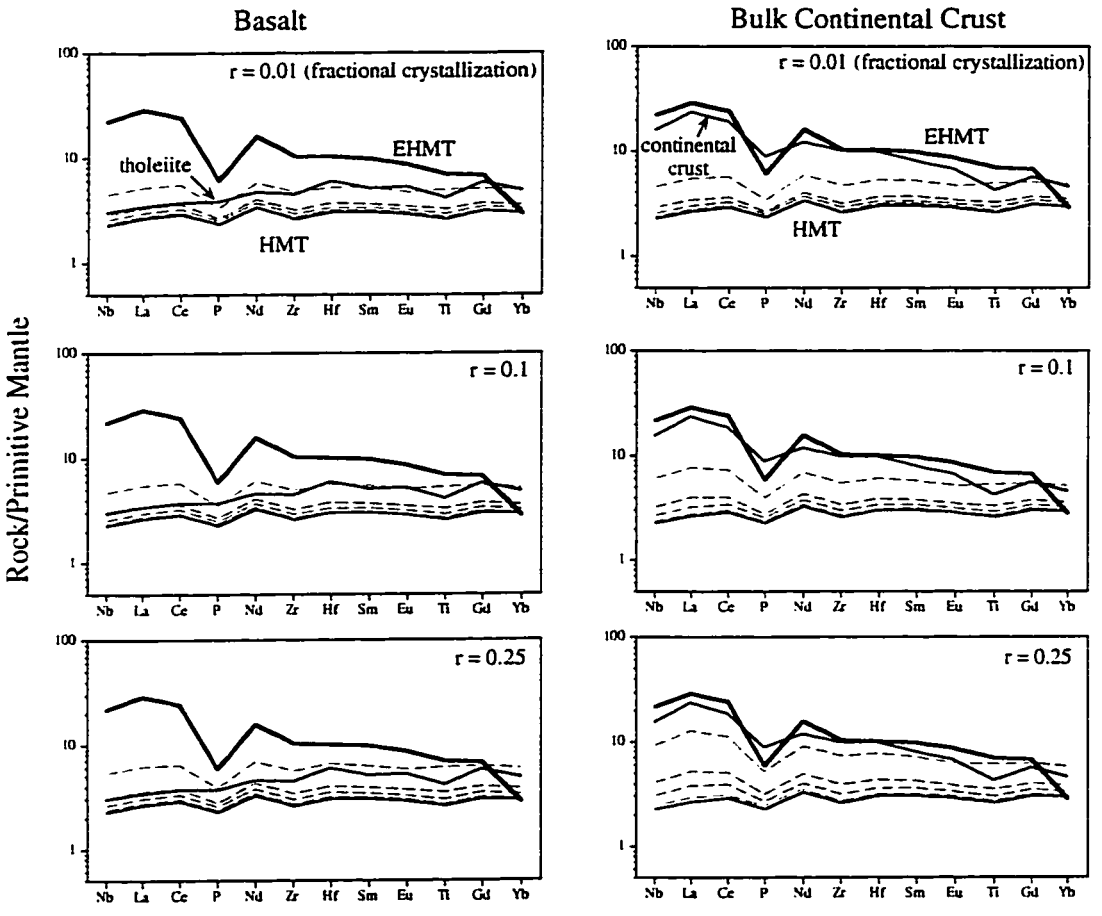

Figure 3.15. Mantle-normalized diagrams, in the style of Fig. 3.13, showing the results of modelling of AFC contamination of HMT (equation 3.1)

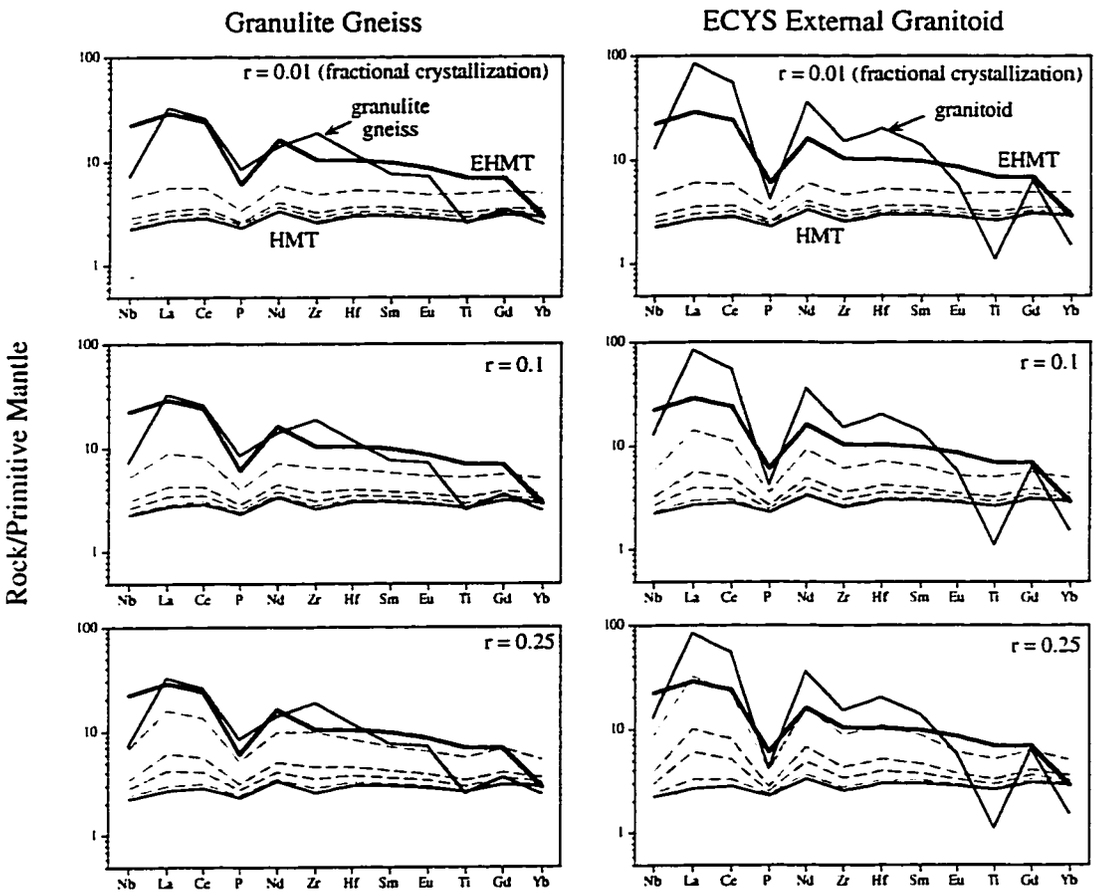

Figure 3.15. (continued)

(1) Cr abundances, which limit the amount of allowable fractional crystallization due to the high D values for Cr in olivine, spinel and clinopyroxene.

(2) La/Yb_n ratios, which monitor the degree of incompatible element enrichment (correspond to slopes of the mantle-normalized multielement patterns).

(3) Gd/Yb_n ratios, which monitor the degree of fractionation of the HREE. These values are only directly available for bulk continental crust and Norseman basalt, but can be interpolated from the mantle-normalized diagrams for the other contaminants.

(4) Fractionation of HFSE from neighbouring REE on the multielement plots.

Consideration of Cr vs. La/Yb_n illustrates that no combination of starting material and contaminant can reproduce the composition of the EHMT (Fig. 3.12). The maximum allowable degree of fractional crystallization during crustal assimilation is limited by Cr dilution to F values > 0.9 , or < 10% crystallization of the original magma mass. Under this constraint, no melts produced can even approach the highly fractionated La/Yb_n of EHMT.

Inspection of Figures 3.13-3.15 confirms these findings in that:

(1) Models which satisfy La and Ce abundances require > 50% crystallization of the primary magma ($F \geq 0.5$), which would excessively dilute the melt in Cr, MgO and Ni. These models also seriously underestimate Nb and Ti abundances, producing large HFSE/REE fractionations that are not observed in the EHMT.

(2) Models which do satisfy Nb and Ti abundances underestimate La, Ce abundances and La/Yb_n values.

(3) All models seriously underestimate Gd/Yb_n values.

As the broadest reasonable ranges of primary melt and contaminant compositions were considered, it is concluded that assimilation of crustal material accompanied by simultaneous fractional crystallization processes cannot have produced the EHMT trace element compositions.

3.4.7.3 Deep assimilation followed by fractional crystallization at higher crustal levels

This model for AFC processes theoretically allows for greater degrees of crustal contamination without concomitant fractional crystallization. Given the results presented in Figures 3.12-3.15, it is evident that only contamination of the ADK starting composition by granulite gneiss or granitoid could possibly emulate the highly fractionated La/Yb_n and Gd/Yb_n values of the EHMT. Results of this modelling are presented in Figures 3.16-3.18. Chromium versus La/Yb_n relationships again limit the

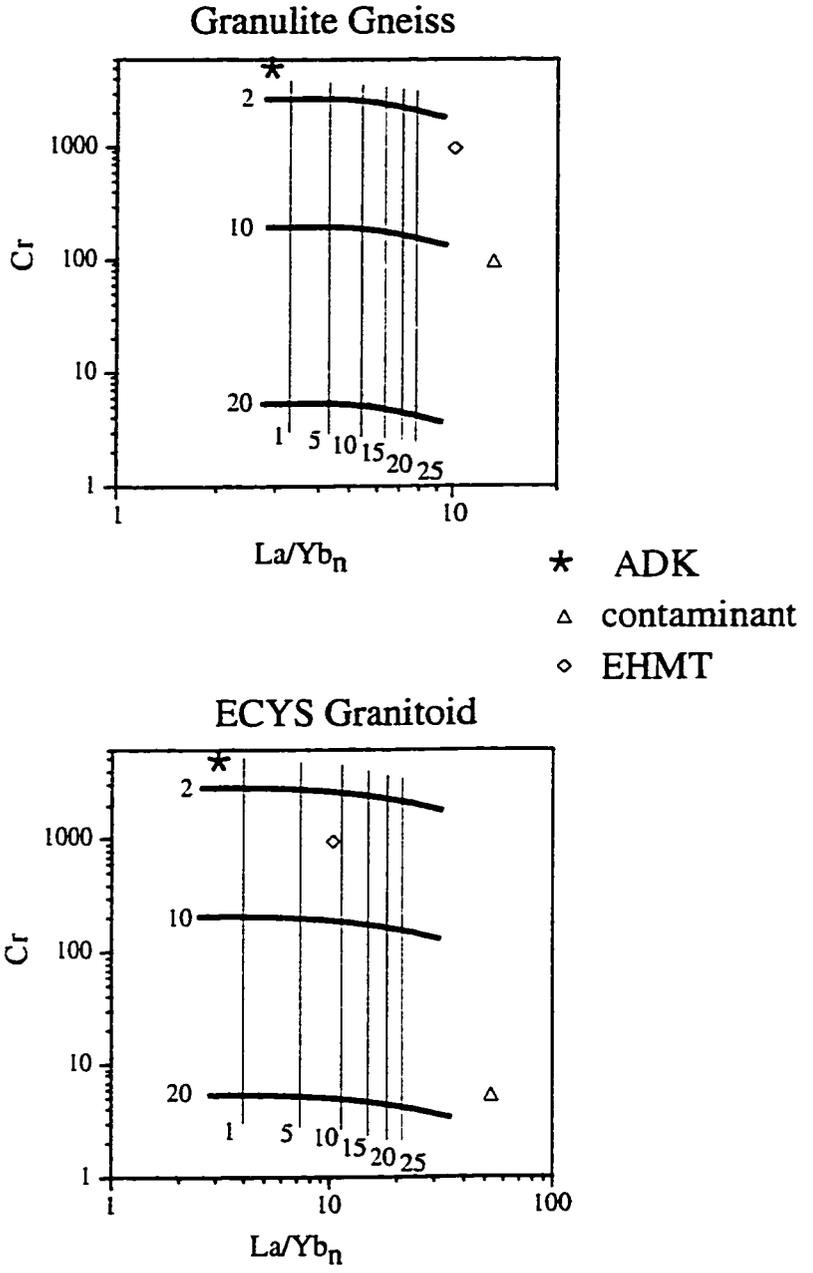

Figure 3.16. Plots of Cr vs La/Yb_n illustrating results of modelling of contamination of ADK by granulite gneiss and granitoid. Modelling assumes that contamination occurs deep in the crust, without simultaneous crystal fractionation, and that crystal fractionation occurs later when the magma has ascended to shallower levels (equation 3.2). Thin lines represent percentage of contamination (in terms of original magma mass), thick lines represent percentage magma mass removed by subsequent fractional crystallization. Fractionating phases are assumed to be olivine + spinel in the proportions 95:05. See text for discussion.

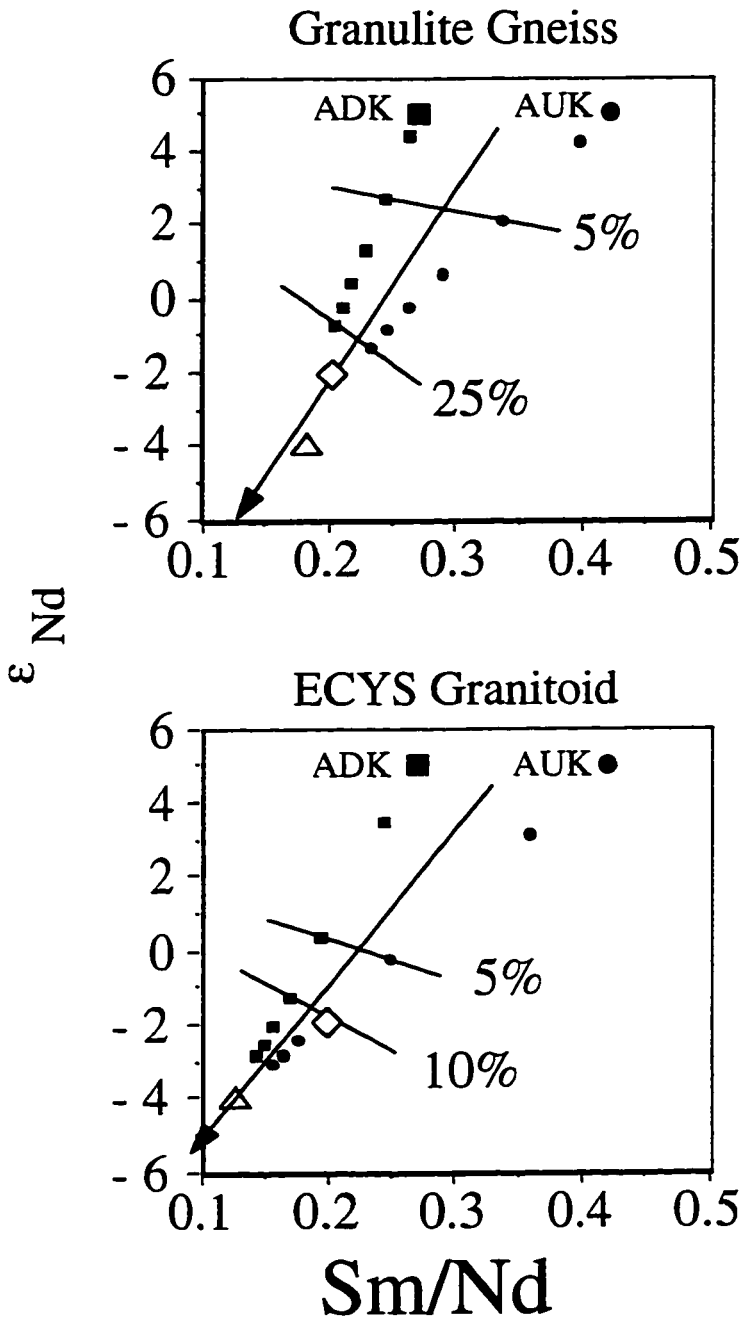

Figure 3.17. Plot of ε_{Nd} vs. Sm/Nd showing results of modelling of contamination of AUK (solid circles) and ADK (solid squares) by granulite gneiss and granitoid (open triangles). Assimilation is assumed to occur deep in the crust without simultaneous crystal fractionation (equations 3.2 and 3.3). EHMT composition is shown for comparison (open diamond). Numbers represent amount of contaminant added, in terms of percentage of original magma mass, and results are shown for 1, 5, 10, 15, 20 and 25%. See text for discussion.

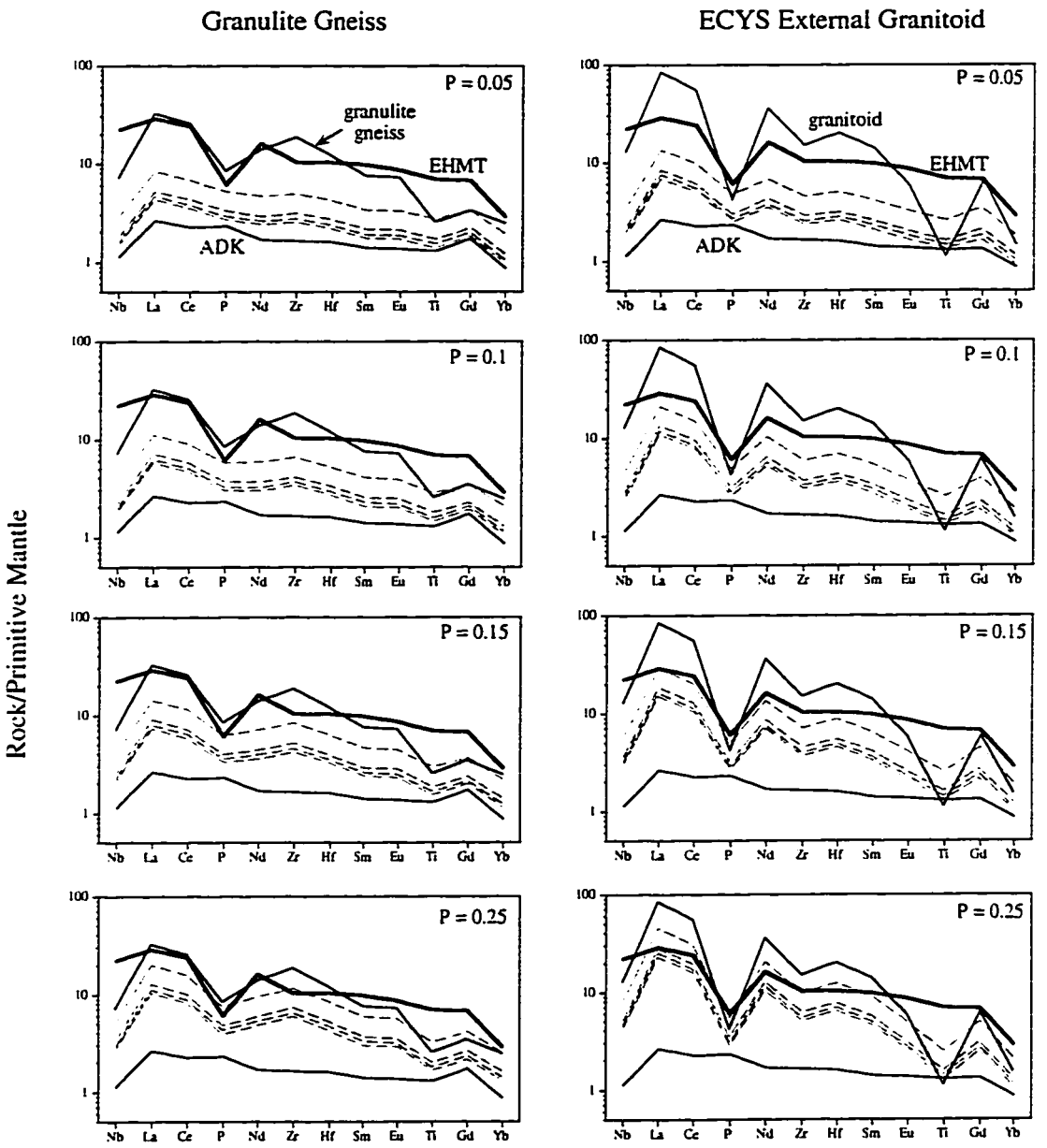

Figure 3.18. Mantle-normalized diagrams illustrating contamination of ADK by granulite and granitoid, for the same boundary conditions as shown in Fig. 3.16. Shaded areas represent compositions achieved by 2 - 50% crystal fractionation of olivine and spinel subsequent to contamination (equation 3.2). See text for discussion.

amount of allowable fractional crystallization to < 10% of the original magma mass, and likely closer to 2%. Inspection of Figure 3.16 reveals that assimilation of > 25% (of the original magma mass, P > 0.25) of the granulite gneiss, or > 10% (P > 0.1) of the granitoid contaminant (or melt equivalent) could possibly create the LREE- enrichment and La/Ybn fractionation found in EHMT. Such degrees of contamination could also account for the negative ε_{Nd} of the EHMT (Fig. 3.17). However, inspection of mantle-normalized trace element patterns (Fig. 3.18) illustrates that at these degrees of assimilation, Nb and Ti values would be significantly underestimated so as to produce large negative Nb and Ti anomalies, which are not observed in the EHMT. Also, resultant Gd/Yb_n values interpolated from these plots would be too low.

3.4.7.4 Summary of crustal contamination modelling

3.4.7.4.1 EHMT genesis

It is concluded from this modelling of trace element behaviour during AFC processes, that no reasonable combination of starting composition and contaminant can produce the combination of extreme incompatible trace element enrichment coupled with the lack of large Nb and Ti anomalies and high Cr and Ni and MgO contents of the EHMT rocks. The LREE enrichment, MgO abundances and ε_{Nd} values of EHMT are similar to those of SHMB (contaminated Al-undepleted komatiites) at Kambalda. However, the following significant differences are noted:

(1) the absolute enrichment of EHMT in HFSE and LREE is larger,

(2) this enrichment is not accompanied by higher SiO_2, as would be expected if significant assimilation of crustal material occurred,

(3) the HREE are strongly fractionated in EHMT (Gd/Yb_n = 2.3 to 2.5) compared to SHMB (Gd/Yb_n = 1.2),

(4) the EHMT also have higher CaO, Cr, Ni contents, and much lower Al_2O_3 contents than SHMB (Table 3.4).

Furthermore, addition of any crustal material to a komatiitic parent should raise the Al_2O_3/TiO_2 ratio of EHMT relative to the parent (Fig. 3.19). All contaminants have Al_2O_3/TiO_2 ratios ≥ 20, whereas Al-undepleted komatiites, characteristic of the southern Norseman-Wiluna belt, have approximately chondritic ratios (Sun and Nesbitt, 1978). Aluminum-depleted komatiites, which have not yet been identifed in the Norseman-Wiluna belt, have $Al_2O_3/TiO_2 \approx$ 10-20 (Figs. 3.10, 3.19; Jochum et al., 1991). EHMT are extremely Al-depleted, with an Al_2O_3/TiO_2 range of 4.0-4.7. This degree of Al depletion could not be achieved without extensive fractionation of an Al-rich phase, which is precluded by the high Cr and Ni abundances in combination with the high MgO

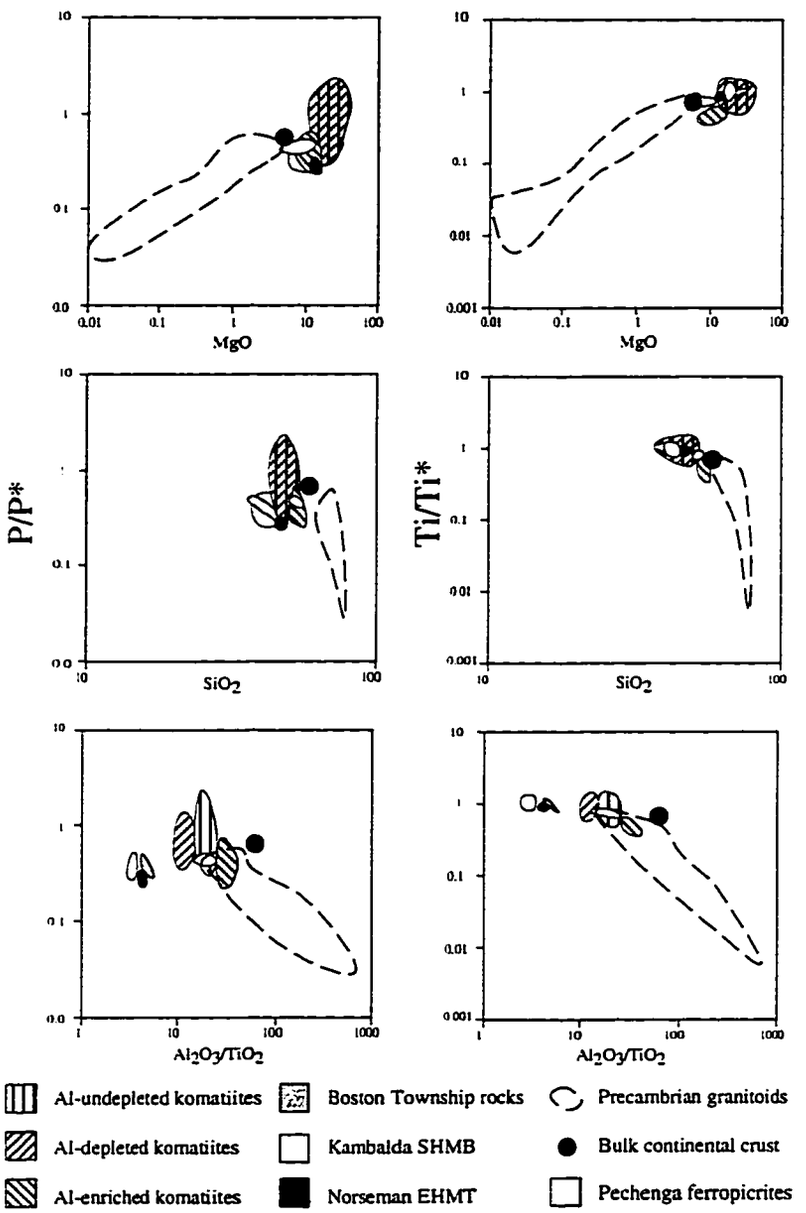

Figure 3.19. Plot of P/P* and Ti/Ti* vs. MgO, SiO_2, and Al_2O_3/TiO_2. The more felsic the material assimilated by a mafic magma, the more extreme the negative P and Ti anomalies, and the more the dilution of refractory elements (MgO, Cr and Ni) that results. Data sources for mafic rock types and bulk continental crust are given in Fig. 3.10, 3.11 and Table 3.4. Data for felsic rocks include Archean felsic intrusions and gneisses from the Norseman Terrane (Perring, 1990), Archean granitoids from the southern ECYS (Cassidy et al., 1991), and average compositions of various granitoid suites from the Abitibi Southern Volcanic Zone and Pontiac subprovinces (Feng and Kerrich, 1992). Modified from McCuaig et al. (1994).

contents of the EHMT.

Accordingly, major and trace element composition of the EHMT, particularly the low Al_2O_3/TiO_2 ratios, strongly fractionated HREE, absolute LREE- and HFSE-enrichments (without increased SiO_2 and diluted Cr and Ni), and the lack of large negative Nb and Ti anomalies cannot be explained by AFC processes alone. Furthermore, the more felsic the assimilant, or the greater the amount of assimilation, the larger the SiO_2, Al_2O_3/TiO_2 and incompatible element enrichment, negative P and Ti anomalies, and dilution of Mg, Cr and Ni that would result (Fig. 3.19). Small degrees of crustal contamination (a few percent) are permissable, as

(1) pre-existing crust has been identified beneath the Norseman area (Chapter 2),

(2) available Pb isotope data for the Woolyeenyer basalts indicates interaction with this older crust (Perring and McNaughton, 1992; Chapter 6), and

(3) minor negative Nb anomalies are present in normalized plots of EHMT, which could result from small degrees of crustal contamination (< 2-5 % from modelling results).

However, it is again stressed that this small degree of allowable contamination cannot account for the trace element and Nd isotope compositions of the EHMT in the modelling presented above (Fig. 3.17). Moreover, there is a distinct lack of high-MgO rocks in the Norseman Terrane representing the less-contaminated volcanic products of a primary komatiitic magma, and a complete lack of ultramafic Al-depleted rocks required by the modelling. Collectively, these data and modelling indicate that the trace element enrichment and Al-depletion of the EHMT is a character of their mantle source and/or melting processes.

The negative ε_{Nd} values of EHMT may be explained by the crustal contamination of a trace element enriched, Al-depleted magma that originally had positive ε_{Nd} values. However, this possibility remaimns unconstrained by the modelling undertaken in this study, inasmuch as no EHMT with positive ε_{Nd} values have been identified.

3.4.7.4.2 ET and THMT genesis

It is also unlikely that the ET and THMT were derived by crustal contamination of high-MgO lavas. Although the degree of LREE enrichment and Gd/Yb_n fractionation observed in THMT can potentially be modelled by large degrees of deep crustal assimilation of an Al-depleted komatiitic magma, the lack of large negative Nb anomalies and the high Cr and Ni abundances in these rocks preclude this as a viable genetic hypothesis.

The ET have lower Cr and Ni contents, and are therefore possible candidates for

crustal contamination processes. The less fractionated trace element pattern and high SiO_2 contents of sample 99941, for example, could represent contamination of Al-undepleted magma by typical Norseman Tholeiite, accompanied by fractional crystallization of clinopyroxene + plagioclase (Fig. 3.8, Table 3.1). However, in order to achieve the absolute abundances of incompatible elements observed in this sample would require an excessive degree of crystallization, or conversely, a melt with enhanced initial incompatible trace element abundances. The high La/Yb_n and Gd/Yb_n of the ET2 samples, however, would still require a trace element enriched, Al-depleted magma (Figs. 3.20, 3.21). In both cases, assimilation of large quantities of more felsic crust is precluded by the lack of large negative Nb anomalies.

Figure 3.20 illustrates the effect of shallow level AFC contamination of EHMT magma by typical Norseman basalt. In all cases, the incompatible element abundances in the contaminated magma are greater than those in EHMT, an effect of concomitant fractional crystallization. As incompatible element concentrations of the ET and THMT are less than those in EHMT, this model for their genesis is not viable.

It is instead proposed that the ET and THMT rocks were formed by variable mixing of two magmas, one approximated by EHMT and the other by HMT, at depth. Figure 3.21 indicates that the Cr contents, and La/Yb_n and Gd/Yb_n values of ET1 are consistent with mixing at depth of an HMT magma with 5-25% EHMT magma, followed by 30-50% fractional crystallization. The ET2 trace element compositions can be approximated by mixing of 20-55% EHMT magma with HMT magma followed by fractional crystallization. Element concentrations of THMT rocks require mixing of 20-75% EHMT magma with HMT magma, followed by <10% fractional crystallization. Normalized trace element patterns produced by this mixing are illustrated in Fig. 3.22, and confirm that this mixing process can approximate the normalized trace element patterns of the ET and THMT, including the Nb concentrations that could not be reproduced with crustal contamination models. The transitional nature of the THMT and ET is also evident from inspection of Figure 3.7, where they plot between the fields of EHMT and HMT + tholeiites.

Therefore, the data and modelling suggest the presence of two end-member magma sources active within the Norseman Terrane during the deposition of mafic volcanics of the Woolyeenyer Formation. One source produced a magma with chondritic to subchondritic Al_2O_3/TiO_2 that was moderately depleted in incompatible elements, of which the HMT dykes are the most primitive examples yet sampled. Products of this source are the tholeiitic basalts and gabbros that constitutes the bulk of the Woolyeenyer Formation. The second source produced Al-depleted, incompatible element enriched

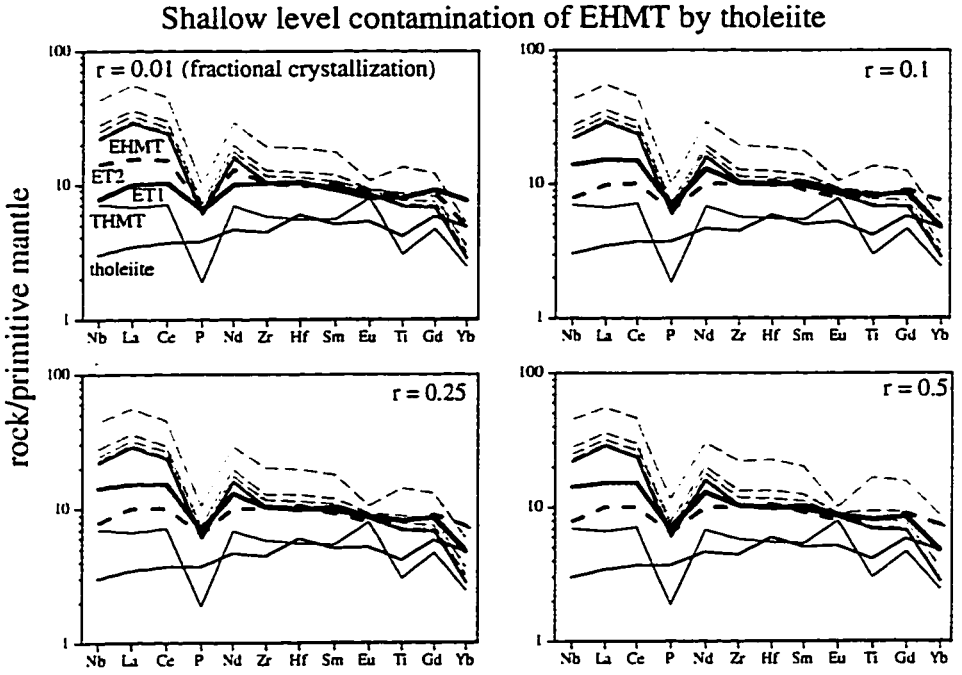

Figure 3.20. Modelling results for contamination of EHMT by tholeiite, assuming AFC processes (equation 3.1). Fractionating phases assumed to be clinopyroxene:orthopyroxene:plagioclase in the proportions 30:30:40. Note that the compositions of the ET and THMT cannot be achieved by shallow level contamination of EHMT by tholeiite, where crystal fractionation accompanies contaminant assimilation.

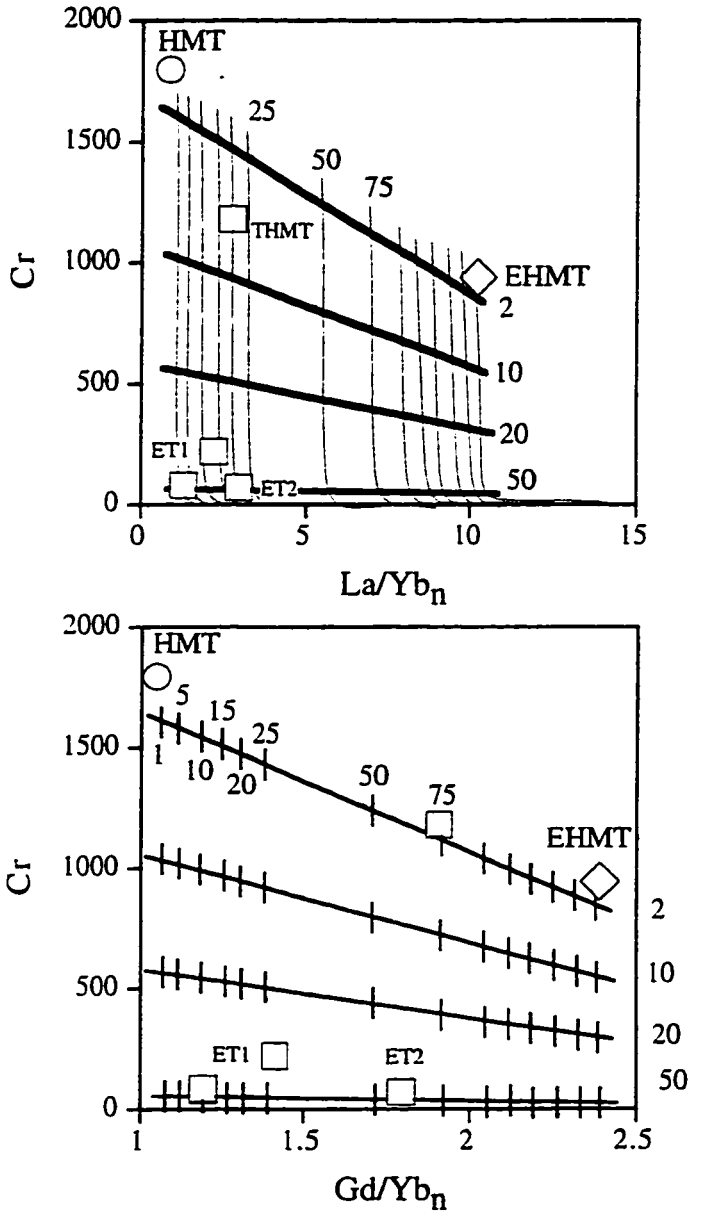

Figure 3.21. Plots of Cr vs. La/Yb$_n$ and Cr vs. Gd/Yb$_n$ showing results of mixing between EHMT and HMT magmas (equation 3.2). Thin lines and notches represent the percentage of EHMT magma added to HMT magma. Thick lines represent the percentage of the magma mass removed by subsequent fractional crystallization of clinopyroxene:orthopyroxene:plagioclase, in the proportions 30:30:50. THMT compositions are consistent with 20-75% addition of EHMT to THMT, with minor subsequent crystallization. The various ET compositions are consistent with 5-50% EHMT magma addition to HMT magma, followed by 40-50% crystal fractionation. Note that this magma mixing could also represent melting of mantle sources with geochemical characteristics transitional to those of HMT and EHMT sources.

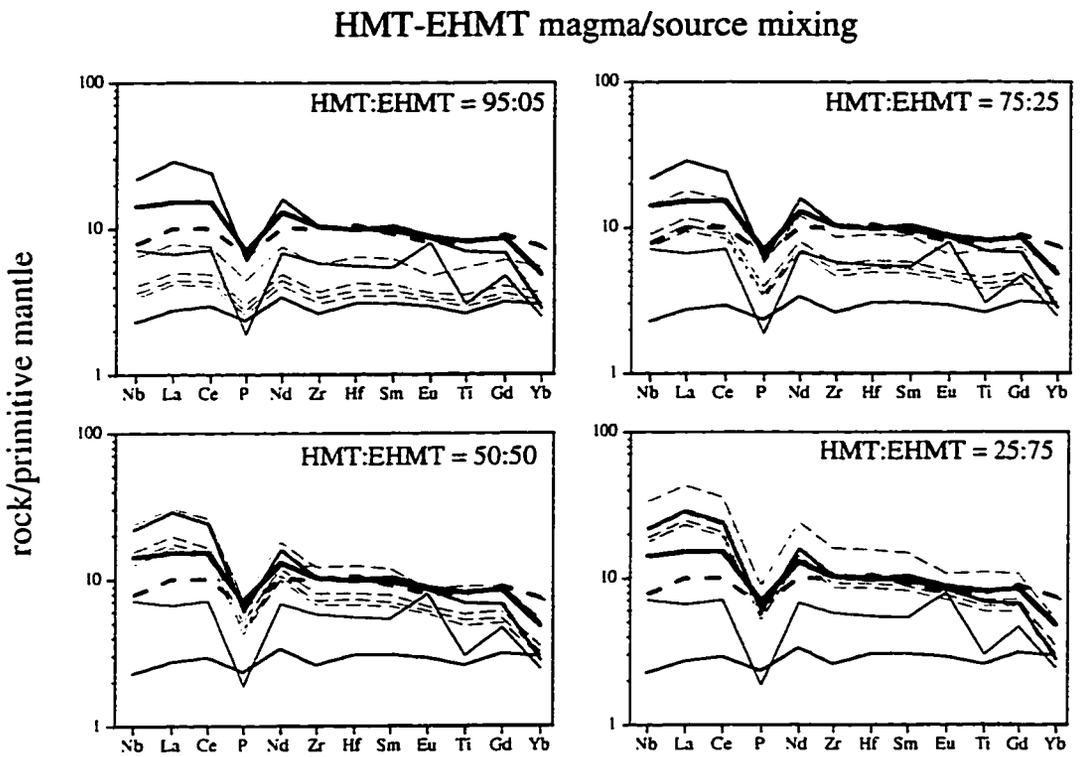

Figure 3.22. Mantle-normalized diagrams showing the spectrum of compositions modelled for HMT-EHMT magma or source mixing. Modelling parameters as for Fig. 3.21.

magmas, of which EHMT are the most primitive examples yet sampled. The geochemistry of the ET and THMT is consistent with mixing of magmas produced by these two sources, or by partial melting of a source with characteristics transitional between the HMT and EHMT sources.

3.5 Characteristics of the HMT and tholeiite magma source

Tholeiites and HMT appear to be cogenetic, in that tholeiite compositions can be produced by fractionation of clinopyroxene and plagioclase from an HMT magma composition. Fractionation of clinopyroxene accounts for the variation in MgO contents between these lithologies (Fig. 3.6). Plagioclase fractionation, which incorporates Al_2O_3 in much greater quantities than TiO_2, may account for some of the variation to subchondritic Al_2O_3/TiO_2 ratios observed in these rock suites, although large degrees of plagioclase fractionation are precluded by the absence of significant Eu anomalies in rocks with lower Al_2O_3/TiO_2. Clinopyroxene fractionation alone accounts for suprachondritic ratios in some HMT samples, inasmuch as clinopyroxene incorporates TiO_2 but excludes Al_2O_3 (Fig. 3.7). It is therefore probable that the primary magmas had approximately chondritic to slightly subchondritic Al_2O_3/TiO_2 ratios.

Trace element patterns of these rock suites are also affected by crystal fractionation. Fractionation of clinopyroxene and plagioclase increases the concentrations of incompatible elements in the residual magma, and fractionate the LREE, producing larger La/Sm_n ratios in the residual magma. For these reasons, the normalized trace element pattern of the mantle source is approximated by the samples that are most depleted in incompatible elements ($La/Sm_n = 0.65$; $La/Yb_n = 0.60$; Fig. 3.8; Table 3.1). Positive ε_{Nd} values for these lithologies indicate that the depletion of these elements in the mantle source occurred in an earlier melting event well before the onset of melting that produced the Norseman mafic lithologies.

These incompatible element depleted mafic lithologies are remarkably common in late Archean terranes worldwide, comprising the bulk of the mafic lithologies in most cases (Sun and Nesbitt, 1978; Arndt and Jenner, 1986; Jochum et al., 1991). These rocks are also similar to mafic lithologies erupted at recent mid-ocean ridges (MORB, Fig. 3.5). Primary melts for such lithologies are derived from the depleted upper mantle, although komatiites are derived from greater depths than recent MORB (Sun and McDonough, 1989). The geochemical characteristics of Norseman tholeiites and HMT are therefore consistent with their derivation from melting of depleted upper mantle, inasmuch as they possess mild depletions in incompatible elements and positive ε_{Nd} values.

3.6 Characteristics of the EHMT mantle source

Whereas the mildly depleted mantle sources inferred for the HMT and tholeiite magmas are typical of the ECYS and late Archean terranes in general, the source of the EHMT is not. This section investigates source characteristics and melting processes that may have operated in the petrogenesis of EHMT magmas. These processes are monitored by a combination of La/Yb_n ratios, which measure the degree of enrichment in incompatible elements, HFSE/HFSE* ratios, which monitor the fractionation of HFSE from REE on mantle-normalized multielement plots, and ε_{Nd} values, which monitor the timing of melting/enrichment events. Particular emphasis is placed on P systematics, as the EHMT have pronounced negative P anomalies, and the behaviour of P in the petrogenesis of mafic lithologies has not been adequately addressed previously.

Processes considered that could produce the EHMT magmas are:

(1) melting of a mantle source that had experienced hydrous metasomatism much prior to melting,

(2) melting of a mantle source that had experienced melt metasomatism much prior to melting, and

(3) retention or fractionation of various minerals during melting or subsequent magma ascent.

During the discussion, comparisons are made to other high-MgO rock suites that display incompatible element enrichments and negative phosphorus anomalies (Table 3.4, Figs. 3.10, 3.11, 3.19).

3.6.1 Mantle Metasomatism

Boninites and Archean mafic shoshonites are high-MgO lithologies which display negative Nb, P and Ti anomalies (Fig. 3.11B), but their MgO, Cr and Ni values are too high to attribute these anomalies to assimilation of continental crust alone. The genesis of these magmas has been ascribed to the mixing of two main components: (1) a refractory mantle source depleted in LREE and other incompatible elements, and (2) a hydrous fluid enriched in LREE relative to HFSE (Cameron et al., 1983; Sun et al., 1989; Wyman and Kerrich, 1989). The concept of preferential transport of REE over HFSE in a hydrous fluid during mantle metasomatism has been well established, and accounts for the characteristic negative Nb, P and Ti anomalies, enrichment of LILE over LREE, and the lack of dilution of refractory elements such as Mg, Cr and Ni in arc basalts (Fig. 3.4; Pearce, 1983; Tatsumi et al., 1986; Weaver, 1991; Maury et al., 1992; Hawkesworth et

al., 1993; Kamenetsky et al., 1995; Pearce and Peate, 1995). However, Norseman EHMT do not show significant fractionation of Nb and Ti from neighbouring REE, thus the possibility of hydrous mantle metasomatism in their petrogenesis is discounted.

The partitioning of HFSE and REE in silicate melts, however, follows the order of incompatibility on normalized trace element diagrams (Fig. 3.4B; Pearce, 1983; Pearce and Peate, 1995). Therefore, during metasomatism of mantle by small volume silicate melts, REE and HFSE may be co-enriched in a manner that produces no fractionation of HFSE from REE, **if** no phases that partition HFSE from REE are retained in the source of the small volume melt. Melt-metasomatized mantle sources have been postulated in the petrogenesis of ferropicrites (e.g. Proterozoic Pechenga region, Hanski, 1992; Hanski and Smolkin, 1995; Boston Township, late-Archean Pontiac subprovince, Stone et al., 1995), which bear marked similarities to EHMT in that they have depleted Al contents, strongly fractionated HREE, extreme incompatible element enrichments, and pronounced negative P anomalies and no significant Nb or Ti anomalies (Table 3.4; Figs. 3.10, 3.11C). The possibility of melt metasomatism in the petrogenesis of EHMT is discussed further in a later section.

3.6.2 Retention or fractionation of a phosphate

Phosphates such as fluorapatite and whitlockite are the most likely repository for P in high-MgO rocks and the upper mantle (Beswick and Carmichael, 1978; Watson, 1980). However, apatite is always one of the last phases to crystallize from a mafic magma, and due to its solubility in mafic melts it is virtually impossible to have apatite as a residual mantle phase during magma genesis (Watson, 1980). Phosphates typically accommodate LREE, and involvement of a phosphate phase should generate correlations between P and LREE. This is not observed in the Norseman EHMT, Boston Township or Pechenga suites, and accordingly, it is difficult to account for negative P anomalies in these high-MgO rocks by invoking the involvement of a phosphate phase.

3.6.3 Retention or fractionation of a P-bearing silicate

Silicates are another possible repository for P in the mantle. In silicate phases, P substitutes for Si in coupled substitutions involving Al, Ti, Na, Ca, and in some phases, cation vacancies (Thompson, 1975; Reid et al., 1976; Bishop et al., 1978; Goodrich, 1984). Phases of interest to this discussion include olivine, orthopyroxene, clinopyroxene, pyrope and majorite garnet, Ca- and Mg-perovskite, and spinel, i.e. the minerals thought to dominate partial melting and crystal fractionation processes in the petrogenesis of high-MgO magmas from 0-25 GPa (0-750 km). Normalized HFSE

anomalies resulting from the involvement of these minerals have been modelled, using the Kd values compiled in Table 3.7, for the following situations:

(1) Rayleigh fractional crystallization (RFC)

$$C_{Li}=C_{Oi}F^{(Di-1)} \quad (3.4)$$

where C_{Li} = concentration of element i in the offspring melt, C_{Oi} = the concentration of element i in the parent liquid, F = the fraction of melt remaining, and D = the bulk distribution coefficient for element i (Shaw, 1970), and

(2) Equilibrium (batch) melting (EBM)

$$C_{Li}=C_{Si}/[D_i(1-F)+F] \quad (3.5)$$

where C_{Si} = the concentration of element i in the source rock, and F is the melt fraction (Shaw, 1970).

Since HFSE/HFSE* values are calculated from data normalized to primitive mantle, C_O and C_S (starting compositions) were taken as primitive mantle, which has no normalized HFSE anomalies. Furthermore, to isolate the effects of individual phases on HFSE/REE and P/REE relationships, it is assumed that only one phase was fractionating or residual, so that D_i values = Kd_i values for the particular phase being modelled. Results of this modelling are presented in Figures 3.23-3.26.

Data on P in these minerals, and mineral-melt Kd's for P, are limited, but available analyses on natural samples and results from experimental charges at 0-25 GPa show that the P contents of olivine, orthopyroxene and spinel are vanishingly small compared to those observed in Ca-perovskite, pyrope and majorite garnet, and clinopyroxene. In all studies the relative partitioning of P into these phases is consistent with Kd in Ca-perovskite > majorite garnet > pyrope garnet > clinopyroxene >>> spinel ≥ orthopyroxene ≥ olivine (Table 3.7; Bishop et al., 1978; Ringwood et al., 1992).

Figures 3.23 and 3.24 show that crystallization of olivine from a melt, or retention of olivine in the source during partial melting, will neither fractionate REE's nor alter

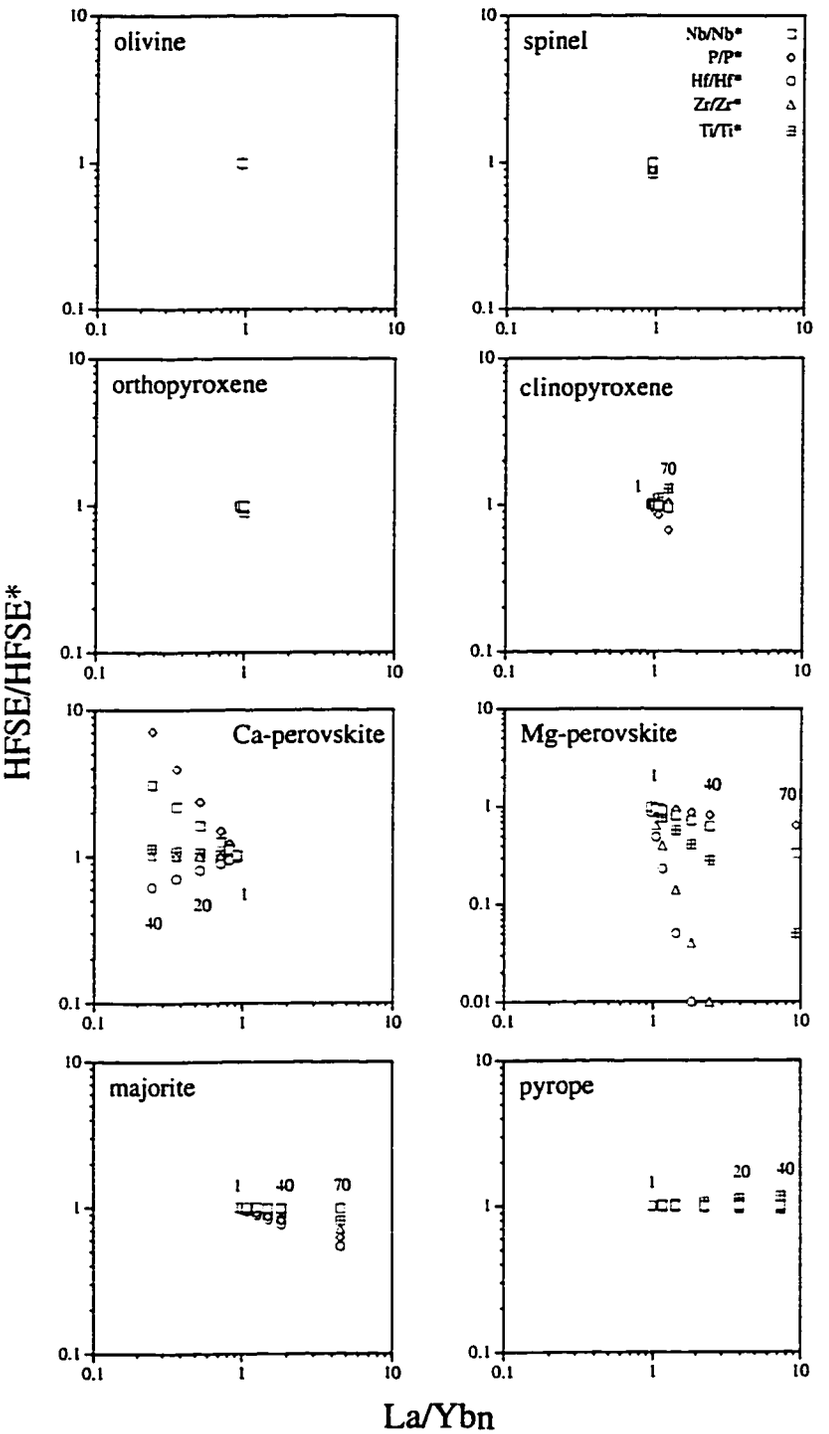

Figure 3.23. Interrelationships between HFSE and REE in melts during perfect Rayleigh fractional crystallization (RFC, equation 3.4) of spinel, olivine, orthopyroxene, clinopyroxene, Ca-perovskite, Mg-perovskite, majorite and pyrope garnet from a melt of primitive mantle composition (HFSE/HFSE* = 1, La/Ybn = 1). HFSE* values are calculated as in Table 3.4. Numbers on the graphs represent the percent of melt that has crystallized, in steps of 1, 5, 10, 20, 30, 40 and 70%. Given uncertainties in Kd values and the assumed RFC, the modelling is approximate. However, asumption of equilibrium crystallization rather than RFC affects the magnitude but not the sense of the HFSE anomalies produced (i.e. positive vs. negative). See text for discussion.

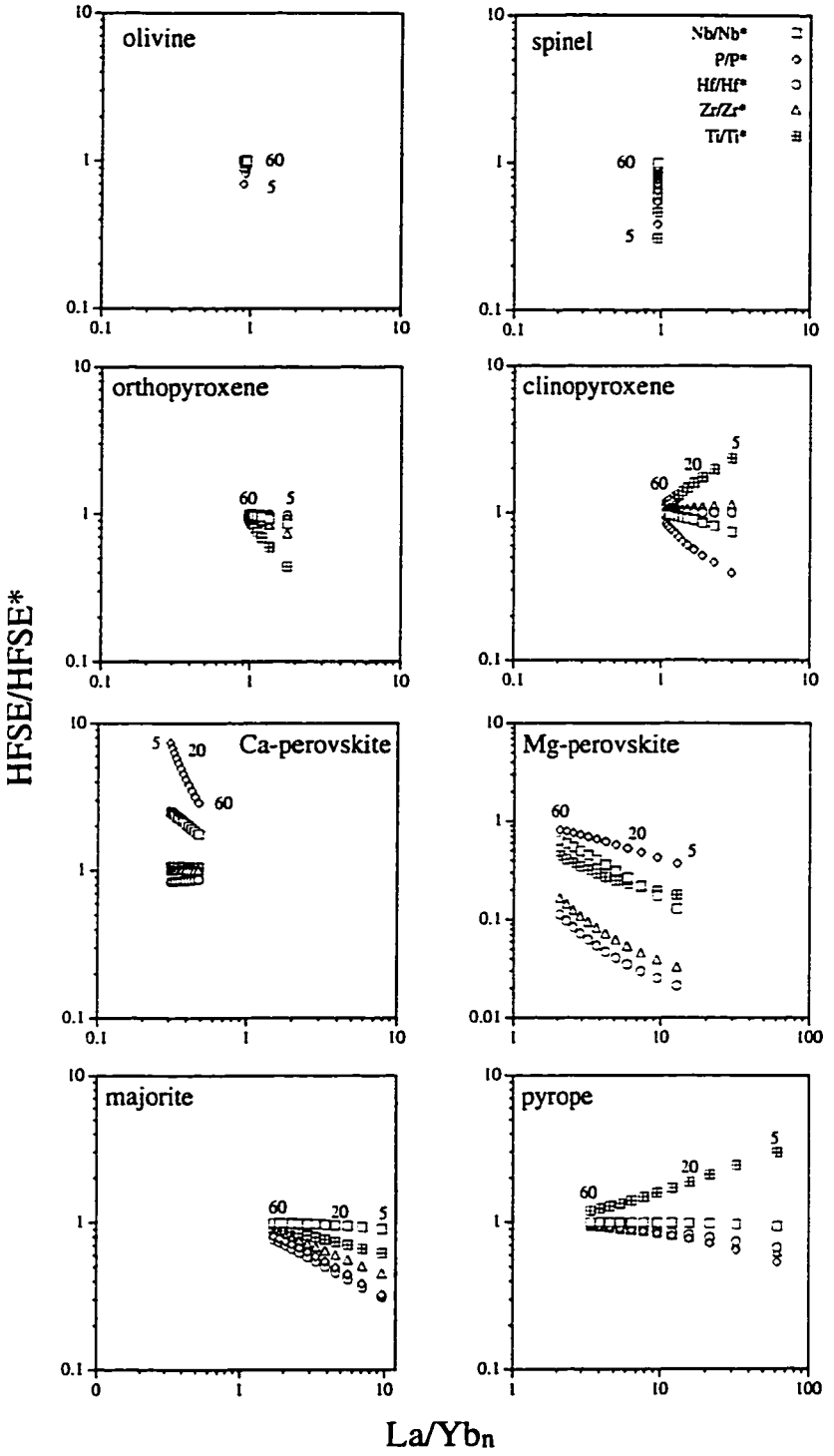

Figure 3.24. Interrelationships between HFSE and REE in melts during equilibrium (batch) melting of primitive mantle (equation 3.5), using a batch size of 5%. Symbols and data sources as for Fig. 3.23, except that numbers on the graphs denote percent melting of the primitive mantle source, in steps of 5%, from 5 to 60%. Modelling is approximate given the uncertainties in Kd values and the assumption that only one phase is residual, and is only designed to isolate the effects of individual phases on the HFSE anomalies produced, not to represent actual conditions during melting. Assumption of accumulative Rayleigh fractional melting rather than equilibrium melting affects the magnitude but not the sense of the anomalies produced. See text for discussion.

HFSE/REE ratios, and thus cannot cause negative normalized P anomalies. This conclusion is supported by the observation that significant P and HFSE anomalies are not observed in rocks where significant olivine accumulation or fractionation has been involved in their petrogenesis, such as MORB, OIB, and some komatiites (Sun and McDonough, 1989; Jochum et al., 1991; Weaver, 1991; Xie et al., 1993). Data on trace element partitioning into orthopyroxene and spinel indicate that these phases incorporate large amounts of HFSE into their structures relative to REE (Kelemen et al., 1990; McKenzie and O'Nions, 1991; Hawkesworth et al., 1993). On the basis of these Kd values, some authors propose that the interaction of melts with orthopyroxene- and spinel-bearing rocks cause the normalized Nb and Ti depletions characteristic of arc basalts (Kelemen et al., 1990). However, only minor HFSE/REE fractionation even after extensive crystallization of these phases from a parental magma is evident in Figure 3.23.

At very low degrees of melting, any negative P anomalies caused by retention of these phases would be accompanied by significant negative Ti anomalies (Fig. 3.24). Covariant Ti and P anomalies are not observed in the Norseman EHMT, Boston Township, or Pechenga rocks. In this context, it is important to note that orthopyroxene, olivine and spinel only partition minute amounts of HFSE and REE, so that any HFSE/REE fractionation caused by these minerals, whether residual in a source or fractionating from a melt, would be overprinted by even minor involvement of clinopyroxene, garnet or perovskite (Table 3.7). Accordingly, orthopyroxene, olivine and spinel are not likely to significantly contribute to the negative P anomalies observed in the Norseman EHMT, Boston Township, or Pechenga rocks.

Ca-perovskite, pyrope garnet, majorite garnet and clinopyroxene are all high pressure phases that can incorporate significant amounts of P into their structures (Thompson, 1975; Reid et al., 1976; Bishop et al., 1978; Exley et al., 1983; Ringwood et al., 1992). No data is available on partitioning of P into the high pressure phase Mg-perovskite. Based on the results obtained for other high pressure phases, it is assumed here that Mg-perovskite also strongly partitions P (Table 3.7). Melts in which clinopyroxene fractionation plays a major role should display only minor normalized P and HFSE anomalies, even after extensive crystallization of the parental magma (Fig. 3.23). These results are in agreement with observations on MORB, OIB and Archean tholeiites and HMT of this study, which show no normalized P anomalies (Figs. 3.5, 3.8; Sun and McDonough, 1989; Weaver, 1991). Melts with clinopyroxene as the predominant residual phase will have negative normalized P anomalies, but there would be concomitant positive Ti anomalies, no Zr or Hf anomalies, and only minor fractionation of LREE/HREE (Fig. 3.24). Furthermore, the primitive mantle source

composition considered has flat normalized patterns. A depleted mantle source, which is common in the Archean, would have initial $La/Yb_n < 1$, making it even more difficult to achieve the La/Yb_n values observed in the Norseman EHMT, Boston Township, and Pechenga rock suites. Furthermore, retention of clinopyroxene in the mantle source does not significantly fractionate the HREE, and cannot account for the Gd/Yb_n values of the incompatible element enriched lithologies. It follows that, whereas it may contribute to negative P anomalies in high-MgO rocks, clinopyroxene alone cannot account for the normalized negative P anomalies in the Norseman EHMT, nor in the Boston Township and Pechenga ferropicrites.

Mg-perovskite may strongly partition P, but it also partitions the HFSE strongly relative to their neighbouring REE, so that resultant normalized HFSE anomalies should be larger than the concomitant P anomaly (Kato et al., 1988). As **pronounced** depletions of **all** HFSE are lacking in the Norseman EHMT, Boston Township and Pechenga ferropicrites, Mg-perovskite fractionation in the mantle source is discounted as the cause of the negative P anomalies in these rock suites. To the author's knowledge, the only experimental data available on P in Ca-perovskite is reported by Ringwood et al. (1992), and indicates that Ca-perovskite can incorporate significant amounts of P into its structure. Ca-perovskite also contains significant amounts of REEs, and fractionates Nb and P relative to neighbouring REE (Kato et al., 1988). However, Ca-perovskite is enriched in LREE and MREE, and magmas with residual Ca-perovskite in their source should show concave downward normalized patterns, large positive normalized Nb and P anomalies, $Gd/Yb_n < 1$ and $La/Yb_n < 1$ (Fig. 3.24); these patterns are not observed in the Norseman, Boston Township, and Pechenga rock suites.

3.6.4 Garnet as a sink for P in the mantle

Garnet is the silicate mineral with the most data available for P. These data, from both natural and experimental samples at pressures ranging from < 2 to 16 GPa, indicate that phosphorous can be incorporated in significant amounts into the pyrope and majorite structures (Thompson, 1975; Reid et al., 1976; Bishop et al., 1978; Exley et al., 1983; Ringwood et al., 1992; Kato et al., 1988). The P data for garnet, together with volume considerations (Thompson, 1975), indicate that the amount of P in garnet increases with increasing pressure, for a given bulk rock composition. These pyrope-majorite series minerals strongly partition HREE, fractionate P relative to Nd, yet do not fractionate Nb, and variably fractionate Zr, Hf and Ti relative to neighbouring REE (Figs. 3.23, 3.24, Table 3.7). As garnet is a solid solution between majorite and pyrope above 5 GPa, with the majorite component increasing with pressure (Ringwood et al., 1992), any partial melt

with a garnet-rich residua, or with significant garnet fractionated from it, would thus:

(1) be LREE-enriched,

(2) have fractionated REE (La/Yb_n and $Gd/Yb_n > 1$),

(3) possess no Nb anomaly,

(4) possess a large negative P anomaly,

(5) possess variably negative Zr and Hf anomalies, and

(6) have potentially a positive, negative or no Ti anomaly.

The magnitudes of the P, Zr, Hf ± Ti anomalies would be dependent upon the garnet composition, and thus the pressure of melting/crystal fractionation (Figs. 3.23, 3.24). Retention of garnet in the source would also deplete the melt in Al, Sc and V (Herzberg et al., 1988; Ohtani et al., 1989; Herzberg, 1992).

The Boston Township and Pechenga ferropicrites have all of these geochemical characteristics, as do the Norseman EHMT, excepting minor negative Nb anomalies in all suites (Table 3.4, Figs. 3.10, 3.11B, 3.25, 3.26). The minor normalized negative Nb may reflect small degrees of crustal assimilation, given that crustal rocks have high La/Nb ratios compared to most mantle reservoirs (Taylor and McLennan, 1985; Jochum et al., 1991). Alternatively, the Kd value for Nb in garnet may be in error. Kelemen et al. (1993) report Kd values for La, Ce and Nb that would produce negative normalized Nb anomalies in melts with garnet residual in the source, thereby corroborating independent evidence for the lack of crustal contamination in the Norseman EHMT, and Boston Township and Pechenga ferropicrites. However, the Kd values quoted in Table 3.7 are used here for purposes of internal consistency among the REE Kd values, and because they are based on consistency in literature surveys rather than a single case study such as that of Kelemen et al. (1993).

Many early-Archean and rare late-Archean Al-depleted komatiites and basaltic komatiites are characterized by the conjunction of low Al_2O_3 contents (Al_2O_3/TiO_2 = 10.5-15.7, CaO/Al_2O_3 = 0.6-2.4), fractionated HREE (Gd/Yb_n = 1.0-1.8), and minor LREE enrichment (ΣREE = 5-29, La/Yb_n = 0.7-4.5). These geochemical features are generally accepted as being caused by garnet retention in the source (Sun and Nesbitt, 1978; Jahn et al., 1982; Herzberg et al., 1988; Ohtani et al., 1989; Herzberg, 1992), a conclusion supported by the modelling of this study (Fig. 3.26). Many of these rocks also possess pronounced negative P anomalies, where P/P* = 0.36-0.49, and P/Nd = 26-33 (Table 3.4, Figs. 3.10, 3.25, 3.26). The evidence for a role for garnet in the petrogenesis of the Norseman EHMT, Boston Township and Pechenga ferropicrites, and other Al-depleted komatiites and basaltic komatiites, combined with theoretical, experimental and empirical evidence on the partitioning of P into mantle phases outlined above,

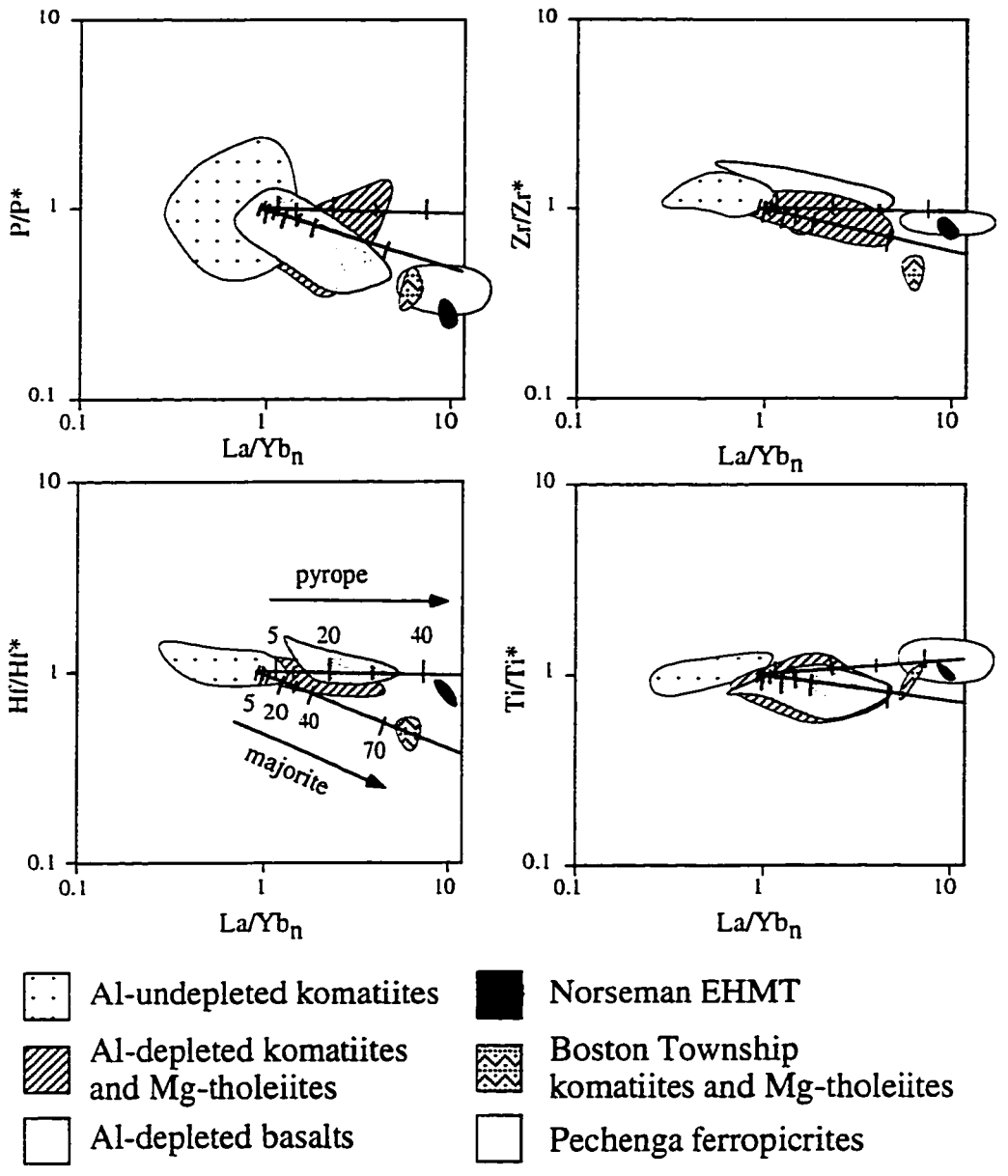

Figure 3.25. Interrelationships between HFSE and REE for Rayleigh fractional crystallization of pyrope and majorite garnet (from Fig. 3.23) as compared to those observed in the Boston Township, Pechenga and Norseman EHMT suites, as well as other Al-depleted and Al-undepleted high-MgO magmas. Data sources listed in Table 3.4. Numbers on the Hf/Hf* graph denote percent of melt that has crystallized. Modified from McCuaig et al. (1994). See text for discussion.

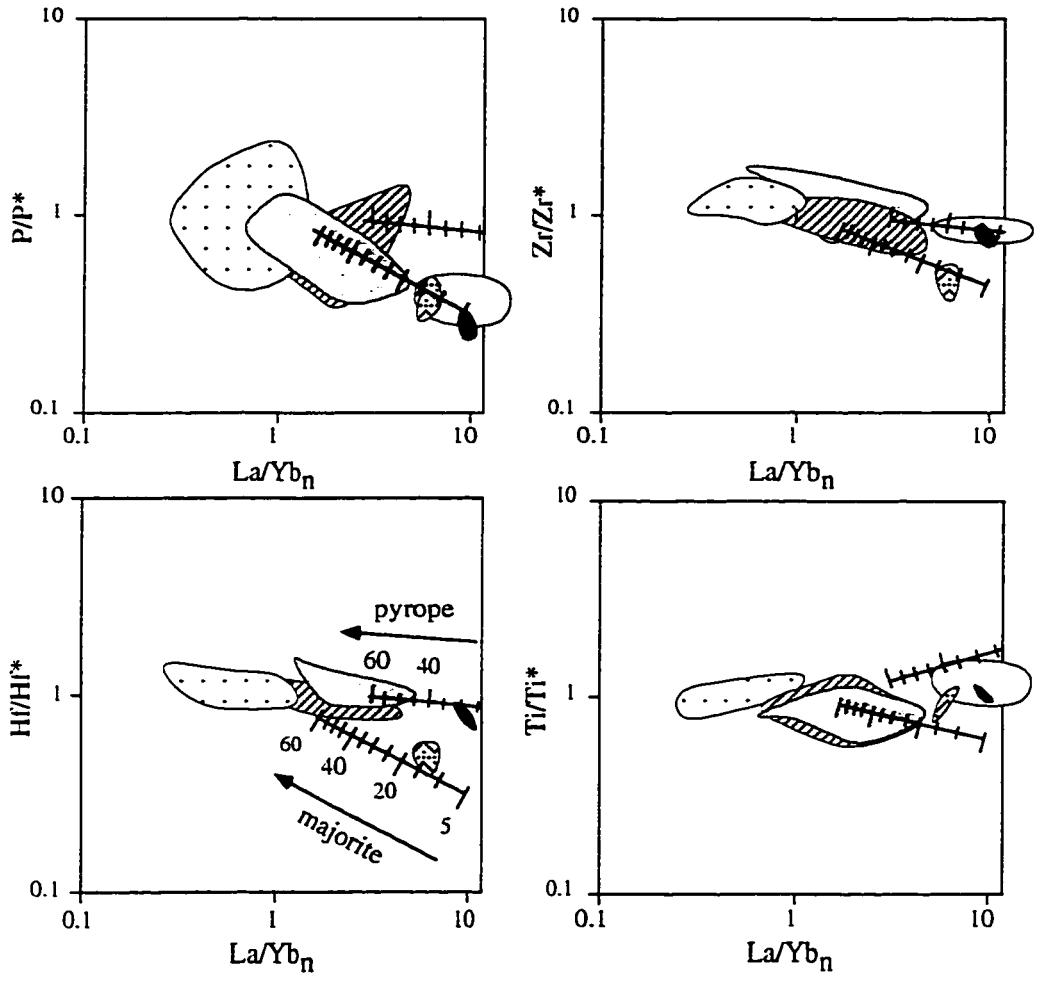

Figure 3.26. Interrelationships between HFSE and REE for pyrope and majorite garnet retention during equilibrium (batch) melting of primitive mantle (from Fig. 3.24) as compared to those observed in various Al-depleted high-MgO rock suites. Numbers on the Hf/Hf* graph denote percent of the source that has melted. Modified from McCuaig et al. (1994). See text for discussion.

collectively suggest that the negative P anomalies are caused by the involvement of garnet in the petrogenesis of these rocks, and that garnet may represent a major repository for P in the mantle.

3.6.5 Depth and mechanism of garnet involvement

Residual garnet in the source of high-MgO magmas, or fractionation of garnet from a high-MgO magma can produce melts with the conjunction of LREE enrichment, fractionated HREE, depleted Al, and negative P, Zr and Hf anomalies without Nb and Ti anomalies. However, in order to produce and preserve the geochemical signatures of the Norseman and Boston Township rocks, garnet must be the dominant fractionating or residual phase controlling REE and HFSE systematics, and the magmas must have little interaction with overlying mantle and crust during diapiric ascent.

Garnet does not appear on the liquidus at pressures below approximately 5 GPa, corresponding to depths < 150 km (Takahashi and Scarfe, 1985), at which point it can begin to significantly affect melt chemistry through crystal fractionation, but at this pressure, phases such as clinopyroxene, orthopyroxene and spinel, may compete with garnet, producing "mixed" geochemical signatures. However, above 8 GPa garnet is the only phase denser than high-MgO melts, and thus the only phase which could effectively separate from a rising melt or upwelling diapir (Herzberg, 1992). Furthermore, between 14-24 GPa majorite garnet is the sole phase on the liquidus (Kato et al., 1988; Ohtani et al., 1989; Herzberg, 1992; Ringwood et al., 1992; Fig. 3.27). To produce the magnitude of the normalized HFSE anomalies and La/Ybn enrichments observed in the Norseman EHMT, Boston Township and Pechenga rocks, over 70 % of the melt must crystallize (Fig. 3.25), a degree of crystallization clearly inconsistent with the observed high contents of compatible elements such as MgO and Cr in these rocks (Table 3.4).

Residual garnet in the source of high MgO magmas would produce normalized HFSE anomalies similar to those produced by fractional crystallization of garnet. However, anomalies observed in the Norseman, Boston Township and Pechenga rocks require only 5 to 30 % melting of primitive mantle (Fig. 3.26). These degrees of partial melting are much more realistic than the >70% crystallization required; thus the preferred model for generation of the normalized HFSE and P anomalies observed in the Norseman and Boston Township rocks is residual garnet in their respective mantle sources, rather than garnet fractionation from a melt or by density separation of garnet in a rising mantle diapir. A combination of these processes is also possible, and would only serve to enhance the Zr, Hf and P anomalies produced. Depending on the bulk composition of the source, garnet may be residual during partial melting at a range of

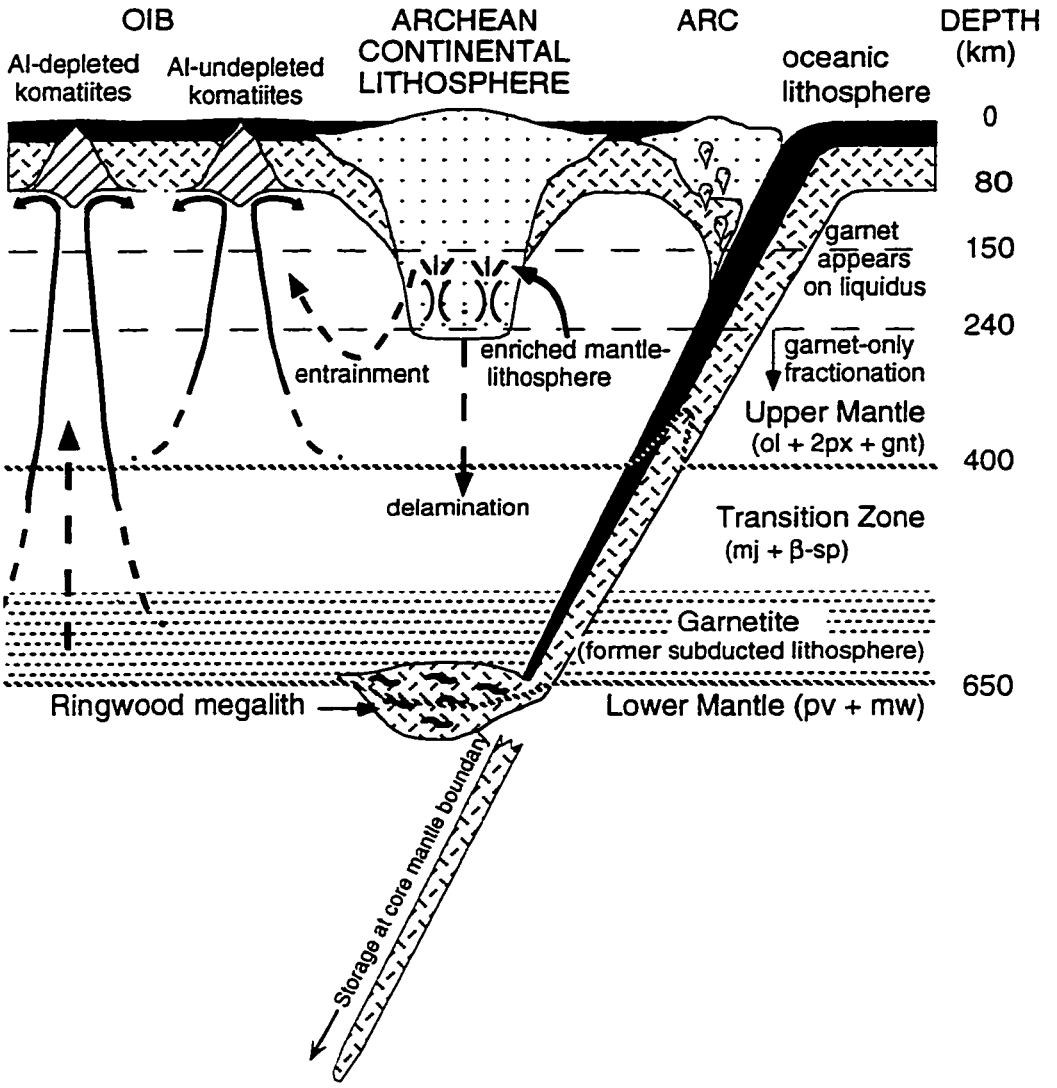

Figure 3.27. Schematic diagram illustrating possible creation, storage, and reactivation scenarios for enriched sources in the Archean mantle. Abbreviations: ol = olivine, px = pyroxene, mj = majorite, b-sp = b-spinel, pv = perovskite, mw = magnesiowüstite. Appearance of garnet on the liquidus after Takahashi and Scarfe (1985); depth of garnet-only fractionation from Herzberg (1992). Storage of subducted material at the 650 km discontinuity or core-mantle boundary, would require development of a mature subduction zone with old, cool, oceanic crust descending. Reactivation of these enriched sources must take place in a mantle plume, with garnet on the liquidus at some stage. Enriched sources in the continental mantle-lithosphere (cf. Menzies, 1990) could be reactivated either by delamination of or entrainment of the enriched source.

pressures from the lower lithosphere throughout the upper mantle, but to produce the distinctive garnet signature, garnet must be the dominant REE and HFSE-bearing residual phase. This would likely occur at > 8 GPa, as discussed above. Deep melting conditions are also supported by elevated Ni contents of Norseman EHMT, and Boston Township and Pechenga ferropicrites, which are comparable to those of some komatiites (Table 3.4), indicating that partial melting may have occurred at high temperatures and pressures, where the distribution coefficient for Ni in olivine is low (cf., Ohtani et al., 1989). Note that the influence of pyrope garnet and majorite garnet can potentially be distinguished by the presence or absence of Zr and Hf anomalies in these rocks. The Boston Township rocks are consistent with the involvement of majorite garnet (distinct negative Zr + Hf anomalies), whereas the Pechenga picrites and Norseman EHMT have only minor negative Zr + Hf anomalies, consistent with the involvement of pyrope garnet (Fig. 3.26). If this interpretation is correct, Zr and Hf anomalies in these rocks serve as indicators of depth of melting: Boston Township rocks, with majorite garnet signatures, melted at deeper levels than Pechenga picrites and Norseman EHMT, which have pyrope garnet signatures. This is the first time that the P/REE and HFSE systematics have been demonstrated as indicators of variable melting depths within the garnet stability field.

From these constraints, production of the distinctive geochemical signatures of the Norseman EHMT, and Boston Township and Pechenga ferropicrites required significant residual pyrope or majorite garnet in the mantle source, involving partial melting at pressures where no significant residual Mg-perovskite, Ca-perovskite, clinopyroxene or any other REE or HFSE-bearing phase caused HFSE/REE fractionations. This must have occurred in a hotter mantle where sources could have been melted at depths where garnet is a significant residual phase. Such anomalously hot conditions can only occur in mantle plumes (cf. Bickle, 1993). These plumes are initiated at thermal instabilities within the earth's interior, likely at the core-mantle boundary or at the 650 km discontinuity (Campbell et al., 1989; Campbell and Griffiths, 1992). The distinctive geochemical signature of the Norseman EHMT, Boston Township and Pechenga rocks, and many other Al-depleted komatiites and basaltic komatiites is common in early Archean rocks, scarcer in late Archean rocks, rare in Proterozoic rocks, and absent in Phanerozoic oceanic basalts. This secular variation in magma geochemistry supports a cooling mantle model, whereby in a younger earth melting could initiate at the greater depths required to retain garnet in the mantle source of plume magmas (Fig. 3.29; Xie et al., 1995).

3.6.6 The argument against garnet involvement, and counter-arguments

Throughout the above discussion, comparisons have been drawn between Norseman EHMT, and ferropicritic magmas of the Boston Township and Pechenga regions, as these rocks all share very similar geochemical characteristics (Table 3.4; Fig. 3.11C). Hanski (1992) considered phase relations in the upper mantle and concluded that the Pechenga and Boston Township primary melts were in equilibrium with either garnet or olivine, but not both, in their mantle sources. As olivine is ubiquitous in the upper mantle, Hanski concluded that these rocks were not in equilibrium with garnet in their mantle source (Fig. 3.28). To account for the enrichment in incompatible elements and elevated FeO_{total} contents in these rocks, Hanski appealed to a mantle source that had been enriched by small-volume silicate melts from underlying mantle, which was then remelted to produce the Pechenga ferropicrites. Hanski and Smolkin (1995) and Stone et al. (1995) then extended this idea to ferropicrites in general. The small-volume silicate melts are strongly enriched in Fe (Kd_{Fe} in olivine $\approx 0.3 * Kd_{Mg}$ in olivine) and incompatible elements relative to their source rocks, and thus enrich the overlying mantle in these elements. Subsequent melting of this enriched mantle source (without residual garnet) is called upon to produce ferropicritic magmas. As the rock suites these workers studied have positive ε_{Nd} values, the enriching event must have occurred immediately prior to ferropicritic magma production, and may have been part of a complex melting process during ascent of a single mantle plume within the mantle (Stone et al., 1995; Figs. 3.27, 3.29).

There are numerous problems with this model, however, and the most pertinent of these are outlined below:

(1) According to the garnet-olivine equilibrium discrimination diagram of Hanski (1992), most Al-depleted rocks of various geological age worldwide are not in equilibrium with garnet + olivine in their mantle source (Fig. 3.28), contrary to the multiple studies which independently verify that garnet is likely residual in the mantle source of these lithologies (e.g. Sun and Nesbitt, 1978; Jahn et al., 1982; Herzberg et al., 1988; Ohtani et al., 1989; Grau et al., 1990; Herzberg, 1992).

(2) There are error ranges associated with the construction of the garnet + olivine equilibrium line in Figure 3.28, which are not indicated by Hanski (1992). As the Norseman EHMT and Pechenga ferropicrites fall very close to the equilibrium line, it is possible that these melts **were** in equilibrium with garnet + olivine in their mantle source.

(3) In a mantle source metasomatized by small-volume silicate melts, Al would be enriched along with Fe and incompatible elements. Elevated Al contents would

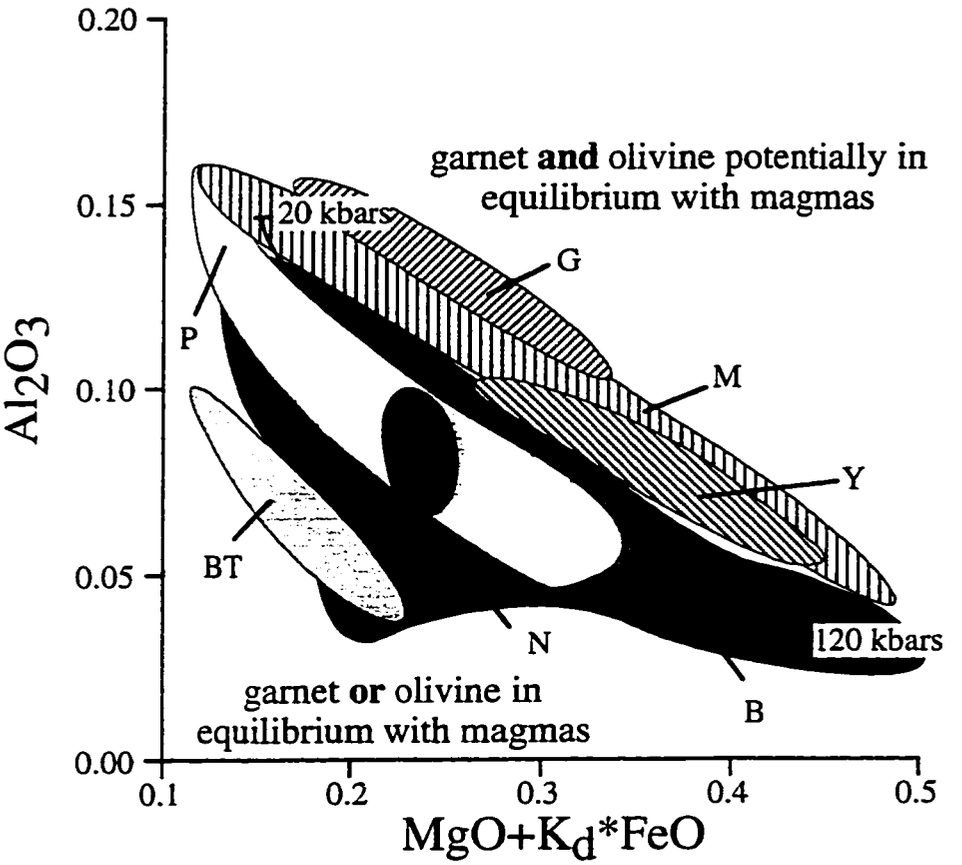

Figure 3.28. plot of mole % Al_2O_3 versus mole % $MgO+K_d*FeO$ diagram for high MgO lithologies, designed to test for garnet + olivine equilibrium in the mantle source. Plot design, garnet-olivine equilibrium line for varying pressure, and all rock fields from Hanski (1992), except EHMT from this study. Hatched fields represent Al-undepleted lithologies, shaded fields represent Al-depleted lithologies. Abbreviations: B = Barberton, BT = Boston Township, G = Gorgona, M = Munro Township, N = Norseman EHMT, P = Pechenga, Y = Yilgarn Craton.

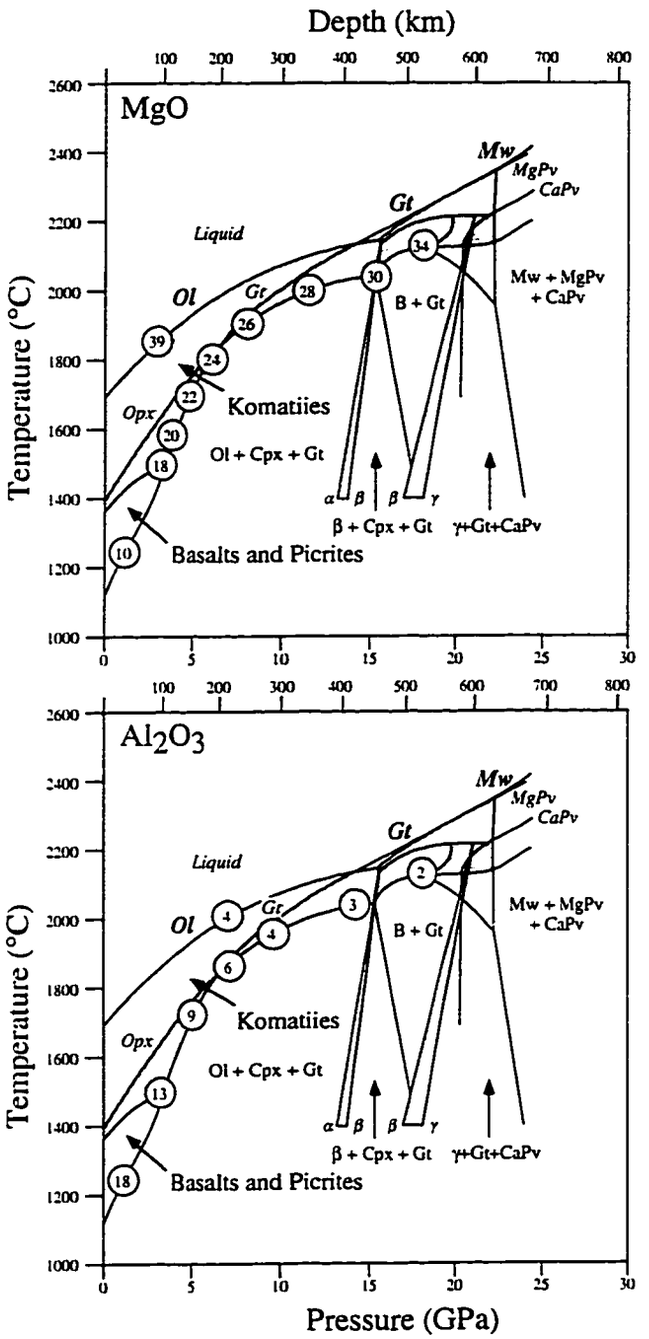

Figure 3.29. MgO and Al2O3 contents of liquids between the solidus and liquidus for a peridotite source with 39wt.% MgO and 4 wt.% Al_2O_3. Shaded region represents komatiite liquids with MgO ≥ 18 wt.% Basalts and picrites are stable at pressures ≤ 3 GPa. From Herzberg (1995). Liquidus minerals in bold italic print, reaction curves limiting the stability of various mantle phases in italic print, and dominant mineral assemblages in plain text. Symbols: Ol = olivine, Opx = orthopyroxene, Cpx = clinopyroxene, Gt = garnet, Mw = magnesiowüstite, MgPv = Mg-perovskite, CaPv = Ca-perovskite, α = olivine, β = modified spinel, γ = spinel. To produce the Al-depleted Norseman EHMT, and the Boston Township and Pechenga picrites, melting must have initiated in the garnet stability field, below 5 GPa, and likely below 8 GPa (see text).

increase the stability field for garnet, which is a major Al-bearing phase in the upper mantle. Such mantle compositions were not considered in the study of Hanski (1992), therefore, Figure 3.28 may not be a valid discrimination diagram for picritic rock types with enrichment in Fe and incompatible elements.

Therefore it is likely that the garnet-olivine equilibrium discrimination diagram constructed by Hanski (1992), although a novel approach to addressing the petrogenesis of high-MgO magmas, is fundamentally flawed in its present form. Aside from these concerns, there are also a number of geochemical characteristics that the petrogenetic model of Hanski (1992), Hanski and Smolkin (1995) and Stone et al. (1995) cannot account for:

(1) Kd values for olivine, orthopyroxene and clinopyroxene presented in Table 3.7 illustrates that it is difficult to strongly fractionate the HREE by small volume partial melting of upper mantle without retaining garnet in the source. Therefore it is unlikely that the Gd/Yb_n values observed in the Norseman, Pechenga, and Boston Township rock suites could be produced by the Hanski (1992) - Stone et al. (1995) models.

(2) Stone et al. (1995) propose that the high Fe contents of the ferropicrites are dictated by the metasomatizing, small-volume, silicate melt, whereas the low Al contents are controlled by the composition of the depleted mantle that was metasomatized. It is possible that incompatible elements are controlled by the metasomatizing melt; however, it is unlikely that one major element (Fe) is controlled by the metasomatizing melt, whereas another (Al) is controlled by the depleted mantle being metasomatized.

In relation to the second point, there is also a mass balance problem: it is unlikely that the Fe content of a small volume melt (say, 1 km^3) will significantly affect Fe concentrations in a much larger volume (say > 100 km^3) of depleted mantle in which Fe is a major constituent. However, if the melt metasomatism is in the form of veins (cf. Wood, 1979; Wilshire et al., 1980), these veins would likely be the first to melt in a later thermal event. In this case, Fe contents of resultant melts could be dictated by the small-volume metasomatizing event, but Al abundances should be co-enriched with Fe.

The only conceivable manner in which the high Fe contents of the ferropicrites can be reconciled with the conjunction of depleted Al contents and strongly fractionated HREE is if the small-volume metasomatizing melt, enriched in Al, stabilized garnet in the metasomatized mantle. This garnet must have been partially retained during subsequent melting to form the ferropicrites.

3.6.7 Petrogenesis of the Norseman EHMT

Norseman EHMT are similar to the Pechenga and Boston Township ferropicrites in terms of their incompatible element enrichment, strongly fractionated HREE, MgO contents, high Ni contents, and strongly depleted Al contents. However, they differ in that the EHMT are not as Fe-enriched. The EHMT have $FeO_{total} < 14$ wt.% (anhydrous), and thus resemble picrites, but are not **ferro**picrites (Hanski, 1992). Norseman EHMT also have negative ε_{Nd} values. The combination of negative ε_{Nd} values and incompatible element enrichment observed in the EHMT cannot be adequately accounted for by crustal contamination of typical komatiites with positive ε_{Nd} values and depleted LREE. These negative values represent either:

(1) crustal contamination of an Al-depleted parental magma derived from a short-term enriched mantle source, as interpreted for the Pechenga and Boston Township komatiites by Stone et al. (1995), or

(2) are a source characteristic, where the EHMT are generated by melting of a long-term enriched mantle source.

If the latter, a time lag between the enrichment of the mantle source in incompatible elements, and subsequent partial melting to produce the EHMT, is necessary to allow the Sm-Nd isotopic system to evolve sufficiently to produce the negative ε_{Nd} values. In this context, the extreme incompatible element enrichment of EHMT, coupled with negative ε_{Nd} values, show marked similarities to some modern enriched-mantle (EM)-OIB (Zindler and Hart, 1986; Sun and McDonough, 1989). Pb, Sr and Nd isotopic data require that the mantle source for many EM-OIB in intraplate environments was isolated for some time between enrichment in incompatible elements and partial melting (Zindler and Hart, 1986; Weaver, 1991 and references therein). However, the present database for Norseman mafic lithologies does not allow resolution of the two petrogenetic scenarios presented above.

If the negative ε_{Nd} values are a source characteristic, it is not known where or when the enrichment in incompatible elements occurred, or where this enriched mantle source was subsequently stored. Extensive trace element and Nd-Pb isotope databases require that many modern EM-OIB contain a component of recycled oceanic crust in their mantle sources. Ringwood (1990) suggested that subducted oceanic crust may descend to the 650-km discontinuity, where density crossovers between pyrolite, harzburgite and basalt cause this subducted crust to be stored in a 70-100 km thick zone. However, there is evidence that some subducted lithosphere penetrates the 650 km discontinuity and is stored at or above the core-mantle boundary (Vidale, 1991; Campbell and Griffiths, 1992; Kerr et al., 1995). In either case, these layers may be subsequently reactivated in mantle

plumes, resulting in the production of incompatible element enriched OIB melts (Fig. 3.27).

Alternatively, Menzies (1990) summarizes evidence for intermittent modification of the depleted continental mantle-lithosphere by small volume, incompatible element enriched asthenospheric melts. The thick subcontinental mantle keel of Archean cratons may promote the preservation potential of these enriched sources (Fig. 3.27). The paucity of EM-OIB in the Archean is, therefore, an important constraint on Archean mantle and tectonic processes, suggesting either that such small volume, enriched melts trapped in the lithosphere were rare, or alternatively that most enriched sources underwent rapid convective dispersal in the asthenosphere. If the geochemical evidence for garnet fractionation in the source of EHMT is valid, then either the Ringwood (1990) model of reactivating subducted material under garnet-stable conditions is possible, or an enriched lithosphere component may have been reactivated near the base of the thick Archean mantle-lithospheric keel (Fig. 3.27).

Crustal formation events ranging from ca. 3.5 to 2.65 Ga are evident in the southern Norseman-Wiluna belt (Chapter 2; Hill et al., 1992 and references therein). The source for the Norseman EHMT may have been enriched during any of these or other events, either by low-degree asthenosphere melts trapped in the mantle-lithosphere, or by storage of subducted crust or delaminated mantle-lithosphere at the 650 km discontinuity or core-mantle boundary. Which of these various enrichment and storage scenarios operated at Norseman cannot yet be determined. However, it remains that an incompatible element enriched mantle or mantle-lithosphere source was produced in the early Archean, preserved, and reactivated ca. 2.7 Ga to produce the EM-OIB-like characteristics of the Norseman EHMT (Fig. 3.27).

3.7 Tectonic setting of the Woolyeenyer Formation

The long-term incompatible element depleted source of the HMT/tholeiites, and the incompatible element enriched source of the EHMT, operated coevally at Norseman. These magmas were also erupted through older continental crust, and appear to have been passively extruded onto this substrate (Chapter 2). These lithologies contain no geochemical signature characteristic of destructive plate margins (cf. Pearce, 1992; Hawkesworth et al., 1993; Pearce and Peate, 1995); therefore, such a tectonic setting for the Wollyeenyer mafic lithologies is dismissed.

The similarity of the HMT-tholeiite association to some modern MORB and ocean plateau sequences indicates either a constructive plate boundary, or intraplate

setting, whereas the similarity of EHMT to EM-OIB and other intraplate mafic magmas, in conjunction with the interpreted retention of garnet in their source, requires a plume origin for these magmas. The HMT-tholeiite and EHMT association may, therefore, represent impingement of an enriched mantle plume onto a constructive plate margin (cf. Iceland, Kerguelen Island), however, the presence of older crust below the Woolyeenyer Formation, and the passive eruption of the lavas onto this substrate, renders this an unlikely scenario.

It is more probable that the HMT, tholeiites and EHMT were all generated during a single plume event. Small volume melts in the hot tail of the plume may have enriched surrounding mantle, which subsequently melted to form the EHMT magmas (cf. Campbell et al., 1989; Kerr et al., 1995). If the enriched source was stored for some time in the convecting mantle, then the EHMT may represent melting in the tail of the plume of enriched mantle material, whereas the HMT and tholeiites result from widespread melting of depleted upper mantle entrained into the head of the plume. Alternatively, if the enriched source was stored in the mantle lithosphere, this source may have been delaminated and entrained into a plume of depleted mantle material, or melted by impingement of a plume of depleted mantle material onto the base of the mantle lithosphere (Fig. 3.27).

3.8 Conclusions

(1) Multiple mafic rock types have been identified within the Woolyeenyer Formation by a combination of major and trace element compositions.

(i) Tholeiitic basalts and gabbros comprise the bulk of the formation, and are characterized by MgO = 4.9-8.4 wt.%, Al_2O_3/TiO_2 = 11.1-23.4 wt.%, flat to slightly depleted mantle-normalized incompatible element patterns with no significant fractionation of HFSE from neighbouring REE (ΣREE = 24-44, La/Yb_n = 0.6-1.1, Gd/Yb_n = 0.9-1.1), and distinctly positive ε_{Nd} values.

(ii) High-MgO tholeiite dykes (HMT) have MgO = 12.5-17.1 wt.%, Al_2O_3/TiO_2 = 14.7-22.4 wt.%, and normalized REE and multielement patterns that mimic those of tholeiites, albeit at slightly lower abundances (ΣREE = 16-28, La/Yb_n = 0.8-1.0, Gd/Yb_n = 1.0-1.1).

(iii) Enriched high-MgO tholeiite dykes (EHMT) have MgO, SiO_2 and Cr contents similar to HMT but with higher Ni contents and extreme Al-depletion, significant enrichment in incompatible elements, fractionated

HREE, moderate negative Nb anomalies and pronounced negative P anomalies (Al_2O_3/TiO_2 = 4.0-4.7, ΣREE = 88-152, La/Yb_n = 9.0-11.0, Gd/Yb_n = 2.3-2.5, Nb/Nb* ≈ 0.57, P/P* ≈ 0.29), and with ε_{Nd} values of -1.9 to -1.2.

(iv) A single transitional high-MgO tholeiite (THMT) has geochemical characteristics between those of HMT and EHMT, with depleted Al_2O_3, incompatible element enrichment and fractionated REE (Al_2O_3/TiO_2 = 6.8, ΣREE = 41, La/Yb_n = 2.5, Gd/Yb_n = 1.9), and a pronounced negative P anomaly.

(v) Incompatible element enriched tholeiites (ET) possess characteristics transitional between EHMT and tholeiites, showing Ti-enrichment, minor Al-depletion, moderate enrichment in incompatible elements and moderate negative P anomalies, (Al_2O_3/TiO_2 = 7.4-13.5, ΣREE = 69-84, P/P* ≈ 0.58, and can be further subdivided into ET1 with moderate REE fractionation (La/Yb_n = 1.2-2.3, Gd/Yb_n = 1.2-1.4) and ε_{Nd} values of -0.2 to +1.0, and ET2 with significant REE fractionation (La/Yb_n = 2.9-3.4, Gd/Yb_n = 1.8-1.9).

(2) The HMT and tholeiites are comagmatic, and positive ε_{Nd} values and incompatible element depletion suggest derivation of these rocks from a similar long-term depleted source. Conversely, detailed modelling and comparison to other mafic rocks types of varied tectonic setting demonstrates that EHMT compositions, with extreme incompatible element enrichment and pronounced negative normalized P anomalies, cannot be generated by (i) post-magmatic hydrothermal alteration, (ii) contamination by continental crust, (iii) hydrous metasomatism of the mantle source, or (iv) fractionation of a phosphorus-bearing phase from the magma, and instead require retention of a phosphorus-bearing phase in the source region of the magma.

(3) Modelling of P/REE and HFSE/REE systematics during partial melting and fractional crystallization processes indicate that the trace element geochemistry of the EHMT and similar suites of high-MgO rocks is consistent with retention of garnet (majorite-pyrope solid solution) in the mantle source, a conclusion supported by their extreme Al-depletion (Al_2O_3/TiO_2 = 4-5) and heavy-REE fractionation (Gd/Yb_n=2.0-2.5). Furthermore, it appears that the magnitude of Hf-Zr anomalies in Al-depleted, high-MgO magmas with fractionated HREE may be an indicator of relative melting depth: pronounced negative Zr, Hf anomalies (e.g. Boston Township komatiites and ferropicrites) indicate the retention of

majorite garnet in the source, and thus were produced at greater depths than those varieties possessing only minor Zr,Hf anomalies (e.g. Norseman EHMT, Pechenga ferropicrites), which indicates pyrope garnet retention in the mantle source.

(4) This is the first study to demonstrate that the P/REE and HFSE/REE systematics of high-MgO magmas can be used to differentiate between majorite and pyrope garnet involvement, and therefore as indicators of melting depths.

(5) Phase relation arguments against garnet retention in the source are found lacking in that (i) aspects of the construction of the garnet + olivine phase equilibrium diagram and the validity of its application to these enriched magmas are questionable, and (ii) these models fail to account for the simultaneous enrichment in Fe, depletion in Al and strong fractionation of HREE in these lithologies. The EHMT and other Al-depleted, high-MgO rocks with similar trace element geochemistry require a mantle source that (i) was enriched in incompatible elements, and (ii) had garnet residual during the melting event that produced the magmas.

(6) Production of the distinctive geochemical signatures of the Norseman EHMT, and similar high-MgO magmas, requires partial melting at temperatures and pressures where garnet is the dominant residual phase in the mantle source, and where no significant residual Mg-perovskite, Ca-perovskite, clinopyroxene or any other REE or HFSE-bearing phase caused HFSE/REE fractionations (ie. between 8 and 24 GPa). Such anomalously hot conditions can only occur in mantle plumes, likely initiated from either the core-mantle boundary or at the 650 km discontinuity. The distinct geochemical signature of the Norseman EHMT, Boston Township and Pechenga rocks, and many other Al-depleted komatiites and basaltic komatiites is common in early Archean rocks, scarcer in late Archean rocks, rare in Proterozoic rocks, and absent in Phanerozoic oceanic basalts. This secular variation in magma geochemistry supports a cooling mantle model, whereby in a younger earth, melting could initiate at the greater depths required to retain garnet in the mantle source of plume magmas.

(7) Generation of the Norseman mafic lithologies requires that incompatible element enriched and depleted sources existed at 2.7 Ga in the mantle source to the Norseman Terrane. The EHMT are the first report of such severely Al-depleted 2.7 Ga lithologies from the Yilgarn Block of Western Australia. Moreover, if the negative ε_{Nd} values are inherited from the mantle source, these rocks also provide the first evidence for preservation of an incompatible element enriched source in the hot Archean mantle or the Archean mantle lithosphere. Modern examples of

coeval operation of diverse mantle magma sources occur in within-plate settings (e.g. Hawaii), or where enriched mantle plumes intersect ocean ridges (e.g. Iceland, Kerguelen). Accordingly, the Norseman mafic rocks may have been formed in an EM-OIB-like setting. As the Norseman basalts were erupted through older continental crust, a plume-related, within-plate tectonic setting is favoured during production of the Woolyeenyer Formation.

CHAPTER 4

SPATIAL DISTRIBUTION AND STRUCTURAL CHARACTER OF THE LODE GOLD DEPOSITS OF THE NORSEMAN TERRANE, WESTERN AUSTRALIA

4.1 Introduction

The genesis of Archean "mesothermal" lode-gold deposits has been the subject of extensive research and debate, particularly within the past two decades. Detailed studies of the large deposits hosted in low- to upper-greenschist facies terranes, such as those at Kalgoorlie (Golding, 1982), Kambalda (Phillips and Groves, 1984; Clark et al., 1989), Hollinger-McIntyre (Spooner et al., 1987) and Kerr-Addison (Kishida and Kerrich, 1987), have characterized these systems in terms of alteration systematics in various lithologies, ore mineralogy, fluid chemistry, metal budgets, and P-T-X_{CO2} conditions of alteration and mineralization. These results have led to the formulation of several genetic models, the most current of which involve:

(1) devolatilization of host greenstones (Groves and Phillips, 1987) or
(2) devolatilization of subcreted/subducted material during regional dynamothermal metamorphism, with mineralization after the metamorphic peak during subsequent uplift of the terranes (Wyman and Kerrich, 1988);
(3) magmatic fluids expelled during the ascent or crystallization of regional granitoid batholiths (Burrows and Spooner, 1989);
(4) devolatilization of the lower crust during granulite facies metamorphism (Cameron, 1988);
(5) degassing of the upper mantle (Fyon et al., 1983; Santosh et al., 1995),
(6) some unspecified combination of models (4) and (5) (Colvine et al., 1988, and references therein), and
(7) deep convection of meteoric waters (Nesbitt et al., 1986; Nesbitt and Muelenbachs, 1989).

Significant deposits exist in higher-grade metamorphic terranes such as the Kolar Schist Belt, India (Hamilton and Hodgson, 1986) and Red Lake, Ontario, Canada (Andrews et al., 1986), but until recently these have been understudied. The past decade

Table 4.1. Characteristics of some high-temperature lode gold deposits hosted by amphibolite facies rocks, with comparisons to giant greenschist facies counterparts in Western Australia and Ontario, Canada

High-Temperature Lode Gold Deposits (Amphibolite-Granulite Facies)

Deposit/Location	Host Rocks	Metamorphism (P,T)	Hydrothermal Alteration (a), b),... denote host rock]	P,T	XCO2	Timing	Sources
Yilgarn Block, Western Australia							
Norseman Terrane, Norseman-Wiluna Belt						Mineralization spans g-schist/amphibolite transition	Golding (1982);
Northern deposits	a) tholeiitic basalts b) high-Mg tholeiites	2-4 kb, 450-575C	a) q, cc, chl, bi, pl(An20-43), sch, tourm	● 3 kb, 420-475 C	>0.09 (projected)	Post-peak metamorphism, syn to late-deformation	McCuaig et al. (1993); this study.
Central deposits	a) tholeiitic basalts b) high-Mg tholeiites	2-4 kb, 500-700 C	a) q, cc, act, bi, pl(An20-65), sch, tourm	● 3 kb, 450-500 C	>0.09 (projected)	Syn to post-peak metamorphism, syn to late-deformation	Mueller (1992); this study; McCuaig et al. (1993).
Southern deposits	a) tholeiitic basalts	2-4 kb, 600-750 C	a) q, cc, di, zo, ksp, act, sch, ga (inner) bi, hb, pl(An35-58) (outer)	● 3-5 kb, 500-600 C	>0.08 (projected)	Syn-peak metamorphism, syn-deformation. Ore cut by pegmatites	McCuaig et al. (1993); this study.
Southern Cross Province							
Marvel Loch	a) komatiites b) gabbro	3 kb, 550-630 C	a) ol, cc, q, di, amph, phl, sch (inner) b) q, di, ga, Ca-amph, pl(>An20), cc, sch	3-5kb, 500-640 C		Post-peak metamorphism; syn-deformation. Ore cut by pegmatites	Ho et al. (1990) Mueller (1988, 1991)
Fraser's	a) mafic rocks b) ultramafic rocks	3 kb, 520-670 C	a) q, di, cc, Ca-amph (inner) bi, crd, cumm, pl (outer)	3-5kb, 520-590 C	0.06-0.47	Syn-peak metamorphism; syn-deformation. Ore cut by pegmatites	Ho et al. (1990) Barnicoat et al. (1991)
Nevoria	a) BIF b) amphibolite	3 kb, 570-610 C	a) q, di, ga, cc, act, sch b) q, di, ga, cc, act-hb, pl, sch	3-5 kb, 550-580 C	0.06-0.47	Post-peak metamorphism; syn-deformation Ore cut by pegmatites	Ho et al. (1990) Mueller (1988)
Griffins Find	a) paragneiss b) mafic orthogneiss	5-7 kb, 700-750 C	a) q, di, ga b) ksp, cpx, tit, q	ca. 6 kb, 700 C	>0.08	Syn-peak metamorphism, late?-deformation	Ho et al. (1990) Barnicoat et al. (1991)
Canada							
Superior Province							
Red Lake, Uchi Belt	a) mafic rocks b) intermediate stocks	low P, low-moderate T	a) q, Fe-dol, ser, chl, cc, tourm (greenschist) a) q, bi, ga (greenschist-amphibolite) a) q, bi, mu, ga, and, sta, crd, chltd, anth, tourm, cc (amphibolite)			Metamorphism, batholiths, shear zones all coeval with mineralization. Mineralization spans g-schist/amphibolite transition	Andrews et al. (1986)
Musselwhite, Sachigo Subprovince	a) oxide facies BIF b) basalts c) pelite	low P, moderate T	veins = q, ab, ga, grun, cc, tourm a) q, mt, grun, bi, hb, ga	3 kb, 530-550 C		Syn-peak metamorphism. Felsic and lamprophyre dykes cut ore.	Hall and Rigg (1986)
Detour, Abitibi Belt	a) mafic rocks b) ultramafic rocks c) felsic porphyries	low P, low-moderate T	veins = q, ksp, pl, cb, act a) q, pl, ksp, bi-phl, ep, ser, chl, (wallrock)			Post-peak metamorphism	Marmont (1986)
Slave Province							
Lupin, Yellowknife Subprovince	a) BIF b) turbidites	low P, low-moderate T	a) q, hb (greenschist-amphibolite) a) q, hb, ap, hed, sch, ep, ga, tit (amphibolite)				Lhotka and Nesbitt (1988)
Brazil							
Crixas, Sao Fransisco Craton	a) amphibolite b) pelite	low P-T	a) Fe-dol, bi, mu, q, chl, ilm, rut, pl(An15-40) b) q, chl, ser, ga, ep, chltd	3 kb, 440-480 C	0.15-0.26	Post-peak metamorphism	Thompson (1986, 1991)
India							
Kolar Schist Belt, Dhawar Craton	a) tholeiites b) komatiites c) IF d) quartzites	low P, 470-540 C	a) q, di, cc, sch, tourm (inner) hb, bi, q (outer)	435 C (veins) 470-540 C (sulphide lodes)		Pre-peak metamorphism; syn-deformation. Ore cut by pegmatites	Hamilton and Hodgson (1986) Siddaiah and Rajamani (1989)
South Dakota, USA							
Homestake, Black Hills Uplift	carbonate facies BIF	3.5-4.9 kb, 370-630 C	chl, sid, q, ank, mu, ab (greenschist) chl, grun, q, bi (greenschist-amphibolite) grun, q, chl, bi, ga (amphibolite)			Post-peak metamorphism, syn- deformation Mineralization spans g-schist/amphibolite transition	Caddey et al. (1991)

Table 4.1 (continued)

Giant Low-Temperature Lode Gold Deposits (Greenschist Facies)

Yilgarn Block, Western Australia							
Golden Mile, Kalgoorlie	a) mafic rocks b) black shale	low P, 350-400 C	mu, q, sid (ank/dol), ab (inner) chl, cc, ank, ab, q (outer)	250-230 C	0.2	Post-peak metamorphism, syn- deformation	Ho et al. (1990)
Victory-Defiance, Kambalda	a) tholeiitic basalts b) high-Mg tholeiites c) ultramafic rocks d) pelites	low P, 450-570 C	a, b) ab, dol, ank, ser (inner) bi, chl, dol, ank, q, ab, cc, ilm, rut (outer) d) ab, bi, act, dol, ank, mu, chl	1.7-2kb, 340-430 C	0.1-0.2	Post-peak metamorphism, late?- deformation	Clark et al. (1986, 1989)
Abitibi Belt, Superior Province, Ontario							
Kerr-Addison, Kirkland Lake	a) ultramafic rocks b) mafic rocks	low P-T	ank, Fe-dol, ab, mu (inner) chl, ank/dol, ab, talc (outer)	270-330 C		Post-peak metamorphism, syn- deformation	Kishida and Kerrich (1987)

Abbreviations used: q = quartz, cc = calcite, ank = ankerite, dol = dolomite, sid = siderite, pl = plag, An = anorthite, ab = albite, ksp = microcline, bi = biotite, phl = phlogopite, amph = amphibole, act = actinolite, act-hb = actinolitic hornblende, hb = hornblende, cumm = cummingtonite, anth = anthophyllite, grun = grunerite, cpx = clinopyroxene, di = diopside, hed = hedenbergite, zo = zoisite, ep = epidote, mu = muscovite, ser = sericite, sta = staurolite, chltd = chloritoid, crd = cordierite, ol = olivine, ga = garnet, chl = chlorite, sch = scheelite, tourm = tourmaline, mt = magnetite, ilm = ilmenite, rut = rutile, tit = titanite. Modified from McCuaig et al. (1993).

has witnessed a resurgence of interest in these deposits, and detailed documentation of high-temperature deposits has been undertaken in numerous Archean terranes including the Murchison (Phillips, 1985), Yellowdine (Barnicoat et al., 1991; Mueller, 1991), and Kalgoorlie (Knight et al., 1993) Terranes, and the Pilbara Block (Neumayr et al., 1993) of Western Australia; the Kolar Schist Belt (Hamilton and Hodgson, 1986); and Hemlo, Ontario (Pan and Fleet, 1995): see Table 4.1 for a summary. Models proposed for the genesis of deposits in higher metamorphic-grade terranes variously include:

(1) prograde metamorphism of typical greenschist-facies-hosted deposits (Phillips, 1985; Hamilton and Hodgson, 1986),

(2) syn-metamorphic mineralization at similar P-T conditions to those suggested by the alteration mineral assemblages, i.e. amphibolite or granulite facies (Andrews et al., 1986; Barnicoat et. al., 1991; Knight et al., 1993; McCuaig et al., 1993; McCuaig and Kerrich,1994), or

(3) syn- or post-peak metamorphic formation as skarns from metasomatic fluids, possibly expelled during the crystallization of regional granitoids (Mueller, 1991; Mueller et al., 1991a; Pan and Fleet, 1995).

Recently, data from these studies of high-temperature deposits have been considered in conjunction with observations from deposits hosted in lower-grade terranes. Groves (1993) points out that the P-T-t and radiogenic isotope data from the higher metamorphic-grade Archean deposits in Western Australia are incommensurate with genetic models that involve devolatilization of host greenstones alone (e.g. Groves and Phillips, 1987). Furthermore, Groves et al. (1992), Groves (1993) and McCuaig and Kerrich (1994) argue that petrogenetic studies, thermodynamic modelling and timing relationships from these deposits point to a genetic continuum of gold mineralization, with deposits forming at conditions that range broadly from sub-greenschist to granulite facies, potentially representing a crustal depth range from < 5 km to about 20 km, or a "crustal continuum" of gold deposition.

The deposits of the Norseman region, Western Australia, are hosted in a sequence of metabasalts that range in metamorphic grade from upper-greenschist to mid-amphibolite facies. Accordingly, this goldfield is well-suited to test the crustal continuum model. As part of this overarching goal, the aims of the following chapters are to:

(1) document the dimensions and nature of gold mineralization and related hydrothermal alteration in the Norseman lode gold deposits;

(2) establish the pre-, syn- or post-peak metamorphic timing of alteration and mineralization based on structural and textural arguments supported by thermodynamic, stable isotope and radiogenic isotope studies,

(3) to elucidate the pressure-temperature-time-deformation-fluid (P-T-t-d-f) history of the Norseman Terrane, and

(4) to draw comparisons to other deposits hosted in upper-greenschist to amphibolite facies terranes, in order to evaluate the crustal continuum model for gold deposition.

Previous studies of the Norseman deposits have variably argued for a pre-peak (Golding, 1982; Keele, 1994; Golding et al., 1990) or post-peak metamorphic (Mueller, 1992; McCuaig et al., 1993) timing for quartz vein deposition and gold mineralization. This question of relative timing is vital: if the deposits have been metamorphosed, a crustal continuum model is unconstrained, whereas syn- to post-peak metamorphic mineralization would support such a model.

4.2 Deposit subdivisions

Gold mineralization is present in all greenstone rock types at Norseman, although the large economic deposits are restricted to the lower members of the Woolyeenyer Formation (Fig. 2.2). All orebodies are subdivided into three groups on the basis of their (1) spatial relationships over 40 km, (2) structural characteristics, and (3) associated hydrothermal alteration. These groups consist of the Northern deposits (Surface Winze, North Royal, Princess Royal Mines), which access auriferous quartz vein networks north of the Jimberlana Dyke, the Central deposits (Regent, Ajax, Viking, Okay), and Southern (Scotia) deposits (Fig. 2.2).

4.3 Northern deposits

The North Royal mine is situated approximately 10 km NNE of the Norseman townsite within the Woolyeenyer Formation. Rock types in and around the mine, in chronological order of emplacement are: (1) NNE-striking, W-dipping (45°) basaltic flows, (2) composite N-striking, E-dipping (50°) gabbroic dykes, (3) NNE-striking, W-dipping (approximately 50°) felsic porphyries of the Ajax suite, (4) Dinky Buoys porphyry suite (of variable attitude), and (5) E-striking, subvertical Proterozoic norite dykes of the Jimberlana Dyke suite. The largest member of this norite dyke suite is the Jimberlana Dyke itself, over 200 km in strike length and over 1 km in width, located approximately 3 km south of the North Royal shaft. The orebodies are hosted in an E-dipping gabbroic dyke complex, with the dykes ranging from tholeiitic to high-magnesian tholeiitic in composition (Chapter 3; Figs. 4.1, 4.2B).

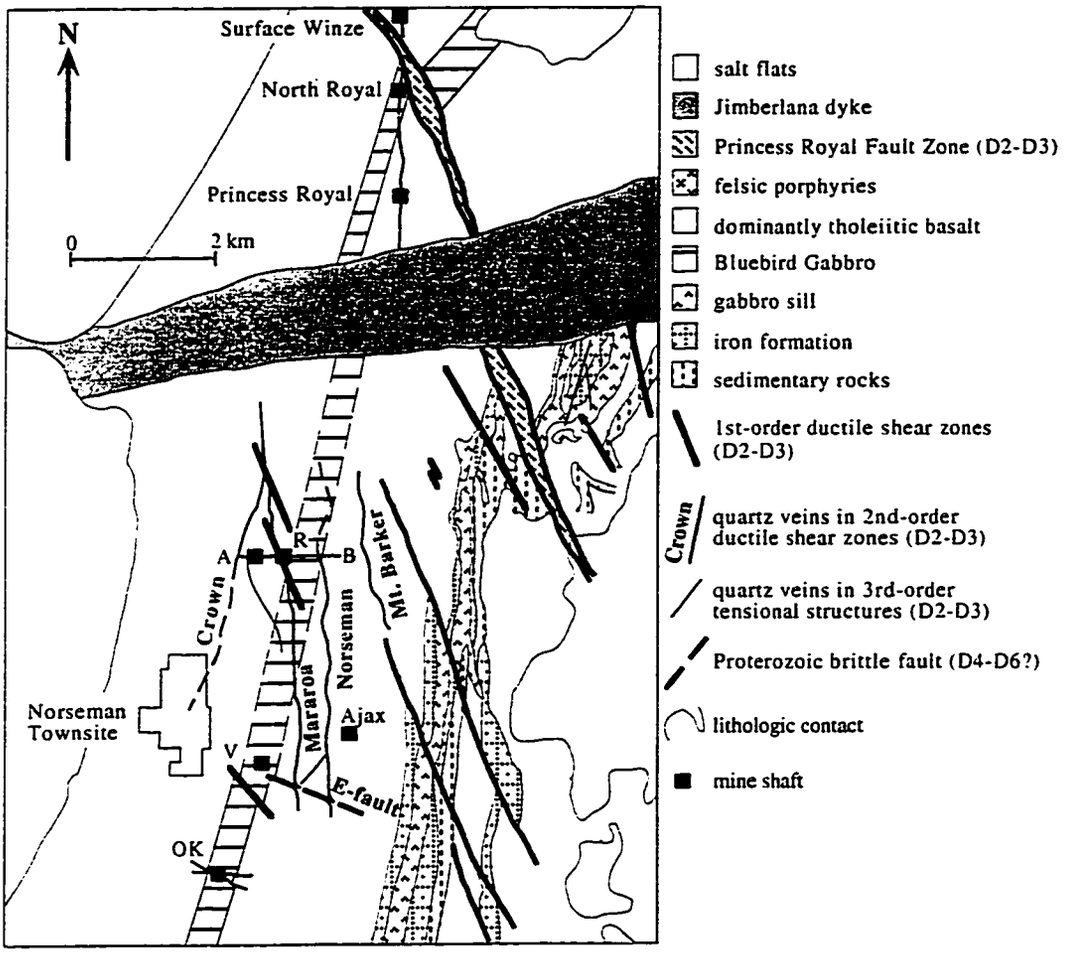

Figure 4.1. Simplified geological map of the Northern and Central deposits, highlighting structural geometry of the auriferous quartz vein system. Modified from Johnson (1988). R = Regent shaft, V = Viking decline. Line AB is the location of the cross section shown in Figure 4.3.

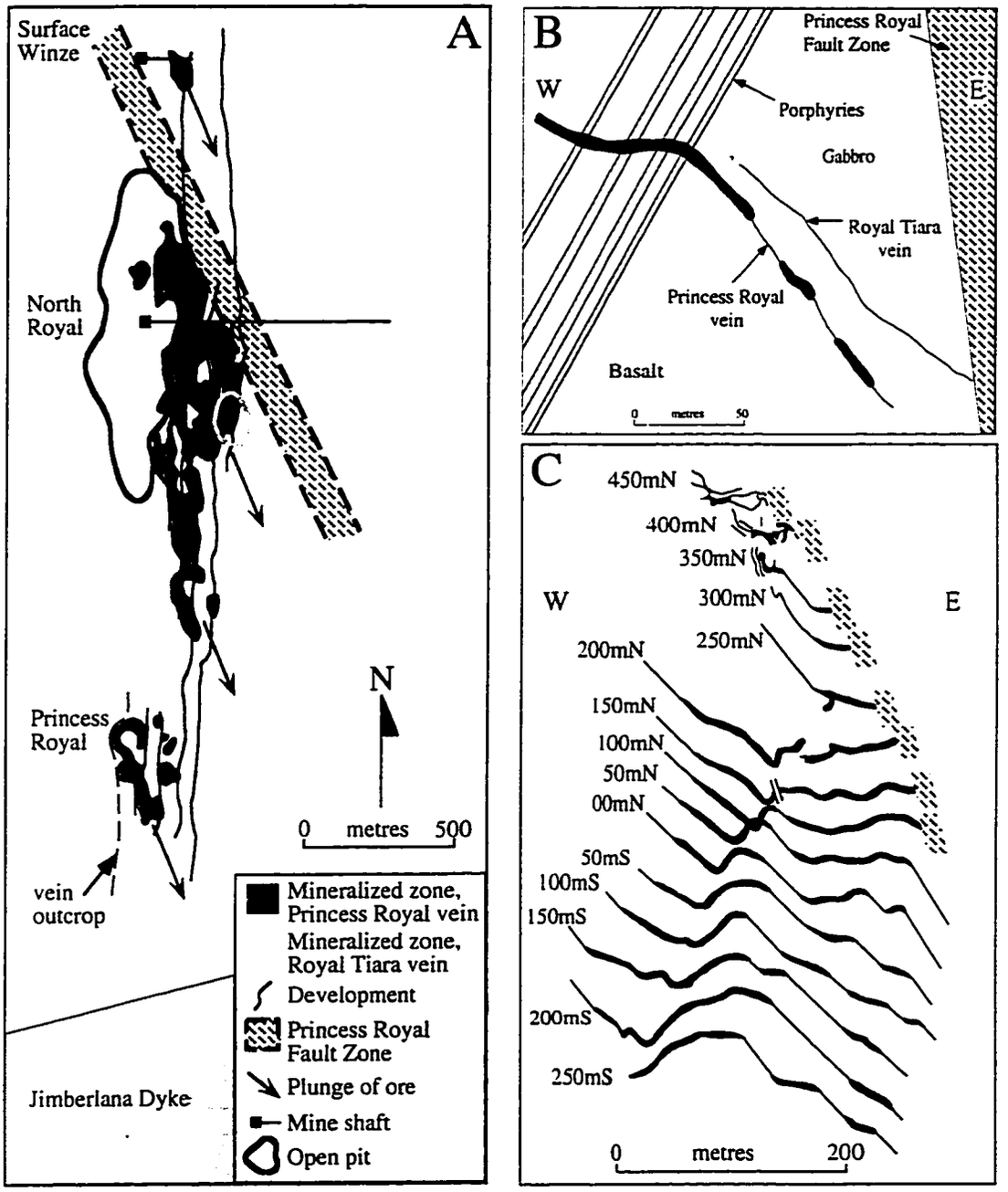

Figure 4.2. Structural geometry of the Northern deposits. (A) Plan projection of the Princess Royal, North Royal, and Surface Winze mine workings, modified after Thomas et al. (1990). (B) Cross section through the North Royal orebodies 250 m south of the North Royal shaft, showing the relationship of the Princess Royal and Royal Tiara reefs to stratigraphy and the Princess Royal Fault Zone. Shaded areas represent mineralized sectors of the Princess Royal vein. Modified from CNGC mapping. (C) Stacked cross sections through the North Royal deposit highlighting the geometry of the Princess Royal vein. Thin portions of the vein are hosted in second-order N-striking, E-dipping ductile shear zones, thicker portions are hosted in third-order NE-striking, SE-dipping structures, which host the majority of the ore. The vein system is truncated by later movement on the Princess Royal Fault zone. After Campbell (1990).

Northern and Central deposits are predominantly hosted in D3 structures, the heirarchy of which (1st-, 2nd and 3rd-order) is illustrated in Figure 4.1. The predominant structure in the Northern deposits is the first-order, NNW-striking, steeply E-dipping (70-90°) Princess Royal Fault zone (Fig. 4.2A), a reverse-dextral ductile shear zone up to 100 m in width. The majority of orebodies are hosted in 3rd-order NE-striking, subhorizontal to SE-dipping laminated quartz veins between N-striking, E-dipping 2nd-order shear zones, and partly within the 2nd-order shear zones. To the NE these structures are truncated by the Princess Royal Fault Zone (Fig. 4.2). Major vein systems identified to date include the Princess Royal, Royal Tiara, and Surface Winze veins, accessed by the North Royal shaft. Ore shoots within these quartz veins plunge at moderate angles towards 160° (Fig. 4.2).

4.4 Central deposits

The Woolyeenyer Formation hosting the Central deposits comprises dominantly tholeiitic basalt flows striking NNE and dipping 50°W. These basalts are intruded by gabbroic dykes striking N and dipping 45°E, which are in turn crosscut by a suite of high-magnesian tholeiite dykes striking NNW to NNE and dipping 25-50°E, and a suite of NW-trending gabbros. Felsic intrusive stocks are sparse in the Regent underground workings, but surface geology indicates that two swarms of Ajax porphyry dykes are in the vicinity of the mine (attitude 025/60°W). In the southern reaches of the Ajax mine, felsic intrusive bodies of the Ajax suite are abundant, constituting the dominant host rock in some cases (Figs. 3.1, 4.1).

Dominant structures in the area comprise NNW-trending, steeply NE-dipping ductile reverse-dextral faults that transect the stratigraphy. Displacement is indicated by the offset of stratigraphy, and a mineral lineation defined by amphibole that plunges shallowly (20°) to the NNW (Keele, 1984). Brittle fabrics are locally developed in these structures, and contain abundant slickensided chlorite. For the most part, these structures are barren of gold mineralization or extensive quartz veins. Quartz veins, where present, occur at intersections with second- and third-order structures described below. At these intersections, quartz veins in the latter structures show variable ductile folding, boudinage, or brittle faulting in a reverse-dextral sense. Such variable style and intensities of deformation of veins indicates that vein emplacement was syn-ductile deformation, but that deformation on the first-order structures locally outlasted quartz vein emplacement.

The first-order D2-D3 ductile shear zones have associated second- and third-order structures that host the orebodies of the Central deposits (Fig. 4.1). Second-order

structures are approximately N-striking (345-025°), moderately E-dipping (30-70°) shear zones at a high angle to the stratigraphy, and are best developed in the lower members of the Woolyeenyer Formation, between the Agnes Venture Slate and the Empress Slate (Fig. 4.3, 4.5). These shear zones commonly follow E-dipping gabbroic dykes, suggesting that the rheological contrast between the W-dipping stratigraphy and E-dipping dykes, particularly high-MgO tholeiitic dykes, controlled shear zone nucleation, propagation, and quartz vein emplacement (e.g. Mararoa vein, Figs. 3.2, 4.3; Hall and Bekker, 1965; Keele, 1984). The second-order structures contain variably deformed veins of laminated to massive quartz, which have remarkable along-strike and down-dip continuity. Major second-order vein systems identified to date include the Crown, Mararoa and Norseman veins accessed by the Regent and Ajax shafts (Figs. 4.2, 4.4, 4.5).

The Crown vein (025/30°E) possesses a strike length of 2.5 km and a downdip extent of approximately 1 km (Figs. 4.2, 4.4). The upper portions of the vein bounded by the A-fault (late brittle structure), B-fault (a first-order, NNW-striking ductile shear zone with late brittle movement), and the South Crown fault, contains ore. Five major orebodies have been delineated which plunge SE and narrow downplunge. No mineralization is present north of B-fault; the vein's orientation here (345/50°E), is an unfavourable attitude for ore development on veins throughout the Central deposits (Fig. 4.4). The updip continuation of the Crown reef west of A-fault also appears to lack economic gold concentrations (Fig. 4.3).

The Mararoa vein, attitude 345-025/45-70°E, is hosted in a high-magnesian tholeiite dyke (Butterfly Dyke, Chapter 3), has a strike length of over 4 km, and extends downdip for at least 1.5 km. Four major orebodies are restricted to segments of the vein striking slightly east of north, with a shallower dip. Ore shoots within the orebodies plunge to the SE (Fig. 4.5).

The Norseman quartz vein system, and its host reverse-dextral shear zone, broadly parallels that of the Mararoa vein. However, the Norseman vein is much less extensively mineralized. As with the Mararoa reef, the Norseman vein orebodies are restricted to NNE-striking segments of the veins. E-fault, a late brittle fault oriented 285/40°N cuts the Mararoa and Norseman orebodies in the southern end of the Ajax mine workings, and marks the southernmost extent of economic mineralization in these giant quartz vein systems (Figs. 4.1, 4.5).

Within the second-order shear zones, quartz veins vary in width from centimetres to > 10 m. Fabrics in the altered wallrocks, such as aligned amphibole (35° towards 010°) and foliation/quartz vein intersections (70° $\rightarrow$ 150°, Keele, 1984), in combination with features such as tensional veins, variably folded veins, laminated veins, breccia veins,

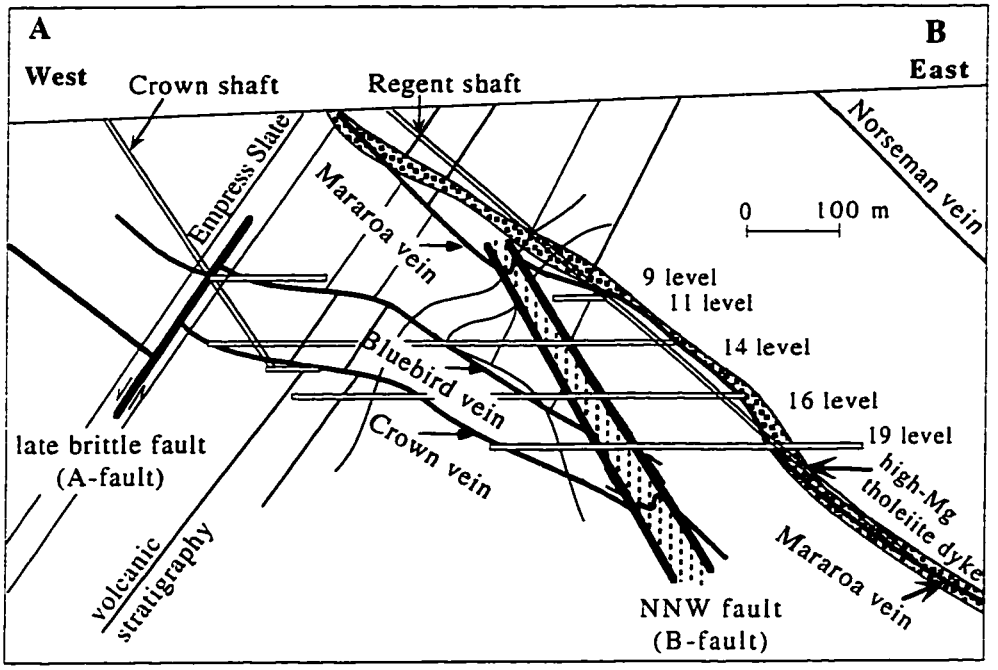

Figure 4.3. Cross section through the Central deposits in the vicinity of the Crown and Regent shafts. The geometrical relationships between the stratigraphy, 1st-order B-fault zone, 2nd-order Crown and Mararoa veins, 3rd-order Bluebird vein, and D4-D6 brittle A-fault are highlighted. Modified from the compilation of CNGC geologist Stuart Taylor (1986).

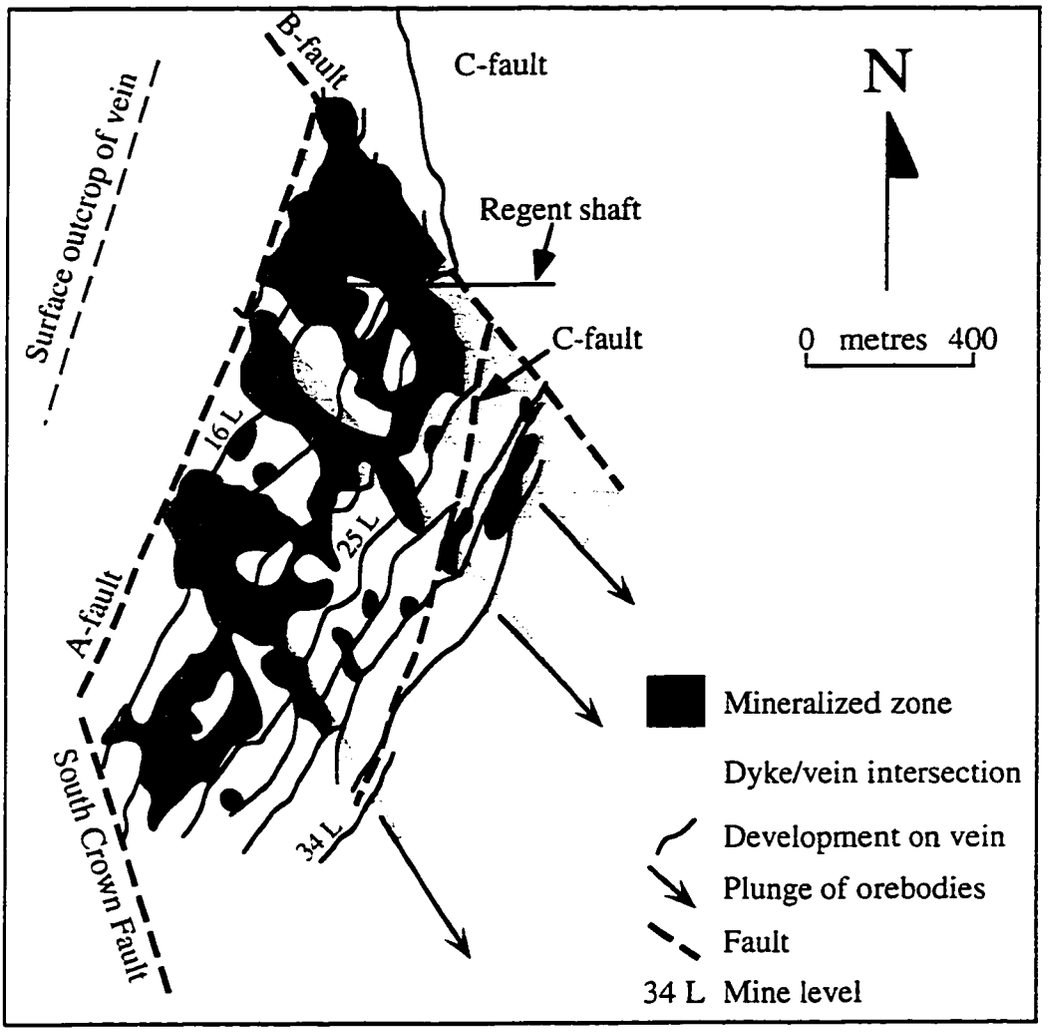

Figure 4.4. Plan projection of orebodies on the Crown vein system, and the relationship of orebody geometry to major faults and intersections with gabbro dykes. The intersections between veins and gabbro dykes form dilational jogs and splays in the vein system, and are intensely mineralized. After Campbell (1990) and Thomas et al. (1990).

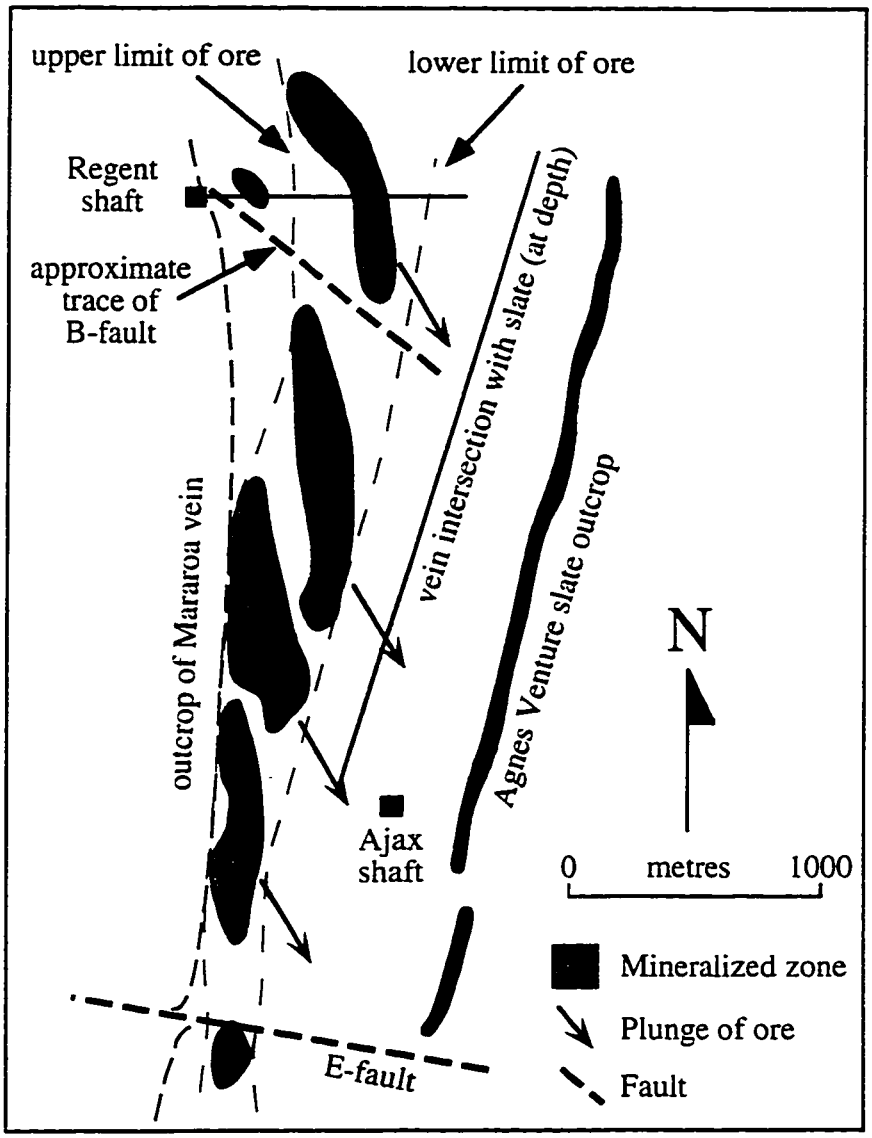

Figure 4.5. Surface outcrop and plan projection of orebodies on the Mararoa vein. The upper and lower limits of mineralization on this vein system broadly parallel vein/stratigraphy intersections. Each orebody is located on a segment of vein which dips more shallowly than the neighbouring barren segments, lending a southeast plunge to ore shoots. With the interpreted reverse-dextral motion on this vein system, these orebodies are thus sited in dilational jogs. After Campbell (1990) and Thomas et al. (1990).

massive quartz and wallrock inclusion alignment, indicate that wallrock shear and quartz vein emplacement occurred synkinematically during brittle-ductile dextral-reverse movement along these structures (Fig. 4.6; Chapter 5; c.f. Ramsay, 1980; Sibson, 1990). Gold orebodies in dilational NNE-striking, more shallowly dipping segments of the second-order structures are thus restricted to dilational jogs (Figs. 4.2-4.5; Connolly, 1936; Campbell, 1990). Brittle post-vein fabrics are sporadically present, and contain retrograde mineral assemblages (see below).

Third-order structures comprise small NE-striking, shallowly SE-dipping (20-30°) tensional footwall or hangingwall splays off of the much more extensive second-order structures (e.g. Bluebird link, Fig. 4.3; Royal Standard vein accessed by Viking decline, Fig. 4.7). Limited width of wallrock alteration haloes (5-50 cm), the lack of intense fabric development in the altered wallrock, and the absence of mesoscopic deformation of the quartz veins (absence of boudinage or folding, except where other structures are intersected) support the interpretation that these were dominantly tensional structures. The geometric relationship of these structures to first- and second-order dextral-reverse shear zones is also consistent with a tensional origin. Ore grades in these quartz veins tend to be evenly distributed along the shallowly dipping segments of these structures, except where intersected by later structures (Fig. 4.7).

West- and WNW-striking subvertical shear zones are abundant in the mine area, and locally host quartz veins and gold mineralization (e.g. OK Mine, Figs. 4.1, 4.8). Where unmineralized, these structures displace the west-dipping stratigraphy, but are crosscut by NNW-striking gabbroic dykes and NNE-striking felsic porphyry dykes. These W- and WNW-striking faults are interpreted to be syn- to early post-depositional D1 listric normal faults (Chapter 2, Keele, 1984). Where mineralized, these structures are ductile in nature and crosscut the gabbro and porphyry dykes, consistent with reactivation during D3 ductile deformation and mineralization (Fig. 4.8).

The OK Mine is a classic example of structural control of orebodies. The two main ore-bearing structures in the mine area are the Main and O2 quartz veins (Fig. 4.8). A number of other quartz veins such as the North, South and New veins have also been small producers, and are morphologically and structurally analogous to the Main vein. The Main vein is hosted in a weakly-developed dextral shear zone, striking 090° and dipping subvertically, that varies from a few centimetres to 2 m in width. Economic gold mineralization is restricted to hydraulically brecciated dilational jogs that occur at the intersection of the vein with the NE-striking porphyry dykes, resulting in oreshoots with westerly plunges.

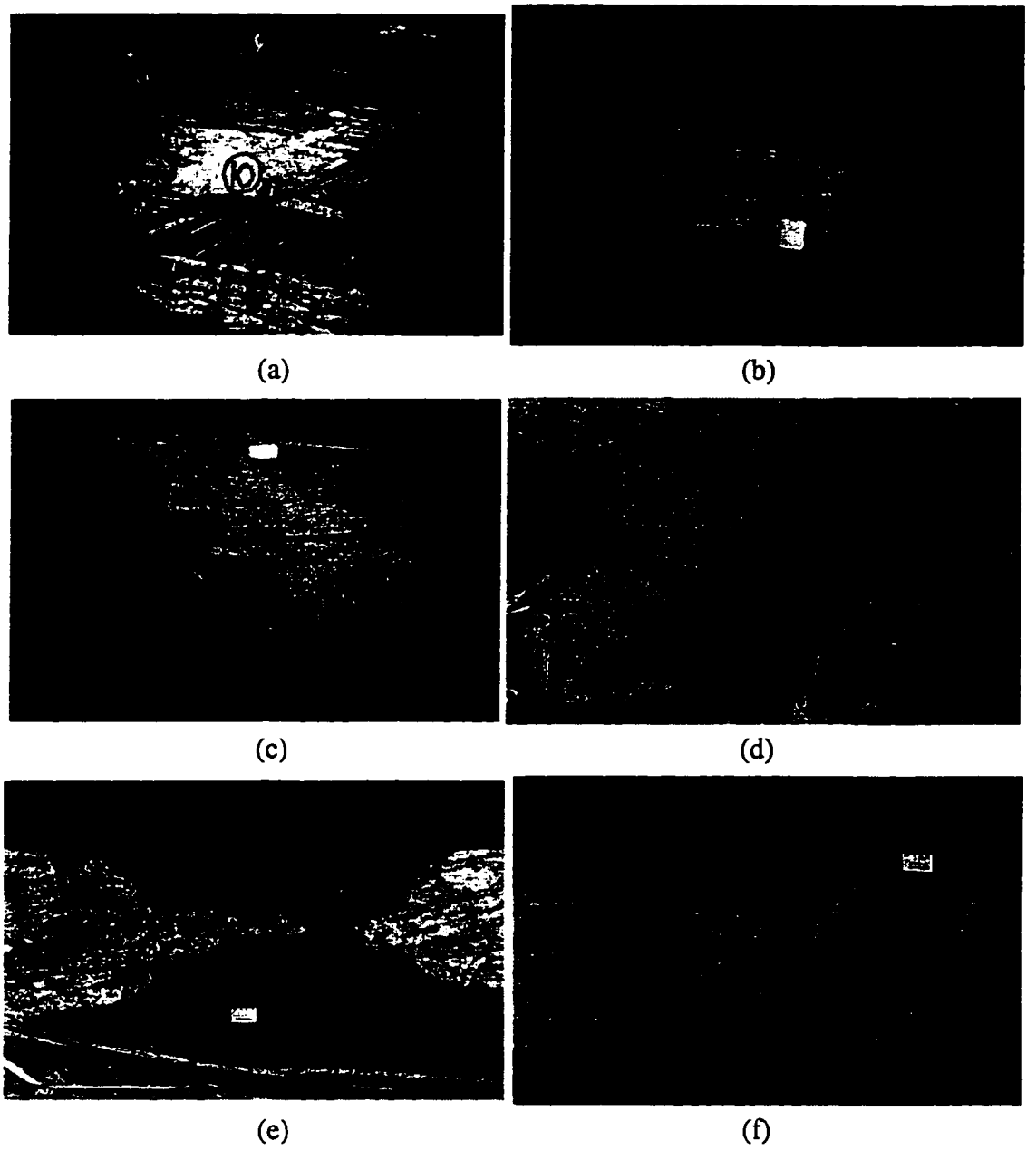

Figure 4.6: Vein morphologies observed in the Northern and Central deposits
(a) Multiple generations of laminated and massive quartz, Crown vein, 14 level, Regent mine. Tensional veins and sense of inclusion separation indicate dextral motion on surrounding shear zone. (b) Laminated and massive quartz, and wallrock inclusions, 5/150N stope, Princess Royal vein. (c) Breccia and massive quartz, 7 level, Norseman vein, Ajax mine. (d) Folded Mararoa vein, B-fault, Regent mine (e) Boudinaged Mararoa vein, 25 level, Regent mine. (f) Brittle disruption of Mararoa vein, 25 level, Regent mine.

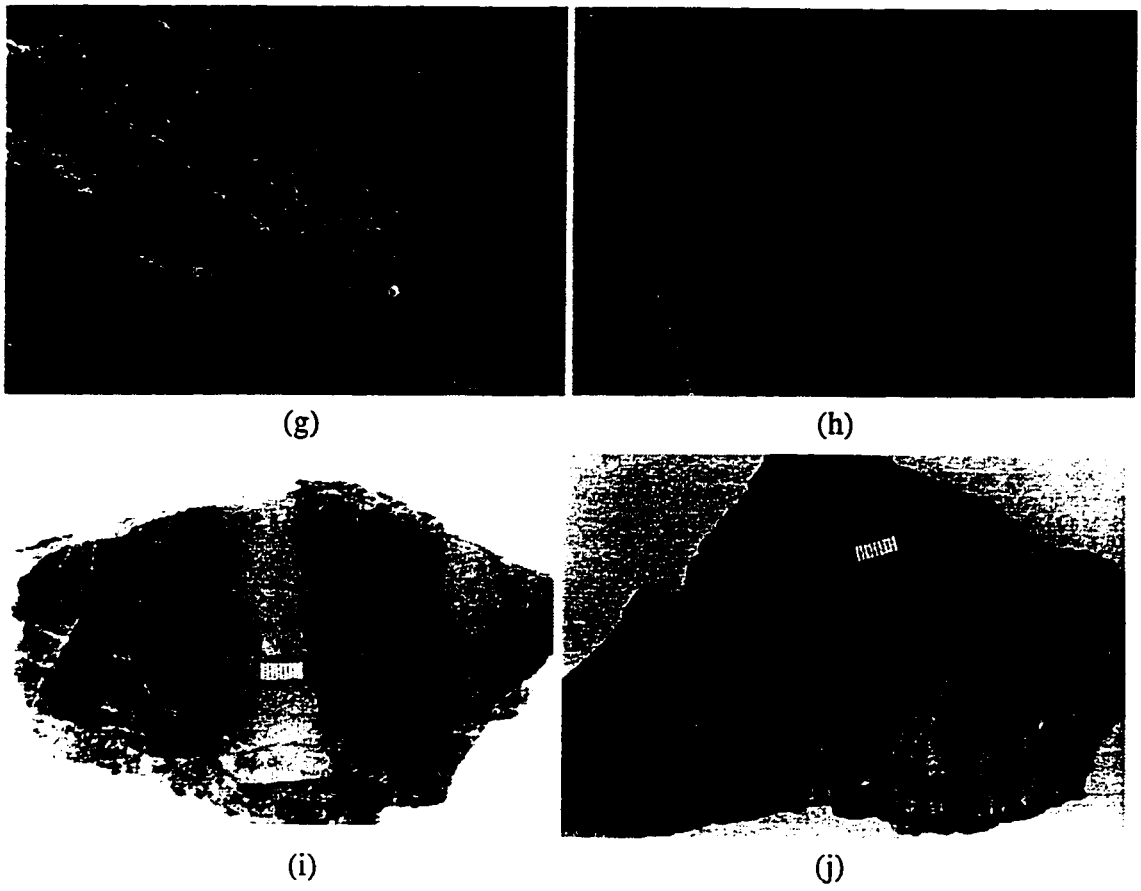

Figure 4.6 (cont.): Vein morphologies observed in the Southern deposits
(g) Discontinuous quartz-clinopyroxene-amphibole-calcite veining within a broad ductile shear zone. The surrounding wallrock is pervasively altered to a biotite-amphibole-plagioclase alteration assemblage. Up is to the left. 7 level, Scotia mine. (h) Discontinuous, banded auriferous quartz-clinopyroxene veins within a ductile shear zone, 7 level, Scotia mine. veins are extremely disrupted by late brittle faults. (i) Quartz vein with amphibole and clinopyroxene alteration selvedges, Scotia mine. (j) Banded clinopyroxene-quartz-carbonate microcline vein, Scotia mine.

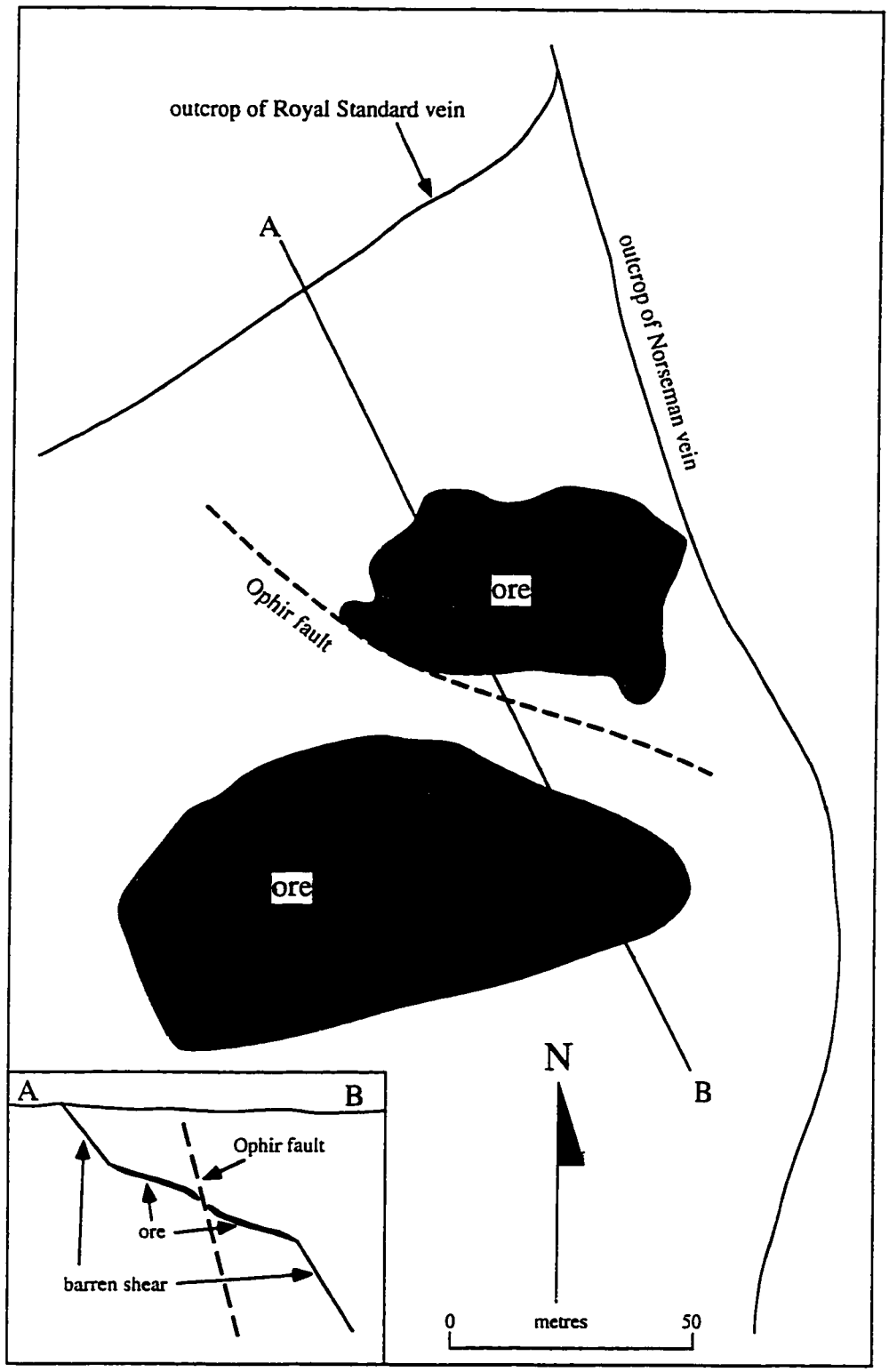

Figure 4.7. Plan projection of orebodies on the 3rd-order Royal Standard vein, a footwall splay of the Norseman vein. Inset shows schematic cross section through the vein. The vein is offset by the brittle (D4-D6) Ophir fault. Modified from geology compiled by CNGC geologists P. Bird and D. Kelley (1989-1991).

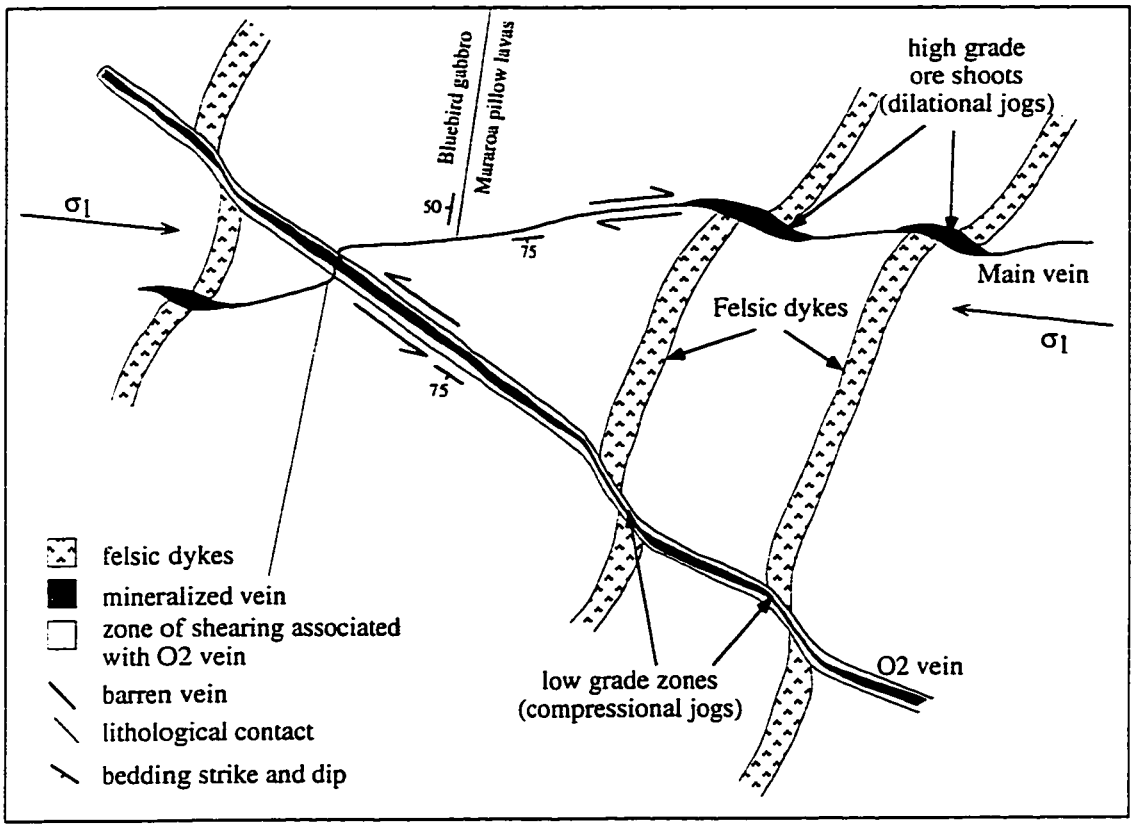

Figure 4.8. Schematic map view of the OK main and O2 veins, highlighting the structural controls on on orebody location (not to scale). On Main vein, mineralization is restricted to dilational jogs, formed where veins intersect felsic porphyry dykes. Conversely, O2 vein is uniformly mineralized except for such vein/dyke intersections, which form compressional jogs and are barren of minerlaization. Note that O2 vein has a strong zone of deformation associated with it. In this zone, both ductile shear fabrics with high-temperature alteration assemblages that formed syn-vein emplacement and mineralization, and cataclasite with associated retrograde minerals, can be found. The retrograde cataclasite formed during reactivation of O2 vein, which produced the offset observed at the Main/O2 vein intersection. Also shown is the interpreted paleostress configuration during formation of the quartz veins. As the veins show only strike-slip displacement associated with them, σ_2 is interpreted to have been subvertical during vein emplacement.

The O2 vein is hosted by a NNW-striking, subvertical, sinistral brittle-ductile shear zone up to 5 m in width. In contrast to the Mararoa vein, the entire length of the O2 vein is mineralized, except at the intersection with the porphyry dykes which host the ore on Main vein. On the O2 reef, such intersections result in compressional jogs, devoid of economic mineralization (Fig. 4.8).

Large scale brittle faults that displace auriferous quartz vein systems are recognized throughout the Northern and Central deposits. Examples are E-fault, which offsets the Norseman and Mararoa veins in the southern workings of the Ajax mine (Figs. 4.1, 4.5); the Ophir fault, which offsets the Royal Standard vein in the Viking decline (Fig. 4.7); A-fault, which offsets the Crown reef (Figs. 4.3, 4.4), and reactivation of the O2 reef in the OK mine, offsetting the other E-striking reefs in this area (Fig. 4.8). All of these structures have brittle fabrics associated with them, including slickensides, breccias, and abundant disaggregated fault cataclasite, which collectively postdate the characteristically ductile ore-bearing structures. These brittle structures attest to disturbance of the Norseman Terrane at times significantly post-mineralization, when the terrane was at much lower temperatures and confining stresses.

4.5 Southern deposits

The Scotia goldfield is located approximately 25 km south of the Norseman Townsite, and approximately 10 km north of the southernmost extension of the Norseman greenstone sequence (Fig. 2.2). In the mine area, the greenstones are approximately 3-4 km wide (Fig. 4.9). The stratigraphic sequence of the greenstones in the Scotia area resembles that surrounding the northern and central deposits. The orebodies are hosted by a shearzone that transects the inferred strike-equivalent of the Woolyeenyer Formation. The mine stratigraphy, listed in chronological order of formation, consists of: (1) N-striking, W-dipping (45°) tholeiitic metabasalts, (2) N-striking, E-dipping (50°) gabbroic sills and dykes, (3) felsic porphyry intrusions (000/80°E), (4) felsic pegmatite dykes having dominant trends of 000/40°W, 000-010/20-30°E), and (5) ENE-striking, subvertical diorite dykes of the Jimberlana Dyke Suite. The entire greenstone sequence is separated from that hosting the Northern and Central deposits by the Proterozoic Dambo Fault (Figs. 2.2, 4.9).

The Southern orebodies at Scotia are distinctive both in terms of their higher metamorphic-grade host rocks and their higher-temperature alteration mineral assemblages (Chapter 5). Structural controls on primary gold mineralization are difficult to constrain, as closely spaced brittle faults of varying orientation disrupt and displace the

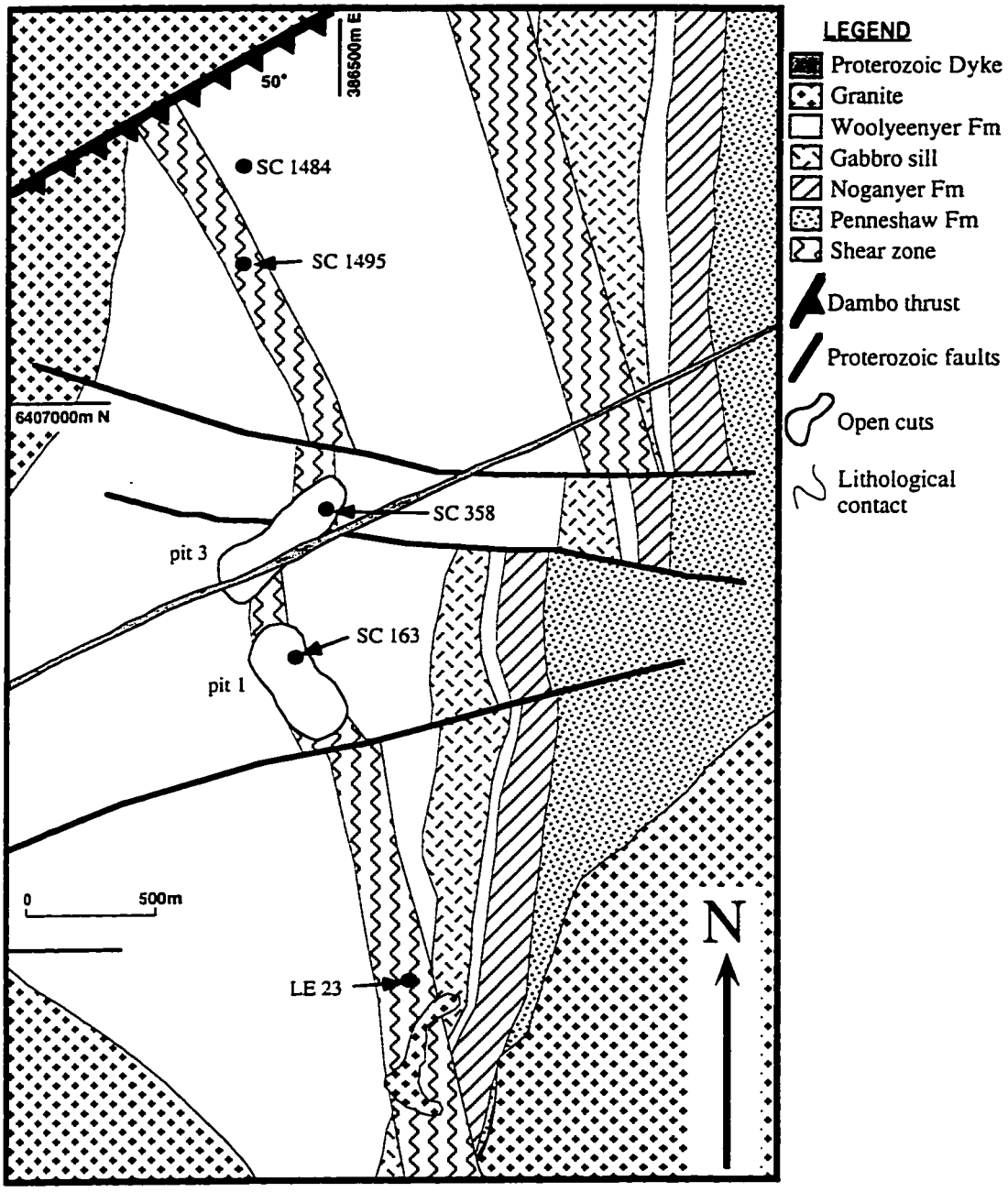

Figure 4.9. Surface geology of the Scotia mine environs (after CNGC mapping). Numbered dots refer to the location of drill holes that were sampled in the course of this study.

orebodies. Gold mineralization occurs in a D3 ductile shear zone striking NNW to N and dipping E, that transects the stratigraphy and, in the mine workings, follows a N-striking, E-dipping (50°) gabbroic dyke (Figs 4.9-4.11). Within the shear zone, weak mineral lineations defined by amphibole grains plunge approximately 50° SW and parallel the foliation/vein intersections.

Most of the ore is hosted in an en echelon array of 5 lenses (ACDEF) of multiple quartz + diopside + calcite veins (D3) within the shear zone. Due to offset by late brittle faults, the ore zones are limited in strike and dip extent (150 X 120 m maximum). Ore shoots are difficult to define due to the disrupted nature of the orebody, but those identified to date plunge to the northeast at 20° (Fig. 4.10). Orebodies crosscut fine-grained felsic porphyry dykes, but are in turn cut by pegmatites having a quartz + plagioclase + muscovite + biotite ± garnet assemblage (Fig. 4.12).

Two orientations of brittle faults (D4-D6) have been identified in the mine. These faults are recognized by their abrupt offsets of ore zones and the abundance of chloritic fault gouge within them. E-striking, subvertical dextral faults average 3-10 cm in width and offset the orebodies by as much as a few metres. Reverse faults, striking NNE, dipping 60°W, and averaging only a few cm in width, also crosscut the orebodies. Smaller-scale WNW-striking faults are also present in the mine workings (Fig. 4.10-4.12). The NE- to ENE-striking Dambo fault appears to have undergone the latest and largest displacement, and offsets stratigraphy, in an apparent sinistral sense, approximately 5 km from the rest of the Norseman Terrane (Figs. 2.2, 4.9).

4.6 Mesoscopic characteristics of veins, and post-emplacement modification

Quartz veins exposed by mining show numerous metre-scale features that would be difficult to elucidate in drill core or hand specimens (Figs. 4.6, 4.13, 4.14). These features are of great importance to the interpretation of paragenetic relationships between deformation, regional metamorphism, hydrothermal alteration, quartz precipitation, and gold mineralization, detailed later in Chapter 5.

The character of the quartz veins differs between Northern, Central and Southern deposits. Veins in Northern and Central deposits are, in detail, similar (Fig. 4.6). However, Northern deposits are characterized by thicker quartz veins (up to 10 m, average 1-3m) and a greater abundance of massive quartz that contains abundant inclusions of wallrock and lacks significant laminations, whereas Central deposits consist of thinner quartz veins (generally < 1-2m) that contain more laminations and

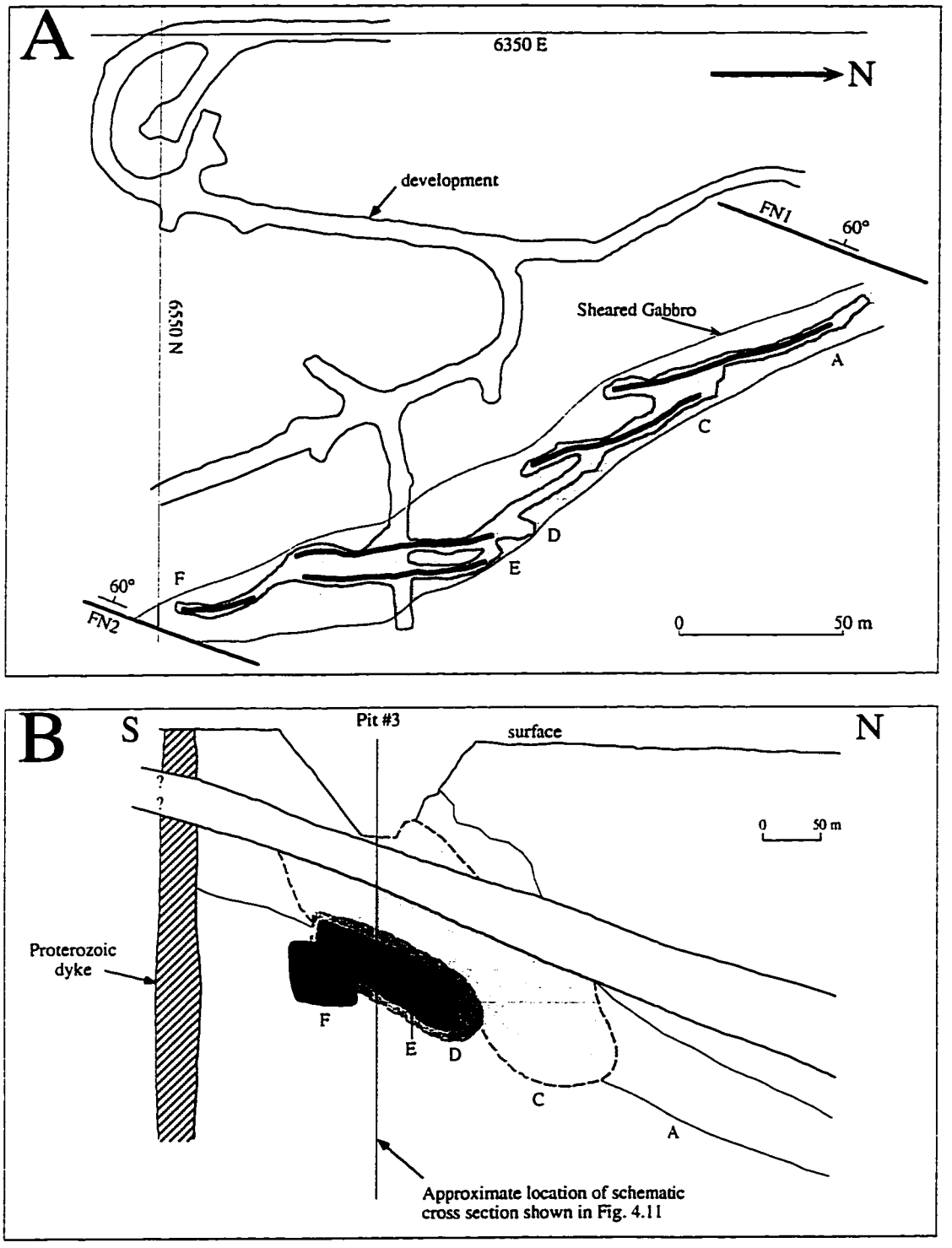

Figure 4.10. A. Plan view of ore lenses, 8 level, Scotia mine. B. Composite long section showing the geometry of ore lenses in the Scotia deposit. Compiled by CNGC geologist Bernie Turner (written communication, 1993). Letters ACDEF refer to individual ore lenses, highlighted by bold lines in (A) and shading in (B). FN1 and FN2 are two large brittle faults (D4-D6) that crosscut and offset the mineralization and host ductile shear zone.

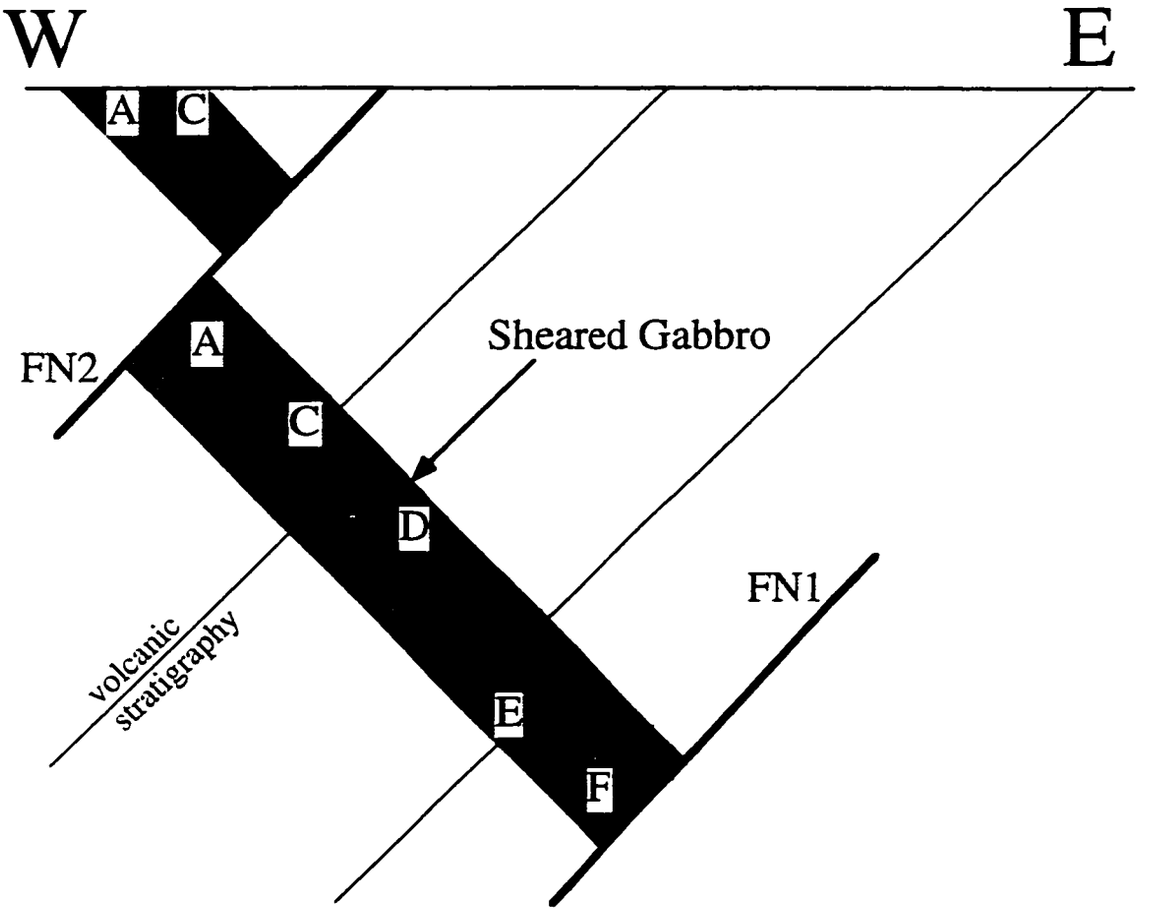

Figure 4.11. Schematic cross section through the Scotia orebody under open pit #3 (pit omitted for clarity). Letters ACDEF refer to individual ore lenses in an east-dipping shear zone that follows a gabbro dyke. FN1 and FN2 are large brittle faults that crosscut and offset the mineralization and host ductile shear zone. Compiled by Bernie Turner (written communication, 1993).

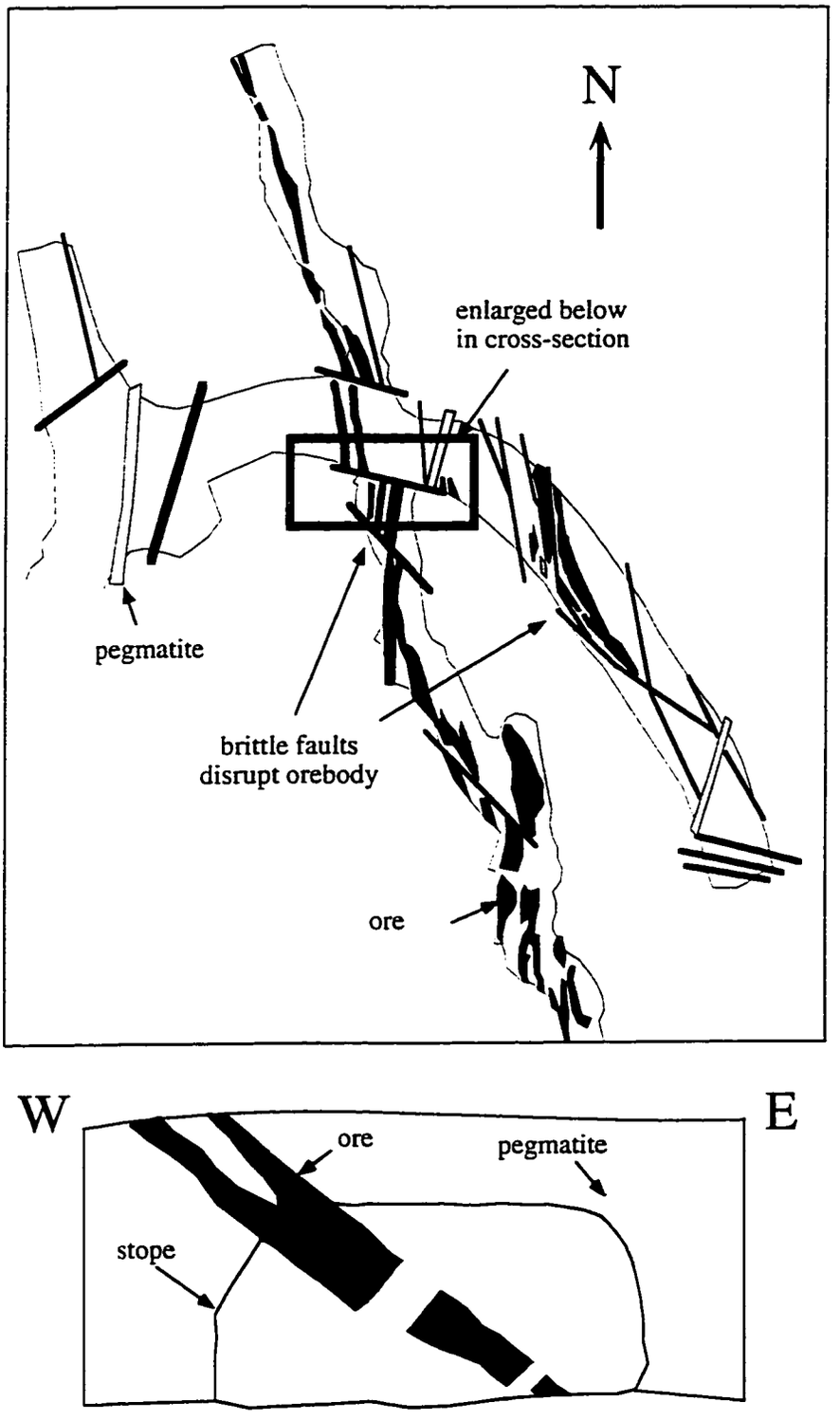

Figure 4.12. A. Plan view of the 7/440 crosscut, 7 level, Scotia mine, showing the detailed geology of two ore lenses. B. Cross section illustrating pegmatite-ore relationships. Note the pegmatite dykes that crosscut the orebodies, and the abundant D4-D6 brittle faults that disrupt the orebodies and pegmatite dykes. Modified from CNGC mapping.

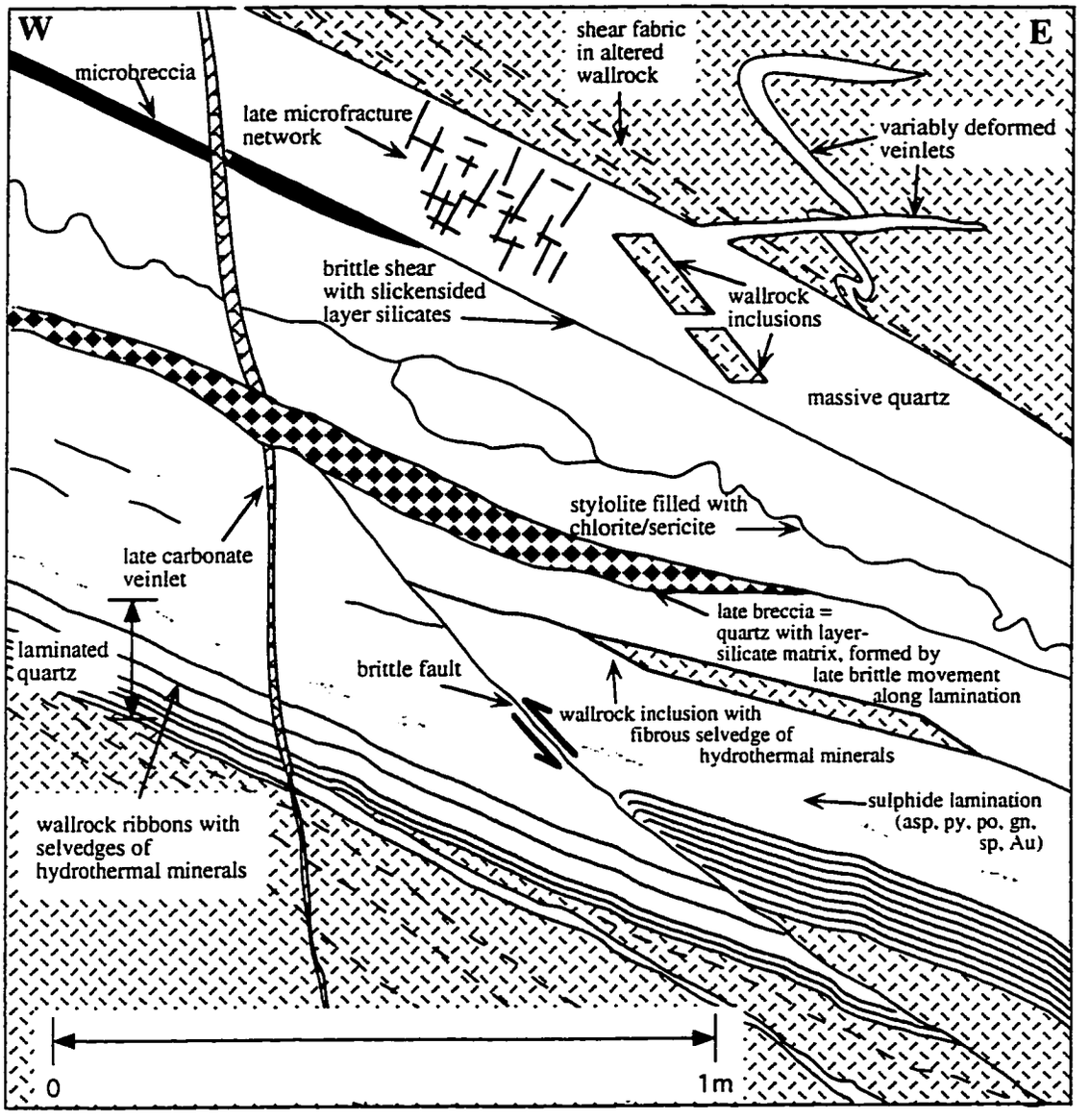

Figure 4.13. Schematic diagram illustrating the complex appearance of Norseman quartz veins produced by the combination of sun- and post-emplacement (D3-D6) deformation and fluid activity.

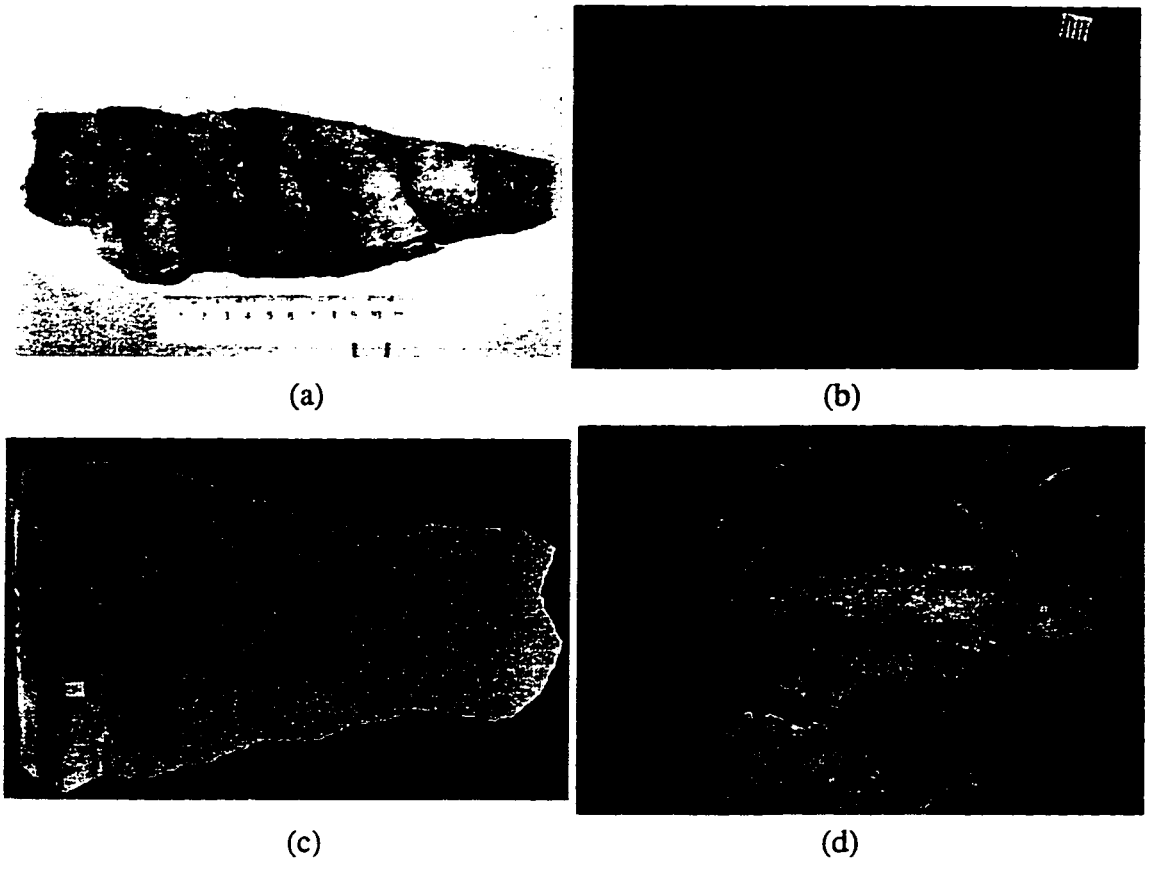

Figure 4.14: Post-emplacement brittle disruption of quartz veins
(a) Black quartz laminations, 16 level, Crown vein. Black colour is caused by dislocations in quartz grains formed during low-temperature britle deformation of the quartz vein. (b) Close-up of (a), showing brittle fractures at center of black quartz laminations, which are infilled by low-temperature mineral assemblages. (c) Quartz slab from the Princess Royal vein showing sulphide rich laminations at right and britle deformation laminations at left (d) Post-emplacement brittle ramping of quartz veins, 5 level, Surface Winze deposit.

proportionately less massive quartz. Quartz veins, especially stringers in the wallrock away from the main veins, are variably folded and boudinaged in both groups of deposits, with less-deformed stringers crosscutting their more intensely deformed counterparts. These relationships indicate emplacement of the veins into active ductile-brittle shear zones.

Vein features within the Scotia orebody are presented in Figure 4.6G-J. The veins within the shear zone are variably deformed, with less- deformed veins crosscutting their more intensely deformed counterparts. Within the ore zones, repeated veining events have produced composite banded veins, up to 6 m in total width (average < 1 m): composite veins comprise alternating bands of quartz, clinopyroxene, calcite, amphibole, biotite and microcline. Individual veins vary in width from a few millimetres to 0.5 metres, are discontinuous, and variably deformed (Fig 4.6H-J). Vein density decreases rapidly into the host shear zone where veins are thin and widely spaced (Fig. 4.6G).

Laminated or banded veins, such as those found in the Norseman lode gold deposits, are generally taken to imply a crack-seal or multiple hydraulic fracturing mechanisms of formation (cf. Ramsay, 1980; Cox, 1987; Hronsky et al., 1990), although this may not always be the case. A variety of vein laminations are developed at Norseman. Some are ribbons of wallrock subparallel to vein margins, and may have formed by a crack-seal mechanism, or more likely by hydraulic fracturing events, as indicated by the presence of wallrock inclusions (Figs. 4.6A-C; 4.13). However, many laminations consist of minerals whose textures imply deposition directly from a hydrothermal fluid, such as rosettes of amphibole, biotite or chlorite, trails of galena + sphalerite + tellurides + cubic pyrite (Fig. 4.14A), and fibrous selvedges to vein and wallrock inclusion margins (Fig. 4.13; see Chapter 5 for discussion of alteration textures).

In contrast to these laminations that formed syn-quartz vein emplacement, other laminations form during post-mineralization modification of the orebodies. Some of the latter are stylolitic in nature, bordered by corroded mineral grains and exhibiting irregular geometries. Other laminations are planes of slip, indicated by orientated layer silicates, quartz slickensides, and black quartz (Fig. 4.14B,C). Microscopically, black quartz has intense structural distortion, signifying "cold workin" or low temperature dislocation glide, consistent with low temperature deformation (Chapter 5). Laminations may contain rock flour or brecciated vein material formed during such movement (Fig. 4.13).

The veins in all deposits are crosscut at wide intervals by D4-D6 brittle faults that offset vein-parallel laminations, and displace quartz vein margins (Figs. 4.6F,H; 4.12). These faults are probably related to larger-scale brittle faults, described above, which offset the orebodies on a regional scale. Some small-scale brittle faults merge with the

quartz vein margins, resulting in thickening of quartz veins by ramping (Fig. 4.14D). Vein minerals, particularily quartz, are typically darker in colour proximal to vein laminations, and are also brecciated near slip planes and stylolites that approximately parallel the vein margins. These slip planes and stylolites are infilled by a matrix of ultra fine-grained layer silicates (Fig. 4.14A-C). The fabrics indicate that these areas were loci for strain during the ductile and brittle deformation episodes. Some late fractures are also infilled by such minerals as carbonate, sericite, prehnite, albite and gypsum (Fig. 4.6I; Fig. 4.14B,C). The significance of these late veinlets will be discussed further in Chapters 5 and 6.

4. 6 Summary

(1) Lode gold deposits at Norseman comprise auriferous quartz veins in ductile-brittle second or higher-order structures related to barren first-order ductile shear zones.

(2) The Norseman gold deposits can be subdivided into three broad groups, Northern, Central, and Southern deposits, on the basis of their spatial distribution and structural style. These subdivisions are corroborated by observations on alteration mineral assemblages detailed in Chapter 5.

(3) Northern and Central deposits comprise massive to laminated quartz veins within narrow ductile shear zones. The proportion of massive + breccia to laminated quartz is generally higher in Northern deposits. The Northern and Central quartz vein systems have remarkable along-strike and down-dip continuity.

(4) Southern deposits comprise discontinuous banded quartz-clinopyroxene veins within a broad ductile shear zone.

(5) Gold orebodies are largely restricted to dilational segments of vein systems.

(6) Veins in all deposits are variably deformed. In combination with the location of orebodies on dilation jogs, the similar alteration assemblages on intensely deformed and less deformed veins within a single deposit (Chapter 5), and observations on alteration textures (Chapter 5), indicates that massive fluid flow, hydrothermal alteration and gold mineralization occurred synkinematic, in a dominantly ductile régime.

(7) Macroscopic and mesoscopic observations on individual quartz veins reveal features such as stylolites, brittle faults, and veinlets with low-temperature mineral assemblages which crosscut the veins and their host shear zones. These features indicate a protracted history of deformation and limited fluid flow **post**-quartz vein emplacement and mineralization in the Norseman Terrane.

CHAPTER 5

PETROGRAPHY, MINERAL CHEMISTRY AND TEXTURAL CHARACTERISTICS OF METAMORPHIC AND HYDROTHERMAL ALTERATION ASSEMBLAGES IN MAFIC LITHOLOGIES OF THE NORSEMAN TERRANE

5.1 Introduction

A fundamental unresolved question in lode gold deposits is whether those examples in higher grade metamorphic terranes, with high temperature alteration mineral assemblages, formed under the ambient metamorphic conditions, or alternatively are metamorphosed equivalents of counterparts formed at lower grade conditions (Table 4.1; Phillips, 1985; Groves et al., 1992). Resolution of this question has a direct bearing on the ore-forming processes for this class of precious metal deposit.

Gold deposits in the Norseman camp are hosted in a terrane with metamorphic grade trending systematically from upper greenschist facies in the north to amphibolite facies conditions in the south. Accordingly, this terrane has the appropriate boundary conditions for addressing the question of timing of gold mineralization. In an attempt to resolve the question, the regional metamorphic mineral assemblages are first documented, to constrain the relative differences in P-T conditions from north to south. The alteration mineral assemblages and paragenesis are then documented, P-T conditions quantified, and compared to ambient metamorphic conditions in each of the Northern, Central, and Southern deposit areas. Macroscopic and mesoscopic structural fabrics are recorded, and compared to morphological characteristics detailed in Chapter 4, to further constrain the thermal and temporal relationships of alteration to deformation and metamorphism. Collectively, the data are used to test the competing hypotheses of pre- versus post-peak mineralization.

5.2 Metamorphism of the Woolyeenyer Formation

The present understanding of regional metamorphism within the Norseman Terrane was outlined in Chapter 2. This section documents the petrographic and mineral compositional characteristics of least-altered assemblages found within mafic lithologies of the terrane. The term least-altered is used in the context of degree of hydrothermal alteration. As all rocks are hydrated to some degree and affected by varying degrees of post-peak metamorphic fluid activity, least-altered assemblages comprise those which most closely approximate regional metamorphic assemblages, in areas distal to shear zones and structurally focused hydrothermal activity.

Determining the grade of metamorphism surrounding the gold deposits proves to be a challenge as there are few interlayered sedimentary horizons in the mafic volcanic sequence of the Woolyeenyer Formation, and none with pelitic compositions that would provide diagnostic mineral assemblages. The sedimentary sequences of the Noganyer and Penneshaw Formations serve as a yardstick for regional metamorphic variation as outlined in Chapter 2; however, given the metamorphic gradient observed through these formations, they do not provide adequate indices of metamorphic grade at mine localities more than 1 km to the west of the Noganyer Formation. Emphasis is therefore placed on mafic lithologies of the Woolyeenyer Formation, as they are the dominant host lithologies, to facilitate comparison to hydrothermal alteration assemblages documented later in this chapter.

5.2.1 Petrography of regional metamorphic assemblages

5.2.1.1 Northern deposits

The environs of the Northern deposits are structurally very disrupted (Chapter 4), consequently allowing pervasive fluid movement through much of the stratigraphic sequence in this area. Of the samples collected in this study, only rarely were assemblages that potentially represent metamorphic assemblages observed. In high-MgO tholeiite of the North Royal Mine (Chapter 3), least-altered assemblages comprise dominantly amphibole and chlorite, with subordinate opaques (ilmenite) and only minor proportions of interstitial quartz and plagioclase (Fig. 5.1A) Amphiboles are actinolitic-hornblende to actinolite, and no zoning is apparent within individual grains (amphibole nomenclature after Leake, 1978, Fig. 5.2A). Chlorites are ripidolites (Appendix A). Igneous textures are rarely observed in these lithologies.

Least-altered assemblages in tholeiitic gabbros that host the Northern deposits comprise dominantly actinolite to hornblende and plagioclase (An_{5-43}), in varying

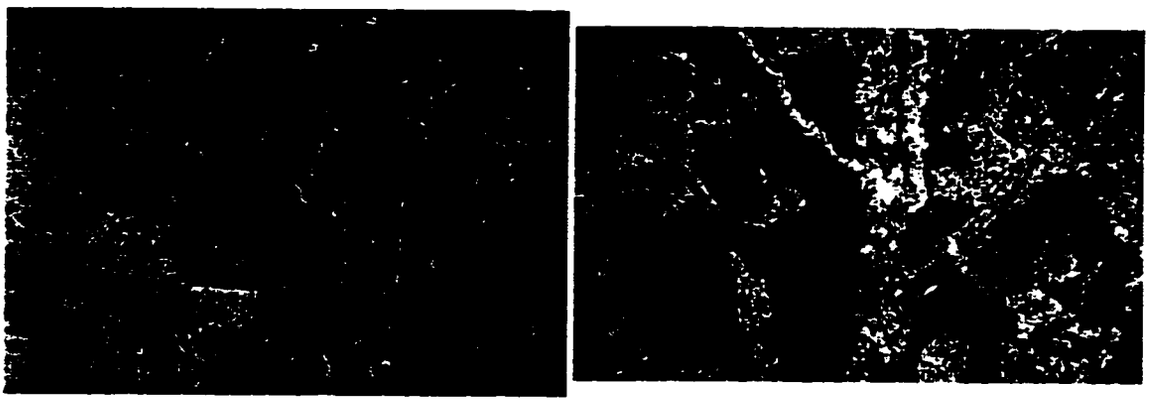

(a) (b)

Figure 5.1: Least-altered metamorphic assemblages in HMT and Tholeiites
(a) Photomicrograph of amphibole-chlorite assemblages, NR-34, North Royal mine. Plane polarized light, field of view 0.5 cm. (b) Metamorphic assemblages in a tholeiitic gabbro, sample SC163-18, Scotia mine. Note the multiple generations of late veinlets representing low-temperature retrogression of peak metamorphic assemblages.

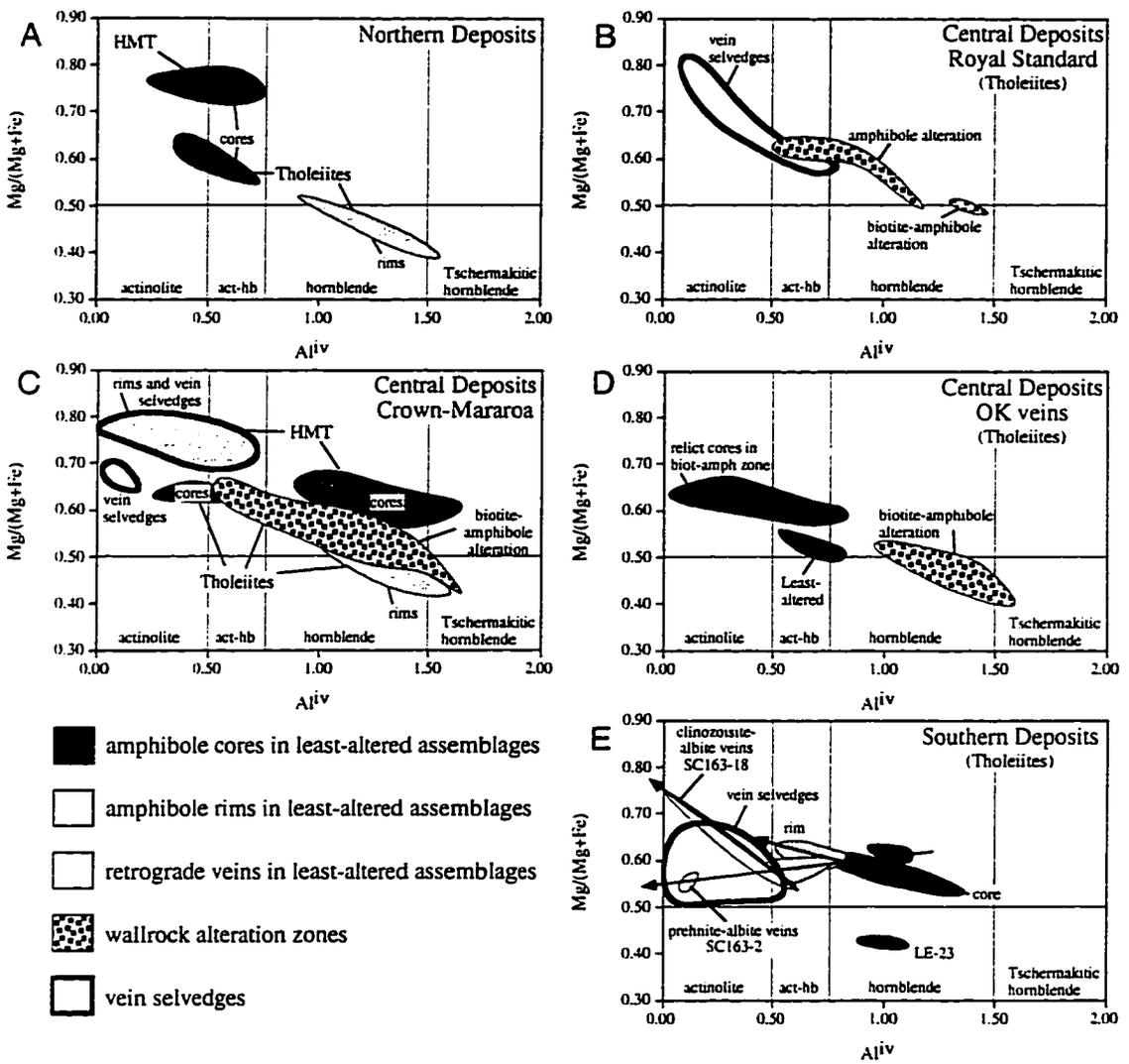

Figure 5.2. Plots of Mg/(Mg+Fe) versus Al^{iv} showing compositional ranges for amphiboles in least-altered metamorphic assemblages and gold-related hydrothermal alteration assemblages for select Northern, Central and Southern deposits. Element values shown are per formula unit, based on 23 oxygen atoms per formula unit in amphibole. Complete analyses of amphibole compositions are given in Appendix A. Fields for least-altered cores, rims, biotite-amphibole alteration assemblages and vein selvedges are distinguished on each diagram. Arrows on the Southern deposits diagram (E) show vectors for retrograde alteration observed through multiple generations of amphibole in least-altered tholeiite: from peak metamorphic cores, to lower-temperature rims, to zoisite-albite-actinolite veins, to prehnite-albite-actinolite veins.

proportions, with minor quartz, epidote, ilmenite and accessory apatite, titanite, leucoxene and biotite (Fig. 5.1B). A distinct paragenesis is evident in all samples. Metamorphic amphiboles are actinolite to actinolitic-hornblende in composition, pseudomorphing primary pyroxenes, with relict pyroxene cores rarely preserved. Finer-grained actinolitic-hornblende to Mg-hornblende forms fibrous rims around the pseudomorphous amphiboles, and along plagioclase cleavage planes and grain boundaries (Figs. 5.1B, 5.2A). Plagioclase (An_{39-43}) comprises well-preserved laths and glomeroporphyritic to (rarely) megaphenocryst patches, lightly dusted by sausseritic alteration and exhibiting relict Carlsbad and albite twinning (Figs. 5.1B, 5.3). Minor quartz, ilmenite and accessory apatite are ubiquitous; ilmenite as skeletal grains up to 200 μm in diameter, and apatite as finer-grained inclusions in plagioclase. This amphibole + plagioclase + ilmenite + apatite metamorphic assemblage is typically retrogressed to quartz + albite ($<An_{10}$) + epidote + chlorite + calcite along plagioclase and amphibole grain boundaries, and crosscut by veins of this mineral assemblage (Figs. 5.1B, 5.3). Ilmenite grains are variably altered to leucoxene ± titanite.

5.2.1.2 Central deposits

Least-altered high-MgO tholeiites in the environs of the Central deposits comprise amphibole + chlorite + ilmenite to amphibole + plagioclase + ilmenite assemblages, with igneous textures well preserved in many instances (Fig. 3.3C, Chapter 3). Amphiboles in these assemblages comprise actinolitic-hornblende to hornblende, which can be rimmed by clear actinolite (Fig. 5.2B-D). Where actinolite rims are observed, hornblende cores are variably altered; this is likely a manifestation of hydrothermal alteration described later in the chapter. Plagioclase (An_{35-38}) exhibits relict Carlsbad twinning. Chlorites are compositionally ripidolite.

Tholeiitic basalts and gabbros hosting the Central deposits are mineralogically similar to those in the Northern deposits area, with an amphibole + plagioclase + ilmenite + quartz ± epidote ± apatite ± biotite assemblage (Fig. 3.3A, 5.1A). Actinolite or actinolitic-hornblende (after primary pyroxene), rimmed by Mg-hornblende, and plagioclase are present (Fig. 5.2B-D). However, the plagioclase cores are more Ca-rich (An_{40-70}) than Northern deposit counterparts, and clear rims coexisting with Mg-hornblende, epidote and chlorite are Ca-rich (An_{70-90}). Conversely, some samples have rims of more sodic plagioclase (An_{15-19}, Fig. 5.3). Both of these assemblages are retrogressed to quartz + chlorite + zoisite + epidote + calcite assemblages, developed along amphibole and plagioclase grain boundaries and in transgranular veinlets. An important distinction between least altered assemblages in Central and Northern deposits

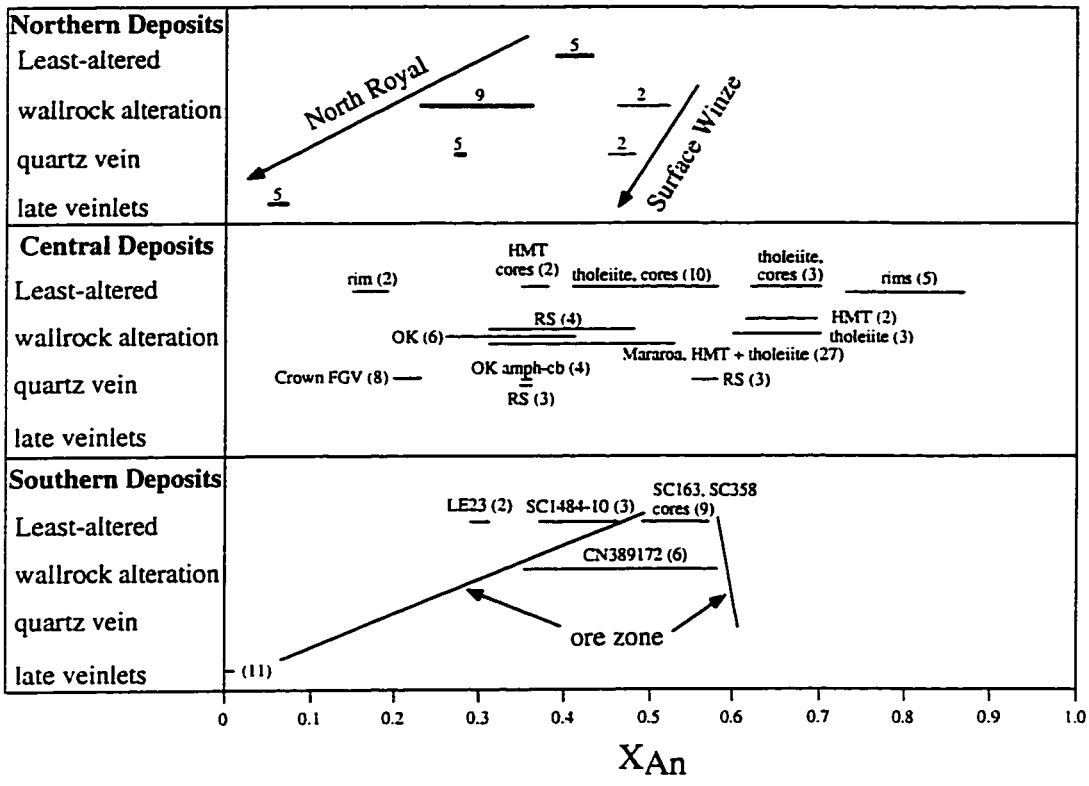

Figure 5.3. Composition of plagioclase from metamorphic and alteration assemblages, quartz vein selvedges and retrograde, post mineralization veinlets from Northern, Central and Southern deposit regions of the Norseman Terrane. Complete mineral analyses are given in Appendix A. Abbreviations: HMT = high-MgO tholeiite, RS = Royal Standard vein, amph-cb = amphibole carbonate veins in the OK mine. Numbers associated with Southern deposit compositions denote drill core from which samples were taken. Cores and rims of plagioclase grains are differentiated for some least-altered samples.

is the degree of epidote + chlorite development. Chlorite and epidote are minor to major constituents of the least altered assemblages in Northern deposits, whereas in Central deposits they usually constitute accessory phases in least-altered assemblages.

5.2.1.3 Southern deposits

Tholeiitic rocks in the Scotia area consist of variable proportions of amphibole and plagioclase, with minor quartz, Mg-chlorite, ilmenite and accessory apatite and titanite. Actinolitic-hornblendes to Mg-hornblendes pseudomorph pyroxene, whereas plagioclase crystals (An_{29-57}) generally show preserved Carlsbad ± albite twinning and are weakly sausseritised (Figs. 5.1C, 5.2E, 5.3). These amphibole-plagioclase assemblages are crosscut by zoisite + actinolite + calcite veinlets, and replaced along amphibole-plagioclase grain boundaries by fine-grained zoisite + actinolite + albite (An_1). Late prehnite + albite (An_1) veinlets crosscut all of the above assemblages.

5.2.2 Thermal history of least-altered assemblages

In mafic rock types, both amphibole and plagioclase compositions are sensitive to changes in metamorphic grade (Liou et al., 1974; Laird, 1980; Spear, 1980; 1981; Plyusnina, 1982; Maruyama et al., 1983; Moody et al., 1983; Blundy and Holland, 1990). An attempt is made to quantify differences in peak metamorphic conditions between the Northern, Central and Southern deposit areas through application of the calibrated amphibole-plagioclase geothermometer of Blundy and Holland (1990). This geothermometer correlates the Si atoms per formula unit (Si_{pfu}) in amphibole and X_{Ab} content of coexisting plagioclase with variations in temperature. In order to apply this geothermometer, the amphibole and plagioclase must have formed under equilibrium conditions, and must coexist with quartz, which buffers the Si content of the amphiboles. The geothermometer is considered to be applicable above 500°C, and for amphiboles with $Si_{pfu} < 7.8$ and plagioclase with $X_{Ab} > 8$, in which range temperatures are believed to be accurate to ± 75°C. Amphibole formula are calculated by normalizing to 23 oxygen atoms per formula unit, and appear to be robust to Fe^{3+}/Fe^{2+} recalculations in amphibole, which are therefore not calculated for the data presented here.

The geothermometer takes the form of:

$$T = (0.677P - 48.98 + Y)/(-0.0429 - 0.008314\ln K) \quad (5.1)$$

where T is temperature in Kelvin, P is pressure in kbar, $K = ((Si_{pfu}-4)/(8-Si_{pfu}))*X_{Ab}$, and $Y = 0$ when $X_{Ab} > 0.5$, or $Y = -8.06 + 25.5(1-X_{Ab})^2$ when $X_{Ab} < 0.5$.

Results of temperature calculations for selected amphibole-plagioclase pairs are summarized in Figure 5.4. Plagioclase and amphibole cores, assumed to have formed in equilibrium, give calculated temperature ranges of 500-550°C for Northern deposits, 500-700°C for Central deposits, and 650-750°C for Southern deposits. With the estimated error in temperature as high as ± 75°C, there is potentially overlap of estimated metamorphic temperatures between the different deposit groups. However, these results correlate reasonably well with the stability ranges for the assemblages observed in least-altered tholeiites, with abundant chlorite and epidote in Northern deposits, less common chlorite and epidote in Central deposits, and rare epidote and chlorite in Southern deposits (cf. Liou et al., 1974; 1983; 1985; Maruyama et al, 1983; Moody et al., 1983).

Within least-altered tholeiites of the Southern deposits, at least three generations of amphibole + plagioclase + quartz assemblages allow tracing of post-peak metamorphic fluid activity, and show a consistent cooling trend (Fig. 5.4). Northern and Central deposits, conversely, exhibit more hornblende-rich rims on actinolitic-hornblende cores and more Ca-rich rims on plagioclase. Temperatures calculated for these assemblages are much higher than those indicated by amphibole and plagioclase cores. It is possible that these hornblende + Ca-plagioclase assemblages represent a thermal overprint of earlier amphibole + plagioclase assemblages, but the temperatures calculated for these assemblages are above the stability of amphibole in metabasalts (ca. 800°C, Spear, 1981). A problem with this interpretation is that these "high-temperature" assemblages coexist with epidote and chlorite (Figs. 3.3A, 5.1B), which should represent lower temperatures than those indicated by amphibole and plagioclase cores, suggesting that the assemblages are retrograde in nature, or represent prograde metamorphism under disequilibrium conditions.

5.2.3 Summary of Metamorphism in the Norseman Terrane

Precise metamorphic conditions experienced by the mafic rocks of the Woolyeenyer Formation are difficult to constrain due to the lack of interlayered rocks of appropriate composition, such as pelites. Nevertheless, a comparison of relative metamorphic grade within the Woolyeenyer Formation from the Northern to Southern deposit areas can be made by comparing variations in mineral assemblage and mineral chemistry between least-altered lithologies in each of these areas.

The textural preservation of plagioclase phenocrysts, coupled with the complete recrystallization of primary pyroxenes to amphibole and lack of abundant chlorite,

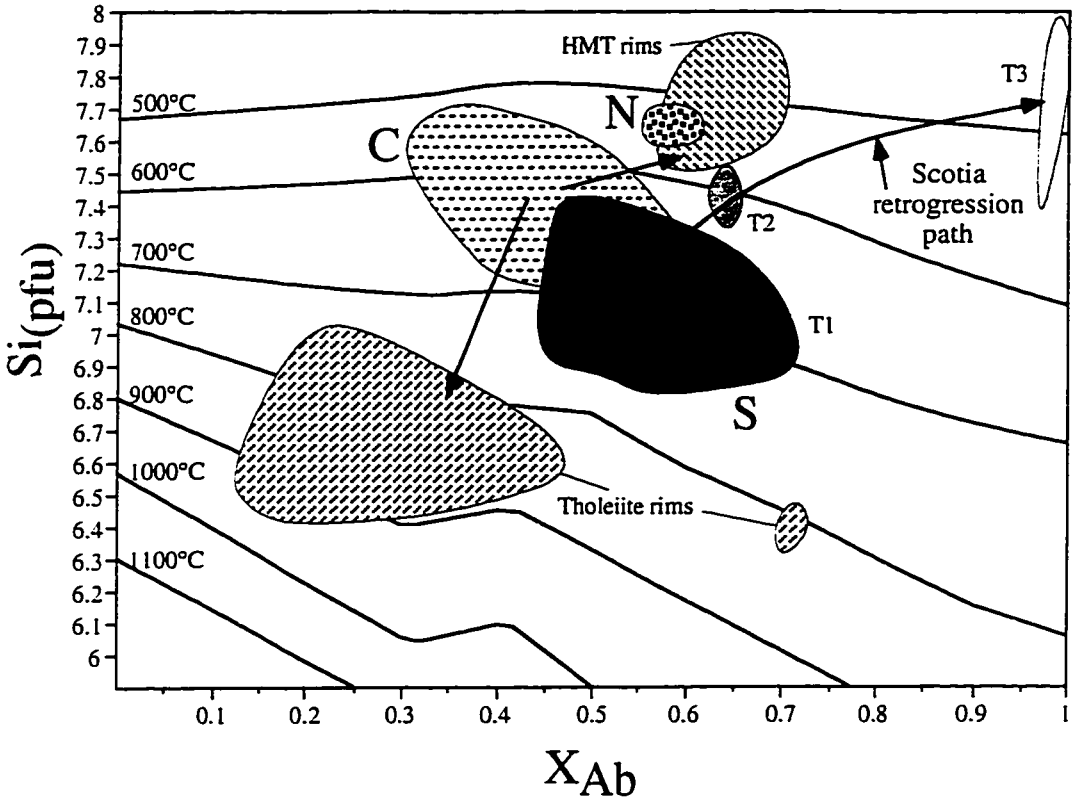

Figure 5.4. A graphical representation of the amphibole-plagioclase geobarometer of Blundy and Holland (1990) (equation 5.1), in coordinates of Si atoms per formula unit in amphibole versus mole proportion of albite in coexisting plagioclase. Solid lines running left to right across the diagram represent isotherms. Fields for coexisting amphibole-plagioclase pairs for least-altered assemblages are shown for Northern (N), Central (C) and Southern (S) deposits. Fields for amphibole-plagioclase rim assemblages in HMT and tholeiites of the Central deposits, and for the three generations of amphibole-plagioclase-quartz assemblages observed in the Southern deposits, are also shown (T1, T2, T3). See text for discussion.

corresponds to the medium-grade metamorphism (lower- to mid-amphibolite facies) style recognized by Binns et al. (1976). These assemblages indicate that the early retrogression of the Norseman greenstones, presumably in sea-floor hydrothermal cells, occurred under conditions of very high heat flow and rapid burial, so as to preserve relict plagioclase yet hydrate and recrystallize primary pyroxene to amphibole (cf. Binns et al. 1976, Barley et al. 1990). Subsequent prograde metamorphism to low-amphibolite facies may be represented by Mg-hornblende rims on actinolite cores in the environs of the Northern and Central deposits. The more extensive development of Mg-hornblende rims, and more calcic plagioclase, in the Central deposits is consistent with slightly higher metamorphic temperatures in the Central *versus* Northern regions, although the unrealistically high temperatures calculated for these assemblages suggest formation under disequilibrium conditions. In the lithologies hosting the Southern deposits, amphibole cores consisting predominantly of Mg-hornblende/actinolitic hornblende, the paucity of actinolite and chlorite, and the presence of calcic plagioclase collectively suggest that these lithologies were metamorphosed to higher metamorphic grades than counterparts in the Central and Northern areas.

The observations of metamorphic assemblages reported above are consistent with those of Hallberg (1970) and Binns et al. (1976), and in combination with the calculated temperatures suggest that lithologies hosting the Northern deposits straddle the greenschist-amphibolite transition (450-550°C, Essene, 1989), those hosting the Central deposits are within the lower-amphibolite facies, and lithologies hosting the Southern deposits have been metamorphosed to upper-amphibolite facies.

Golding (1982) compared least-altered assemblages at Norseman to petrogenetic grids constructed from studies of metamorphosed mafic rocks. This approach yielded estimated peak metamorphic temperatures of 475 -500°C in the vicinity of the Northern deposits at an estimated pressure of 2-4 kb, based on assemblages of oligoclase/andesine + hornblende ± chlorite in mafic lithologies, and 500 ± 50°C in the environs of the Central deposits, based on assemblages of hornblende + actinolite + plagioclase in mafic lithologies, and tremolite + chlorite ± calcite ± quartz assemblages in high-MgO lithologies. Amphibole-plagioclase geothermometry performed by Mueller (1992) indicated temperatures of 500-575°C for rocks hosting the Central deposits. The results of Golding (1982) and Mueller (1992) also corroborate those of this study. However, the report of prehnite-pumpellyite and greenschist facies assemblages in the vicinity of the Southern deposits (Spray, 1985) is not supported by the current study. The dominant assemblage preserved in the environs of the Southern deposits is hornblende/actinolitic-hornblende and calcic plagioclase of the amphibolite facies, and the low-grade

assemblages denoted by prehnite + albite veins are paragenetically late.

The pressure of metamorphism is largely unconstrained at Norseman. Stratigraphic reconstructions of Mueller (1992) estimate that metamorphism may have taken place at 3 kb. Sedimentary rocks of the lower Noganyer Formation contain andalusite in the vicinity of both the Central and Southern deposits and lack kyanite (Keele 1984; Spray 1985), indicating that peak metamorphism in the Norseman Terrane occurred under P-T conditions below those of the aluminosilicate triple point (ca. 3.75 kb, 500°C, Holdaway, 1971). Application of the hornblende geobarometer of Hammarstrom and Zen (1986) to a tonalite body in the vicinity of the Central deposits yields a crystallization pressure of 1.7 ± 0.5 kbars (Kent, 1994; Chapter 2). As this tonalite body is interpreted to be broadly coeval with the thermal peak of metamorphism, this is the best quantitative estimate of minimum pressure conditions of metamorphism within the Woolyeenyer Formation.

Fifty kilometres east of Norseman, the Dambo Fault juxtaposes granulite facies rocks in its hangingwall against amphibolite facies rocks in the footwall (Fig. 2.2, M.E. Clark pers. comm. 1992). This suggestion of south-over-north thrusting along the Dambo Fault implies that the greenstones south of the Dambo Fault, in the vicinity of Southern deposits, have seen deeper crustal levels relative to the Central and Northern areas.

Retrograde mineral assemblages in veinlets, vug fillings (Hallberg 1970) and along grain boundaries may represent passage of the Norseman Terrane through the greenschist and prehnite-pumpellyite metamorphic facies during uplift and cooling, or episodic fluid infiltration through pre-existing structures during post-cratonization events.

5.3 Hydrothermal alteration associated with lode gold deposits

Hydrothermal alteration assemblages contiguous with quartz-dominated veins in shear zones, faults or fracture systems (fluid conduits) reflect open system chemical and isotopic metasomatic interaction of fluids advecting upwards through the crust with adjacent wallrocks as they approach chemical, isotopic, and thermal equilibrium (Fig. 5.5; see Korzhinskii, 1970, for a general treatment of metasomatic theory). Factors controlling alteration associated with lode gold orebodies and their host hydrothermal plumbing systems are divisible into variables that include:

(1) the tectonic régime and resultant stress field in which the deposits are formed,
(2) composition of the host lithologies,
(3) composition of the hydrothermal fluid (X_{fluid}),

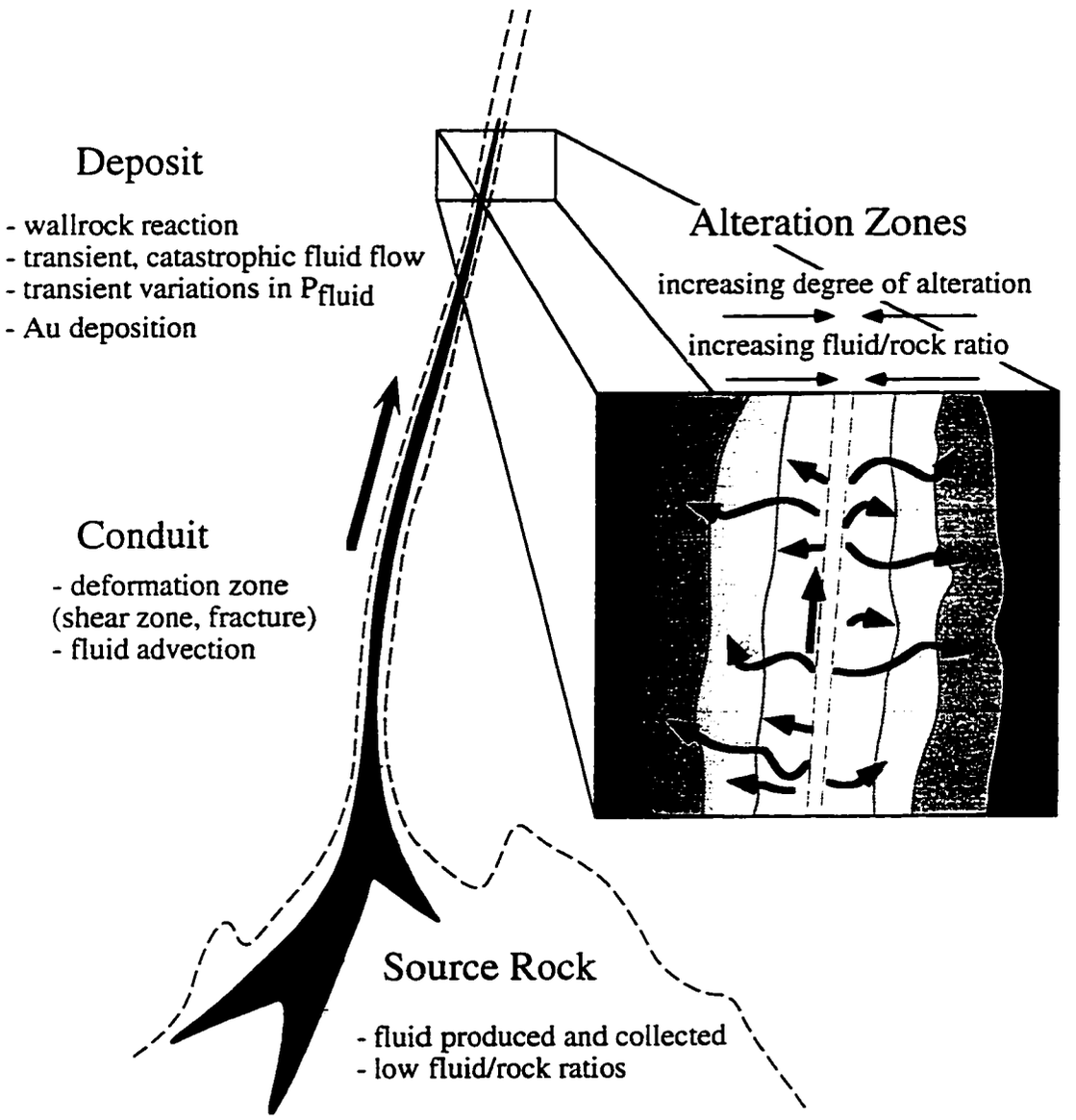

Figure 5.5. Schematic diagram of processes of fluid sourcing, focussed flow, infiltration into wallrocks and resultant hydrothermal alteration as envisaged for lode gold systems. After Ridley (1990).

(4) the temperatures (T), and

(5) pressures (P) at which hydrothermal alteration and gold mineralization occur.

Complex interplay of these five parameters influence properties such as the rheologies of rock units and effective fluid pressures, as well as the mechanisms of deformation, fluid/rock interaction and metasomatic reaction that operate. Collectively, the above factors control the architecture of hydrothermal plumbing systems from the terrane to microscopic scale, and the structural and chemical 'traps' in which gold is deposited (McCuaig and Kerrich, 1994).

Norseman is well-suited for terrane-scale investigations of hydrothermal alteration because the gold deposits are hosted in mafic lithologies of similar composition, and in a uniform far-field stress regime. Therefore, differences outlined in alteration mineralogy allow investigation of variations in the P-T-X_{fluid} of alteration on the terrane scale.

5.3.1 Alteration zonation and mineralogy associated with the Norseman lode gold deposits

The mineralogy of alteration assemblages associated with lode gold deposits is varied, and zonations are noted

(1) with increasing distance orthogonally away from the fluid conduit(s),

(2) between host lithologies of differing bulk composition, and

(3) regionally with temperature ± pressure of formation.

The most marked changes in alteration mineralogy occur perpendicular to the fluid conduits. These zones may range from millimetres to tens of metres or more in thickness, and correlate with the width, strain intensity, and abundance of quartz veins within the host shear zones, and are defined by the presence of diagnostic mineral assemblages. There is no direct correlation, however, between alteration intensity and the width of individual quartz veins.

Alteration mineralogy in the wallrocks surrounding all deposits is zoned laterally toward the fluid conduits, from least-altered metamorphic assemblages, through outer to inner alteration zones. Inner, or proximal alteration zones immediately adjacent to quartz veins, or towards areas of greatest fluid flux, reflect fluid-dominated metasomatic reactions. Note that the term **vein selvedge** in the following discussion is used to denote the mineral assemblages in the veins at the immediate contact between the quartz veins and wallrock. This zone is generally a few millimetres to a few centimetres in width. The mineralogical zones more distal from the vein reflect a decreasing gradient of fluid/rock ratio, as well as chemical gradients (discussed below), and represent progressive infiltration of the fluid into the wallrock.

Boundaries between alteration zones may be knife sharp or gradational over centimetres to metres with sharp boundaries common in proximal alteration zones, whereas diffuse boundaries predominate in distal alteration zones. The most distal alteration zones grade into least-altered regional metamorphic assemblages. Examples of such lateral alteration zonation are summarized for tholeiite-hosted quartz veins in Fig. 5.6 The greatest complexity usually occurs in inner alteration zones due to narrow zone widths and the episodic nature of deformation and fluid infiltration, which act in concert to produce alteration zones with complex crosscutting relationships. These zones are progressive in nature, such that proximal alteration zones overprint their distal counterparts. Thus the zonation of mineral assemblages away from the fluid conduits can be viewed as metasomatic reaction fronts (e.g., Korzhinskii, 1970; Kishida and Kerrich, 1987; Clark et al., 1989).

The paragenetic sequence of mineral assemblages and structures identified in both the least-altered wallrocks detailed above and fluid-dominated shear zones in the lode gold deposits described below indicate that the deposits have evolved through a number of temperature ± pressure régimes and fluid events. Therefore, it is imperative that hydrothermal wallrock alteration envelopes be examined in a broad context from several different standpoints, including: a spatial distribution, or lateral zonation away from veins and shear zones; differences in alteration assemblages between deposits (Fig. 5.6); and a temporal framework, or change in alteration mineralogy and deformation mechanisms with time (Fig. 5.7).

5.3.2 Petrography of hydrothermal alteration assemblages

5.3.2.1 Northern deposits

The Princess Royal Fault Zone possesses a planar to anastamosing ductile fabric defined by the alignment of chlorite, biotite, and quartz-carbonate veins that have been transposed subparallel to the shear zone margins. The fabric varies in intensity, with weakly deformed blocks of basalt, porphyry and high-MgO gabbro surrounded by zones of intense fabric development, in which the original rock type is generally unrecognizable. Throughout the fault zone, primary igneous textures are destroyed, and the least-altered metamorphic mineralogy of amphibole + plagioclase + quartz in tholeiites is completely replaced by chlorite + carbonate + quartz ± plagioclase. Biotite is abundant in discrete zones of intense fabric development (Fig. 5.8A).

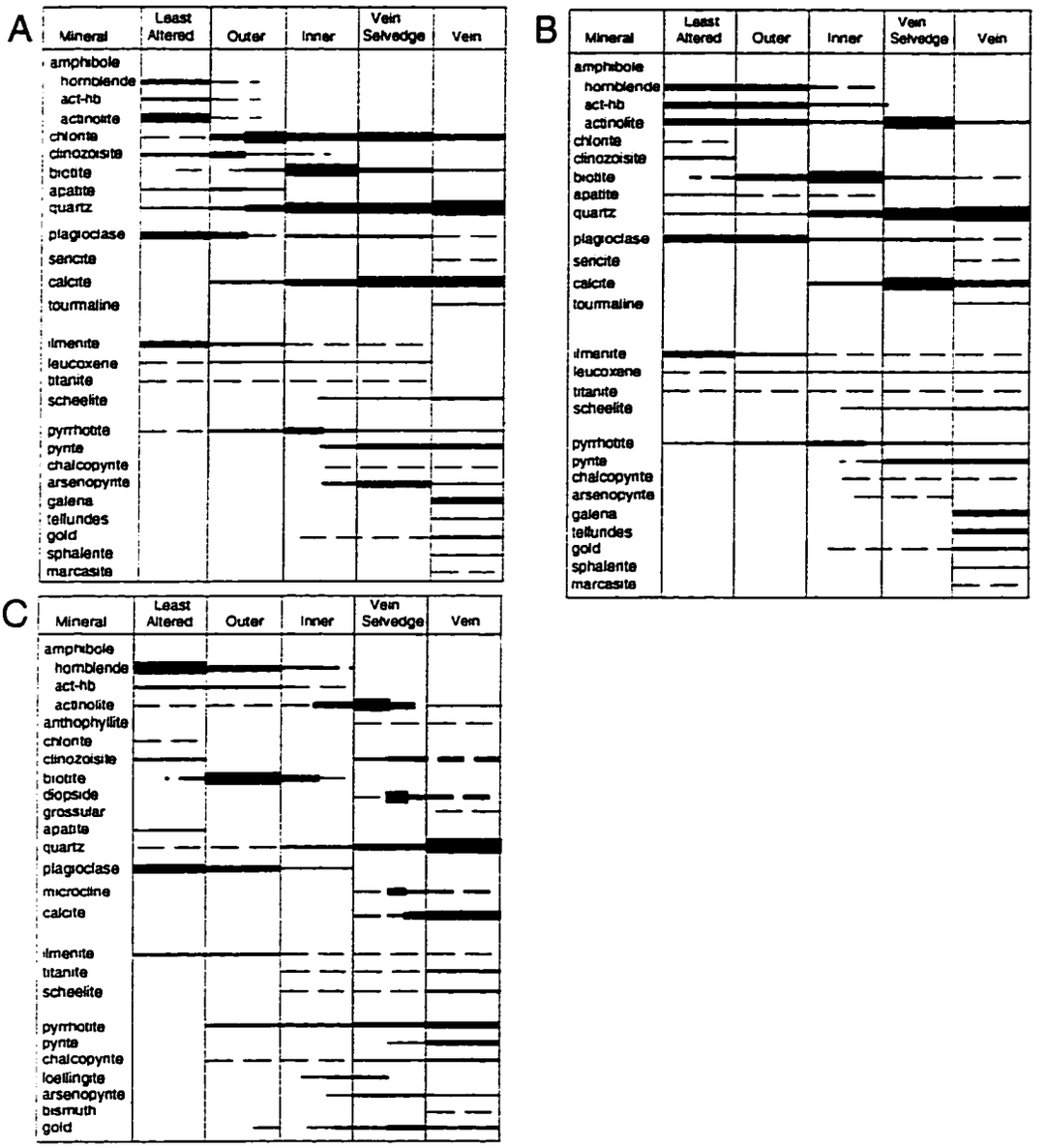

Figure 5.6. Zonation of alteration mineral assemblages surrounding tholeiite-hosted lode gold deposits of the Norseman Terrane. Least-altered metamorphic assemblages are at the left of each diagram, quartz vein assemblages are at the right. Thickness of bars corresponds to the relative abundance of the minerals. Zone widths are not to scale, indicating only the relative spatial relationships between alteration assemblages. **A.** Northern deposits. **B.** Central deposits. **C.** Southern deposits. From McCuaig et al. (1993).

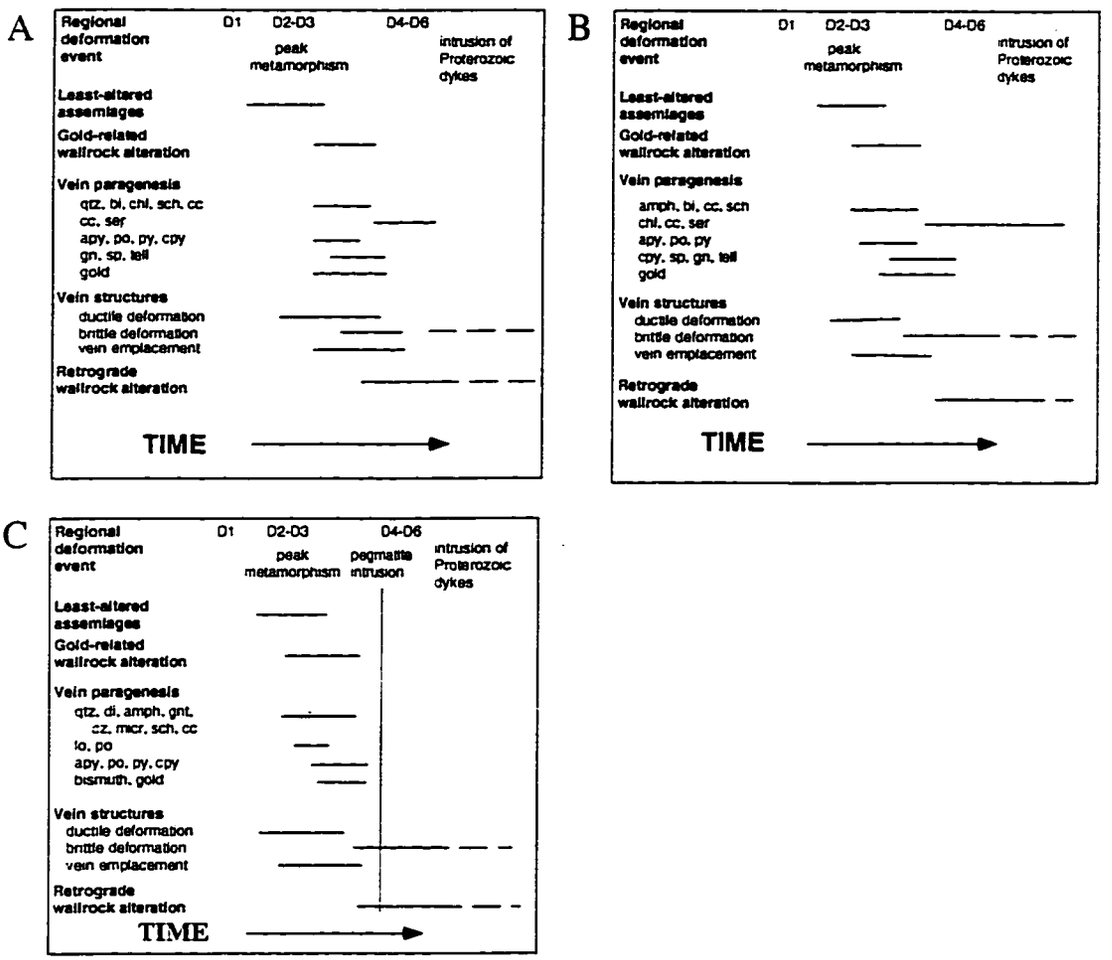

Figure 5.7. Paragenetic evolution of lode gold deposits within the Norseman Terrane, based on textural observations of gold related alteration assemblages and structural observation of vein morphologies and host shear zones. **A.** Northern deposits. **B.** Central deposits. **C.** Southern deposits. Modified from McCuaig et al. (1993).

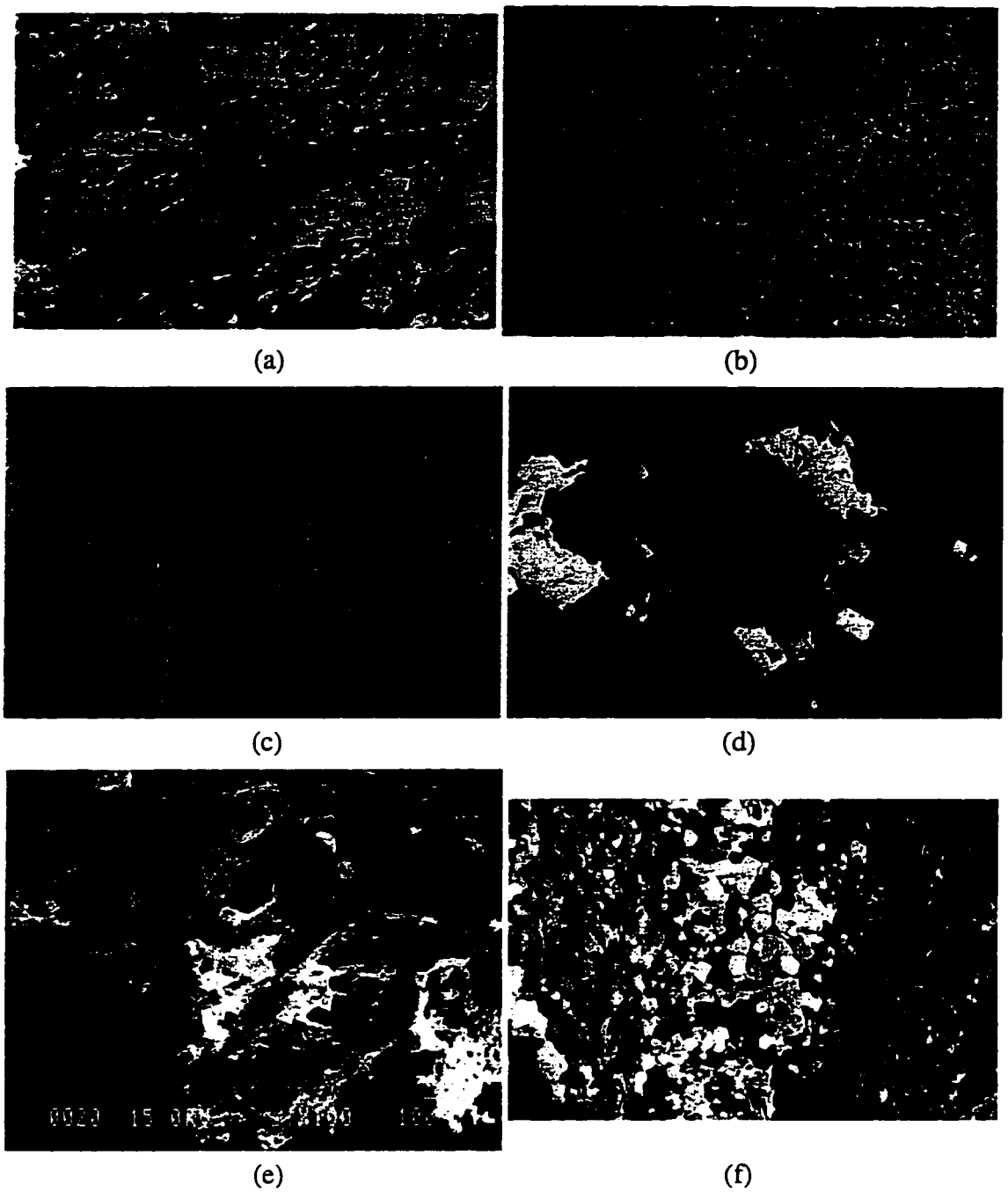

Figure 5.8: Photomicrographs of alteration assemblages in Northern Deposits
(a) Chlorite-quartz-carbonate alteration defining a foliation within the Princess Royal Fault Zone. (b) Amphibole in HMT at the margin of the Royal Tiara vein, partially retrogressed to chlorite-carbonate-quartz assemblages. (c) banded monomineralic chlorite, and biotite-carbonate-quartz selvedges at the margin of the Princess Royal vein. (d) Gold associated with pyrite and galena in quartz, North Royal mine (e) SEM photo of wire gold and gold casts of pyrite grains, indicating that gold precipitated on preexisting pyrite crystals (f) Recovered quartz subgrains at the margin of the Princess Royal vein.

In HMT, least-altered assemblages of amphibole + chlorite ± plagioclase ± quartz are altered to chlorite + carbonate + quartz. Biotite can be present locally but is notably less abundant than in lithologies with tholeiitic precursors. Amphibole is preserved in many of the HMT precursors within the PRFZ, and can be oriented at high angles to the fabric. However, these amphiboles are typically corroded, fractured, and rotated into the fabric, exhibiting subgrain development and undulose extinction. The amphiboles are also variably altered to chlorite and calcite (Fig. 5.8B). Collectively, these observations indicate that the amphiboles are deformed and unstable within the PRFZ (Archer, 1990; McCuaig, 1990). Quartz grains in these assemblages show extensive subgrain development, and subgrains are generally well recovered, showing only minor undulose extinction. In some localities, evidence that pressure solution processes were operative is given by elongate quartz crystals with straight, truncated long edges bounded by chlorite+ biotite + opaque bands (Fig. 5.8A).

Quartz-carbonate veining is common within the fault zone. Coarse chlorite + carbonate selvedges to some of these veins have been observed, generally oriented parallel to the fabric. Quartz within these veins is dynamically recrystallized, with subgrains exhibiting undulose extinction and serrated grain boundaries, with moderate degrees of recovery (Fig. 5.8A). Late carbonate + quartz veinlets cut all of the above alteration assemblages and earlier quartz + carbonate veins. Brittle faults are also present within the PRFZ, and occur as isolated thin fractures, or as discrete zones of fractures with anastamosing fabric filled with disaggregated fault cataclasite.

In lode-gold deposits hosted within tholeiites, the least-altered assemblages are amphibole-bearing, and are progressively altered to outer chlorite- and then to inner chlorite + biotite-bearing assemblages with increasing proximity to the auriferous quartz veins. Concomitantly, there is complete destruction of metamorphic amphibole, plagioclase and all primary textures, and an increase in the abundance of calcite and sulphide minerals (Fig. 5.6A). This mineralogical zonation is consistent with wholerock geochemical variations across the alteration zones, which reflect the progressive addition of volatiles (H_2O, CO_2) and K_2O into the wallrock from the hydrothermal fluid (Section 5.4; McCuaig and Kerrich, 1990). In the biotite + chlorite zone, biotite and chlorite possess mutually overprinting relationships. Note that plagioclase proximal to the vein is slightly less calcic than its metamorphic precursor (Fig. 5.3).

In high-MgO lithologies, least-altered assemblages of amphibole + chlorite ± quartz ± plagioclase are altered to chlorite + carbonate + quartz ± biotite with increasing proximity to the vein margins. Amphibole may persist through inner alteration assemblages to the vein margin, but is variably altered to chlorite + calcite + quartz, and

possesses multiple fractures infilled by these minerals (Fig. 5.8B). Biotite alteration is only sporadically developed in these HMT lithologies, even in the innermost alteration zones. Vein selvedges are commonly mono- or bi-mineralic, consisting of carbonate, chlorite or biotite, occuring as aggregates, subradial rosettes, or aligned plates, sporadically intergrown with quartz + sulphides ± scheelite ± tourmaline (Fig. 5.8C). Hydrothermal amphibole has not been documented in vein or vein selvedge assemblages within the Northern deposits.

Pyrrhotite is the dominant sulphide in the outer and inner alteration zones. Pyrite and arsenopyrite are locally abundant adjacent to the veins. Where sulphides are abundant, ilmenite is progressively altered to leucoxene, titanite and Fe-sulphides. However, ilmenite is typically a stable phase at the vein margins in sulphide-poor areas.

Earliest mineral assemblages in the quartz veins consist of fine-grained chlorite, subordinate amounts of biotite, and locally abundant tourmaline fibres intimately intergrown with quartz, euhedral arsenopyrite or pyrite crystals, and granular aggregates of carbonate, chlorite and scheelite adjacent to vein selvedges and wallrock inclusions. Aggregates of carbonate, chlorite and scheelite, and trails of euhedral arsenopyrite or pyrite crystals also occur as isolated patches in quartz, or on early fractures in quartz (Fig. 5.8D). Later galena, sphalerite, Ag-Pb-Au tellurides (altaite, hessite, petzite) and native gold rim and fill fractures in the earlier pyrite/arsenopyrite, or are sited along quartz grain boundaries (Figs 5.8D,E). As these minerals occur also as rare isolated inclusions in arsenopyrite and pyrite, and never crosscut quartz grain boundaries, they are interpreted to have been introduced during or shortly after the main phase of quartz deposition (Fig. 5.7B). Gold occurs as free grains within the quartz veins (>98%), but also is present in a sporadic dispersion halo at abundances of >10 ppb up to a few metres from the vein margins (McCuaig, 1989; McCuaig and Kerrich 1990; Section 5.4).

Deformation fabrics are variably developed in these wallrock assemblages, and are defined by the alignment of chlorite and biotite, and occasionally by compositional banding with alternating quartz-carbonate and biotite-chlorite zones. This compositional banding is likely a result of closely spaced small-scale vein emplacement within the wallrock. Chlorite and biotite in quartz veins have a characteristic "accordion" texture.

Quartz fabrics vary throughout the quartz veins, even in a single locality, from quartz with intense subgrain development but well recovered subgrain boundaries (Fig. 5.8E), to coarse-grained quartz (>2 cm), with extreme undulose extinction and highly serrated subgrain boundaries (cf. Fig. 5.9G). Mortar texture, where large quartz grains are rimmed by mantles of subgrains, is sporadically developed. In general, grain size decreases proximal to vein margins, wallrock inclusions, and vein laminations, and

towards zones of post-quartz brittle deformation. However, the bulk of the quartz observed in thin section in Northern deposits exhibits only moderate subgrain development, has highly undulose extinction, and has well-serrated grain boundaries. These quartz grains are often moderately aligned at high angles to the vein margins (cf. Fig. 5.9H). A recovered quartz microstructure signifies relatively higher temperatures and/or slower strain rates, whereas serrated subgrains indicate relatively lower temperatures and/ or faster strain rates.

These hydrothermal alteration assemblages associated with quartz vein emplacement and gold mineralization in ductile-brittle shear zones are locally retrogressed to calcite, sericite, chlorite and albite ($An<10$) along vein margins and along narrow brittle fractures that crosscut all other assemblages. Sericite and chlorite are commonly along stylolites and brittle fractures in the quartz veins. Calcite + quartz + chlorite veinlets crosscut the veins and wallrock fabrics at high angles, and may be weakly deformed. Many brittle fractures within the quartz veins are filled by brecciated quartz and fault gouge (Chapter 4) The latest mineral assemblage comprises gypsum precipitated from groundwater along brittle fractures.

5.3.2.2 Central deposits

Alteration assemblages in 1st-order shear zones were evaluated through observation of B-fault, a ductile-brittle shear zone that transects the Regent mine stratigraphy and deforms the Mararoa and Crown quartz vein systems (Chapter 4). Where this structure transects tholeiitic lithologies, mineral assemblages comprise amphibole + plagioclase + quartz + ilmenite, with biotite alteration locally developed. Where HMT are cut by this shear zone, the mineral assemblage consists of amphibole + chlorite + quartz + ilmenite. A well developed ductile fabric pervades the structure, defined by the alignment of amphibole + chlorite, and rodding of quartz. Brittle fabrics are only locally developed, in the form of anastamosing patterns of discrete fractures filled with chlorite and ultra-fine grained fault cataclasite.

Folded, locally auriferous, laminated quartz veins are present throughout B-fault. Alteration surrounding these veins is similar to that surrounding the auriferous quartz veins in second-order structures documented below. Vein selvedges of carbonate and monomineralic, fibrous amphibole are ubiquitous (Fig. 5.9A). The similarities between hydrothermal alteration surrounding folded quartz veins in B-fault, and that surrounding the Mararoa and Crown veins, indicates that B-fault was active during mineralization and acted as a conduit for ore fluids.

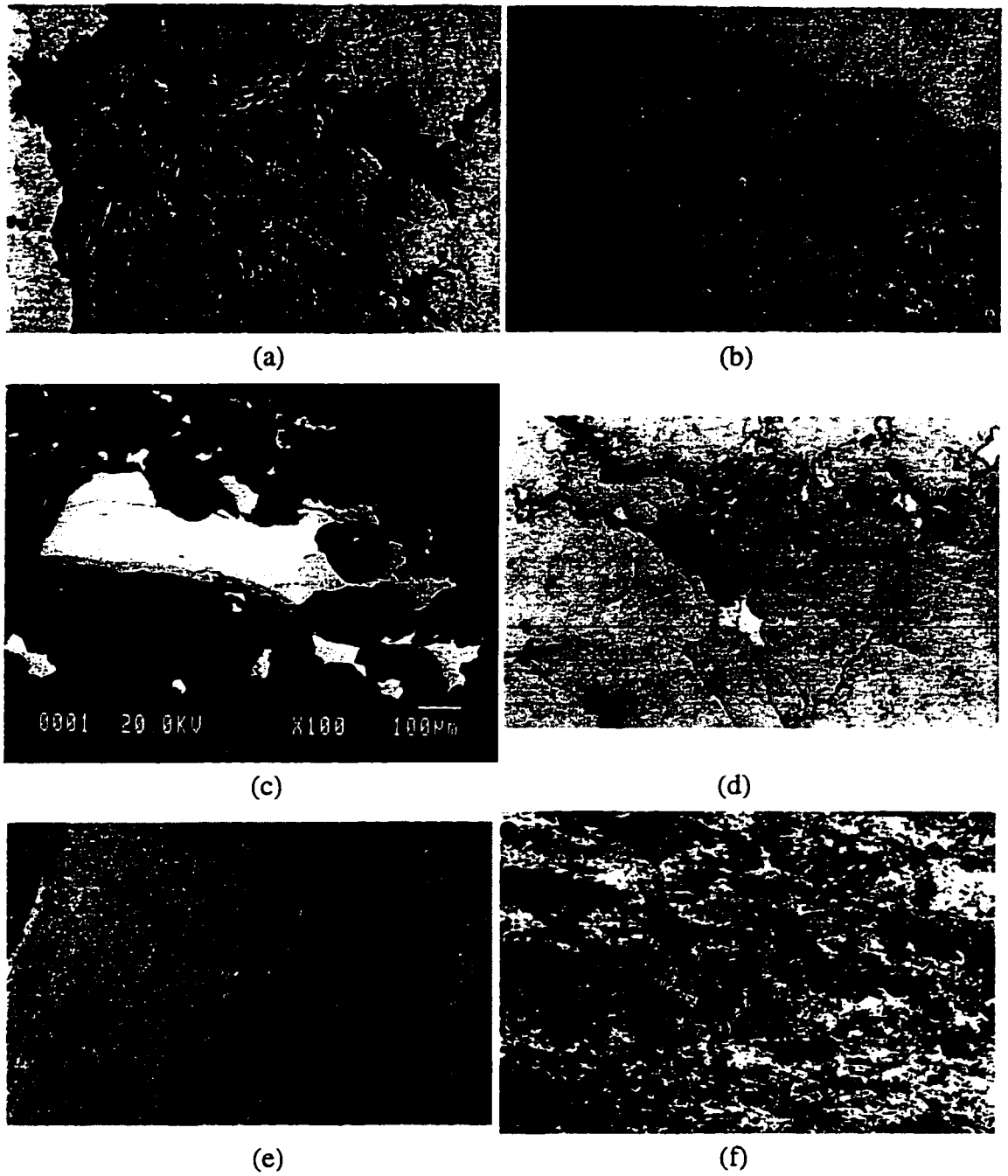

Figure 5.9: photomicrographs of alteration assemblages in Central deposits
(a) Monomineralic amphibole lamination in quartz, fringed by acicular amphibole, B-fault, Regent mine. (b) Fibrous amphibole selvedge, 25 level, Crown vein. (c) SEM photo of multiple fracture and sulphide generations, OK Main vein. Au is intergrown with biotite and plagioclase away from the late fracture. (d) sericite and galena growth on stylolitic lamination in the Norseman vein, Ajax mine. (e) Foliated amphibole-biotite-quartz-plagioclase-ilmennite alteration, S13-D, Mararoa vein. (f) Prismatic amphibole overgrowing aligned amphibole-biotite-quartz-plagioclase alteration, O2 rein, OK mine.

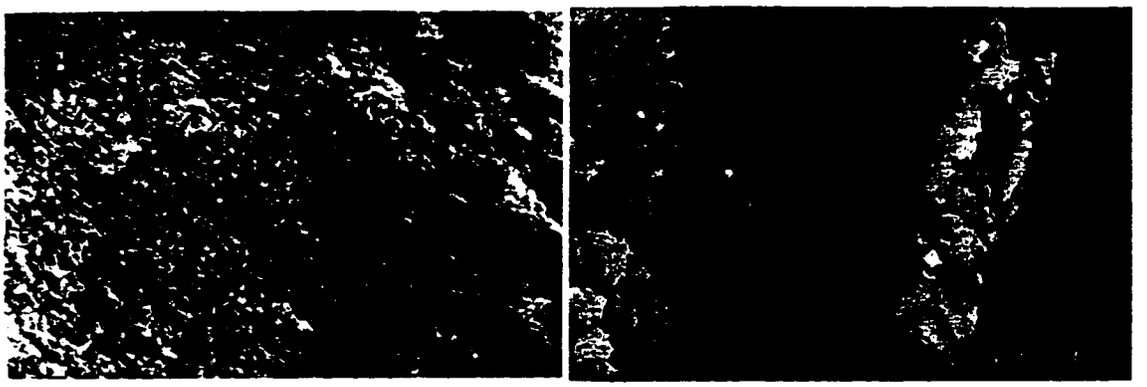

(g) (h)

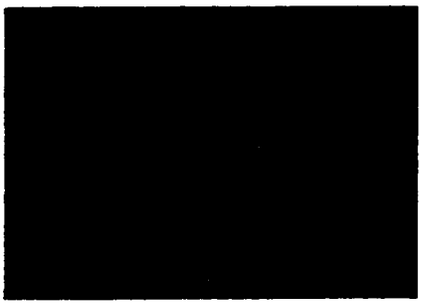

(i)

Figure 5.9 (cont.): Alteration associated with Central deposits
(g) Mutually intergrown prismatic amphibole and aligned biotite shown in 5.9f. (h) Serrated grain boundaries and undulose extinction in quartz, Mararoa vein, Regent mine. (i) Photo of thin section of Royal Standard vein margin, exhibiting varying degrees of recovery in quartz and alteration minerals.

Hydrothermal alteration envelopes surrounding auriferous quartz veins in tholeiitic lithologies within the Central deposits consist of three gradational zones (Fig 5.6B). With increasing proximity to the veins, these are:

(1) actinolitic-hornblende + hornblende + plagioclase + epidote (least-altered metamorphic assemblage, Fig. 3.3A),

(2) hornblende + actinolite + biotite + plagioclase (outer zone, and

(3) biotite + quartz + actinolite + plagioclase or calcite (inner zone).

Inner alteration zones are dominated by biotite, with subordinate actinolite and plagioclase or calcite (Fig. 5.9B). Plagioclase recrystallized throughout this alteration sequence, exhibiting a range of compositions, from An_{20-70} (Fig. 5.3); it tends to be the stable Ca-rich phase in quartz-rich inner alteration zones, whereas calcite is stable in quartz-poor inner zones. In HMT, least-altered assemblages of amphibole + chlorite + plagioclase ± quartz are progressively altered to amphibole + chlorite + quartz + carbonate with increasing proximity to the vein margins. Biotite occurs sporadically.

A sharp transition marks the vein margins, where inner alteration zone assemblages are bounded by actinolite + quartz + calcite ± biotite ± plagioclase vein selvedges (Figs. 5.6B, 5.9B). Actinolite is present as fibrous rosettes in the quartz vein, and typically exhibits progressive grain-coarsening towards the centre of fibrous aggregates (Figs. 5.9A,B), whereas calcite or plagioclase are present as medium to coarse-grained granular aggregates. Any of these minerals may form mono- or bi-mineralic mineralic vein selvedges up to a few centimetres in width.

Sulphides are locally abundant in the wallrock adjacent to the veins, but are generally less abundant than in the Northern deposits. Pyrrhotite is the dominant sulphide in the inner and outer alteration zones, whereas pyrite dominates the quartz veins and vein selvedges. As in the Northern deposits, metamorphic ilmenite is generally altered to titanite and leucoxene, but may be a stable phase at the vein margins and, rarely, within the quartz veins. Arsenopyrite is abundant in inner alteration zones of some deposits (e.g. OK veins, parts of Crown vein) but is notably scarce in others (e.g. Mararoa, Norseman veins).

Veins within the shear zones comprise over 90% quartz, intimately intergrown with subordinate calcite, actinolite, pyrite, scheelite and tourmaline. Euhedral pyrite grains within the quartz are fractured and infilled by galena, the tellurides hessite, altaite, petzite and sylvanite, and native gold. Galena, sphalerite and gold also are localized along quartz grain boundaries, generally away from later brittle fractures and stylolites (Fig. 5.9C). Stylolites appear to have preferentially nucleated along bands of wallrock or sulphide trails, and ore minerals may be located adjacent to or on the stylolite surfaces.

An example is at the southern end of the Mararoa and Norseman reefs where the brittle E-fault offsets the veins (Fig. 4.1). In stopes adjacent to this structure, galena, sphalerite, sericite, chalcopyrite, tellurides and gold are intimately intergrown along stylolitic fractures in the veins (Fig. 5.9D). Significantly, galenas from this assemblage yield Proterozoic Pb-Pb paleoisochron ages, and suggest that Proterozoic remobilization of Pb, Zn, Te and Au has occurred locally in the Norseman deposits (Chapter 6).

The alteration zones adjacent to the quartz veins possess a variably developed fabric, which is subparallel to oblique to the vein margin. In tholeiites, this fabric consists of domains of strongly aligned biotite + amphibole anastamosing around domains of randomly oriented amphibole and random to weakly aligned biotite, and around quartz + plagioclase aggregates (Fig. 5.9E). Some amphiboles appear to overprint the aligned biotite/chlorite (Fig. 5.9F). This amphibole texture was previously described as decussate, and interpreted as a metamorphic overprint of the hydrothermal alteration assemblages (Golding, 1982; Keele, 1984). However, the amphiboles are not decussate, but rather tend to be aligned with the fabric more often than at high angles to it. Figs. 5.9F and 5.9G illustrate that a fabric defined by ilmenite is preserved in amphiboles at high angles to the fabric, whereas it is destroyed in aligned amphibole and biotite. The amphibole and biotite also display mutually penetrative crystal edges (Fig. 5.9G). Detailed probe traverses show no reaction rim around the amphibole, or in the biotite. Furthermore, quartz and plagioclase in the matrix exhibit varying degrees of dynamic recovery, with undulose extinction well developed in some grains. If the amphibole was a metamorphic overprint, more annealed textures would be expected.

It is proposed here that this texture formed during deformation and alteration at broadly syn-peak metamorphic temperatures. The biotite and amphibole formed together, with the amphibole, being a more prismatic mineral, tending to crystallize with less of a preferred dimensional orientation than the biotite. The chlorite and biotite accommodate much of the strain as they crystallize, allowing the prismatic amphibole to crystallize at variable angles to the fabric. In fine-grained basalts, amphiboles become progressively coarser towards the vein margin, typically consisting of aggregates of fibrous crystals which grade into optical continuity towards the centre of the larger composite crystal. Some coarse, optically continuous amphiboles actually consist of very fine-grained acicular amphibole crystals that are parallel to the fabric defined by aligned biotite or chlorite (Fig. 5.9G). Therefore, amphiboles which are oriented at high angles to the wallrock fabric can form by the aggregation of numerous acicular amphibole fibres which, individually, grow parallel to the wallrock fabric. The mutually penetrative crystal boundaries and the fact that some amphiboles have rotated into the fabric are also

consistent with the biotite/chlorite and amphibole forming synchronously during syntectonic hydrothermal alteration.

Vein quartz in the Central deposits exhibits varying degrees of recovery, from coarse grains (up to 1 cm) with extremely undulose extinction and serrated grain boundaries, to completely recovered subgrains with 120° triple boundaries (Figs. 5.9H,I). Mortar textures are well developed, and abundant. Quartz grain size decreases towards vein margins, wallrock inclusions, and zones of brittle deformation. In general, the degree of subgrain formation and dynamic recovery is greater, and the average grain size smaller, than in quartz veins of the Northern deposits. Extreme undulose extinction in quartz grains is more common in grains proximal to zones of late brittle deformation.

Retrograde assemblages, overprinting the above hydrothermal assemblages, occur in three stages:

(1) chlorite (ripidolite) + sericite + carbonate along stylolitic laminations and fractures in the quartz veins and wallrocks (Fig. 5.9D),

(2) quartz + carbonate veinlets that crosscut the veins and wallrock assemblages (Fig. 4.14C),

(3) late chlorite (penninite) + prehnite + albite veinlets (An<1) that crosscut alteration zones in the wallrock, and

(4) gypsum veinlets that crosscut all of the above assemblages.

These assemblages collectively produce millimetre-scale bleached zones in wallrock adjacent to brittle fractures, and this bleaching is best developed along the margins of the quartz veins, suggesting that vein/wallrock contacts may have acted as a preferred conduit for the percolation of fluids since Archean times. No large scale quartz vein emplacement appears to be related to these assemblages. The paragenetic sequence of alteration in the Central deposits is summarized in Figure 5.7B.

5.3.2.3 Southern deposits

In the Scotia orebodies, the banded nature of the ore zones produces complex overlapping alteration envelopes. However, a consistent sequence of alteration zones can be observed around isolated veinlets in tholeiitic host rocks (Figs. 5.6C, 5.10A). Throughout a large section of the host shear zone, the metamorphic assemblage of hornblende + plagioclase (An_{48-57}) + epidote + ilmenite is altered to an outer zone of biotite + hornblende + plagioclase (An_{35-58}; Figs. 5.3, 5.10A,B). With increasing proximity to the veins, the biotite + hornblende + plagioclase assemblage is progressively replaced by actinolite, then clinopyroxene (diopside) + calcite + microcline, and less commonly quartz + amphibole + zoisite + microcline, over a few millimetres to

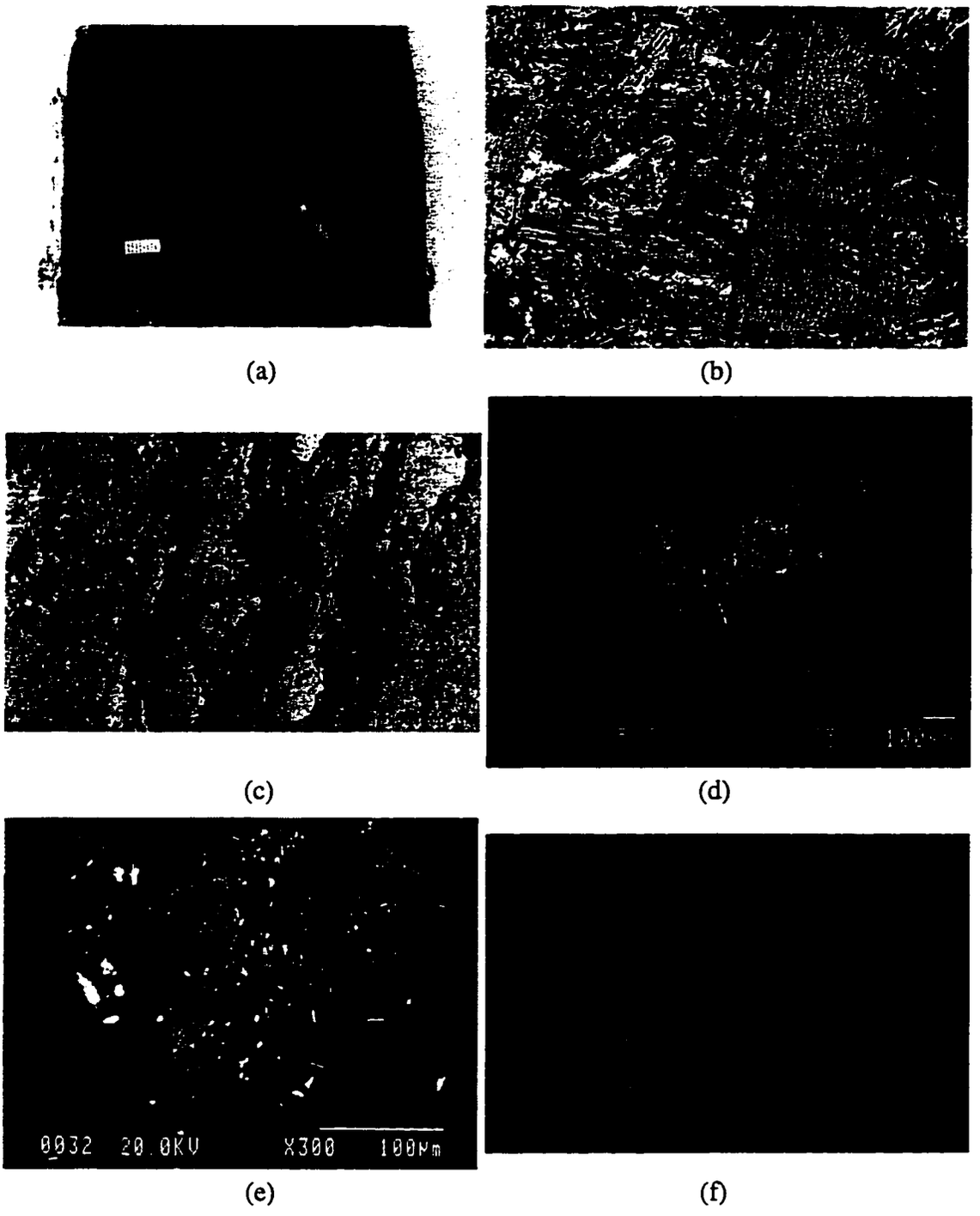

Figure 5.10: Alteration associated with Southern deposits
(a) Biotite-plagioclase-amphibole, amphibole, clinopyroxene, calcite and quartz assemblages are progressively developed towards quartz veins in the Scotia deposit. (b) Amphibole-biotite relationships in wallrock alteration, Scotia mine (c) Amphibole-clinopyroxene-quartz banding on the scale of a thin section, Scotia mine (d) Loellingite rimmed by Au, Bi and arsenopyrite, Scotia mine. (e) Au, Bi, and tellurides intimately intergrown with quartz, amphibole, and microcline, Scotia deposit. (f) Au and telluride inclusion

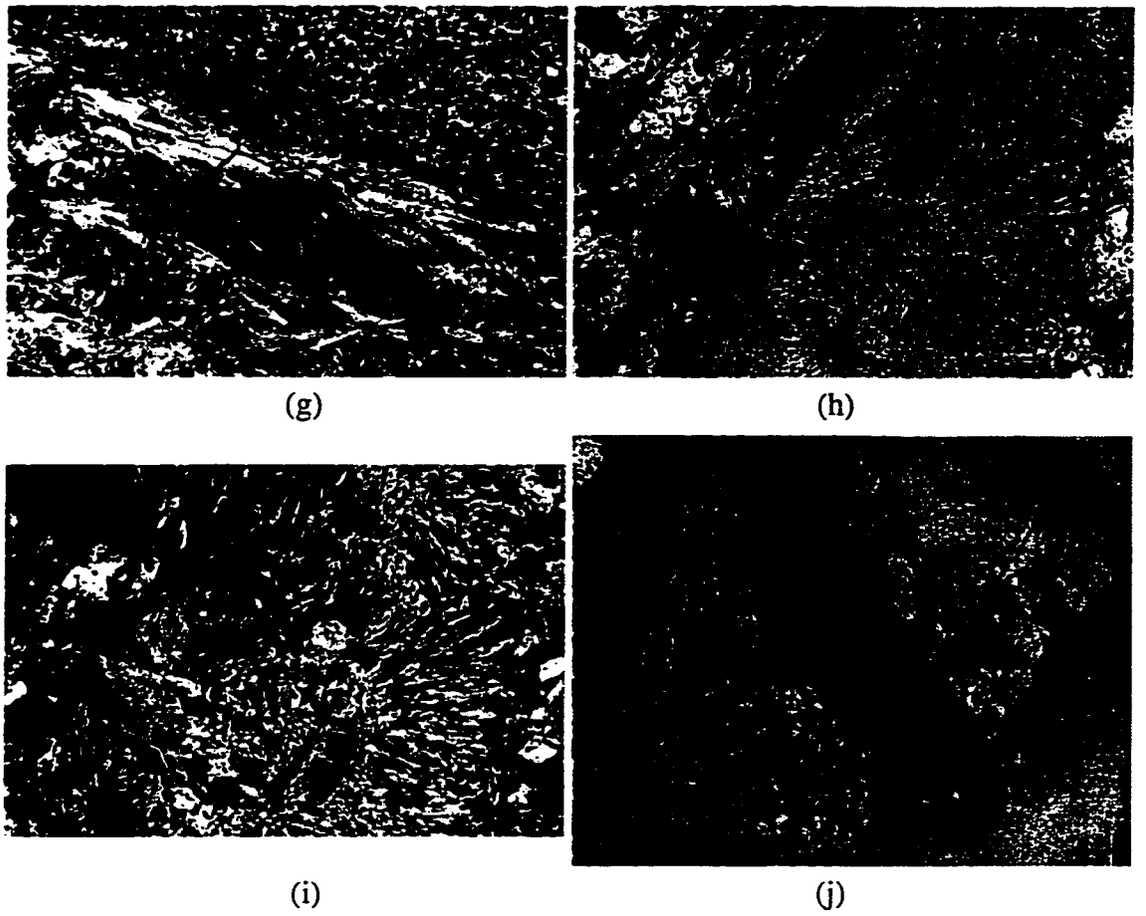

Figure 5.10 (cont.): Alteration associated with Southern deposits
(g) Variably deformed amphibole in an amphibole-qtz alteration assemblage. Sample SCPV, Scotia mine, crossed nicols. An S-C fabric is partially preserved in this sample. (h) Rosettes of amphibole at the margin of a quartz vein, Scotia deposit, plane polarized light. (i) As in (h), under crossed nicols (j) Photo of thin section exhibiting variable degrees of subgrain development and recovery in quartz, sample CN380170g, Scotia mine. The wallrock lamination separating the two varieties of quartz is rimmed by fibrous amphibole on both sides.

centimetres (Figs. 5.2E, 5.6C, 5.10A,C). The actinolite, clinopyroxene or calcite may form distinct, monomineralic bands in the veins (Figs. 4.6I, 5.10A,C). Garnet occurs sporadically, associated with calcite + quartz (R. Waugh, pers. comm. 1990).

Ilmenite is partially altered to titanite and pyrrhotite throughout the shear zone. Proximal to the margins of the veins, in the biotite + amphibole + plagioclase and amphibole inner zones, löellingite ($FeAs_2$) is progressively rimmed by gold + bismuth and then arsenopyrite (Fig. 5.10D). Pyrrhotite is the dominant sulphide in the veins, associated with chalcopyrite. Fractures within clinopyroxene and quartz are infilled by actinolite + pyrrhotite + chalcopyrite. Gold and bismuth are disseminated throughout the quartz as isolated inclusions <10 μm in diameter (Fig. 5.10E), or as inclusions in arsenopyrite (Figs. 5.10D,F).

Significantly, the diopside-bearing veins found outside the mineralized shear zone do not contain gold, often contain garnet, and typically lack a biotite-bearing alteration zone. Many of these 'barren' veins are found throughout the Scotia stratigraphy. This implies that the quartz-diopside-carbonate-amphibole veins may have been introduced in an event separate from that which formed the biotite and introduced the gold into the shear zone (S. Peters, pers. comm., 1990). Similar assemblages in lode gold deposits of the Yellowdine Terrane have been referred to as gold Skarns by Mueller (1988; 1990; 1991), who interpreted them as orthomagmatic phenomena. However, amphibole is introduced with diopside in the veins (Fig. 5.10C). Amphibole selvedges to diopside-quartz veins are variably deformed (Figs. 5.10G,H); therefore diopside + quartz + amphibole + plagioclase veins are interpreted as synchronous with deformation, fluid flow, and potassium metasomatism.

Quartz grains in the veins are generally equigranular and well recovered, exhibiting little undulose extinction and 120° grain boundaries (Fig. 5.10J). However, quartz grains with well developed mortar texture, serrated grain boundaries, and well developed undulose extinction are also observed in late stage quartz cutting earlier recovered quartz. Both the dynamically recovered and non-recovered quartz varieties are associated with diopside + amphibole + calcite assemblages Fig. 5.10J). Amphibole + zoisite + microcline assemblages have only been observed in the variety characterized by less recovered quartz. Clinopyroxene grains are typically poikiloblastic and elongate, with grains as long as 2 cm and 1 mm wide being in optical continuity along their entire length, indicating formation as stretched crystals in a dynamic environment.

Quartz + clinopyroxene + actinolite + calcite + microcline and quartz + amphibole + zoisite + microcline assemblages retrogress to quartz + albite ($An_{<1}$) + chlorite + calcite ± sericite assemblages along cleavage planes and grain boundaries. Brittle

fractures and faults crosscutting the vein are also filled with chlorite + quartz + albite + sericite, and the youngest fractures are filled with prehnite + albite (Figs. 4.6I,J). The sequence of alteration and mineralization in Southern orebodies is shown in Figure 5.7C.

5.4 Whole Rock Geochemistry

Whole-rock geochemistry of hydrothermal alteration assemblages associated with lode-gold deposits has been addressed by various authors (Kerrich et al., 1977; Kerrich, 1983; Clark et al., 1986, 1989; Kishida and Kerrich, 1987; Böhlke, 1989; Golding et al., 1990; Mikucki et al. 1990, Lesher et al., 1991). Such studies have made significant contributions to our understanding of alteration processes. In all cases, geochemical variations correlate with mineralogical changes, showing marked variations laterally away from the fluid conduits, but little variation within an individual lithology along strike or down dip within any given deposit. However, the chemical changes within a deposit are strongly dependent upon host rock composition (Kishida and Kerrich, 1987; Clark et al., 1986, 1989; Böhlke, 1989; Mikucki et al., 1990).

Geochemical changes that accompany the mineralogical zonation detailed previously were investigated by analyzing samples from drill core through representative Northern, Central, and Southern orebodies. Samples were selected to represent all alteration zones, from least-altered metamorphic assemblages through distal alteration zones to inner alteration zones. Major and trace element abundance were determined by methods outlined in Chapter 3. Representative data for alteration zones in HMT and tholeiite hosts for each deposit type are given as Table 5.1.

5.4.1 Major elements

Figure 5.11 graphically presents select whole-rock geochemical data data as element concentrations versus depth down drill core. Host lithologies are all mafic, and on these diagrams, MgO contents serve to distinguish HMT from tholeiitic protoliths. These diagrams illustrate that, in terms of measured abundance, all deposits are characterized by increased relative abundance of volatiles (H_2O, CO_2, H_2S, measured as loss on ignition (LOI)) and K_2O, within individual lithologies, with increasing proximity towards the auriferous quartz veins. Note however, that absolute abundance of K_2O are lower in HMT host rocks than in tholeiitic counterparts (e.g. Royal Tiara vein, Northern deposits; Mararoa vein, Central deposits; SC358-11, Southern deposits). The HMT are apparently less efficient scrubbers of K from the hydrothermal fluid, explaining why biotite alteration is sporadic within these lithologies. Inner zones of amphibole alteration

Table 5.1. Geochemical analyses for altered mafic rocks

Northern deposits

Sample	PRS 1177-1	PRS1177-3	PRS1177-4	PRS1177-5	PRS1177-7	PRS1177-9	PRS1177-11	PRS1177-12	PRS1177-13	PRS1177-14	PRS1177-15
Depth* (m)	211 34	229.67	238.46	250.41	267.76	272.92	329.46	331.41	344.08	351 04	351 92
Major elements											
SiO2 %	47 5	49.1	43.7	39.4	52.4	48.2	48 4	44.2	47 5	45.5	45.7
TiO2 %	1 37	1 16	1.13	1.04	0.97	0.91	0.61	0.69	0 56	0.65	0 64
Al2O3 %	12.2	12.5	11 2	13.6	10.3	14.5	9 69	9.76	9.95	9 55	9.99
Fe2O3 %	16.4	11 8	13.5	11.5	11	11 2	12.4	12.3	12.6	12.8	12.8
MnO %	0 2	0.21	0.26	0.24	0 2	0.24	0.18	0.19	0.2	0 22	0 21
MgO %	5.36	5.49	5.11	5.56	5.32	5.41	15 8	14.3	16	15.4	14 8
CaO %	6 93	8	12.7	13.1	9.41	9.52	5.75	5.81	5 34	7 79	7 6
Na2O%	3.02	3 49	0.78	0 58	0 69	1.7	0.19	0 04	0.11	0 07	0.11
K2O %	0.1	0.06	1.03	4.5	1.36	1 3	0.1	0.73	0 61	0.06	0.1
P2O5 %	0.11	0 09	0.1	0.1	0 09	0.07	0.06	0.07	0 05	0 06	0.06
LOI %	7 62	8.7	11 2	9 62	9 08	7 47	6.16	12.3	6.31	7 93	7 93
Total	100.81	100.6	100.71	99.24	100.82	100.52	99.34	100.39	99 23	100.03	99.94
Trace elements											
La	3 28	2.67	4.71	4.61	4.21	2.41	2.1	2.12	1.71	1 83	1 85
Ce	8.79	7 07	12.12	11 93	10 88	6.61	5.57	5.56	4 51	4.92	4 68
Pr	1 39	1.15	1 83	1 83	1 63	1.08	0 88	0 83	0.74	0.8	0.7
Nd	7 54	6.15	9.6	9 62	8.04	5.89	4.59	4 32	3.8	4.52	4 03
Sm	2.41	2.05	2.74	3.09	2.26	1 84	1 36	1 37	1.13	1 26	1 24
Eu	0 93	0 69	0.92	0.96	0.8	0.67	0.5	0.41	0 46	0.45	0 38
Gd	3 46	2.82	3.62	4 23	2.67	2.6	1.63	1.71	1 45	1 77	1 68
Tb	0.56	0.5	0.58	0.65	0.41	0.46	0.29	0.3	0.25	0 3	0 28
Dy	4 14	3.8	3.84	4 62	2.81	3.24	2.11	2.02	1 86	2.16	2.09
Ho	0.85	0.82	0.8	0 95	0.58	0 71	0.46	0.43	0.39	0 43	0 41
Er	2.67	2.58	2.42	2.9	1.75	2.21	1 39	1 39	1.2	1 32	1 34
Tm	0.41	0.38	0.35	0.44	0.26	0.33	0.2	0.21	0.18	0 21	0.18
Yb	2.76	2.53	2.41	2.9	1 66	2.24	1 3	1.36	1.1	1 36	1.3
Lu	0.41	0 39	0.36	0.42	0 24	0.34	0.21	0.22	0.18	0 21	0.21
Th	0.5	0 36	1	1.17	0.75	0 29	0.21	0.64	0.74	0.49	0.49
U	0 09	0.07	0 24	0.57	0.12	0.06	0.05	0.06	0.04	0.04	0.04
Cs	0.11	0.1	0.99	1.92	1.17	0.75	0.94	6.16	6.37	0 66	0.94
Tl	0.09	0.29	0.54	1.6	0.65	0.71	0.05	0.24	0.23	0 03	0.07
Rb	2.7	0.9	39.4	186.2	56.7	47 8	3.8	35 4	29.9	2.5	4 1
Sr	78	76	60	62	53	73	23	54	21	22	23
Ba	24	10	252	530	511	160	9	94	71	6	10
Nb	3.16	2.75	4.13	4.05	3.91	2.13	1.7	1 92	1.46	1.77	1 69
Ta	0.21	0.17	0.27	0.24	0.26	0.14	0.11	0.14	0.13	0.11	0.11
Zr	67	55	70	64	65	49	36	36	29	33	32
Hf	2.18	1.75	2.44	2.05	2.05	1 5	0 95	1.12	0.99	1 04	0 93
Y	21	21	21	24	15	18	12	11	10	11	11
V	366	314	288	275	230	274	204	205	187	189	201
Sc	45	41	36	39	30	40	34	31	34	31	32
Cr	62	109	62	81	46	262	1600	1500	1650	1490	1470
Co	47	48	50	48	40	52	64	66	66	63	62
Ni	39	42	59	57	51	119	363	341	379	335	333
Cu	85	103	88	104	57	103	68	6	40	49	144
Zn	102	117	117	157	108	96	124	103	110	117	111
Pb	5.5	4.1	3.4	4.0	4.8	12.3	1.3	1.1	0.9	1 1	1 7
Be	1 9	1.5	1.9	2.9	2.5	1.9	1 4	2.1	1 3	1.7	1 9
Bi	0.04	0.07	0.1	0.26	0.09	0.16	0.03	0.02	0.02	0 03	0 02
Cd	2	2	2	2	2	2	2	2	2	2	2
W	10	10	10	10	10	21	10	10	10	10	10
Ag	0.5	0.5	0.5	0.5	0.5	0.5	0.5	0.5	0.5	0.5	0.5
Au	5	9	11	5	4	3	14	1	13	1	5
As	3	3	7	50	16	4	3	3	6	3	3
Mg#	22	29	25	29	29	29	52	50	52	51	50
Al2O3/TiO2	8.9	10 8	9.9	13.1	10.6	15.9	15.9	14 1	17 8	14.7	15.6
CaO/Al2O3	0.57	0 64	1.13	0.96	0.91	0.66	0 59	0.60	0.54	0 82	0.76
Total REE	40	34	46	49	38	31	23	22	19	22	20
(La/Yb)cn	0 78	0.70	1 29	1.05	1 67	0.71	1 07	1 03	1.03	0.89	0.94
(La/Sm)cn	0 84	0 80	1 06	0.92	1.14	0.80	0.95	0.95	0.93	0.89	0.92
(Gd/Yb)cn	1 02	0.90	1.22	1.18	1.30	0.94	1.02	1.02	1 07	1 05	1 05
Zr/Hf	31	31	28	31	32	33	38	32	29	32	35
Nb/Ta	15	16	15	17	15	15	15	14	11	16	15
Ti/Zr	123	126	97	98	89	111	102	116	117	117	119
Nb/Th	6.3	7.6	4.1	3.5	5.2	7.3	8.1	3.0	2.0	3.6	3.4
La/Nb	1 04	0.97	1.14	1.14	1.08	1.13	1 24	1.10	1.17	1.03	1.09
La/Th	6.6	7 4	4.7	3.9	5.6	8.3	10.0	3.3	2.3	3.7	3.8
Zr/La	20.37	20 60	14.76	13.79	15.44	20.40	17 04	16.79	16.81	18.20	17 36

Sample locations and descriptions are detailed in Appendix C.
*Depth is measured down the drill core axis.
Major elements reported in weight percent. Trace elements reported in ppm except for Au reported in ppb

Table 5.1. continued

Northern deposits

Sample	PRS1177-16	PRS1177-17	PRS1177-18	PRS1177-19	PRS1177-20	PRS1177-21	PRS1177-22	PRS1177-24	PRS1177-26	PRS1177-27	PRS1177-28
Depth m	352.61	353.53	355.95	360.58	361.03	371 2	378.61	383.52	385.11	386.03	387 04
SiO2 %	44	45.1	47.3	49.3	49.6	48.4	45 8	46.1	43.9	45.8	40.2
TiO2 %	0.43	0.38	0.43	0.65	1.15	0.75	0.75	0 75	0.68	0.86	1 58
Al2O3 %	11	10.5	12.1	15.2	13.5	15.8	15.1	13.9	13.4	13.3	14
Fe2O3 %	10.9	10.7	11	12.4	15	13.2	13.2	11.6	11.7	10.8	17 7
MnO %	0.18	0.19	0.17	0.22	0.26	0.22	0.19	0.2	0.24	0.26	0.19
MgO %	14 6	14.2	13.8	7 73	5.63	6.6	7 75	6 7	6.54	5.79	6 45
CaO %	8.16	8.26	6.39	10.4	9.32	11.6	7.67	10.3	11	11.9	7 69
Na2O%	0.05	0.07	1.35	2.02	3.4	1 98	2.35	1 93	1 62	2.18	2.36
K2O %	0.72	0.02	0.04	0.39	0.18	0.2	0.88	0.94	1.3	1.42	3.17
P2O5 %	0.04	0 04	0.04	0.06	0.1	0.06	0.07	0.06	0 06	0.06	0.14
LOI %	10.1	9 85	7 08	2.08	1.93	2	7	7.77	9.39	8.31	7 16
Total	100.18	99.31	99.7	100.45	100.07	100.81	100.76	100.25	99 83	100.68	100.64
La	1	1.13	1 29	1.84	4.16	2.04	2.38		1.93		6 83
Ce	2.51	3.01	3.33	4.76	10.68	5.34	6.35		5.09		17 34
Pr	0 4	0.48	0.55	0.74	1 63	0.85	1.03		0.82		2.64
Nd	1.88	2.31	3.07	4.15	8.6	4.45	5.16		4 32		13 36
Sm	0.72	0.74	0.84	1.2	2.68	1.47	1 69		1.49		3 56
Eu	0.28	0.45	0.41	0.51	0.96	0.61	0.4		0.64		0.99
Gd	0.98	1 01	1.16	1 85	3.5	2.13	2.31		2.03		4 11
Tb	0.16	0.17	0.21	0.33	0.6	0.36	0.4		0.36		0 63
Dy	1.1	1 38	1 55	2.46	4 23	2.74	3.15		2.66		4 43
Ho	0.22	0 29	0.32	0.52	0 91	0.57	0.65		0.56		0 86
Er	0 68	0.9	1	1 68	2.65	1 86	2.02		1 8		2.57
Tm	0.12	0.14	0.15	0.25	0.4	0.28	0 3		0 28		0 37
Yb	0.78	0.92	1.05	1.79	2.77	1.87	2.07		1 89		2.36
Lu	0.11	0.15	0.16	0.24	0.41	0.28	0.33		0.29		0.35
Th	0 48	0.34	0.22	0.21	0.46	0.22	0.28		0.24		0.72
U	0 02	0.03	0.03	0.05	0.13	0.05	0.05		0.04		0.17
Cs	3.12	0.25	0.19	0.22	0.23	0.23	2.98		1.72		5 88
Tl	0.2	0.01	0	0.05	0.35	0.34	0.64		0.64		1.23
Rb	29.3	0.4	0.5	12.9	1.4	4.1	37 0		38.4		127 6
Sr	38	35	30	93	91	94	65		58		86
Ba	70	1	8	39	22	32	108		119		259
Nb	0.8	0.86	1	1.4	3.36	1.7	1.95		1.51		5.91
Ta	0 06	0.07	0.08	0.1	0.22	0.09	0.12		0.09		0.34
Zr	15	20	21	34	68	38	41	42	39	35	89
Hf	0.57	0.56	0 62	1.11	2.04	1.33	1.01				2.4
Y	6	7	8	13	22	15	16		15		21
V	132	149	178	219	301	235	211		224		327
Sc	29	34	38	40	40	38	40		38		42
Cr	1470	1310	1390	256	112	185	242	200	222	206	61
Co	63	60	58	57	56	39	42	37	54	50	61
Ni	321	299	285	125	69	86	105	82	119	102	66
Cu	82	29	10	110	89	95	143	202	76	96	84
Zn	107	92	94	108	138	88	100	78	103	95	103
Pb	2.1	1 3	1 2	3.1	3.8	2.8	2.8		3.0		11 9
Be	1 7	1.2	1.7	2.0	2.0	1 4	1.1	1.4	1.7	1 9	3.4
Bi	0 03	0.02	0.02	0.03	0.11	0.11	0.11		0.14		0.19
Cd	2	2	2	2	2	2	2	2	2	2	2
W	10	10	10	10	10	10	10	10	10	10	43
Ag	0.5	0.5	0.5	0.5	0.5	0.5	0.5	0.5	0.5	0.5	4
Au	130	3	2	10	15	8	2	40	48	5	
As	5	3	16	43	35	11	30	3	20	3	185
Mg#	54	53	52	35	24	30	34	33	33	32	24
Al2O3/TiO2	25 6	27 6	28.1	23.4	11.7	21.1	20.1	18.5	19.7	15.5	8.9
CaO/Al2O3	0.74	0.79	0.53	0.68	0.69	0.73	0.51	0 74	0.82	0.89	0 55
Total REE	11	13	15	22	44	25	28	0	24	0	60
(La/Yb)cn	0.85	0.81	0.81	0.68	0.99	0.72	0.76		0.67		1.91
(La/Sm)cn	0 85	0.94	0.94	0.94	0.95	0.85	0.87		0.80		1.18
(Gd/Yb)cn	1 02	0 89	0.90	0.84	1.02	0.92	0.90		0.87		1 41
Zr/Hf	27	36	34	31	33	29	41		#DIV/0!		37
Nb/Ta	13	12	13	14	15	19	16		17		17
Ti/Zr	168	114	123	113	102	118	110	107	105	147	106
Nb/Th	1.7	2.5	4 5	6.7	7.3	7.7	7 0		6.3		8.2
La/Nb	1 25	1 31	1.29	1.31	1.24	1 20	1 22		1.28		1.16
La/Th	2.1	3.3	5.9	8.8	9.0	9.3	8.5		8.0		9 5
Zr/La	15.31	17 70	16 28	18.72	16.30	18.63	17 23		20.21		13.03

Table 5.1. continued

	Northern deposits					Central Deposits (Mararoa)					
Sample	PRS1177-29	PRS1177-30	PRS1177-31	PRS1177-32	PRS1177-33	PRS1177-34	PRS1177-35	S1113-A	S1113-B	S1113-C	S1113-D
Depth m	387.66	387.97	389.19	397.16	390.78	403.65	446.41	131.64	146.89	151.88	152.05
SiO2 %	36.1	45.7	42.8	45.8	36.5	48.5	47.7	48.6	50	49.5	49.9
TiO2 %	1.43	1.26	1.16	1.11	0.95	0.81	0.56	1.05	0.88	0.98	0.95
Al2O3 %	14.9	12.6	11.1	13.8	18.8	14.2	11.3	14.8	16.4	15.4	15.4
Fe2O3 %	14.2	14.1	13.3	16	15	11.9	12	13.1	11.2	12.3	12.4
MnO %	0.31	0.26	0.27	0.24	0.19	0.22	0.21	0.21	0.18	0.19	0.2
MgO %	7.37	5.75	5.09	9.2	9.65	8.45	14.8	7.51	6.54	6.74	6.82
CaO %	11.2	7.96	9.98	9.11	6.97	11.3	7.45	9.91	12.1	11.1	11.3
Na2O%	2.71	2.1	1.91	2.16	2.68	2.43	1.37	2.54	1.96	1.91	1.85
K2O %	3.49	1.9	1.29	0.15	1.59	0.18	0.17	0.15	0.12	0.23	0.13
P2O5 %	0.1	0.11	0.1	0.09	0.08	0.07	0.05	0.09	0.08	0.09	0.08
LOI %	4.7	4.47	8.85	2.77	8.47	2.39	3.93	1.39	0.93	1.54	1
Total	96.51	96.21	95.85	100.43	100.68	100.45	99.54	99.35	100.39	99.98	100.03
La		7.05			2.93	2.46	2.07	3.29	3.35	3.2	3.09
Ce		18.23			7.78	6.42	5.06	8.66	8.77	8.38	8.29
Pr		2.72			1.2	1	0.75	1.37	1.39	1.33	1.28
Nd		13.49			6.26	5.45	3.86	7.4	7.23	6.99	6.97
Sm		3.5			1.99	1.7	1.13	2.08	2.07	2.19	2.09
Eu		1.34			0.64	0.62	0.41	0.86	0.91	0.8	0.85
Gd		3.94			2.65	2.38	1.51	2.98	2.86	2.83	2.92
Tb		0.61			0.41	0.4	0.24	0.52	0.46	0.5	0.47
Dy		4.21			2.61	2.82	1.81	3.4	3.33	3.48	3.53
Ho		0.81			0.49	0.56	0.42	0.72	0.68	0.71	0.7
Er		2.34			1.25	1.84	1.24	2.24	2.1	2.08	2.06
Tm		0.33			0.18	0.28	0.18	0.34	0.31	0.31	0.32
Yb		2.11			1.13	1.86	1.25	2.11	1.9	2.09	1.93
Lu		0.31			0.18	0.26	0.19	0.34	0.3	0.29	0.29
Th		0.87			0.4	0.27	0.36	0.33	0.29	0.52	0.29
U		0.12			0.08	0.06	0.08	0.07	0.08	0.78	0.08
Cs		2.54			1.94	0.1	0.18	0.3	0.31	0.73	0.42
Tl		0.82			0.2	0.01	0.01	0.02	0	0	0
Rb		67.8			50.2	3.3	4.6	0.8	0.9	3.0	1.9
Sr		86			83	94	68	109	146	119	112
Ba		150			216	24	32	28	21	21	18
Nb		4.77			2.34	2.18	1.51	2.96	2.74	2.68	2.8
Ta		0.31			0.15	0.16	0.11	0.18	0.15	0.16	0.16
Zr	85	77	86	64	56	44	29	62	58	57	47
Hf		2.34			1.19	1.37	0.9	1.73	1.65	2.02	0.95
Y		20			12	14	10	19	16	16	16
V		291			263	226	193	292	238	275	277
Sc		39			45	39	36	44	36	38	39
Cr	62	66	53	275	385	385	1540	215	235	274	272
Co	44	42	38	74	73	50	67	59	43	44	43
Ni	59	55	47	209	157	156	351	102	83	89	91
Cu	397	233	164	153	49	135	128	86	92	91	117
Zn	126	116	128	145	149	112	92	116	94	100	107
Pb		4.0			5.0	1.5	3.5	2.0	1.8	2.4	1.9
Be	3.1	2.0	1.4	1.9	1.8	1.8	1.4	4.0	2.0	2.0	2.0
Bi		0.12			0.09	0.03	0.04	0.04	0	0.51	0.02
Cd	2	2	2	2	2	2	2	2	2	2	2
W	128	20	20	10	10	10	10	10	10	18	20
Ag	0.5	0.5	0.5	0.5	0.5	0.5	0.5	0.5	0.5	0.5	0.5
Au	1700	710	2400	19	33	10	15	1	6	4	8
As	3	3	3	21	58	17	11	32	11	31	9
Mg#	31	26	25	33	36	38	52	33	33	32	32
Al2O3/TiO2	10.4	10.0	9.6	12.4	19.8	17.5	20.2	14.1	18.6	15.7	16.2
CaO/Al2O3	0.75	0.63	0.90	0.66	0.37	0.80	0.66	0.67	0.74	0.72	0.73
Total REE	0	61	0	0	30	28	20	36	36	35	35
(La/Yb)cn		2.20			1.71	0.87	1.09	1.03	1.16	1.01	1.06
(La/Sm)cn		1.24			0.90	0.89	1.13	0.97	0.99	0.90	0.91
(Gd/Yb)cn		1.51			1.90	1.04	0.98	1.14	1.22	1.10	1.23
Zr/Hf		33			47	32	32	36	35	28	49
Nb/Ta		15			16	14	14	16	18	17	18
Ti/Zr	101	98	81	104	102	109	115	102	91	103	121
Nb/Th		5.5			5.9	8.1	4.2	9.0	9.4	5.2	9.7
La/Nb		1.48			1.25	1.13	1.37	1.11	1.22	1.19	1.10
La/Th		8.1			7.3	9.1	5.8	10.0	11.6	6.2	10.7
Zr/La		10.92			19.11	18.09	14.09	18.84	17.31	17.81	15.21

Table 5.1. continued

Central Deposits (Mararoa)

Sample	S1113-E	S1113-F	S1113-G	S1113-I	S1113-J	S1113-K	S1113-L	S1113-M	S1113-N	S1113-O	S1113-P	S1113-Q
Depth m	152.58	154.32	156.4	158.07	159.25	159.9	160.56	161.12	162.95	163.6	164.9	166.17
SiO2 %	48.4	50.1	49.3	49.8	48.5	49.9	49	49.1	47.7	48	48	47.6
TiO2 %	1.03	1.01	1.06	1.06	1.12	1.04	0.94	0.85	0.69	0.62	0.57	0.46
Al2O3 %	15.8	15.2	15.2	15.3	15.5	15.2	14.8	15.3	10.2	12.2	10.2	10.7
Fe2O3 %	12.9	12.4	13.5	12.8	13	12.7	12.3	11.7	13.1	12	12.8	12.5
MnO %	0.21	0.2	0.22	0.2	0.19	0.2	0.2	0.18	0.22	0.2	0.22	0.2
MgO %	7.85	7.02	6.7	6.86	7.07	6.85	6.91	6.68	14.8	14.6	15	15.3
CaO %	10.1	11.2	11	10.9	10.1	10.5	11.8	10.7	8.6	6.9	8.43	7.81
Na2O%	2.16	1.68	1.97	2.05	2.17	1.9	1.28	1.86	0.32	0.24	0.36	0.32
K2O %	0.1	0.16	0.22	0.27	0.72	0.71	0.84	1.17	0.4	1.03	0.87	0.8
P2O5 %	0.09	0.09	0.08	0.09	0.08	0.09	0.09	0.1	0.06	0.06	0.04	0.04
LOI %	1.62	1.39	0.85	0.85	0.93	1.31	1.47	1.85	4	4.23	3.39	4.08
Total	100.26	100.45	100.1	100.18	99.38	100.4	99.63	99.49	100.09	100.08	99.88	99.81
La	2.75	4.58	3.1	3.89	3.25	3.08	3.3	3.53	1.44	1.33	1.79	0.95
Ce	7.61	11.11	8.18	9.96	8.27	8.18	8.81	9.54	4	3.42	4.75	2.63
Pr	1.26	1.68	1.27	1.59	1.33	1.26	1.36	1.49	0.64	0.53	0.78	0.45
Nd	6.63	8.54	6.89	8.19	6.66	7.04	7.13	7.6	3.49	2.75	3.96	2.36
Sm	2.15	2.49	2.03	2.55	1.96	2.11	2.24	2.23	1.25	0.82	1.21	0.86
Eu	0.81	0.91	0.78	0.96	0.8	0.66	0.68	0.81	0.38	0.32	0.48	0.34
Gd	3.03	3.25	2.87	3.2	2.83	2.94	2.98	2.91	1.65	1.15	1.6	1.09
Tb	0.5	0.51	0.46	0.54	0.48	0.47	0.51	0.51	0.3	0.23	0.27	0.19
Dy	3.43	3.68	3.37	3.88	3.28	3.43	3.57	3.64	2.11	1.76	1.91	1.41
Ho	0.74	0.78	0.71	0.82	0.7	0.7	0.71	0.77	0.45	0.38	0.41	0.29
Er	2.33	2.38	2.24	2.51	2.08	2.11	2.22	2.31	1.43	1.19	1.27	0.93
Tm	0.36	0.36	0.32	0.35	0.32	0.32	0.34	0.35	0.21	0.19	0.2	0.14
Yb	2.13	2.17	2.01	2.24	2	1.93	2.25	2.16	1.47	1.24	1.26	1.01
Lu	0.29	0.31	0.29	0.35	0.32	0.28	0.32	0.31	0.23	0.21	0.2	0.16
Th	0.32	0.88	0.34	0.6	0.39	0.34	0.62	0.44	0.76	0.54	0.37	0.67
U	0.07	0.14	0.7	0.24	0.22	0.26	16.01	6.18	0.1	0.08	0.05	0.06
Cs	0.45	0.48	0.74	1.27	4.53	3.71	3.17	6.91	1.64	6.19	8.58	7.22
Tl	0	0	0	0	0	0	0	0	0.09	0.19	0.15	0.14
Rb	1.5	3.4	4.4	7.0	21.3	20.1	26.1	41.2	16.5	40.5	35.9	31.0
Sr	105	133	110	118	100	80	72	141	24	62	30	34
Ba	27	23	27	36	65	73	97	182	63	101	41	59
Nb	2.95	3.39	2.78	3.19	2.78	3	2.85	3.04	1.63	1.51	1.42	0.87
Ta	0.16	0.2	0.16	0.19	0.16	0.17	0.16	0.18	0.13	0.13	0.13	0.1
Zr	55	68	66	59	46	49	54	53	36	27	26	22
Hf	1.06	2.17		2.24	1.01	1.1	2.5	1.47	1.18	0.89	0.76	0.92
Y	17	17	16	17	15	15	16	17	12	10	10	8
V	272	274	248	258	256	245	254	234	212	206	212	179
Sc	40	40	40	40	41	39	38	39	39	39	38	35
Cr	268	266	293	286	315	301	283	292	1500	1570	1460	1610
Co	52	52	59	59	57	50	58	50	67	68	66	67
Ni	102	104	102	96	104	92	109	99	363	365	366	361
Cu	66	113	32	71	34	72	90	110	9	3	26	4
Zn	108	141	115	121	147	128	120	104	110	103	98	104
Pb	2.5	9.2	7.2	4.5	6.6	4.7	6.6	18.1	3.2	1.6	1.2	2.2
Be	4.0	16.0	7.0	3.0	2.0	2.0	2.0	2.0	2.0	2.0	2.0	2.0
Bi	0.03	0.63	0.03	0.63	0.07	0.03	0.68	0.13	0.05	0.04	0.04	0.06
Cd	2	2	2	2	2	2	2	2	2	2	2	2
W	10	10	10	10	10	10	10	19	10	10	10	10
Ag	0.5	0.5	0.5	0.5	0.5	0.5	0.5	0.5	0.5	0.5	0.5	0.5
Au	14	5	3	1	2	1	1	19	1	1	1	2
As	43	3	25	8	3	5	39	5	105	69	45	13
Mg#	34	33	30	32	32	32	33	33	49	51	50	51
Al2O3/TiO2	15.3	15.0	14.3	14.4	13.8	14.6	15.7	18.0	14.8	19.7	17.9	23.3
CaO/Al2O3	0.64	0.74	0.72	0.71	0.65	0.69	0.80	0.70	0.84	0.57	0.83	0.73
Total REE	34	43	35	41	34	35	36	38	19	16	20	13
(La/Yb)cn	0.85	1.39	1.02	1.15	1.07	1.05	0.97	1.08	0.65	0.71	0.94	0.62
(La/Sm)cn	0.79	1.13	0.94	0.94	1.02	0.90	0.91	0.97	0.71	1.00	0.91	0.68
(Gd/Yb)cn	1.15	1.21	1.16	1.16	1.15	1.23	1.07	1.09	0.91	0.75	1.03	0.87
Zr/Hf	52	31	#DIV/0!	26	46	45	22	36	31	31	34	24
Nb/Ta	18	17	17	17	17	18	18	17	13	12	11	9
Ti/Zr	112	89	96	108	146	127	104	97	115	135	132	125
Nb/Th	9.2	3.9	8.2	5.3	7.1	8.8	4.6	6.9	2.1	2.8	3.8	1.3
La/Nb	0.93	1.35	1.12	1.22	1.17	1.03	1.16	1.16	0.88	0.88	1.26	1.09
La/Th	8.6	5.2	9.1	6.5	8.3	9.1	5.3	8.0	1.9	2.5	4.8	1.4
Zr/La	20.00	14.85	21.29	15.17	14.15	15.91	16.36	14.92	25.00	20.64	14.50	23.28

Table 5.1. continued

	Central Deposits (Mararoa)							Central deposits (OK Mine)				
Sample	S1113-R	S1113-S	S1113-T	S1113-U	S1113-	S1113-W	S1113-Y	S657-1	S657-2	S657-3	S657-4	S657-5B
Depth m	166.75	168.42	169.36	169.58	170.17	180.25	184.9	397.36	401.43	401.9	402.7	403.09
SiO2 %	47.9	47.4	47.8	48.9	50.2	50.2	49.3	50.5	49.8	49.5	47.1	36.7
TiO2 %	0.57	0.56	0.51	0.56	0.74	0.86	0.95	0.94	0.91	0.91	0.88	1.11
Al2O3 %	9.29	9.99	10.9	11.9	14.4	14.4	15.7	14.7	14.3	14.6	13.6	20
Fe2O3 %	13.3	13.2	12.3	12.2	11.8	12.4	12.2	12.5	11.7	12.7	10.5	8.77
MnO %	0.23	0.22	0.22	0.2	0.19	0.19	0.19	0.27	0.26	0.25	0.24	0.09
MgO %	15.5	16	13.9	12	8.42	7.99	6.76	5.79	6.66	6.59	4.59	3.31
CaO %	9.5	8.35	9.93	11.1	11.4	10.7	11.7	12.2	10	11	12.4	21.2
Na2O%	0.27	0.28	0.53	0.92	2.05	2.3	1.8	1.82	2.36	1.92	1.79	0.01
K2O %	0.38	0.26	0.76	0.49	0.14	0.15	0.11	0.19	1.19	0.43	2.15	1.44
P2O5 %	0.04	0.05	0.03	0.04	0.06	0.07	0.09	0.06	0.06	0.06	0.08	0.05
LOI %	3.23	3.85	3	2	0.77	0.85	1	0.77	1.77	1.54	4.23	4.77
Total	100.21	100.16	99.88	100.31	100.17	100.11	99.8	99.76	99.03	99.52	97.56	97.45
La	1.57	1.45	1.19	0.85	2.02	2.87	3.39	2.84	2.54	2.37	2.38	4.35
Ce	3.99	4.03	3.01	2.24	5.76	7.91	8.61	7.4	6.67	6.41	6.51	10.7
Pr	0.64	0.63	0.49	0.38	0.94	1.26	1.36	1.21	1.13	1.04	1.05	1.62
Nd	3.38	3.38	2.74	2.02	5.28	6.77	6.96	6.49	6.26	5.52	5.72	8.61
Sm	1.13	0.94	0.87	0.77	1.7	2.14	2.16	2.2	2.04	1.87	1.92	2.57
Eu	0.5	0.43	0.49	0.18	0.5	0.81	0.83	0.76	0.9	0.68	0.52	1.66
Gd	1.4	1.27	1.03	1.26	2.35	2.99	2.93	3.3	2.94	2.54	2.72	4
Tb	0.23	0.23	0.18	0.23	0.39	0.51	0.48	0.56	0.51	0.45	0.47	0.66
Dy	1.85	1.64	1.27	1.68	2.81	3.54	3.34	4.15	3.75	3.34	3.63	5.3
Ho	0.38	0.35	0.29	0.39	0.61	0.73	0.7	0.89	0.79	0.73	0.8	1.24
Er	1.2	1.13	0.84	1.17	1.75	2.24	2.16	2.8	2.4	2.39	2.47	4.15
Tm	0.17	0.16	0.14	0.17	0.27	0.33	0.31	0.43	0.36	0.35	0.36	0.62
Yb	1.18	1.15	0.86	1.14	1.62	2.01	2.1	2.84	2.42	2.5	2.5	4.33
Lu	0.18	0.17	0.14	0.19	0.26	0.3	0.32	0.4	0.38	0.38	0.38	0.76
Th	0.29	0.26	0.35	0.19	0.23	0.29	0.25	0.65	0.28	0.26	0.49	0.33
U	0.04	0.04	0.03	0.02	0.04	0.47	0.06	0.06	0.05	0.05	0.06	0.12
Cs	1.39	0.88	2.51	2.11	0.4	0.07	0.15	0.03	0.71	0.6	0.89	0.64
Tl	0.03	0.04	0.11	0.1	0.03	0	0	0.3	0.77	0.48	0.86	0.63
Rb	14.7	10.5	34.1	20.8	1.6	0.5	0.6	0.9	50.3	15.8	77.5	39.2
Sr	30	24	39	63	66	85	111	80	75	77	86	13
Ba	42	22	81	30	30	21	19	30	157	42	275	84
Nb	1.2	1.3	0.71	0.88	1.78	2.55	2.64	2.3	2.06	2.06	2.1	3.63
Ta	0.11	0.14	0.09	0.05	0.12	0.14	0.18	0.13	0.14	0.13	0.12	0.16
Zr	24	29	18	19	37	51	56	62	38	48	48	63
Hf	0.76	0.73	0.71	0.79	1.18	1.11	1.19	1.57	1.16	1.43	1.84	1.97
Y	9	9	7	11	13	16	18	23	19	19	20	34
V	206	180	215	271	272	298	245	313	283	299	286	406
Sc	39	32	36	42	40	46	37	46	42	44	42	57
Cr	1670	1710	1510	1460	327	322	268	234	219	217	199	251
Co	77	72	69	68	44	46	50	56	57	60	53	50
Ni	381	396	342	324	115	120	96	99	101	101	112	122
Cu	26	14	7	3	17	51	95	35	18	66	111	41
Zn	96	98	97	93	85	103	101	154	127	126	99	41
Pb	1.2	0.5	1.5	1.7	3.6	1.8	1.9	3.9	3.3	3.0	3.2	1.7
Be	2.0	5.0	2.0	2.0	2.0	2.0	2.0	2.0	2.0	2.0	2.0	2.0
Bi	0.05	0.05	0.06	0.08	0.05	0.02	0.04	0.13	0.16	0.16	0.21	0.43
Cd	3	2	2	2	2	2	2	2	2	2	2	2
W	10	10	10	10	10	10	10	10	10	10	30	54
Ag	0.5	0.5	0.5	0.5	0.5	0.5	0.5	0.5	0.5	0.5	0.5	0.5
Au	13	21	1	1	6	1	2	5	7	8	27	48
As	3	79	145	148	13	3	3	3	27	23	1870	19
Mg#	50	51	49	46	38	36	32	29	33	31	27	25
Al2O3/TiO2	16.3	17.8	21.4	21.3	19.5	16.7	16.5	15.6	15.7	16.0	15.5	18.0
CaO/Al2O3	1.02	0.84	0.91	0.93	0.79	0.74	0.75	0.83	0.70	0.75	0.91	1.06
Total REE	18	17	14	13	26	34	36	36	33	31	31	51
(La/Yb)cn	0.88	0.83	0.91	0.49	0.82	0.94	1.06	0.66	0.69	0.63	0.63	0.66
(La/Sm)cn	0.85	0.95	0.84	0.68	0.73	0.82	0.96	0.79	0.76	0.78	0.76	1.04
(Gd/Yb)cn	0.96	0.90	0.97	0.90	1.18	1.21	1.13	0.94	0.98	0.82	0.88	0.75
Zr/Hf	31	39	25	24	31	46	47	39	33	33	26	32
Nb/Ta	11	9	8	18	15	18	15	18	15	16	18	23
Ti/Zr	145	117	170	177	120	100	102	91	144	114	110	105
Nb/Th	4.1	5.0	2.0	4.6	7.7	8.8	10.6	3.5	7.4	7.9	4.3	11.0
La/Nb	1.31	1.12	1.68	0.97	1.13	1.13	1.28	1.23	1.23	1.15	1.13	1.20
La/Th	5.4	5.6	3.4	4.5	8.8	9.9	13.6	4.4	9.1	9.1	4.9	13.2
Zr/La	15.04	19.86	15.13	22.35	18.32	17.91	16.49	21.83	14.96	20.15	20.18	14.51

Table 5.1. (continued)

Central deposits (OK Mine)

Sample	S657-5A	S657-6	S657-9	S657-10	S657-11	S657-12	S657-13	S657-14	S657-15	S657-17	S657-18	S657-19
Depth m	403.22	405.46	407.5	408.66	409.18	409.9	415.37	416.86	421.91	427.93	448.91	476.67
SiO2 %	42.7	38.6	44.8	47.5	53.2	50.2	48.5	50	47.80	51.80	52.70	49.80
TiO2 %	1.02	0.93	0.85	1.02	0.99	0.98	1	0.96	0.99	0.94	0.98	1.60
Al2O3 %	15.1	14.3	13.8	15.6	15.5	15.1	15.5	14.4	13.70	14.50	15.60	13.30
Fe2O3 %	12.5	10.1	11.8	10.7	11.6	11.8	11.4	12.6	15.20	11.70	11.40	14.60
MnO %	0.2	0.26	0.22	0.2	0.21	0.26	0.24	0.27	0.29	0.26	0.25	0.23
MgO %	6.68	5.32	4.64	4.82	4.67	6.4	5.41	6.52	6.78	6.52	4.93	6.07
CaO %	6.9	12.7	11.2	9.06	9.01	11.2	11.3	9.88	12.20	10.50	12.00	10.70
Na2O%	2.23	2.05	1.38	2.45	2.49	1.91	2.11	1.37	1.27	2.39	1.89	1.95
K2O %	3.74	3.38	3.37	2.84	0.91	0.69	0.82	0.88	0.42	0.30	0.16	0.34
P2O5 %	0.09	0.06	0.07	0.08	0.07	0.08	0.08	0.08	0.08	0.08	0.07	0.15
LOI %	5.62	7.7	5.16	3.7	0.77	1.31	1.85	2.62	0.70	0.47	0.47	0.62
Total	96.78	95.4	97.29	97.97	99.42	99.93	98.21	99.58	99.43	99.46	100.45	99.36
La	2.94	2.29	2.15	2.98	2.8	2.7	2.92	2.67		2.25	2.54	9.84
Ce	8.11	6.36	5.94	8.1	7.51	7.24	7.58	7.36	4.00	6.70	7.37	25.54
Pr	1.27	1.07	0.98	1.3	1.19	1.18	1.22	1.18		1.02	1.13	3.44
Nd	7.07	5.54	5.38	7.21	6.53	6.31	6.36	6.61		5.48	6.16	15.85
Sm	2.21	1.91	1.87	2.29	2.2	2.11	2.2	2.21		2.09	2.14	4.41
Eu	0.77	0.82	0.63	0.71	1.07	0.81	0.9	0.82		0.62	0.85	1.51
Gd	3.09	2.79	2.77	3.39	3.18	3.03	3.29	3.2		2.99	3.04	4.95
Tb	0.54	0.47	0.48	0.56	0.53	0.5	0.55	0.56		0.51	0.55	0.72
Dy	3.86	3.63	3.59	4.11	3.82	3.69	4.16	3.95		3.61	3.79	4.66
Ho	0.83	0.74	0.78	0.84	0.79	0.76	0.89	0.9		0.78	0.81	0.88
Er	2.58	2.34	2.43	2.55	2.48	2.36	2.81	2.67		2.47	2.45	2.55
Tm	0.39	0.37	0.38	0.39	0.37	0.36	0.44	0.41		0.38	0.38	0.36
Yb	2.61	2.47	2.37	2.44	2.4	2.27	2.85	2.76		2.46	2.63	2.22
Lu	0.39	0.4	0.38	0.36	0.36	0.35	0.45	0.4		0.40	0.38	0.35
Th	0.3	0.24	0.2	0.53	0.28	0.24	0.56	0.26		0.27	0.24	1.14
U	0.07	0.05	0.04	0.05	0.06	0.07	0.1	0.06		0.04	0.05	0.21
Cs	1.91	4.16	5.06	6.39	1.89	1.24	2.02	1.76		0.74	0.04	0.26
Tl	1.27	1.33	1.28	1.25	0.68	0.56	0.69	0.7				
Rb	114.7	145.4	148.1	135.6	35.7	30.0	41.3	43.5	23.0	28.0	1.4	11.0
Sr	79	123	78	68	92	93	75	65	50	90	92	163
Ba	430	190	160	243	87	51	63	288	71	101	27	70
Nb	2.26	2.3	1.98	2.35	2.33	2.29	2.42	2.25	1.5	2.41	2.57	9.82
Ta	0.15	0.13	0.12	0.15	0.14	0.14	0.14	0.13		0.14	0.14	0.51
Zr	53	52	44	51	43	47	53	44	56	64	59	112
Hf	1.63	1.61	1.46	1.99	1.5	1.38	1.83	1.27		1.55	1.15	2.91
Y	20	19	19	21	20	19	22	22	22	23	23	26
V	326	300	281	325	321	319	329	312	266	327	347	372
Sc	49	46	41	49	48	48	50	45	42	51	44	44
Cr	243	217	196	241	243	235	225	202	205	206	219	90
Co	59	56	55	66	48	54	46	43	59	61	51	58
Ni	123	101	108	123	103	106	99	92	89	126	125	64
Cu	81	61	186	163	104	14	384	143	460	95	71	139
Zn	71	55	100	107	126	139	124	133	152	118	122	101
Pb	1.7	6.2	4.4	5.6	5.1	3.6	4.4	2.6	2.0	1.6	1.8	1.4
Be	2.0	2.0	2.0	2.0	2.0	2.0	2.0	2.0	2.0	1.5	1.6	2.3
Bi	0.21	0.27	0.17	0.26	0.19	0.16	0.22	0.16				
Cd	2	2	2	2	2	2	2	2	2	2.00	2.00	2.00
W	62	79	11	63	10	10	10	10	5	12.00	5.00	5.00
Ag	0.5	0.5	0.5	0.5	0.5	0.5	0.5	0.5	0.5	0.50	0.50	0.50
Au	53	410	490	550	27	2	66	17	4	1	1	2
As	28	11200	115	2560	21	50	14	11	8	39	33	58
Mg#	32	31	25	28	26	32	29	31	28	32	27	26
Al2O3/TiO2	14.8	15.4	16.2	15.3	15.7	15.4	15.5	15.0	13.8	15.4	15.9	8.3
CaO/Al2O3	0.46	0.89	0.81	0.58	0.58	0.74	0.73	0.69	0.89	0.72	0.77	0.80
Total REE	37	31	30	37	35	34	37	36		32	34	77
(La/Yb)cn	0.74	0.61	0.60	0.81	0.77	0.78	0.68	0.94		0.60	0.64	2.92
(La/Sm)cn	0.82	0.74	0.71	0.80	0.78	0.79	0.82	0.92		0.66	0.73	1.37
(Gd/Yb)cn	0.96	0.92	0.95	1.13	1.07	1.08	0.94	1.05		0.99	0.94	1.81
Zr/Hf	32	32	30	25	29	34	29	35		41	51	39
Nb/Ta	15	18	17	16	17	16	17	17		17	18	19
Ti/Zr	116	107	115	121	138	126	114	129	106	88	100	85
Nb/Th	7.5	9.6	9.9	4.4	8.3	9.5	4.3	8.7		8.9	10.7	8.6
La/Nb	1.30	1.00	1.09	1.27	1.20	1.18	1.21	1.19		0.93	0.99	1.00
La/Th	9.8	9.5	10.8	5.6	10.0	11.3	5.2	10.3		8.3	10.6	8.6
Zr/La	17.92	22.66	20.60	17.02	15.36	17.24	18.06	16.56		28.44	23.23	11.43

Table 5.1. continued

	Central deposits (OK Mine)											
Sample	S657-20	S657-21	S657-2	S657-23	S657-24	S657-2	S657-27	S657-28	S657-29	SC 1484-1	SC 1484-2	SC 1484-3
Depth m	482.5	484.38	485.12	486.24	486.71	487.87	490.45	494.39	521.13	43.7	45.4	45.8
SiO2 %	49.80	50.90	47.90	46.00	46.10	49.00	49.80	50.70	51.10	52.1	50.1	49.4
TiO2 %	1.78	0.97	1.59	1.75	2.01	1.72	1.73	1.14	0.95	0.24	1.32	1.23
Al2O3 %	13.10	15.00	14.00	13.20	14.50	13.20	13.20	15.10	14.60	4.24	14.3	13.7
Fe2O3 %	15.40	12.40	15.40	12.90	15.80	14.90	15.20	12.30	11.90	15.5	14.7	14.5
MnO %	0.25	0.24	0.33	0.20	0.36	0.25	0.22	0.26	0.24	0.33	0.21	0.23
MgO %	5.86	6.23	6.99	4.80	9.30	6.91	5.81	6.19	6.66	4.6	6.93	6.8
CaO %	10.60	9.38	9.63	10.70	2.56	8.12	10.50	10.60	11.70	16.1	8.27	9.35
Na2O%	2.05	2.59	2.12	1.74	2.45	1.85	1.86	3.01	1.92	0.23	2.57	2.32
K2O %	0.37	0.76	0.66	1.33	0.22	0.94	0.41	0.28	0.14	0.12	0.43	0.43
P2O5 %	0.15	0.08	0.14	0.16	0.16	0.14	0.15	0.09	0.08	0.04	0.11	0.11
LOI %	0.54	0.62	1.77	6.54	6.08	2.47	0.62	0.31	0.47	1.23	1.39	1
Total	99.9	99.17	100.53	99.32	99.54	99.5	99.50	99.98	99.76	94.75	100.42	99.14
La	10.48			11.16			10.73	4.16	2.79	7.95	4.16	3.74
Ce	26.62	6.00	17.00	27.99	11.00	20.00	26.78	11.31	7.75	16.63	11.19	10.35
Pr	3.58			3.79			3.59	1.61	1.18	2.21	1.75	1.62
Nd	17.53			18.15			17.39	8.36	6.83	9.22	9.44	8.5
Sm	4.54			4.92			4.71	2.64	2.34	1.82	2.81	2.76
Eu	1.47			1.35			1.56	1.01	0.85	0.53	1.07	0.96
Gd	5.13			5.09			5.02	3.69	3.20	1.93	3.97	3.73
Tb	0.77			0.74			0.74	0.61	0.55	0.27	0.68	0.62
Dy	4.79			4.55			4.61	4.29	3.94	1.7	4.63	4.5
Ho	0.90			0.90			0.91	0.92	0.85	0.33	1.01	0.96
Er	2.54			2.59			2.57	2.72	2.60	1	3.1	2.76
Tm	0.36			0.37			0.36	0.42	0.41	0.14	0.47	0.42
Yb	2.34			2.19			2.21	2.66	2.56	0.98	2.88	2.83
Lu	0.33			0.33			0.33	0.40	0.41	0.14	0.46	0.42
Th	1.14			1.22			1.17	0.42	0.27	1.35	0.63	0.73
U	0.21			0.21			0.21	0.09	0.05	0.25	0.45	0.31
Cs	0.14			5.79			0.33	0.11	-0.01	0.33	3.06	2.67
Tl										0.47	0.39	0.32
Rb	9.6	51.0	10.0	64.6	10.0	50.0	13.6	4.9	0.7	4.3	40.9	40.4
Sr	155	83	72	96	18	45	163	134	133	34	117	107
Ba	63	188	102	165	102	255	87	80	34	16	168	166
Nb	10.00	2.5	6.5	9.44	7.9	7.0	10.38	3.78	2.55	1.11	3.38	3.22
Ta	0.52			0.58			0.55	0.22	0.14	0.08	0.21	0.19
Zr	113	52	96	113	125	118	108	52	52	49	86	52
Hf	3.01			3.08			2.75	1.51	1.25	1	1.49	1.77
Y	26	19	21	23	21	19	27	25	24	10	25	23
V	461	269	317	422	330	293	458	417	405	85	349	345
Sc	43	41	39	41	36	32	43	53	53	12	45	45
Cr	62	204	137	60	104	92	63	207	215	46	221	165
Co	67	60	59	57	43	52	65	67	59	36	46	45
Ni	61	126	92	60	64	64	65	127	122	59	68	74
Cu	179	229	963	123	157	134	160	72	117	1066	119	67
Zn	117	162	140	95	75	106	131	119	108	192	108	110
Pb	2.1	2.0	3.0	3.2	2.0	2.0	1.6	2.1	1.3	70.2	504.7	6.3
Be	2.6	2.3	2.3	2.9	1.9	2.2	2.4	1.6	1.6	9.3	0.6	0.5
Bi										14.03	0.35	0.25
Cd	2.00	2	2	2.00	2	2	2.00	2.00	2.00	2	0.5	0.5
W	5.00	10	5	24.00	5	5	5.00	5.00	5.00	110	10	10
Ag	0.50	0.5	0.5	0.50	0.5	0.5	0.50	0.50	0.50	3.8	0.2	0.2
Au	3	28	130	61	15	6	6	3	2			
As	43	64	40	30	81	22	5	11	8			
Mg#	25	30	28	24	34	29	25	30	33	20	29	29
Al2O3/TiO2	7.4	15.5	8.8	7.5	7.2	7.7	7.6	13.2	15.4	17.7	10.8	11.1
CaO/Al2O3	0.81	0.63	0.69	0.81	0.18	0.62	0.80	0.70	0.80	3.80	0.58	0.68
Total REE	81			84			82	45	36	44.85	47.62	44.17
(La/Yb)cn	2.95			3.36			3.20	1.03	0.72	8.11	1.44	1.32
(La/Sm)cn	1.42			1.39			1.40	0.97	0.73	4.37	1.48	1.36
(Gd/Yb)cn	1.78			1.88			1.84	1.12	1.01	1.97	1.38	1.32
Zr/Hf	38			37			39	34	42	49	58	29
Nb/Ta	19			16			19	17	18	14	16	17
Ti/Zr	94	112	99	93	96	87	96	131	110	29	92	142
Nb/Th	8.8			7.7			8.9	9.0	9.4	0.8	5.4	4.4
La/Nb	1.05			1.18			1.03	1.10	1.09	7.16	1.23	1.16
La/Th	9.2			9.1			9.2	9.9	10.3	5.9	6.6	5.1
Zr/La	10.82			10.13			10.07	12.50	18.64	6.16	20.67	13.90

Table 5.1. (continued)

Southern deposits												
Sample	SC 1484-5	SC 1484-8	SC 1484-10	SC 1484-11	SC 358-1	SC 358-2	SC 358-3	SC 358-7	SC 358-11	SC 358-15	SC 358-24	SC 358-25
Depth m	171 3	227 25	244.6	250	43.1	105.6	108.8	121.3	123.6	130.5	143.3	143.6
SiO2 %	49 57	54	47 8	46.9	50	49.2	49.6	48.3	43.1	48 2	47 2	49.5
TiO2 %	1.2	0.86	1 01	1 07	0.92	0.9	0.91	0.89	0.96	0 82	1 07	0.86
Al2O3 %	13.52	13.8	14.9	14.5	15.4	14.9	14.9	15.7	13.7	14 8	17 1	14 8
Fe2O3 %	14 15	8.44	13.4	13.9	11.3	12.5	11.8	12.4	12.1	12.5	13.2	12 5
MnO %	0.21	0.24	0.17	0.28	0.24	0.23	0.24	0.22	0.2	0.28	0.22	0.26
MgO %	6.64	2.81	7 84	8.51	7.35	8.19	7.34	7.31	15.7	8.35	8.7	8.15
CaO %	9 23	14.8	9.17	9.49	9.09	9.06	9 23	8.31	9.51	8.99	5 31	9 71
Na2O%	2.26	1 99	2.27	2.27	2.33	2.19	2.43	1 9	0.91	1.45	2.52	2.03
K2O %	0.44	0.63	0.24	0.44	0.79	1 09	1.01	1.71	0.46	1 29	0.92	0.99
P2O5 %	0.1	0 07	0.09	0.07	0.08	0.08	0.08	0.08	0 07	0.07	0.09	0.08
LOI %	1	2.08	1.77	1	1.16	1.77	1 39	2.77	3.47	1 54	3.31	1 7
Total	98.39	99.77	98.73	98.52	98.75	100.2	99.02	99 7	100.27	98.44	99.78	100.72
La	3.92	4 61	3.66	3.31	2.44	2.57	2.19	2.53	3	2.64	3.02	2.82
Ce	10.52	10 83	9.56	9.52	6.85	7.2	6 34	7 17	8 28	7 04	8.35	7 56
Pr	1 65	1 65	1 48	1.55	1.11	1.16	1.11	1.17	1 29	1.15	1 37	1 24
Nd	8.79	8 5	7 81	8.23	5.94	6 38	5.99	6.25	6.34	6.02	7 35	6.87
Sm	2.71	2 23	2.55	2.52	2.12	2.07	1 97	2.12	1 69	2.02	2.41	2.12
Eu	0.99	1 3	0.8	0 64	0.79	0.86	0.74	0.8	0.57	0.8	0.79	0.76
Gd	3.56	2.9	3.3	3.39	2.84	2.94	2.81	2.83	2.28	2.75	3.38	2.99
Tb	0.6	0 46	0.56	0.5	0.51	0.48	0.47	0.49	0.38	0.46	0.54	0.51
Dy	4 39	3	3.85	3.19	3.77	3.63	3.39	3.43	2.79	3.32	3.91	3.54
Ho	0.9	0 62	0.8	0.58	0.8	0.74	0.72	0.71	0 58	0.7	0.82	0.76
Er	2.72	1 8	2.4	1.52	2.45	2.29	2.17	2.2	1.81	2.08	2.56	2.3
Tm	0.42	0.26	0.39	0.21	0.38	0.36	0.32	0.32	0.27	0.31	0.36	0.37
Yb	2.73	1 64	2.33	1.39	2.4	2.15	2.1	2.07	1.67	1 97	2.37	2.16
Lu	0.42	0.25	0.36	0.22	0.35	0.31	0.31	0.32	0.26	0.32	0.34	0.35
Th	0.53	0.48	0.65	0.47	0.53	0.36	0.35	0.46	0.35	0.32	0.51	0.41
U	0.36	0 36	1 06	0.17	0.54	0.21	0.1	0.1	0.24	0.16	0.14	1 93
Cs	2.67	0 87	1 51	0.86	1.13	4.56	3.28	15 47	2.06	3.68	4 88	4 02
Tl	0 3	0.26	0.14	0.15	0.22	0.32	0.34	0.95	0.18	0.37	0.34	0.46
Rb	39 8	40.1	19.5	30.0	42.1	52.1	58.2	119.4	29.2	70 8	42 8	58.3
Sr	105	62	136	114	128	102	104	98	20	87	130	105
Ba	165	83	38	113	102	162	185	301	39	222	346	297
Nb	3.17	6.44	2.88	2.24	2.25	2.23	2.23	2.25	2.41	1.96	2.77	2.55
Ta	0.2	0.57	0.19	0.17	0.14	0.15	0.13	0.14	0.14	0.12	0.18	0.16
Zr	64	48	64	61	53	55	61	41	63	63	67	43
Hf	1.35	0.76	1.1	1.21	1.37			1.1		0.88	1 55	0.85
Y	23	16	20	13	19	18	18	18	14	17	20	19
V	341	213	306	167	303	274	267	289	264	256	321	253
Sc	44	31	41	22	45	39	39	42	39	40	48	37
Cr	144	202	276	304	295	246	301	294	457	611	437	494
Co	45	33	45	52	51	45	45	38	47	50	48	46
Ni	71	85	115	133	109	116	109	107	92	159	139	144
Cu	66	67	127	1	110	166	88	239	56	23	63	133
Zn	108	96	96	116	96	102	108	136	148	186	94	138
Pb	71 3	3.1	22.6	4.2	80.0	7 3	145.8	23.7	32.1	9.4	115.1	16 5
Be	0 9	95 8	0.5	1 2	0.4	0.3	0.4	0.5	0.2	0.4	0.0	0 5
Bi	0.29	0.32	0.21	0.31	0.23	0.72	0.32	0 66	0 55	0.74	0 21	0 28
Cd	1	0.5	0.5	1	0.5	0.5	0.5	1	0.5	1	0 5	0.5
W	10	10	10	10	10	10	10	30	40	10	10	10
Ag	0.2	0 2	0.2	0.2	0.2	0.2	0.2	0.6	0.2	0.2	0.2	0.2
Au												
As												
Mg#	29	22	34	35	36	36	35	34	53	37	36	36
Al2O3/TiO2	11 3	16.0	14.8	13.6	16.7	16.6	16.4	17 6	14.3	18 0	16.0	17 2
CaO/Al2O3	0.68	1 07	0.62	0.65	0.59	0 61	0.62	0.53	0.69	0.61	0.31	0 66
Total REE	44.32	40.05	39.85	36.77	32.75	33.14	30.63	32.41	31.21	31 58	37.57	34.35
(La/Yb)cn	1.44	2.81	1 57	2.38	1.02	1.2	1.04	1.22	1 8	1 34	1 27	1 31
(La/Sm)cn	1.45	2.07	1 44	1.31	1.15	1.24	1.11	1.19	1.78	1 31	1.25	1 33
(Gd/Yb)cn	1.3	1.77	1 42	2.44	1.18	1.37	1.34	1.37	1.37	1.4	1 43	1 38
Zr/Hf	47	63	58	50	39	#DIV/0!	#DIV/0!	37	#DIV/0!	72	43	51
Nb/Ta	16	11	15	13	16	15	17	16	17	16	15	16
Ti/Zr	112	107	95	105	104	98	89	130	91	78	96	120
Nb/Th	6.0	13.4	4.4	4.8	4.2	6.2	6.4	4.9	6.9	6.1	5.4	6.2
La/Nb	1.24	0.72	1.27	1.48	1.08	1.15	0.98	1.12	1.24	1.35	1 09	1.11
La/Th	7 4	9.6	5.6	7.0	4.6	7.1	6.3	5.5	8.6	8.3	5.9	6.9
Zr/La	16.33	10.41	17.49	18.43	21.72	21.40	27.85	16.21	21 00	23.86	22.19	15 25

Table 5.1. (continued)

Southern deposits				
Sample	SC 358-27	SC 358-28	SC 358-29	SC 358-31
Depth m	144.1	144.6	144.7	145.6
SiO2 %	49.5	51.7	37 5	53 3
TiO2 %	1 46	1 25	0.61	1.2
Al2O3 %	15.3	15.2	8 33	14.5
Fe2O3 %	14 6	13 8	7 95	11
MnO %	0 29	0.29	0 32	0.23
MgO %	7 36	6.31	4.42	4.75
CaO %	4 87	6.73	25	8.21
Na2O%	3.21	3.16	1.92	4.47
K2O %	0.73	0.59	0.45	0.24
P2O5 %	0.11	0.11	0.08	0.1
LOI %	1 77	0.54	13.5	0.62
Total	99 28	99.75	100.11	98.68
La	3.57	4.39	3.07	2.8
Ce	9 82	11 48	7.62	8.44
Pr	1.6	1 83	1.19	1.42
Nd	9 63	9.44	6.21	8.13
Sm	2.85	3.08	1.59	2.56
Eu	0.92	1 07	0.79	0.9
Gd	3.89	4.07	2.43	3 64
Tb	0 67	0.7	0.4	0.61
Dy	4 59	5 07	2.9	4.39
Ho	0 96	1 06	0 63	0.97
Er	2.66	3.13	1 98	2.85
Tm	0.39	0.48	0 29	0 44
Yb	2.4	3.16	1.81	2.85
Lu	0 37	0 46	0.3	0 42
Th	0.36	0 59	0.26	0.34
U	0.14	0.16	0 26	0.14
Cs	3.71	1 23	1	0.21
Tl	0.32	0.14	0.25	0.06
Rb	32.9	27 9	26.0	7 8
Sr	124	125	50	110
Ba	146	92	83	44
Nb	3.06	3.45	1.7	2.97
Ta	0.2	0.2	0.11	0.19
Zr	87	89	41	75
Hf				
Y	22	26	16	23
V	432	349	185	351
Sc	53	48	24	47
Cr	165	149	36	163
Co	46	45	29	45
Ni	65	62	31	65
Cu	140	40	77	5
Zn	146	172	128	78
Pb	25.0	4.1	18.5	3.2
Be	0.1	0.3	0.1	0.2
Bi	0.2	0.2	0.19	0.19
Cd	0.5	0.5	0.5	0.5
W	10	10	10	10
Ag	0.2	0.2	0.2	0.2
Au				
As				
Mg#	30	28	32	27
Al2O3/TiO2	10.5	12.2	13.7	12.1
CaO/Al2O3	0.32	0 44	3.00	0.57
Total REE	43.32	49.42	31.21	40.42
(La/Yb)cn	1.49	1 39	1.7	0.98
(La/Sm)cn	1 25	1 43	1 93	1.09
(Gd/Yb)cn	1 62	1.29	1.34	1.28
Zr/Hf	#DIV/0!	#DIV/0!	#DIV/0!	#DIV/0!
Nb/Ta	15	17	15	16
Ti/Zr	101	84	89	96
Nb/Th	8.5	5.8	6.5	8.7
La/Nb	1.17	1.27	1.81	0.94
La/Th	9.9	7 4	11 8	8 2
Zr/La	24.37	20.27	13.36	26.79

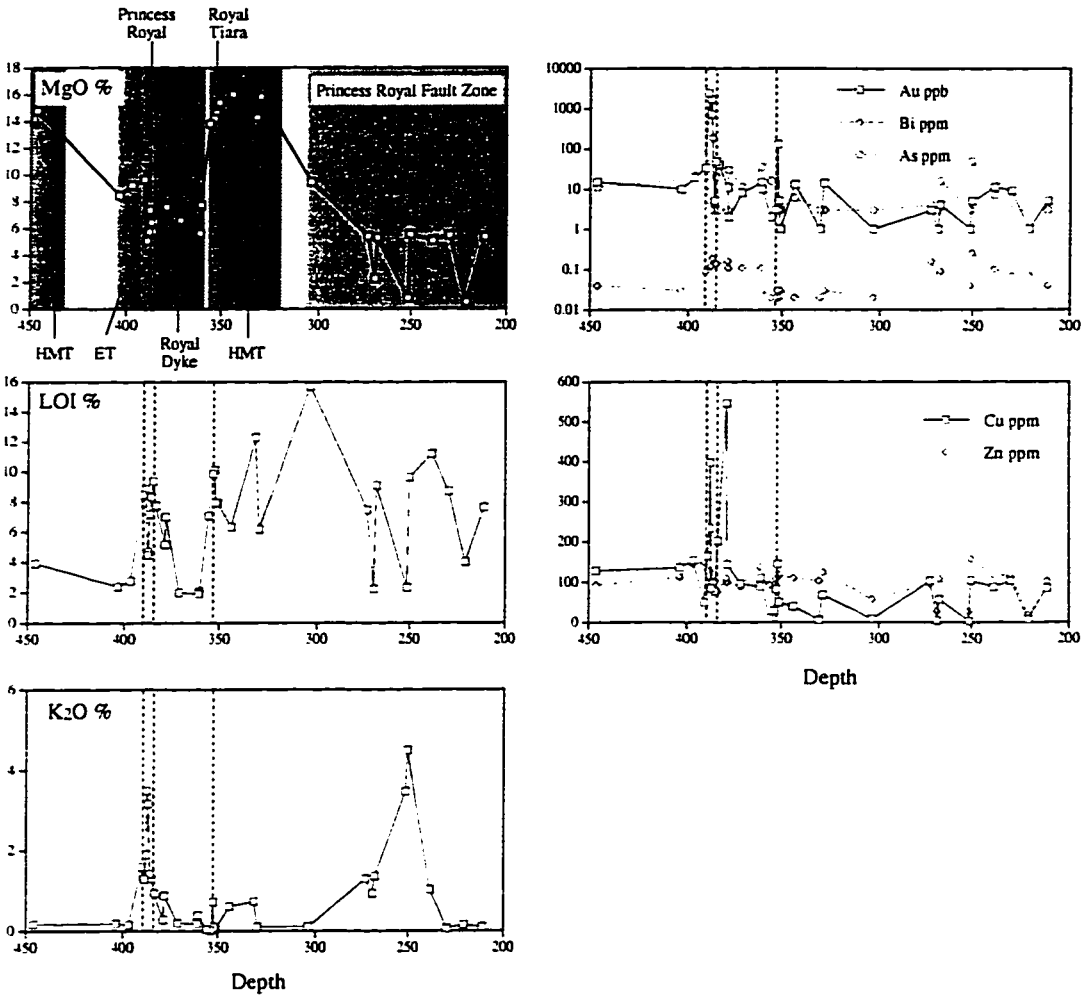

Figure 5.11A. Plots of element concentration versus depth down drill core PRS1177 (North Royal coordinates 255m N, 545m E, oriented 50° towards 270°, Fig. 4.2) for the Princess Royal and Royal Tiara veins of the Northern deposits. Lithologies and strutures are labelled on the plot of MgO concentration. The auriferous quartz veins, indicated by vertical dashed lines, are hosted within an east-dipping gabbro dyke complex. The dyke complex comprises HMT, ET, and tholeiitic intrusives (Royal Dyke). Alteration envelopes surrounding the quartz veins are characterized by progressive increases in K_2O and volatiles (LOI) with increasing proximity to the auriferous veins. Enrichment in K_2O is not as pronounced in HMT lithologies, where biotite is only sporadically developed. Note that the Princess Royal Fault Zone displays a similar alteration pattern.

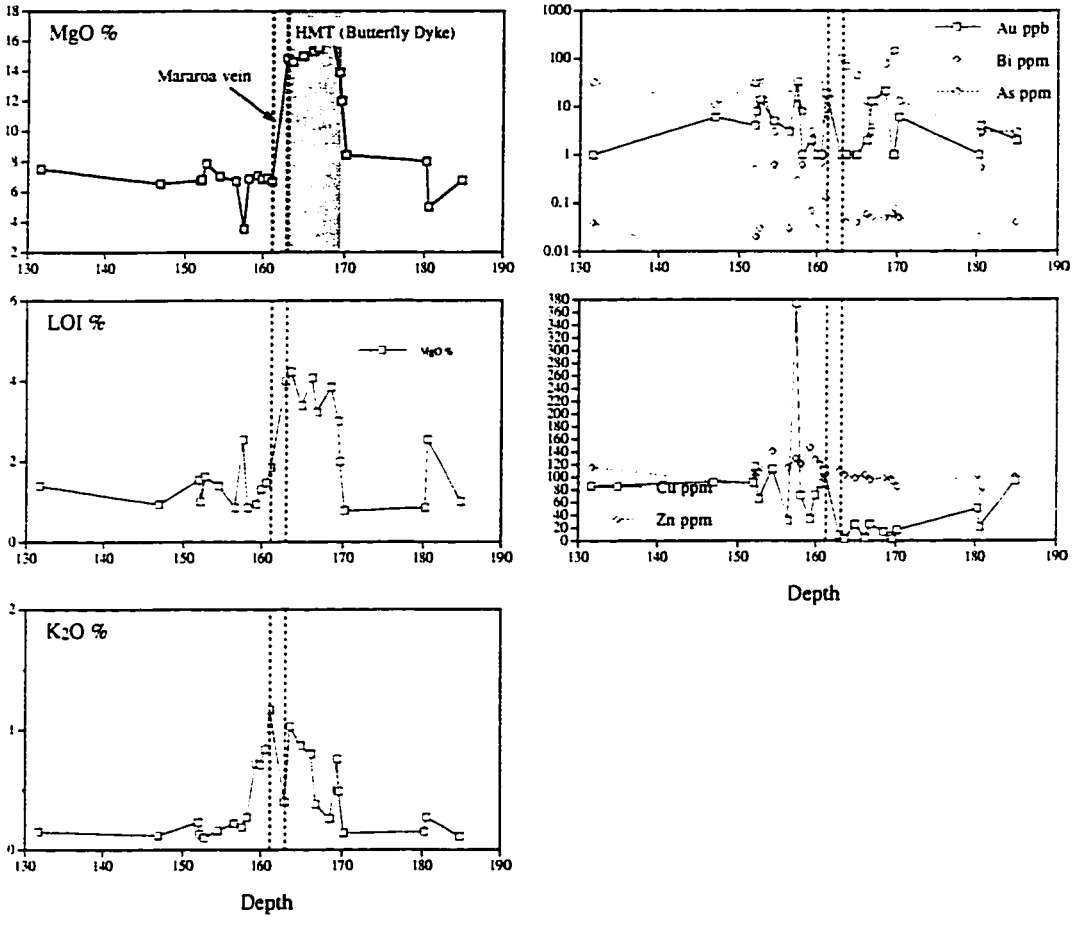

Figure 5.11B. Plots of element concentration versus depth down drill core S1113 through the Mararoa vein of the Central deposits (coordinates 2235mN, 100 mE, vertical). The vein is hosted at the contact between the HMT Butterfly Dyke and tholeiitic volcanics of the Woolyeenyer Formation (Figs. 3.1, 3.2, 4.1, 4.3).

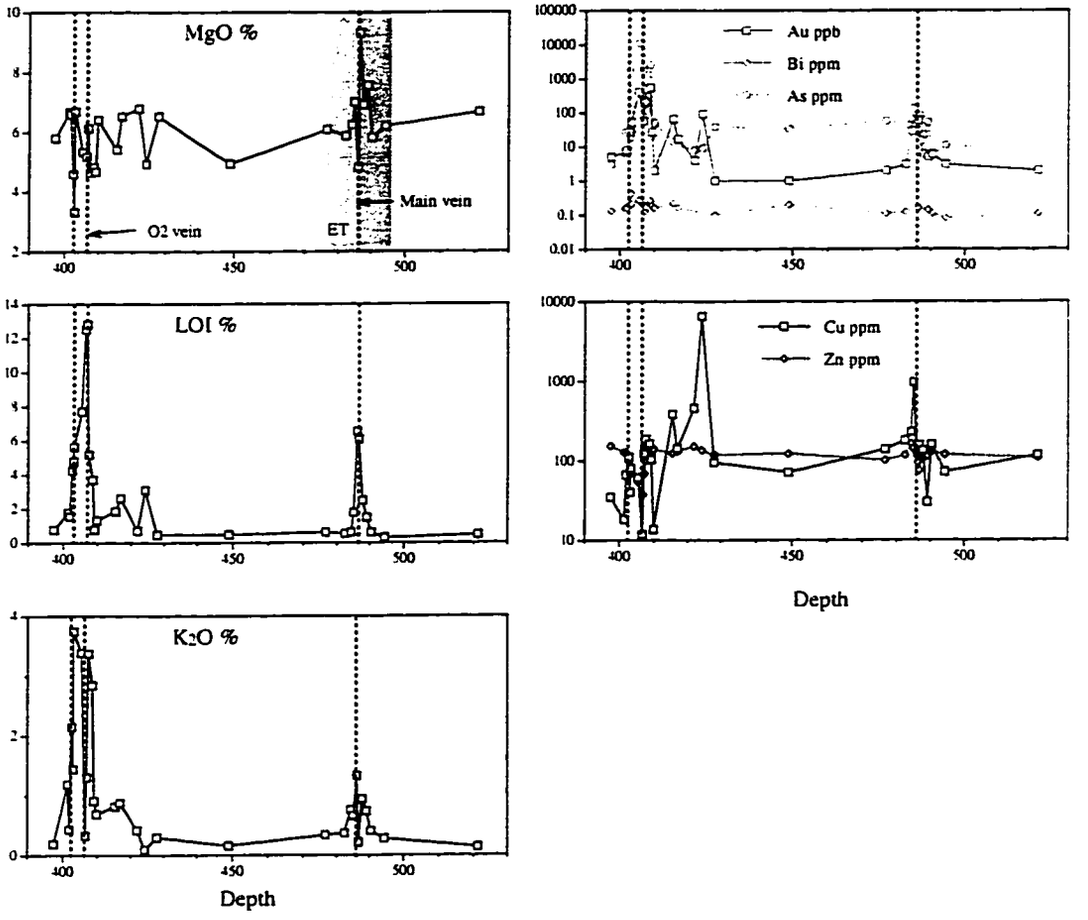

Figure 5.11C. Plot of element concentration versus depth down drill core S657 through the Main and O2 veins of the OK Mine, Central deposits (coordinates 2670m S, 850m W, 48° towards 350°; Figs. 4.8).

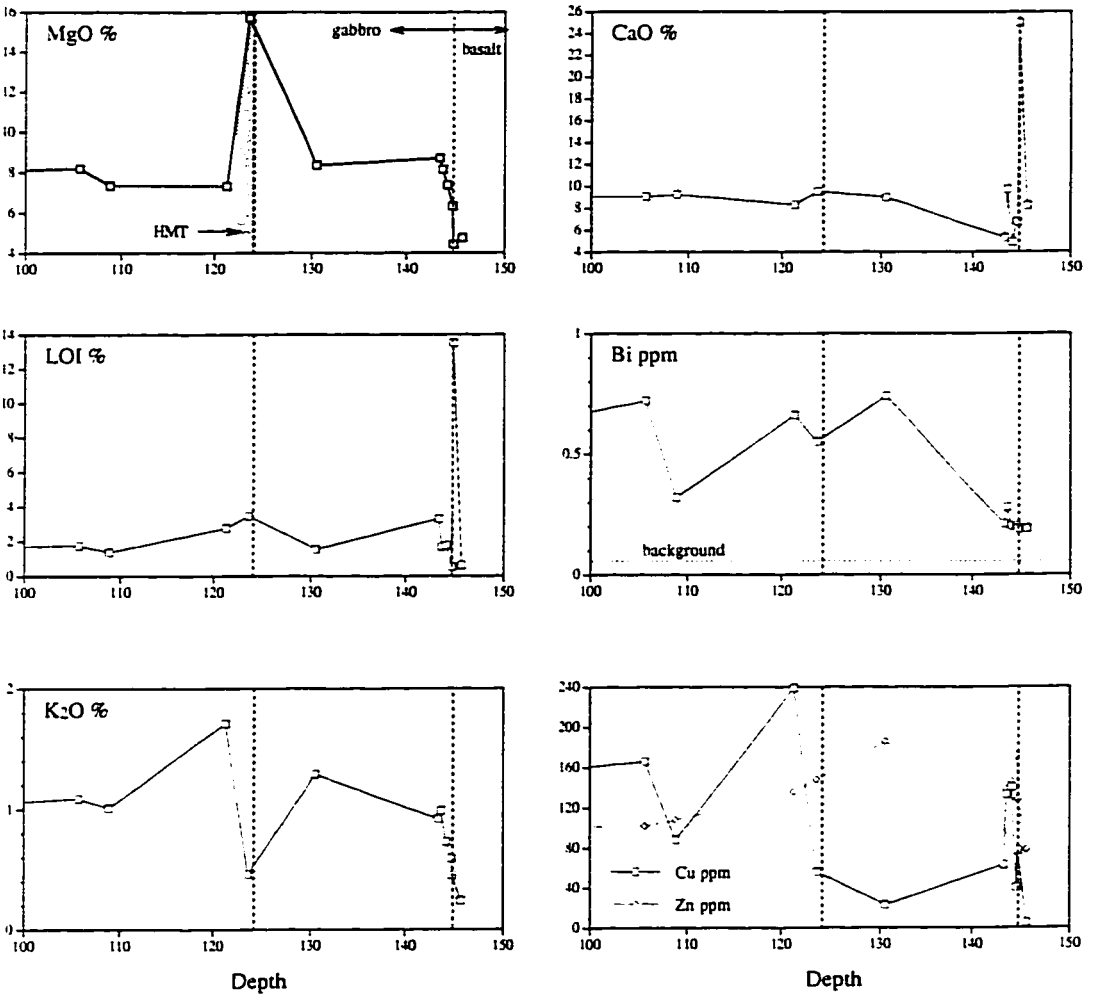

Figure 5.11D. Plots of element concentration versus depth down drill core SC358 through the Scotia ore zone, Southern deposits (Fig. 4.9). Lithologies are labelled on the MgO diagram, ore zones are dashed vertical lines. A ductile shear fabric pervades the gabbro, which is altered to amphibole + biotite + plagioclase. The ore zone adjacent to the HMT contains no clinopyroxene, possessing only biotite + amphibole + plagioclase and amphibole + plagioclase alteration selvedges. Biotite is only sporadically developed in the HMT, which has not fixed K from the hydrothermal fluid. The ore zone near the contact with the basalt contains banded clinopyroxene + calcite + quartz veins, and shows a corresponding decrease in K2O contents and increase in CaO and volatile abundances.

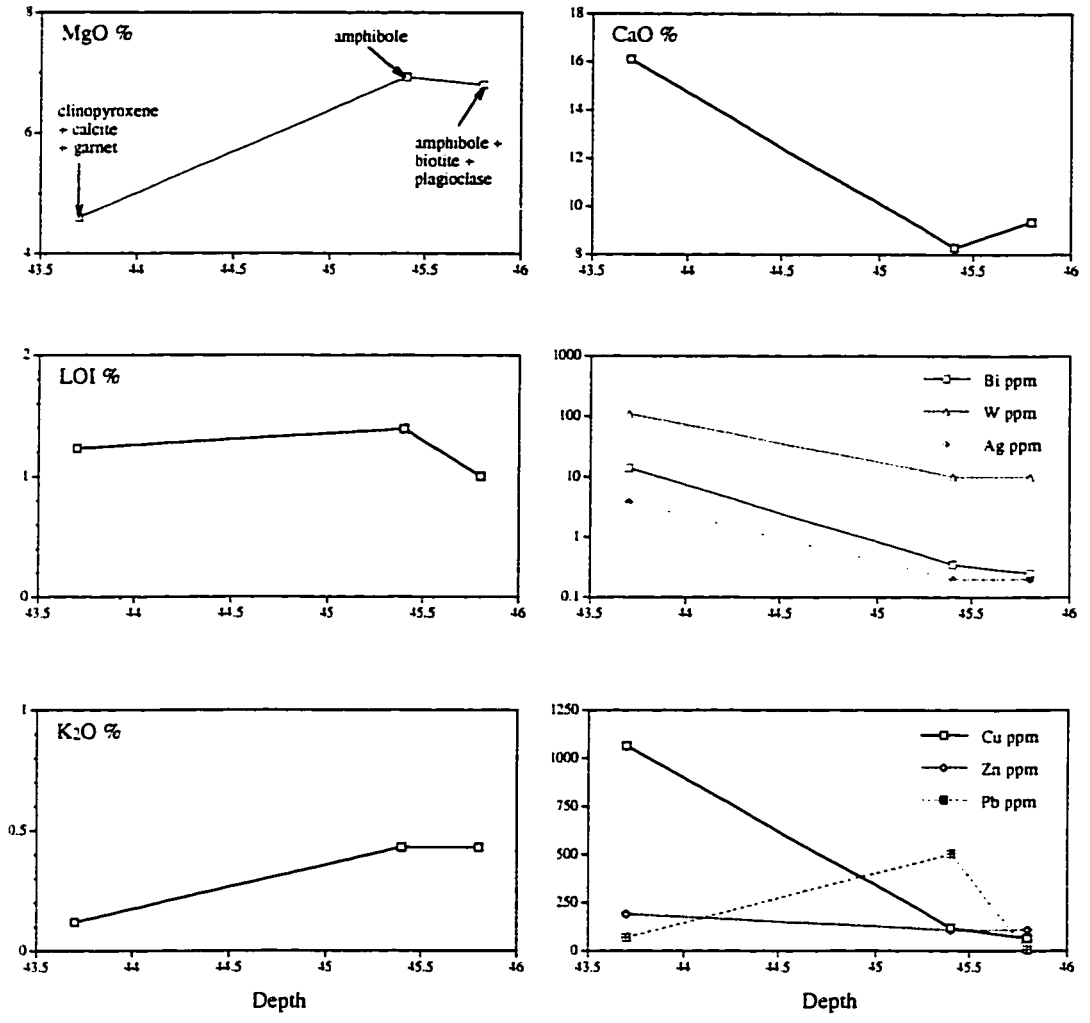

Figure 5.11E. Plots of element concentration versus depth down drill core SC1484, highlighting an intersection through a ductiley sheared gabbro with clinopyroxene + calcite + garnet alteration, but subeconomic concentrations of gold (Fig. 4.9; CNGC unpublished data). The three alteration zones characteristic of Southern deposits are present: biotite + amphibole + plagioclase, amphibole-dominated selvedges to the fluid conduits, and clinopyroxene + calcite ± garnet in the fluid conduit. K2O abundances decrease towards the conduit, whereas CaO contents increase markedly. LOI values remain relatively uniform throughout these alteration zones. Although this intersection contains subeconomic gold values (CNGC unpublished data), Bi, Ag, and W are systematically enriched in the fluid conduit, as they are in the Scotia ore zones. This element inventory, coupled with the ductile nature of the shear zone, implies that this hydrothermal activity was related to that which formed the Scotia deposits.

in the Central and Southern deposits, and diopside in the Southern deposits, can show relative K_2O depletion, as there are no mineral phases in these assemblages that fix potassium (e.g. S1113-N, Mararoa vein; SC358-29, Scotia deposit).

Behaviour of CaO and Na_2O is varied in the Norseman deposits. Northern deposits show enrichments of CaO with increasing degree of hydrothermal alteration due to greater abundance of calcite in alteration zones surrounding these deposits, whereas Na_2O contents remain relatively constant, varying only with the amount of plagioclase in the precursor lithologies.

Relative abundances of CaO and Na_2O in lithologies hosting the Central deposits vary irregularily with degree of alteration. For example, CaO (Na_2O) is depleted in the alteration halo of the Main Vein, OK mine, whereas it is enriched in the alteration associated with the adjacent O2 vein. Conversely, CaO is relatively uniform through alteration in tholeiites hosting the Mararoa vein, but is erratically distributed in HMT in the immediate footwall of the same quartz vein. These variations are due to (a) variations in the amount of precursor plagioclase in the host lithologies, and (b) the abundance of calcite in the alteration haloes. Calcite is markedly less abundant in Central deposits in comparison to their Northern counterparts.

In Southern deposits, CaO is enriched in innermost alteration haloes, consistent with the high modal abundance of diopside + calcite. Na_2O is variably enriched or depleted. As with potassium, Na abundance is intrinsically lower in HMT lithologies.

5.4.2 Trace elements

Figures 5.12 and 5.13 show the effects of hydrothermal alteration on extended primitive-mantle-normalized multielement diagrams. Alteration sequences are illustrated for rocks with similar protoliths. Note that the LILE closely follow K, and are variably disturbed even in least-altered lithologies. U contents are also variably affected by hydrothermal alteration (Fig. 5.12). Despite variations in the above elements, the remainder of the elements presented on these diagrams (REE, HFSE, compatible trace elements) appear to be robust during hydrothermal alteration, retaining their primary magmatic signatures (Fig. 5.13). It is these alteration-insensitive elements that are used in interpreting the petrogenesis of mafic precursor lithologies in Chapter 3.

The amount of dilution of trace elements, due to overall volume gain or loss during hydrothermal alteration, can be estimated from the variation of absolute aundances of elements between least altered and most altered rocks on Figures 5.12 and 5.13. Note that in many cases (e.g. Figs. 5.13 C,D,E,I), zero or minor dilution is apparent, indicating that alteration occurred at relatively constant volume.

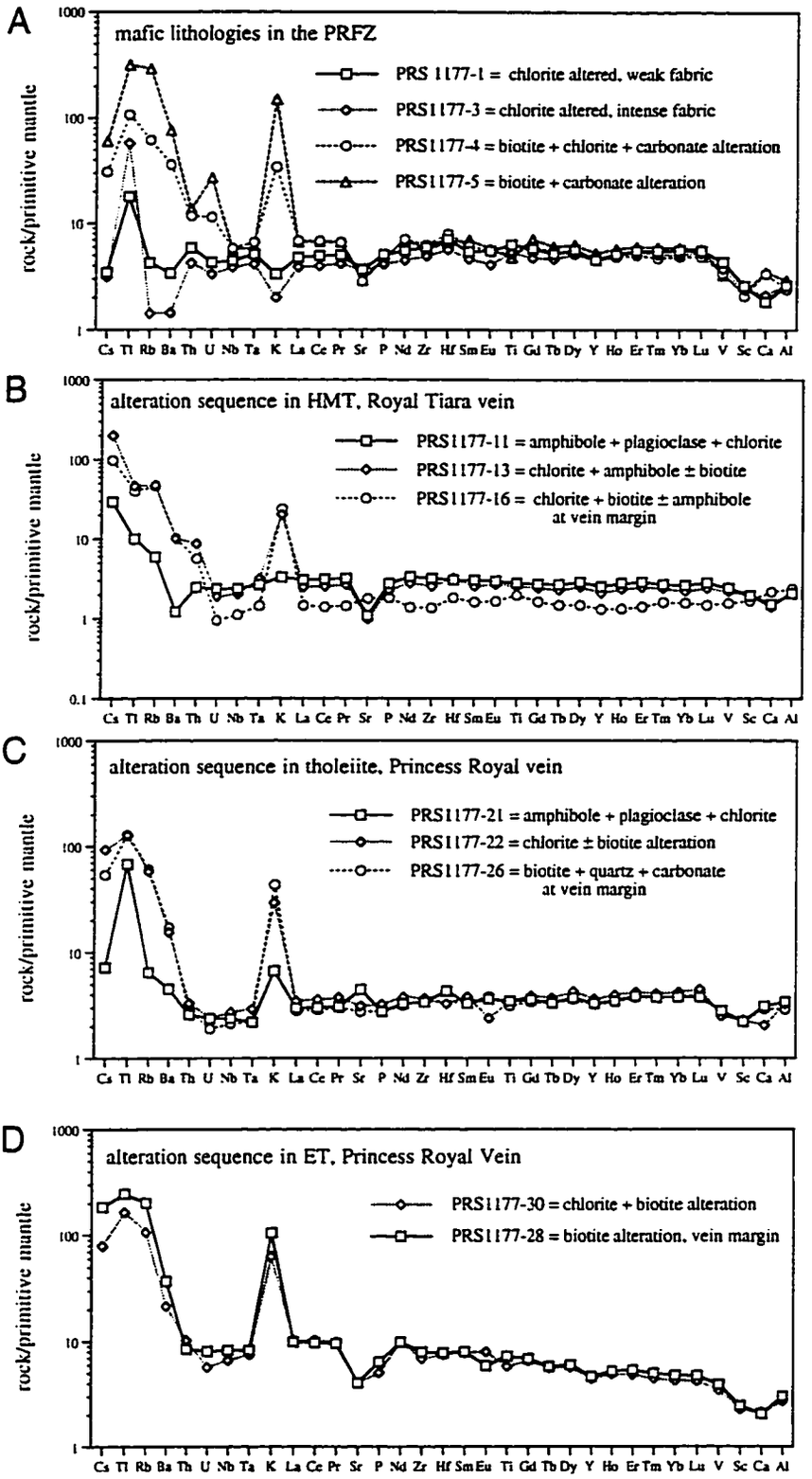

Figure 5.12 A-D. Mantle-normalized multielement diagrams for gold-related alteration sequences in various lithologies, North Royal Mine, diamond drill hole PRS1177. Normalizing factors and order of elemenets after Sun and McDonough (1989) and Sun et al. (1989).

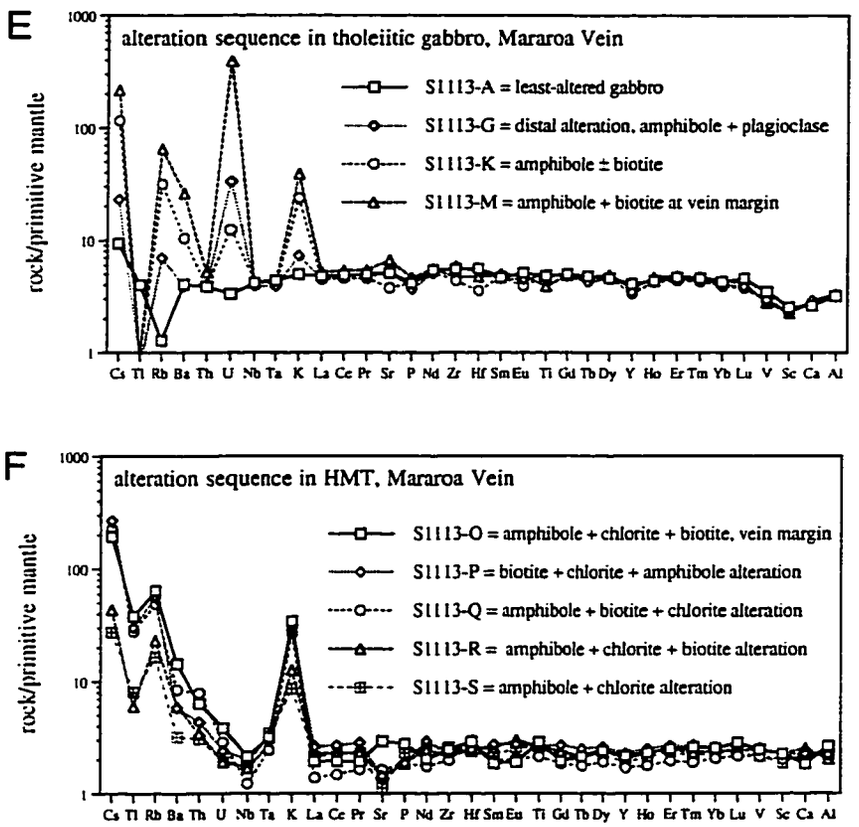

Figure 5.12 E-F. mantle-normalized multielement diagrams for gold-related hydrothermal alteration sequences in HMT and tholeiite, Mararoa vein, Central deposits. Samples are from diamond drill core S1113.

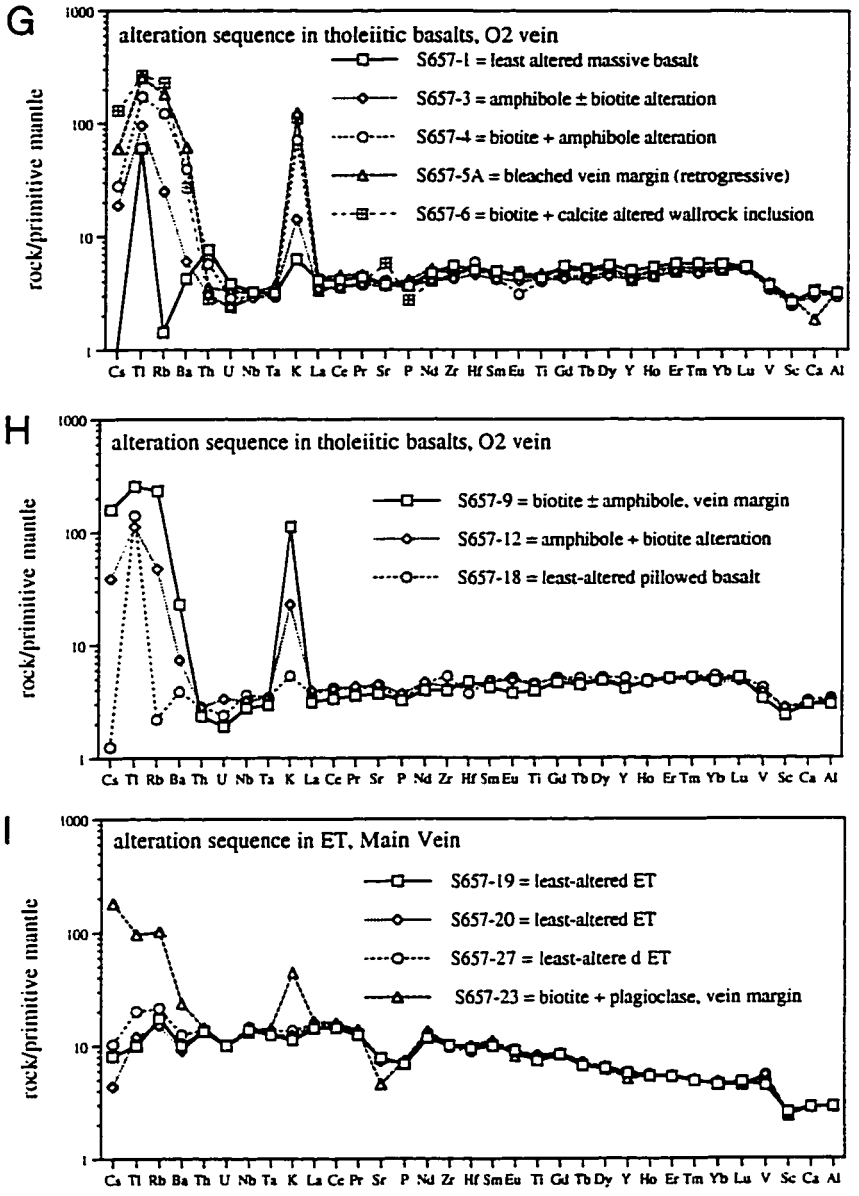

Figure 5.12 G-I. Mantle-normalized multielement plots for gold-related hydrothermal alteration sequences surrounding the O2 and Main veins, OK mine, Central deposits. Samples from drill hole S657.

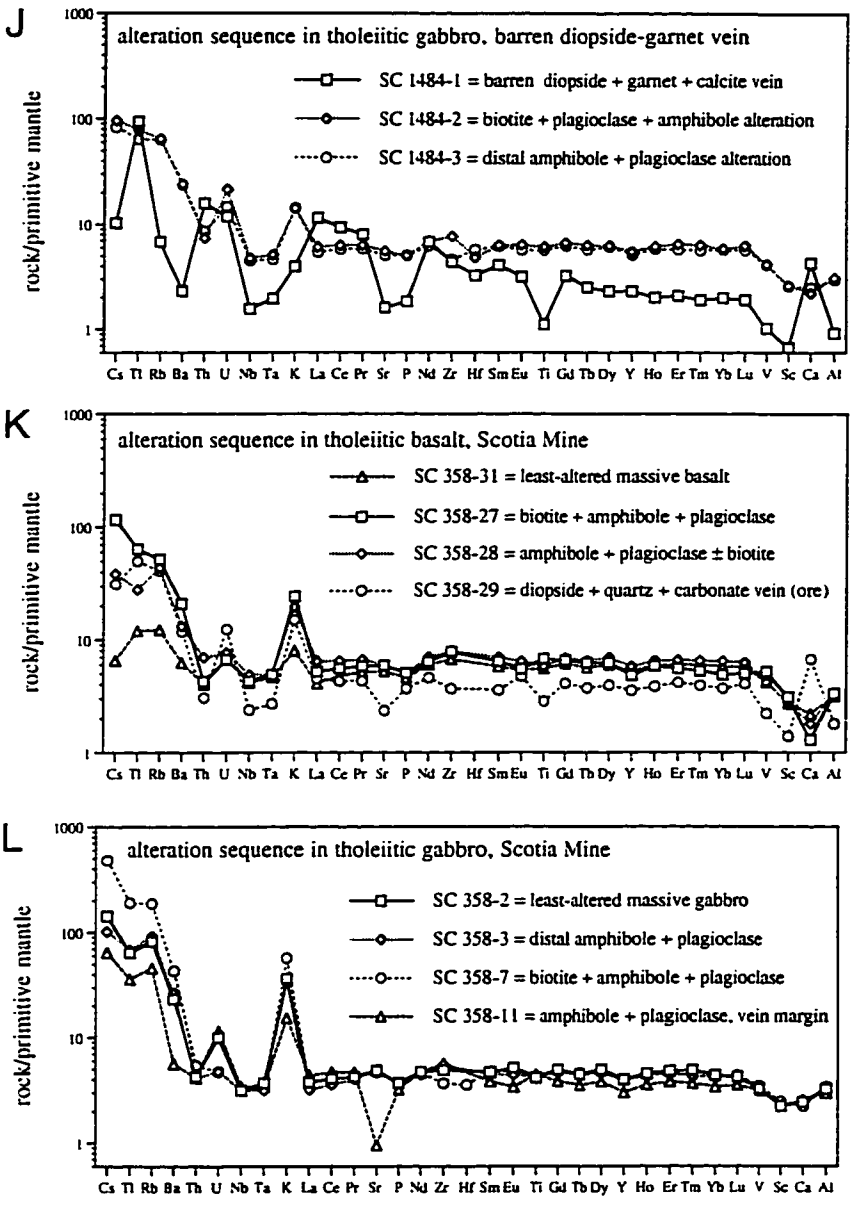

Figure 5.12 J-L. Mantle-normalized multielement plots for hydrothermal alteration sequences in the Southern deposits. Samples from drill cores SC1484 (J) and SC358 (K-L).

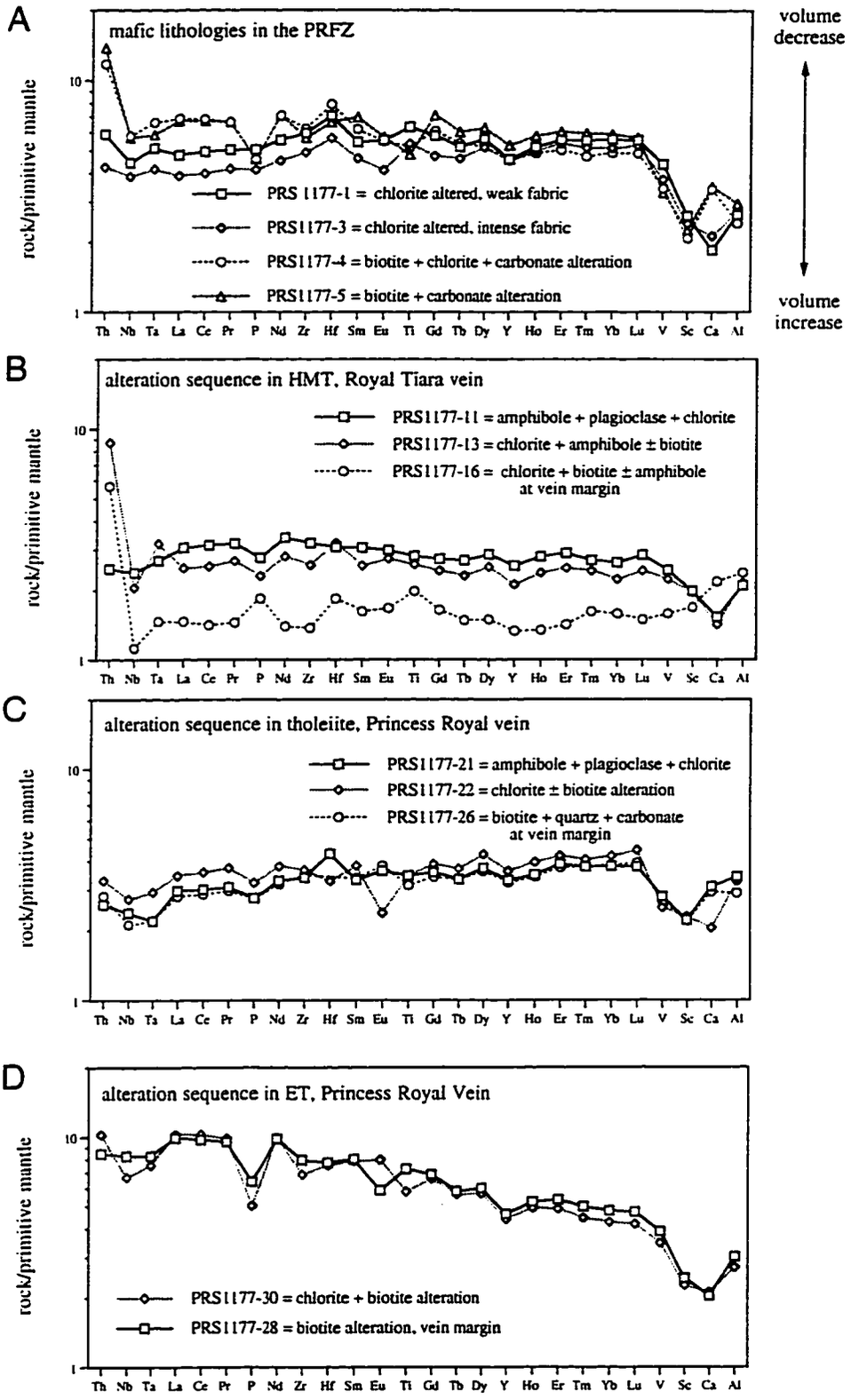

Figure 5.13 A-D. Abbreviated mantle-normalized multielement diagrams as for Figures 5.12 A-D, but with most mobile elements removed. Note the relative immobility of the remaining elements. Vectors describing the effect on element abundances of volume increase or decrease during alteration are also shown.

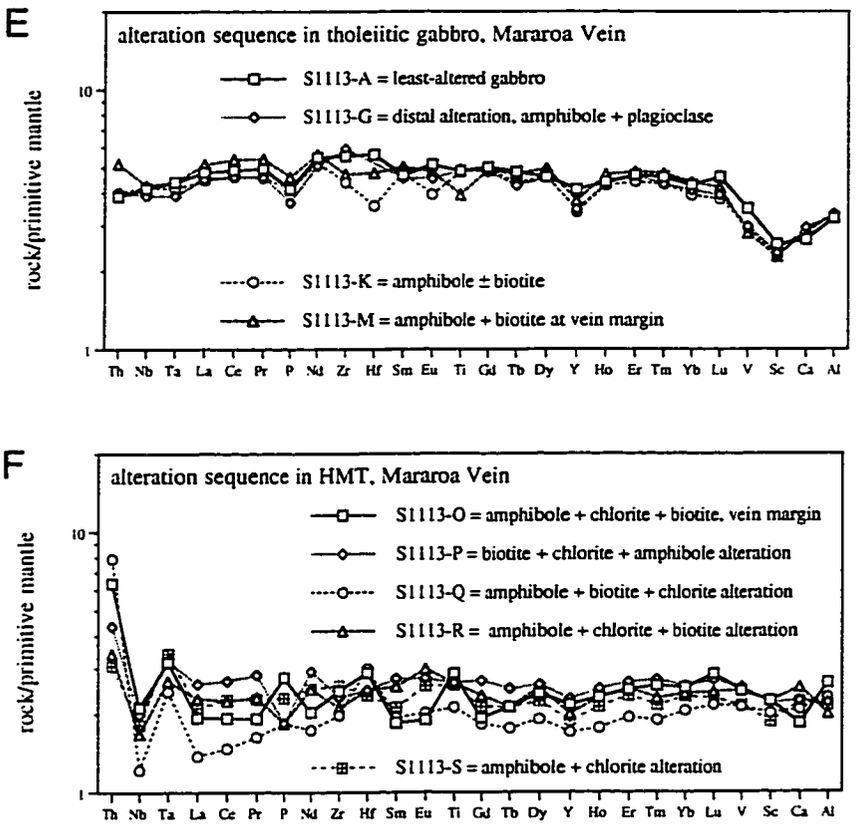

Figure 5.13 E-F. Abrreviated mantle-normalized multielement diagrams for Figures 5.12 E-F, with most mobile elements removed.

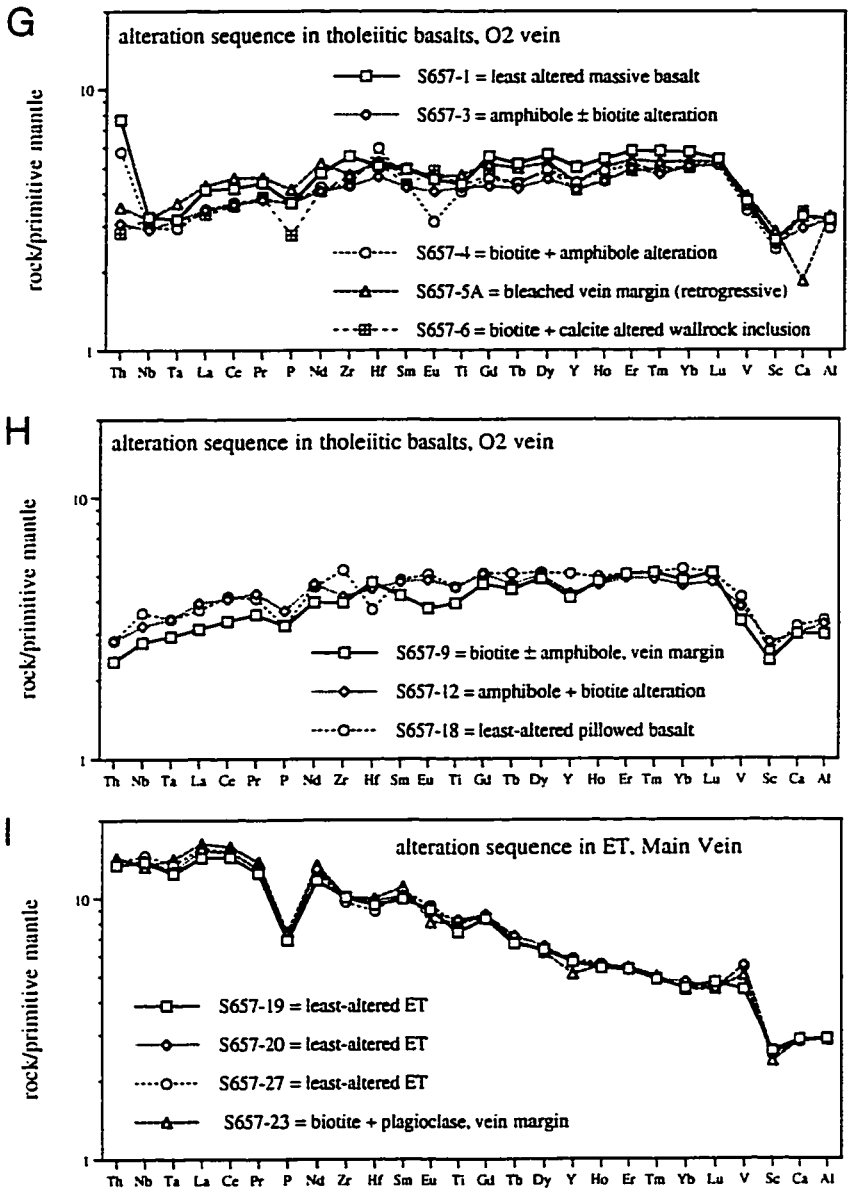

Figure 5.13 G-I. Abbreviated mantle-normalized multielement plots for Figures 5.12 G-I, with most mobile elements removed. O2 and Main veins, OK mine, Central deposits.

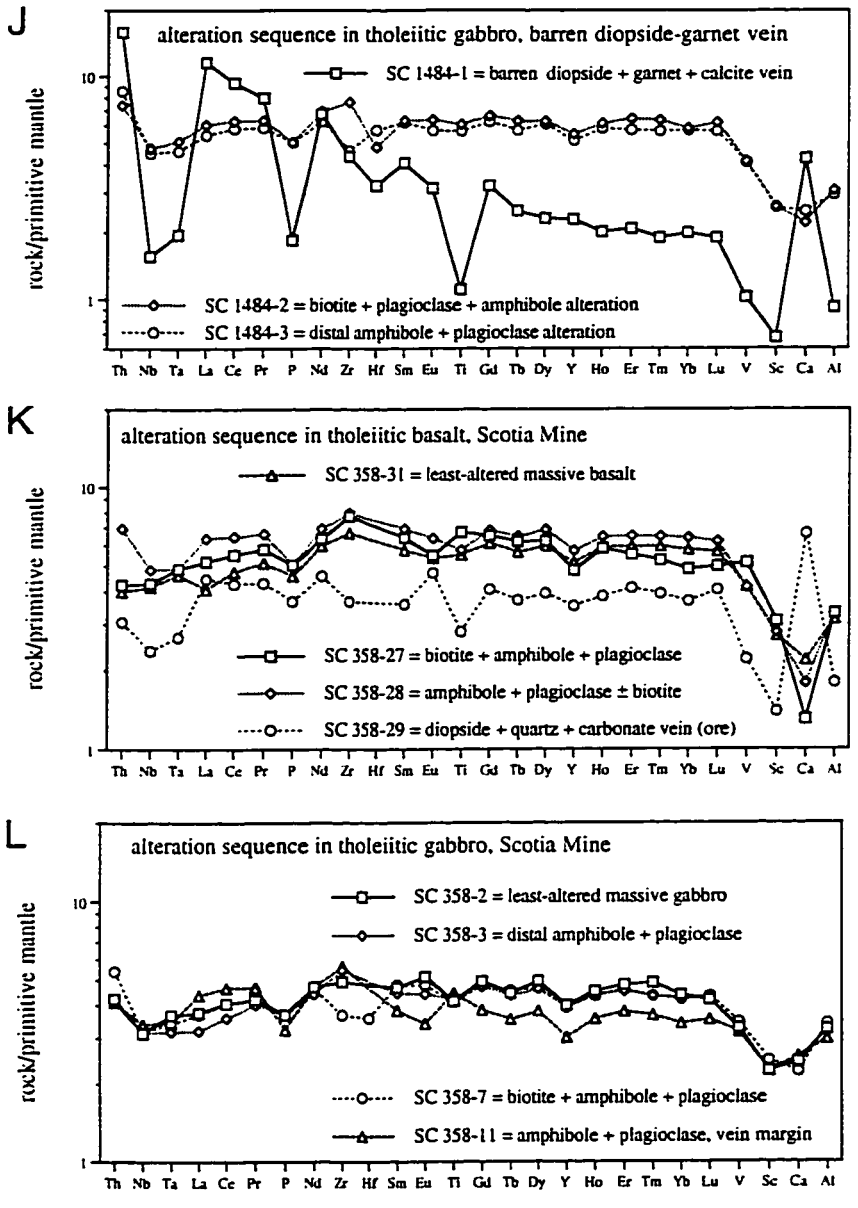

Figure 5.13 J-L. Abbreviated mantle-normalized multielement plots for Figures 5.12 J-L, with most mobile elements removed.

5.4.3 Comparison to other studies

The patterns of geochemical alteration observed in the Norseman deposits corroborate calculations of chemical mass balance conducted on suites of rocks representing a wide range of alteration intensities, from numerous Au, Ag-vein deposits, which have shown that in general high field-strength elements (HFSE: Th, Nb, Ta, Zr, Hf, Ti, Y, P, Al, Ga), rare-earth elements (REE: La through Lu) and compatible trace elements such as Sc, V, Cr and Ni are usually alteration insensitive, or isochemical, such that variations in absolute abundances arise from volume changes during hydrothermal alterations, generally due to the deposition of large amounts of quartz veins (Kerrich, 1983; Lesher et al., 1991). Comparison of mass balance studies between deposits formed at low temperature (greenschist facies) and high temperature (^{3} amphibolite facies) illustrate that most deposits are characterized by enrichments of precious metals (Au, Ag), associated rare elements (±As, Sb, Se, Te, Bi, W, B), LILE (K, Rb, Ba, Li, Cs, Tl) and volatiles (H_2O, CO_2, CH_4, H_2S). Low temperature deposits, however, may show Na enrichment in addition to, or instead of, potassium metasomatism. This is evident in the Norseman-Wiluna belt of Western Australia, where a change from Na to K metasomatism can be seen between deposits hosted within similar lithologies along the same major structure. High temperature deposits are characterized by substantial additions of Ca to inner alteration zones, and depletion of Na (Mikucki et al., 1990). The reasons for these variations are unclear, but likely result from the progressive modification of the alkali content of the fluid as it continuously reacts with the rocks it advects through, which in turn is controlled by the mineral assemblages stable in the P-T regimes the fluid encounters. Within a single lithological type, therefore, Ca is fixed at high P-T, K at all P-T, and Na at low P-T. Other major elements such as Fe and Mg show variable enrichments or depletions both between alteration zones in a single deposit (cf. Clark et al., 1986, 1989; Kishida and Kerrich, 1987; Mikucki et al., 1990), and between different deposits (Mikucki et al., 1990).

5.4.4 LILE systematics

As potassium metasomatism is a characteristic feature of many lode gold deposits, consideration of LILE systematics may provide constraints on fluid sources and the genetic origin of lode gold deposits, as discussed in detail by Kerrich (1989c). Coherent behaviour of K, Rb, Ba, Cs and Tl is present over three orders of magnitude in K content (Fig. 5.14), shown by K/Cs (1000-20000), K/Tl (10000-70000), K/Rb (95-1000) and K/Ba ratios (10-200) that encompass the ratios of 'average crust' (K/Rb = 286,

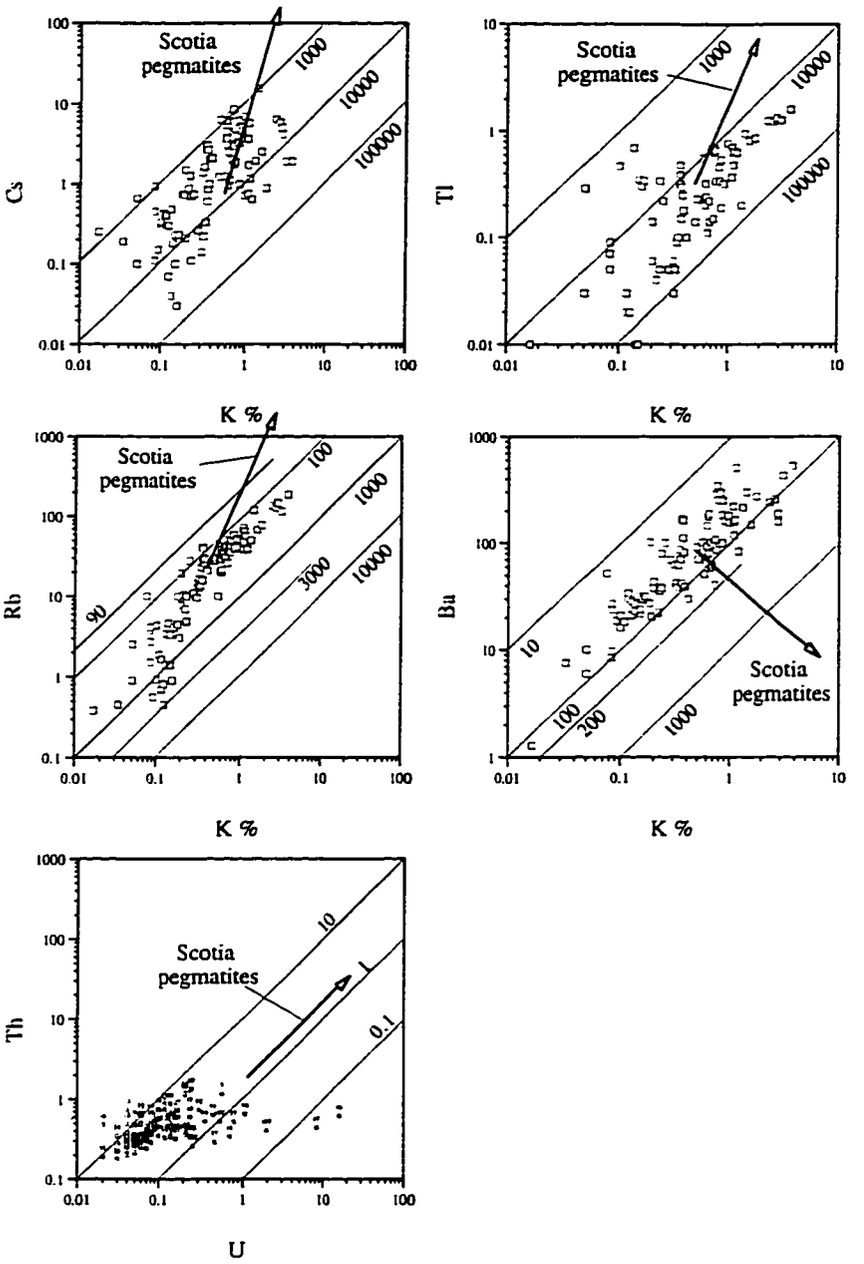

Figure 5.14. Plots of Cs, Tl, Rb, Ba (in ppm) versus K (%), and Th versus U (in ppm) for mafic lithologies of the Norseman Terrane. All degrees of alteration are represented, from least-altered metamorphic assemblages to banded clinopyroxene veins. Also indicated is the fractionation vector for late-stage magmatic fluids as defined by three pegmatites from the Southern deposits area (SC1484-4, SC1484-8, SCpeg8, Appendix B). The LILE (K, Rb, Ba, Tl) are coenriched with K over 3 orders of magnitute, unlike trends observed in magmatic-derived fluids. Note also that U and Th are decoupled in the hydrothermal fluid, as U is mobile in aqueous fluids, but Th solubility is limited to silicate melts.

K/Ba = 37; Taylor and McLennan, 1985), and is independent of host lithology or K-bearing alteration phase (muscovite, K-feldspar, biotite). In deposits hosted by felsic intrusive rocks with high initial LILE contents, it may be difficult to discern whether the LILE ratios observed in alteration reflect those in the hydrothermal fluid. However, in deposits hosted by mafic-ultramafic volcanic rocks, with low initial LILE abundances, the enhanced measured levels of K, Rb and Ba must result exclusively from their co-enrichment by the hydrothermal ore-forming system (Kerrich, 1989c; Perring and Barley, 1990).

These LILE correlations contrast with those in fluids sources from magmatic, sea floor hydrothermal, or granulite formation processes. Deposits formed from dominantly magmatic ore fluids such as Cu-, and Mo-porphyry deposits, Sn-W greisens, and certain pegmatites, display interelement trends between K, Rb, Ba, Cs and Tl that are in keeping with the characteristic partitioning trends of late-stage magmatic systems, where during progressive fractional crystallization of magmas, K/Rb, K/Cs, and K/Tl decrease, whereas K/Ba ratios increase (Fig. 5.14).

Volcanic hosted base metal sulfide deposits formed in the submarine environment are characterized by quite distinct K-Rb-Ba interelement systematics compared to either their lode gold or magmatic-related counterparts. Marine water has much larger K/Rb (3,300) and K/Ba (19,900) ratios (Holland, 1978) such that the alteration of volcanic rocks by seawater at low temperature acts to shift K/Rb and K/Ba ratios from typical igneous values towards higher ratios (Munha et al., 1980; Armbrust and Gannicott, 1980). Many granulites are depleted in LILE, leading some workers to postulate that the LILE enrichments characteristic of lode gold deposits may indicate ore fluids produced during granulitization processes in the lower crust (Cameron, 1988; Colvine et al., 1988). However, many LILE depleted granulites possess high K/Rb and K/Cs ratios, and alteration assemblages associated with lode gold deposits do not show corresponding LILE ratios.

While these processes, in theory, can effectively discriminate between fluid sources, it is important to stress that resultant LILE ratios from these processes may remain within the main trend of igneous rocks as defined by Shaw (1968), and thus LILE ratios of alteration assemblages alone cannot unequivocally discriminate between fluid sources (Kerrich, 1989c; Perring and Barley, 1990; Perring et al., 1990). LILE systematics alone can only be used as a fluid source discriminant where

(1) the absolute abundances of LILE in the alteration are much greater than those of the host lithologies, such that the LILE ratios result strictly from the hydrothermal fluid,

(2) K/Rb, K/Cs and K/Tl ratios of the alteration are greater than those of intrusions suspected as possible fluid sources, and

(3) K/Rb, K/Cs, K/Tl and K/Ba ratios are greater than those in the host lithologies.

In these cases, such as in the Norseman Terrane, the coherent behaviour of K, Rb and Ba in the lode gold deposits is unlike the trends observed in magmatic-related, or massive base metal sulfide deposits; accordingly a different origin for the gold deposits is likely, involving neither dominantly magmatic nor heated marine hydrothermal fluids.

5.4.5 Metal inventory

Although Au, Ag, W, Te, Pb and Bi are variably enriched in the veins (Mueller, 1992), as indicated by locally abundant free gold, scheelite, tellurides and galena, abundances of these elements generally drop to subeconomic or background values within millimetres to centimetres of the veins (Fig. 5.11). Exceptions to this rule occur in the Scotia orebodies, where biotitic alteration haloes in tholeiitic gabbro can contain economic concentrations of Au (CNGC, unpublished data). Nevertheless, the majority of the Au in the Southern deposits is concentrated in the quartz-clinopyroxene veins. Similarily, some Northern and Central deposits contain gold-enriched alteration haloes, with Au concentrations as high as 100 times that of background (1000 vs. 1-10 ppb), but economic concentrations of gold are generally restricted to the quartz veins (Fig. 5.11).

The lack of economic Au concentrations in altered wallrocks is of interest for two reasons: (1) the concentration of Au in the quartz veins results in thinner mining widths, and is therefore of economic importance, and (2) gold distribution acts as an indicator of depositional mechanisms for Au. Thus, in the Norseman deposits, wallrock reaction mechanisms for Au deposition are only of significance in the Southern deposits, of minor significance in the tholeiite-hosted veins of the Northern deposits, and generally insignificant in the Central deposits.

Lode gold deposits of the Norseman Terrane are characterized by a metal and trace element inventory consisting of Au, Ag, As, Te, W, Bi, generally with low levels of Cu, Zn, Pb, and Au/Ag ratios averaging 5 (Mueller, 1992). Deposits are variably enriched in one or more of the above elements, often with extreme interdeposit and even intradeposit variations in relative enrichments (A. Thomas, 1988, unpublished data). This metal budget variation closely complies with those observed in many other Archean lode gold deposits (Kerrich, 1983; Colvine et al., 1988; Perring et al., 1990).

Reasons for the enrichment of rare elements (eg. Au - 2ppb crustal average), yet absence of enrichment of abundant elements (eg. Cu - 60 ppm crustal average) are not well understood, but likely relate to differences in transport of the elements by the

hydrothermal fluid. The source rocks (average crust) have much more abundant S than Cl. Sulphur will readily complex Au and associated elements, but not the base metals Cu, Pb, Zn, which prefer Cl complexes (Seward, 1973). Hydrothermal fluids associated with lode gold deposits are generally accepted as possessing low salinities, which would discourage significant base metal solubility. In addition, the source regions likely evolved fluids under low water/rock ratios (0.05, Fyfe and Kerrich, 1984). Under these conditions, rare elements will not exceed their solubility in the ambient fluid, whereas limited contents of abundant elements may be constrained by solubility (Kerrich and Fyfe, 1988). Moderate enrichment of Pb along with Au in the Norseman veins suggests that Au and Pb are often coprecipitated, thus either Pb shares similar complexing ligands with Au, or Pb complexes are destabilized by processes that destabilize Au complexes.

Significant variations in rare element and metal inventory are common, even on the scale of single deposits. The reasons for these variations on such localized scales is not understood, but likely stems from differing physico-chemical conditions of the fluid and depositional mechanisms that operated at the sites of mineralization (see transport and deposition of gold section below).

5.5 Arsenopyrite geothermometry

Many of the lode gold deposits of the Norseman Terrane contain arsenopyrite in their vein or vein selvedge alteration assemblages; therefore an attempt was made to constrain the P-T of alteration by application of the calibrated arsenopyrite geothermometer of Kretschmar and Scott (1976). This geothermometer relates the atomic percent of As in arsenopyrite, in combination with coexisting Fe-As-S assemblages, to temperature of arsenopyrite formation.

Compositions of arsenopyrite from arsenopyrite-rich deposits of the Norseman Terrane, including the Surface Winze, Princess Royal, OK Main and O2, and Scotia, deposits, and the Higginsville deposit of the southern Kalgoorlie Terrane, were determined by electron microprobe, and are given in Table 5.2 and presented graphically in Figure 5.15. The data plot approximately along the pyrite-löellingite join at 33.3 at.% Fe, but in detail are more Fe-rich, with average Fe contents ranging between 34-35 at.%. Accordingly, the arsenopyrite requires at least two other Fe-S or Fe-As phases (pyrite, löellingite, pyrrhotite) to buffer its composition to a unique value at a given temperature (Kretschmar and Scott, 1976; Sharp et al., 1985). All samples from the Higginsville, Northern and Central deposits conform to the < 1 at.% Co + Ni stipulation for application of the calibrated geothermometer (Kretschmar and Scott, 1976). Some samples from the

Table 5.2 Microprobe analyses of arsenopyrite and löellingite from gold deposits of the Kalgoorlie-Norseman Terranes

Sample	Pt#	S	Fe	As	Co	Ni	Total*	point description
Higginsville								
HIG-1 = asp with Au at edge of quartz vein. No Fe sulphides coexist, but po common in altered wallrock, py common in other veins								
	1	0.3262	0.3422	0.3286	0.0008	0.0020	98.16	asp core
	2	0.3356	0.3438	0.3198	0.0005	0.0000	99.63	asp core, #1 rerun
	3	0.3296	0.3473	0.3223	0.0006	0.0002	97.07	rim of #1
	4	0.3343	0.3415	0.3229	0.0007	0.0006	99.52	rim, #3 rerun
	5	0.3511	0.3485	0.2994	0.0002	0.0003	98.86	darker core
	6	0.3294	0.3491	0.3207	0.0004	0.0000	98.23	brighter rim of #5
	7	0.3175	0.3406	0.3389	0.0011	0.0016	98.84	brighter rim, #6 rerun
	8	0.3248	0.3501	0.3225	0.0005	0.0010	97.65	darker asp band intergrown with #10
	9	0.3290	0.3480	0.3209	0.0003	0.0011	99.57	dark asp #8 rerun
	10	0.3066	0.3421	0.3457	0.0013	0.0038	98.85	bright band, intimately zoned with #8
Northern deposits								
CN389173-C (Surface Winze, 5/350 stope) = asp in vein, coexisting with py								
	11	0.3478	0.3467	0.3048	0.0006	0.0000	99.77	dark band in asp core
	12	0.3308	0.3503	0.3181	0.0003	0.0004	98.33	bright band in core of #11
	13	0.3240	0.3477	0.3278	0.0004	0.0000	100.45	cryptic 'veinlet', cuts #11 &#12
	14	0.3272	0.3550	0.3167	0.0002	0.0004	98.15	dark zone, near asp rim
	15	0.3228	0.3526	0.3234	0.0004	0.0006	99.14	bright zone, at rim of asp #14
	16	0.3153	0.3504	0.3323	0.0018	0.0000	99.93	cryptic 'veinlet', cuts intimate zoning
	17	0.3561	0.3466	0.2966	0.0003	0.0000	99.68	darkest asp core zone found
	18	0.3215	0.3418	0.3320	0.0044	0.0001	99.13	bright zone, with #17
	19	0.3201	0.3511	0.3280	0.0002	0.0004	98.93	bright asp edge, cuts #'s 20 & 21
	20	0.3433	0.3504	0.3050	0.0007	0.0001	98.66	dark zone in core of #19
	21	0.3359	0.3519	0.3106	0.0005	0.0010	99.67	bright zone in core of #19
SW-14B = immediately adjacent to CN389173-C, coexisting with pyrite								
	22	0.3470	0.3480	0.3043	0.0005	0.0000	100.05	dark asp core
	23	0.3247	0.3470	0.3245	0.0031	0.0000	98.24	slightly brighter rim on #22
	24	0.3167	0.3479	0.3294	0.0035	0.0021	99.33	rim, #23 rerun
	25	0.3360	0.3490	0.3141	0.0005	0.0000	98.39	dark asp core
	26	0.3410	0.3476	0.3101	0.0003	0.0006	99.54	dark core, #25 rerun
	27	0.3228	0.3456	0.3280	0.0023	0.0010	99.91	brighter rim on 25
	28	0.3383	0.3335	0.3188	0.0041	0.0048	99.64	asp core
	29	0.3326	0.3460	0.3206	0.0007	0.0000	99.28	inclusion-rich zone in 28
	30	0.3287	0.3462	0.3220	0.0010	0.0016	100.11	rim of 28
NR-35 (North Royal, 5/150N stope) = coexisting with pyrite								
	31	0.3437	0.3475	0.3082	0.0002	0.0000	99.49	asp with Au, tellurides, py
	32	0.3443	0.3501	0.3050	0.0002	0.0002	99.15	asp with Au, tellurides, py
	33	0.3412	0.3529	0.3053	0.0003	0.0000	98.34	asp inclusion in py, rimmed by Au
	34	0.3420	0.3438	0.3138	0.0001	0.0001	100.03	asp inclusion in py, rimmed by Au
Central Deposits								
OKM 3/585-2 (OK Mine, Main Vein, 3/585 stope) = coexisting with pyrrhotite								
	35	0.3333	0.3423	0.3205	0.0030	0.0008	99.21	inclusion-rich dark zone in asp core
	36	0.3219	0.3398	0.3347	0.0013	0.0016	100.56	inclusion-free bright rim of #35
	37	0.3511	0.3417	0.3033	0.0035	0.0000	99.43	inclusion-free dark zone in #35
	38	0.3171	0.3411	0.3376	0.0036	0.0003	99.86	inclusion-free bright zone in #35
	39	0.3443	0.3431	0.3092	0.0033	0.0001	98.19	dark asp core, some inclusions
	40	0.3575	0.3432	0.2947	0.0034	0.0011	99.36	dark core, #39 rerun
	41	0.3155	0.3454	0.3338	0.0047	0.0004	98.92	bright rim on #39
	42	0.3241	0.3408	0.3294	0.0048	0.0008	98.32	bright area of #39 rim
	43	0.3229	0.3391	0.3346	0.0019	0.0013	100.31	bright area of #39 rim, #42 rerun
	44	0.3206	0.3413	0.3354	0.0013	0.0012	98.72	darker edge of #39 rim
	45	0.3097	0.3442	0.3398	0.0043	0.0016	98.16	middle of #39 rim
	46	0.3082	0.3476	0.3371	0.0049	0.0016	97.89	middle of rim,#45 rerun
CN275938 (OK Mine, O2 Vein, 10 level) = coexisting with pyrrhotite ± pyrite								
	47	0.3463	0.3458	0.3047	0.0021	0.0008	99.39	asp core
	48	0.3204	0.3380	0.3348	0.0034	0.0033	99.72	bright partial rim on #47
	49	0.3474	0.3465	0.3043	0.0012	0.0003	99.23	dark edge of #47
	50	0.3052	0.3476	0.3416	0.0022	0.0031	99.21	bright rim on #47, touching po
	51	0.3485	0.3449	0.3033	0.0021	0.0007	100.28	asp core
	52	0.3204	0.3363	0.3349	0.0040	0.0041	100.96	bright edge patch in #51
	53	0.3213	0.3231	0.3307	0.0211	0.0037	98.92	semi-bright corner on #51

Table 5.2 (continued)

Sample	Pt#	S	Fe	As	Co	Ni	Total*	point description
	54	0.3098	0.3343	0.3470	0.0045	0.0043	100.28	bright asp edge
	55	0.3407	0.3428	0.3148	0.0016	0.0000	98.73	dark core of #54, with po
	56	0.3214	0.3368	0.3351	0.0032	0.0034	100.19	bright patch in #54, with po
	57	0.3580	0.3414	0.2987	0.0004	0.0013	100.12	dark core of #54
	58	0.3463	0.3421	0.3076	0.0027	0.0002	100.01	dark asp
Southern Deposits								
SC-3 (CN380170-G) asp coexisting with lö or po								
	59	0.0222	0.2636	0.6390	0.0172	0.0571	101.23	löellingite inclusion in asp #61
	60	0.0074	0.2416	0.6552	0.0185	0.0768	101.18	löellingite inclusion in asp #61
	61	0.2822	0.3291	0.3728	0.0097	0.0060	100.18	asp by löellingite inclusion
	62	0.2880	0.3372	0.3638	0.0076	0.0032	99.22	centre of asp #61
	63	0.2889	0.3309	0.3648	0.0083	0.0071	98.75	centre of asp #61
	64	0.2983	0.3319	0.3582	0.0068	0.0047	99.94	near rim of #61
	65	0.3331	0.3282	0.3276	0.0070	0.0039	99.68	µm thin rim of #61
	66	0.3517	0.3447	0.3023	0.0005	0.0006	99.37	µm thin dark rim on #61
	67	0.2779	0.3343	0.3713	0.0095	0.0065	98.58	centre of asp with lö inclusion
	68	0.2994	0.3281	0.3582	0.0076	0.0065	99.78	bright rim on asp
	69	0.3176	0.3438	0.3348	0.0033	0.0003	99.05	dark core of #68
	70	0.2945	0.3381	0.3577	0.0044	0.0053	100.18	bright asp rim
	71	0.3199	0.3256	0.3371	0.0067	0.0106	99.79	dark asp rim
	72	0.2837	0.3068	0.3647	0.0132	0.0316	99.59	bright asp core with löellingite #73
	73	0.0331	0.2955	0.6293	0.0130	0.0287	102	löellingite inclusion in asp #72

* Element concentration reported in mole proportion, totals for each analysis are reported in wt. %.
Abbreviations: asp = arsenopyrite, lö = löellingite, po = pyrrhotite, py = pyrite.
Lines at right denote analyses from the same grain

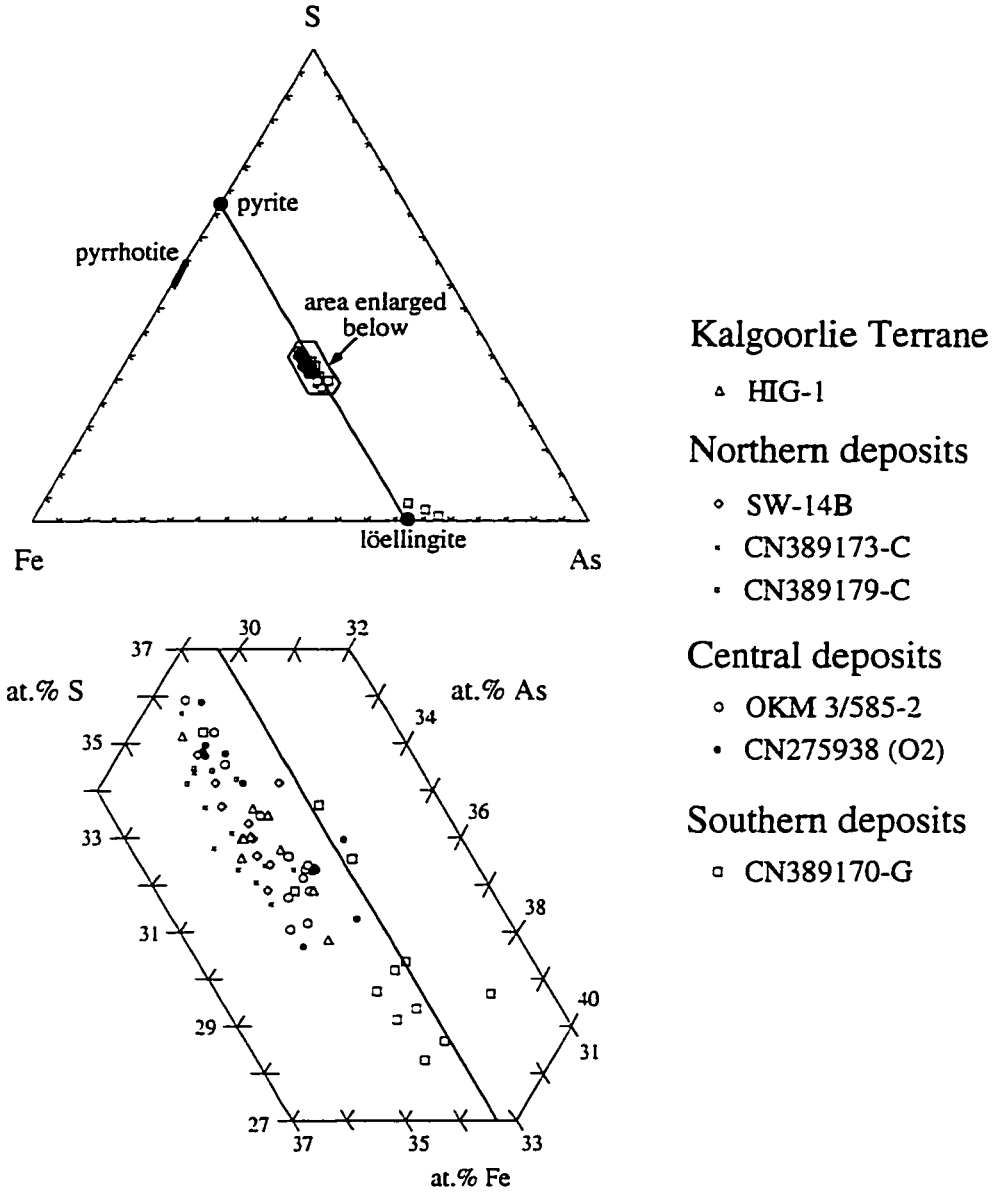

Figure 5.15 Triangular plot showing the compositional range of arsenopyrites from deposits of the Norseman and Kalgoorlie Terranes. Solid line through both diagrams represents the pyrite-löellingite join at 33.3 at.% Fe. Data is listed in Table 5.2.

Scotia deposit do not meet this requirement, with Co + Ni contents proportional to As content (Table 5.2). Samples with Co + Ni > 1 at.% are included in the calculations, as measured As contents for these samples are within error of As contents of coexisting arsenopyrite that do pass the Co + Ni < 1 at.% criterion.

Results of the analyses are plotted on Figure 5.16, a phase diagram for the system Fe-As-S, from which temperatures of arsenopyrite formation can be graphically interpolated. The Higginsville arsenopyrite has no coexisting Fe-S or Fe-As phases on the scale of the thin section, but pyrite is common elsewhere in the vein, and pyrrhotite is a common alteration mineral elsewhere in the adjacent altered wallrocks. Thus the data is plotted for this entire range of possible equilibrium assemblages, resulting in a calculated $T_{equilibrium}$ range of 340-550°C , and average compositions yield 360-450°C. As-rich and As-poor compositions alternate throughout single crystals in an oscillatory fashion, encompassing this entire compositional range.

Arsenopyrite from Northern deposits are in equilibrium with pyrite, and exhibit a broad range of composition through oscillatory zoned bands, consistent with temperatures of formation $\geq$ 490°C. Crystals possess rims and cryptic veinlets which crosscut these oscillatory zones, are more As-rich, and yield average temperatures of 470°C. Average core compositions yield a $T_{equilibrium}$ range of 380-410°C. Arsenopyrite from the Princess Royal vein are also oscillatory zoned, do not show As-rich rims, and calculated $T_{equilibrium}$ range from 340-415°C.

Arsenopyrite samples from the OK deposits are in equilibrium with pyrrhotite and possibly pyrite. These arsenopyrites demonstrate extreme compositional variation and complex oscillatory zonation, with a distinct compositional gap between As-poor and As-rich bands. Most samples, however, show As-rich rims that truncate other zones, for which calculated $T_{equilibrium}$ ranges from 420-510°C (Figs. 5.16, 5.17A,B).

Southern deposits show the greatest variation in arsenopyrite composition. Löellingite cores of large arsenopyrite crystals coexist with As-rich arsenopyrite (Fig. 5.9D), and indicate $T_{equilibrium}$ of 540-630°C. Arsenopyrite rims on these crystals, and centres of arsenopyrite crystals without löellingite cores, are complexely zoned (Fig. 5.17C), with variably As-poor or As-rich rims, and a calculated $T_{equilibrium}$ range of 420-590°C. Very thin rims on some crystals in wallrock laminations possess lower As contents and exhibit a large compositional range, consistent with $T_{equilibrium}$ < 475°C. These sporadic rims may indicate either later arsenopyrite growth, or re-equilibration with late stage fluids which variably retrogressed main-stage alteration assemblages at Scotia.

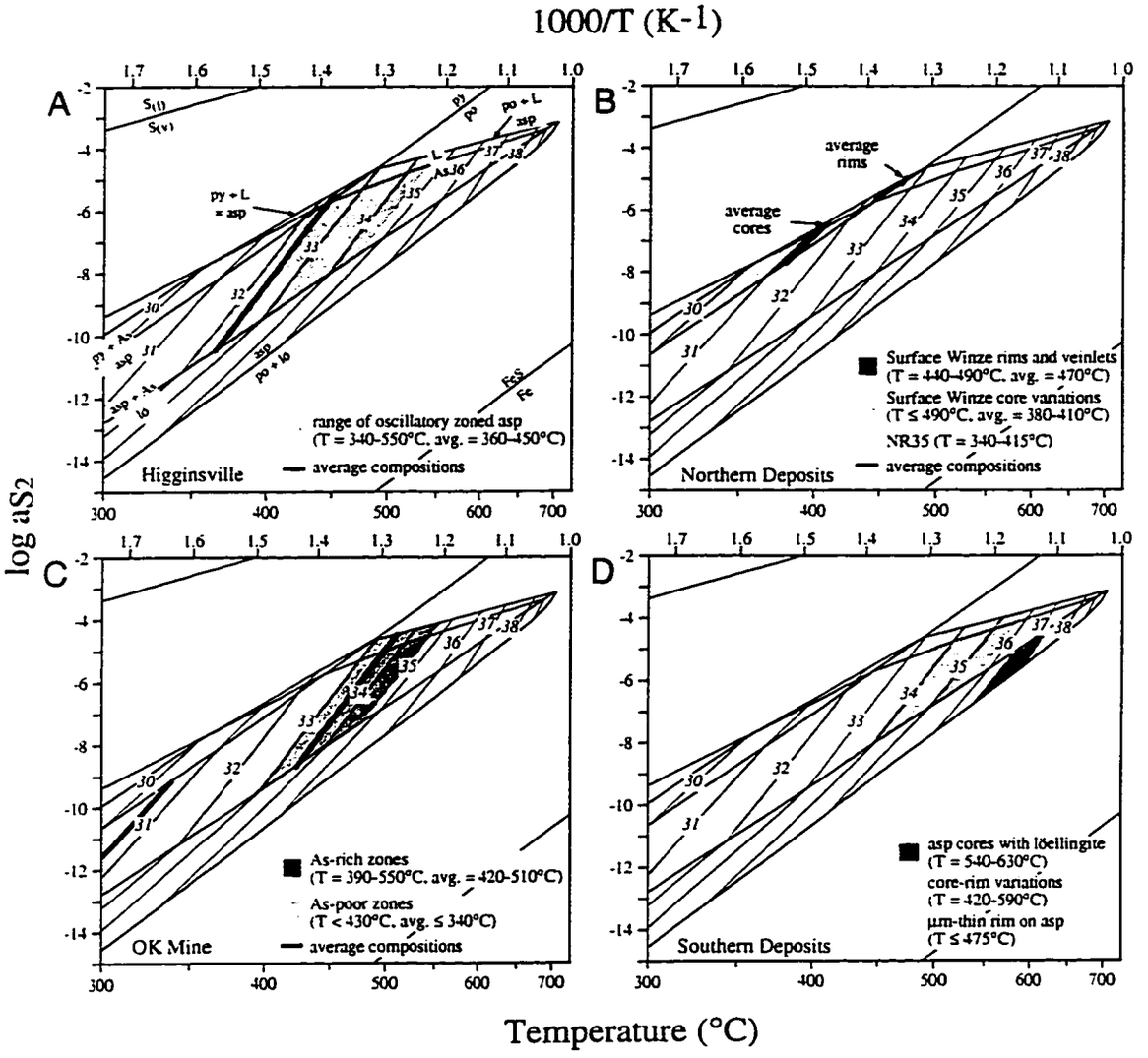

Figure 5.16. Plots of log a_{S2} vs. temperature showing phase relationships in the Fe-As-S system, and arsenopyrite geothermometer results for arsenopyrite compositions reported in Table 5.2. (A) Higginsville deposit, (B) Princess Royal (NR35) and Surface Winze deposits (Northern deposits), (C) OK mine (Central deposit), (D) Scotia deposit (Southern deposit). Reaction lines are labelled in (A). Isopleths for atomic % As in arsenopyrite are labelled on all diagrams (thin lines). Abbreviations: asp = arsenopyrite, L = liquid, lö = löellingite, po = pyrrhotite, py = pyrite. Diagram and application of the arsenopyrite geobarometer after Kretschmar and Scott (1976) and Sharp et al. (1985).

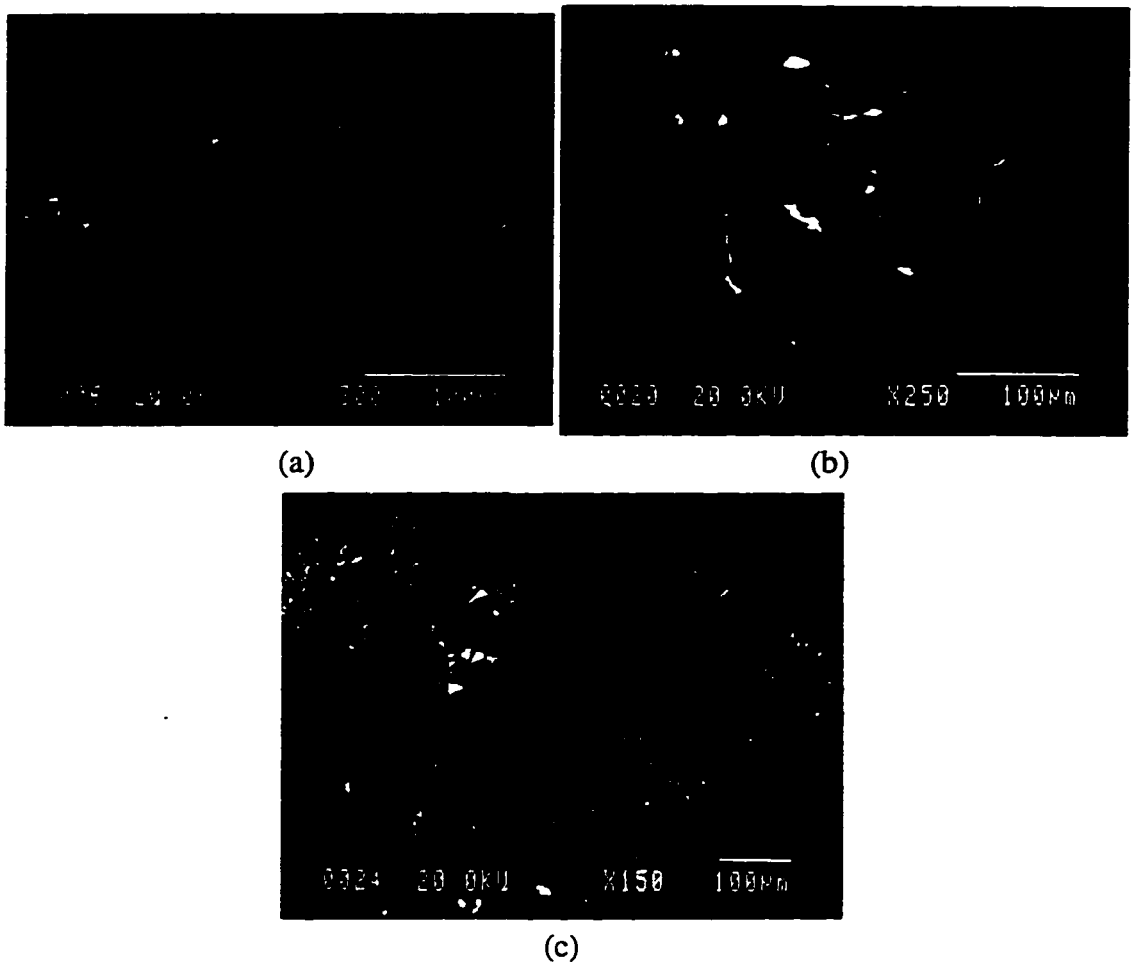

Figure 5.17: Backscattered electron microprobe photos of compositional zoning in arsenopyrite

(a) Compositional zoning in arsenopyrite, sample CN380170G, Scotia mine (b) Complex compositional zoning in arsenopyrite in quartz, sample OK 3585, OK main vein. Bright grains are native gold (c) Complex compositional zoning in arsenopyrite in quartz, sample OK 3585, OK main vein. Bright grains are native gold.

5.6 Oxygen Isotope Geothermometry

In an attempt to further constrain temperatures of hydrothermal alteration, coexisting silicate mineral pairs from coarse-grained alteration selvedges were separated for oxygen isotope analysis, and application of calibrated quartz-mineral oxygen isotope geothermometers. Analytical methods, data, and calculated temperatures, assuming equilibrium, are presented in Table 5.3. $\delta^{18}O$ values of vein quartz in the Norseman lode gold deposits range from 10.0-12.4‰, with variations of up to 2‰ detected within a single quartz vein system (Crown vein, Fig. 5.18). The majority of the analyses for all deposits cluster between 11.0 and 12.0‰. Quartz from the Junction and Higginsville deposits of the Kalgoorlie Terrane is slightly more ^{18}O-enriched, with $\delta^{18}O$ values ranging from 12.2-12.8‰. Where possible, quartz-mineral pairs in contact and apparent textural equilibrium were selected for determination of temperatures. Where samples are not touching, the entire range of quartz values within the deposit was used to calculate a range of temperatures, and these samples are indicated in Table 5.3. This results in a maximum range of calculated temperatures.

Quartz-chlorite and quartz-biotite pairs from the Junction deposit yield temperatures of formation of 390-400°C. Close compliance of calculated temperatures from two different quartz-mineral geothermometers supports the assumption that these minerals record equilibrium temperatures of formation.

Five quartz-biotite pairs from the Princess Royal vein have been calculated from data of Golding (1982), and yield a temperature range of 400-430°C. The tight grouping of calculated temperatures is again evidence that equilibrium is preserved in these samples.

Quartz-biotite and quartz-amphibole from the Central deposits yield formation temperatures of 440-540°C, corroborating temperatures calculated by arsenopyrite geothermometry. A single quartz muscovite pair from the OK Main vein yields a temperature of 350°C, contrasting greatly with temperatures calculated from amphibole and biotite on other Central deposit veins, and with those calculated from arsenopyrite from Main vein. Therefore, the temperature range of Central deposits is considered to be in the range calculated from quartz-biotite, quartz-amphibole, and arsenopyrite geothermometers. The muscovite, although a rare alteration mineral in the mafic-hosted deposits, appears to be part of the main stage quartz vein assemblage, and is slightly deformed in thin section. It is therefore possible that this sample does not record oxygen isotope equilibrium.

Table 5.3 $\delta^{18}O$ and δD values (‰), calculated temperatures, and calculated isotope compositions (‰) of fluids in equilibrium with silicates from lode gold deposits of the Norseman and Kalgoorlie Terranes

Mine *Vein* Sample#	Mineral	$\delta^{18}O_{min}$	δD_{min}	T (°C)	$\delta^{18}O_F$	δD_F
KALGOORLIE TERRANE						
Junction						
Molybdenum-quartz						
Ju-1 moly	quartz	12.8				
Au-quartz						
Ju-1 massive	quartz	12.2			8.1	
	chlorite	5.8		400		
Ju-2	quartz	12.4			8.1	
	biotite	4.6	-100	390		-49
Higginsville						
HIG-1	quartz	12.7		360–450 (asp)	7.7-9.6	
NORSEMAN TERRANE						
Surface Winze						
SW-14	quartz	10.0		380–470 (asp)	5.6-7.6	
North Royal						
Princess Royal						
NRM-7	quartz	11.5				
NR-11	quartz	10.3				
NR-35	quartz	11.7		340–420 (asp)	6.1-8.1	
PRS-28	quartz	10.4				
	biotite		-98			-48 to -52
Golding (1982)	quartz	10.4-11.9 (17)				
	biotite	3.9-4.7 (6)	-50 to -59 (5)	400–430 (5)	7.3-8.3[A]	-1 to -12[A]
Regent						
Crown						
C22	quartz	11.4				
16/70 FWa	biotite	4.9	-88	440–450		-43 to -44
16/70 FWb2	quartz	11.4			8.2-9.6[B]	
	quartz	11.6			8.4-9.8[B]	
	quartz	11.3			8.1-9.5[B]	
	amphibole	6.7		500-540		-51 to -55
	amphibole	6.8	-83			
Golding (1982)	quartz	10.4-12.4 (25)				
B-fault						
Golding (1982)		11.0-12.1 (5)				
Mararoa						
surface	quartz	10.1				
Golding (1982)	quartz	11.3-12.4 (4)				
Ajax						
South Norseman						
AJ-1	quartz	11.6				
AJ-2	quartz	11.6				
AJ-5	quartz	11.6				
Viking Decline						
Royal Standard						
RS-12	quartz	11.8				
	amphibole	6.5		480	9.2	
OK						
Main vein						
3/585	quartz	11.4				
OK-26	muscovite	8.3	-50	350	6.1	-12 to -27[C]
O2 vein						
OKD2	quartz	12.3				
AK102	amphibole	6.5		450	9.2	

Table 5.3 (continued)

Mine *Vein* Sample#	Mineral	$\delta^{18}O_{min}$	δD_{min}	T (°C)	$\delta^{18}O_F$	δD_F
Regional quartz veins						
CN353305a	quartz	11.1				
CN353305b	quartz	10.8				
Lonesome prospect						
CN353306	quartz	13.9				
"Late tectonic granitoid, SE Scotia"						
SESCCGV	quartz	10.4			7.5 - 8.6	
		10.0			7.1 - 8.2	
	diopside	5.7		490-520		
	amphibole	4.8	-81	460-480		-44 to -53
	garnet	5.7		510-540		
"West shore, Lake Dundas"						
"massive, white"	quartz	9.8				
"deformed, grey"	quartz	10.4				
Scotia						
Underground						
CN380171	quartz	11.1				
	quartz	11.1				
CN380172	quartz	11.8			10.2[D]	
	anthophyllite	7.7		570		
SCPV	quartz	11.5			9.4-9.8	
	quartz	10.9			8.8-9.2	
	amphibole	6.6	-70	510-550		-39 to -43
SC7/440N drv	quartz	11.2				
SC2 early	quartz	11.3				
SC3	bulk quartz	10.9			9.2-9.6	
	massive quartz	11.1			9.4-9.8	
	massive quartz	10.6			8.9-9.3	
	amphibole	6.9		560-610		
SCPEG	muscovite	6.9	-58			
Core						
SC163-62	gypsum		-123			
SC163-66a	quartz	11.6			9.5[E]	
	amphibole		-61	510[E]		-30 to -43[F]
SC163-66b	quartz	11.1			9.4	
	amphibole	6.8		550		
SC358-33	diopside	6.3				
	amphibole	6.4	-65			-27 to -42[G]
SC358-40b	quartz	11.0			8.7	
	diopside	6.4		500		
SC358-54	quartz	11.6			8.5	
SC358-55	diopside	6.4		450		
SC358-78	quartz	11.2				
SC358-96	quartz	11.3				
SC358-99a	amphibole		-62			-24 to -39[G]

Oxygen and hydrogen isotope analyses were carried out at the University of Saskatchewan. Hydrogen isotope compositions were determined using the uranium method of Godfrey (1962) as modified by Kyser and O'Neil (1984). Oxygen was extracted using the BrF_5 technique described by Clayton and Mayeda (1963). Duplicate analyses indicate a reproducibility of ± 0.3‰ for oxygen values and ± 5‰ for hydrogen isotope values. $\delta^{18}O$ values of 9.6‰ for NBS-28 quartz and δD values of -65‰ for NBS-30 biotite were obtained using these techniques. $\delta^{18}O$ and δD values are reported relative to V-SMOW.

All temperatures are calculated from quartz-mineral oxygen isotope fractionations, except where noted as calculated from arsenopyrite geothermometry. Fractionation factors used are: quartz-chlorite, Wenner and Taylor (1971); quartz-muscovite, Eslinger et al. (1979); quartz-biotite, quartz-amphibole, quartz-garnet, Bottinga and Javoy (1975); quartz-diopside, Clayton and Keiffer (1992); quartz-water, Clayton et al. (1972); muscovite-water, biotite-water, amphibole-water, Suzuoki and Epstein (1976).

A Calculated from five biotite-quartz pairs of Golding (1982).

B Calculated using temperature range calculated from both quartz-amphibole and quartz-biotite fractionation factors.

C Calculated using temperature range calculated from both quartz-amphibole and quartz-muscovite fractionation factors.

D Calculated using quartz-hornblende and hornblende water fractionation factors.

E Calculated using amphibole SC-166b.

F Calculated using combined temperature range of SC-166a and SC-166b.

G Calculated using entire temperature range calculated for samples from Scotia, 450°-610°C.

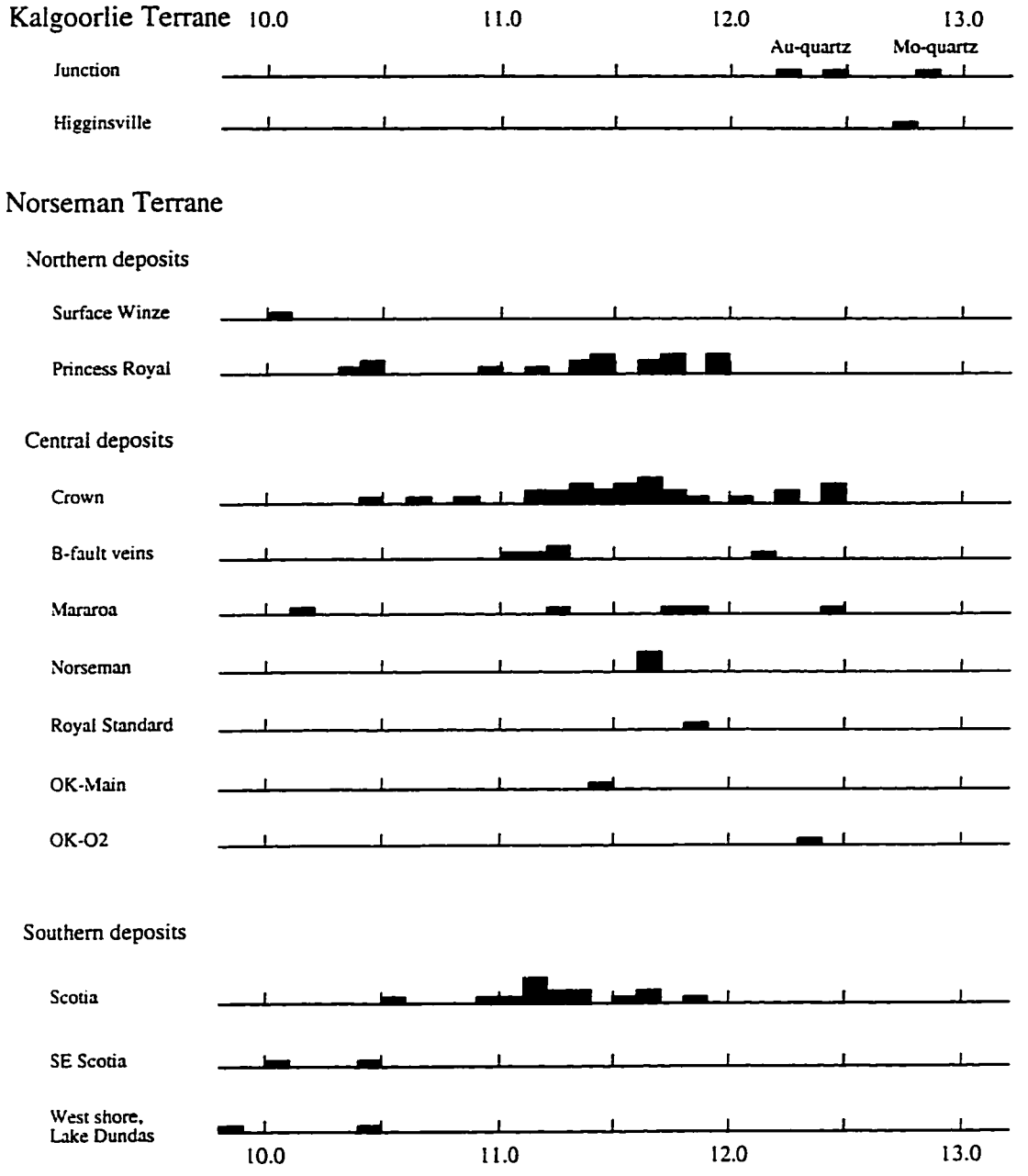

Figure 5.18. Histogram of $\delta^{18}O_{quartz}$ values for lode gold deposits of the Norseman and Kalgoorlie Terranes. Data from Table 5.3.

Quartz-clinopyroxene and quartz-amphibole pairs indicate that temperatures of formation of hydrothermal alteration assemblages associated with the Southern deposits occurred at temperatures of 450-610°C, with all but two quartz-mineral pairs clustering in the range 500-570°C, in close compliance with those calculated from the arsenopyrite geothermometer. Again, the tight clustering of calculated temperatures from multiple samples, two independent quartz-mineral geothermometers, and arsenopyrite geothermometry indicates that equilibrium temperatures of formation are preserved in these samples.

A barren, shear-zone hosted quartz-diopside-amphibole-garnet vein adjacent to, and crosscutting, a late-tectonic granitoid to the southeast of Scotia yield temperatures from quartz-clinopyroxene, quartz-garnet and quartz-amphibole temperatures of 460-540°C. It is interesting to note that in this sample, garnet appears to have formed with clinopyroxene, which is then retrogressed to amphibole. Calculated temperatures from each mineral pair system corroborate these petrogenetic relationships, with quartz-garnet, quartz-clinopyroxene, and quartz-amphibole geothermometers yielding progressively lower temperatures (Table 5.3)

5.7 Phase Equilibria

Isobaric phase relations for critical vein selvedge assemblages for the Norseman deposits in the system KCMASH are presented in Figure 5.19, along with calculated temperature ranges from arsenopyrite and oxygen isotope mineral-pair geothermometers. Thermodynamic calculations in construction of this diagram were made assuming mineral activities of unity, and therefore may not represent exact T-X_{CO_2} ranges of stability. However, the diagram still serves to illustrate the relative temperature-X_{CO_2} ranges between the various deposits and, despite potential errors associated with each geothermometer, there is a relative thermal zonation between deposits that is corroborated by all three methods. The data indicate increasing relative temperatures of hydrothermal alteration from north to south within the terrane, with Northern deposits yielding approximate formation temperatures of 420-475°C, Central deposits 470-500°C, and Southern deposits 490-540°C. Note that these changes in mineralogy and calculated temperatures of alteration correlate with changes in peak metamorphic temperatures throughout the terrane, at $T_{alteration} \leq T_{metamorphism}$ in all cases. This thermal zonation within the Norseman Terrane also correlates with structural style of the gold deposits, from massive + breccia + laminated quartz within ductile-britle shear zones in Northern deposits, to laminated + massive + breccia within ductile-brittle shear zones in

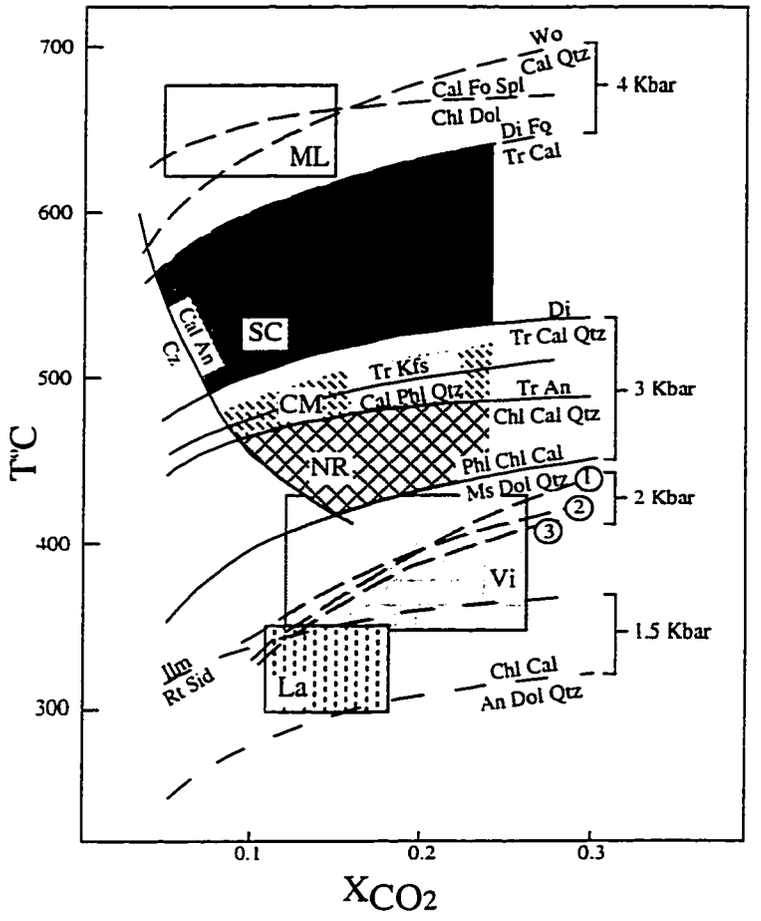

Figure 5.19. T-XCO_2 phase diagram showing isobaric equilibrium curves for mineral assemblages at specific deposits of the Yilgarn Block, Western Australia, constructed using the thermodynamic database of Holland and Powell (1990). Deposits: La = Lancefield, Hronsky and Ridley (1992); Vi = Victory, Clark et al. (1989); NR, CM and SC = North Royal, Crown-Mararoa and Scotia, respectively, of the Norseman Terrane, McCuaig et al. (1993); ML = Marvel Loch, Mueller et al. (1991b). Reactions for the Victory mine are: (1) Ms + Dol = Bt + Chl + Cal; (2) Bt + Chl + Dol = Tr + Ms; (3) Bt + Chl + Dol + Act + Ms. Abbreviations: Act = actinolite; An = anorthite; Bt = biotite; Cal = calcite; Di = diopside; Fo = forsterite; Ilm = ilmenite; Kfs = K-feldspar; Phl = phlogopite; Rt = rutile; Sid = siderite; Spl = spinel; Tr = tremolite; Wo = wollastonite. Redrawn from McCuaig and Kerrich (1994), McCuaig et al. (1993) and Mikucki and Ridley (1993). A thermal zonation of hydrothermal alteration assemblages is apparent within the Norseman Terrane, with temperatures increasing from north (NR) to south (SC).

Central deposits to thin, discontinuous, banded veins within broad ductile shear zones in Southern deposits. These relationships are summarized in Figure 5.20.

5.8 Relative timing of alteration, deformation, metamorphism, and fluid flow: textural evidence

The above sections document that the Norseman lode gold deposits contain high-temperature alteration assemblages, but the question remains: what is the timing of the alteration assemblages with respect to the peak of metamorphism? Are the high-temperature assemblages formed during high-temperature fluid flow, or were lower-temperature alteration assemblages subjected to prograde metamorphism, which produced the high-temperature minerals observed at present? Tectonic fabrics and microstructures that form in quartz veins and contiguous alteration haloes surrounding lode gold deposits can reveal information on the deformation mechanisms that operated during hydrothermal activity. Fabrics may also constrain the relative timing of hydrothermal alteration, mineralization, and quartz vein emplacement to deformation and metamorphism. Few studies have used microtextures in assessing hydrothermal alteration processes and conditions of formation of hydrothermal ore deposits (Bain, 1933; Kerrich and Allison, 1978; 1980; McCuaig and Kerrich, 1994).

5.8.1 Deformation and fluid flow

Numerous studies have demonstrated that the deformation of wallrocks, fluid pressure fluctuations and intermittent fluid flow, metasomatic alteration, and mineralization are inextricably linked in lode gold deposit systems (e.g., Kerrich, 1986; Sibson et al., 1988; Cox et al., 1990, 1991). The progressive alteration of wallrock causes new minerals to form, which affect the wallrocks' resultant permeability and response to stress. The formation of phyllosilicate minerals, such as chlorite, biotite, and muscovite by hydration reactions, may impart a fabric to the rocks, decreasing wallrock competency and generating a mechanical anisotropy. In combination, these two attributes focus deformation in the structures. Focused deformation will increase permeability, allowing greater infiltration of hydrothermal fluids, and thus further alteration, which in turn leads to progressive deformation. This cycle is referred to as the process of strain softening. The anisotropic fabric has an additional effect in that the tensile strength orthogonal to the fabric is less than parallel to the fabric. Consequently, hydraulic fractures preferentially open parallel to the fabric generating fabric-parallel vein systems rather than stockworks (Fig. 5.21; Kerrich, 1986).

Figure 5.20. Summary diagram illustrating the correlation of alteration mineralogy and orebody morphology observed in mafic host lithologies with increasing metamorphic grade (bottom) for the crustal continuum of lode gold deposits. Selected Archean deposits are shown as examples (top). For the deposits, the solid heavy line indicates the calculated temperature range of alteration and mineralization. Filled diamonds anchoring the low-temperature end indicate T(mineralization) calculated from fluid inclusion data; filled diamonds anchoring the high-temperature end indicate T(mineralization calculated from phase equilibria or stable isotope geothermometry. Where both fluid inclusion and phase equilibria/stable isotope temperature estimates are available for a single deposit, the phase equilibria and stable isotope estimates are invariably higher (McCuaig and Kerrich, 1994). Abbreviations: hem = hematite; mag = magnetite; rt = rutile; ilm = ilmentite; py = pyrite; po = pyrrhotite; apy = arsenopyrite; lö = löellingite; ank = ankerite; dol = dolomite; cal = calcite; mu = muscovite; bt = biotite; am = amphibole; di = diopside.

Deposit key and data sources: North America (all deposits directly from Colvine, 1989, and references therein) 1 Ross; 2 Kirkland Lake; 3 Dome; 4 Hollinger-McIntyre; 5 Couchenor-Willans; 6 Campbell; 7 Dickenson; 8 Madsen; 9 Geraldton; 10 Doyon; 11 Bousquet; 12 Musselwhite; 13 Sigma-Lamaque; 14 Lupin; 15 Detour. Western Australia: 16a,b Wiluna (a = early, b = late, Hagemann et al., 1993); 17 Lancefield (Ho et al., 1990); 18 Golden Mile (Ho et al., 1990); 19 Mt. Charlotte (Ho et al., 1990); 20 Harbour Lights (Ho et al., 1990); 21 Sons of Gwalia (Ho et al., 1990); 22 Hunt (Ho et al., 1990); 23 Victory-Defiance (Clark et al., 1989); 24 North Royal (MCuaig et al., 1993); 25 Crown-Mararoa (McCuaig et al., 1993); 26 Scotia (McCuaig et al., 1993); 27 Fraser's (Ho et al., 1990); 28 Nevoria (Ho et al., 1990); 29 Marvel Loch (Mueller et al., 1991); 30 Griffin's Find (Ho et al 1990); 31 Lady Bountiful (Cassidy and Bennett, 1993); 32 Granny Smith (Cassidy, 1992); 33 Porphyry (Cassidy, 1992); 34 Great Eastern (Cassidy, 1992); 35 Westonia (Cassidy, 1992). Modified from McCuaig and Kerrich (1994).

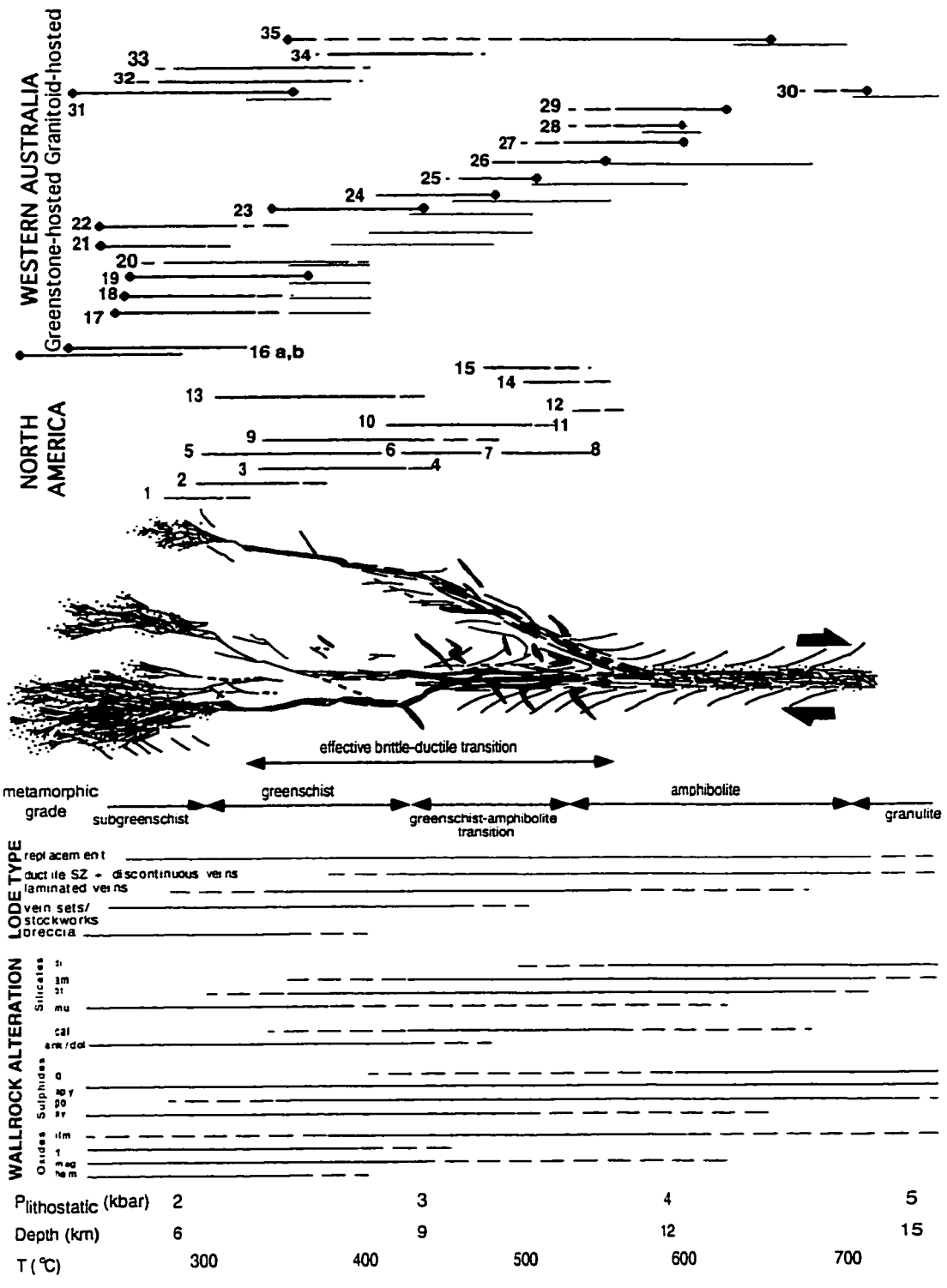
WESTERN AUSTRALIA
Greenstone-hosted Granitoid-hosted
NORTH AMERICA
effective brittle-ductile transition
metamorphic grade
subgreenschist
greenschist
greenschist-amphibolite transition
amphibolite
granulite
LODE TYPE
replacement
ductile SZ - discontinuous veins
laminated veins
vein sets/ stockworks
breccia
WALLROCK ALTERATION
Silicates
Sulphides
Oxides
Plithostatic (kbar)
Depth (km)
T (°C)

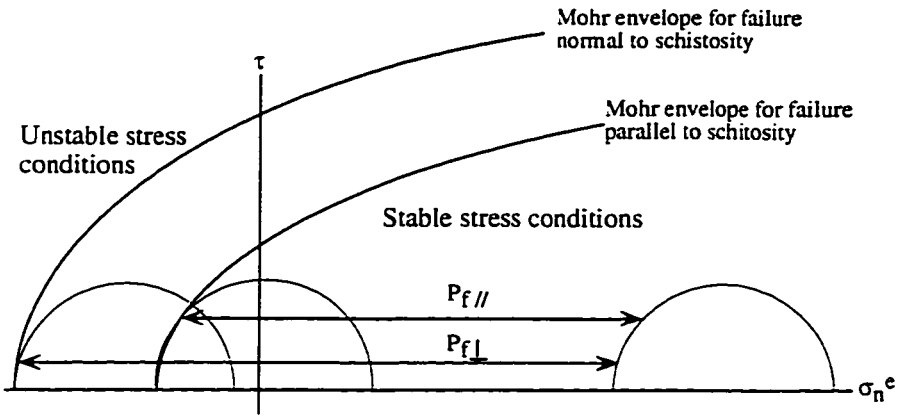

Figure 5.21. Mohr's circle schematically depecting stress conditions of hydraulic fracturing in synkinematic lode gold systems. Relative failure envelopes for host rocks at angles perpendicular and parallel to schistosity are also shown. Failure generally occurs parallel to fabrics, focussing subsequent fluid flow and further failure into discrete shear zones. After Kerrich (1986).

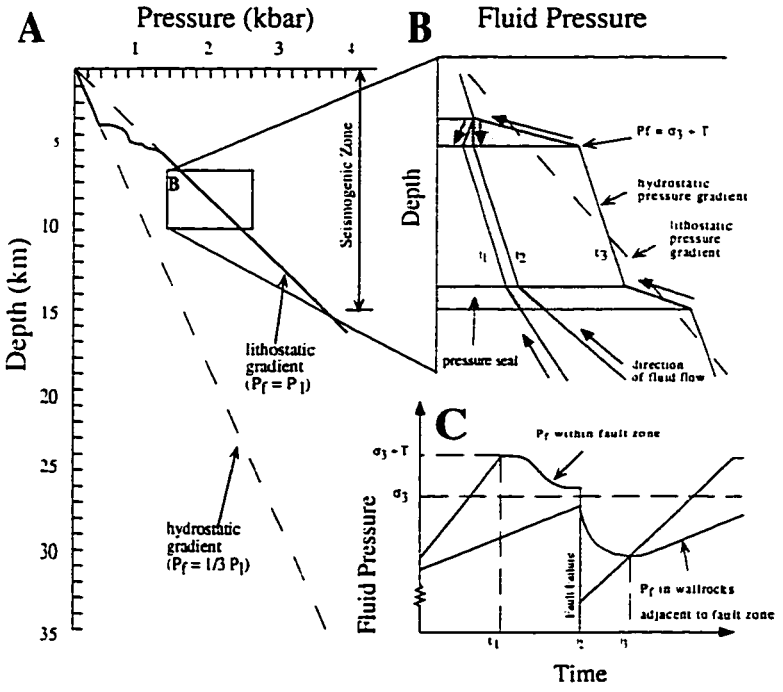

Figure 5.22. Fluid pressure fluctuations associated with lode gold hydrothermal systems. (A) Fluid pressure versus depth (solid line), after Thompson and Connolly (1992). Seismogenic zone from Sibson (1990). (B) Details of fluid (Pf) pressure fluctuations with time (t1, t2, t3) along the lithostatic pressure gradient during episodic seismic failure, hydraulic fracture, catastrophic fluid flow, vein emplacement and mineral deposition (Cox et al., 1990). Pressure seals may be relatively impermeable lithologies, or mineralized segments of faults. (C) Fluid pressure cycling in wallrocks and fault zones during seismic events depicted in (B) (after Cox et al., 1990).

Conversely, the precipitation of various anhydrous minerals with prismatic crystal habits such as quartz, carbonate, and plagioclase will increase the competency of the wallrocks, as it is difficult to impart a fabric to these minerals, and may even cement anisotropic fabrics. This strain hardening process increases the competency of the wallrocks and can inhibit further fluid infiltration and hydrothermal alteration. Therefore, the type of alteration produced can have a profound effect on the extent of alteration haloes through the competitive nature of the strain softening and hardening processes.

The cycle between strain softening by fabric development and strain hardening by hydrothermal mineral precipitation contributes to fault-valve behaviour in the fluid conduits (Figs. 5.21, 5.22) and is visually manifested in the development of banded (laminated) veins. During successive hydraulic fracture events, structures tend to break outside of the veins beyond the zone of wallrock cementation, such that successive selvedges of wallrock become rafted into the veins, generating a banded structure (cf., Cox et al., 1991, and primary references therein). Spectacular examples of banded veins occur in the Norseman camp (McCuaig et al., 1993; Chapter 4). Between brittle failure events, ductile mechanisms operate and impart ductile fabrics to wallrocks and previously deposited quartz. Brittle events reflect high fluid pressures and fast strain rates, whereas intervening ductile flow occurs under conditions of relatively lower fluid pressures and strain rates. This brittle-ductile behaviour, so characteristic of lode gold deposits, indicates that the hydrothermal fluids responsible for alteration and mineralization were at approximately lithostatic pressures and underwent transient sublithostatic to supralithostatic fluid cycling (Figs. 5.21, 5.22).

5.8.2 Deformation mechanisms

The development of petrofabrics within mineral assemblages is dependent upon:

(1) the susceptibility of minerals within the assemblage to adopt fabrics, for example: mica-chlorite-amphibole = high susceptibility; whereas quartz-feldspar-carbonate-clinopyroxene = low susceptibility,

(2) the deformation mechanisms that are operating,

(3) the relative rates of dynamic recrystallization and recovery of crystals, and

(4) the degree of fabric cementation by mineral precipitation. The second and third factors are competing processes that are dependent on temperature, differential stress, strain rate, and fluid pressure (Pf), which controls effective confining stress as illustrated in Figures 5.21-5.23.

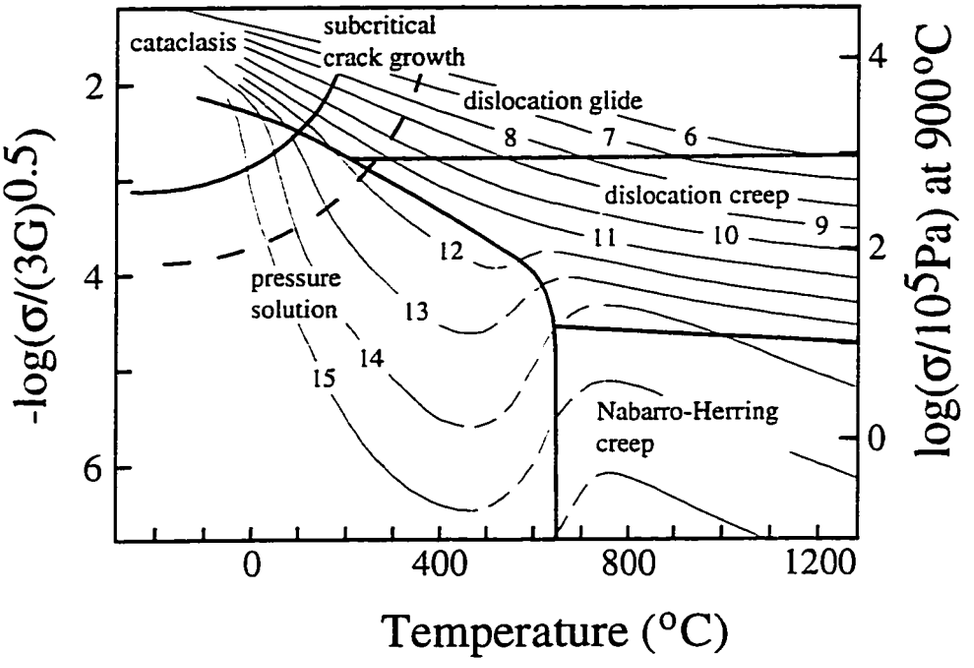

Figure 5.23. Deformation mechanism map for quartz (grain size = 100 μm), showing variations in deformation mechanisms with temperature, differential stress, and strain rate (after Rutter, 1976). Contoured numbers represent -log strain rate, vertical axis approximates -log differential stress.

Steady-state deformation of mineral grains under geologically reasonable conditions may occur by one, or some combination, of the following processes:

(1) cataclasis, involving repeated grain fracturing and frictional sliding of rock particles,

(2) intercrystalline (grain boundary) diffusive mass transport, e.g., pressure solution or Coble creep, or

(3) dislocation mechanisms, involving the glide of solid-state defects (dislocations) in crystal lattices or glide and climb (Fig. 5.23; Rutter, 1976; Kerrich and Allison, 1978).

Dynamic recrystallization involves the formation of undulose extinction, mortar texture, and subgrains in which dislocations have re-organized into new (sub)grain boundaries. Recovery of deformed mineral grains occurs by two basic processes, the migration of subgrain boundaries and the formation of new grain boundaries, which can combine in a number of ways to return strained grains to states of low free energy, with coarser grain size, straight grain boundaries, and triple junction (foam texture) microstructure. These mechanisms dominantly involve dislocation migration and boundary diffusive processes (Drury and Urai, 1990). Distinct microtextures result from complex interplay of these processes and can be used to constrain the temperature-time-deformation-fluid (T-t-d-f) evolution of hydrothermal alteration associated with lode gold deposits. Examples are documented above and discussed below for the Norseman quartz veins and wallrock alteration assemblages. In general, dynamic recrystallization by dislocation glide dominates at temperatures corresponding to greenschist metamorphic facies whereas dynamic recovery by dislocation climb predominates at ambient temperatures of the amphibolite facies.

5.8.3 Quartz vein fabrics

Comparison of quartz textures from veins associated with the Norseman lode gold deposits allows variations in deformation and recrystallization mechanisms, with both temperature and strain rate, to be recognized. At high temperatures and confining stress corresponding to amphibolite facies conditions, ductile deformation dominates. Deformation is accommodated in broad shear zones that may contain discontinuous and highly deformed quartz veins (Hronsky et al., 1990; Sibson, 1990; McCuaig et al., 1993) and microstructures in these veins are produced by dislocation migration mechanisms. Recovery rates of mineral grains will equal or exceed those of deformation and dynamic recrystallization, such that quartz veins may possess equant crystals with little or no undulose extinction, and 120° grain boundary intersections. No primary depositional

features are preserved in this variety of quartz. The veins of the Southern deposits are excellent examples of these processes.

At intermediate temperatures and confining stress (greenschist facies), vein geometries comprise breccias through to laminated veins in ductile shear zones (Fig. 5.24) with abundant evidence of hydraulic fracturing (Sibson, 1990). Under these conditions brittle and ductile deformation mechanisms operate (dislocation mechanisms + boundary diffusive mass transport). However, rates of dynamic recrystallization exceed recovery rates producing undulose extinction and serrated grain boundaries with variable subgrain formation (Fig. 5.9H). Primary depositional features are generally destroyed in this variety of quartz. The extensive quartz vein systems of the Northern and Central deposits exhibit these characteristics. The smaller, more equant grain size and higher degrees of recovery in the Central deposits is consistent with slightly higher temperatures of vein emplacement relative to Northern deposits.

At very low temperatures and effective confining stress (sub-greenschist facies), brittle deformation (cataclasis, pressure solution) processes dominate, producing abundant fault gouge, breccia, and stockworks. Microstructures observed in such environments include fractured grains, stylolites and fault gouge along discrete planes with little dynamic recovery of grains. Between these planes of strain accommodation, the quartz veins will be relatively undeformed. These features are observed in and adjacent to brittle structures within the quartz veins of all Norseman deposits (Figs. 4.14A,B,C). As these brittle features crosscut the quartz veins and the contiguous wallrock alteration envelopes, they are interpreted as significantly post quartz-vein emplacement.

Note that multiple quartz types may be found in a single lode gold deposit (e.g. Figs. 5.9I, 5.10I). Microscopic textures such as intragranular fractures in quartz grains with undulose extinction or subgrain mantles indicate cyclical variation in deformation mechanisms. These microtextures are consistent with macroscopic features such as variably deformed quartz veins, mutually crosscutting laminated, massive, and brecciated quartz (Fig. 4.6), and variably developed ductile fabrics in alteration haloes surrounding brittley-emplaced veins (Figs. 5.10G,H). Collectively these textures indicate fluctuations between brittle and ductile behaviour within the plumbing systems of lode gold deposits, which are controlled in turn by cyclic variations in fluid pressure (effective confining stress).

Variations in deformation mechanisms within individual lode gold quartz veins with time has also been documented. Quartz from high-T deposits showing significant degrees of dynamic recovery can be crosscut by later stage quartz that show more

undulose extinction and less recovery, and both may be cut by later stylolites or brittle fractures containing fault gouge or retrogressive mineral assemblages (e.g., Figs. 4.6, 4.14, 5.9I, 5.10I; McCuaig et al., 1993). These features record the uplift and cooling of the Norseman Terrane after mineralization and quartz-vein emplacement.

5.8.4 Wallrock alteration fabrics

Within the wallrocks and vein selvedges, deformation and recrystallization processes operate in the same manner, but are complicated by the presence of multiple mineral phases with contrasting rheological properties and by the variable transmission of strain through fault/shear zones. In brittle-dominated plumbing systems formed at lower temperatures, strain accommodation occurs on discrete planes and fabrics in the wallrock alteration haloes may not be extensively developed. In contrast, ductile-dominated plumbing sytems accommodate strain in broad shear zones, imparting well developed tectonic fabrics to wallrock alteration assemblages (cf. Hronsky et al., 1990, and primary references therein).

Lode gold deposits formed at low and intermediate temperatures ($\leq$ upper-greenschist facies) possess alteration assemblages with aligned preferred dimensional orientations, particularily of phyllosilicate minerals, which overprint metamorphic assemblages (e.g. Northern deposits). These deposits are generally considered as forming syn-late deformation and post-peak metamorphism. However, deposits formed at high temperature ($\geq$ lower-amphibolite facies) show large degrees of dynamic recovery in alteration assemblages (e.g. Central and Southern deposits). In these cases, it becomes difficult to distinguish between deposits that formed at these high temperatures (cf., Barnicoat et al., 1991; Mueller and Groves, 1991; Knight et al., 1993; McCuaig et al., 1993; Neumayer et al., 1993a,b; McCuaig and Kerrich, 1994) and deposits which formed at lower temperatures and then were subsequently metamorphosed during a later thermal event (cf., Golding and Wilson, 1982; Keele, 1984; Hamilton and Hodgson, 1986; Hodgson, 1993).

The micro- and meso-structural observations of alteration assemblages associated with these high-T deposits is crucial to resolving this dilemma. Variable deformation of veins and their contiguous alteration assemblages in the shear zones indicate synkinematic formation of deposits. Specifically, minerals such as amphibole and biotite in these deposits may be both aligned with and overprint the tectonic fabric on the scale of a single thin section, and while extensive dynamic recovery is apparent in the vein and alteration assemblages, rosettes of fibrous minerals, such as amphibole and chlorite, are also present (e.g., Figs. 5.9A,B, 5.10I; McCuaig et al., 1993). Multiple generations of

sulphides are often apparent with deformed crystals overgrown by, or coexisting with, less deformed or pristine crystals (e.g., Figs. 5.8D, 5.9C,D, 5.17A-C; Bain, 1933). Alteration selvedges immediately adjacent to the veins are often mono- or bi-mineralic in nature (e.g. Figs 5.8C, 5.9A,B, 5.10A, 5.10G-I). These fibrous and monomineralic assemblages have a high thermodynamic variance and are indicative of formation within an open hydrothermal system (Korzhinskii, 1970; Ridley, 1990; Barnicoat et al., 1991; McCuaig et al 1993; Mikucki and Ridley, 1993). If the deposits had been subsequently metamorphosed, more equigranular, polymineralic assemblages (low thermodynamic variance) would be expected. Another key observation is that in these high T deposits, löellengite, where present, is always rimmed by arsenopyrite (Fig. 5.10D). If the deposits had been subsequently metamorphosed, arsenopyrite would be rimmed by löellengite due to desulphidation reactions that occur during prograde metamorphism (e.g., Barnicoat et al. 1991; McCuaig et al., 1993; Neumayer et al., 1993a,b). Oscillatory zoning is also observed in silicate vein minerals in some deposits, and in arsenopyrite in the Norseman deposits (Figs. 5.17A-C). This texture is unlikely to survive a prograde metamorphic event.

In conclusion, the sum of microstructural, macrostructural, and metamorphic observations signify that these high-temperature deposits formed synkinematically, and close to peak metamorphic conditions, in gross rheological and thermal equilibrium with the host terranes. One of the clearest demonstrations of this characteristic is at Red Lake, Ontario, where Andrews et al. (1986) mapped out the transition from deposits in greenschist facies rocks with greenschist grade alteration assemblages to counterparts in amphibolite facies rocks with amphibolite grade alteration assemblages (Table 4.1). Similar transitions between deposits have been identified in the Yilgarn Block of Western Australia, in the lower- to middle-amphibolite facies (Coolgardie Domain, Knight et al., 1993; Table 4.1) and in upper-greenschist to lower-amphibolite facies (Norseman Terrane; McCuaig et al., 1993, this study, Table 4.1). The observation that hydrothermal alteration assemblages typically overprint peak regional metamorphic assemblages does not necessarily imply timing of mineralization significantly post-peak metamorphism. Rather, there is compelling evidence in high-T lode gold deposits that the mineralizing event occurred under P-T conditions close to peak regional metamorphism, but that the hydrothermal fluids imposed greater activities of H_2O, CO_2, and S in fluid conduits than in ambient metamorphic rocks. Deposits formed at temperatures less than amphibolite facies appear to have formed during the waning stages of regional metamorphism.

5.9 A crustal continuum of gold deposition

Separate deposits formed at significantly different temperatures within similar lithologies feature distinct alteration assemblages (e.g., Andrews et al., 1986; Colvine et al., 1988; Mueller and Groves, 1991; Cassidy, 1992; Groves et al., 1992; Groves, 1993; McCuaig et al., 1993; McCuaig and Kerrich, 1994). The variation in key alteration minerals, structural style, and microtextures with temperature and pressure for mafic lithologies hosting lode gold deposits is summarized in Figure 5.20 and correlates directly with the metamorphic grade of the host rocks. Principal variations in alteration mineralogy to note with increasing temperature include:

(1) In greenschist facies deposits, quartz and carbonate (ankerite, Fe-dolomite) generally constitute the principal gangue minerals and carbonate is also present in the alteration assemblages that envelop the vein systems. In deposits formed in amphibolite facies, carbonate is generally restricted to vein assemblages and is invariably calcite.

(2) Dominant Fe- and As-sulphides change from pyrite to pyrrhotite and arsenopyrite to loellingite, respectively.

(3) Plagioclase compositions become increasingly calcic, from albite in greenschist facies deposits to oligoclase-andesine in amphibolite facies.

(4) Abundant Ca-bearing minerals predominate in inner zones of high T deposits, including amphibole, clinopyroxene, epidote, and grossular garnet.

Hydrothermal alteration and gold mineralization can therefore occur at a variety of crustal levels, from subgreenschist to potentially granulite facies, and forms a 'crustal continuum ' of lode gold deposits (Groves et al., 1992; Groves, 1993; McCuaig and Kerrich, 1994). Hydrothermal alteration and gold mineralization in each of the examples in Figure 5.20 is interpreted as synkinematic and syn- to post-peak metamorphic.

5.10 Transport and deposition mechanisms for gold

5.10.1 Transport of gold in solution

The mechanisms of gold sourcing, transport, and deposition are extremely complex and have been reviewed by various workers (e.g., Seward, 1973, 1991; Cathles, 1986; Romberger, 1986; 1990; Kerrich and Fyfe, 1988; Shenberger and Barnes, 1989; Letnikov and Vilor, 1990; Mikucki and Groves, 1990; Hayashi and Ohmoto, 1991). Thermodynamic data on gold-complexing ligands is only available for a few possible

ligands and narrow ranges of P and T (generally < 1 kbar, < 300°C). Thus data is lacking for the P-T conditions of many lode-gold forming hydrothermal systems. However, this limited database suggests that gold is transported as a thiosulphide complex under greenschist and subgreenschist facies conditions as $(Au(HS)_2)^-$, and amphibolite facies conditions potentially as $(AuHS)^0$ (Seward, 1973, 1991; Shenberger and Barnes, 1989; Mikucki and Groves, 1990).

Thioarsenide complexes (Romberger, 1986) and carboxyl and carboxyl-chloride complexes (Kerrich and Fyfe, 1981; Fyfe and Kerrich, 1984) may also be important carriers of gold. Gold-chloride complexes are probably insignificant contributors to gold solubility at temperatures less than 400°C, but may be important at higher temperatures (Fig. 5.24A; Mikucki and Groves, 1990; Romberger, 1990) Base metals readily form soluble complexes with chloride, which suggests that characteristically low abundances in lode gold deposits would require gold to be deposited without affecting the stability of base metal-chloride complexes (Kerrich and Fyfe, 1988).

5.10.2 Deposition of gold from solution

Regardless of the actual gold concentrations in lode gold-forming fluids, in order to form an economic orebody it is necessary to induce a change in the fluid chemistry that will efficiently remove gold from solution by destabilizing gold complexes. Based on available data (Figs. 5.24A,B), destabilization could be accomplished by:

(1) cooling the fluid,
(2) oxidation of the fluid,
(3) reduction of the fluid,
(4) increasing pH of the fluid, especially for chloride complexes,
(5) lowering ΣS in the fluid, specifically for thiosulphide complexes,
(6) or, more likely, a combination of the above mechanisms.

This modification of fluid chemistry can be achieved by one or more of the following methods:

(1) large-scale pressure and temperature gradients along the fluid plumbing system,
(2) reaction of the fluid with the wallrocks surrounding the fluid conduit,
(3) transient pressure fluctuations inducing phase immiscibility in the fluid,
(4) fluid mixing,
(5) chemisorption onto preexisting sulphides, point defects, or gold grains.

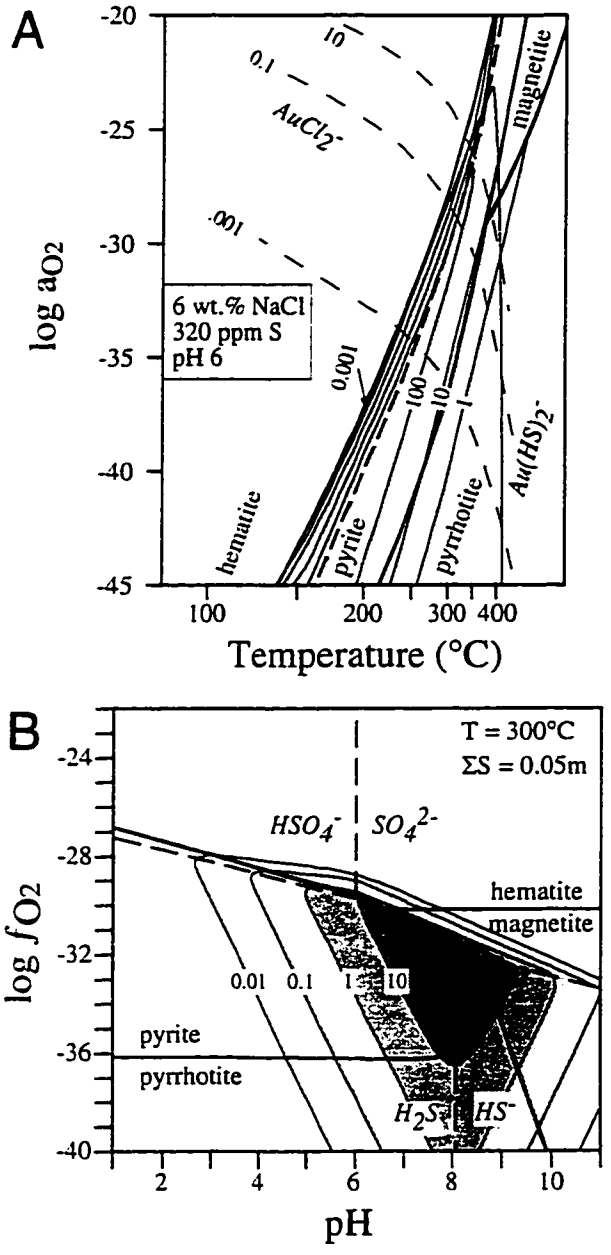

Figure 5.24. (A) Aqueous solubility of gold as a function of temperature and oxygen activity, from Romberger (1990). Heavy solid lines demark stability limits of Fe-sulphide/Fe-oxide phases (plain text), heavy dashed line represents the boundary between aqueous sulphate and sulphide fields (italics). Thin solid lines are solubility contours in ppb for gold-bisulphide complexes ($Au(HS)_2^-$ only), thin dashed lines are solubility contours in ppb for gold-chloride complexes. Shaded area is the field in which gold-bisulphide complexes dominate. Note that consideration of $AuHS^0$ complexes would expand the field of gold-sulphide dominance to higher temperatures (cf. Mikucki and Groves, 1990). (B) Calculated gold solubilities in ppm, in the form of $Au(HS)_2^-$, as a function of pH and oxygen fugacity. Solubility contours are in ppm. From Roberts (1988).

5.10.2.1 Broad pressure and temperature gradients as a depositional mechanism for gold

Broad pressure and temperature gradients, such as those found in geothermal and epithermal systems, are unlikely to exist in lode gold environments on the scale of a single deposit, based on the lack of vertical zonation in alteration assemblages, uniform oxygen isotope values for quartz, or trapping temperatures for fluid inclusions, which is evidence for broadly isothermal conditions of alteration and vein emplacement (McCuaig and Kerrich, 1994). However, such P-T gradients may be important on the terrane scale, such that gold deposition is favoured in a certain P-T "window" (e.g., Phillips and Powell, 1993). If P-T gradients are a dominant control on gold deposition on a terrane scale, then deposits should correlate with metamorphic isograds (e.g., Red Lake, Ontario, Andrews et al., 1986; Alpine Fault, New Zealand, Craw and Koons, 1989). This correlation with metamorphic grade is also apparent at Norseman, where the largest orebodies (Crown, Mararoa, North Royal) straddle the greenschist-amphibolite facies transition. Such depositional controls may explain the location of the majority of giant lode gold deposits worldwide in greenschist facies environments.

5.10.2.2 Fluid-wallrock reaction as a depositional mechanism for gold

Gold sited dominantly in alteration haloes surrounding quartz veins or in replacement bodies within select lithologies, was likely deposited as a direct result of metasomatic fluid-rock interaction. There are many possible mechanisms by which this can occur.

Sulphidation of the wallrocks has been demonstrated as an efficient gold deposition mechanism and is commonly invoked as the dominant depositional mechanism for many large replacement orebodies (e.g., Kambalda, Clark et al., 1986, 1989; Neall and Phillips, 1987; BIF-hosted deposits, Neumayer et al., 1993a,b). In this process, H_2S from the fluid is consumed by the formation of Fe-sulphides in the wallrocks of the fluid conduit. The loss of sulphur, or decrease in a_{S2} in the fluid, destabilizes the gold-sulphur complexes causing gold to precipitate by reactions (unbalanced) involving $(Au(HS)_2)^- + FeO(\text{silicate, oxides}) \rightarrow Au + FeS_2$. If this process is dominant, the gold grades in resultant orebodies should correlate with the total sulphide content of the adjacent wallrocks. Note that iron from wallrock phases is consumed in the reaction. This may leave ferromagnesian silicates in the wallrocks surrounding orebodies more magnesium-rich than those external to the orebody.

Intense **K and CO_2 metasomatism** can also cause gold deposition (Fyfe and Kerrich, 1984; Kishida and Kerrich, 1987). These metasomatic processes release H_2 into the hydrothermal fluid, thus decreasing the pH of the fluid and potentially causing gold to

precipitate. If K and/or CO_2 metasomatism contributes to the deposition of gold in an orebody, significant gold grades should occur in the wallrocks adjacent to the quartz veins and gold grades should correlate with the dynamic alteration fronts (e.g., Kerr-Addison, Ontario, Kishida and Kerrich, 1987; Alleghany, California, Böhlke, 1989).

Reaction of primary ore fluid with **graphitic wallrocks** produces significant quantities of methane through reactions such as $2C+2H_2O = CH4+CO_2$. This methane causes reduction of the ore fluid and results in gold precipitation (e.g., Cox et al., 1991). Carbon isotope compositions of vein carbonates may indicate if this process was operative (cf., Kerrich, 1990b).

At Norseman, significant concentrations of Au in wallrock alteration are only found in some tholeiite-hosted veins within the North Royal, OK (O2 vein) and Scotia deposits (Fig. 5.11; CNGC unpublished data). In the North Royal and OK mine, even where economic gold concentrations occur in wallrock alteration envelopes, the bulk of the gold is still located within the quartz veins. In these situations, gold in the wallrock correlates with sulphide content, indicating that sulphidation processes are locally important in precipitating gold.

In the Scotia mine, biotite-amphibole-plagioclase alteration within the host shear zone, and adjacent to the quartz-clinopyroxene veins, often contains marginally economic gold concentrations (average ≈ 3 g/t; CNGC unpublished data; R. Waugh, pers. comm. 1990). Metamorphic ilmenite is altered to pyrrhotite throughout the altered shear zone and, therefore, sulphidation may play a role in concentrating this gold. However, the intense K-metasomatism may also be partially responsible for the even distribution of gold through the biotite alteration zones in the deposit. Although the host shear zones contain economic concentrations of gold, it is important to note that the bulk of the gold is contained within the banded quartz-clinopyroxene veins (average Å 10-40 g/t; R. Waugh, pers. comm. 1990).

5.10.2.3 Phase immiscibility as a depositional mechanism for gold

As summarized earlier, phase separation in ore fluids may arise from transient pressure drops during seismic events. This process generally results in an increase in the pH of the ore fluid, as the acid volatile species H_2S, CO_2, and SO_2 partition into the vapour phase. An increase in the oxygen fugacity of the fluid also occurs, because the reduced volatile species CH_4, H_2S, and H_2 partition into the vapour phase more readily than their oxidized counterparts CO_2, SO_2, and H_2O (Drummond and Ohmoto, 1985; Naden and Shepherd; 1989; Mikucki and Groves, 1990). Examination of Figure 5.24B reveals that increasing pH and oxygen fugacity may have competing effects on gold

solubility and can actually increase the solubility of gold in the ore fluid. Whether or not gold will precipitate depends on the initial redox and pH conditions of the fluid and the relative magnitude of the $f(O2)$ and pH increases.

The total sulphur content of the fluid decreases as H_2S is exsolved into the vapour phase during phase immiscibility (Mikucki and Groves, 1990). This can lead to gold precipitation through reactions such as $(Au(HS)_2)^- + 1/2H_2 = Au + H_2S + HS^-$. Whether or not gold actually precipitates depends on the relative magnitude of sulphur loss versus pH and $f(O_2)$ increases. Sudden pressure drops during quartz vein formation are common in lode gold systems (Cox, 1990; Sibson, 1990), and the resultant phase immiscibility provides a possible gold depositional mechanism. This process operates strictly within the fluid conduit, and can be used to explain orebodies in which gold is sited dominantly within veins. It was commonly believed that at temperatures and pressures above the greenschist-amphibolite transition, phase separation was rare, but as shown in Figure 5.25, addition of solutes (Ho et al., 1992) or volatiles such as CH_4 or N_2 (Naden and Shepherd, 1989) push the solvus to higher P-T conditions. Furthermore, recent experimental data suggest that phase immiscibility may be common in moderate-salinity fluids under high-T, moderate-P conditions (e.g., Johnson, 1991). Shock nucleation processes during seismic events may aid phase immiscibility under conditions where a two-phase fluid would not be supported under ambient conditions (Kerrich, 1989a).

At Norseman, the ubiquitous occurrence of native gold in quartz veins, and the location of gold orebodies in dilation sites on the quartz vein systems, suggests that phase immiscibility may have been the dominant mechanism for gold deposition.

5.10.2.4 Fluid mixing as a depositional mechanism for gold

Fluid mixing is unlikely in the majority of lode gold systems due to the uniformity between calculated ore fluid compositions from lode gold deposits of all ages and geographic location (Kerrich, 1989b; Phillips and Powell, 1993). However, recent studies have demonstrated that fluid mixing does occur on two distinct scales.

(1) Mixing of two externally derived fluids. Potential examples of this process include mixing of deeply sourced fluid + surface waters in some sub-greenschist facies environments, and mixing of metamorphic + deeper (magmatic?, mantle-derived?) fluids in some higher temperature deposits.

(2) Mixing of internally derived endmember fluids. In these situations, the primary ore fluid infiltrates wallrock, where metasomatic reactions modify the fluid chemistry. This modified fluid resides in the wallrocks until a subsequent seismic

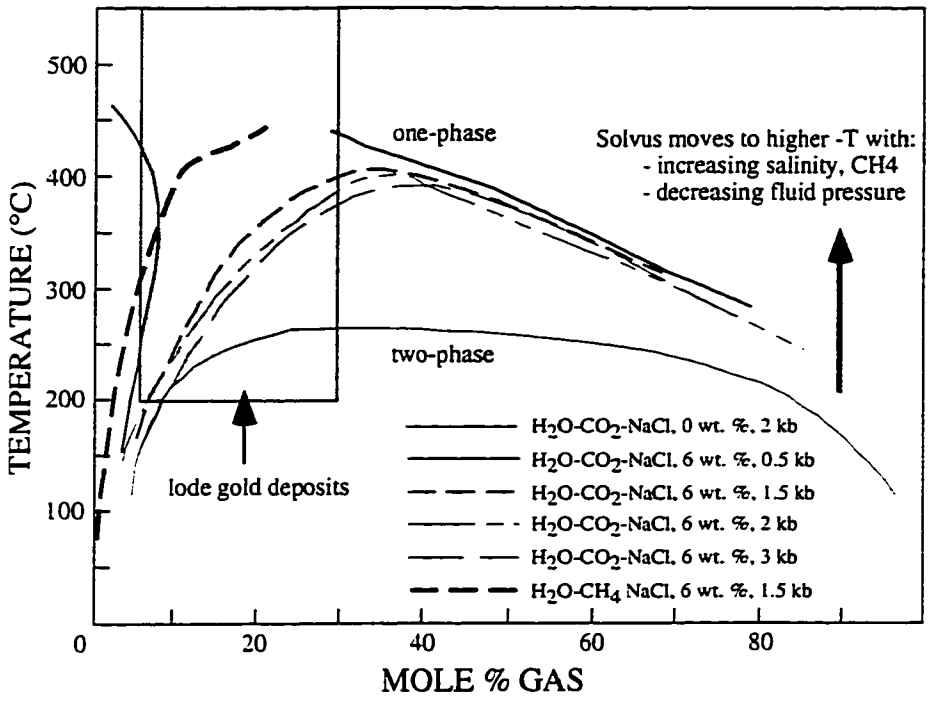

Figure 5.25. Temperature versus fluid composition phase diagram for the H_2O-CO_2-NaCl and H_2O-CH_4-NaCl systems, redrawn from Ho et al., 1992) and Naden and Shepherd (1989). Note that the solvus moves to higher temperatures with (1) increased salinity, (2) increased CH_4 or N_2 content, and (3) decreasing fluid pressure. At higher temperatures, fluid immiscibility may be aided by shock nucleation processes during seismic events, in combination with large pressure drops within the fluid conduits. From McCuaig and Kerrich (1994).

event allows the fluid to reenter the fluid conduits and mix with primary ore fluid, potentially causing gold deposition (e.g., Cox et al., 1991).

It is unlikely that option (1) has occurred at Norseman, as uniform alteration assemblages within a given deposit, and narrow ranges of oxygen isotope values in vein quartz, are consistent with broadly isothermal conditions of alteration from a single ore fluid within any one deposit. Option (2) may occur, in that the transient nature of deformation and catastrophic fluid movement through the mineralized structures could allow evolved fluids from the wallrock to mix with new pulses of original hydrothermal fluid. This scenario could also explain the location of gold predominantly within the veins, without invoking phase immiscibility.

Thus, fluid inclusions and stable and radiogenic isotope data are potential monitors as to whether these processes have operated (see previous sections).

5.10.3 Siting of gold versus introduction of gold: remobilization and chemisorption processes

In many deposits the majority of the gold, if not all, appears paragenetically late Often native gold or, more rarely, tellurides or sulphosalts are observed occupying fractures in sulphides, quartz veins, and silicate and carbonate gangue (e.g., Figs. 5.8D,E; Robert and Brown, 1986b; Hamilton and Hodgson, 1986; Fedorowich et al., 1991; De Ronde et al., 1992; Cassidy and Bennett, 1993; McCuaig et al., 1993). This relation has led some workers to speculate that gold was introduced post-vein emplacement and alteration.

However, there are abundant examples of deposits with gold bound in sulphide lattice structures (e.g., Cathlineau et al., 1989; Neumayer et al., 1993a), gold as inclusions in sulphides (e.g., Figs. 5.8D, 5.10F; Andrews et al., 1986; Barnicoat et al., 1991; Caddey et al., 1991; Fedorowich et al., 1991; Gebbre-Merriam et al., 1991; Goldfarb et al., 1991; De Ronde et al., 1992; Hagemann et al., 1993; McCuaig et al., 1993), silicate and carbonate gangue (e.g., Figs. 5.9C, 5.10E; Caddey et al., 1991; Cassidy, 1992), and gold in textural equilibrium with sulphides or silicates (e.g., Figs. 5.9C, 5.10E; Andrews et al., 1986; Robert and Brown, 1986b; Peters and Golding, 1989; Caddey et al., 1991; Fedorowich et al., 1991; Gebbre-Merriam et al., 1991; De Ronde et al., 1992; Cassidy and Bennett, 1993; Hagemann et al., 1993; McCuaig et al., 1993). In these examples, at least part of the gold must be introduced and deposited coevally with hydrothermal alteration and quartz vein emplacement.

The study of Neumayer et al. (1993a) is particularly relevant in that it demonstrates that gold sited at löellingite-arsenopyrite boundaries, a common texture

observed in higher temperature deposits, was initially introduced as lattice-bound gold with löellingite, then locally exsolved during retrogression of löellingite to arsenopyrite. Similarly, other studies have demonstrated that gold mineralization was likely continuous throughout protracted and episodic histories of quartz vein emplacement and hydrothermal alteration (Peters and Golding, 1989; Cox et al., 1991; De Ronde et al., 1992; McCuaig et al., 1993). The breakdown of gold-bearing pyrite during recrystallization or deformation (e.g., $Fe(Au)S_2 = FeS_2 + Au$) may also lead to the remobilization of gold into paragenetically-late sites, even though the gold was originally introduced during earlier stages of alteration (Romberger, 1986).

At lower temperatures, gold may be locally mobilized and redeposited on the surface of pre-existing sulphides or point defects by chemisorption processes (Jean and Bancroft, 1985). Such ore modification processes may explain the common presence of gold on fractures in, or as rims on, sulphides at Norseman (Figs. 5.8D,E).

Collectively, these observations demonstrate that the final siting of gold need not equate with the initial mode of gold introduction and deposition. Gold may be remobilized a number of times, as suggested by complexly reset isotopic systems, which indicate numerous post-fluid events in Precambrian terranes (Chapter 6; Kerrich and Cassidy, 1994; McCuaig and Kerrich, 1994, Ansdell and McCuaig, 1996).

5.11 Summary and conclusions

(1) Metamorphic assemblages in tholeiitic metabasalts within the Norseman Terrane indicate a broad zonation in metamorphic grade, from upper greenschist facies in the environs of the Northern deposits, to lower amphibolite facies in the Central deposits area, to mid-amphibolite facies in the Southern deposits area.

(2) Zonation of hydrothermal alteration assemblages associated with lode gold deposits of the Norseman Terrane are recognized on three scales: (i) laterally away from the quartz veins (fluid conduits), (ii) between host rocks of different bulk composition (HMT versus tholeiite), and (iii) regionally, between Northern versus Central versus Southern deposit areas.

(3) The lateral alteration zones may have distinct boundaries between zones over millimetres to centimetres, or be gradational over a few metres, with zone boundaries commonly correlating with zones of variable fabric development and heterogeneous fluid infiltration. Sharp contacts occur between inner alteration zones in the wallrock immediately adjacent to the vein, and vein selvedges deposited directly from the hydrothermal fluid at the margins of the quartz veins.

(4) The lateral zonation of alteration assemblages reflects the progressive addition of LILE (K_2O, Cs, Rb, Ba) and volatiles (H_2O, CO_2, H_2S) from the fluid. Mantle-normalized trace element patterns for all REE, HFSE, P, V, Sc, and Al are relatively unaffected by even the most intense alteration. These elements therefore preserve primary magmatic geochemical ratios, and can be used to interpret the petrogenesis of the mafic lithologies of the Norseman terrane, even where the rocks are hydrothermally altered.

(5) In contrast to the marked lateral variations in alteration away from fluid conduits, remarkably little variation is observed parallel to the fluid conduits within a single host lithology; thus alteration zones are often described as alteration envelopes surrounding fluid conduits. However, a fluid conduit in a single deposit that transects two lithologies of contrasting bulk composition will have different mineral assemblages in the different lithologies. Within a single lithology in any given deposit, the alteration zones may be traced parallel to the fluid conduits, both down dip and along strike, for hundreds of metres showing little variation in mineralogy within individual zones, implying relatively uniform conditions of vein emplacement and metasomatism.

(6) The paragenetic sequence of hydrothermal alteration assemblages identified in both the least-altered assemblages and quartz-veined shear zones indicate that the Norseman Terrane and associated gold deposits have evolved through a number of pressure-temperature regimes. Therefore, it is imperative that the hydrothermal wallrock alteration envelopes associated with the quartz veins be examined in both a spatial framework: lateral zonation away from veins, and differences in alteration assemblages between mines; and a temporal framework: change in alteration mineralogy and deformation styles with time.

(7) Arsenopyrite geothermometry, oxygen-isotope mineral-pair geothermometry, and phase equilibria considerations constrain hydrothermal alteration to temperatures of 420-475°C for Northern deposits, 470-500°C for Central deposits, and 490-540°C for Southern deposits. These results indicate a broad thermal zonation of temperatures of alteration from north to south within the Norseman Terrane, which corroborates the interpreted zonation of metamorphic grade.

(8) Variably deformed veins and contiguous alteration assemblages indicate that all deposits formed during deformation. Quartz fabrics in the veins show generally increasing degrees of dynamic recovery from Northern to Southern deposits, consistent with the interpreted regional zonation of temperatures of hydrothermal alteration and quartz vein emplacement. However, varying degrees of

dynamically recovered quartz are observed in each deposit, an observation consistent with the interpreted post-peak metamorphic, synkinematic timing of the hydrothermal alteration and quartz vein emplacement.

(9) Gold deposition can occur at various crustal levels, and is generally synkinematic and syn- to post-peak metamorphic. There is, therefore, a crustal continuum of gold deposition within the crust. Separate deposits formed at significantly different temperatures within similar lithologies feature distinct alteration assemblages which usually correlate directly with the metamorphic grade of the host rocks. Principal variations in alteration mineralogy with increasing temperature include:

(i) In greenschist facies deposits, quartz and carbonate (ankerite, Fe-dolomite) generally constitute the principal gangue minerals and carbonate is also present in the alteration assemblages that envelop the vein systems. In deposits formed in amphibolite facies, carbonate is generally restricted to vein assemblages and is invariably calcite.

(ii) Dominant Fe- and As-sulphides change from pyrite to pyrrhotite and arsenopyrite to löellingite, respectively.

(iii) Plagioclase compositions become increasingly calcic,

(iv) Abundant Ca-bearing minerals predominate in inner zones of high T deposits.

CHAPTER 6

^{40}Ar-^{39}Ar AND Pb ISOTOPE SYSTEMATICS: CONSTRAINTS ON PRIMARY MINERALIZATION AGES, ORE FLUID SOURCES, AND POST-MINERALIZATION RESETTING EVENTS

6.1 Introduction

Lode gold deposits in Archean terranes worldwide are sited in, or proximal to, Archean structures. Deposits of this type are manifestations of terrane-scale hydrothermal systems with large vertical and lateral extent (Groves et al., 1992; Groves, 1993; McCuaig and Kerrich, 1994). Multiple theories of fluid sources for such deposits have been proposed including mantle degassing (Fyon et al., 1983), granulitization of the lower crust (Cameron, 1988), metamorphic devolatization of host greenstones (Groves and Phillips, 1987), or of subcreted or subducted material during dynamothermal regional metamorphism (Wyman and Kerrich, 1988), fluids expelled during the ascent or crystallization of granitoid melts (Burrows and Spooner, 1987), and deep circulation of meteoric waters (Nesbitt et al., 1986). This fluid/solute source debate has yet to be resolved.

All Archean lode gold deposits show some degree of later, usually minor and localized, modification in terms of structural reactivation, retrograde mineral parageneses, or isotopic resetting (cf. Cassidy and Bennett, 1993; McCuaig et al., 1993; Kent and McDougall, 1995), although this post-mineralization history has been largely ignored in many studies of lode gold deposits. Proterozoic reactivation has been documented in structures associated with Archean lode gold deposits (Kerrich and Cassidy, 1994 and references therein), and there is increasing evidence that many gold lodes are sited where such Proterozoic reactivation of the Archean structural hosts has occurred (cf. Guha and Kanwar, 1987; Perring and McNaughton, 1990). This observation raises the imperative for means to recognize and document the special characteristics of reactivated mineralization, to distinguish between remobilized versus reintroduced gold, and hence potentially to predict the primary and secondary enrichment processes and structures for future discoveries.

Radiogenic isotope studies of mineral deposits can provide three types of information:

(1) the primary age of mineralization,

(2) the source of ore and gangue constituents, and

(3) the time or times of secondary disturbance.

This chapter synthesizes the results of Ar and Pb isotope studies on the Norseman lode gold deposits. Reviews of the application of these radiogenic isotope systems to ore deposits are available (Doe and Zartman, 1979; Faure, 1986; Kerrich, 1991).

In recent years substantial advances in the understanding of the formation of hydrothermal ore deposits have arisen from the application of isotopic dating techniques to hydrothermal minerals within these deposits (e.g. Claoué-Long et al., 1990; Richards and McDougall ,1990; Goldfarb et al., 1991). This has enabled workers to develop chronologies for different phases of hydrothermal activity within individual deposits and mineral fields, and also enabled recognition of temporal relations between hydrothermal mineralization and geological events within mineralized regions. The latter has been particularly useful in testing genetic models for the formation of different types of hydrothermal mineralization (e.g. Richards and McDougall, 1990).

Isotopic ages of hydrothermal minerals associated with Archean gold deposits in Australia and Canada have been used to place constraints on the timing of Archean gold mineralization. The interpretation of these ages has a direct bearing on the origin of gold mineralization and the nature of the processes responsible for generation of gold-bearing fluids. The ^{40}Ar-^{39}Ar step heating technique has proved particularly useful, in that it can be applied to a wide variety of hydrothermal minerals, including muscovite, K-feldspar, biotite, and amphibole (e.g. Clark et al., 1989; Claoué-Long et al., 1990; Wong et al., 1991; Barnicoat et al.,1991; Hanes et al., 1992; Wang et al., 1993; Zweng et al., 1993; Groves, 1993; Kerrich and Cassidy, 1994, Kent and McDougall, 1995). However, many of the conclusions drawn from this work are controversial, with much of the current debate centering around the possibility that radiometric ages of hydrothermal phases have been affected by isotopic resetting, and thus record ages younger than the true age of mineralization (Miller et al., 1991; Kerrich and Cassidy, 1994; Powell et al., 1995).

Galena (PbS) and altaite (PbTe) are minerals that contain abundant Pb, but virtually exclude Th and U from their structure, and thus hydrothermal galena and altaite can potentially preserve the primary Pb-isotope composition of the fluid(s) from which they precipitated. Therefore, analysis of these minerals from lode gold deposits can provide the initial Pb-isotope compositions of the ore-forming fluids, which in turn can

constrain rocks with which the hydrothermal fluids exchanged. The Pb isotope composition of Pb-rich ore minerals are therefore useful in addressing the problems of timing and solute source outlined above. Gold cannot be used as an isotopic tracer given its monoisotopic character (^{197}Au). Consequently, Pb, Sr and Nd isotope studies of hydrothermal minerals are commonly used to obtain information on gold source rocks, in combination with stable isotopes as summarized in Chapter 5.

This chapter reports new ^{40}Ar-^{39}Ar data on hydrothermal and igneous minerals, which is combined with existing geochronological data to further constrain the timing of Au mineralization in the overall thermo-tectonic evolution of the Norseman Terrane. Extremely disturbed ^{40}Ar-^{39}Ar spectra are then further examined in the context of post-mineralization resetting of the ^{40}Ar-^{39}Ar system.

All available Pb-isotope data for the Norseman Terrane is then presented. These data, modelled within the geochronological framework for the evolution of the Norseman Terrane, are used to constrain fluid sources and the architecture of the hydrothermal plumbing systems associated with lode gold deposits. Extremely radiogenic ore galena and altaite compositions are then investigated in terms of complex post-mineralization isotope resetting events.

6.2 ^{40}Ar-^{39}Ar systematics

6.2.1 Sample selection and description

In an attempt to date gold-related hydrothermal alteration at Norseman, six samples for ^{40}Ar-^{39}Ar step heating analysis were selected from four well-characterized study areas: the Scotia mine in the Southern deposits, the OK Main vein, and the Crown vein from the Central deposits, and the Princess Royal vein from the Northern deposits.

At the Scotia mine, quartz - muscovite - albite - biotite - garnet pegmatites crosscut ore bodies in many locations, and are invariably post-mineralization (Chapter 4; McCuaig et al. 1993). Samples of muscovite from the pegmatite (SCPEG8), and of amphibole from the vein selvedge alteration (SCPV) from the 7/440 crosscut (Fig. 4.15) were analyzed. The muscovite is very coarse grained, forming books up to 3 cm across. Euhedral grains approximately 0.5 cm across were handpicked for analysis. Amphibole from foliated, ore-related alteration is subhedral and medium grained, with individual grains up to 0.5 cm in length (Fig. 5.10G). Ore zones, pegmatites and Proterozoic dolerite dykes are disrupted by multiple generations of brittle faults (Chapter 4, McCuaig et al. 1993). These structures are variably filled with assemblages of chlorite - quartz - albite - sericite, and prehnite - albite, fine-grained cataclasite, and gypsum. The brittle

nature of these faults, the multiple generations of these structures as indicated by cross-cutting relationships, and the variable low-temperature alteration assemblages associated with them, collectively indicate that brittle deformation occurred a number of times after, at lower pressures and temperatures than gold mineralization and pegmatite intrusion.

A hydrothermal muscovite from the OK Main vein was selected for analysis (OK-26). Muscovite is rare in the mafic-hosted lode gold deposits at Norseman, usually restricted to fine-grained sericite on stylolites and late brittle fractures within the quartz veins. The OK-26 sample is unique in that the muscovite is coarse grained, occurring as euhedral books up to 0.5 cm in diameter and 0.1 cm thick. This muscovite is intergrown with what appears to be main stage quartz + arsenopyrite at the selvedge of Main vein, and is mildly deformed. Significantly, the biotite in the adjacent wallrock is intergrown with muscovite, a feature uncharacteristic of this vein system. Late-stage carbonate veins up to a few mm wide follow the vein selvedge, brecciating quartz, wallrock alteration, and muscovite grains. Main vein is not mineralized at this location, but a high grade ore shoot within a dilational jog on the vein system occurs approximately 100 m to the east along the same vein (Fig. 4.10).

Amphibole and biotite were separated from the vein selvedge and adjacent wallrock alteration of the Crown vein, at the base of the 16/70 stope (Fig. 4.4). The vein selvedge to this laminated auriferous quartz vein comprises a fibrous amphibole + granular calcite and plagioclase (e.g. Fig. 5.9B). Adjacent wallrock alteration comprises biotite + calcite + amphibole, and exhibits a well-developed foliation, with mineral grains aligned subparallel to the vein margin. The quartz vein is boudinaged at this point, and coarse gold is visible along the footwall vein selvedge where sampled. The quartz vein also shows evidence of post-emplacement brittle modification, with brittle fractures crosscutting the quartz, and stylolites that have nucleated on vein laminations that were originally bands of biotite-altered wallrock. Biotite and amphibole are variably retrogressed to chlorite- and sericite-bearing assemblages along these structures and along the vein selvedges. Amphibole and biotite separates from this sample are generally fine grained, although grains > 250 μm in width were hand-picked for analyses.

Biotite from the Princess Royal Vein was separated from sample PRS-28 from diamond drill core PRS-1177 (Appendix C). This sample is a biotite-plagioclase-pyrite-pyrrhotite altered wallrock inclusion. Vein selvedges bordering the inclusion comprise combinations of chlorite + calcite + plagioclase + biotite + quartz + pyrite. A ductile fabric is present in the wallrock inclusion, defined by anastamosing bands of biotite surrounding aggregates of plagioclase + biotite + quartz. However, biotite within these

bands is often randomly oriented. Individual biotite grains, 100-150 μm in diameter, were selected for analysis. In thin section, no obvious intergrowth with chlorite is apparent; biotite grains are subhedral and appear pristine.

6.2.2 ^{40}Ar-^{39}Ar analytical methods

Mineral separates from all samples were prepared to >99% purity, using standard heavy liquid and magnetic techniques, with aliquots for analyses further refined by hand-picking. Samples analyzed by the ^{40}Ar-^{39}Ar technique were irradiated for 116 hours in position 5c of the water-moderated, enriched uranium research reactor at McMaster University, Hamilton, Ontario, Canada using international hornblende standard HB3GR as a flux monitor. Argon was extracted at Queen's University, Kingston, Ontario, Canada, using a Lindberg tubular furnace and analyzed using a MS-10 mass spectrometer. Linear regression of isotope ratios for each step was carried out according to the procedures summarized in McDougall and Harrison (1988).

^{40}Ar-^{39}Ar for samples are tabulated, and resultant spectra illustrated, in Figure 6.1, with data reported as isotopic ratios of argon released in each step. Ages from plateau-like segments in release spectra are calculated using gas-fraction weighting of individual steps and associated errors, and include the error in J. All ages were calculated using the decay constants of Steiger and Jaeger (1977) and with errors expressed as 2σ.

6.2.3 ^{40}Ar-^{39}Ar results

Release spectra for the SCPEG8 muscovite and SCPV amphibole are combined with release spectra for similar samples from the Scotia mine of Kent (1994) and presented in Fig. 6.2. The ^{40}Ar-^{39}Ar spectra for the muscovite samples, both taken from pegmatite dykes, exhibit well-developed plateau-like segments which comprise > 90% of argon released. Muscovite from sample SCPEG8 exhibits a plateau between steps 3 - 19 comprising 97% of argon released, and corresponding to an apparent age of 2612 ± 4 Ma (Fig. 6.1A). The plateau-like segment for the muscovite reported by Kent (1994) is within experimental error of SCPEG8, although the median values are some 20 Ma different. This may be due to interlaboratory variations or could reflect some real age difference between these two samples.

All samples of hydrothermal biotite and hornblende from the Scotia Mine have ^{40}Ar-^{39}Ar release spectra which are erratic and do not display plateau-like segments. Hornblende samples analyzed display increasingly older apparent ^{40}Ar-^{39}Ar ages with progressive gas release. The youngest step ages range between ca. 1000 - 1600 Ma and the oldest step ages between 1900 - 2400 Ma (Figs. 6.1B, 6.2). In sample SCPV the

6.1A **ScPeg Musc**

Run: jf-35 103/14 Mass: 16.1 mg
Date: December 2 1992 J Value: 0.02325

Total 39Ar: 20.168 E-8 cm3 NTP Approx. 7.6% K
Integrated Age 2612.8 +/- 4.4 Ma
Plateau Age: 2612.5 +/- 4.0 Ma (97.4% of 39Ar, steps marked by *)

	Temp C	40/39	36/39	37/39	Vol 39A E-8 cm3	Fraction 39Ar	%40Ar Rad.	Age Ma	+/-	Error 2 sigma
	500	208.043	0.2783	0.009	0.032	0.002	60.78	2473.0	+/-	148.8
	600	150.305	0.0121	0.079	0.268	0.013	97.81	2877.4	+/-	5.1
*	700	140.804	0.0002	0.008	4.550	0.228	99.95	2619.5	+/-	3.5
*	750	140.598	0.0008	0.001	2.363	0.117	99.83	2615.9	+/-	2.0
*	800	140.430	0.0009	0.000	1.761	0.087	99.80	2613.7	+/-	6.1
*	850	139.724	0.0010	0.001	2.285	0.113	99.80	2608.7	+/-	2.2
*	900	139.784	0.0004	0.000	3.995	0.198	99.91	2608.6	+/-	2.5
*	950	140.037	0.0010	0.000	3.173	0.157	99.78	2609.6	+/-	4.3
*	1000	140.007	0.0011	0.000	1.518	0.075	99.77	2609.1	+/-	5.5
	1200	141.358	0.0138	0.128	0.225	0.011	97.11	2585.4	+/-	18.8

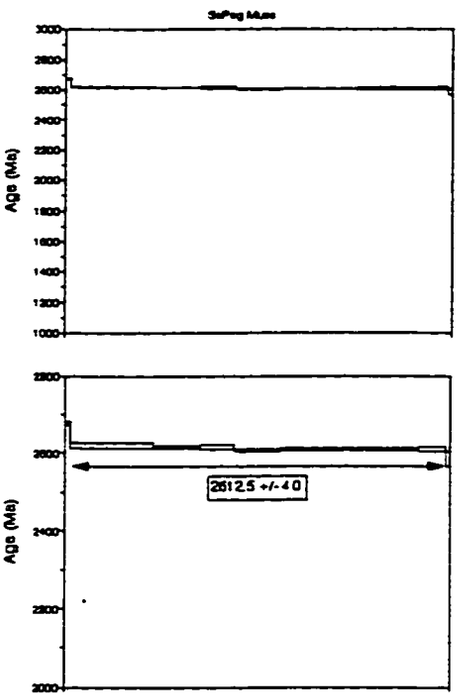

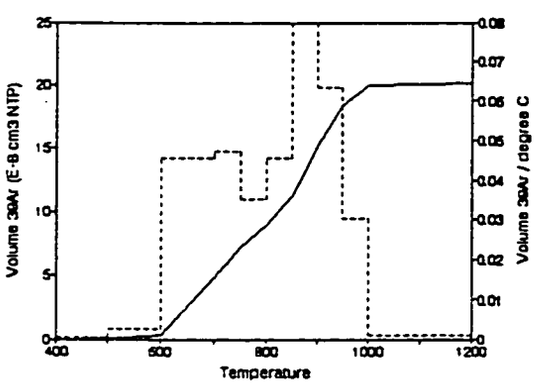

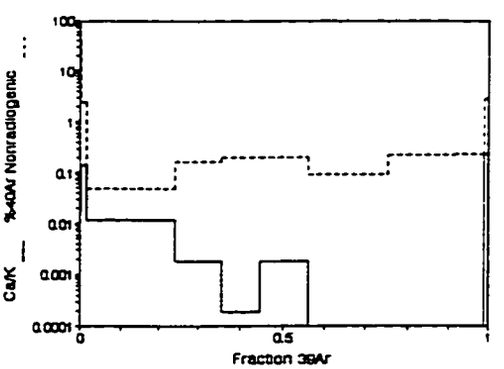

6.1B SCPV amphibole, Scotia deposit

Run: JF-48 103/11 Mass: 50.4 mg
Date: December 18 1992 J Value: 0.02323

Total 39Ar: 4.635 E-8 cm3 NTP Approx. 0.56% K
Integrated Age: 1999.4 +/- 7.3 Ma

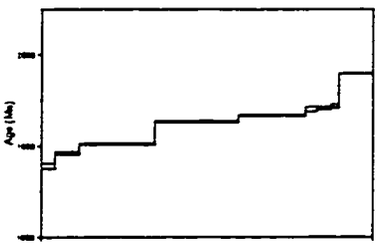

Temp C	40/39	36/39	37/39	Vol 39Ar E-8 cm3	Fraction 39Ar	%40A Rad.	Age Ma	+/-	Error 2 sigma
600	68.143	0.0183	2.054	0.196	0.042	92.07	1625.5	+/-	22.8
700	71.673	0.0076	2.025	0.333	0.072	96.88	1736.1	+/-	12.5
800	75.429	0.0024	1.082	1.044	0.225	99.07	1817.2	+/-	5.5
900	88.613	0.0036	5.280	1.200	0.259	98.80	2011.3	+/-	3.8
950	93.182	0.0040	4.891	0.919	0.198	98.73	2070.8	+/-	6.4
975	99.367	0.0121	5.290	0.159	0.034	96.41	2121.7	+/-	21.3
1000	100.229	0.0126	5.367	0.188	0.041	96.30	2131.0	+/-	12.5
1050	104.837	0.0236	6.268	0.111	0.024	93.35	2150.0	+/-	13.9
1200	123.412	0.0099	15.856	0.484	0.104	97.63	2434.4	+/-	3.3

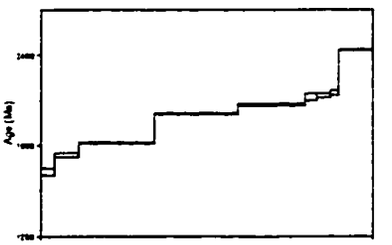

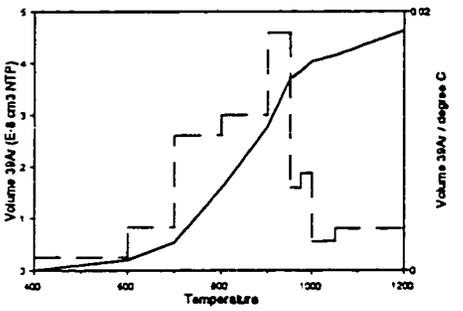

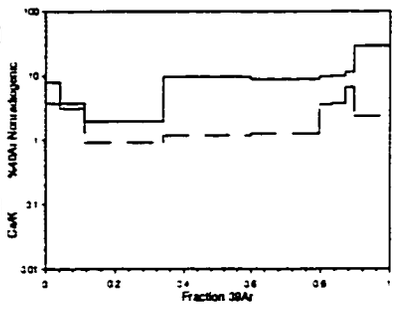

O.K. 26 Musc

Run: kd-37 139/37
Date: October 25, 1995

Mass: 21.0 mg
J Value: 0.03416

Total 39 Ar: 37.220 x E-8 cm3 NTP
Integrated Age: 2594.9 +/- 10.6 Ma
Plateau Age: 2598.7 +/- 9.3 Ma (96.4% of 39Ar, steps marked by *)

Approx. 7.3% K

Temp C	40/39	36/39	37/39	Vol 39A E-8 cm3	Fraction 39Ar	%40Ar Rad.	Age Ma	+/-	Error 2 sigma
600	101.299	0.0238	0.001	0.518	0.015	93.03	2597.4	+/-	97.7
*675	96.852	0.0024	0.001	1.339	0.040	99.25	2624.5	+/-	10.9
*725	96.006	0.0007	0.001	0.889	0.026	99.74	2619.3	+/-	15.2
*800	95.256	0.0007	0.001	6.003	0.178	99.74	2608.5	+/-	12.9
*850	95.262	0.0003	0.001	3.068	0.091	99.89	2610.6	+/-	16.1
*900	82.618	0.0001	0.001	3.274	0.097	99.94	2619.7	+/-	23.7
*950	91.390	0.0004	0.001	4.029	0.119	99.83	2552.8	+/-	35.8
*1000	93.497	0.0006	0.001	8.076	0.238	99.80	2583.6	+/-	5.0
*1050	94.971	0.0003	0.001	6.643	0.196	99.88	2606.2	+/-	4.3
1200	92.502	0.0323	0.001	n/a	n/a	88.67	2424.2	+/-	249.1

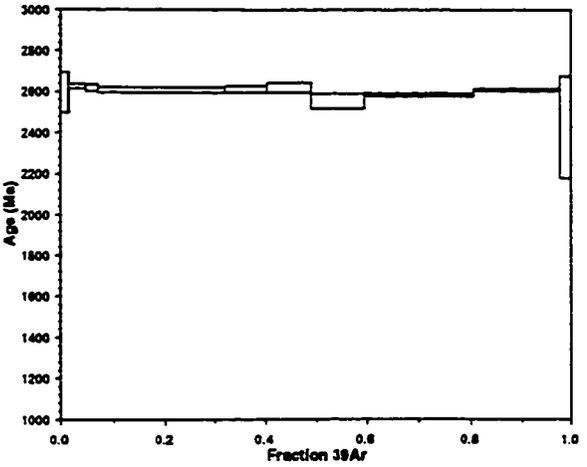

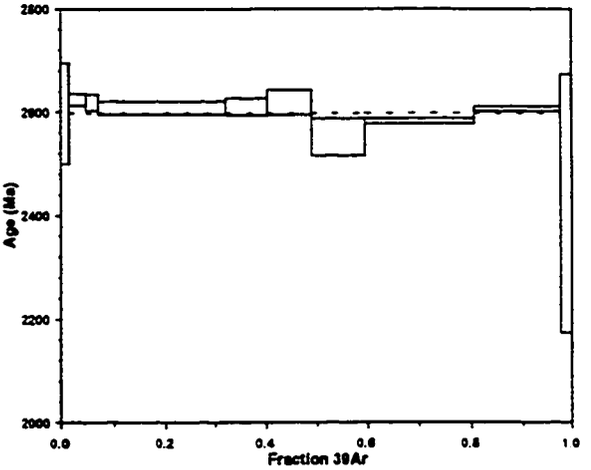

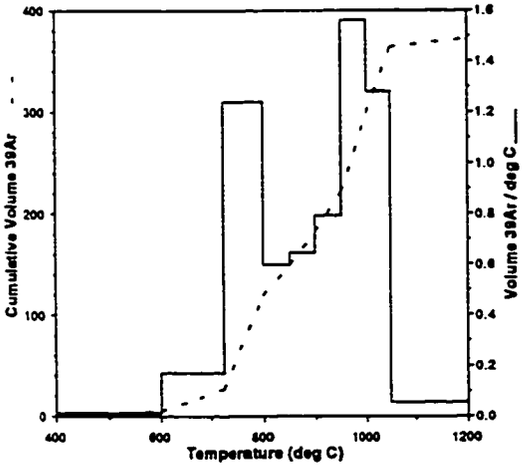

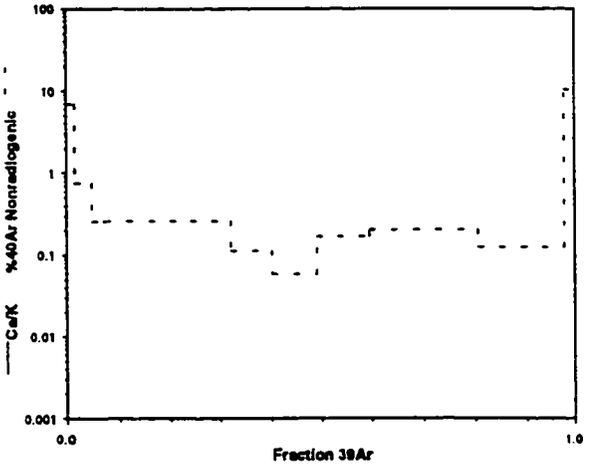

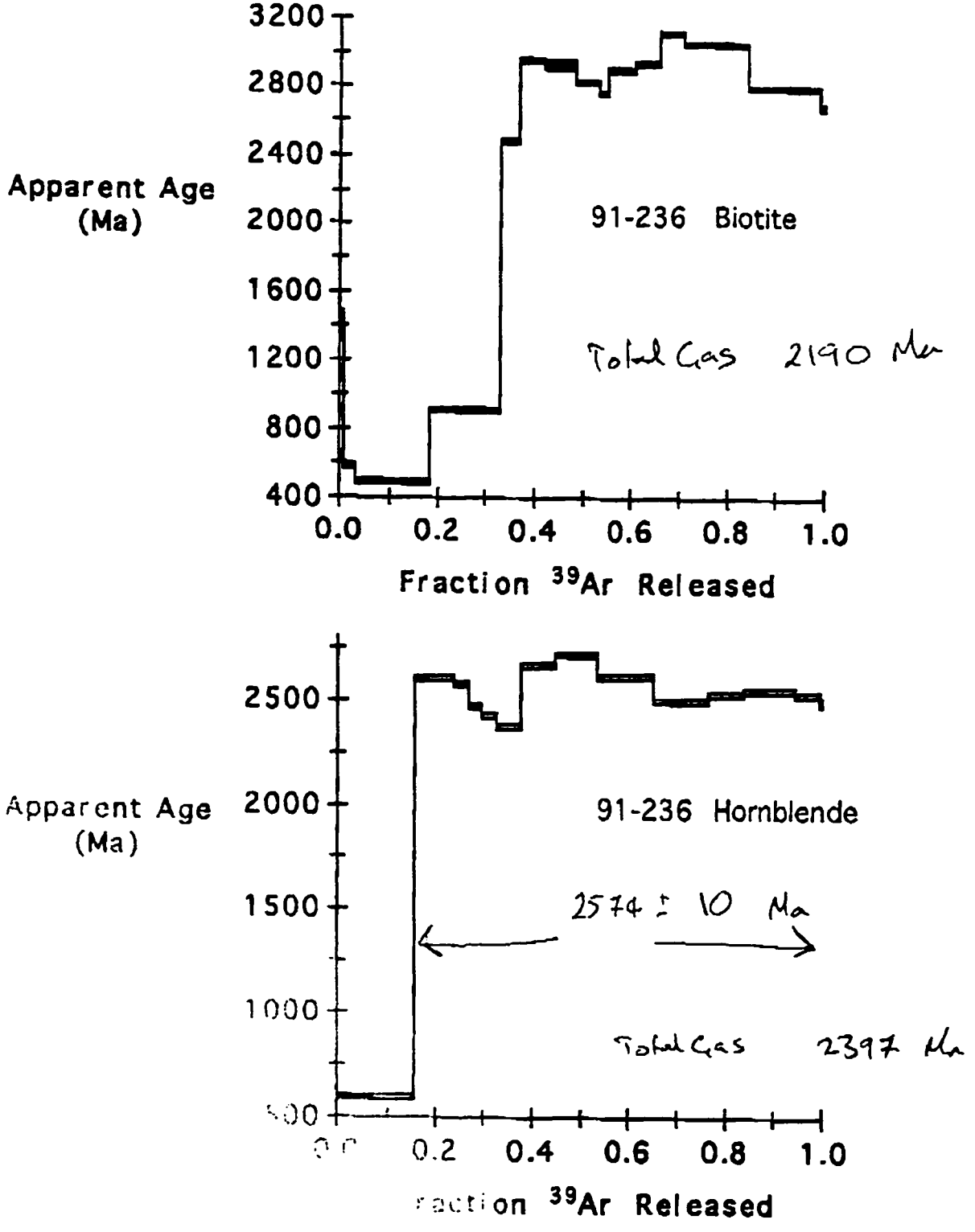

6.10 Age spectra for hydrothermal amphibole and biotite from the OK mine, Norseman *From Adam Kent*

6.1E 16/70 amphibole, Crown Vein, Central deposits

Run: JF-50 103/12 Mass: 20.4 mg
Date: December 19 1992 J Value: 0.02324

Total 39Ar: 1.133 E-8 cm3 NTP Approx. 0.34% K
Integrated Age: 2438.1 +/- 16.9 Ma
Plateau Age: 2543.4 +/- 16.5 Ma (64.7% of 39Ar, steps marked by *)

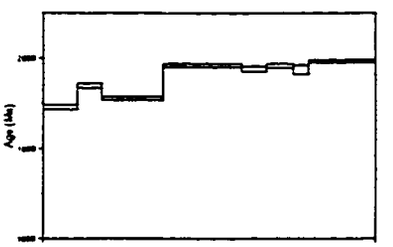

	Temp C	40/39	36/39	37/39	39Ar E-8 cm3	Fraction 39Ar	%40Ar Rad.	Age Ma	+/-	Error 2 sigma
	600	105.710	0.0192	0.662	0.112	0.099	94.62	2167.8	+/-	20.8
	700	124.496	0.0296	1.365	0.082	0.072	92.96	2357.0	+/-	22.1
	800	109.391	0.0132	4.450	0.206	0.182	96.45	2242.3	+/-	14.1
*	880	133.737	0.0110	13.753	0.273	0.241	97.57	2538.0	+/-	14.8
*	930	134.259	0.0199	8.853	0.084	0.074	95.61	2507.7	+/-	21.1
*	980	135.012	0.0143	10.038	0.090	0.080	96.86	2534.7	+/-	18.5
*	1050	138.063	0.0370	12.738	0.052	0.046	92.08	2501.1	+/-	40.6
*	1200	138.287	0.0141	13.736	0.234	0.206	96.98	2575.1	+/-	10.7

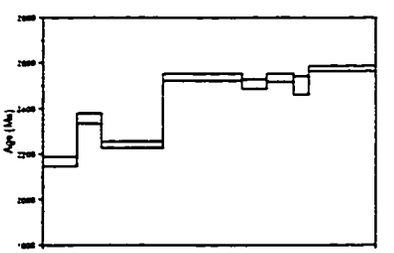

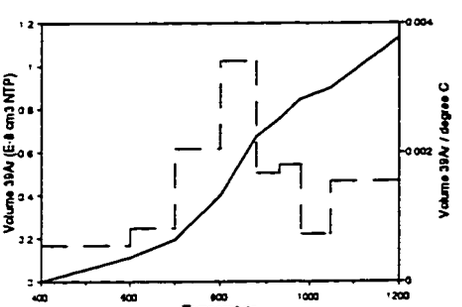

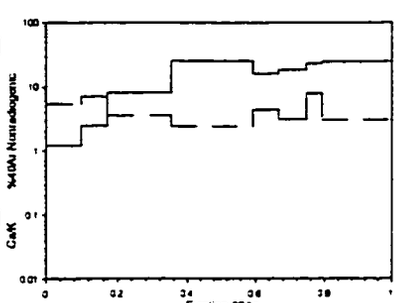

6.1F 16-70 biotite. Crown vein. Central deposits

Run: JF-18 103/13 Mass: 15.2 mg
Date: October 26 1992 J Value: 0.02324

Total 39Ar: 7.271 E-8 cm3 NTP Approx. 2.9% K
Integrated Age: 2517.4 +/- 4.8 Ma
Plateau Age: 2695.9 +/- 4.7 Ma (48.6% of 39Ar, steps marked by *)

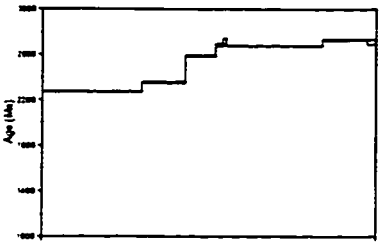

	Temp C	40/39	36/39	37/39	vol 39Ar E-8 cm3	Fraction 39Ar	%40Ar Rad.	Age Ma	+/-	Error 2 sigma
	500	118.427	0.0322	0.007	2.135	0.294	91.96	2275.8	+/-	2.6
	550	120.036	0.0150	0.015	0.949	0.130	96.31	2353.7	+/-	6.6
	600	141.996	0.0137	0.020	0.646	0.089	97.15	2591.5	+/-	5.5
*	650	153.603	0.0208	0.081	0.160	0.022	95.99	2683.9	+/-	11.7
*	700	162.706	0.0407	0.470	0.076	0.010	92.61	2715.0	+/-	26.8
*	800	148.802	0.0064	0.012	2.140	0.294	98.72	2678.6	+/-	2.0
*	850	156.719	0.0147	0.032	0.478	0.066	97.23	2729.9	+/-	6.5
*	900	156.806	0.0137	0.244	0.483	0.066	97.42	2733.8	+/-	2.9
*	1000	156.842	0.0229	1.257	0.193	0.027	95.68	2710.4	+/-	20.3
	1200	246.440	0.5880	8.114	0.010	0.001	29.50	1800.0	+/-	336.9

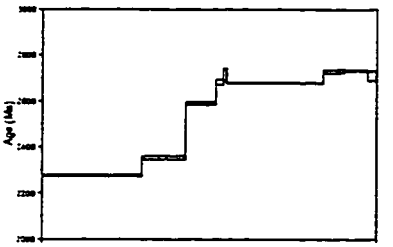

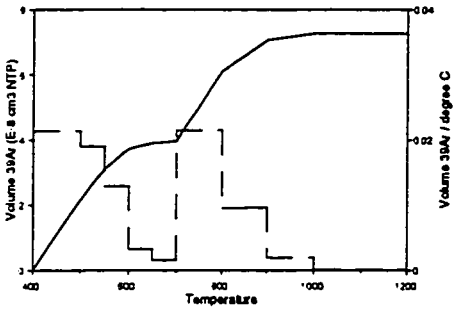

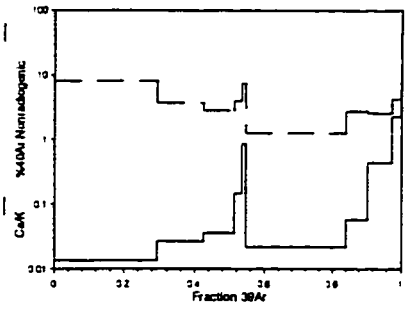

6.1G. PRS1177-28 biotite, Princess Royal vein

Run: JF-85 117/15 Mass: 8.0 mg
Date: April 25 1993 J Value: 0.02463

Total 39Ar: 6.439 E-8 cm3 NTP Approx. 4.6% K
Integrated Age: 2512.4 +/- 7.9 Ma
Plateau Age: 2721.5 +/- 8.2 Ma (70.2% of 39Ar, steps marked by *)

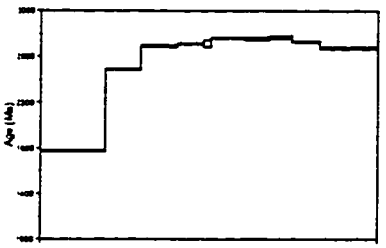

	Temp C	40/39	36/39	37/39	Vol 39Ar E-8 cm3	Fraction 39Ar	%40Ar Rad.	Age Ma	+/-	Error 2 sigma
	500	73.844	0.0193	0.003	1.265	0.196	92.27	1777.0	+/-	8.1
	550	122.049	0.0041	0.008	0.656	0.102	99.01	2490.2	+/-	6.0
*	600	141.398	0.0041	0.001	0.701	0.109	99.15	2694.5	+/-	6.8
*	650	143.845	0.0051	0.011	0.519	0.081	98.96	2715.9	+/-	6.4
*	700	145.938	0.0118	0.008	0.148	0.023	97.61	2716.9	+/-	32.8
*	790	148.361	0.0037	0.012	0.639	0.099	99.27	2763.9	+/-	5.5
*	840	148.482	0.0059	0.024	0.464	0.072	98.82	2758.6	+/-	9.2
*	890	150.137	0.0069	0.046	0.413	0.064	98.63	2771.7	+/-	11.0
*	940	145.727	0.0064	0.045	0.523	0.081	98.69	2730.4	+/-	4.7
*	1200	140.889	0.0076	0.038	1.110	0.172	98.41	2679.0	+/-	8.3

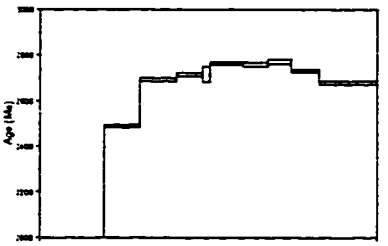

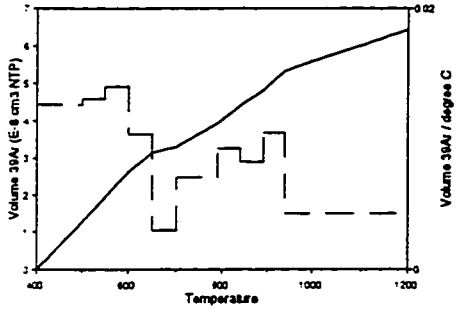

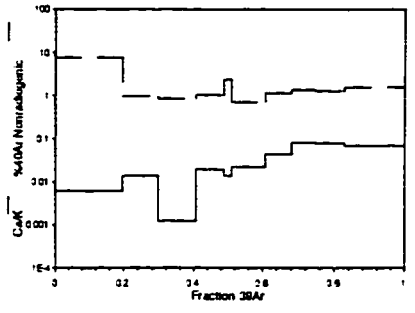

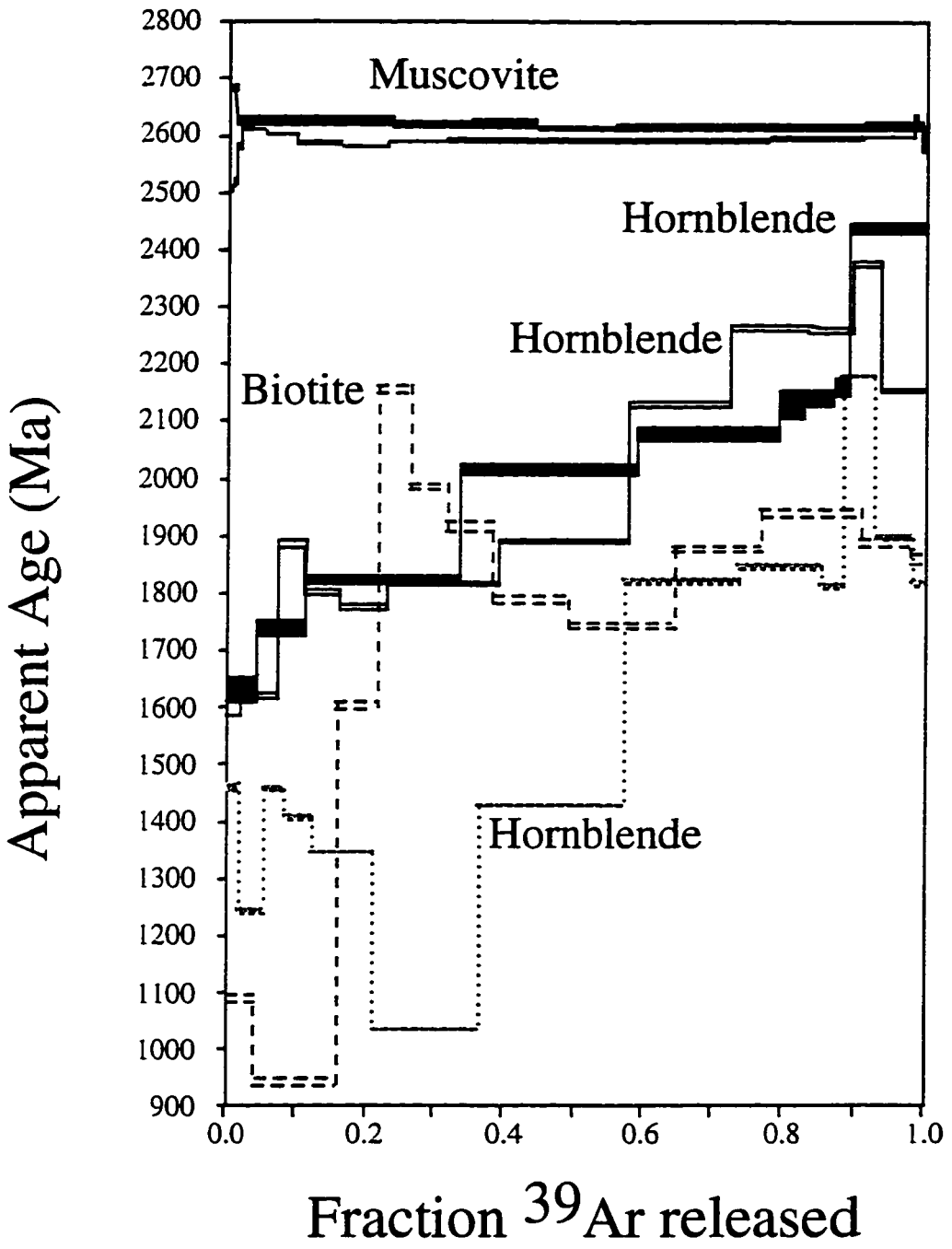

Figure 6.2. 40Ar-39Ar spectra for all samples from the Scotia mine

increase in ages is broadly monotonic and regular whereas in the samples of Kent (1994), the hornblende ^{40}Ar-^{39}Ar spectra are more irregular. Total gas ages for these samples range between 1570 to 2000 Ma (Kent and McCuaig, submitted). The single biotite sample analyzed also exhibits an irregular ^{40}Ar-^{39}Ar release spectrum (Fig. 6.2). Ages increase rapidly from 944 to 2153 Ma in the early stages of gas release, followed by a saddle-shaped region. The total gas age for this sample is 1751 ± 12 Ma, and the saddle shaped region (steps 5-12) has an integrated age of 1859 ± 12 Ma (Kent, 1994; Kent and McCuaig, in prep.).

Hydrothermal muscovite from the Main vein yields a release spectra with a well-developed plateau. This plateau in the spectra comprises 96.4% of ^{39}Ar released, and corresponds to an apparent age of 2599 ± 9 Ma (Fig. 6.1C). In contrast, hydrothermal biotite and amphibole from the O2 vein yield disturbed spectra, with poorly developed plateau segments corresponding to ages of ca. 2850 Ma and 2574 ± 10 Ma, respectively (Adam Kent, unpublished data, Fig. 6.1D).

Amphibole from wallrock and vein selvedge assemblages adjacent to the Crown vein exhibits a disturbed Ar release spectra. A moderately well-defined plateau-like segment can still be defined, however, comprising steps 4 through 8 and 64.7% of the ^{39}Ar released. This plateau corresponds to an age of 2543 ± 17 Ma (Fig. 6.1e). Biotite from the same location also exhibits an irregular release spectra. A plateau-like segment, comprising steps 4 through 9 and 49.6% of the ^{39}Ar released, yields an age of 2696 ± 5 Ma (Fig. 6.1F).

The biotite sample selected from the Princess Royal vein yields a convex-upward Ar release spectra. Steps 3 through 10 approximate a plateau-like segment, comprise 70.2% of the Ar released, and yields an age of 2722 ± 8 Ma (Fig. 6.1G).

6.2.4 Discussion of ^{40}Ar-^{39}Ar data

6.2.4.1 Age of pegmatite emplacement, Scotia mine

All available geochronological data for the Norseman Terrane is compiled in Figure 6.3. Note that the ages of plateau-like segments from pegmatite muscovites are also within error of a 2620 ± 36 Ma Sm-Nd isochron (garnet-albite) age of sample 91-237 (Kent, 1994) for these rocks. Intrusion of pegmatites of comparable composition to those at Scotia occurred elsewhere within the Yilgarn Block at this time (Bloem et al., 1995, Kent et al., in prep.), and was accompanied by widespread granitoid emplacement and metamorphism within middle- to lower-crustal regions (Kent et al. in prep.).

The slightly lower median values of the muscovite ^{40}Ar-^{39}Ar ages relative to the Sm-Nd internal isochron is consistent with the ^{40}Ar-^{39}Ar ages recording the time of

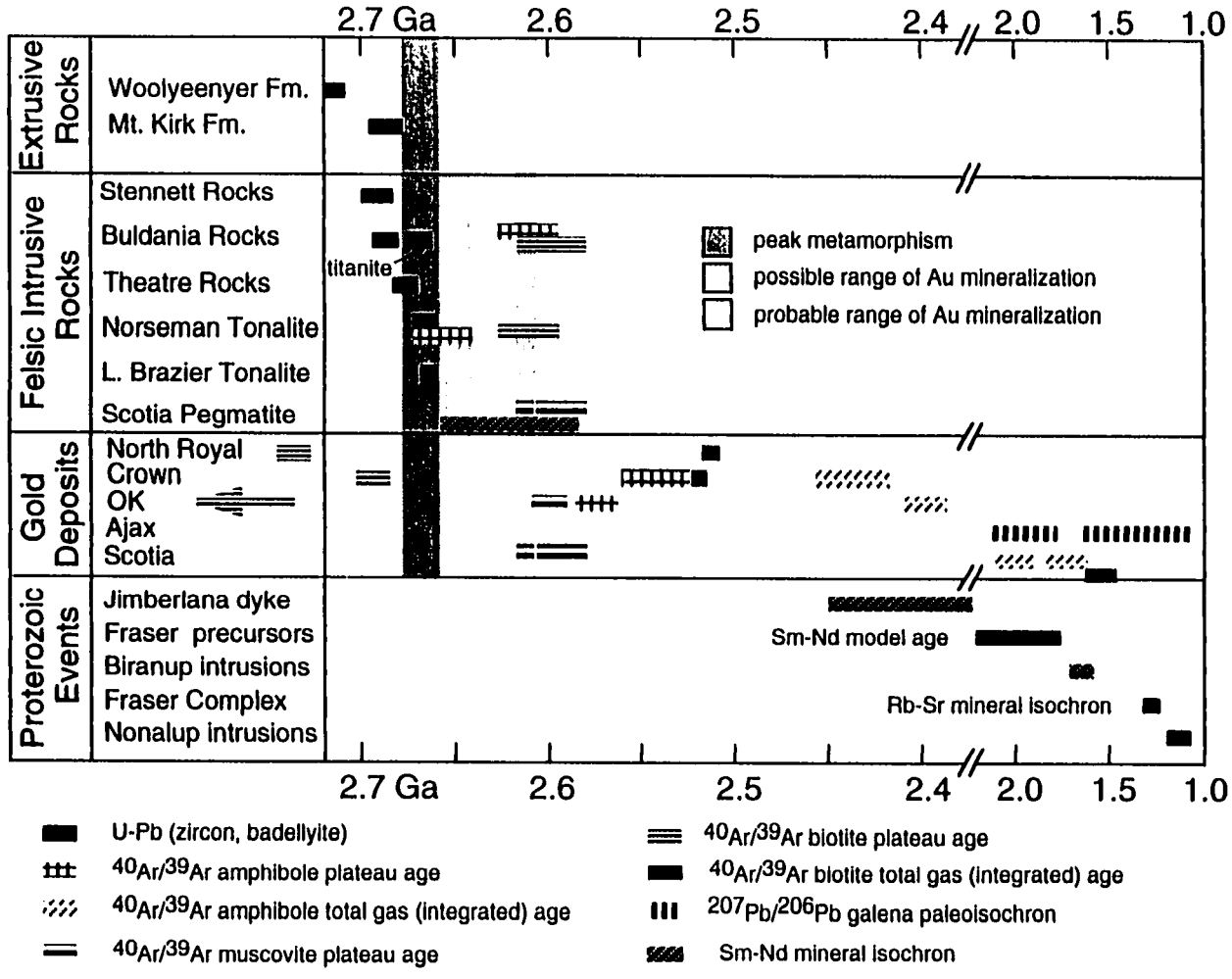

Figure 6.3 Compilation of available geochronological data for the Norseman Terrane and the Proterozoic Faser-Albany orogen. Data sources: Campbell and Hill (1988); Hill et al. (1989; 1992), Fletcher et al. (1987; 1991); Myers (1993); Kent, 1994; this study.

cooling of the pegmatite through the closure temperature for diffusion of Ar in muscovite (350 ± 50°C; McDougall and Harrison 1988). Considering that metamorphic and mineralization temperatures in this area were considerably above the closure temperature of muscovite (Chapter 5; McCuaig et al. 1993) it is probable that the muscovite ^{40}Ar-^{39}Ar ages represent the cooling of the pegmatite samples through the muscovite closure temperature, and provide a minimum estimate for the time of dyke emplacement. Evidence from ^{40}Ar-^{39}Ar dating of granitoids from elsewhere in the Norseman region suggests that this area cooled through the closure temperature of hornblende, biotite and muscovite, an approximate temperature range of 550 - 300°C, at ca. 2600 Ma (Fig. 6.3; Kent 1994; Chapter 2), consistent with the interpretation of the ca. 2600 Ma ages of muscovite from the pegmatites at Scotia as the result of slow cooling.

As gold-mineralized structures are cut by pegmatite dykes, this provides a minimum estimate of the timing of gold mineralization at the Scotia Mine. Gold mineralization at Scotia occurred prior to 2600 - 2630 Ma, which is consistent with field relations and radiometric ages which indicate a widespread gold mineralization event in the Yilgarn Craton at ca. 2630 Ma (e.g. Clark et al., 1989; Barnicoat et al.,1991, Wang et al., 1993; Groves, 1993; Bloem et al., 1995; Kent and McDougall, 1995; Kent and Hagemann, submitted).

6.2.4.2 Hydrothermal muscovite, OK mine

The muscovite from the OK mine, which appears intimately intergrown with main stage quartz veining, yields an apparent age within the range of ages obtained for muscovite from the Scotia pegmatite. This result corroborates the interpretation that the time interval 2590-2610 Ma represents final cooling of the Norseman Terrane through the closure temperature of muscovite (350 ± 50°C).

6.2.4.3 Age of gold mineralization

The above data, in combination with other available geochronological data on the evolution of the Norseman Terrane compiled on Figure 6.3, and the textural and geothermometry evidence detailed in Chapter 5, provide constraints on the age of gold mineralization. A minimum age for gold mineralization is provided by the ^{40}Ar-^{39}Ar ages obtained for igneous and hydrothermal muscovite, from two separate locations, which are identical within error at approximately 2600 Ma. It is likely that gold mineralization occurred significantly prior to this date, however, for the reasons detailed below.

(1) The pegmatite dykes at Scotia are emplaced in a brittle tectonic regime, and a

different far-field stress regime (as determined by dyke attitude) in comparison to the ductile, high-temperature mineralization and hydrothermal alteration.

(2) The mean age of the pegmatite as determined by an internal Sm-Nd isochron, although within error of the ^{40}Ar-$^{39}Ar_{muscovite}$ age, suggests a slightly older age of emplacement of ca. 2620 Ma.

(3) The mineralization in the Southern and Central deposits occurred at 50° C to as much as 300°C above the theoretical closure temperature for Ar diffusion in muscovite, so that the hydrothermal muscovite in the OK mine may have formed significantly prior to 2600 Ma.

(4) As was established in Chapter 5, the high-temperature hydrothermal alteration in the Central and Southern deposits occurred synkinematically, and syn- to post-peak metamorphism. Peak metamorphism is constrained by a ^{40}Ar-^{39}Ar age on amphibole from a tonalite intrusion immediately south of the OK mine. This age of 2656 ± 15 Ma suggests that the Norseman Terrane had cooled through the theoretical closure temperature for Ar diffusion in this amphibole sample (580 ± 50°C, Kent, 1994) by ca. 2640 Ma. As hydrothermal alteration assemblages associated with the Central and Southern lode gold deposits contain amphibole, and geothermometry suggests that the amphibole formed at a temperature close to its Ar-Ar closure temperature (well above the closure temperature for muscovite), it is likely that the gold deposits formed closer to 2640 Ma than 2600 Ma.

Thus, hydrothermal alteration and lode gold mineralization in the Norseman terrane is constrained to have occurred between 2640 Ma and 2610 Ma, although consideration of textures and calculated temperatures of alteration assemblages versus those of pegmatite emplacement suggest that mineralization occurred closer to 2640 Ma.

6.2.4.4 Disturbance of ^{40}Ar-^{39}Ar spectra in hydrothermal amphibole and biotite

Whereas both igneous and hydrothermal muscovite exhibit well developed plateaux in their ^{40}Ar-^{39}Ar release spectra, hydrothermal biotite and amphibole yield erratic release spectra. The release spectra of the hydrothermal biotite and amphibole have only poorly developed or no plateau-like segments that correspond to apparent ages that are either much too old, as for biotite from the Northern and Central deposits, or too young, as for all amphiboles and biotite from Southern deposits. The cause of the erratic ^{40}Ar-^{39}Ar spectra observed in these hydrothermal minerals is uncertain. In general, erratic spectra may be due to a number of factors, including:

(1) Recoil of ^{39}Ar into finely intergrown phases, such as chlorite (in biotite), or exsolution lamellae (in amphibole) during sample irradiation (e.g. Harrison and

Fitzgerald, 1986; Lo and Onstott, 1989). In all samples, biotite is occasionally observed to be finely intergrown with chlorite, and the low potassium contents of these biotites suggest that this intergrowth may be widespread on a submicroscopic scale (Fig. 6.2; Kent, 1994; Kent and McCuaig, submitted). The saddle-shaped spectrum exhibited by the Scotia biotite sample is similar to spectra observed in other biotite samples known to contain intergrown chlorite. However, recoil effects due to biotite-chlorite intergrowths should not lower or raise the apparent ages of these samples by > 100 Ma, as is observed. Amphiboles in the hydrothermal alteration assemblages often contain inclusions of quartz and ilmenite, but intimate intergrowths with other phases such as chlorite or biotite, are only rarely observed under the petrographic microscope in the analyzed samples. Microprobe analyses of numerous amphiboles indicate that hydrothermal hornblende and actinolite can both be present in a single sample (Chapter 5). Usually hornblende cores are rimmed by actinolite, although coexisting actinolite and hornblende can occur on grain boundaries, and vein selvedges, where the intergrowth is temporally related to the gold-related hydrothermal alteration. Radiogenic argon obtained from these samples should emanate mostly from the hornblendes, given their relatively higher K contents. Recoil effects due to hornblende-actinolite intergrowth may disturb Ar release spectra, and may explain the young ages obtained for hydrothermal amphiboles from the Central deposits. Recoil effects should not, however, cause the calculated ages to be lower than the intergrowth formation age by > 600 Ma, as is observed in the Southern deposits (Fig. 6.1; Kent and McCuaig, submitted).

(2) Incorporation of multiple components of extraneous argon of non-atmospheric isotopic composition (e.g. Heizler and Harrison, 1988). Addition of extraneous argon may have occurred at the time of crystallization of the mineral phases, or may have been "trapped" at some later time, possibly during interaction between the mineral and a fluid. However, the highly radiogenic nature of the argon released from the majority of steps from these samples indicates that this effect was most probably minimal (Fig. 6.1). However, incorporation of extraneous radiogenic Ar may be the cause of the anomalously old apparent ^{40}Ar-^{39}Ar ages calculated for biotites from the Northern and Central deposits.

(3) ^{40}Ar-^{39}Ar release spectra from minerals such as biotite and hornblende may also be complicated by the known propensity for hydrous minerals to degas in a non-Arrhenius fashion under vacuum conditions (McDougall and Harrison, 1988). The degassing of these minerals is poorly understood, and may be particularly

complex where different minerals are intergrown or exsolved into different phases. However, the effects of non-Arrhenius degassing should not lower the calculated age spectra for the samples by the > 600 Ma observed.

On balance, non of the effects outlined above can adequately account for the extremely disturbed spectra of hydrothermal amphibole and biotite from the Scotia deposit.

6.2.4.5 Resetting of ^{40}Ar-^{39}Ar systematics in hydrothermal biotite and hornblende

The above results provide an insight into the ^{40}Ar-^{39}Ar systematics of hydrothermal minerals in amphibolite-facies Archean gold deposits. Hydrothermal biotite and hornblende, which from textural relations demonstrably formed during gold mineralization and associated hydrothermal alteration (Chapter 5; McCuaig et al., 1993), have plateau (or total gas, if no plateau) ^{40}Ar-^{39}Ar ages which are ca. 25 - 1000 Ma younger than the minimum age of mineralization, as given by the 2600 - 2630 Ma ^{40}Ar-^{39}Ar and Sm-Nd ages from cross-cutting pegmatite dykes and hydrothermal muscovite. This is despite the fact that, in two cases at Scotia, samples of pegmatite and hydrothermal minerals came from within several metres of each other.

The close spatial association of disturbed hydrothermal minerals and the relatively undisturbed pegmatite muscovite at Scotia allows insight into the nature of the processes responsible for argon loss in hydrothermal biotite and hornblende. Simple reheating of the Scotia Mine and environs cannot explain the observed argon loss. Hornblende and biotite with total gas ^{40}Ar-^{39}Ar ages of 1572 Ma and 1751 Ma, respectively, occur within a few metres of muscovite with a plateau age of 2610 Ma. Estimates for the closure temperature of argon diffusion in hornblende (500 ± 50 °C; Harrison, 1981) are considerably higher than that of muscovite (350 ± 50°C; Jaeger, 1979; McDougall and Harrison, 1988), thus any thermal disturbance capable of causing argon loss from hornblende would also be expected to completely reset argon systematics within muscovite in the adjacent pegmatite.

It is concluded from the above considerations that the observed release spectra must be the result of isotopic resetting at temperatures below that of the closure of argon diffusion in muscovite (and thus also hornblende). The most likely explanation for the observed argon loss in hydrothermal hornblende and biotite may lie in the movement of fluids through the Scotia deposit at some time after mineralization. Late fluid infiltration within the Scotia mine is recorded by the presence of low temperature alteration assemblages associated with the numerous brittle faults that dissect the orebody (Chapter

4). Interaction and exchange between these late fluids and hydrothermal biotite and hornblende may have removed argon from these phases at temperatures below that of the closure temperature of muscovite. Fluid movement must also have occurred on the grain boundary scale through foliated hydrothermal alteration assemblages to produce the degree of resetting observed in the samples. Muscovite within the unfoliated and thus relatively impermeable pegmatites remained apparently unaffected by this fluid movement, and retains an Archean age.

Such a scenario may also produce the disturbed ^{40}Ar-^{39}Ar spectra of amphiboles from the Central deposits. These deposits are also transected by numerous small scale, and less common large scale, brittle faults (Chapter 4). The brittle nature of these structures, in combination with the low temperature hydrothermal assemblages found associated with them, indicate formation in a low P-T environment (Chapters 4, 5). Fluid movement along such structures, and percolation along grain boundaries in the foliated alteration assemblages, could explain why hydrothermal amphiboles are disturbed, whereas amphibole in a relatively impermeable tonalite body nearby is not (Fig. 6.3). Significantly, hydrothermal muscovite in the OK mine is affected by later deformation and fluid movement, along the vein selvedge, as evidenced by kinked grains, undulose extinction and cross-cutting carbonate, yet the Ar spectra in this sample is apparently undisturbed. This observation corroborates other studies, which indicate that muscovite is relatively less prone to isotopic resetting below its theoretical closure temperatures than biotite (Hess et al., 1987; Dunlap et al., 1991).

Miller et al. (1991) document a similar scenario in metamorphic hornblende and biotite at temperatures considerably lower than the accepted closure temperatures of hornblende. Miller et al. (1991) demonstrated that reset hornblendes have excess structural water and anomalous δD values, and interpreted this to indicate that exchange between the hornblende and fluid was the most probable cause of argon loss. However, the δD values of hydrothermal amphiboles and biotites from the Norseman lode gold deposits are consistent with those expected for Archean lode gold fluids, indicating that the hydrogen isotope systematics were not affected by the fluids that reset argon isotopes at low temperatures. It is unlikely that the late fluids fortuitously maintained isotopic equilibrium with their contiguous fluid conduits, such that they were rock-buffered and thus did not displace calculated fluids from the expected range for Archean lode gold deposits (Fig. 6.4). The argon and hydrogen isotope data collectively indicate that Ar isotope systematics are easier to disturb than H isotope systematics. Argon is unbound in the crystal lattice of minerals and may be easier to lose during late brittle deformation and fluid percolation.

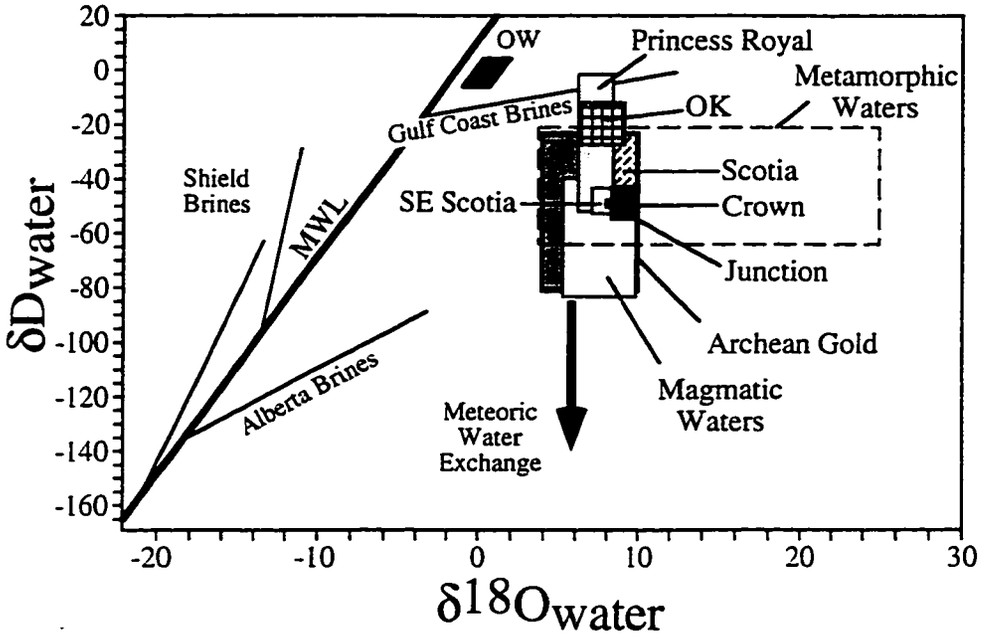

Figure 6.4 δD versus $\delta^{18}O$ diagram showing the compositional ranges of fluids involved in hydrothermal alteration associated with lode gold deposits of the Kalgoorlie and Norseman Terranes, as calculated from the isotopic compositions of quartz and hydrous silicates that are assumed to be in isotopic equilibrium, compared to those from other Archean lode gold deposits (Table 5.4; Kerrich, 1989). Also shown are the fields for metamorphic, magmatic, ocean and meteoric waters (after O'Neil, 1987). Fields for basinal brines (Alberta, Gulf Coast) and shield brines are taken from Kerrich (1989).

6.3. Pb isotope studies

6.3.1 Introduction

Studies of the Pb-isotopic compositions of galena and altaite from Archean lode gold deposits have recognized trends on two scales: (1) regional variations of least radiogenic compositions, which are interpreted as the best estimates of initial ore fluid Pb, on the scale of entire terranes (Franklin et al, 1983; Browning et al., 1987; McNaughton et al., 1990; 1992, 1993; Ho et al., 1992; Perring and McNaughton, 1992), and (2) local variations within single mining camps or deposits to anomalously radiogenic compositions (Franklin et al., 1983; Browning et al., 1987; Moritz et al., 1990; Perring and McNaughton, 1990; 1992; Hattori, 1993; Cassidy and McNaughton, in prep; McNaughton et al., in prep).

The Pb isotope data from the Norseman Terrane appear to be unique in that they show the widest range in Pb-isotope compositions for galena and altaite of any lode gold district, and include the most radiogenic Pb of any lode gold deposit in the Yilgarn Craton (Browning et al., 1987; Perring and McNaughton, 1990, 1992). However, studies by Browning et al. (1987), Perring (1990), and Perring and McNaughton (1990, 1992), were either reconnaissance in nature, or restricted to a few deposits such that unique interpretation of the controls on the within-camp variation of initial Pb composition was hampered by the lack of sufficient three-dimensional coverage of the Norseman gold deposits.

The aims of this section are to present Pb-isotope data that better reflect the regional and local controls of structure, host lithology and spatial distribution on the observed Pb isotope variation of galena and altaite at Norseman. The implications that these Pb data hold for genetic models for lode gold deposits within the southern ECYS, the nature of the crust beneath the Norseman Terrane, and the post-mineralization modification of these deposits, is also discussed.

6.3.2 Sample selection and analytical methods

Samples analyzed for this project were carefully selected to provide relatively complete three-dimensional coverage of the Norseman area, and to help constrain the various possible controls on Pb-isotope composition. Galena and altaite samples were selected from a wide variety of paragenetic sites: isolated in quartz, proximal to vein laminations, on sheared vein laminations, fracture-fillings in pyrite, and fracture coatings in quartz. Unfortunately, no suitable material for determination of initial Pb isotope composition was found in the Scotia deposits at the southern end of the Norseman

Terrane. Microcline from these deposits is too fine-grained and extensively retrogressed, and no galena has been detected in the samples collected from the mine. Samples from the Poseidon South pit at Higginsville have also been analyzed to provide better regional coverage of the southern Norseman-Wiluna belt, and to allow comparison of initial Pb in the Norseman Terrane to that in the nearest deposit in the Kalgoorlie Terrane to the north (Fig. 6.5).

Galena and altaite grains from the selected samples were removed from hand specimens with the point of a clean scalpel. Galena generally predominates over altaite, but the proportions of these two minerals can vary substantially both within and between deposits. Galena and altaite are in textural equilibrium and cannot be practically separated, and thus were analyzed together in some cases. Galena was dissolved in 3N HCl made up from reagents distilled in quartz stills under clean room conditions. Any visible residue was dissolved in 3N HNO_3 and assumed to be altaite, but may have contained some residual galena. Lead from all samples was purified using anion exchange resin in an HBr-HCl medium. Isotopic determinations were carried out by Neal McNaughton on a VG 354 solid-source mass-spectrometer at Curtin University of Technology. Measured ratios were corrected for mass fractionation by normalization to replicate analyses of SRM-981 lead. The Broken Hill galena standard was analysed during the period of analysis and gave data within accepted errors. Analytical precision in the Pb isotopic ratios is approximately 0.15% (2σ) or better. The Pb isotope data and details of sample locations are presented in Table 6.1.

6.3.3. Results

The Pb-isotope data are graphically presented in Figure 6.6. Data of Browning et al. (1987) and McNaughton et al. (1990) are also presented for reference. In $^{207}Pb/^{204}Pb$ versus $^{206}Pb/^{204}Pb$ isotope coordinates, two distinct linear arrays are present; a steep array of least-radiogenic compositions from each deposit, and a shallower array trending to much more radiogenic compositions (Fig. 6.6A). The least-radiogenic galena and altaite are in textural equilibrium, are paragenetically related to hydrothermal alteration and quartz vein emplacement, and provide the closest approximation of the Pb-isotopic composition of the Archean auriferous fluid that formed the Norseman quartz vein systems. These galena and altaite are termed "early". "Late" galena and altaite comprise the radiogenic compositions that are quite distinct from those of the early galena and

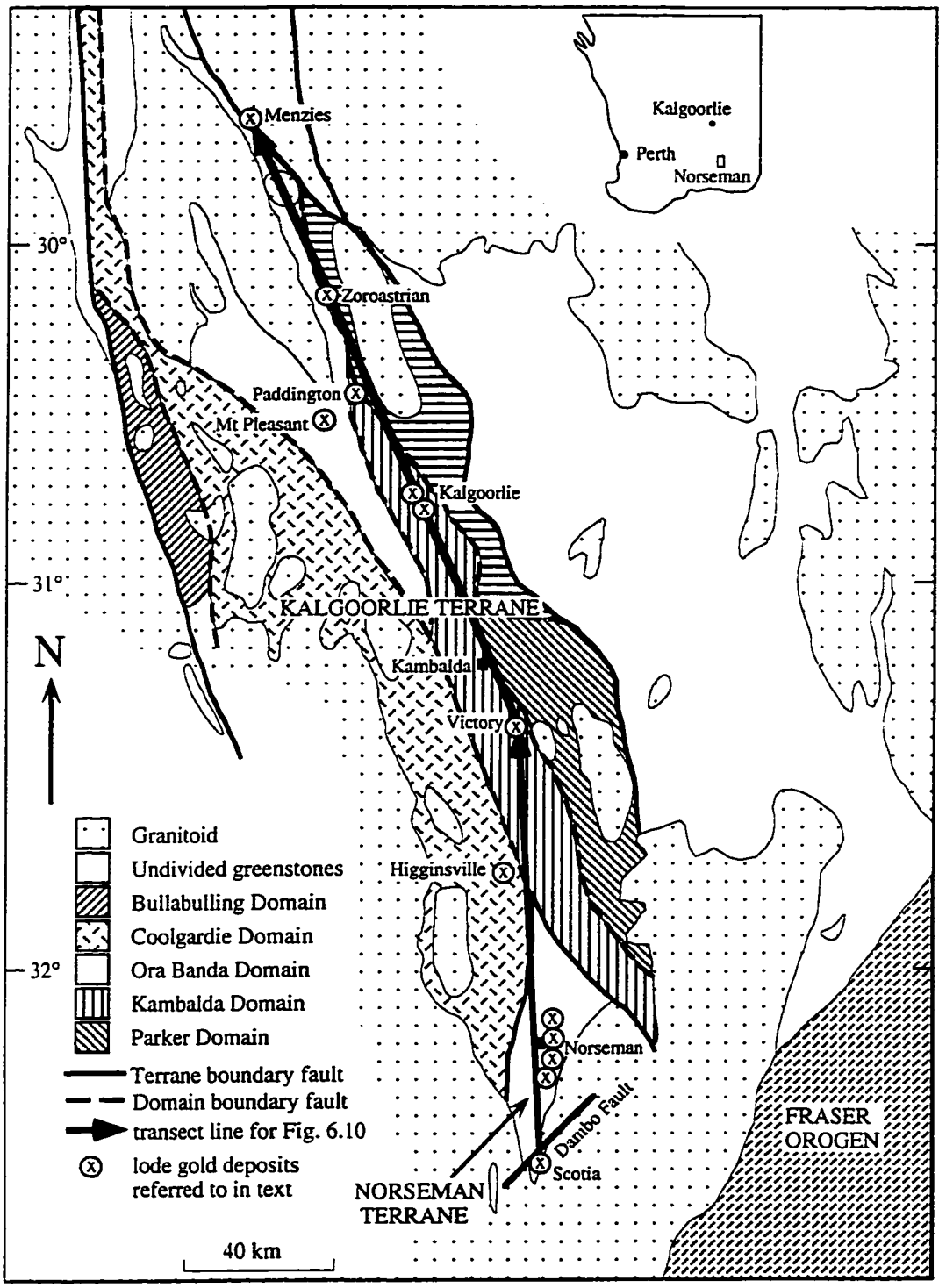

Figure 6.5. Simplified geology of the Norseman and southern Kalgoorlie Terranes, showing the locations of lode gold deposits discussed in the text. After Swager et al. (1990, 1992).

Table 6.1 Pb-isotope composition of galena and altaite from the Higginsville and Norseman deposits

Sample #	Mine	Vein	Location	206Pb/ 204Pb	207Pb/ 204Pb	208Pb/ 204Pb	Ref.	Dist. from Penn. (km)	Proximity to felsic rocks (m)	Proximity to large brittle structures (m)	Sample description
Early Galenas from lode gold deposits											
HIGGINSVILLE											
Hig-1	Poseidon South	Main	N end	13.789	14.879	33.508	1		>100	?	e.g. gn + FGV + asp isolated in qtz, gabbro host
Hig-2	"	"	"	13.786	14.875	33.501	1		>100	?	"
F711	"	?????	?????	13.791	14.832	33.527	2		>100	?	"
NORSEMAN TERRANE											
Norseman 1	Regent	?????	?????	14.065	15.174	33.868	3	?	>100	?	no details available
Norseman 2	"	"	"	14.044	15.111	33.685	3	?	>100	?	"
Norseman 3	"	"	"	14.037	15.139	33.803	3	?	>100	?	"
Norseman 4	"	"	"	14.009	15.085	33.646	3	?	>100	?	"
Norseman 5	"	"	"	13.995	15.091	33.702	3	?	>100	?	"
Norseman 6	"	"	"	14.027	15.093	33.625	3	?	>100	?	"
Norseman 7	"	"	"	14.035	15.131	33.739	3	?	>100	?	"
UWA 108336	Ajax	Mararoa	10/1400 stope	14.028	15.107	33.630	4	2.30	<100	>200	gn in qtz, mafic host
UWA 108337	"	Mararoa	"	14.050	15.115	33.631	4	2.30	<100	>200	"
UWA 108354	"	Mararoa	10/1200 stope	14.047	15.125	33.659	4	2.28	<10	<10	gn in qtz
UWA 108357	"	Mararoa	12/1282 stope	14.074	15.141	33.709	4	2.23	<30	<10	"
UWA 108358	"	Mararoa	"	14.063	15.126	33.662	4	2.23	<30	<10	"
UWA 108362	OK	Main	5/610 stope	14.049	15.121	33.653	4	3.30	<1	>300	gn in qtz, mafic/felsic contact
NR-35	North Royal	Main	5/150N stope	14.019	15.101	33.655	1	5.60	<100	>50	gn + FGV + py + sp isolated in deformed qtz
NR-35-1	"	"	"	14.015	15.095	33.672	1	5.60	<100	>50	vein, gabbro host, ~50m from PRFZ
NR-5/450	"	"	5/450S stope	14.079	15.128	33.775	1	5.20	<30	>100	gn + py + FGV on lamination in qtz vein, mafic host
RT-10/390	North Royal	Royal Tiara	10/390 stope	13.953	15.043	33.595	1	5.10	>100	>10	alt + gn isolated in boudinaged qtz vein, mafic host
S3151-1	East of Regent	Mt. Barker	S3151, 126m	14.112	15.170	33.673	1	2.50	<1	?	gn + sp +po on lamination in qtz vein,
S3151-2	"	"	"	14.115	15.168	33.664	1	2.50	<1	?	host = mafic/felsic contact
M11/76-2	Regent	Mararoa	11/76 stope	13.996	15.083	33.599	1	2.95	>100	>100	gn + alt + FGV isolated in boudinaged qtz, mafic host
RM-1	"	"	29 lvl, 1900mN	14.059	15.153	33.775	1	2.33	>100	>100	gn adjacent to brittle fracture in qtz vein, mafic host
RM-22	"	"	29 lvl, 2160mN	14.040	15.120	33.665	1	2.34	>100	>100	"
RM-71	"	"	25 lvl, 2075mN	14.058	15.160	33.789	1	2.43	>100	<100	gn + alt from centre of boudinaged qtz vein, mafic host
RM-74	"	"	"	14.022	15.105	33.655	1	2.43	>100	<100	e.g. gn from neck of boudinaged qtz vein, mafic host
RM-99-1	"	"	11 lvl, 2050mN	14.021	15.117	33.734	1	2.80	>100	<100	f.g. gn + alt in deformed qtz vein, mafic host
C-12	Regent	Crown	14 lvl vertical	13.985	15.078	33.617	1	3.10	>200	>300	gn + sulphides isolated in qtz vein, mafic host
C20	"	"	16 lvl X-cut	13.987	15.085	33.649	1	2.90	>300	>300	"
AJ-23a-2	Ajax	Norseman	7 lvl, 900mS	14.151	15.179	33.807	1	1.86	<100	>100	e.g. gn isolated in qtz, mafic host
AJ-23b	"	"	"	14.095	15.153	33.690	1	1.86	<100	>100	e.g. gn on lamination in qtz vein, 3cm from AJ-23a

Table 6.1 (continued)

Sample #	Mine	Vein	Location	206Pb/ 204Pb	207Pb/ 204Pb	208Pb/ 204Pb	Ref.	Dist. from Penn. (km)	Proximity to felsic rocks (m)	Proximity to large brittle structures (m)	Sample description
AJ-34	"	"	7/656 stope	14.060	15.124	33.671	1	1.86	>100	>100	e.g. gn + sp + FGV isolated in qtz, mafic host
AJ-56-1	Ajax	Mararoa	10 lvl, 1200mS	14.144	15.148	33.726	1	2.24	<1	<20	e.g. gn isolated in qtz along mafic/felsic contact
AJ-56-2	"	"	"	14.126	15.182	33.852	1	2.24	<1	<20	"
AJ-75	Ajax	Mararoa	12 lvl, 1150mS	14.082	15.137	33.693	1	2.20	>100	<30	e.g. gn + FGV in fracture in py, mafic host
RS-11	Viking	Royal Standard	450W stope	14.088	15.164	33.795	1	2.35	>100	<30	e.g. gn isolated in qtz, mafic host
RS-13-1	"	"	"	14.096	15.181	33.821	1	2.07	>100	<30	e.g. gn on sulphide-rich lamination in qtz vein,
RS-13-2	"	"	"	14.068	15.135	33.677	1	2.07	>100	<30	mafic host
OK-L	OK	O2/Main	6 lvl, 850mW	14.042	15.117	33.671	1	3.55	<30	<1	e.g. gn isolated in qtz, mafic host
OKM 3/585-1	OK	Main	3/585 stope	14.062	15.129	33.687	1	3.30	<1	>300	e.g. gn in qtz vein at mafic/felsic contact
Late Galenas from lode gold deposits											
AJ-5	Ajax	Norseman	7/1530 stope	14.417	15.225	33.835	1		<1	<20	e.g. gn + alt (+ ser + FGV ± sp) on fractures in qtz and
AJ-4-1	"	"	"	14.167	15.193	33.838	1		<1	<20	py, felsic host
AJ-4-2	"	"	"	15.123	15.432	34.254	1		<1	<20	"
AJ-4-3	"	"	"	15.511	15.302	35.075	1		<1	<20	"
AJ-23a-1	Ajax	Norseman	7 lvl, 900mS	14.280	15.192	33.828	1		<100	>100	e.g. gn isolated in qtz, mafic host
AJ-58 gn	Ajax	Mararoa	10 lvl, 1200mS	20.639	16.970	37.143	1		<1	<20	microfaulted gn crystals in qtz <5m from AJ-56
AJ-58 gn2	"	"	"	18.374	16.375	35.905	1		<1	<20	hosted at mafic/felsic contact
AJ-58 gn3	"	"	"	20.410	16.914	37.007	1		<1	<20	"
UWA108355	"	"	10/1200 stope	14.901	15.377	34.054	4		<10	<20	gn +Au on fractures in qtz and py
UWA108355a	"	"	"	14.930	15.380	34.054	4		<10	<20	"
UWA108355b	"	"	"	14.870	15.365	34.020	4		<10	<20	"
UWA108355c	"	"	"	14.896	15.376	34.051	4		<10	<20	"
UWA108355d	"	"	"	14.759	15.357	34.023	4		<10	<20	"
UWA108356	"	"	12/1282 stope	14.664	15.318	33.908	4		<30	<20	"
UWA108356a	"	"	"	15.372	15.540	34.208	4		<30	<20	"
UWA108356b	"	"	"	15.104	15.471	34.114	4		<30	<20	"
UWA108356c	"	"	"	15.238	15.503	34.164	4		<30	<20	"
UWA108356d	"	"	"	15.279	15.513	34.163	4		<30	<20	"
UWA108356e	"	"	"	15.217	15.497	34.138	4		<30	<20	"
UWA108356f	"	"	"	15.424	15.562	34.262	4		<30	<20	"
UWA108356g	"	"	"	14.940	15.415	34.038	4		<30	<20	"
UWA108357a	"	"	"	14.584	15.298	33.915	4		<30	<20	"
UWA108357b	"	"	"	14.529	15.245	33.895	4		<30	<20	"
UWA108357c	"	"	"	14.664	15.313	34.033	4		<30	<20	"

references: 1 = this study, 2 = Cater (1992), 3 = Browning et al. (1987), 4 = Perring and McNaughton (1990)
abbreviations: alt = altaite, FGV = free gold visible, gn = galena, po = pyrrhotite, lvl = mine level, py = pyrite, qtz = quartz, ser = sericite, sp = sphalerite

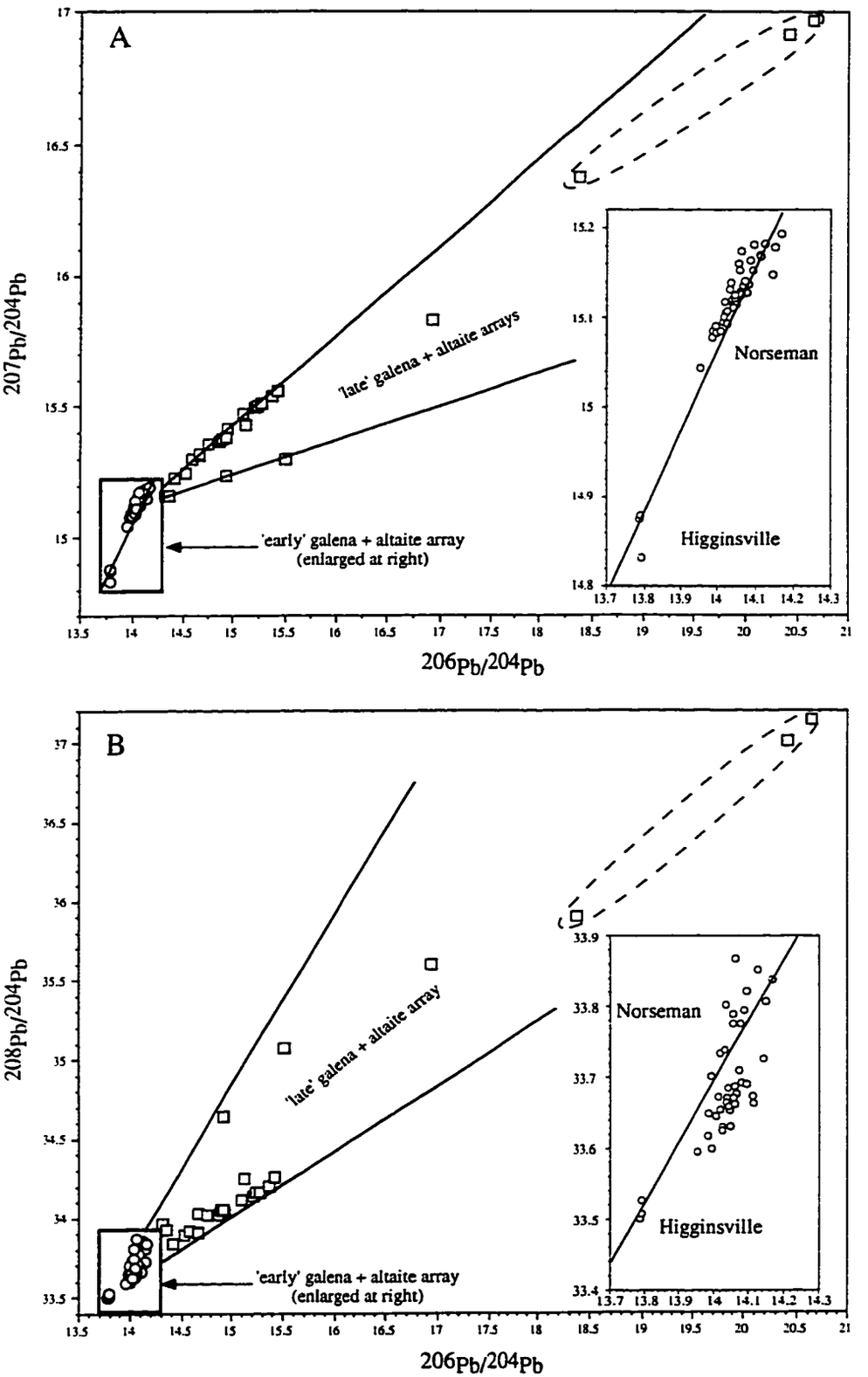

Figure 6.6. Plots of (A) $^{207}Pb/^{204}Pb$ vs. $^{206}Pb/^{204}Pb$ and (B) $^{208}Pb/^{204}Pb$ vs. $^{206}Pb/^{204}Pb$ for all galena and altaite samples from the Norseman and Higginsville lode gold deposits. Early vs. late galena + altaite arrays are indicated. Samples enclosed by the dashed line are from sample AJ58, and were taken from within 2 cm of each other.

altaite, are in textural equilibrium with each other, and are sited in fractures within the quartz veins and earlier sulphides. The two generations of galena + altaite can also be distinguished as linear arrays of differing slope in $^{208}Pb/^{204}Pb$ versus $^{206}Pb/^{204}Pb$ isotope coordinates (Fig. 6.6B).

6.3.4. Discussion of Pb data

6.3.4.1 Early galena + altaite: Pb isotope compositions as a tracer of Pb source reservoirs

Because galena and altaite incorporate large amounts of Pb, but virtually exclude Th and U in their crystal structures, these ore minerals may potentially preserve the Pb isotope composition of the fluid(s) from which they precipitated (Doe and Stacey, 1974; Franklin et al., 1983; Browning et al., 1987; Moritz et al., 1990; Perring and McNaughton, 1992; Ho et al., 1992; McNaughton et al., 1992; 1993; Hattori, 1993). In lode gold deposits such as those of the Norseman Terrane where galena and altaite show extreme variation in Pb-isotopic compositions, the least radiogenic compositions are taken as the closest approximation of the Pb-isotopic composition of the original ore forming fluid. This is a valid assumption, as any post-mineralization disturbance of the Pb isotopic composition of these minerals, such as Pb from in-situ decay of U or Th in included or adjacent silicates, or later isotopic resetting, would result in more radiogenic compositions.

There are many potential sources of Pb that the Norseman ore fluids may have encountered, including the host greenstones, upper mantle, basement rocks beneath the greenstones, felsic stocks that intrude the greenstone belt, and the large external granitoid batholith complexes that bound the greenstone terranes. The initial Pb compositions of these potential source reservoirs at the time of their formation and at the time of lode gold mineralization (taken as ca. 2630 Ma, see discussion of Ar data) are plotted with early galena and altaite data from lode gold deposits of the Norseman and southern Kalgoorlie Terranes on Figures 6.7 and 6.8.

The initial Pb isotopic composition of the host greenstones at the time of their formation is preserved in Pb-rich sulphides in syngenetic massive sulphide deposits, including VMS and komatiite-hosted Cu-Ni ores, that are coeval with their enclosing greenstones (Franklin et al., 1983; Browning et al., 1987). As the mafic-ultramafic volcanic sequences that dominate the Norseman-Wiluna belt are mantle-derived, these sulphides also provide the best estimate of mantle Pb isotopic compositions at the time of greenstone formation. However, since some mafic-ultramafic magmas are contaminated by continental crust (Arndt and Jenner, 1986; Compston et al., 1986; Claoué-Long et al., 1988), their isotopic composition reflects that of mantle-derived

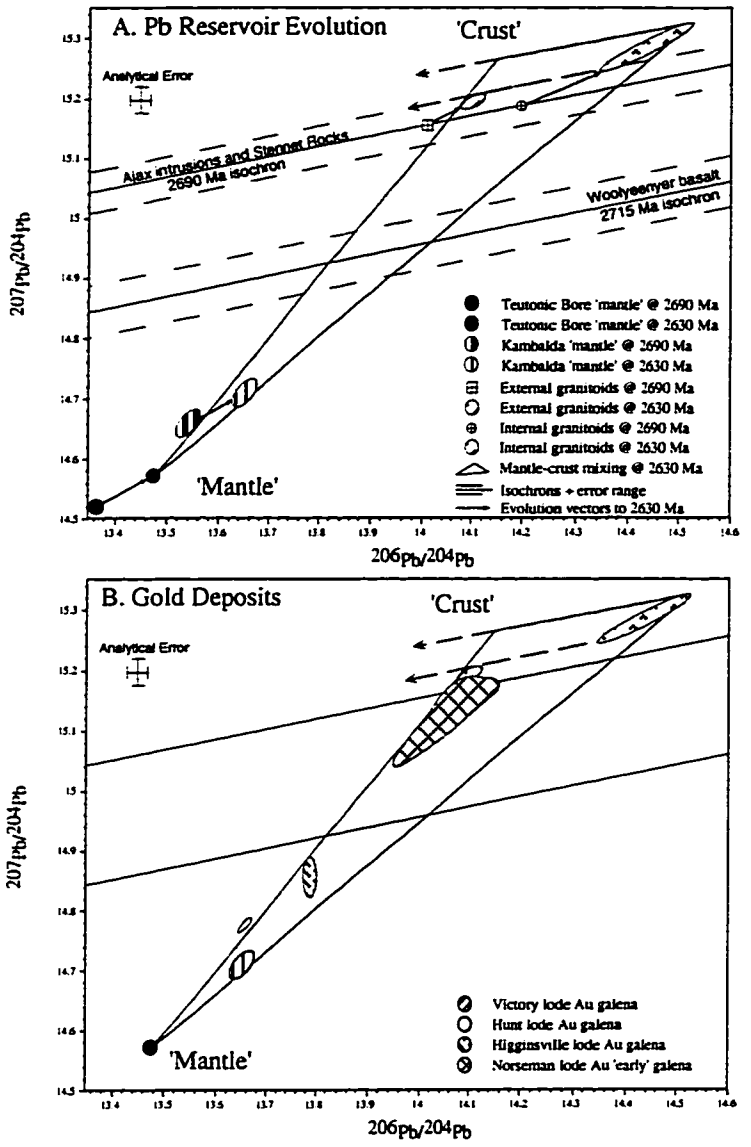

Figure 6.7. Plot of (A) composition and evolution of possible Pb reservoirs for the Norseman Terrane, and (B) early galena and altaite data from the Norseman and Higginsville lode gold deposits in $^{207}Pb/^{204}Pb$ vs. $^{206}Pb/^{204}Pb$ space, and comparison to data from other lode gold deposits of the southern Kalgoorlie Terrane, 'mantle' and host rocks at the time of mineralization (ca. 2630 Ma). Lode gold early galena and altaite data reflect mixing of Pb from two reservoirs: mantle or mantle-derived greenstones, and older crust or felsic intrusions derived from older crust. Data sources: Teutonic Bore 'mantle' @ 2690 Ma (pyrite in VMS ore) from McNaughton et al. (1990); Kambalda 'mantle' @ 2700 Ma (pyrite in Cu-Ni ores) from Browning et al. (1987); Victory and Hunt lode gold galena, and internal granitoids initial ratios @ 2690 Ma (crossed circle), isochron and evolution to 2630 Ma from Perring (1990) and Perring and McNaughton (1992); External granitoids initial ratios (crossed square), isochron and evolution to 2630 Ma calculated using data of Oversby (1975) and a U/Pb_{zircon} age of 2690 Ma (Campbell and Hill, 1988). Mantle compositions were evolved from syngenetic sulphide ore formation to 2630 Ma using a mantle $^{238}U/^{204}Pb$ range of 7.5-8.0 (Moorbath and Taylor, 1981). Woolyeenyer basalt isochron from Perring and McNaughton (1992) and a $U/Pb_{badellyite}$ age of 2715 Ma (Hill et al., 1992).

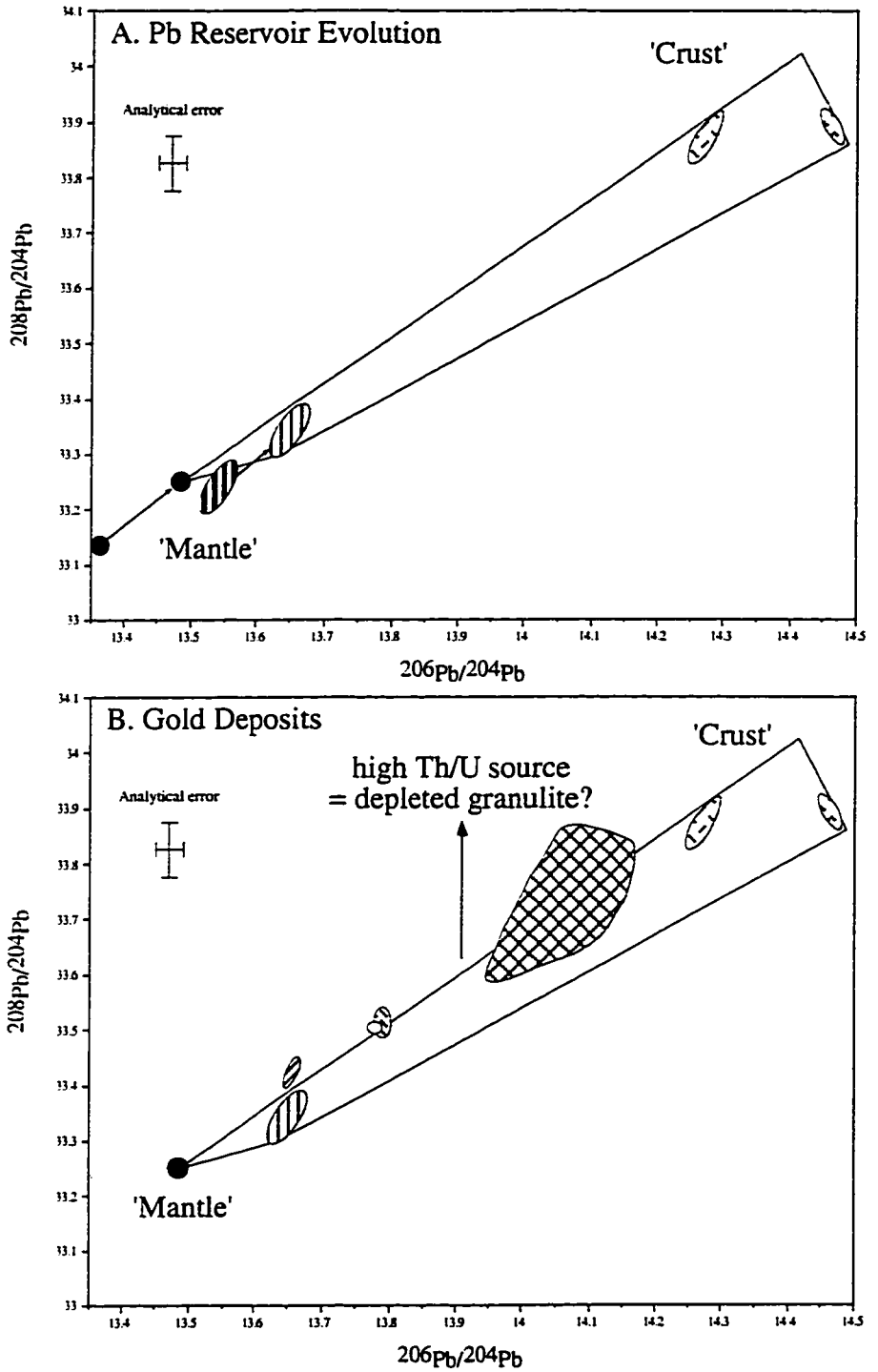

Figure 6.8. Plot of (A) Possible Pb reservoirs evolved to the time of mineralization (ca. 2630Ma), and (B) early galena and altaite data from the Norseman and Higginsville lode gold deposits in $^{208}Pb/^{204}Pb$ vs. $^{206}Pb/^{204}Pb$ space, compared to data from other lode gold deposits of the southern Kalgoorlie Terrane, 'mantle' and felsic intrusive rocks at the time of mineralization Potential mantle-crust mixing field at 2630 Ma is shown. Data sources, modelling parameters, and fileds as for Fig. 6.7. Mantle compositions evolved to 2630 Ma using a Th/U ratio of 4.2 for Teutonic Bore (McNaughton et al., 1990), and 3.8 for Kambalda (Roddick, 1984).

magma + assimilant, and thus 'mantle' is stated in parentheses on Figures 6.7 and 6.8. For the northern Norseman-Wiluna belt, the initial Pb isotopic ratios of the host greenstones and underlying mantle are represented by the Teutonic Bore VMS deposit (ca. 2690 Ma, Pidgeon, 1986; Pb data of McNaughton et al., 1990), whereas that of the Kalgoorlie Terrane is best approximated by the komatiite-hosted Cu-Ni deposits at Kambalda (ca. 2700 Ma, Claoué-Long et al., 1988; Pb data of Browning et al., 1987; Perring, 1990).

No syngenetic massive sulphide deposits have yet been identified in the Norseman Terrane, therefore the best estimate of the initial Pb isotopic ratio of the greenstones is whole-rock data for the Woolyeenyer basalts (Perring and McNaughton, 1992). The isochron for these basalts is also shown on Figure 6.7, constructed through the least radiogenic whole-rock data of Perring and McNaughton (1992). At the time of mafic volcanism, the Pb isotope composition of the Woolyeenyer Basalts would have fallen somewhere to the left of the whole-rock data along this isochron.

Older crust is known to underlie the Norseman Terrane from direct age dates on felsic volcanic units of the Penneshaw Formation, xenocrystic zircons within both external granitoid batholiths and felsic volcaniclastic units of the Penneshaw Formation, and detrital zircons of the Noganyer Formation (Chapter 2; Campbell and Hill, 1988). The external granitoid bodies that bound the Norseman Terrane, and internal granitoids that intrude the greenstone stratigraphy, are derived from this older crust (Oversby, 1975; Perring and McNaughton, 1990; 1992). These granitoids possess extremely radiogenic initial Pb compositions, as estimated from least-radiogenic acid-washed K-feldspar, age corrected to a U-Pb_{zircon} crystallization age of 2690 Ma. Isochrons for both granitoid suites, constructed through the initial ratios, are nearly coincident and pass through the most-radiogenic Norseman early galena and altaite data. Although these samples may not have behaved as closed systems to Pb, the Pb isotope composition of K-feldspars appear to be relatively undisturbed, and can be used to calculate initial Pb isotope ratios for the Ajax intrusions (Oversby, 1975; Perring and McNaughton, 1992). As initial ratios determined from acid-washed K-feldspars are maximum estimates, the true initial ratios, if different, would lie to the left along the isochron. Thus the evolved compositions of internal and external intrusions are considered maximum estimates, with the true compositions at the time of mineralization lying along lines parallel to the isochron (dashed arrows, Fig. 6.7; Perring and McNaughton, 1990; 1992).

From Figure 6.7 it is apparent that ore fluids from which early galena and altaite in lode gold deposits formed required at least two Pb source reservoirs: (1) the mantle, or mantle-derived greenstone lithologies (basalts, komatiites), and (2) older crust that underlies the greenstones, or felsic intrusive rocks derived from this substrate. This

mixing trend is referred to as the 'mantle'-crust mixing line (McNaughton et al., 1990). The Norseman early galena and altaite data fall between the calculated external and internal granitoid whole-rock Pb isotopic compositions and the projected positions of the Woolyeenyer basalt whole-rock Pb isotopic compositions at the time of mineralization. The isotopic signature of the ore fluid was dominated by the felsic lithologies as the felsic rocks, although volumetrically minor within the Woolyeenyer Formation, contain much greater Pb abundances than the Woolyeenyer mafic volcanic rocks. This result supports the conclusions of previous workers who have studied the Pb composition of lode gold galena within the Norseman Terrane (McNaughton et al., 1990; 1992; 1993; Ho et al., 1992; Perring and McNaughton, 1992).

Thorogenic data support the interpretation of mantle + crustal Pb input. However, the scatter of galena and altaite data away from the mantle-crust mixing line to higher $^{208}Pb/^{204}Pb$ ratios suggests that a third component may be required (Fig. 6.8). This third Pb source with a high Th/U ratio may be represented by depleted granulites in the lower crust (Browning et al., 1987; Perring and McNaughton, 1992).

6.3.4.2 Early galena + altaite: Regional variation of Pb-isotopic compositions within lode gold deposits of the Norseman Terrane

Inspection of Figures 6.7 and 6.8 reveals that Pb isotopic compositions of early galena and altaite from the Norseman lode gold deposits, while broadly constrained to the mantle-crust mixing line, display interdeposit scatter outside of the range of analytical error. To further investigate this within-camp variation, Pb isotope data from early galena and altaite of the Norseman deposits are plotted versus proximity to older crust on Figure 6.9, with all samples subdivided by mine. Two major controls on the Pb isotopic composition of galena and altaite within the Norseman deposits are apparent on Figure 6.9: (1) proximity to felsic intrusions, and (2) proximity to older crust.

Within individual deposits, the most important control on the Pb isotopic composition of early galena and altaite is their proximity to felsic intrusions. Galena and altaite from lodes hosted within or proximal to large felsic bodies possess more radiogenic compositions than those hosted in Woolyeenyer Formation basalts. This effect is best illustrated in samples from the Mararoa vein in the Ajax Mine, and from samples from the North Royal deposits. This variation in isotopic composition reflects local Pb contributions to an ore fluid that was externally derived and whose Pb composition was constrained by the mantle-crust mixing line.

Factoring out this local control of proximity to felsic intrusions, a regional variation of early galena + altaite Pb isotopic composition exists within the Norseman

Terrane. In the broadest sense, galena + altaite compositions become more radiogenic to the south (compare North Royal mafic-hosted vs. Regent vs. Ajax mafic-hosted samples), to the east (Crown vs. Mararoa vs. Norseman versus Mt. Barker vein samples), and with increasing depth along individual veins (compare Regent Mararoa vein samples, sampled over a downdip extent of 550m). Taken as a whole, this three-dimensional variation reflects proximity of the samples to the older Penneshaw Formation and to the eastern edge of the Norseman Terrane, with more radiogenic samples from locations closer to this older crust (Fig. 6.9). The isotopic variation at Norseman also corresponds roughly with the regional temperature zonation of hydrothermal alteration defined by McCuaig et al. (1993), with more radiogenic compositions associated with deposits formed at higher temperatures.

Departure of data from the Northern deposits from the linear trend defined by the Central deposit samples may be due to the base of the greenstones lying closer than projected to the Northern deposits, a curvilinear variation of Pb isotopic compositions away from older crust, or their proximity to a major fault zone (PRFZ, Chapter 4), but the database from these deposits is too limited to resolve these possibilities.

6.3.4.3 Early galena + altaite: Regional variation of Pb compositions in the Kalgoorlie-Norseman Terranes

McNaughton et al. (1990; 1992; 1993), Ho et al. (1992) and Perring and McNaughton (1992) demonstrated that the Pb-isotopic compositions of galena from gold deposits at Norseman were markedly different than those from gold deposits of the Kambalda Domain (Kalgoorlie Terrane) further north, with the Norseman galena yielding much more radiogenic compositions. Both mafic volcanic and felsic intrusive rocks of the Norseman Terrane were also found to be more radiogenic than their counterparts at Kambalda. The difference in the isotopic composition of the host rocks was interpreted as reflecting the coeval crustal Pb in each terrane, with a greater contribution of older crust preserved in lithologies of the Norseman Terrane. Isotopic compositions of galena in both terranes were interpreted as mixing of Pb from mantle or mantle-derived rocks with Pb from older crustal reservoirs or rocks derived from this substrate, as illustrated in Figs. 6.7 and 6.8 and discussed previously, reflecting the local crustal cross-section traversed by the mineralizing fluids.

Two galena samples from the Higginsville lode gold deposits in the Coolgardie Domain of the Kalgoorlie Terrane, approximately halfway between the Victory-Defiance and Norseman lode gold deposits (Fig. 6.5), were analyzed to further investigate existing Pb-isotope variations on the scale of the southern Norseman-Wiluna belt. Galena from

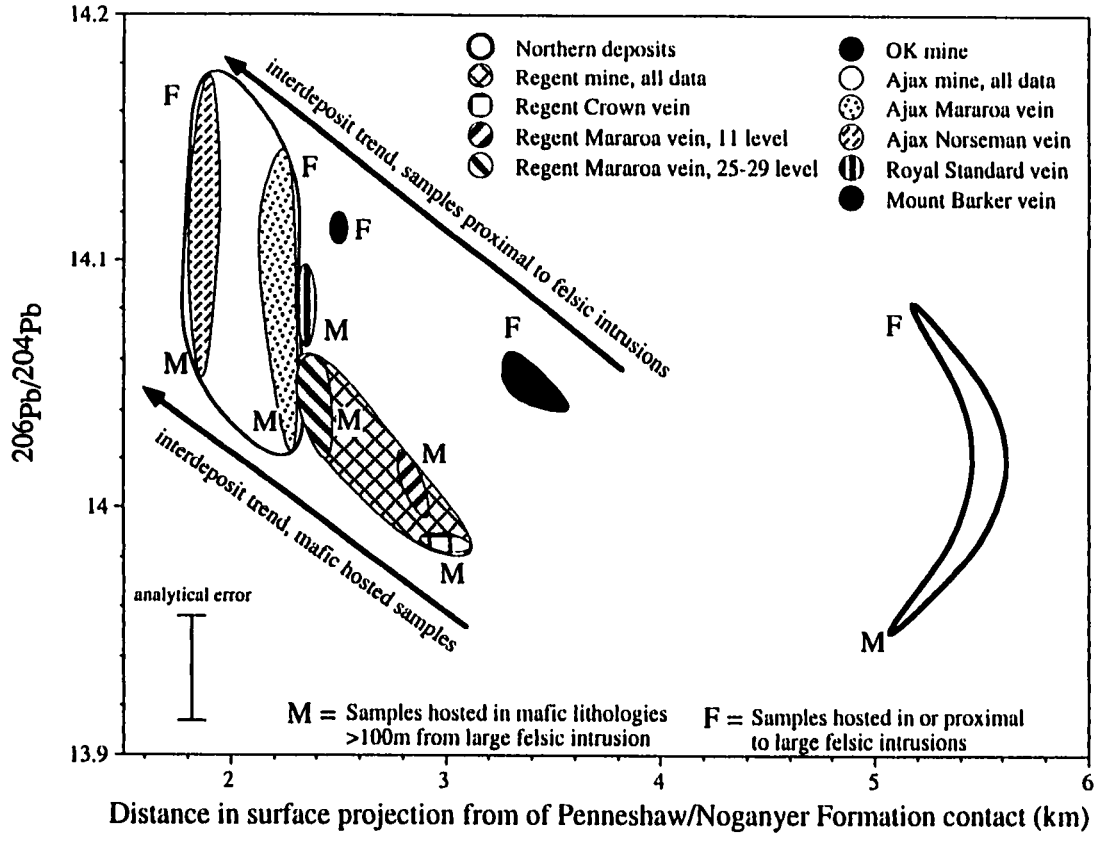

Figure 6.9. Variation of $^{206}Pb/^{204}Pb$ compositions of early galena and altaite from Norseman lode gold deposits with distance from the Penneshaw Formation/Noganyer Formation contact, illustrating the controls of proximity to felsic intrusions (Northern deposits, Ajax Mine) versus increasing proximity to the contact on early galena and altaite compositions. Samples are subdivided by mine and vein system, and classed according to proximity to felsic intrusions. Note that the Regent and Ajax Mines both access the Mararoa quartz vein system. Exact distance from the Penneshaw contact is difficult to estimate as the Penneshaw/Noganyer contact dips west (≈50°) and the auriferous quartz veins dip east (25 - 60°). As the vertical thickness of the greenstones at Norseman is not sufficiently well established, spatial relationships are drawn in the horizontal plane. The distance from each shaft to contact was measured from 1:25000 scale map, and individual samples were projected to surface and their horizontal distance to the outcrop of the Penneshaw Formation was calculated relative to the shaft. Actual distance of each sample to the contact should be > the calculated distance. On the terrane scale, galena + altaite compositions become more radiogenic with increasing proximity to older crust. Within deposits, compositions become more radiogenic with proximity to felsic intrusives (Northern deposits, Ajax Mine), and with depth (Regent Mine).

these deposits fall on the mantle-crust mixing line joining the early galena and altaite of the Norseman deposits and those of the Kambalda deposits (Figs. 6.7, 6.8), indicating that the variation in initial Pb isotopic compositions of the ore fluids may have been gradational from Norseman to Kambalda. This regional variation in initial Pb isotopic compositions broadly corresponds to the temperature of deposit formation (Norseman > Higginsville > Kambalda, Chapter 5; Clark et al., 1989), and with the proximity of the deposits to the southern end of the Norseman-Wiluna belt (Fig. 6.10). This gradation in Pb isotopic composition with more radiogenic compositions from deposits nearer the northern and southern edges of the Kalgoorlie and Norseman terranes, respectively, reflects the interaction of the ore fluids with progressively more sialic and radiogenic basement towards the greenstone margins, and requires that the conduits along which auriferous fluids advected were crustal-scale lineaments that transected the greenstone lithologies and penetrated underlying older sialic crust. Samples which deviate from this trend are proximal to the Menzies-Boorara shear zone, a crustal-scale, terrane bounding shear zone. The anomalously radiogenic data from these deposits indicate that their ore fluids were dominated by the older basement Pb reservoir, which the structure transects.

The Norseman and Menzies lode gold deposits are both sited proximal to the margins of their respective greenstone belts, yet the Pb data from the Norseman deposits are extremely radiogenic by comparison. As it seems probable that ore fluids at both Menzies and Norseman would be dominated by the older sialic crustal Pb reservoir, the data suggest that the sialic basement underlying the Norseman Terrane may be older and more radiogenic than the basement to the Kalgoorlie Terrane. This interpretation is supported by the report of extremely old detrital zircons in sediments of the Noganyer Formation of the Norseman Terrane (3650-3670 Ma, Campbell and Hill, 1988), compared to the oldest xenocrystic zircons in greenstones of the Kambalda Domain of the Kalgoorlie Terrane (ca. 3400-3500 Ma, Compston et al., 1986; Claoué-Long et al., 1988).

6.3.4.4 Late galena + altaite: Uranogenic Pb isotope linear arrays from the Norseman lode gold deposits

Linear arrays of Pb isotope data projecting to extremely radiogenic compositions in $^{207}Pb/^{204}Pb$ versus $^{206}Pb/^{204}Pb$ coordinates for galena and altaite from the Norseman lode gold deposits (Fig. 6.6A) have a number of possible origins, including: (1) mixing between two different Pb reservoirs at the time of mineralization, (2) post-mineralization mixing of Pb from two or more reservoirs which had the same initial Pb isotope composition at the time of mineralization forming (a) isochrons, or

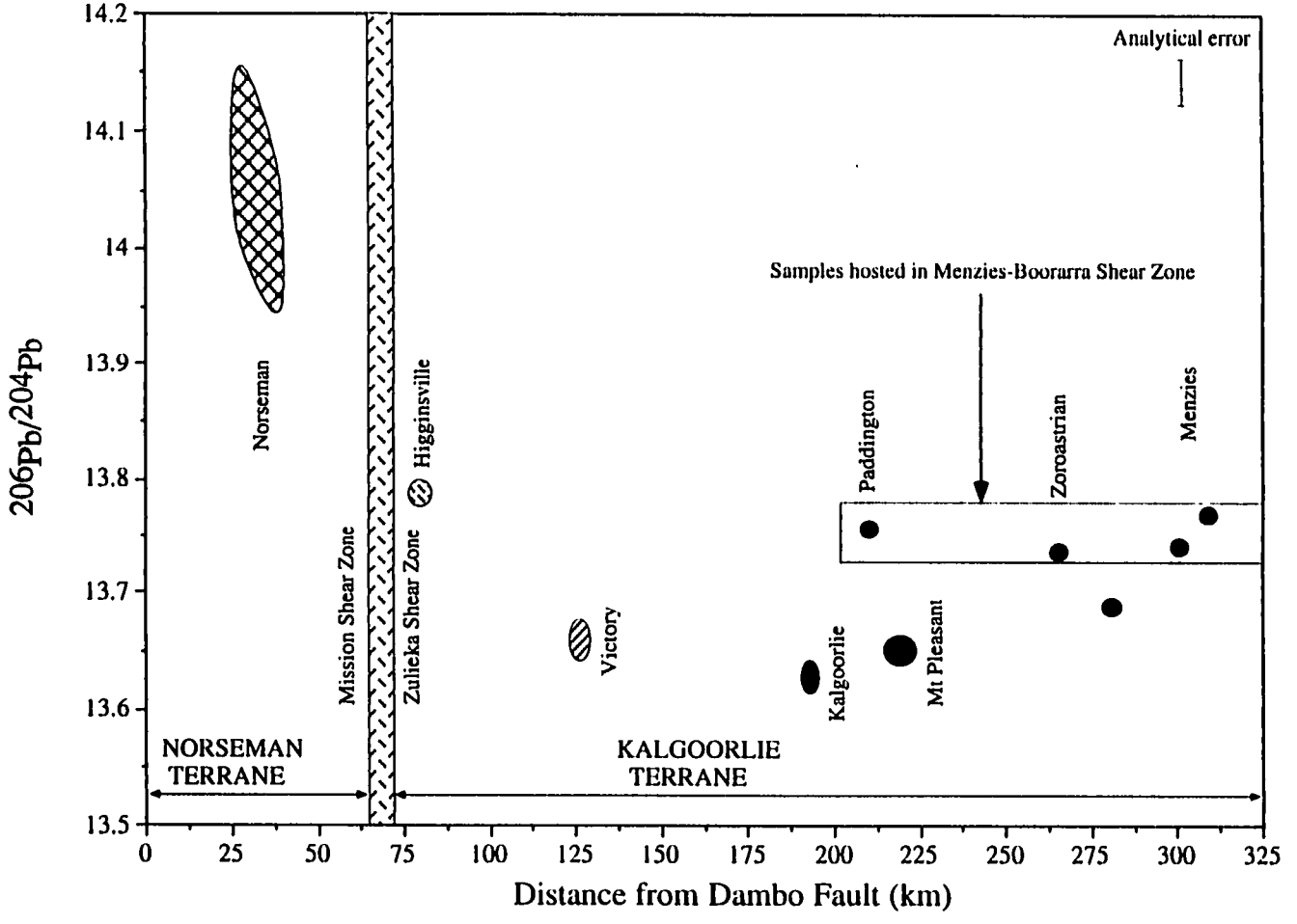

Figure 6.10. Variation of $^{206}Pb/^{204}Pb$ compositions of early galena and altaite from lode gold deposits of the Norseman and Kalgoorlie Terranes from the Dambo fault at the southern end of the Norseman Terrane to Menzies at the northern end of the Kalgoorlie Terrane, with the Mission and Zulieka shear zones forming the boundary between the two terranes. Transect line is shown in Fig. 6.5. Kalgoorlie Terrane data (black) from Fig. 4 of McNaughton et al. (1993). More radiogenic compositions towards the the terrane margins are interpreted as reflecting the increasing proportion of older crust vs. greenstone lithologies that the ore fluids exchanged with. Samples hosted within the Menzies-Boorarra shear zone have ore fluid Pb compositions dominated by older crustal Pb, as the shear zone transects older basement. The extremely radiogenic compositions of the Norseman ore fluids suggest that the felsic substrate to the Norseman greenstones may be older than that beneath the Kalgoorlie Terrane.

(b) paleoisochrons, or (3) post-mineralization mixing of Pb from two or more unrelated reservoirs (McNaughton et al., in prep.).

Hypothesis (1) has been proposed by Hattori (1993) to explain extremely radiogenic compositions of galena and altaite from the Archean Kirkland Lake deposit, Abitibi Subprovince, Canada. This hypothesis can be rejected for the Norseman data because no rocks with such extremely radiogenic Pb compositions could have plausibly existed in the Archean. Norseman has the most radiogenic early galena composition of any Yilgarn lode gold deposit, and the Norseman Terrane has the most radiogenic host rocks yet found in the Norseman-Wiluna belt (Perring and McNaughton, 1992). However, these felsic lithologies anchor the most radiogenic end of the mantle-crust mixing line (Fig. 6.7), and the least radiogenic ends of the extremely radiogenic linear arrays.

Accordingly, these linear arrays must be caused by post-mineralization galena + altaite growth, hence they are referred to as 'late' galena and altaite. Isochrons, which form due to the addition of radiogenic Pb to the galena or altaite crystal by the in-situ decay of U in included or adjacent silicates, possess a slope in uranogenic Pb-isotope space corresponding to the age of galena and altaite growth. Four low-Pb telluride samples with high $^{206}Pb/^{204}Pb$ relative to $^{207}Pb/^{204}Pb$ values (Fig. 6.6A) are consistent with the addition of Pb by in situ decay of U since the time of mineralization (Fig. 6.11).

The other two linear arrays of late galena + altaite data on Figure 6.6A have slopes much too steep to be isochrons, as they would yield ages much older than the host rocks which the lode gold deposits crosscut. These arrays may be interpreted as paleoisochrons, in which the slope of the array corresponds to the age of new galena + altaite growth, or as mixing of Pb from two unrelated Pb reservoirs, in which case the slope of the array has no age significance. The distinction between these two possibilities is that in the case of paleoisochrons, the source of Pb that forms the most radiogenic end of the array had the same initial Pb isotope ratio as the least-radiogenic end at the time of original galena + altaite growth. Even when this is the case, post-mixing in-situ decay could significantly modify the paleoisochron (e.g. sample 108355, Fig. 6.11), producing scatter in the array and thus an inaccurate calculated age. The best test for a paleoisochron versus a linear array with no age significance is (1) evidence that the two Pb reservoirs had the same isotopic composition at the time of mineralization, (2) a linear array that combines a slope with low error with a low mean standard weighted deviation (MSWD), and (3) a resultant age that has geological significance, in that it can be correlated with events dated by other geochronological techniques. The

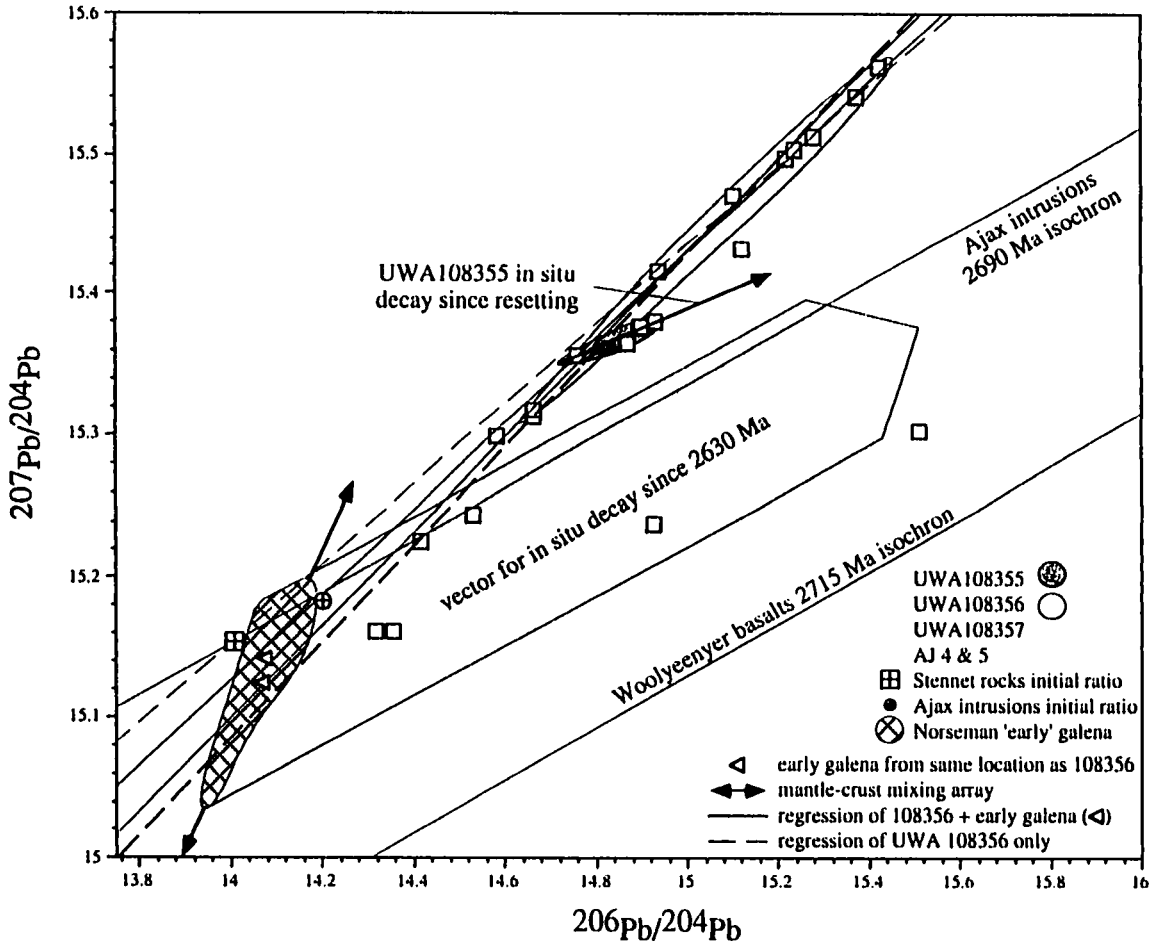

Figure 6.11. Regression of late galena + altaite Pb data from sample UWA108355 and UWA108356 in $^{207}Pb/^{204}Pb$ vs. 206Pb/204Pb isotopic space. Two possible regressions are shown for sample UWA108356: data from sample UWA108356 alone (dashed line), and data from sample UWA108356 combined with early galena + altaite samples UWA108357 and UWA108358 from the same stope. Details of regressions are listed in Table 6.2. Data from UWA108356 represents new galena + altaite growth long after the mineralization event. Data from four low-Pb tellurides are consistent with in situ U decay since the time of Primary Archean mineralization. The data for UWA108355 represent in situ U decay since the time of Proterozoic galena + altaite growth. Data sources as for Figure 6.7 and Table 6.1

age of a paleoisochron may be calculated by graphically solving the equation:

$$\text{slope} = (1/137.88)(e^{\lambda 2t1} - e^{\lambda 2t2})/(e^{\lambda 1t1} - e^{\lambda 1t2}) \quad (6.1)$$

where t_1 is the age of gold mineralization and primary galena formation, t_2 is the age of resetting or Pb mobility event, and λ_1 and λ_2 are the decay constants for ^{238}U and ^{235}U, respectively (Jaffey et al., 1971). For the Norseman case, a broad mineralization age range of 2630 to 2675 Ma was utilized to include maximum probable variation in the resultant calculations.

As discussed previously, the initial Pb isotope ratios of felsic intrusions are interpreted to be the same as the most radiogenic early galena and altaite data from the Norseman deposits, thus satisfying the first of the requirements for a paleoisochron. In order to investigate the possibility that the Norseman uranogenic Pb isotope linear arrays do represent paleoisochrons, the arrays were studied on a sample by sample basis. Seven samples yield galena or altaite with anomalously radiogenic (late) Pb isotope compositions (Table 6.1). Regression details for the uranogenic Pb data from these samples are presented in Table 6.2, and are graphically displayed in Figures 6.11-6.13.

Sample UWA108356 consists of galena ± altaite infilling fractures in quartz and earlier sulphides in a quartz vein proximal to a large felsic intrusion of the Ajax suite, and is within _ 20 m of E-Fault, a large brittle structure which crosscuts and offsets the auriferous quartz veins by several tens of metres (Chapters 4, 5). This structure displays retrogression of high temperature gold-related amphibole-biotite alteration in the basalts, and sericite-plagioclase in felsic intrusions, to chloritic gouge. These retrogressive alteration assemblages are only very weakly developed at the sample location, and are restricted entirely to within millimetres of late brittle fractures which transect the quartz veins and their contiguous high temperature alteration assemblages. Uranogenic Pb data for sample UWA108356 produces a linear array, and considerable heterogeneity is exhibited on the scale of centimetres (Perring and McNaughton, 1990). Regression of data from this sample alone (dashed lines on Fig. 6.11) yields an age of 1915 +270/-330 Ma (Table 6.2). Early galena + altaite samples UWA108357 and UWA108358 are from the same stope as 108356 (Perring and McNaughton, 1990), and therefore probably had the same Pb isotope ratio at the time of mineralization. Regressing these data with those from sample UWA108356 yields a slope with a corresponding paleoisochron age of 1945 +135/-150 Ma and a mean standard weighted deviation (MSWD) of 0.33 (Fig.

TABLE 6.2

Slope and regression details of linear uranogenic Pb isotope arrays for late galenas from the Norseman lode gold deposits. Regression of data follows York (1969). See text for discussion

Sample	n	MSWD	Slope ± 2σ	Paleoisochron age {isochron} Ma±2σ	comments
Isochrons					
UWA108355	5	0.13	0.13601±0.16130	{2177+779/-1750}	in-situ decay since $t_{resetting}$
Paleoisochrons					
ca. 1950 event					
UWA108356	8	0.32	0.31248±0.02988	1915+270/-330	Proterozoic resetting
UWA108356 + early galena 108357 and 108358	10	0.33	0.31584±0.01284	1945+135/-150	Proterozoic resetting
ca. 1500 event					
AJ58	3	0.08	0.26350±0.01202	1410+170/-190	Proterozoic resetting
AJ58 + early galena AJ56	5	4.99	0.27883±0.00708	1585+105/-120	meaningless, high MSWD

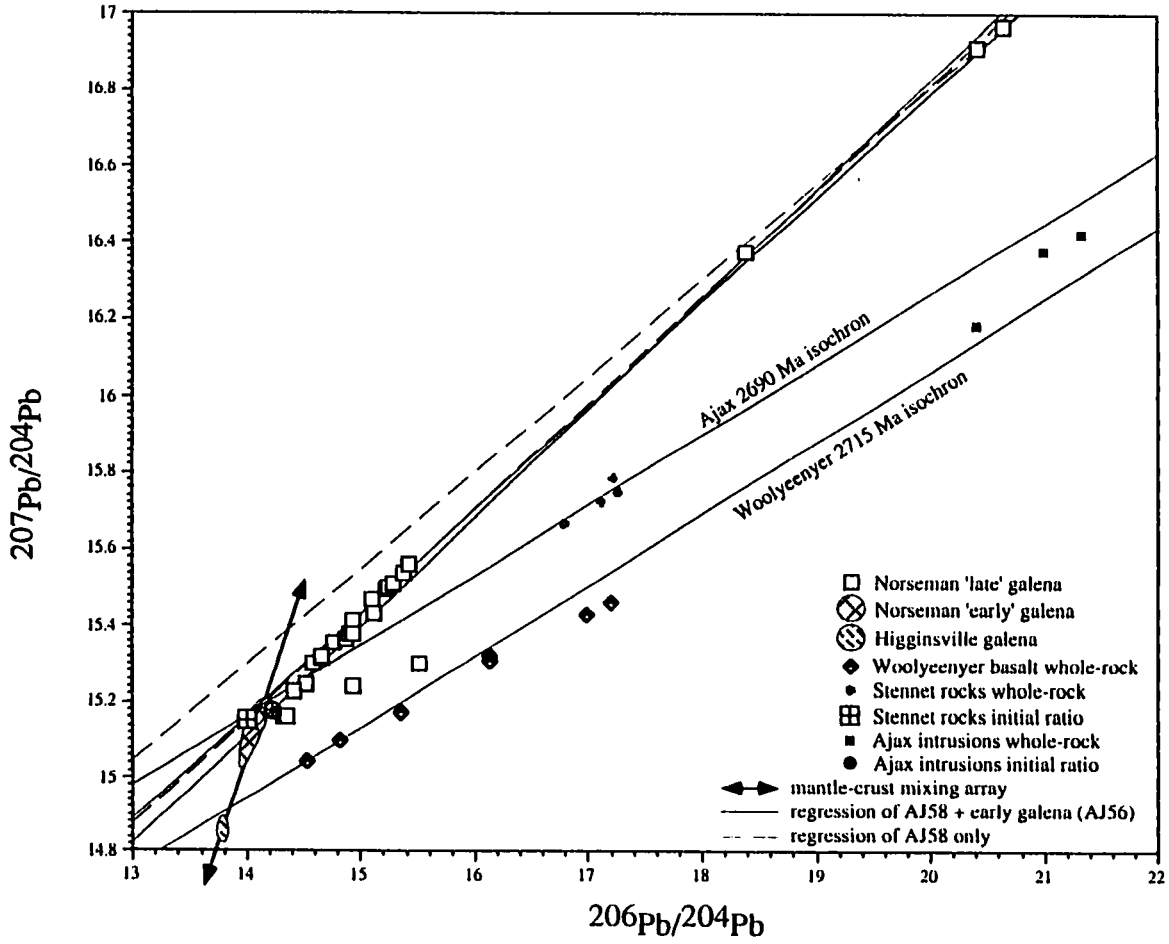

Figure 6.12. Regression of late galena + altaite Pb data from sample AJ58 in $^{207}Pb/^{204}Pb$ vs. $^{206}Pb/^{204}Pb$ isotopic space. Two possible regressions are shown: data from sample AJ58 alone (dashed line), and data from sample AJ58 combined with early galena + altaite sample AJ56 from the same location. Details of regressions are listed in Table 6.2. The scatter in late galena + altaite data to extremely radiogenic compositions requires that new galena + altaite growth occurred long after the original mineralization event, and involved mixing of Pb from the early galena + altaite with much more radiogenic Pb from felsic intrusive rocks. Data sources: Stennet Rocks from Oversby (1975); Ajax intrusions and Woolyeenyer basalts from Perring and McNaughton (1990, 1992); other data sources as listed in Table 6.1 and Fig. 6.7. Analytical error is smaller than symbol size.

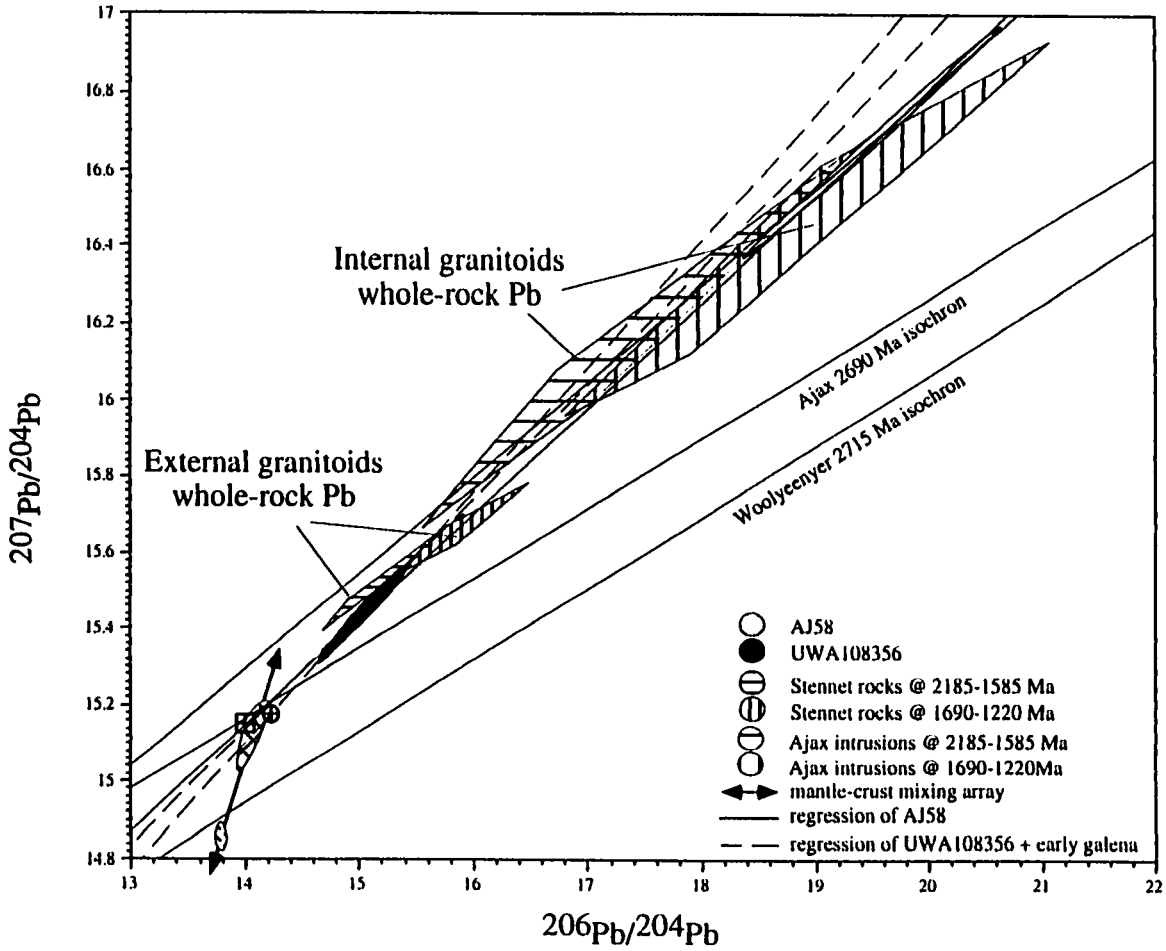

Figure 6.13. Regression of late galena + altaite Pb data in $^{207}Pb/^{204}Pb$ vs. $^{206}Pb/^{204}Pb$ isotopic space, and interpretation of these data as mixing between early galena + altaite and evolved Pb from internal granitoids (Ajax intrusions). Modelling parameters: Ajax intrusions μ = 11.96 - 22.26 (Perring and McNaughton, 1990); Stennet Rocks μ = 5.98 - 8.02 (Oversby, 1975); age ranges given in Table 6.2 and in legend. If interpreted as paleoisochrons, samples UWA108356 and AJ58 yield two different ages outside of error, and require that two distinct galena + altaite growth events occurred in the Norseman auriferous quartz veins during the Proterozoic.

6.11, Table 6.2). The paleoisochron determined above for sample UWA108356 is considered to be more accurate than the 2000±300 Ma paleoisochron obtained by Perring and McNaughton (1990) in that (1) better age constraints are available on the timing gold mineralization, and (2) Perring and McNaughton (1990) regressed all late galena, including data from different sample locations and samples which have been affected by varying amounts of in-situ decay, and therefore represent mixed Pb populations.

Sample AJ58 comprises coarse grained galena ± altaite crystals at the brittle-deformed margin of the Mararoa quartz vein. The crystals have been microfractured and faulted, and possess the most radiogenic Pb compositions for galena or altaite yet discovered in an Archean lode gold deposit, exhibiting considerable sample heterogeneity on the scale of a few centimetres (Fig. 6.6). The quartz vein is hosted at the contact between a large internal granitoid body and tholeiitic basalt of the Woolyeenyer Formation. The sample location is within ≈ 20 m of E-fault. Regression of the uranogenic Pb data for this sample alone is illustrated as dashed lines on Figure 6.12, and yields a paleoisochron age of 1410 +170/-190 Ma (Table 6.2). Note that his regression envelope barely passes within error of the early galena + altaite data. Sample AJ56 comprises coarse grained galena + altaite crystals isolated in the relatively undeformed centre of the quartz vein, less than 5 m from sample AJ58, and should have had the same initial Pb isotope composition at the time of mineralization. However, regression of the combined data (solid line on Fig. 6.12) yields a slope with a relatively high MSWD of 4.99, indicating that the samples are not easily related (Table 6.2). It is therefore likely that sample AJ58 has experienced at least two periods of post-mineralization Pb addition: an initial event perhaps coeval with that which affected UWA108356, and a second event which produced the extremely radiogenic galena. Thus, the linear array of AJ58 data only has age significance in that it is consistent with an event causing galena growth after the resetting of UWA108356. The actual age calculated can be used as a broad constraint on the timing of this event, but may be in significant error.

Lead for this Proterozoic galena + altaite growth was supplied by two sources: (1) the early galena and altaite which define the least radiogenic end of the arrays, and (2) extremely radiogenic Pb introduced during Proterozoic events. Given the fact that ore metals have experienced remobilization during the Proterozoic events, it is important to determine whether this radiogenic endmember was a local source such as the internal felsic intrusions, or a source external to the terrane such as the huge granitoid batholiths bounding the terrane. To distinguish between internal versus external sources, the initial Pb isotope compositions of these two rock types were evolved over the age ranges of the

two paleoisochrons determined above. Maximum error ranges in age were taken into account, including both retrogressions of late galena + altaite arrays alone as well as arrays anchored by appropriate early galena + altaite compositions as discussed above (Table 6.2, Fig. 6.13). From these calculations it is apparent that sources external to the terrane cannot account for the radiogenic endmember of the uranogenic linear arrays, whereas the internal sources can (Fig. 6.13). For sample AJ58, the extremely radiogenic Pb isotope compositions cannot be obtained from evolving the felsic intrusion whole rock data, and requires exotic Pb input, likely leached from minerals with high U contents, and therefore high proportions of radiogenic Pb, such as monazite or zircon.

Late galena data from samples UWA108357, AJ4 and AJ5 (Table 6.1) appear to have been affected by a combination of Proterozoic galena growth and in-situ decay. Regression of these data produce slopes with large errors and high MSWDs, and thus yield meaningless ages (Table 6.2). Note also that the isochron calculated for sample UWA108355 represents in-situ U decay since the time of new Proterozoic galena + altaite growth (Table 6.2, Fig. 6.11).

For the linear arrays of uranogenic Pb data discussed above to represent true paleoisochrons, the calculated ages must be geologically meaningful. Figure 6.3 compiles the available geochronology for the Archean Norseman Terrane, and the adjacent Proterozoic Fraser Orogen to the southeast (Fig. 6.5). The paleoisochron age for sample UWA108356 corresponds to the genesis of precursor rocks to the Fraser Complex, Fraser Orogen, as determined from Sm-Nd modelling (Fletcher et al., 1991). The paleoisochron for sample AJ58, although of uncertain age significance, is within error of voluminous granitoid intrusion into the Biranup complex of the Fraser Orogen (Myers, 1993 and references therein). The paleoisochrons also correspond to total gas (no plateau) ^{40}Ar-^{39}Ar ages obtained on gold-related biotite and amphibole alteration minerals in the Scotia deposit at the southern end of the Norseman Terrane.

Significantly, the two linear arrays for samples AJ58 and UWA108356, respectively, yield distinct slopes of calculated error ranges, indicating that there was at least two periods of new galena + altaite growth in the Archean quartz veins at Norseman. Most of the late galena and altaite detected thus far are from the southern end of the Mararoa and Norseman veins in the Ajax mine workings, within a few 10's of metres of the E-fault (Table 6.1, Chapter 4). E-fault is a large brittle structure which significantly offsets the Mararoa and Norseman reefs and their host volcanic stratigraphy, whereas all major structures hosting lode gold deposits in the Norseman area are dominantly ductile. The implication is that E-fault was active at multiple times during the Proterozoic, and that this activity was accompanied by fluid movement and

ore metal remobilization through the adjacent auriferous quartz veins. Gold has been documented associated with both early and late galena and altaite (Perring and McNaughton, 1990), indicating that these fluid events may have locally remobilized the Archean lode gold concentrations. A single late galena sample from the Regent Mine indicates that the resetting event is not restricted to the vicinity of E-fault, corroborating evidence from reset ^{40}Ar-^{39}Ar systematics in hydrothermal amphibole in these deposits. It is interesting that Sr isotope data from hydrothermal scheelites from Norseman mirrors Pb isotope data from galena + altaite. Scheelites with the most radiogenic compositions are from the Ajax mine within approximately 300 m of the E-fault ($^{87}Sr/^{86}Sr = 0.7042$, Mueller et al., 1991b). It is possible that very radiogenic scheelites have had their Sr isotope ratios partially reset by the Proterozoic event that formed the late galena + altaite.

6.3.4.5 Late galena + altaite: Thorogenic Pb isotope linear arrays

Lead isotope data for late galena + altaite samples AJ58 and UWA108356 also form linear arrays in $^{208}Pb/^{204}Pb$ versus $^{206}Pb/^{204}Pb$ space. Knowledge of t_1 and t_2 allows the Th/U of the source of the evolved Pb to be calculated using the equation:

$$\text{slope} = {}^{208}Pb/{}^{206}Pb = ({}^{232}Th/{}^{238}U)(e^{\lambda 3 t1} - e^{\lambda 3 t2})/(e^{\lambda 1 t1} - e^{\lambda 1 t2}) \qquad (6.2)$$

where t_1, t_2 and λ_1 are as previously defined, and λ_3 is the decay constant for ^{232}Th (LeRoux and Glendenin, 1963). Regression details and calculated Th/U ratios are given in Table 6.3. Model (time-integrated) Th/U ratios for Stennet Rocks and Ajax intrusions are calculated for comparison to late galena + altaite arrays by the equation:

$$\begin{aligned} \text{slope} &= ({}^{208}Pb/{}^{204}Pb_n - {}^{208}Pb/{}^{204}Pb_i)/({}^{206}Pb/{}^{204}Pb_n - {}^{206}Pb/{}^{204}Pb_i) \\ &= ({}^{232}Th/{}^{238}U)(e^{\lambda 3 to_{-1}})/(\varepsilon \lambda 1 to_{-1}) \end{aligned} \qquad (6.3)$$

where $^{208}Pb/^{204}Pbn$ and $^{206}Pb/^{204}Pbn$ are the whole-rock Pb isotope compositions as measured today, $^{208}Pb/^{204}Pb_i$ is the initial Pb isotope ratio determined from least radiogenic acid washed K-feldspar, and $^{206}Pb/^{204}Pb_i$ is the initial Pb isotope ratio determined from least radiogenic acid washed K-feldspar age corrected to a formation age (t_o) of 2690Ma (Oversby, 1975; Perring and McNaughton, 1990; 1992). The calculated Th/U for these lithologies are also presented in Table 6.3.

Figure 6.14 illustrates that the Pb forming the late galena + altaite isotopic compositions must have evolved in a source with a time-integrated Th/U of 1.44-2.24. Lead reservoirs such as the Woolyeenyer basalts (Th/U = 3.70-4.75) and the external

TABLE 6.3

Slope and regression details of linear thorogenic Pb isotope arrays and calculated Th/U ratios. ($^{208}Pb/^{204}Pb$)i, ($^{206}Pb/^{204}Pb$)i = initial ratios calculated from least radiogenic acid-washed K-feldspar. ($^{208}Pb/^{204}Pb$)n, ($^{206}Pb/^{204}Pb$)n = measured whole-rock Pb isotope ratios. Stennet Rocks data from Oversby (1975), Ajax data from Perring and McNaughton (1990).

Sample	n	MSWD	Slope ± 2σ	Paleoisochron age range in Ma	Th/U
Late Galenas					
ca. 1950 event					
UWA108356	8	0.37	0.43437±0.06592	1585 - 2185	1.44 - 2.03
ca. 1500 event					
AJ58	3	0.11	0.54445±0.02654	1220 - 1580	1.99 - 2.24
AJ58 +AJ56	5	4.99	0.51278±0.02034	1465 - 1690	1.92 - 2.11
Host Rocks					
Woolyeenyer basalts	7	7.37	1.06484±0.04696	2700-2715	3.70 - 4.75

Model Th/U calculations for rocks not showing linear arrays of thorogenic data

Sample	$t_{formation}$ (Ma)	$(^{206}Pb/^{204}Pb)_i$	$(^{208}Pb/^{204}Pb)_i$	$(^{206}Pb/^{204}Pb)_n$	$(^{208}Pb/^{204}Pb)_n$	Th/U
Stennet Rocks						
71-905a	2690	14.008	33.834	17.122	37.894	4.74
71-906b	2690	14.008	33.834	17.228	36.248	2.73
Ajax Porphyry						
UWA108327	2690	14.194	33.865	22.228	37.374	1.59
UWA108328	2690	14.194	33.865	20.387	38.078	2.47

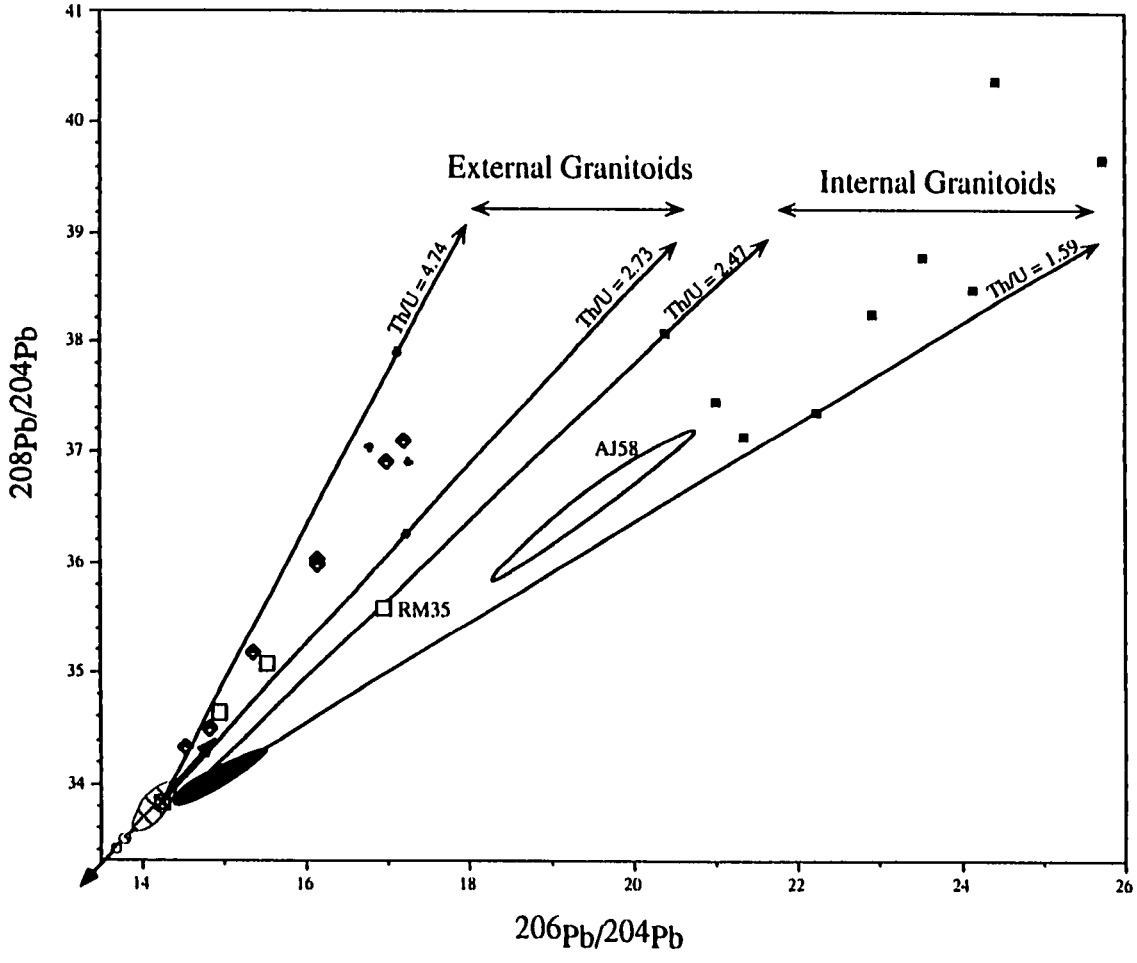

Figure 6.14. Plot of Norseman galena + altaite Pb data in $^{208}Pb/^{204}Pb$ vs. $^{206}Pb/^{204}Pb$ isotopic space. Ranges of model Th/U ratios for internal granitoids (Ajax intrusions) and external granitoids (Stennet Rocks) are given, along with whole rock data for the Woolyeenyer basalts. These data support the interpretation of late galena + altaite as mixing of Pb from early galena + altaite and evolved Pb from Ajax intrusives, as the Ajax intrusives are the only lithologies with sufficiently low Th/U. Symbols, fields and data sources as for Fig. 6.12.

granitoid batholiths (Stennet Rocks Th/U = 2.73-4.74) have Th/U ratios that are much too high to have supplied this radiogenic Pb. Therefore, the only reasonable source for this Pb is the internal Ajax intrusions (Th/U = 1.59-2.47), supporting the conclusions drawn from the uranogenic Pb data.

6.4 Implications of ^{40}Ar-^{39}Ar and Pb isotope studies

6.4.1 Cryptic fluid movement through Archean structures

In the Norseman Terrane, post-mineralization fluid movement resulting in argon loss in amphibole and biotite and new galena + altaite growth was most likely related to tectonic activity within Proterozoic orogenic belts immediately to the south. The Norseman Terrane is situated less than 100 km from the southern and eastern boundary of the Yilgarn Craton (Fig. 6.5), and is affected by a zone of deformation along the southern margin of the Yilgarn, which is attributed to Proterozoic interaction between the Yilgarn Craton and the Albany-Fraser Province (Whitaker, 1990). Several major orogenic episodes, involving high grade metamorphism and granitoid emplacement, occurredwithin the Albany-Fraser Province between ca. 1900 -1100 Ma (Gee, 1979). These tectonic events may have caused successive pulses of fluid movement along Archean structures adjacent to the cratonic margin, such as those which host gold mineralization in the Norseman Terrane. This interpretation is supported by the following observations:

(1) Pb isotope results from ore sulfides associated with gold mineralization in the Norseman and Kalgoorlie Terranes record at least two Proterozoic fluid events, one ca. 2000 Ma, a later event ca. 1100 Ma, and potentially multiple events between these dates that have collectively reset Pb isotopic compositions of gold-related galena (this study; Perring and McNaughton, 1990; Cassidy and McNaughton, in prep.).

(2) Cross-cutting brittle fractures, containing lower temperature mineral assemblages (chlorite - quartz - sericite - albite; albite-prehnite; gypsum) than the hydrothermal assemblages associated with mineralization are common in the Norseman lode gold deposits. Lower temperature, retrogressive, mineral assemblages (sericite - albite - chlorite - calcite) are also found along cleavage planes and grain boundaries within ore zones (Chapters 4, 5; McCuaig et al., 1993).

Recognition of resetting of argon systematics in hydrothermal hornblende and biotite that are petrographically fresh and have apparently pristine stable isotope

compositions, at temperatures below the closure temperature for argon diffusion in muscovite, has important ramifications for the interpretation of results from ^{40}Ar-^{39}Ar analysis. Where isotopic resetting of this style has occurred the criteria required to assess the validity of isotopic ages differ from those used to detect thermal resetting. Thus the thermal history of a sample becomes largely secondary when compared to the fluid history of a sample, and factors such as permeability, proximity to fluid conduits, duration of exposure to the fluid, and crystal microstructure determine the degree of isotopic disturbance (e.g. Miller et al., 1991). In addition, this study has shown that, although investigation of the stable isotope systematics of dated minerals offers perhaps the best means for determining whether fluid-mineral interaction has occurred at some time after mineralization (e.g. Miller et al., 1991; Kerrich and Cassidy, 1994), Ar isotope systematics can be severely disturbed even in situations where hydrogen and oxygen isotope compositions appear unaffected.

These results are especially relevant to mineral deposits, such as Archean gold deposits, which are associated with major crustal structures that have experienced long post-mineralization fluid movement histories (Kerrich and Cassidy 1994). In this situation there is considerable opportunity for "cryptic" argon loss to have occurred within hydrothermal minerals. Interpretations from previous studies on Archean gold deposits that have assessed the possibility of argon loss only under purely thermal regimes (e.g. Hanes et al. 1991, Zweng et al. 1993) will require reassessing in light of the results outlined herein.

6.4.2 Remobilization of Gold

That gold is intimately related to both early and late galena + altaite implies that Au is either remobilized or introduced during both of the distinct galena-forming events. Studies of ore textures indicate that paragenetically late gold exists at all mines at Norseman. However, late galena + altaite are largely restricted to the Ajax mine proximal to (a) E-fault and (b) abundant felsic rocks of the Ajax intrusive suite. The lack of abundant late galena + altaite in areas that are distal to E-fault, yet still proximal to or hosted in felsic intrusive rocks, would indicate that the Proterozoic fluid advection was restricted to the vicinity of late brittle structures. The lack of significant low-temerature retrogressive alteration away from these brittle structures further indicates that this late Pb-Au-Te mobility was restricted to the brittle structures. However, it is important to note that although the fluid circulation was locally restricted to brittle structures, the entire fluid system may have been kilometers in scale as the paleoisochron ages correspond to tectonic events in the Proterozoic Fraser Orogen $\approx$ 60 km to the southeast.

Gold is often sited in paragenetically late sites within mesothermal quartz veins; however, the identification of "late gold" by itself does not imply significant remobilization of gold or late introduction of gold. Gold may be the one of the last phases to precipitate from the fluid (along with tellurides, galena, etc.), or may be easily remobilized on a millimetre to centimetre scale during late deformation or sulphide recrystallization (i.e. the geometry of the orebody does not change, gold is simply recrystallized as coarser grains in "late sites" in situ, see Chaspter 5 for a discussion). It is only the Pb isotope data that provides any clue to the timing of Au remobilization. Ore texture observations of Au as both inclusions and fracture fillings in pyrite, the concentration of gold proximal to the Archean quartz veins and not in the brittle structures remote from these veins, and the two distinct galena-forming events collectively provide compelling evidence for the local remobilization rather than reintroduction of gold during the Proterozoic. From the current database, it can only be concluded that remobilization has occurred in the vicinity of E-fault in the Ajax mine. However, this study raises the possibility that cryptic remobilization of gold associated with late brittle faults and fluid interaction may be a common feature in Archean lode gold deposits (cf. Boyle, 1969; Guha and Kanwar, 1987).

6.5. Conclusions

(1) Pegmatites which crosscut, and thus postdate gold-bearing structures at the Scotia gold mine have ca. 2600 Ma muscovite ^{40}Ar-^{39}Ar and Sm-Nd (garnet - albite) ages. Identical ages are obtained from a hydrothermal muscovite in the Central deposits, and suggests that this represents a cooling age, recording the time at which the Norseman Terrane cooled through the theoretical blocking temperature for Ar diffusion in muscovite. This provides a minimum age for gold mineralization. This cooling age, considered in combination with constraints on the timing of peak metamorphism within the terrane and the high-temperature, synkinematic, and syn- to post-peak metamorphic nature of the mineralization, constrains the mineralizaing event to between 2610 and 2640 Ma, and likely closer to 2640 Ma. This timing for gold mineralization in the Norseman Terrane is consistent with data from elsewhere that suggests that much of the gold mineralization in the Yilgarn Craton occurred between ca. 2630 and 2600 Ma.

(2) Analyses of galena and altaite from lode gold deposits of the Archean Norseman Terrane, Yilgarn Craton, Western Australia yield the most variable Pb-isotopic compositions for these minerals yet found in any Archean lode gold deposit. Two

distinct types of linear arrays are recognized in $^{207}Pb/^{204}Pb$ versus $^{206}Pb/^{204}Pb$ isotope coordinates: (a) a steep array encompassing the variation in least-radiogenic galena + altaite ("early") from all of the gold orebodies, and (b) shallower arrays extending to extremely radiogenic compositions from galenas that can show extreme heterogeneity on the scale of a few centimetres ("late" galena + altaite).

(3) The steep array of early galena and altaite Pb isotopic compositions is interpreted as representing variability of the ore fluid Pb isotope composition at the time of mineralization. This variation in isotopic composition reflects mixing of Pb from two sources: mantle or mantle-derived mafic-ultramafic volcanic and intrusive rocks, and older crust underlying the greenstones or felsic intrusive rocks derived from this basement. Felsic and older basement sources dominate the Pb isotope signature, as these sources contain higher Pb abundances than the mafic greenstones. The steep array of early galena Pb isotope compositions is also evident in $^{208}Pb/^{204}Pb$ versus $^{206}Pb/^{204}Pb$ isotopic space, consistent with a mantle-crust Pb mixing trend, but scatter of data to high $^{208}Pb/^{204}Pb$ ratios may require a third component with high Th/U ratios, perhaps represented by depleted granulites.

(4) Lead isotope compositions of early galena and altaite from the Norseman lode gold deposits, although broadly constrained to the mantle-crust mixing line, display interdeposit trends of both uranogenic and thorogenic data outside of the range of analytical error. Two controls on the Pb isotopic composition of these ore minerals have been identified: (a) proximity to felsic intrusive rocks, with more radiogenic compositions in galena + altaite from gold lodes hosted in or near large felsic intrusive bodies, and (b) a three dimensional spatial variation, with more radiogenic compositions occurring to the south on the camp scale, and with increasing depth within individual deposits. The latter spatial variation correlates with proximity of the deposits to the greenstone margins, with more radiogenic compositions towards the margins, and reflects the proportion of older sialic crust versus mafic greenstone lithologies with which the ore fluid exchanged.

(5) Comparison of data from Norseman early galena and altaite with Pb isotope data from Higginsville and Victory lode gold deposits of the Kalgoorlie Terrane indicates that the regional variation in ore fluid Pb isotope compositions between the Kalgoorlie and Norseman Terranes recognized by Perring and McNaughton (1992) may be gradational in nature.

(6) Lead isotope data for early galena and altaite from the Norseman lode gold deposits are much more radiogenic than Pb isotope data from the lode gold deposits at Menzies at the northern margin of the Kalgoorlie Terrane. As both deposit areas are proximal to the greenstone margins and should be dominated by the older crust Pb isotope signature of the mantle-crust mixing line, the extremely radiogenic Norseman early galena and altaite suggest that the basement to the Norseman greenstones may be older than that of the Kalgoorlie Terrane.

(7) Hydrothermal biotite and hornblende from the Scotia mine that demonstrably formed during gold mineralization have highly disturbed ^{40}Ar-^{39}Ar spectra with total gas ages ranging between 1571 ± 12 to 1989 ± 12 Ma. This is despite the fact that in two cases pegmatite and hydrothermal ore samples came from within two metres of each other.

(8) The close spatial association between isotopically disturbed hydrothermal minerals and relatively undisturbed pegmatite minerals and hydrothermal muscovite precludes simple reheating as the explanation of the observed argon loss. Instead argon loss is interpreted as the result of interaction between hydrothermal minerals and low temperature fluids moving through ore zones during Proterozoic orogenic activity within the Albany - Fraser Province to the south. Muscovite within pegmatite dykes at Scotia, and within the quartz veins in the OK mine, remained relatively undisturbed during these episodes, due to reduced amount of fluid movement within the relatively impermeable pegmatites and quartz veins, or to the resistance of muscovite to isotopic resetting below its closure temperature relative to amphibole and biotite. In this situation, factors such as permeability, proximity to fluid pathways, microstructures, and chemical reactivity may be more important in governing ^{40}Ar-^{39}Ar systematics in hydrothermal minerals than factors known to influence volume diffusion.

(9) Although the Norseman example is an extreme case, more subtle forms of this fluid resetting phenomenon may be difficult to recognize and may lead to erroneous conclusions concerning the age of hydrothermal alteration and origin of gold mineralization in Archean terranes.

(10) Late galena and altaite have been discovered proximal to a large brittle structure, E-fault, that offsets the gold orebodies, and are considered to represent Pb-mineral growth significantly post-mineralization. Modelling indicates that Pb for this new galena + altaite growth is contributed from early galena + altaite, and evolved Pb from the felsic host lithologies. As the felsic intrusions and early ore

galenas have similar initial Pb isotopic compositions, these mixing arrays of uranogenic Pb isotope data can be interpreted as paleoisochrons. Regression of late galenas from two separate locations indicate that at least two distinct galena growth events occurred during the Proterozoic: one ca. 1950 ± 150 Ma, and one ca. 1400 ± 100 Ma. Both ages correlate to geologic events recorded in the Proterozoic Fraser Orogen 60 km to the southeast, and to the fluid-reset ^{40}Ar-^{39}Ar ages of alteration minerals in the Scotia deposits at the southern end of the Norseman Terrane.

(11) Gold is associated with both early and late galena, therefore, gold was either remobilized or reintroduced during the Proterozoic events. However, the restriction of late galena and significant gold concentrations to the conjunction of brittle structures and Archean quartz reefs argues for local gold remobilization rather than gold reintroduction during the Proterozoic event. This cryptic ore remobilization may be a common feature in Archean lode gold deposits where large later structures intersect auriferous quartz veins. If so, Pb-isotope data combined with documentation and radiometric dating of brittle structures and their associated hydrothermal alteration may be a practical exploration tool, serving as pathfinders to high-grade remobilized ore.

CHAPTER 7

SUMMARY OF RESEARCH

7.1 Problems in Archean geology: research objectives

A longstanding and widely debated question in Archean terranes concerns the nature of the extensive sequences of mafic-ultramafic lavas that are preserved in them. In particular, the extent and amount of geochemical variation within and between these sequences is poorly resolved. Questions remain as to the nature of their mantle source, specifically the mineralogical and geochemical nature of the mantle sources of mafic-ultramafic lavas, and to the depth and degree of partial melting that produced them. Complications also arise from the interaction of parental magmas with overlying mantle and lithosphere as they ascend and are emplaced in the upper crust. The geochemical effects of the latter processes are only cursorily understood.

The genesis of Archean lode gold deposits, so abundant in late Archean terranes worldwide, also remains enigmatic. Specific questions concerning these mineral deposits include the timing of high temperature alteration assemblages with respect to metamorphism and deformation of their host terranes. Are these high-temperature assemblages formed by high-temperature fluid flow, or alternatively are they the product of prograde metamorphism of lower temperature alteration assemblages? The source of the fluids is also debated, and is variously ascribed to magmatic sources, devolatization of host greenstones, meteoric water, devolatization of the lower crust, subcretion of material to the mantle lithosphere, and/or mantle degassing. In many terranes, geochronological data from hydrothermal minerals in gold deposits is at odds with geochronological data constraining the thermotectonic evolution of the host terranes, leading to wide disparity in the interpreted ages of Archean lode gold mineralization.

The Norseman Terrane is an ideal place to investigate these problems. The Norseman Terrane contains an extensive sequence of ca. 2.7 Ga mafic lavas and dykes, which are known to overlie older sialic crust. The Norseman Terrane also hosts extensive lode gold mineralization. The gold deposits collectively possess a variation in alteration mineralogy that represents a broad range in temperature within similar host rocks and in a

similar structural setting.

7.2 Archean mafic magmatism in the Norseman Terrane

The Woolyeenyer Formation of the Norseman Terrane has been previously described as a 'monotonous' sequence of basalts and comagmatic gabbros, with limited mineralogical and geochemical diversity. Quite to the contrary, this study has demonstrated great geochemical diversity among these mafic lithologies that cannot be distinguished petrographically, and has identified six major rock types:

(1) Tholeiitic basalts and gabbros that comprise the bulk of the Woolyeenyer Formation,

(2) High-magnesian tholeiite dykes (HMT), with similar trace element characteristics to the tholeiites, albeit at lower absolute abundances,

(3) Enriched high-magnesian tholeiites (EHMT), with enrichments in incompatible elements, fractionated HREE and marked Al-depletion,

(4) Transitional high-MgO tholeiites (THMT), with geochemical characteristics between those of HMT and EHMT,

(5) Enriched tholeiites (ET), with geochemical characteristics transitional between tholeiites and EHMT. This last group can be further subdivided into ET1, with flat HREE and enriched LREE, and ET2, with fractionated HREE, enriched LREE, and Al-depletion.

Consideration of whole-rock geochemistry and limited, but invariably positive, ε_{Nd} values indicate that tholeiites and HMT are likely comagmatic, produced by partial melting of mildly depleted upper mantle.

Detailed modelling of crustal assimilation processes indicates that the EHMT magmas cannot be produced by contamination of high-MgO parental magmas associated with HMT and tholeiites. Rather, the EHMT require that their mantle source was enriched in incompatible elements prior to generation of the EHMT magmas. Furthermore, modelling of P/REE and HFSE/REE systematics during mantle melting processes require that pyrope garnet was retained in the mantle source of the EHMT during partial melting. This suggests depths of melting greater than 150 km depth in a hot mantle plume.

Trace element modelling also suggests that the THMT formed by magma mixing between EHMT and HMT lavas, or by partial melting of a mixed mantle source. ET2 lavas are similarily mixtures between EHMT and tholeiite magmas. ET1 may be due to mixing of EHMT and tholeiite lavas, or may result from limited crustal contamination of

tholeiitic or HMT magma.

7.3 Mafic magmatism through time

The EHMT resemble trace element enriched picrites and Al-depleted basaltic komatiites identified elsewhere in Archean and (rarely) Proterozoic terranes. A debate continues in the literature as to the petrogenesis of such magmas, particularly their depth of melting, and whether garnet is retained in their mantle sources. This study demonstrates that garnet retention in the source is required in the generation of these magmas, and were thus melted at depths greater than 150 km (5 GPa), and likely greater than 240 km (8Gpa), where garnet is a stable phase on the liquidus. Such deep melting can only be achieved in the anomalously hot environment of mantle plumes.

Furthermore, this study demonstrates that P/HFSE and REE/HFSE systematics potentially be used to distinguish between majorite garnet versus pyrope garnet retention in mafic magma sources. The variation in the magnitude of normalized Zr, Hf and P anomalies may thus be an indicator of depth of melting in Al-depleted high-MgO magmas.

The common occurrence of mafic-ultramafic rocks with majorite garnet retention geochemical signatures in the early Archean, their sparse occurrence in the late Archean, rare occurrence in the Proterozoic, and absence in Phanerozoic terranes, supports a cooling mantle model. In a hotter Archean mantle, melting could regularly initiate at depths where majorite garnet is stable. As the mantle cooled, the depth at which melting could initiate became progressively shallower. At present, it appears that even in mantle plume environments, melting does not initiate at depths where majorite garnet is stable on the liquidus.

7.4 Long term versus short term enrichment of the EHMT source, and implications for mantle dynamics

The negative ε_{Nd} values of the EHMT may indicate that the mantle source of these magmas was enriched in incompatible elements much prior to their genesis. If so, this is the first identification of an enriched source being preserved in the hot Archean mantle. For an enriched source to be preserved in the Archean would require that lithosphere be subducted and stored at depth in the mantle (650 km discontinuity or core-mantle boundary), or that enriched mantle lithosphere be delaminated and entrained into deep mantle plumes. The possibility that such enriched sources can occur may require

that rocks from other Archean terranes, displaying the conjunction of trace-element enrichment, Al-depletion and negative ε_{Nd} values, be re-appraised by the methodology followed in this study.

Alternatively, the negative ε_{Nd} values of the EHMT may result from crustal contamination of an incompatible-element-enriched, Al-depleted magma. This model remains unconstrained by the modelling undertaken in this study, inasmuch as EHMT with positive ε_{Nd} values have not yet been identified.

Resolution of these scenarios awaits the results of a detailed Sm-Nd and Pb isotope study of Norseman mafic lithologies, which is presently being undertaken.

7.5 Archean lode gold deposits of the Norseman Terrane

Arsenopyrite and stable-isotope mineral pair geothermometry, and T-XCO2 phase equilibria, indicate that alteration assemblages associated with lode gold deposits of the Norseman Terrane formed at high temperatures. Furthermore, a thermal zonation of alteration assemblages is apparent throughout the terrane, from 420-475°C in Northern deposits, through 450-500°C in Central deposits, to 500-600°C in Southern deposits. This thermal zonation correlates with the peak metamorphic grade of the mafic lithologies that host the deposits, from upper-greenschist facies in the Northern deposits environs, through lower-amphibolite facies in the Central deposits area, to mid- to upper amphibolite facies in the environs of the Southern deposits.

Many lode gold deposits with high-temperature mineral assemblages, and particularly those of the Norseman Terrane, have been interpreted previously as forming pre-peak metamorphism. Therefore, a focus of this study was to confirm or refute this interpretation of pre-peak metamorphic mineralization by a detailed documentation of orebody morphology and textures of quartz veins and contiguous alteration assemblages. The following observations support a syn- to post-peak metamorphic timing of hydrothermal alteration and gold mineralization:

(1) Orebodies restricted to dilational jogs on ductile-brittle reverse-dextral to strike-slip shear zones.

(2) Quartz vein morphologies indicate synkinematic formation in ductile-brittle shear zones from overpressured fluids. Evidence includes:
   (a) the presence of breccia veins
   (b) laminated veins, suggesting formation from fluid flow during multiple seismic events
   (c) separation of wallrock inclusions and tension gashes consistent with vein

formation during reverse-dextral movement on the host shear zones.

(3) Quartz vein morphology varies from north to south, from massive + breccia + laminated veins in Northern deposits, to laminated + massive + breccia veins in Central deposits, to discontinuous banded veins in Southern deposits. This zonation of vein morphology is consistent with increasing temperatures (and/or pressures) of vein emplacement, and corroborates the regional zonation of metamorphic facies and alteration temperatures.

(4) Veins in all deposits are variably deformed, indicating syn-to late-kinematic formation.

(5) Vein quartz shows varying degrees of dynamic recovery in all deposits, corroborating syn-to late-kinematic vein formation.

(6) Vein quartz fabrics show progressively greater degrees of dynamic recovery from Northern deposits to Southern deposits, consistent with vein formation at progressively higher temperatures. from north to south.

(7) In all deposits, fibrous rosettes of alteration minerals can be observed. Such textures would not likely survive a subsequent prograde metamorphic event.

(8) Arsenopyrite in all deposits posesses complex oscillatory zoning, which would not likely survive a prograde metamorphic event.

(9) In Southern deposits, arsenopyrite rims löellingite, the opposite relationship to that expected from prograde metamorphism.

In combination, the above observations support a syn- to late-kinematic and syn- to post-peak metamorphic timing of fluid flow, vein emplacement, hydrothermal alteration and primary gold mineralization. As a corollary, any model of pre-, or significantly post-metamorphic gold mineralization can be ruled out.

7.6 Ore fluid sources

A detailed Pb isotope study of ore galenas from the Northern and Central deposits was undertaken with the aim of identifying potential Pb sources, and therefore potential fluid sources and flow paths. Pb isotope compositions of the ore fluids were highly variable in the Norseman deposits, contrary to observations on other gold camps in the ECYS. Ore fluid Pb at Norseman was invariably more radiogenic than the host lithologies, and becomes progressively more radiogenic with increasing proximity to older crust, and with increasing proximity to internal felsic intrusions. The data require Pb input to the ore fluid from:

(1) older crust underlying the greenstones

(2) intrusions derived from older crust,

(3) host greenstones,

(4) a high Th/U source, potentially depleted lower crustal granulites.

These interpretations require that the ore fluid Pb at Norseman was derived in part from older sialic crust underlying the Norseman Terrane or partially exchanged with such crust, and then partially equilibrated with the host greenstones. Therefore, the master plumbing system for the Norseman lode gold deposits was crustal in scale, penetrating into, and potentially through, the lower crust.

Ore fluid Pb at Norseman is much more radiogenic than any deposit in the Kalgoorlie Terrane, suggesting that the sialic basement to the Norseman Terrane is older than that underlying the adjacent Kalgoorlie Terrane. This interpretation corroborates the report of the oldest xenocrystic zircons from the ECYS in the Noganyer Formation of the Norseman Terrane (Campbell and Hill, 1988).

Calculated oxygen and hydrogen isotope compositions of the ore-forming fluids are consistent with a metamorphic or magmatic fluid source.

7.7 Geochronology of mineralization and the P-T-t-d-f evolution of the Norseman Terrane.

7.7.1 Age of mineralization

The minimum age of mineralization in the Norseman Terrane is constrained by $^{40}Ar/^{39}Ar$ ages on igneous muscovite from a pegmatite cross-cutting the Southern deposits and hydrothermal muscovite from a Central deposit to >2610 Ma. However, the following points argue for an older mineralization age:

(1) The brittle emplacement of the pegmatite, and its subhorizontal attitude, indicate that it significantly postdates mineralization.

(2) An older internal Sm-Nd isochron has been obtained on the pegmatite (ca. 2620 Ma),

(3) The coincidence of the igneous and hydrothermal muscovite ages, combined with the post-mineralization nature of the pegmatite, support interpretation of this 2610 Ma age as a cooling age,

(4) Structural observations on orebody and quartz vein morphologies, quartz and alteration mineral textures, and the correlation of calculated temperatures of alteration with regional metamorphic grade, collectively support a timing of fluid flow and concomitant hydrothermal alteration close to the thermal peak of metamorphism (ca. 2640-2665 Ma).

The confirmation of ca. 2630 Ma gold mineralization at Norseman places this

gold camp in the 2680-2630 Ma gold mineralization range recognized globally, including Canada, Finland, South Africa, Brazil and Australia.

7.7.2 Post-mineralization history of the Norseman Terrane

Whereas $^{40}Ar/^{39}Ar$ ages on muscovite indicate cooling of the Norseman Terrane through ca. 350°C at 2610 Ma, amphibole and biotite in the Scotia deposit have extremely disturbed Ar isotope systematics, yielding apparent $^{40}Ar/^{39}Ar$ ages ranging from ca. 2400 to 1000 Ma. Thermal resetting of the amphibole is precluded by the higher closure temperature for Ar diffusion in amphibole compared to muscovite (ca. 500°C vs. 350°C, respectively), in combination with the fact that igneous muscovite and hydrothermal amphibole samples are only metres apart. Therefore, the Ar isotope systematics of amphibole and biotite have been variably disturbed below their theoretical closure temperatures during the Proterozoic. This resetting is interpreted as having occurred by cryptic fluid movement trough the Scotia orebody during tectonic events recorded in the Proterozoic Fraser Orogen, some 100 km to the southeast of Scotia.

Similarly, Pb isotope systematics of ore galenas within the Central deposits show disturbance post-mineralization. Linear arrays of Pb isotope compositions of these 'late' galenas are interpreted as paleoisochrons, and indicate at least two periods of post-mineralization galena growth: one ca. 1950 Ma, and one at an indeterminate time later. These late galenas are restricted largely to areas proximal to late brittle faults, corroborating evidence from Ar systematics at Scotia that cryptic fluid movement has occurred through the Norseman Terrane during the Proterozoic.

References

Anderson, A.T., Greenland, L.P. (1969) Phosphorus fractionation diagram as a qualitative indicator of crystallisation differentiation of basaltic liquids. *Geochim. Cosmochim. Acta* **33**, 493-505.

Andrews, A.J., Hugon, H., Durocher, M., Corfu, F., Lavigne, M.J. (1986) The anatomy of a gold-bearing greenstone belt: Red Lake, Northwestern Ontario, Canada. In Macdonald, A.J. (ed.) Gold '86, an international symposium on the geology of gold deposits, Toronto, Ontario. Proceedings volume, 3-22.

Archer, N.R. (1990) Observations on alteration at the North Royal. Internal report to Central Norseman Gold Corporation (unpubl.)

Archibald, N.J., Bettenay, L.F., Binns, R.A., Groves, D.I., Gunthorpe, R.J. (1978) The evolution of Archean greenstone terrains, Eastern Goldfields Province, Western Australia. *Precambrian Res.* **6**, 103-131.

Armbrust, G.A., Gannicott, R.A. (1980) K/Rb ratios as a source indicator for hydrothermal fluids of the Seneca volcanogenic massive sulphide deposit, British Columbia. *Econ Geol.* **75**, 466-477.

Arndt, N.T., Jenner, G.A. (1986) Crustally contaminated komatiites and basalts from Kambalda, Western Australia, *Chem. Geol.* **56,** 229-255.

Arndt, N.T., Nisbet, E.G. (1982) Komatiites. George Allen and Unwin, London, 526 p.

Arth, J.G. (1976) Behaviour of trace elements during magmatic processes - a summary of theoretical models and their applications. *J. Res. U.S. Geol. Surv.* **4**, 41-47.

Bain, G.W. (1933) Wall rock mineralization along Ontario gold deposits: Economic *Geology* **28**, 705-745.

Barley, M.E. (1986) Incompatible-element enrichment in Archean basalts: a consequence of contamination by older sialic crust rather than mantle heterogeneity. *Geology* **14**, 947-950.

Barley, M.E., Groves, D.I. (1987) Hydrothermal alteration of Archean supracrustal sequences in the central Norseman-Wiluna belt, Western Australia: a brief review. *Geol. Dept. (Key Centre) and Univ. Extension, The Univ. of West. Aust. Publ.* **11**, 51-66.

Barley, M.E., Groves, D.I. (1990) Dechipering the tectonic evolution of Archean greenstone belts: the importance of contrasting histories to the distribution of mineral deposits in the Yilgarn Block. *Precambrian Res.* **46**, 3-20.

Barley, M.E., Groves, D.I., McNaughton, N.J. (1990) Regional hydrothermal alteration in greenstone belts. In Ho, S.E., Groves, D.I., Bennett, J.M. (eds.) Gold deposits of the Archaean Yilgarn Block, Western Australia: nature, genesis and exploration guides. *Geol. Dept. and Univ. Extension, Univ. of West. Aust. Publ.* **20**, 55-59.

Barnicoat, A.C, (1989) The genesis of amphibolite-facies gold deposits: a model, and the example of Fraser mine, Southern Cross. Key Centre report, Department of Geology, University of Western Australia (unpubl.)

Barnicoat, A.C., Fare, R.J., Groves, D.I., McNaughton, N.J. (1991) Synmetamorphic lode-gold deposits in high-grade Archaean settings. *Geology* **19,** 921-924.

Bau, M. (1991) Rare-earth mobility during hydrothermal and metamorphic fluid-rock interaction and the significance of the oxidation state of europium. *Chem. Geol.* **93**, 219-230.

Bekker, C. (1963) The "greenstones" of the Norseman district. M.Sc. thesis, University of Western Australia (unpubl.).

Beswick, A.E., Carmichael, I.S.E. (1978) Constraints on mantle source compositions imposed by phosphorous and the rare-earth elements, *Contrib. Mineral. Petrol.* **67**, 317-330.

Bettenay, L.F. (1988) Granitoid batholiths of the Eastern Goldfields Province, Tilgarn Block: characteristics and significance to gold mineralization. *Geol. Dept. (Key Centre) and Univ. Extension, The Univ. of West. Aust. Publ.* **12**, 227-237.

Bickle, M.J. (1990) Archean magmatism: 3rd International Archean Symposium, Extended Abstracts, Geoconferences (WA) Perth, 143-145.

Bickle, M.J. (1993) Plume origin for komatiites. *Nature* **365**, 390-391.

Binns, R.A., Gunthorpe, R.J., Groves, D.I. (1976) Metamorphic patterns and development of greenstone belts in the eastern Yilgarn Block, Western Australia. In Windley, B.F. (ed.) *The early history of the Earth.* John Wiley and Sons, New York, 303-313.

Bishop, F.C., Smith, J.V., Dawson, J.B. (1978) Na, K, P, and Ti in garnet, pyroxene and olivine from peridotite and eclogite xenoliths from African kimberlites. *Lithos* **11**, 155-173.

Bloem, E.J.M., Mcnaughton, N.J., Groves, D.I., Ridley, J.R. (1995) An indirect lead isotope age determination of gold mineralization at the Corinthia mine, Yilgarn Block, Western Australia. *Aust. J. Earth Sci.* **42**, 447-451.

Blundy, J.D., Holland, J.B. (1990) Calcic amphibole equilibria and a new amphibole-plagioclase geothermometer. *Contrib. Mineral. Petrol.* **104**, 208-224.

Böhlke, J.K. (1989) Comparison of metasomatic reactions between a common CO_2-rich vein fluid and diverse wall rocks: intensive variables, mass transfers, and Au mineralization at Alleghany, California. *Econ. Geol.* **84**, 291-327.

Bottinga, Y., Javoy, M. (1975) Oxygen isotope partitioning among the minerals in igneous and metamorphic rocks. *Rev. Geophys. Space Phys.* **13,** 401-418.

Boyle, R.W. (1979) The geochemistry of gold and its deposits. *Canada. Geol. Surv. Bull.* **280**, 544 p.

Brookins, D.G. (1989) Aqueous geochemistry of rare earth elements. *Rev. Mineral.* **21**, 201-226.

Browning, P., Groves, D.I., Blockley, J.G. and Rosman, K.J.P. (1987) Lead isotope constraints on the age and source of gold mineralization in the Archean Yilgarn Block, Western Australia. *Econ. Geol.* **82**, 971-986.

Burrows, D.R., Wood, P.C., Spooner, E.T.C. (1986) Carbon isotope evidence for a magmatic origin for Archean gold-quartz vein ore deposits: *Nature* **321**, 851-854.

Burrows, D.R. and Spooner, E.T.C. (1987) Generation of a magmatic H_2O-CO_2 fluid enriched in Au, Mo and W within an Archean sodic granodiorite stock, Mink Lake, northwestern Ontario. *Econ. Geol.* **82**, 1931-1957.

Burrows, D.R., Spooner, E.T.C. (1989) Relationships between Archean gold quartz vein-shear zone mineralization and igneous intrusions in the Val d'Or and Timmins areas, Abitibi Subprovince, Canada. In: Keays, R.R., Ramsay, W.R.H., Groves, D.I. (eds.) The geology of gold deposits: the perspective in 1988. *Econ. Geol. Mono.* **6**, 424-444.

Caddey, S.W., Bachman, R.L., Campbell, T.J., Reid, Rolland, R.R., Robert, P.O. (1991) The Homestake gold mine, an early Proterozoic iron-formation hosted gold deposit, Lawrence County, South Dakota. *U.S. Geol. Surv. Bull.* **1857-J**.

Cameron, E.M. (1988) Archean gold: relation to granulite formation and redox zoning in the crust. *Geology* **16**, 26-29.

Cameron, W.E., McCulloch, M.T., Walker, D.A. (1983) Boninite petrogenesis: chemical and Nd-Sr isotopic constraints, *Earth Planet. Sci. Lett.* **65**, 75-89.

Campbell, I.H., Griffiths, R.W. (1990) Implications of mantle plume structure for the evolution of flood basalts. *Earth Planet. Sci. Lett.* **99**, 79-93.

Campbell, I.H., Griffiths, R.W. (1992) The changing nature of mantle hotspots through time: implications for the chemical evolution of the mantle. *J. Geology* **92**, 497-523.

Campbell, I.H., Hill, R.I. (1988) A two stage model for the formation of granite-greenstone terrains of the Kalgoorlie-Norseman area, Western Australia. *Earth Planet. Sci. Lett.* **90**, 11-25.

Campbell, I.H., Griffiths, R.W., Hill, R.I. (1989) Melting in an Archean mantle plume: heads its basalts, tails its komatiites. *Nature* **339**, 697-699.

Campbell, I.H., Lesher, C.M., Coad, P., Franklin, J.M., Gorton, M.P., Thurston, P.C. (1984) Rare-earth element mobility in alteration pipes below massive Cu-Zn sulphide deposits. *Chem. Geol.* **45**, 181-202.

Campbell, J.D. (1990) Hidden gold: the Central Norseman story. *Aust. Institute of Mining and Metall. Mono.* **16**, 68p.

Cassidy, K.F. (1992) Archaean granitoid-hosted gold deposits in greenschist to amphibolite facies terrains: a highP-T to low P-T depositional continuum

equivalent to greenstone-hosted deposits, Ph.D. thesis, The University of Western Australia, Nedlands (unpublished), 296 p.

Cassidy, K.F., McNaughton, N.J. (in prep.) Source and Proterozoic remobilization of ore metals in Archean lode gold deposits: lead isotope evidence from quartz-sulphide veins at the Lady Bountiful mine, Yilgarn Craton, Western Australia.

Cassidy, K.F., Barley, M.E., Groves, D.I., Perring, C.S. and Hallberg, J.A. (1991) An overview of the nature, distribution and inferred tectonic setting of granitoids in the late-Archaean Norseman-Wiluna Belt, *Precambrian Res.* **51**, 51-83.

Cassidy, K.F. and Bennett, J.M. (1993) Gold mineralisation at the Lady Bountiful Mine, Western Australia: an example of a granitoid-hosted Archaean lode gold deposit. *Mineral. Deposit.* **28**, 388-408.

Cater, I. (1992) The nature and controls on gold mineralisation in the Poseidon South gabbro-hosted deposit, Higginsville, Western Australia. UWA B.Sc. Hons. thesis, unpubl., 56p.

Cathelineau, M., Boiron, M-C., Holliger, P., Marion, P., Denis, M. (1989) Gold in arsenopyrites: crystal chemistry, location and state, physical and chemical conditions of deposition, *in* Keays, R.R., Ramsay, W.R.H. and Groves, D.I., eds., The Geology of Gold Deposits: The Perspective in 1988: *Econ. Geol. Mono.* **6**, 328-341.

Cathles, L.M. (1986) The geologic solubility of gold from 200-350°C, and its implications for gold-base metal ratios in vein and stratiform deposits. In Clark, L.A. (ed.), Gold in the Western Shield: *Canadian Inst. of Mining and Metall. Spec. Volume* **38**, 187-210.

Cattell, A., Arndt, N. (1987) Low-and high-alumina komatiites from a late Archaean sequence, Newton Township, Ontario. *Contrib. Mineral. Petrol.* **97**, 218-227.

Chapman, J.S., Offe, L.A. (1993) RP180 - documentation of the Butterfly Dyke, Norseman. Internal report to Western Mining Corporation K/3527 (unpubl.), 35 p.

Chauvel, C., Dupré, B., Jenner, G.A. (1985) The Sm-Nd age of Kambalda volcanics is 500 Ma too old! *Earth Planet. Sci. Lett.* **74**, 315-324.

Clague, D.A. (1987) Hawaiian alkaline volcanism. In *Alkaline Igneous Rocks* (eds. J.G. Fitton, and B.G.J. Upton), *Geol. Soc. Spec. Publ.* **30**, 227-252.

Claoué-Long, J.C., Thirlwall, M.F., Nesbitt, R.W. (1984) Revised Sm-Nd systematics of Kambalda greenstones, Western Australia. *Nature* **307**, 697-701.

Claoué-Long, J.C., Compston, W., Cowden, A. (1988) The age of the Kambalda greenstones resolved by ion-microprobe: implications for Archaean dating methods. Earth Planet. Sci. Lett. 89: 239-259.

Claoué-Long, J.C., King, R.W., Kerrich, R. (1990) Archean hydrothermal zircon in the Abitibi greenstone belt: constraints on the timing of gold mineralization. *Earth and Planetary Science Letters* **98**, 109-128.

Clark, M.E., Archibald, N.J. and Hodgson, C.J. (1986) Structural and metamorphic setting of the Victory gold mine, Kambalda, Western Australia. In Macdonald, A.J. (ed.) Gold '86, an international symposium on the geology of gold deposits, Toronto, Ontario. Proceedings volume: 243-254.

Clark, M.E., Carmichael, D.M., Hodgson, C.J., Fu, M. (1989) Wall-rock alteration, Victory gold mine, Kambalda, Western Australia: processes and P-T-X_{CO2} conditions of metasomatism. In: Keays, R.R., Ramsay, W.R.H., Groves, D.I. (eds.) The geology of gold deposits: the perspective in 1988. *Econ. Geol. Mono.* **6**, 445-459.

Clayton, R.N., Keiffer, S.W. (1992) Oxygen isotopic thermometer calibrations. in H.P. Taylor, Jr., J.R. O'Neil, I.R. Kaplan (eds.) Stable Isotope Geochemistry: a Tribute to Samuel Epstein. *The Geochemical Soc. Spec. Publ.* **3**, 3-10.

Clayton, R.N., O'Neil, J.R., Mayeda, T.K. (1972) Oxygen isotope exchange between quartz and water. *J. Geophys. Res.* **77**, 3057-3067.

Colvine, A.C. (1989) An empirical model for the formation of Archaean gold deposits: products of final cratonization of the Superior province, Canada. In: Keays, R.R., Ramsay, W.R.H., Groves, D.I. (eds.) The geology of gold deposits: the perspective in 1988. *Econ. Geol. Mono.* **6**, 37-53.

Colvine, A.C., Fyon, J.A., Heather, K.B., Marmont, S., Smith, P.M., Troop, D.G. (1988) Archaean lode gold deposits in Ontario. *Ontario Geol. Surv. Misc. Pap.* **139**, 136p.

Compston, W., Williams, I.S., Campbell, I.H., Gresham, J.J. (1986) Zircon xenocrysts from the Kamblada volcanics: age constraints and direct evidence for older continental crust below the Kamblada-Norseman greenstones. *Earth Planet. Sci. Lett.* **76**, 299-311.

Condie, K.C. (1990) Geochemical characteristics of Precambrian basaltic greenstones. In *Early Precambrian Basic Magmatism* (eds. R.P. Hall, and D.J. Hughes), 40-55. Blackie.

Connolly, H.J.C. (1936) A contour method of revealing some ore structures. *Econ Geol* **31**, 259-271.

Cox, S.F. (1987) Antitaxial crack-seal vein microstructures and their relationship to displacement paths. *J. Struct. Geol.* **9**, 779-787.

Cox, S.F., Etheridge, M.A., Wall, V.J. (1990) Fluid pressure regimes and fluid dynamics during deformation of low-grade metamorphic terranes: implications for the genesis of mesothermal gold deposits, *in* Robert, F., Sheahan, P.A. and Green S.B., eds., Greenstone Gold and Crustal Evolution, NUNA Conference Volume, 46-53.

Cox, S.F., Wall, V.J., Etheridge, M.A., Potter, T.F. (1991) Deformational and metamorphic processes in the formation of mesothermal vein-hosted gold deposits - examples from the Lachlan Fold Belt in central Victoria: *Ore Geol. Rev.* **6**, 391-423.

Craw, D. and Koons, P.O. (1989) Tectonically-induced hydrothermal activity and gold mineralization adjacent to major fault zones, *in* Keays, R.R., Ramsay, W.R.H. and Groves, D.I., eds., The Geology of Gold Deposits: the Perspective in 1988: *Econ. Geol. Mono.* **6**, 463-470.

DePaolo, D.J. (1981) Trace elements and isotopic effects of combined wallrock assimilation and fractional crystallization. *Earth Planet. Sci. Lett.* **53**, 189-202.

de Ronde, C.E.J., Spooner, E.T.C., de Wit, M.J., Bray, C.J. (1992) Shear zone-related, Au quartz vein deposits in the Barberton greenstone belt, South Africa: field and petrographic characteristics, fluid properties, and light stable isotope geochemistry: *Econ. Geol.* **87**, 366-402.

Doe, B.R., Stacey, J.S. (1974) The application of lead isotopes to the problems of ore genesis and ore prospect evaluation: a review. *Econ. Geol.* **69**, 757-776.

Doe, B.R., Zartman, R.E. (1979) Plumbotectonics 1. the Phanerozoic. in H.L. Barnes (ed.), *Geochemistry of Hydrothermal Ore Deposits, 2nd ed.* Holt, Reinhart and Winston, New York, 450-479.

Doepel, J.J.G. (1973) Explanatory notes on the Norseman 1:250000 geological sheet (SI 51-02), Western Australia. Geological Survey of Western Australia.

Drummond, B.J. (1988) A review of crust/upper mantle structure in the Precambrian areas of Australia and implications for Precambrian crustal evolution. *Precambrian Res.* **40/41**, 101-116.

Drummond, S.E., Ohmoto, H. (1985) Chemical evolution and mineral deposition in boiling hydrothermal systems: *Econ. Geol.* **80**, 126-147.

Drury, M.R., Urai, J.L. (1990) Deformation-related recrystallization processes: *Tectonophysics* **172**, 235-253.

Dunlap, J.D., Tessier, C., McDougall, I., Baldwin, S. (1991) Ages of deformation from K/Ar and ^{40}Ar-^{39}Ar dating of white micas. *Geology* **19**, 1213-1216.

England, P.C., Richardson, S.W. (1977) The influence of erosion upon the mineral facies of rocks from different metamorphic environments. *J. Geol. Soc. London* **134**, 201-213.

England, P.C., Thompson, A.B. (1984) Pressure-temperature-time path of regional metamorphism I. Heat transfer during the evolution of regions of thickened continental crust: *J. Petrology*, **25**, 894-928.

Eslinger, E.V., Savin, S.M., Yeh, H. (1979) Oxygen isotope geothermometry of diagenetically altered shales. *SEPM Spec. Publ.* **26**, 113-124.

Essene, E.J. (1989) The current status of thermobarometry in metamorphic rocks. In Daly, J.S., R.A. Cliff, B.W.D. Yardley (eds.) Evolution of Metamorphic belts. **Geol. Soc. Spec. Publ. 43**, 1-44.

Exley, R.A., Smith, J.V., Dawson, J.B. (1983) Alkremite, garnetite and eclogite xenoliths from Bellsbank and Jagersfontein, South Africa. *Am.. Mineral.* **68**, 512-516.

Faure, G. (1986) *Principles of Isotope Geology, 2nd edition.* John Wiley and Sons, New York, 589 p.

Faure, G. (1991) *Principles and applications of inorganic geochemistry.* MacMillan Publishing Company, New York, 626 p.

Fedorowich, J., Stauffer, M., Kerrich, R. (1991) Structural setting and fluid characteristics of the Proterozoic Tartan Lake gold deposit, Trans-Hudson orogen, northern Manitoba: *Econ. Geol.* **86**, 1434-1467.

Fedorowich, J.S., Richards, J.P., Jain, J.C., Kerrich, R., Fan, J. (1993) A rapid method for REE and trace-element analysis using laser sampling ICP-MS on direct fusion whole-rock glasses. *Chem. Geol.* **106**,.

Feng, R., Kerrich, R. (1992) Geochemical evolution of granitoids from the Archean Abitibi Southern Volcanic Zone and the Pontiac subprovince, Superior Province, Canada: Implications for tectonic history and source regions, *Chem. Geol.* **98**, 23-70.

Fletcher, I.R., Libby, W.G., Rosman, K.J.R. (1987) Sm-Nd dating of the 2411 Ma Jimberlana dyke, Yilgarn Block, Western Australia. *Aust. J. Earth Sci.* **34**, 523-525.

Fletcher, I.R., Myers, J.S., Ahmat, A.L. (1991) Isotopic evidence on the age and origin of the Fraser Complex, Western Australia: a sample of mid-Proterozoic lower crust. *Chem. Geol.* **87**, 197-216.

Franklin, J.M., Roscoe, S.M., Loveridge, W.D., Sangster, D.F. (1983) Lead isotope studies in the Superior and Southern provinces. *Geol. Surv. Can. Bull.* **351**: 60p.

Fujimaki, H., Tatsumoto, M., Aoki, K-i. (1984) Partition coefficients of Hf, Zr, and REE between phenocrysts and groundmasses, *Jour. Geophys. Res.* **89**, B662-B672.

Fyfe, W.S., Kerrich, R. (1984) Gold: natural concentration processes, *in* Foster, R.P., ed., Gold '82. *Geol. Soc. Zimbabwe Spec, Publ.* **1**, 99-127.

Fyon, J.A., Crocket, J.H., Schwarcz, H.P. (1983) Application of stable isotope studies to gold metallogeny in the Timmins-Porcupine camp: *Ontario Geol. Surv. Open File Report* **5464**: 182p.

Fyon, J.A., Crocket, J.H., Schwarcz, H.P. (1984) The Carshaw and Malga iron-formation-hosted gold deposits of the Timmins area, In: Colvine, A.C. (Editor) The Geology of Gold in Ontario: *Ontario Geol. Surv. Misc. Paper* **110**, 98-110.

Gebre-Mariam, M., Groves, D.I., Ho, S.E., McNaughton, N.J., Vearncombe, J.R. (1991) The Archaean lode-gold deposit at Racetrack, near Kalgoorlie, Western Australia: a transitional mesothermal-epithermal hydrothermal system, in Pagel and Leroy (eds.), *Source, Transport and Deposition of Metals*: Balkema, Rotterdam, 661-664.

Gee, R.D. (1979) Structure and tectonic style of the Western Australian shield. *Tectonophysics* **58**, 327-369.

Gee, R.D., Baxter, J.L., Wilde, S.A., Williams, I.R. (1981) Crustal development in the Archaean Yilgarn Block, Western Australia. In: J.E. Glover and D.I Groves (eds.), Archaean Geology: Second International Symposium, Perth, 1980. *Geol. Soc. Aust. Spec. Publ.* **7**, 43-56.

Gee, R.D., Myers, J.S., Trendall, J.F. (1986) Relation between Archean high-grade gneiss and granite-greenstone terrain in Western Australia. Precambrian Res. 33, 87-102.

Glover, J.E., Ho, S.E. (eds. 1990) The Archean: Terrains, Processes and Metallogeny. *Geol. Dept. and Univ. Extension, Univ. of West. Aust. Publ.* **22**, 435 p.

Goldfarb, R.J., Snee, L.W., Miller, L.D., Newberry, R.J. (1991) Rapid dewatering of the crust deduced from ages of mesothermal gold deposits *Nature* **354,** 296-298.

Golding, S.D. (1982) An isotopic and geochemical study of gold mineralization in the Kalgoorlie-Norseman region, Western Australia. Ph.D. thesis, University of Queensland (unpubl.).

Golding, S.D., Clark, M.E., Keele, R.A., Wilson, A.F., Keays, R.R. (1990) Geochemistry of Archean epigenetic gold deposits in the Eastern Goldfields Province, Western Australia. *Geol. Dept. (Key Centre) and Univ. Extension, Univ. of West. Aust. Publ.* **23,** 141-176.

Golding, S.D., Wilson, A.F. (1982) Geochemical and stable isotope studies of the Crown and Mararoa Reefs, Norseman, Western Australia. *Revista Brasileita de Geosciecias* **12** (1-3), 445-456.

Goodrich, C.A. (1984) Phosphoran pyroxene and olivine in silicate inclusions in natural iron-carbon alloy, Disko Island, Greenland *Geochim. Cosmochim. Acta* **48**, 1115-1126.

Grau, G., Chauvel, C., Arndt, N.T., Cornichet, J. (1990) Aluminum depletion in komatiites and garnet fractionation in the early Archean mantle: Hafnium isotopic constraints. *Geochim. Cosmochim. Acta* **54,** 3095-3101.

Greenough, J.D., Fryer, B.J., Robinson, P.T. (1990) Geochemical effects of alteration on mafic rocks from Indian Ocean site 706. *Proceedings of the Ocean Drilling Program, Scientific Results* **115**, 85-92.

Groves, D.I. (1993) The crustal continuum model for late Archean lode gold deposits of the Yilgarn Block, Western Australia. *Mineral. Deposit.* **28**, 366-374.

Groves, D.I., Phillips, G.N. (1987) The genesis and tectonic controls on Archaean gold deposits of the Western Australian Shield: a metamorphic replacement model. *Ore Geol. Rev.* **2**, 287-322.

Groves, D.I., Barley, M.E., Cassidy, K.F., Fare, R.J., Hagemann, S.G., Ho, S.E., Hronsky, J.M.A., Mikucki, E.J., Mueller, A.G., McNaughton, N.J., Ridley, J.R., Vearncombe, J.R. (1990) Sub-greenschist to granulite-hosted Archaean

lode-gold deposits: a depositional continuum from deep-sourced hydrothermal fluids in crustal-scale plumbing systems. In Glover, J.E., Ho, S.E. (eds.) The Archaean: terrains, processes and metallogeny. *Geol. Dept. (Key Centre) and Univ. Extension, The Univ. of West. Aust. Publ.* **22**, 325-337.

Guha, J., Kanwar, R. (1987) Vug brines in fluid inclusions: a key to understanding secondary gold enrichment processes and the evolution of deep brines in the Canadian Shield. In: P. Fritz and S.K. Frape (Editors), Saline Water and Gases in the Crystalline Rocks. *Geol. Assoc. Can. Spec. Pap.* **33**, 95-101.

Hagemann, S,G., Groves, D.I., Ridley, J.R. (1993) The Wiluna lode-gold deposits, Western Australia: an example of a high crustal-level Archaean lode-gold system, *in* Hach-Ali, F., Torres-Ruiz, J. and Gervilla, F. (eds.) *Current research in geology applied to ore deposits*, 469-472.

Hall, H.I.E., Bekker, C. (1965) Gold deposi*ts of Norseman. In McAndrew, J. (ed.) Geology of Australian ore deposits. 8th Commonwealth Mining and Metallurgy Congress*, Melbourne, 101-107.

Hall, R.S., Rigg, D.M. (1986) Geology of the West Anticline Zone, Musslewhite prospect, Opapimiskan Lake, Ontario, Canada. In Macdonald, A.J. (ed.) Gold '86, an international symposium on the geology of gold deposits, Toronto, Ontario. Proceedings volume, 124-136.

Hallberg, J.A. (1970) The petrology and geochemistry of metamorphosed Archaean basic volcanic and related rocks between Coolgardie and Norseman, Western Australia. Ph.D. thesis, University of Western Australia (unpubl.).

Hallberg, J.A. (1972) Geochemistry of Archaean volcanic belts in the Eastern Goldfields region of Western Australia, *J. Petrol.* **13**, 45-56.

Hallberg, J.A., Williams, D.A.C. (1972) Archaean mafic and ultramafic rock associations in the Eastern Goldfields region, Western Australia. *Earth Planet. Sci. Lett.* **15**, 191-200.

Halleran, A.D., Russell, J.K. (1990) Trace elements formulated as pearce element ratios II: recognition of open system behaviour. *Geol. Assoc. Canada Short Course Notes* **8**.

Hamilton, J.V., Hodgson, C.J. (1986) Mineralization and structure of the Kolar gold field, India. In Macdonald, A.J. (ed.) Gold '86, an international symposium on the geology of gold deposits, Toronto, Ontario. Proceedings volume, 270-283.

Hammarstrom, J.M., Zen, E-An. (1986) Aluminum in hornblende: an empirical igneous geobarometer. *Am. Mineral.* **71**, 1297-1313.

Hammond, R.L., Nisbet, B.W. (1992) Towards a structural and tectonic framework for the central Norseman-Wiluna belt, Western Australia. In Glover, J.E., Ho, S.E. (eds.) The Archaean: terrains, processes and metallogeny. *Geol. Dept. (Key Centre) and Univ. Extension, The Univ. of West. Aust. Publ.* **22**, 39-50.

Hanes, J.A., Archibald, D.A, Hodgson, C.J. (1992) Dating Archaean auriferous quartz vein deposits in the Abitibi greenstone belt, Canada: ^{40}Ar-^{39}Ar evidence

for a 70-100 m.y.-time gap between plutonism-metamorphism and mineralisation. *Econ. Geol.* **87**, 1849-1861.

Hanski, E.J. (1992) Petrology of the Pechenga ferropicrites and cogenetic, Ni-bearing gabbro-wehrlite intrusions, Kola Peninsula, Russia. *Geol. Surv. Finland. Bull.* **367**, 192 p.

Hanski, E.J., Smolkin, V.F. (1995) Iron- and LREE-enriched mantle source for early Proterozoic intraplate magmatism as exemplified by the Pechenga ferropicrites, Kola Peninsula, Russia. *Lithos* **34**, 107-125.

Harrison, T.M., FitzGerald, J.D. (1986) Exsolution in hornblende and its consequences for ^{40}Ar-^{39}Ar age spectra and closure temperature. *Geochim. Cosmochim. Acta*, **50**, 247-253.

Hattori, K. (1993) Diverse metal sources of Archaean gold deposits: evidence from in situ lead-isotope analysis of individual grains of galena and altaite in the Ross and Kirkland Lake deposits, Abitibi Greenstone belt, Canada. *Contrib. Mineral. Petrol.* **113**,185-195.

Hawkesworth, C.J., Gallagher, K., Hergt, J.M., McDermott, F. (1993) Trace element fractionation processes in the generation of island arc basalts, *Phil. Trans. R. Soc. Lond.* **A 342**, 179-191.

Hayashi, K-I., Ohmoto, H. (1991) Solubility of gold in NaCl- and H_2S-bearing aqueous solutions at 250-350 C: *Geochim. Cosmochim. Acta* **55**, 2111-2126.

Henderson, P. (ed. 1984) *Developments in geochemistry 2: Rare Earth Element Geochemistry*. Elsevier, Amsterdam, 510 p.

Herzberg, C. (1992) Depth and degree of melting of komatiites, *J. Geophys. Res.* **97**, 4521-4540.

Herzberg, C.T. (1995) Generation of plume magmas through time: an experimental perspective. In: J.N. Ludden and N.T. Arndt (eds.), Mafic Magmatism through Time. *Chem. Geol.* **126**, 1-16.

Herzberg, C., Feigenson, M., Skuba, C., Ohtani, E. (1988) Majorite fractionation recorded in the geochemistry of peridotites from South Africa. *Nature* **332**, 823-826.

Hess, J.C., Lippolt, H.J., Wirth, R. (1987) Interpretation of ^{40}Ar-^{39}Ar spectra of biotites: evidence from hydrothermal degassing experiments and TEM studies. *Chem. Geol.* **66**, 137-149.

Hill, R.I., Compston, W. (1986) Age of granite emplacement, southeastern Yilgarn Block, Western Australia. Res. School Earth Sci., Austr. Nat. Univ., Ann. Rep. 1986, 70-71.

Hill, R.I., Campbell, I.H., Compston, W. (1989) Age and origin of granitic rocks in the Kalgoorlie-Norseman region of Western Australia: implications for the origin of Archaean crust. *Geochim. Cosmochim. Acta* **53**, 1259-1275.

Hill, R.I., Chappell, B.W., Campbell, I.H. (1992) Late Archaean granites of the southeastern Yilgarn Block, Western Australia: age, geochemistry, and origin. *Trans. Royal Soc. Edinburgh: Earth Sci.* **83**, 211-226.

Ho, S.E., Bennett, J.M., Cassidy, K.F., Hronsky, J.M.A., Mikucki, E.J., Sang, J.H., (1990) Fluid inclusion studies, *in* Ho, S.E., Groves, D.I. and Bennett, J.M. eds., Gold deposits of the Archaean Yilgarn Block, Western Australia: Nature, Genesis and Exploration Guides: *Geol. Dept. and Univ. Extension, Univ. of West. Aust. Publ.* **20**, 198-211.

Ho, S.E., Groves, D.I., Bennett, J.M. (eds.) (1990) Gold deposits of the Archaean Yilgarn Block, Western Australia: nature, genesis and exploration guides. *Geol. Dept. and Univ. Extension, Univ. of West. Aust. Publ.* **20.**

Ho, S.E., Groves, D.I., McNaughton, N.J., Mikucki, E.J. (1992) The source of ore fluids and solutes in Archaean lode-gold deposits of Western Australia. *J. Volcan. Geotherm. Res.* **50**, 173-196.

Hodgson, C.J. (1989) The structure of shear-related, vein type gold deposits: a review: *Ore Geol. Rev.* **4**, 231-273.

Hodgson, C.J. (1993) Mesothermal lode-gold deposits. in Kirkham, R.V., Sinclair, W.D., Thorpe, R.I., Duke, J.M. (eds.) Mineral Deposit Modelling. *Geol. Assoc. Canada Spec. Pap.* **40**, 635-678.

Holdaway, M.J. (1971) Stability of andalusite and the aluminum silicate phase diagram. *Am. J. Sci.* **271**, 97-131.

Holland, H.D. (1978) *The chemistry of the atmosphere and oceans.* Wiley Interscience, New York.

Holland, T.J.B., Powell, R. (1990) An enlarged and updated internally consistent dataset with uncertainties and correlations: the system K_2O-Na_2O-CaO-MgO-FeO-Fe_2O_3-Al_2O_3-TiO_2-SiO_2-C-H_2-O_2: *J. Metamorphic Geol.* **8**, 89-124.

Hronsky, J.M.A., Cassidy, K.F., Grigson, M.W., Groves, D.I., Hagemann, S.G., Mueller, A.G., Ridley, J.R., Skwarnecki, M.S., Vearncombe, J.R. (1990) Deposit and mine-scale structure. In Ho, S.E., Groves, D.I., Bennett, J.M. (eds.) Gold deposits of the Archaean Yilgarn Block, Western Australia: nature, genesis and exploration guides. *Geol. Dept. Univ. Extension, Univ. West. Aust. Publ.* **20**, 38-54.

Huppert, H.E., Sparkes, R.S.J. (1985) Cooling and contamination of mafic and ultramafic lavas during ascent through continental crust. *Earth Planet. Sci.Lett.* **74**, 371-386.

Irwin, W.P. (1973) Terranes of the western Paleozoic and Triassic belt in the southern Klamath Mountains, California. *U.S. Geol. Surv. Prof. Paper* **800-C**, C103-C111.

Isles, D.J., Harman, P.G., Cunneen, J.P. (1989) The contribution of high resolution aeromagnetics to Archean gold exploration in the Kalgoorlie region, Western

Australia. In: Keays, R.R., Ramsay, W.R.H., Groves, D.I. (eds.) The geology of gold deposits: the perspective in 1988. *Econ.Geol. Mono.* **6**, 389-397.

Jaffey, A.H., Flynn, K.F., Glendenin, L.E., Bentley, W.C., Essling, A.M. (1971) Precision measurement of half-lives and specific activities of 235U and 238U. *Phys. Rev.* **C4**, 1889p.

Jäger, E. (1979) Introduction to geochronology. In Jäger, E.and J.C. Hunziker (eds.) *Lectures in Isotope Geology*. Spinger -Verlag, Berlin.

Jahn, B-m., Gruau, G., Glickson, A.Y. (1982) Komatiites of the Onverwacht Group, South Africa: REE geochemistry, Sm/Nd age and mantle evolution. *Contrib. Mineral. Petrol.* **80**, 25-40.

Jean, G.E., Bancroft, G.M. (1985) An XPS and SEM study of gold deposition at low temperature on sulphide mineral surfaces: concentration of gold by adsorption/reduction: *Geochim. Cosmochim.Acta* **49**, 979-987.

Jemielita, R.A., Davis, D.W., Krogh, T.E. (1990) U-Pb evidence for Abitibi gold mineralization postdating greenstone magmatism and metamorphism. *Nature* **346**, 831-834.

Jenner, G.A., Longerich, H.P., Jackson, S.E., Fryer, B.J. (1990) ICP-MS --- a powerful tool for high-precision trace-element analysis in Earth sciences: evidence from analysis of selected U.S.G.S. reference samples. *Chem. Geol.* **83**, 133-148.

Jochum, K.P., Arndt, N.T., Hoffman, A.W. (1991) Nb-Th-La in komatiites and basalts: constraints on komatiite petrogenesis and mantle evolution. *Earth Planet. Sci. Lett.* **107**, 272-289.

Jochum, K.P., Seufert, H.M., Thirlwall, M.F. (1990) Multielement analysis of 15 international standard rocks by isotope dilution spark-source mass spectrometry. *Geostand. Newslett.* **14**, 469-473.

Johnson, E.L. (1991) Experimentally determined limits for H_2O-CO_2-NaCl immiscibility in granulites: *Geology* **19**, 925-928.

Johnson, K. (1988) The Norseman Gold Deposits. In Groves, D.I., Barley, M.E., Ho, S.E., Hopkins, G.M.F. (eds.) Bicentennial Gold '88 Excursion Guidebook. Western Australian gold deposits. *Geol. Dept. Univ. Extension, Univ. West. Aust. Publ.***14**, 114-121.

Jolly, W.T., Hallberg, J.A. (1990) Role of crustal contamination in heterogeneous Archean volcanics from the Leonora region, Western Australia. *Precambrian Res.* **48**, 75-98.

Kato, T., Ringwood, A.E., Irifune, T. (1988) Experimental determination of element partitioning between silicate perovskites, garnets and liquids: constraints on early differentiation of the mantle. *Earth Planet Sci. Lett.* **89**, 123-145.

Kamenetsky, V.S., Sobolev, A.V., Joron, J.-L., Semet, M.P. (1995) Petrology and geochemistry of cretaceous ultramafic volcanics from Eastern Kamchatka. *J. Petrol.* **36**, 637-662.

Keele, R.A. (1984) Emplacement and deformation of Archaean gold-bearing quartz veins, Norseman, Western Australia. Ph.D. thesis, University of Leeds (unpubl.).

Kelemen, P.B., Johnson, K.T.M., Kinzler, R.J., Irving, A.J. (1990) High-field strength element depletions in arc basalts due to mantle-magma interaction. *Nature* **345**, 521-524.

Kelemen, P.B., Shimuzu, N., Dunn, T. (1993) Relative depletion of niobium in some arc magmas and the continental crust: partitioning of K, Nb, La and Ce during melt/rock reaction in the upper mantle. *Earth Planet. Sci. Lett.* **120,** 111-134.

Kent, A.J.R. (1994) Geochronological constraints on the timing of Archean gold mineralization in the Yilgarn Craton, Western Australia. Ph.D. thesis, The Australian National University (unpubl.).

Kent, A.J.R., Hagemann, S.G. (submitted) Constraints on the timing of lode-gold mineralization in the Wiluna greenstone belt, Yilgarn Craton, Western Australia. Submitted to Aust. J. Earth Sci. July/95.

Kent, A.J.R., McCuaig, T.C. (submitted) Proterozoic disturbance of $^{40}Ar/^{39}Ar$ systematics in Archean hydrothermal biotite and amphibole from the Scotia lode gold deposit, Norseman, Western Australia. Submitted to Geochim. Cosmochim. Acta

Kent, A.J.R., McDougall, I. (1995) $^{40}Ar/^{39}Ar$ and U-Pb age constraints on the timing of gold mineralization in the Kalgoorlie gold field, Western Australia. *Econ. Geol.* **90**, 845-859.

Kerr, A.C., Saunders, A.D., Tarney, J., Berry, N.H., Victoria, L.H. (1995) Depleted mantle-plume geochemical signatures: No paradox for plume theories. *Geology* **23**, 843-846.

Kerrich, R. (1983) Geochemistry of gold deposits in the Abitibi greenstone belt: *Canadian Inst. Mining and Metall. Spec. Paper* **27**, 75 p.

Kerrich, R. (1986) Fluid infiltration into fault zones: chemical, isotopic and mechanical effects: *J. Pure Applied Geophys.***124,** 225-268.

Kerrich, R. (1989a) Geodynamic setting and hydraulic regimes: Shear zone hosted mesothermal gold deposits, in Bursnall, J.T., ed., Mineralization and Shear Zones: *Geol. Assoc. Canada Short Course Notes* **6,** 89-128.

Kerrich, R. (1989b) Geochemical evidence on the sources of fluids and solutes for shear zone hosted mesothermal Au deposits, in Bursnall, J.T., ed., Mineralization and Shear Zones: *Geol. Assoc. Canada Short Course Notes* **6**, 129-197.

Kerrich, R. (1989c) Source processes for Archean Au-Ag vein deposits: evidence from lithophile-element systematics of the Hollinger-McIntyre and Buffalo Ankerite deposits, Timmins. *Can. J. Earth Sci.* **26,** 755-781.

Kerrich, R. (1991) Radiogenic isotope systems applied to mineral deposits, *in* Heaman, L. and Ludden, J.N. eds., Application of Radiogenic Isotope Systems to Problems in Geology: *Mineral. Assoc. Canada Short Course Notes* **19**, 365-421.

Kerrich, R. (1993) Perspectives on genetic models for lode gold deposits: *Mineral. Deposit.* **28**, 362-365.

Kerrich, R., Allison, I. (1978) Flow mechanisms in rocks: microscopic and mesoscopic structures, and their relation to physical conditions of deformation in the crust: *Geoscience Canada* **5**, 110-118.

Kerrich, R., Cassidy, K.F. (1994) Temporal relationships of lode gold mineralization to accretion, magmatism, metamorphism and deformation - Archean to present: a review. *Ore Geol. Rev.* **9**, 263-310.

Kerrich, R., Feng, R. (1992) Archean geodynamics and the Abitibi-Pontiac collision: implications for advection of fluids at transpressive collisional boundaries and the origin of giant quartz vein systems. *Earth Sci. Rev.* **32**, 33-60.

Kerrich, R., Fyfe, W.S. (1981) The gold-carbonate association: source of CO_2 and CO_2-fixation reactions in Archean lode gold deposits. *Chem. Geol.* **33**, 265-294.

Kerrich, R., Fyfe, W.S. (1988) The formation of gold deposits with particular reference to Archean greenstone belts and Yellowknife, in Contribution to the Geology of the Northwest Territories, Volume 3: Northwest Territory Geology Division, Yellowknife, 37-61.

Kerrich, R., Fyfe, W.S., Gorman, B.E., Allison, I. (1977) Local modification of rock chemistry by deformation. *Contrib. Mineral. Petrol.* **65**, 183-190.

Kishida, A., Kerrich, R. (1987) Hydrothermal alteration zoning and gold concentration at the Kerr-Addison Archaean lode gold deposit, Kirkland Lake, Ontario. *Econ. Geol.* **82**, 649-690.

Knight, J.T., Groves, D.I., Ridley, J.R. (1993) District-scale structural and metamorphic controls on Archean lode-gold mineralization in the amphibolite facies Coolgardie Goldfield, Western Australia: *Mineral. Deposit.* **28**, 436-456.

Korzhinskii, D.S. (1970) *Theory of metasomatic zoning.* Oxford University Press, London. 162 p.

Kretschmar, U., Scott, S.D. (1976) Phase relations involving arsenopyrite in the system Fe-As-S and their application. *Canadian Mineralogist* **14**, 364-386.

Kushel, E., Smith, I.E.M. (1992) Rare earth mobility in young arc-type volcanic rocks from northern New Zealand. *Geochim. Cosmochim. Acta* **56**, 3951-3955.

Kyser, T.K., Kerrich, R. (1991) Retrograde exchange of hydrogen isotopes between hydrous minerals and water at low temperatures, *in* Taylor, H.P., O'Neil, J.R. and Kaplan, I.R., eds., Stable isotope geochemistry: a tribute to Samuel Epstein. *Geochem. Soc. Spec.Publ.* **3**, 409-422.

Laird, J. (1980) Phase equilibria in mafic schist from Vermont. *J. Petrol.* **21**, 1-37

Langmuir, C.H.,Klein, E.M., Plank, T. (1992) Petrological systematics of mid-ocean ridge basalts: constraints on melt generation beneath ocean ridges, in: Mantle Flow and Melt Generation at Mid-Ocean Ridges, J.P. Phipps, D.K. Blackman and J.M. Sinton, eds., *Am.Geophys. Union Geophysic. Mono.* **71**, 183-280.

Leake, B.E. (1978) Nomenclature of amphiboles. *Canadian Mineralogist* **16**, 501-520.

LeRoux, L.J., Glendenin, L.E. (1963) Half life of thorium-232. In: Proceedings of National Conference on Nuclear Energy, Pretoria: 77-78.

Lesher, C.M., Phillips, G.N., Groves, D.I., Campbell, I.H. (1991) Immobility of REE and most high field-strength elements and first transition series metals during Archean gold-related hydrothermal alteration of metabasalts at the Hunt mine, Western Australia, *in* Ladiera, E.A., ed., Proceedings of Brazil Gold 91: an International Symposium on the Geology of Gold: Balkema, Rotterdam, p. 327-334.

Letnikov, F.A., Vilor, N.V. (1990) Gold in the Hydrothermal Process: *Geol. Dept. (Key Centre) Univ. Extension, Univ.West. Aust. Publ.* **19**, 110 p.

Lécuyer, C., Grau, G., Anhausser, C.R., Fourcade, S. (1994) The origin of fluids and the effects of metamorphism on the primary chemical compositions of Barberton komatiites: new evidence from geochemical (REE) and isotopic (Nd, O, H, 39Ar/40Ar) data. *Geochim. Cosmochim. Acta* **58**, 969-984.

Lhotka, P.G., Nesbitt, B.E. (1988) Geology of unmineralized and gold-bearing iron formation, Contwoyo Lake - Point Lake region, Northwest Territories, Canada. *Canadian Jour. Earth Sci.* **26**, 46-64.

Libby, J.W., Barley, M.E., Eisenlohr, B.N., Groves, D.I., Hronsky, J.M.A., Vearncombe, J.R. (1990) Craton-scale deformation zones. In Ho, S.E., Groves, D.I., Bennett, J.M. (eds.) Gold deposits of the Archaean Yilgarn Block, Western Australia: nature, genesis and exploration guides. *Geol. Dept. (Key Centre) Univ. Extension, Univ.West. Aust. Publ.* **20**,30-37.

Lindstrom, D.J. (1976) Experimental study of the partitioning of the transition metals between clinopyroxene and coexisting silicate liquids. PhD. thesis, University of Oregon (unpubl.).

Liou, J.G., Kim, H.S., Maruyama, S. (1983) Prehnite-epidote equilibria and their petrologic applications. *J. Petrol.* **24**, 321-342.

Liou, J.G., Kuniyoshi, S., Ito, K. (1974) Experimental studies of the phase relations between greenschist and amphibolite in a basaltic system. *Am. J. Sci.* **274**, 613-632.

Liou, J.G., Maruyama, S, Cho, M. (1985) Phase equilibria and mineral parageneses of metabasites in low-grade metamorphism. *Mineral. Magazine* **49**, 321-333.

Lo, C-H., Onstott, T.C. (1989) ^{39}Ar recoil artefacts in chloritized biotite. *Geochim. Cosmochim. Acta* **53**, 2697-2711.

Ludden, J., Gelinas, L., Trudel, P. (1982) Archean metavolcanics from the Rouyn-Noranda district, Abitibi Greenstone Belt, Quebec. 2. Mobility of trace elements and petrogenetic constraints, *Can. J. Earth Sci.* **19**, 2276-2287.

MacGeehan, P.J. (1983) Norseman metamorphism and deformation - a time frame for dating the emplacement of gold mineralization. Internal report to Western Mining Corporation, memorandum XK 15/83, 16 p.

Marmont, S. (1986) The geological setting of the Detour Lake gold mine, Ontario, Canada. In Macdonald, A.J. (ed.) Gold '86, an international symposium on the geology of gold deposits, Toronto, Ontario. Proceedings volume: 81-96.

Marsh, J.S. (1991) REE fractionation and Ce anomalies in weathered Karoo dolerite. *Chem. Geol.* **90**, 189-194.

Maruyama, S., Kazuhiro, S., Liou, J.G. (1983) Greenschist-amphibolite transition equilibria at low pressures. *J. Petrol.* **24**, 583-604.

Maury, R.C., Defant, M.J., Joron, J-L. (1992) Metasomatism of the sub-arc mantle inferred from trace elements in Philippine xenoliths. *Nature* **360**, 661-663.

McCuaig, T.C. (1989a) Archean gold deposits of Norseman, W.A.: documentation and preliminary geochemistry. Internal report to Central Norseman Gold Corporation (unpubl.), 111 p.

McCuaig, T.C. (1989b) Characterizing hydrothermal alteration at Norseman, W.A.: a preliminary report. Internal report to Central Norseman Gold Corporation (unpubl.), 41 p.

McCuaig, T.C. (1990) Patterns of hydrothermal alteration associated with gold deposits in high- and low-MgO lithologies in the Norseman Terrane. Technical Report, Western Mining Corporation (unpubl.) 72 p.

McCuaig, T.C. (1992) Formal report RP214: Butterfly Dyke petrochemistry. Internal report to Central Norseman Gold Corporation (unpubl.), 11 p.

McCuaig, T.C., Kerrich, R. (1990) Characterizing Archaean Au-mineralization at Norseman, W.A.: pre- or post-peak metamorphic timing? In Glover, J.E., Ho, S.E. (compilers) Third International Archaean Symposium, Perth, Western Australia. Extended abstracts volume: 421-423.

McCuaig, T.C., Kerrich, R. (1994) P-T-t-deformation-fluid characteristics of lode gold deposits: evidence from alteration systematics, In: Lentz, D.R. (Editor) Alteration and Alteration Processes Associated with Ore-forming Systems: *Geol. Assoc. Canada Short Course Notes* **11**, 339-379.

McCuaig, T.C., Kerrich, R., Groves, D.I., Archer, N. (1993) The nature and dimensions of regional and local gold-related hydrothermal alteration in tholeiitic metabasalts in the Norseman goldfields: the missing link in a crustal continuum of gold deposits? *Mineral. Deposita* **28**, 420-435.

McCuaig, T.C., Kerrich, R., Xie, Q. (1994) Phosphorus and high field strength element anomalies in Archean high-magnesian magmas as possible indicators of source mineralogy and depth. *Earth Planet. Sci. Lett.* **124**, 221-239.

McDougall, I., Harrison, T.M. (1988) *Geochronology and Thermochronology by the $^{40}Ar/^{39}Ar$ Method*, pp. 212. Oxford University Press, New York.

McGoldrick, P.J. (1993) Norseman 1:100000 sheet 3233. Australia 1:100000 series, Geol. Surv. West. Aust.

McKenzie, D., O'Nions, R.K. (1991) Partial melt distributions from inversion of rare earth element concentrations, *J. Petrol.* **32**, 1021-1091.

McNaughton, N.J., Dahl, N. (1987) A geochronological framework for gold mineralization in the Yilgarn Block, Western Australia. *Geol. Dept. (Key Centre) and Univ. Extension, The Univ. of West. Aust. Publ.* **11**, 29-50.

McNaughton, N.J., Cassidy, K.F., Dahl, N., Groves, D.I., Perring, C.S., Sang, J.H. (1990) Constraints on genesis of primary gold deposits: lead isotope studies. *Geol. Dept (Key Centre) and Univ. Extension, Univ. West. Aust. Publ.* **20**: 226-236.

McNaughton, N.J., Cassidy, K.F., Dahl, N., de Laeter, J.R., Golding, S.D., Groves, D.I., Ho, S.E., Mueller, A.G., Perring, C.S., Sang, J.H., Turner, J.V. (1992) The source of ore components in lode gold deposits of the Yilgarn Block, Western Australia. *Geol. Dept. (Key Centre) and Univ. Extension, The Univ. of West. Aust. Publ.* **22**, 351-363.

McNaughton, N.J., Groves, D.I., Jackson, S., Newton, P., Sang, J.H. (in prep.) Lead isotope compositions of sulphides in Archean lode gold deposits of the Yilgarn Block, Western Australia: monitors of cryptic Proterozoic events.

McNaughton, N.J., Groves, D.I., Witt, W.K. (1993) The source of lead in Archaean lode gold deposits of the Menzies-Kalgoorlie-Kambalda region, Yilgarn Block, Western Australia. *Mineral. Deposita* **28**, 495-502.

Menzies, M.A. (1990) Archaean, Proterozoic, and Phanerozoic lithospheres. In *The Continental Mantle* (ed. M.A. Menzies), 67-86.

Michard, A. (1989) Rare earth element systematics in hydrothermal fluids. *Geochim.Cosmochim Acta* **53**, 745-750.

Michard, A., Albarède, F,. (1986) The REE content of some hydrothermal fluids. *Chem. Geol.* **55**, 52-60.

Mikucki, E.J., Groves, D.I. (1990) Gold transport and depositional models, *in* Ho, S.E., Groves, D.I. and Bennett, J.M. eds., Gold deposits of the Archaean Yilgarn Block, Western Australia: Nature, Genesis and Exploration Guides. *Geol. Dept. (Key Centre) and Univ. Extension, The Univ. of West. Aust. Publ.* **20**, 278-284.

Mikucki, E.J., Groves, D.I., Cassidy, K.F. (1990) Wallrock alteration in sub-amphibolite facies gold deposits. In Ho, S.E., Groves, D.I., Bennett, J.M. (eds.) Gold deposits of the Archaean Yilgarn Block, Western Australia: nature, genesis and exploration guides. *Geol. Dept. (Key Centre) and Univ. Extension, The Univ. of West. Aust. Publ.* **20**, 60-78.

Mikucki, E.J., Ridley, J.R. (1993) The hydrothermal fluid of Archean lode gold deposits at different metamorphic grades: compositional constraints from ore and wallrock alteration assemblages: *Mineral. Deposita* **28**, 469-481.

Miller, W.M., Fallick, A.E., Leake, B.E., MacIntyre, R.M., Jenkin, G.R.T. (1991) Fluid disturbed hornblende K-Ar ages from the Dalradian rocks of Connemara, Western Ireland. *J. Geol. Soc. London* **148,** 985-992.

Moody, J.B., Meyer, D., Jenkins, J.E. (1983) Experimental characterization of the greenschist/amphibolite boundary in mafic systems. *Am. J. Sci.* **283**, 48-92.

Moorbath, S., Taylor, P.N. (1981) Isotopic evidence for continental growth in the Precambrian. In: Kröner, A. (Editor) *Precambrian Plate Tectonics. Developments in Precambrian geology 4.* Elsevier, Amsterdam. 491-525.

Moritz, R.P., Crocket, J.H., Dickin, A.P. (1990) Source of lead in the gold-bearing quartz-fuchsite vein at the Dome mine, Timmins area, Ontario, Canada. *Mineral. Deposita* **25**, 272-280.

Morris, P.A. (1990) Archean volcanics at Norseman, Western Australia - tholeiitic and alkalic magma? In *Third International Archaean Symposium, Perth, 1990, Extended Abstracts Volume*, 207-208. Geoconferences (W.A.) Inc.

Morris, P.A. (1992) Geochemistry and volcanology of mafic and ultramafic volcanics in the Norseman-Menzies and adjacent areas, Eastern Yilgarn Craton, *Geol. Surv. West. Aust. Report* **36.**

Morris, P.A., Kagami, H. (1989) Nd and Sr systematics of Miocene to Holocene volcanic rocks from Southwest Japan: volcanism since the opening of the Japan Sea. *Earth Planet. Sci. Lett.* **92**, 335-346.

Mueller, A.G. (1988) Archaean gold-silver deposits with prominent calc-silicate alteration in the Southern Cross greenstone belt, Western Australia: analogues of Phanerozoic skarns. In Ho, S.E. and Groves, D.I. (eds.) Recent advances in understanding Precambrian gold deposits. *Geol. Dept. (Key Centre) and Univ. Extension, The Univ. of West. Aust. Publ.* **11**, 141-163.

Mueller, A.G. (1990) The nature and genesis of high-and medium temperature Archaean gold deposits in the Yilgarn Block, Western Australia, including a specific study of scheelite-bearing gold skarn deposits. Ph.D thesis, University of Western Australia (unpubl.).

Mueller, A.G. (1991) The Savage Lode magnesian skarn in the Marvel Loch gold-silver mine, Southern Cross greenstone belt, Western Australia. Part I: Structural setting, petrography, and geochemistry. *Canadian J. Earth Sci.* **28**, 659-685.

Mueller, A.G. (1992) Petrogenesis of amphibole-biotite-calcite alteration and laminated gold-silver quartz veins in four Archaean shear zones of the Norseman district, Western Australia. *Canadian J. Earth Sci.* **29**, 388-417.

Mueller, A.G., Groves, D.I. (1991) The classification of Western Australian greenstone-hosted gold deposits according to wallrock-alteration mineral assemblages: *Ore Geol. Rev.* **6**, 291-331.

Mueller, A.G., Groves, D.I., Delor, C.P. (1991a) The Savage Lode magnesian skarn in the Marvel Loch gold-silver mine, Southern Cross greenstone belt, Western Australia. Part II: Pressure-temperature estimates and constraints on fluid sources. *Canadian J. Earth Sci.* **28**, 686-705.

Mueller, A.G., de Laeter, J.R., Groves, D.I. (1991b) Strontium isotope systematics of hydrothermal minerals from epigenetic Archaean gold deposits in the Yilgarn Block, Western Australia. *Econ. Geol.* **86**, 780-809.

Munha, J., Fyfe, W.S., Kerrich, R. (1980) Adularia, the characteristic mineral of felsic spilites. *Contrib. Mineral. Petrol.* **75**, 15-19.

Myers, J.S. (1993) Precambrian history of the West Australian Craton and adjacent orogens. *Annu. Rev. Earth Planet. Sci.* **21**, 453-485.

Naden, J., Shepherd, T.J. (1989) Role of methane and carbon dioxide in gold deposition: *Nature* **342**, 793-795.

Neall, F.B. (1985) The application of thermodynamics to the study of two Archaean hydrothermal gold deposits in Western Australia. Ph.D thesis, University of Western Australia (unpubl.).

Neall, F.B., Phillips, G.N. (1987) Fluid-wallrock interaction in an Archaean hydrothermal gold deposit: a thermodynamic model for the Hunt Mine, Kambalda. *Econ. Geol.* **82**, 1679-1694.

Nesbitt, B.E., Muehlenbachs, K. (1989) Geology, geochemistry and genesis of mesothermal lode gold deposits in the Canadian Cordillera: evidence for ore formation from evolved meteoric water. In: Keays, R.R., Ramsay, W.R.H., Groves, D.I. (eds.) The geology of gold deposits: the perspective in 1988. *Econ. Geol. Mono.* **6**, 553-563.

Nesbitt, B.E., Murowchick, J.B., Muehlenbachs, K. (1986) Dual origins of lode gold deposits in the Canadian Cordillera. *Geology* **14**, 506-509.

Neumayer, P., Cabri, L.J., Groves, D.I., Mikucki, E.J., Jackman, A.J. (1993a) The mineralogical distribution of gold and relative timing of gold mineralization in two Archean settings of high metamorphic grade in Australia: *Canadian Mineralogist* **31**, 711-725.

Neumayer, P., Groves, D.I., Ridley, J.R., Koning, C.D. (1993b) Syn-amphibolite-facies Archaean lode-gold mineralization in the Mt. York district, Pilbara Block, Western Australia, *Mineral. Deposita* **28,** 457-468.

Nisbet, E.G. (1987) *The Young Earth.* G. Allen and Unwin, London.

Ohtani, E., Kawabe, I., Moriyama, J., Nagata, Y. (1989) Partitioning of elements between majorite garnet and melt and implications for petrogenesis of komatiite, *Contrib. Mineral. Petrol.* **103**, 263-269.

O'Neil, J.R. (1986) Theoretical and experimental aspects of isotope fractionations, *in* Valley, J.W., Taylor, H.P. Jr. and O'Neil, J.R. eds., Stable Isotopes in High Temperature Geological Processes: *Mineral. Soc. Am., Rev. Mineral.* **16,** 1-40.

Oversby, V.M. (1975) Lead isotope systematics and ages of Archaean acid intrusives in the Kalgoorlie-Norseman area, Western Australia. *Geochim. Cosmochim. Acta* **39**, 1107-1125.

Pan, Y., Fleet, M.E. (1995) The late Archean Hemlo gold deposit, Ontario, Canada: a review and synthesis. *Ore Geol. Rev.* **9**, 455-488.

Pan, Y., Fleet, M.E., Barnett, R.L. (1994) Rare-earth mineralogy and geochemistry of the mattagami lake volcanogenic massive sulphide deposit, Quebec. *Canadian Mineralogist* **32**, 133-147.

Pearce, J.A. (1983) Role of the subcontinental lithosphere in magma genesis at active continental margins. In *Continental Basalts and Mantle Xenoliths* (eds. C.J. Hawkesworth, and M.J. Norry), 230-249. Shiva Geological Series.

Pearce, J.A., Peate, D.W. (1995) Tectonic implications of the composition of volcanic arc magmas. *Annu. Rev. Earth Planet. Sci.* **23**, 251-285.

Percival, J., Ludden, J. (chairmen, 1995) Precambrian '95 Program and Abstracts. International conference on tectonics and metallogeny of early/mid Precambrian orogenic belts, Montreal, 327 p.

Perring, C.S. (1990) The significance of 'porphyry' intrusions to Archaean gold mineralization in the Norseman-Wiluna Belt of Western Australia. Ph.D. thesis, University of Western Australia (unpubl.).

Perring, C.S., Barley, M.E. (1990) K/Rb ratios. *in* Ho, S.E., Groves, D.I. and Bennett, J.M. eds., Gold deposits of the Archaean Yilgarn Block, Western Australia: Nature, Genesis and Exploration Guides: *Geol. Dept. (Key Centre) and Univ. Extension, The Univ. of West. Aust. Publ.* **20**, 263-267 .

Perring, C.S., McNaughton, N.J. (1990) Proterozoic remobilization of ore metals within Archaean gold deposits: lead-isotope evidence from Norseman, Western Australia. *Aust. J. Earth Sci.* **37**, 369-372.

Perring, C.S., McNaughton, N.J. (1992) The relationship between Archaean gold mineralization and spatially associated minor intrusions at the Kambalda and Norseman gold camps, Western Australia: lead isotope evidence. *Mineral. Deposita* **27**, 10-22.

Perring, C.S., Groves, D.I., Shellabear, J.N. (1990) Ore geochemistry, *in* Ho, S.E., Groves, D.I. and Bennett, J.M. eds., Gold deposits of the Archaean Yilgarn Block, Western Australia: Nature, Genesis and Exploration Guides: *Geol. Dept. (Key Centre) and Univ. Extension, The Univ. of West. Aust. Publ.* **20**, 93-101.

Peters, S.G. (1993a) Nomenclature, concepts and classification of oreshoots in vein deposits: *Ore Geol. Rev.* **8.**, 3-22.

Peters, S.G. (1993b) Formation of oreshoots in mesothermal gold-quartz vein deposits: examples from Queensland, Australia: *Ore Geol. Rev.* **8.**, 277-301.

Peters, S.G., Golding, S.D. (1989) Geologic, fluid inclusion, and stable isotop studies of granitoid-hosted gold-bearing quartz veins, Charters Towers, Northeastern

Australia, *in* Keays, R.R., Ramsay, W.R.H. and Groves, D.I., eds., The Geology of Gold Deposits: the Perspective in 1988: *Econ. Geol. Mono.* **6**, 260-273.

Phillips, G.N. (1985) Interpretation of Big Bell/Hemlo-type gold deposits: precursors, metamorphism, melting and genetic constraints. *Trans. Geol. Soc. S. Afr.* **88**, 159-173.

Phillips, G.N., Groves, D.I. (1984) Fluid access and fluid-wallrock interaction in the genesis of the Archaean gold-quartz vein at Hunt mine, Kambalda, Western Australia. In: Foster, R.P. (ed.) Gold '82: the geology, geochemistry and genesis of gold deposits. *Geol. Soc. Zimbabwe Spec.Publ.* **1**, 689-712.

Phillips, G.N., de Nooy, D. (1988) High-grade metamorphic processes which influence Archaean gold deposits, with particular reference to Big Bell, Australia. *J. Metamorphic Geology* **6**, 95-114.

Phillips, G.N., Powell, R. (1993) Link between gold provinces: *Econ. Geol.* **88**, 1084-1098.

Pidgeon, R.T. (1986) The correlation of acid volcanics in the Archaean of Western Australia. *West. Aust. Min. Petrol. Res. Inst. Rep.* **27**, 77p.

Pidgeon, R.T., Wilde, S.A. (1990) The distribution of 3.0 Ga and 2.7 Ga volcanic episodes in the Yilgarn Craton of Western Australia. *Precambrian Res.* **48**, 309-325.

Plyusnina, L.P. (1982) Geothermometry and geobarometry of plagioclase-hornblende bearing assemblages. *Contrib Mineral. Petrol.* **80**, 140-146.

Powell, W.G., Hodgson, C.J., Hanes, J.A., Carmichael, D.M., McBride, S., Farrar, E. (1995) $^{40}Ar/^{39}Ar$ geochronological evidence for multiple postmetamorphic hydrothermal events focused along faults in the Southern Abitibi greenstone belt. *Can. J. Earth Sci.* **32**, 768-786.

Ragland, P.C. (1989) Basic Analytical Petrology. Oxford University Press, Oxford, 369 p.

Ramsay, J.G. (1980) The crack-seal mechanism of rock deformation. *Nature* **284**, 135-139.

Rattenbury, M.S. (1993) Tectonstratigraphic terranes in the northern Eastern Goldfields. In: An international conference on crustal evolution, metallogeny and exploration of the Eastern Goldfields, extended abstracts, *AGSO Record* **1993/54**, 73-75.

Redman, B.A., Keays, R.R. (1985) Archean basic volcanism in the Eastern Goldfields Province, Yilgarn Block, Western Australia. *Precambrian Res.* **30**, 113-152.

Reid, A.M., Brown, R.W., Dawson, J.B., Whifield, G.G., Siebert, J.C. (1976) Garnet and pyroxene compositions in some diamondiferous eclogites, *Contrib. Mineral. Petrol.* **58**, 203-220.

Richards, J.P., McDougall, I. (1990) Geochronology of the Porgera gold deposit, Papau New Guinea: resolving the effects of excess argon on K-Ar and ^{40}Ar-^{39}Ar age

estimates for magmatism and mineralization. *Geochim. Cosmochim. Acta* **54**, 1397-1415.

Ridley, J.R. (1990) Constraints from alteration assemblages on gold-bearing hydrothermal fluid composition and source. In Ho, S.E., Groves, D.I., Bennett, J.M. (eds.) Gold deposits of the Archaean Yilgarn Block, Western Australia: nature, genesis and exploration guides. *Geol. Dept. (Key Centre) and Univ. Extension, The Univ. of West. Aust. Publ.* **20**, 268-272.

Ridley, J.R. (1993) Implications of metamorphic patterns to tectonic models of the Eastern Goldfields. In: An international conference on crustal evolution, metallogeny and exploration of the Eastern Goldfields, extended abstracts, *AGSO Record* **1993/54**, 95-100.

Ridley, J.R., Barnicoat, A.C. (1990) Wallrock alteration in amphibolite-facies gold deposits. In Ho, S.E., Groves, D.I., Bennett, J.M. (eds.) Gold deposits of the Archaean Yilgarn Block, Western Australia: nature, genesis and exploration guides. *Geol. Dept. (Key Centre) and Univ. Extension, The Univ. of West. Aust. Publ.* **20**, 79-86.

Ringwood, A.E. (1990) Slab-mantle interactions. *Chem. Geol.* **82**, 187-207.

Ringwood, A.E., Kesson, S.E., Hibberson, W., Ware, N. (1992) Origin of kimberlites and related magmas, *Earth Planet. Sci. Lett.* **113**, 521-538.

Robert, F., Brown, A.C. (1986a) Archean gold-bearing quartz veins at the Sigma mine, Abitibi greenstone belt, Quebec: Part I. Geologic relations and formation of the vein system: *Econ. Geol.* **81**, 578-592.

Robert, F., Brown, A.C. (1986b) Archean gold-bearing quartz veins at the Sigma mine, Abitibi greenstone belt, Quebec. Part II. Geologic relations and formation of the vein systems. *Econ. Geol.* **81**, 593-616.

Roberts, R.G. (1988) Archean lode gold deposits, *in* Roberts, R.G. and Sheahan, P.A., eds., Ore Deposit Models: *Geol. Assoc. Canada, Geoscience Canada Reprint Series* **2**, 1-19.

Rock, N.M.S. (1989) Kimberlites as varieties of lamprophyres: implications for geological mapping, petrological research and mineral exploration, in: Kimberlites and Related Rocks. *Geol. Soc. Amer. Spec. Publ.* **14**, 46-59.

Roddick, J.C. (1984) Emplacement and metamorphism of Archaean mafic volcanics at Kambalda, Western Australia - geochemical and isotopic constraints. *Geochim. Cosmochim. Acta* **48**, 1305-1318.

Romberger, S.B. (1986) The solution chemistry of gold applied to the origin of hydrothermal deposits, *in* Clark, L.A., ed., Gold in the Western Shield. *Canadian Inst. Mining Metall. Spec.Vol.* **38**, 168-186.

Romberger, S.B. (1990) The transport and deposition of gold in hydrothermal systems, *in* Robert, F., Sheahan, P.A. and Green S.B, eds., Greenstone Gold and Crustal Evolution, NUNA Conference Volume, 61-66.

Rutter, E.H. (1976) The kinetics of rock deformation by pressure solution: *Phil. Trans. of Royal Soc. London* **A283**, 203-219.

Salters, V.J.M., Shimuzu, N. (1988) World-wide occurrence of HFSE-depleted mantle, *Geochim. Cosmochim. Acta* **52**, 2177-2182.

Seward, T.M. (1973) Thio complexes of gold and the transport of gold in hydrothermal ore solutions. *Geochim. Cosmochim. Acta* **37**, 370-399.

Seward, T.M. (1991) The hydrothermal geochemistry of gold, *in* Foster, R.P., ed., *Gold Metallogeny and Exploration:* Blackie, 37-62.

Seyfried, W.E., Mottl, M.J., Bischoff, J.L. (1978) Seawater/basalt ratio effects on the chemistry and mineralogy of spilites from the ocean floor. *Nature* **275**, 211-213.

Sharp, Z.D., Essene, E.J., Kelly, W.C. (1985) A re-examination of the arsenopyrite geothermometer: pressure considerations and applications to natural assemblages. *Canadian Mineralogist* **23**, 517-534.

Shaw, D.M. (1968) A review of K-Rb fractionation trends by covariance analysis. *Geochim. Cosmochim. Acta* **32**, 573-601.

Shaw, D.M. (1970) Trace element fractionation during anatexis. *Geochim. Cosmochim. Acta* ***34***, 237-242.

Shenberger, D.M., Barnes, H.L. (1989) Solubility of gold in aqueous sulphide solutions from 150 to 350°C. *Geochim. Cosmochim. Acta* **53**, 269-278.

Shirey, S.B. (1991) The Rb-Sr, Sm-Nd and Re-Os isotopic systems: a summary and comparison of their applications to the cosmochronology and geochronology of igneous rocks. *in* Heaman, L. and Ludden, J.N. eds., Application of Radiogenic Isotope Systems to Problems in Geology: *Mineral. Assoc. Canada Short Course Notes* **19**, 103-166.

Sibson, R.H. (1990) Faulting and fluid flow. In Nesbitt, B.E. (ed.) Fluids in tectonically active regimes of the continental crust. *Mineral. Assoc. Canada Short Course Notes* **18**, 93-132.

Sibson, R.H., Robert, F., Poulsen, H. (1988) High angle faults, fluid pressure cycling and mesothermal gold-quartz deposits: *Geology* **16**, 551-555.

Siddaiah, N.S., Rajamani, V. (1989) The geologic setting, mineralogy, geochemistry, and genesis of gold deposits of the Archaean Kolar Schist Belt, India. *Econ. Geol.* **84**, 2155-2172.

Smith, A.D., Ludden, J.N. (1989) Nd isotopic evolution of the Precambrian mantle. *Earth Planet. Sci. Lett.* **93**, 14-22.

Sofoulis, J. (1963) Explanatory notes on the Boorabin 1: 250000 Geological Sheet (SI 51-13), Western Australia. Geol. Surv. West. Aust., Perth, 24 p.

Spear, F.S. (1980) NaSi-CaAl exchange equilibrium between plagioclase and amphibole: an empirical model. *Contrib. Mineral. Petrol.* **72**, 33-41.

Spear, F.S. (1981) An experimental study of hornbelende stability and compositional variability in amphibolite. *Am. J. Sci.* **281**, 697-734.

Spooner, E.T.C., Bray, C.J., Wood, P.C., Burrows, D.R., Callan, N.J. (1987) Au-quartz vein and Cu-Au-Ag-Mo-anhydrite mineralization, Hollinger-McIntyre Mines, Timmins, Ontario, $\delta^{13}C$, values (McIntyre), fluid inclusion gas chemistry, pressure (depth) estimation, and H_2O-CO_2 phase separation as a precipitation and dilation mechanism. Grant 236; *Ontario Geol. Surv. Misc. Paper* **136**, 35-56.

Spray, J.G. (1985) Dynamothermal transition zone between Archaean greenstone and granitoid gneiss at Lake Dundas, Western Australia. *J. Structural Geology* **7**, 187-203.

Steiger, R.H., Jaeger, E. (1977) Subcommission on geochronology: convention on the use of decay constants in geo- and cosmochronology. *Earth Planet. Sci. Lett.* **36**, 359-362.

Stone, W.E., Crocket, J.H., Dickin, A.P., Fleet, M.E. (1995) Origin of Archean ferropicrites: geochemical constraints from the Boston Creek Flow, Abitibi greenstone belt, Ontario, Canada. *Chem. Geol.* **121**, 51-71.

Sun, S-s. (1984) Geochemical characteristics of Archean ultramafic and mafic volcanic rocks: implications for mantle composition and evolution, in: *Archean Geochemistry*, A. Kroner et al., eds., Springer-Verlag, Berlin-Heidelberg, 25-46.

Sun, S-s., Nesbitt, R.W. (1978) Chemical heterogeneity of the Archean Mantle, composition of the earth and mantle evolution. *Earth Planet. Sci. Lett.* **35**, 429-448.

Sun, S-s., Nesbitt, R.W. (1978) Petrogenesis of Archean ultrabasic and basic volcanics: evidence from rare-earth elements. *Contrib. Mineral. Petrol.* **65**, 301-325.

Sun, S-s., McDonough, W.F. (1989) Chemical and isotopic systematics of oceanic basalts: implications for mantle composition and processes, in, Magmatism in the Ocean Basins, A.D. Saunders, M.J. Norry (eds.), *Geol. Soc. Spec. Publ.* **42**, 313-345.

Sun, S-s., Nesbitt, R.W., Sharaskin, A.Y. (1979) Geochemical characteristics of mid-ocean ridge basalts. *Earth Planet. Sci. Lett.* **44**, 119-138.

Sun, S-s., Nesbitt, R.W., McCulloch, M.T. (1989) Geochemistry and petrogenesis of Archean and early Proterozoic siliceous high-magnesian basalts, in: *Boninites and Related Rocks*, A.J. Crawford (ed.), Allen and Unwin, 148-173.

Suzuoki, T., Epstein, S. (1976) Hydrogen isotope fractionation between OH-bearing minerals and water. *Geochim. Cosmochim. Acta* **40**, 1229-1240.

Swager, C. (1993) Stratigraphy and structure in the Southeastern Goldfields Province, *in* An international conference on crustal evolution, metallogeny and exploration of the Easten Goldfields: extended abstracts, *AGSO Record* **1993/94**, 69-72.

Swager, C., Griffin, T.J., Witt, W.K., Wyche, S., Ahmat, A.L., Hunter, W.M., McGoldrick, P.J. (1990) Geology of the Archaean Kalgoorlie Terrane - an explanatory note. *Geol. Surv. West. Aust. Record* **1990/12**. 55 p.

Swager, C.P., Witt, W.K., Griffin, T.J., Ahmat, A.L., Hunter, W.M., McGoldrick, P.J., Wyche, S. (1992) Late Archaean granite-greenstones of the KalgoorlieTerrane, Yilgarn Craton, Western Australia. *Geol. Dept. (Key Centre) and Univ. Extension, The Univ. of West. Aust. Publ.* **22**, 107-122.

Takahashi, E., Scarfe, C.M. (1985) Melting of Peridotite to 14 GPa and the genesis of komatiite. *Nature* **315**, 566-568.

Tatsumi, Y., Hamilton, D.L., Nesbitt, R.W. (1986) Chemical characteristics of fluid phase released from a subducted lithosphere and origin of arc magmas: evidence from high-pressure experiments and natural rocks. *J. Volcanology and Geothermal Res.* **29**, 293-309.

Taylor, S.R., McLennan, S.M. (1981) The composition and evolution of the continental crust: rare earth evidence from sedimentary rocks. *Philos. Trans. R. Soc. London* **Ser. A**, 381-399.

Taylor, S.R., McLennan, S.M. (1985) *The Continental Crust: Its Composition and Evolution*, Blackwells Scientific, Oxford, 312 p.

Tetley, N., McDougall, I., Heydegger, H.R. (1980) Thermal neutron interferences in the ^{40}Ar-^{39}Ar dating technique. *Journal of Geophysical Research* **85**, 7201-7205.

Thomas, A. (1990) Report: the stratigraphic project, 1983. Internal report to Central Norseman Gold Corporation (unpubl.).

Thomas, A., Johnson, K., MacGeehan, P.J. (1990) Norseman Gold Deposits. In: Hughes, F.E.(Editor) Geology of the mineral deposits of Australia and Papua New Guinea. *Aust. Inst. Mining Metall. Mono.* **14**, 493-504.

Thompson, A.B., Connolly, J.A.D. (1992) Migration of metamorphic fluid: some aspects of mass and heat transfer: *Earth Sci. Rev.* **32**, 107-121.

Thompson, A.B., England, P.C. (1984) Pressure-temperature-time paths II. Their inference and interpretation using mineral assemblages in metamorphic rocks. *J. of Petrology* **25**, 929-955.

Thompson, J.B.Jr. (1959) *Local equilibrium in metasomatic processes.* In Abelson P.H. (ed.) Researches in geochemistry. John Wiley and Sons, New York, 427-457.

Thompson, M.L. (1986) Petrology of the Crixas gold deposit, Brazil: Evidence for gold associated with hydrothermal alteration, subsequent to metamorphism. In Macdonald, A.J. (ed.) Gold '86, an international symposium on the geology of gold deposits, Toronto, Ontario. Proceedings volume: 284-296.

Thompson, M.L. (1991) Wall-rock alteration related to Au mineralization in the low-amphibolite facies: Crixas gold mine, Goias, Brazil. *Canadian Mineralogist* **29**, 461-480.

Thompson, R.N.. (1975) Is upper-mantle phosphorus contained in sodic garnet? *Earth Planet. Sci. Lett.* **26**, 417-424.

Vidale, J.E. (1991) A snapshot of whole mantle flow. *Nature* **370**, 16-17.

Wang, L.G., McNaughton, N.J., Groves, D.I. (1993) An overview of the relationship between granitoid intrusions and gold mineralization in the Archean Murchison Province, Western Australia. *Mineral. Deposita* **28,** 482-494.

Watkins, K.P., Hickman, A.H. (1988) Geology of the Murchison Province: Field Excursion Guide. Geol. Surv. West. Aust., Perth, 22 p.

Watkins, K.P., Hickman, A.H. (1990) Geological evolution and mineralization of the Murchison Province, Western Australia. *Geol. Surv. West. Aust. Bull.* **137**, 267 p.

Watson, E.B. (1980) Apatite and phosphorous in mantle source regions: an experimental study of apatite/melt equilibria at pressures to 25 Kbar, *Earth Planet. Sci. Lett.* **51**, 322-335.

Weaver, B.L. (1991) The origin of ocean island basalt end-member compositions: trace element and isotopic constraints. *Earth Planet. Sci. Lett.* **104**, 381-397.

Weaver, B.L., Tarney, J. (1984) Empirical approach to estimating the composition of the continental crust. *Nature* **310,** 575-577.

Wenner, D.B., Taylor, H.P.Jr. (1971) Temperatures of serpentinization of ultramafic rocks based on $^{18}O/^{16}O$ fractionation between coexisting serpentine and magnetite. *Contrib. Mineral. Petrol.* **32,** 165-185.

Whitaker, A. (1990) The southern Yilgarn Block, Western Australia: a view derived from interpretation of the regional aeromagnetic and gravity data. *Third International Archaean Symposium*, Perth, Geoconferences W.A. (inc.), 89-90.

Williams, P.R. (1993) A new hypothesis for the evolution of the Eastern Goldfields Province. In: An international conference on crustal evolution, metallogeny and exploration of the Eastern Goldfields, extended abstracts, *AGSO Record* **1993/54**, 77-83.

Wilshire, H.G., Pike, J.E.N., Meyer, C.E., Schwarzmann, E.C. (1980) Amphibole-rich veins in lherzolite xenoliths, Dish Hill and Deadmann Lake, California. *Am. J. Sci.* **280-A**, 76-593.

Wilson, M. *Igneous Petrogenesis*. Chapman and Hall, London.

Witt, W.K. (1991) Regional metamorphic controls on alteration associated with gold mineralization in the eastern goldfields province, Western Australia: Implications for the timing and origin of Archaean lode-gold deposits. *Geology* **19**, 982-985.

Wong, L., Davis, D.W., Krogh, T.E., Robert, F. (1991) U-Pb zircon and rutile chronology of Archaean greenstone belt metallogeny. *Earth Planet. Sci. Lett.* **104**, 337-349.

Wood., D.A., Joron, J.L., Treuil, M. (1979) A re-appraisal of the use of trace elements to classify and discriminate between magma series erupted in different tectonic settings. *Earth Planet. Sci. Lett.* **45**, 326-336.

Wood, S.A. (1990a) The aqueous geochemistry of the rare-earth elements and yttrium 1: review of available low-temperature data for inorganic complexes and the inorganic REE speciation of natural waters. *Chem. Geol.* **82,** 159-186.

Wood, S.A. (1990b) The aqueous geochemistry of the rare-earth elements and yttrium 1: Theoretical predictions of speciation in hydrothermal solutions to 350°C at saturation water vapour pressure. *Chem. Geol.* **88**, 99-125.

Wood, S.A., Williams-Jones, A.E.(1994) The aqueous gheochemistry of the rare-earth elements and yttrium 4: Monazite solubility and REE mobility in exhalative massive sulphide-depositing environments. *Chem. Geol.* **115**, 47-60.

Woodall, R. (1988) Gold in 1988. Bicentenial Gold '88 Extended Abstracts, Oral Programme, Melbourne, 1-12.

Woodall, R. (1990) Gold in Australia. In: Hughes, F.E.(Editor) Geology of the mineral deposits of Australia and Papua New Guinea. *Aust.Inst. Mining Metall. Mono.* **14**, 45-67.

Woodhead, J., Eggins, S., Gamble, J. (1993) High field strength and transition element systematics in island arc and back-arc basin basalts: evidence for multi-phase melt extraction and a depleted mantle wedge. *Earth and Planet. Sci. Lett.* **114**, 491-504.

Wyman, D.A., Kerrich, R. (1988) Alkaline magmatism, major structures and gold deposits: implications for greenstone belt metallogeny. Econ. Geol. 83: 454-461.

Wyman, D.A., Kerrich, R. (1989) Archean lamprophyre dykes of the Superior Province, Canada: distribution, petrology, and geochemical characteristics, *J. Geophys. Res.* **94**, 4667-4696.

Xie, Q., Kerrich, R., Fan, J. (1993) HFSE/REE fractionations recorded in three komatiite-basalt sequences, Abitibi greenstone belt: implications for multiple plume sources and depths. *Geochim. Cosmochim. Acta* **57**, 4111-4118.

Xie, Q., Jain, J., Sun, M., Kerrich, R., Fan, J. (1994) Multiple-element analysis of low-level international standards BIR-1: results by ICP-MS, *Geostand. Newslett.* **18,** 53-63.

Xie, Q., McCuaig, T.C., Kerrich, R. (1995) Secular trends in the melting depths of mantle plumes: evidence from HFSE/REE systematics of Archean high-Mg lavas and modern oceanic basalts. In: J.N. Ludden and N.T. Arndt (editors), Mafic Magmatism through Time. *Chem. Geol.* **126**, 29-42.

York, D. (1969) Least squares fitting of a straight line with correlated errors. *Earth Planet. Sci. Lett.* **5**, 320-324.

Zindler, A., and Hart, S. (1986) Chemical geodynamics. *Ann. Rev. Earth Planet. Sci.* **14**, 493-571.

Zweng, P.L., Mortensen, J.K., Dalrymple, G.B. (1993) Thermochronology of the Camflo deposit, Malartic, Quebec: implications for magmatic underplating and the formation of gold-bearing quartz veins.. *Econ Geol.* **88**, 1700-1721.

Appendix A

Microprobe analyses of minerals

The following tables list selected microprobe analyses of silicate and oxide mineral assemblages associated with lode gold deposits of the Norseman Terrane. Compositions reported are representative of the entire range of composition observed for each mineral. The tables are progressively subdivided by mineral, mine, and sample number.

Analyses were performed on a Jeol 8600 Superprobe, using wavelength dispersive spectrometery, and standard reference materials for calibration.

Appendix A1 Representative microprobe analyses of amphiboles from metamorphic and hydrothermal assemblages

Mine	Sample	Comments	SiO2	TiO2	Al2O3	Cr2O3	FeO	MnO	MgO	CaO	NiO	Na2O	K2O	F	Cl	P2O5	TOTAL
Junction																	
	JU-1																
		vein margin	54.9	0.03	1.23	0.01	12.52	0.15	17.13	11.35		0.22	0	0	0.02		97.56
		vein margin	51.45	0.07	3.67	0.01	14.07	0.1	14.89	11.08		0.62	0	0	0.01		95.96
North Royal																	
	NR-11																
		core	54.21	0.05	1.97		9.67	0.26	17.79	12.86		0.27	0	0	0.02		97.1
		(core to rim	54.19	0.1	2.57		10.15	0.27	17.73	12.41		0.44	0	0	0.01		97.87
		traverse)	53.53	0.13	3.55		10.38	0.26	17.08	12.26		0.46	0	0	0		97.65
			52.84	0.15	3.65		10.37	0.28	17.06	12.17		0.44	0	0	0		96.96
			52.74	0.15	3.72		10.25	0.3	16.78	12.47		0.42	0	0	0		96.83
			53.1	0.13	3.48		9.66	0.23	17.38	12.91		0.39	0	0	0.02		97.3
		rim	52.76	0.17	4.12		10.19	0.18	17.13	12.28		0.43	0	0	0		97.26
	NR-14																
		core	50.42	0.22	6.08		10.45	0.23	16.07	12.34		0.78	0	0	0.03		96.62
		core	53.01	0.15	3.74		9.26	0.19	17.61	12.15		0.51	0	0	0.01		96.63
		rim	50.02	0.22	3.84		8.22	0.23	16.78	15.81		0.39	0	0	0.02		95.53
		rim	52.44	0.2	4.97		9.31	0.26	17.34	12.28		0.55	0	0	0.02		97.37
	NR-18																
		rim	40.99	0.13	14.53		17.52	0.36	6.48	11.29		1.05	0.22	0	0.07	0	92.64
		rim	42.06	0.3	12.17		17.16	0.27	7.31	11.15		0.9	0.19	0	0.03	0	91.54
		rim	45.57	0.27	9.32		15.63	0.32	9.48	11.12		0.7	0	0	0.02	0	92.43
		core	47.52	0.18	7.48		14.83	0.26	10.56	11.39		0.62	0	0	0.03	0	92.87
		core	49.29	0.12	5.25		14.09	0.28	12.14	11.39		0.44	0	0	0.01	0	93.01
	PRS-21																
		least-altered	44.18	0.37	11.73		18.4	0.28	8.79	11.77		0.85	0.17	0	0.05		96.58
		least-altered	52.52	0.17	3.44		14.11	0.19	14.69	12.31		0.31	0	0	0.03		97.76
Regent																	
	CN389157																
		vein	45.16	0.45	11.13	0.2	16.85	0.23	9.82	12.05		0.93	0.16	0	0.01		96.99
		vein	42.53	0.48	14	0.19	16.79	0.23	8.51	11.89		1.32	0.36	0	0.01		96.3
		vein	43.04	0.42	13.45	0.03	16.12	0.25	9.15	11.89		1.12	0.28	0	0.02		95.76
		vein	44.67	0.55	11.32	0.1	16.94	0.18	9.9	11.77		0.96	0.28	0	0.01		96.67
		vein	49.38	0.28	6.27	0	16.96	0.28	11.51	11.7		0.54	0	0	0		96.91
		vein	42.17	0.82	14.23	0.07	18.31	0.27	7.86	11.85		1.17	0.39	0	0.02		97.15
	S1113-A																
		amph-rim	44.09	0.22	12.92		17.86	0.27	8.69	12.3		1.19	0	0	0		97.54
		amph-core	52.56	0.15	4.01		13.7	0.22	14.44	12.7		0.34	0	0	0		98.12
		amph-core	52.93	0.1	3.31		14.04	0.32	14.56	12.68		0.3	0	0	0.01		98.25
		amph-rim	44.16	0.28	11.71		19.14	0.3	8.59	12.31		0.92	0.19	0	0.04		97.64
		amph-rim	44.61	0.28	11.83		18.46	0.26	8.97	12.22		0.94	0.13	0	0.04		97.74
		amph-rim	42.96	0.32	13.3		18.6	0.27	9.35	11.47		1.08	0	0	0.02		97.37
		amph-core	50.75	0.18	5.69		13.97	0.22	13.89	12.62		0.49	0	0	0.02		97.83
		amph-core	49.16	0.28	6.42		16.78	0.22	11.89	12.38		0.55	0	0	0.04		97.72
		amph-core	47.84	0.7	5.14		21.78	0.41	10.26	10.51		0.51	0	0	0.21		97.36
		amph-core	52.16	0.07	3.72		14.31	0.25	14.16	12.75		0.27	0	0	0.01		97.7
	CN380911																
		act-rim	51.96	0.13	3.91	0.04	13.68	0.26	14.38	12.26	0.08	0.3	0	0	0		96.99
		act-rim	51.75	0.13	4.76	0.01	14.51	0.26	14.08	11.92	0.03	0.3	0	0	0.15		97.89
		hble-core	45.01	0.35	11.54	0.1	17.3	0.25	9.57	11.82	0.04	0.98	0	0	0.23		97.18
		hble-core	43.15	0.43	13.96	0	18.45	0.27	8.08	11.8	0.06	1.05	0.28	0	0.18		97.7
	AB213763																
		act-rim	52.44	0.03	2.32	0	11.24	0.21	17.08	11.82	0.05	0.18	0	0	0.03		95.39
		act-rim	53.91	0.07	1.68	0.07	10.72	0.15	18.02	12.45	0.06	0.13	0	0	0.12		97.37
		hble-core	43.96	1.27	9.2	0	14.59	0.26	11.99	11.52	0.06	0.92	0	0	2.97		96.74
		hble-core	47.62	0.27	7.43	0.18	14.1	0.23	13.96	11.99	0.05	0.69	0	0	0.05		96.56
	AB213797																
		hble-core	47.19	0.42	9.18	0.06	17.35	0.35	10.55	11.64	0	0.78	0	0	0.24		97.75
		hble-core	43.49	0.57	12.23	0	18.91	0.35	8.69	11.4	0.04	1.17	0.2	0	0.36		97.4
	AB217759																
		act-hb - rim	50.32	0.13	5.8	0.48	11.77	0.27	15.27	12.16	0	0.43	0	0	0.15		96.77
		act-rim	52.71	0.15	4.19	0.01	11.28	0.31	16.25	12.35	0.04	0.31	0	0	0.05		97.64
		hble-core	46.27	0.3	10.58	0.51	13.19	0.3	12.57	11.88	0.01	0.86	0	0	0		96.46
		hble-core	47.58	0.23	9.03	0.5	12.63	0.27	13.55	12.23	0	0.82	0	0	0.22		97.06
		hble-core	46.94	0.18	9.81	0.22	13.43	0.31	13.48	11.73	0.04	0.8	0	0	0		96.93
Ajax																	
	AB372686																
		hble-core	43.56	3.2	11.39	0	13.78	0.26	12.19	11.21	0.04	0.97	0.14	0	1.81		98.54
		hble-core	44.93	2.79	9.05	0.06	14.23	0.35	13.12	11.01	0	0.8	0.18	0	2.25		98.76
		act-rim	55.99	0	0.45	0	8.49	0.23	19.91	12.63	0.01	0.05	0	0	0		97.75
		act-rim	54.32	0.07	2.65	0.34	9.52	0.27	18.45	12.34	0.08	0.2	0	0	0.15		98.38
Royal Standard																	
	RS-2a																
		on frac in vein	50.02	0.15	6.07		15.81	0.31	12.49	11.71		0.47	0	0	0.01		97.03
		on frac in vein	49.01	0.28	6.65		16.11	0.35	12.54	11.57		0.49	0	0	0		96.99
		on frac in vein	50.87	0.3	4.99		14.9	0.28	13.35	11.64		0.39	0	0	0.01		96.72
	RS-2b																
		vein	54.75	0	0.57		8.38	0.21	19.37	12.27		0.04	0	0	0		95.58
		vein	55.58	0	0.51		8.93	0.25	19.2	12.02		0.03	0	0	0.01		96.52
		vein	55.52	0	0.79		9.13	0.22	19.1	12.1		0.03	0	0	0		96.89
		selvedge	53.63	0	2.59		13.01	0.3	15.83	11.96		0.12	0	0	0.01		97.44
		wallrock	48.93	0	8.22		14.15	0.26	13.18	12.23		0.62	0.13	0	0		97.71
	RS-3																
		amph-zone	52.09	0.37	5.18		14.5	0.44	13.6	12.23		0.44	0	0	0	0	98.85
		amph-zone	50.42	0.48	6.46		14.96	0.32	13	12.37		0.44	0	0	0	0	98.45
		amph-zone	46.15	0.27	9.62		18.6	0.25	10.6	11.74		1	0	0	0.01	0	98.24
	RS-10																
		amph-biotite	44.16	0.23	13.08		17.12	0.36	9.14	12.28		1.11	0.18	0	0.01	0.07	97.74
		amph-biotite	44.56	0.35	11.36		17.53	0.32	10.1	11.8		0.93	0	0	0	0	96.95
		amph-zone	46.81	0.32	9.56		17.02	0.48	10.98	12.35		0.8	0	0	0.02	0	98.34
		amph-zone	50.4	0.13	4.95		14.05	0.36	14.06	12.24		0.34	0	0	0	0	96.53
Okay																	
	OK-2																
		poikiloblastic	42.59	0.28	14.25		18.01	0.28	7.73	11.63		1.13	0.13	0	0		96.03
		poikiloblastic	44.63	0.45	11.96		17.23	0.41	9.3	11.74		0.96	0	0	0.03		96.71
		relict, aligned	51.41	0.15	4.36		16.49	0.46	13.48	11.28		0.35	0	0	0		97.98

		relict, aligned	48.86	0.35	6.92		15.99	0.4	12.4	11.99		0.51	0	0	0.01		97.43
	OK-4																
		vein	53.66	0.03	2.66		13.35	0.46	15.52	12.13		0.24	0	0	0		98.05
		vein	48.73	0.05	7.46		15	0.43	12.65	11.32		0.74	0	0	0.03		96.41
	OKu10																
		biotite zone	48.46	0.22	8.09		15.22	0.21	12.14	12.3		0.61	0	0	0	0	97.25
		biotite zone	44.69	0.33	11.17		17.68	0.43	9.93	11.85		0.96	0	0	0.03	0	97.07
	OK-10																
		least-altered	48.35	0.33	6.86		18.11	0.32	10.38	12.35		0.59	0	0	0.03		97.32
		least-altered	50.75	0.22	4.76		17.12	0.28	12.02	12.45		0.42	0	0	0		98.02
	OK-11																
		least-altered	46.98	0.28	8.28		17.07	0.46	10.53	12.23		0.82	0.07	0	0.01		96.73
		least-altered	46.06	0.28	9.69		17.95	0.44	9.97	11.99		0.88	0	0	0		97.26
	OK-12																
		amph-biot zone	42.7	0.32	12.91		19.16	0.44	7.74	11.81		1.27	0	0	0.04		96.39
		amph-biot zone	47.04	0.28	9.01		17.3	0.35	10.94	11.84		0.9	0	0	0		97.66
	OK-13																
		biot-amph zone	41.89	0.6	13.66		18.8	0.32	6.98	12.33		1.04	0.46	0	0.02		96.1
		biot-amph zone	46.87	0.12	9.16		17.28	0.31	10.58	12.26		0.75	0	0	0.01		97.34
Scotia																	
	SC163-18																
		amph-core	49.4	0.32	7.92	0.29	14.99	0.23	12.44	11.38	0.08	0.67	0	0	0		97.71
		amph-core	48.51	0.48	11.09	0.15	16.13	0.26	10.51	11.39	0.05	0.98	0.14	0	0.01		97.69
		amph-rim	49.48	0.38	6.9	0	14.5	0.27	12.82	11.75	0.08	0.65	0	0	0.02		96.84
		amph-rim	50.21	0.33	5.71	0	13.92	0.31	13.23	11.89	0	0.62	0	0	0.03		96.24
		act-zois veins	51.67	0.3	5.48	0.13	15.19	0.23	12.63	11.82	0.01	0.51	0	0	0		97.96
		act-zois veins	50.57	0.33	5.63	0.04	16.98	0.25	11.79	11.96	0.03	0.44	0	0	0		98.01
		act-preh veins	54.68	0.03	3.31	0	13.6	0.22	14.36	12.83	0.03	0.15	0	0	0		99.2
		act-preh veins	56.14	0.02	0.66	0	10.61	0.19	17.08	12.89	0	0	0	0	0.01		97.59
		ab-preh veins	70.49	0.02	18.76	0.03	0.01	0	0.02	0.04	0	11.19	0.04	0	0		100.59
		ab-preh veins	69.76	0	18.97	0	0	0	0	0.04	0.03	11.08	0.04	0	0		99.92
	CN389171-e																
		with cpx	53.27	0.22	4.16	0.04	16.72	0.35	12.92	12.22	0.03	0.39	0	0	0.01		100.32
		with cpx	55.99	0.05	1.1	0	13.93	0.22	15.42	12.47	0	0.07	0	0.09	0		99.34
		with cpx	53.66	0.18	4.01	0	13.46	0.27	14.36	12.26	0	0.36	0	0	0		98.55
	CN389170																
		vein	54.6	0.1	0.28	0.04	17.93	0.34	12.09	12.3	0	0.05	0	0	0.02		97.74
		vein	53.23	0.12	2.65	0	19.1	0.37	11.87	11.81	0.03	0.26	0	0	0.01		99.44
		vein	50.72	0.32	5.08	0.03	18.67	0.39	11.57	11.95	0	0.46	0	0	0.03		99.21
		lamination	44.41	0.37	13.19	0.12	14.04	0.52	11.21	11.77	0	1.36	0.19	0	0.02		97.19
		lamination	48.37	0.22	9.5	0.1	11.18	0.4	14.61	11.94	0	1.13	0	0	0		97.44

Appendix A2 Representative analyses of biotite from alteration assemblages

Mine Sample	Comments	SiO2	TiO2	Al2O3	Cr2O3	FeO	MnO	MgO	CaO	NiO	Na2O	K2O	F	Cl	P2O5	TOTAL
Junction																
JU-1																
	vein	38.42	0.23	13.79	0	15.8	0.08	15.72	0		0.05	9.26	0.01	0.01		93.36
JU-2																
	vein	34.38	1.67	17.19	0	20.78	0.05	10.33	0		0.07	9.14	0	0.03		93.63
	vein	35.09	1.85	15.89	0	20.71	0.09	10.55	0.03		0.15	8.95	0.07	0.02		93.39
	vein	35.11	1.48	15.27	0.04	21.99	0.05	10.46	0.06		0.05	9.08	0.21	0.03		93.82
	vein	34.98	1.77	16.36	0.04	20.82	0.09	10.41	0.04		0.05	9.31	0	0.02		93.88
	vein	35.28	2.1	16.06	0	21.24	0.09	10.3	0.01		0.04	9.31	0	0.02		94.46
Higginsville																
HIG-1																
	vein margin	36.5	1.6	16.95		13.82	0.08	14.66	0.01		0.07	9.53	0	0.02		93.23
	vein margin	37.01	1.57	16.5		13.68	0.17	15.17	0		0.05	9.67	0	0		93.82
CN389164																
	vein margin	39.02	1.97	15.04	0.04	15.37	0.13	14.94	0.03	0	0.04	9.13	0	0.02		95.72
	vein margin	40.09	1.52	15.51	0.07	15.17	0.12	15.55	0.01	0	0.08	8.91	0	0		97.02
	vein margin	35.66	1.6	16.38	0	15.82	0.19	17.53	0.04	0.01	0.04	5.47	0	0.02		92.75
	vein margin	38.55	1.82	16.87	0.04	15.77	0.17	15.34	0	0	0.07	8.77	0	0		97.39
Surface Winze																
SW-14																
	vein margin	36.95	1.75	17.78	0	16.84	0.14	11.97	0	0	0.08	9.64	0	0.03		95.17
	vein margin	36.78	1.8	17.57	0.01	16.38	0.17	12.25	0	0	0.09	9.14	0	0.06		94.24
	vein margin	36.86	1.75	18.21	0	15.79	0.18	12.09	0	0	0.03	9.3	0	0.03		94.23
North Royal																
NR-14 (HMT)																
	vein margin	37.82	1.35	13.85		12.16	0.06	17.23	0		0.09	8.52	0	0.03		91.11
	vein margin	39.02	1.43	14.44		12.54	0.1	17.46	0		0.08	8.66	0.02	0.03		93.78
	vein margin	38.55	1.48	14.28		12.39	0.12	17.41	0.03		0.09	9.19	0	0.03		93.57
	vein margin	37.76	1.55	14.47		12.74	0.14	16.98	0.06		0.08	8.83	0.02	0.01		92.66
	vein margin	38.02	1.48	14.25		12.2	0.14	17.38	0		0.08	8.55	0.13	0		92.23
NR-2																
	biotite	35.3	1.72	16.38		20.35	0.12	10.73	0		0.07	9.17	0.07	0.04		93.95
	biotite	35.86	1.77	16.19		20.28	0.12	10.71	0.03		0.05	9.48	0.11	0.05		94.65
NR-4 (Princess Royal Fault Zone)																
	biotite	36.26	0.95	18.33		18.14	0.1	11.18	0		0.11	9.55	0	0.03		94.65
	biotite	35.49	1.17	17.97		18.64	0.08	10.76	0.04		0.09	9.59	0	0.03		93.86
	biotite	36.07	1.2	18.1		18.47	0.09	11.08	0		0.08	9.43	0	0.04		94.56
NR-8 (Princess Royal Fault Zone)																
	biotite	37.37	1.53	14.25		16.22	0.04	15.87	0		0.11	8.42	0	0.02		93.83
	biotite	38.06	1.57	13.89		15	0.06	16	0.08		0.11	8.59	0	0.04		93.4
NR-22																
	chlor-biot zone	36.07	1.73	15.55		18.05	0.13	11.29	0.03		0.05	8.03	0	0.03		90.96
	chlor-biot zone	37.16	1.63	15.4		18.26	0.13	11.39	0.17		0.11	8.18	0	0.06		92.49
	chlor-biot zone	36.71	1.9	15.57		18.14	0.17	11.13	0		0.03	7.99	0	0.05		91.69
PRS-24																
	biot-chlor zone	35.81	2	15.74		19.98	0.14	11.74	0.04		0.08	8.73	0	0.07		94.32
	biot-chlor zone	35	2.09	15.97		20.3	0.13	11.76	0		0.07	8.26	0	0.04		93.62
NR-25																
	biotite zone	35.6	1.57	16.16		16.98	0.09	11.31	0.01		0.12	8.48	0	0.06		90.38
	biotite zone	36.35	1.67	18.44		17.21	0.1	11.21	0		0.11	8.96	0	0.06		92.11
NR-26																
	wallrock incl.	36.01	1.73	15.76		17.87	0.12	10.46	0		0.05	8.91	0	0.03		90.94
	wallrock incl.	35.49	1.65	16.14		18.27	0.17	10.38	0.01		0.04	8.81	0	0.04		91
	wallrock incl.	35.73	1.62	15.95		18.13	0.18	10.79	0		0.04	8.6	0	0.04		91.08
NR-34																
	vein selvedge	35.45	1.45	16.82		17.26	0.1	11.21	0		0.12	8.99	0	0.04		91.44
	vein selvedge	35.94	1.78	16.63		17.06	0.06	11.09	0.01		0.04	8.97	0	0.02		91.62
	vein selvedge	36.22	1.57	16		17.06	0.1	11.32	0		0.11	8.56	0	0.04		90.98
	vein selvedge	36.88	1.57	16.12		17.6	0.12	11.54	0		0.07	8.54	0	0.05		92.49
Regent																
CN389157																
	vein	34.25	1.75	16.84	0.39	19.91	0.08	11.54	0.04		0.04	7.87	0	0.01		92.72
	vein	35.77	1.63	16.82	0.15	16.93	0.1	11.92	0		0.11	9.26	0	0.03		92.71
	vein	35.56	1.63	16.97	0.19	17.72	0.12	12	0.01		0.08	9	0	0.03		93.3
	vein	35.71	2.05	16.61	0.09	18.77	0.15	11.42	0.03		0.05	8.99	0	0.02		93.88
	vein	36.3	1.97	16.48	0.03	18.14	0.21	11.52	0		0.11	9.76	0	0.02		94.53
AB213759 (HMT)																
	wallrock alt	35.32	0.65	16.53	0.25	17.48	0.14	17.08	0.07	0.06	0.11	5.49	0	0.34		93.51
	wallrock alt	36.39	0.85	16.8	0.42	17.07	0.06	16.17	0.06	0.03	0.05	6.85	0	0.41		95.15
Okay																
OK-2																
	biot-amph zone	35.41	2.3	16.44		19.48	0.22	11.37	0.01		0.13	8.48	0	0.03		93.87
	biot-amph zone	34.89	2.37	16.36		20.06	0.15	11.14	0		0.18	8.5	0	0.03		93.7
OK-6																
	wallrock incl.	35.56	2.04	15.8		18	0.19	12.19	0.06		0.11	8.54	0.05	0.03		92.57
	wallrock incl.	36.5	1.97	15.29		18	0.23	12.19	0.01		0.18	8.84	0.04	0.03		93.28
OKu10																
	biot-amph zone	34.34	1.75	17.29		17.91	0.22	13.61	0.34		0.04	6.96	0	0.02	0	92.48
	biot-amph zone	34.91	1.7	16.63		16.76	0.22	13.41	0.17		0.04	7.34	0	0.02	0.09	93.29
OK-12																
	amph-biot zone	35.47	2.44	15.91		19.43	0.13	10.58	0.03		0.11	8.91	0	0.06		93.07
	amph-biot zone	34.59	1.88	15.89		20.76	0.18	10.94	0.04		0.01	7.82	0	0.02		92.13
OK-13																
	biot-amph zone	35.47	2.17	15.66		22.02	0.04	9.75	0.04		0.01	9.19	0	0.04		94.39
	biot-amph zone	34.96	1.93	15.4		21.11	0.17	9.8	0		0.09	9.01	0	0.05		92.52
OK-26																
	with muscovite	35.11	1.75	17.14		18.49	0.14	12.39	0.17		0.05	7.82	0	0.06		93.11
	with muscovite	33.65	1.75	17.27		19.37	0.21	12.73	0.1		0.03	6.49	0	0.06		91.65
Viking Decline (Royal Standard vein)																
RS-10																
	biot-amph zone	33.87	1.38	16.99		19.53	0.19	13.3	0.15		0.07	6.83	0	0.03	0.02	92.36

Appendix A3 Representative chlorite analyses from metmorphic and hydrothermal alteration assemblages

Mine	Sample	Comments	SiO2	TiO2	Al2O3	Cr2O3	FeO	MnO	MgO	CaO	NiO	Na2O	K2O	F	Cl	P2O5	TOTAL
Junction																	
	JU-1																
		32 vein	26.46	0.05	19.42	0.03	20.24	0.1	19.9	0		0	0	0	0.02		86.21
		38 vein	26.57	0.07	19.35	0	20.44	0.1	19.67	0.01		0	0	0	0.01		86.22
		39 vein	26.93	0.07	19.2	0.03	20.26	0.08	19.8	0.06		0	0	0	0		86.42
	Ju-2																
		17 vein	24.32	0.07	21.75	0	25.06	0.1	14.69	0		0.01	0	0	0		86
		19 vein	24.65	0.08	20.95	0	25.61	0.17	14.94	0.01		0.03	0	0	0.01		86.44
Higginsville																	
	CN389164																
		4 vein	27.55	0.07	19.93	0.01	17.77	0.05	21.36	0.07	0	0.03	0	0	0		86.83
		10 vein	27.92	0.07	20.77	0.1	18.24	0.12	21.64	0.01	0.06	0.01	0	0	0.01		88.94
		13 vein	26.91	0.1	20.48	0	17.48	0.21	21.01	0.03	0	0.11	0	0	0		86.32
Surface Winze																	
	SW-14																
		38 vein	26.23	0.05	21.6	0	21.37	0.12	18.75	0	0	0	0	0	0		88.12
		43 vein	26.36	0.1	20.71	0.06	20.78	0.25	17.92	0	0	0	0	0	0		86.17
North Royal																	
	NR-11 (HMT)																
		42 amph-chlor zone	27.77	0	19.24		16.21	0.06	22.62	0.03		0	0	0	0.02		85.95
		43 amph-chlor zone	27.55	0.1	19.16		15.95	0.14	22.98	0.03		0	0	0	0.02		85.93
		44 amph-chlor zone	27.58	0.1	19.14		15.54	0.13	23.28	0.03		0	0	0	0.02		85.82
		53 amph-chlor zone	27.36	0.1	19.73		15.79	0.21	22.3	0.04		0	0	0	0.01		85.54
	NR-14 (HMT)																
		9 vein margin	28.56	0.03	17.74		13.88	0.12	24.62	0		0.01	0	0	0		84.96
		14 vein margin	28.58	0.05	17.91		13.42	0.13	25.75	0.11		0	0	0	0		85.95
		15 vein margin	29.07	0.18	17.65		13.23	0.14	25.49	0.03		0	0	0	0.01		85.8
		30 vein margin	28.3	0.05	19.22		13.75	0.09	24.77	0.01		0.01	0	0	0		86.2
	NR-18 (tholeiite)																
		80 chlor-ep-ab veins	25.84	0.03	19.86		22.32	0.26	15.4	0.03		0.03	0	0	0.02	0	83.79
		81 chlor-ep-ab veins	26.46	0.05	19.05		22.15	0.27	16.27	0.06		0.01	0	0	0.01	0	84.33
		82 chlor-ep-ab veins	26.12	0.03	18.54		21.33	0.25	16.22	0.03		0.01	0	0	0	0	82.53
		85 chlor-ep-ab veins	25.05	0.05	20.01		22.1	0.3	15.22	0.11		0.01	0	0	0.01	0	82.86
		87 chlor-ep-ab veins	26.1	0.05	18.8		22.11	0.34	16.08	0		0.03	0	0	0.01	0	83.52
	NR-2 (Princess Royal Fault Zone)																
		62 chlorite	25.05	0.03	21.12		24.03	0.21	15.16	0.04		0.04	0	0	0.02		85.7
		63 chlorite	25.31	0.07	20.27		24.82	0.17	16.58	0.11		0	0	0	0		87.33
		68 chlorite	26.14	0.1	19.78		23.74	0.13	16.47	0		0	0	0	0.01		86.37
	NR-4 (Princess Royal Fault Zone)																
		77 chlorite	24.86	0.07	21.73		22.77	0.23	16.65	0.04		0	0	0	0.01		86.36
		78 chlorite	24.09	0.02	21.48		22.59	0.23	16.91	0.04		0	0	0	0.01		85.37
		82 chlorite	25.01	0.03	21.94		23.08	0.21	16.32	0		0	0	0	0.01		86.6
		83 chlorite	25.59	0.03	21.22		23.12	0.15	17.1	0		0.01	0	0	0		87.22
	NR-8 (Princess Royal Fault Zone)																
		33 chlorite	27.68	0.07	18.18		17.21	0.04	22.5	0		0	0	0	0		85.68
		34 chlorite	27.06	0.08	18.37		17.01	0.09	22.32	0.03		0	0	0	0		84.96
		36 chlorite	28.3	0.07	18.14		16.65	0	22.72	0.01		0	0	0	0		85.89
		37 chlorite	27.96	0.1	18.04		16.43	0.09	22.95	0		0.04	0	0	0.01		85.62
	NR-22																
		3 chlor-biot zone	26.1	0.08	20.14		20.6	0.26	16.85	0		0.03	0	0	0.01		84.07
		9 chlor-biot zone	25.78	0.08	19.78		20.46	0.18	16.96	0.03		0	0	0	0.01		83.28
		10 chlor-biot zone	26.19	0.08	19.65		21.09	0.31	16.83	0.01		0.01	0	0	0.02		84.19
	PRS-21																
		40 chlor-ep-ab veins	25.48	0.05	19.92		22.81	0.22	17.11	0.08		0.05	0	0	0.03		85.75
		44 chlor-ep-ab veins	25.72	0.05	19.76		23.76	0.25	16.83	0.06		0.03	0	0	0.03		86.48
	PRS-24																
		31 biot-chlor zone	25.29	0.05	20.09		22.95	0.21	17.71	0.04		0.01	0	0	0.01		86.35
		32 biot-chlor zone	25.14	0.05	20.95		22.45	0.23	16.98	0.06		0	0	0	0.01		85.87
		35 biot-chlor zone	25.44	0.08	20.84		22.35	0.22	17.73	0		0.01	0	0	0		86.67
	NR-26																
		59 wallrock incl.	25.12	0.07	20.73		22.02	0.22	15.98	0.06		0	0	0	0		84.2
		66 wallrock incl.	24.9	0.03	20.63		22.27	0.34	15.35	0		0	0	0	0		83.52
		68 wallrock incl.	25.74	0.02	19.07		21.14	0.23	16.47	0.01		0	0	0	0		82.68
		70 wallrock incl.	25.63	0.05	21.16		21.42	0.23	16.3	0.03		0.01	0	0	0		84.83
	NR-34																
		12 vein	25.61	0.07	20.92		20.16	0.18	16.81	0.03		0	0	0	0.02		83.8
		15 vein	25.78	0.05	20.77		20.24	0.19	17.28	0.03		0.01	0	0	0.01		84.36
		17 vein	25.5	0.1	20.41		20.44	0.15	16.47	0		0	0	0	0.01		83.08
		38 vein	25.05	0.03	20.77		20.87	0.26	16.1	0.03		0.01	0	0	0		83.12
Princess Royal																	
	PR-F																
		8 vein	25.03	0.05	21.14	0.13	25	0.28	15.44	0.03		0	0	0	0.02		87.11
		9 vein	24.73	0.02	20.78	0.07	24.55	0.27	15.47	0		0.01	0	0	0.01		85.9
		10 vein	24.56	0.08	21.18	0	25.22	0.22	15.01	0		0	0	0	0.02		86.28
Regent																	
	AB213759 (HMT)																
		45 amph-chlor-biot	26.61	0.07	20.97	0.63	19.57	0.14	21.16	0.01	0.1	0	0	0	0.17		89.43
		47 amph-chlor-biot	26.53	0.05	20.18	0.45	19.16	0.1	21.04	0.01	0.03	0	0	0	0		87.54
	S1113-A																
		22 chlor-ep-ab	25.05	0.03	19.84		25.73	0.23	14.36	0.59		0.04	0	0	0.02		85.89
		24 chlor-ep-ab	29.16	0.4	17.27		23.48	0.25	13.4	2.2		0.08	0	0	0.01		86.25
		13 chlor-ep-ab	24.88	0.05	20.9		23.3	0.21	15.8	0.01		0	0	0	0.01		85.16
	S1113-11C (HMT)																
		54 chlor-biot-amph	25.8	0.08	21.43		17.93	0.21	20.94	0.03		0	0	0	0		86.42
		51 chlor-biot-amph	25.97	0.13	21.58		18.36	0.22	20.36	0		0	0	0	0		86.62
		52 retrogressive	27.62	0.32	19.69		19.71	0.19	18.94	0.01		0.03	0	0	0		86.51
		53 retrogressive	28.03	0.27	18.61		20.85	0.17	17.18	0.06		0.01	0.53	0	0.01		85.72
Ajax																	
	AB372686 (HMT)																
		27 amph-chlor	31.45	0.97	16.57	0.69	16.09	0.18	19.93	0.06	0.1	0	1.3	0	0.41		89.75
		28 amph-chlor	27.64	0.08	20.24	0.91	15.73	0.13	23.58	0.03	0.06	0.03	0	0	0.11		88.53

Viking Decline																
RS-2a																
6 retrogressive	26.59	0.08	19.48		20.39	0.19	16.91	1.25		0.04	0	0	0.02		84.94
10 retrogressive	27.96	0.05	21.43		20.47	0.22	15.29	0.06		0.01	1.12	0	0		86.61
RS-2b																
19 retrogressive	25.95	0	21.09		22.17	0.18	17.49	0		0	0	0	0.01		86.88
23 retrogressive	26.85	0.17	19.42		22.54	0.32	16.35	0.11		0	0.34	0	0		86.1
24 retrogressive	29.44	0.08	18.38		22.18	0.25	14.76	0.1		0.03	1.88	0	0.02		87.11
26 retrogressive	26.74	0.02	16.87		27.56	0.32	13.56	0.1		0.01	0	0	0.01		85.18
RS-3																
2 amph-chlor zone	26.53	0.07	19.69		22.49	0.22	17.54	0.04		0	0	0	0	0.02	86.6
5 amph-chlor zone	25.93	0.05	19.97		22.37	0.12	17.44	0.08		0.03	0	0	0.01	0	86
RS-10																
58 retrogressive	25.97	0.12	21.01		23.22	0.34	16.61	0.04		0	0	0	0	0	87.31
59 retrogressive	25.48	0.05	19.9		23.22	0.35	17.64	0.07		0	0	0	0	0	86.71
Okay																
OKD-2																
24 vein	25.54	0.08	20.95	0	23.63	0.23	16.5	0.03		0.03	0	0	0.03		87.01
28 vein	25.84	0.05	19.78	0.06	22.64	0.17	17.58	0.03		0	0	0	0.01		86.15
OK-3																
49 retrogressive	28.56	0.47	16.31		21.84	0.36	17.92	0.08		0	0.29	0	0.04		85.87
50 retrogressive	28.22	0.27	16.53		22.67	0.36	17.66	0.06		0	0	0	0.04		85.81
51 retrogressive	27.88	0.2	17.14		22.09	0.34	17.68	0.14		0	0	0	0		85.47
52 retrogressive	28.75	0.25	16.46		22.32	0.27	18.41	0.1		0	0	0	0.03		86.59
53 retrogressive	29.01	0.7	16.33		21.6	0.39	17.73	0.28		0.01	0.3	0	0.02		86.37
54 retrogressive	28.47	0.2	16.84		21.82	0.3	18.02	0.06		0	0	0	0		85.71
63 retrogressive	27.88	0.4	16.04		21.79	0.37	17.73	0.13		0	0	0	0		84.34
OK-14																
29 retrogressive	30.08	0.02	14.68		20.04	0.22	19.7	0.1		0.04	0	0	0.03		84.91
30 retrogressive	30.04	0.03	15.12		20.15	0.26	20.53	0.1		0.08	0	0	0.02		86.33
32 retrogressive	30.27	1.2	16.99		23.22	0.32	14.59	0.04		0.01	1.79	0	0.03		88.46
33 retrogressive	29.33	1.28	16.25		25.27	0.31	13.98	0.07		0.01	1.33	0	0		87.83
34 retrogressive	25.14	0.08	20.01		25.67	0.27	15.22	0.03		0	0	0	0.03		86.45
35 retrogressive	25.44	0.08	20.18		25.87	0.3	15.12	0		0.01	0	0	0.01		87.01
36 retrogressive	29.93	0	15.66		20.82	0.27	19.93	0.11		0.05	0	0	0.01		86.78
38 retrogressive	30.23	0.03	15.34		20.42	0.31	19.42	0.11		0.04	0	0	0.03		85.93
Scotia																
SC163-18																
55 retrogressive	26.36	0.08	20.22	0	24.02	0.13	15.34	0.06	0.04	0	0	0	0		86.25
CN389170																
50 retrogressive	27.23	0	18.74	0.06	26.59	0	13.31	0.7	0	0.11	0	0	0.02		86.75
40 retrogressive	34.85	0	13.26	0.09	13.97	0.71	24.57	0.57	0.03	0.16	0	0	0.08		88.28
CN389172																
13 retrogressive	30.23	1.12	18.31	0.29	19.44	0.13	16.53	1.85	0.11	0	0.7	0	0.02		88.72
8 retrogressive	29.63	1.45	16.84	0.23	21.5	0.18	17.31	0.55	0.11	0.03	0.72	0	0.01		88.56
4 retrogressive	26.98	0.07	20.03	0	18.67	0.09	20.56	0.01	0.04	0.01	0	0	0		86.45

Appendix A4 Representative analyses of feldspars from metamorphic and hydrothermal assemblages

Mine	Sample	Comments	SiO2	TiO2	Al2O3	Cr2O3	FeO	MnO	MgO	CaO	NiO	NA2O	K2O	F	Cl	P2O5	TOTAL
Junction																	
	JU-1																
		36 vein	68.37	0	19.25	0	0.04	0	0	0.04		11.51	0.06	0	0		99.26
		37 vein	68.33	0.07	19.18	0.01	0	0	0	0.15		11.71	0.05	0	0		99.49
	JU-2																
		15 vein	68.35	0	19.1	0.01	0.06	0	0	0.04		11.57	0.07	0	0		99.19
		16 vein	68.76	0	19.22	0	0	0	0	0.08		11.58	0.06	0	0		99.69
Higginsville																	
	HIG-1																
		56 vein	67.92	0	18.61		0	0	0.02	0.13		11.35	0.12	0	0.02		98.16
		57 vein	67.97	0	18.67		0	0	0	0.06		11.08	0.06	0	0.01		97.84
		60 vein	66.79	0	19.12		0.08	0	0.02	0.43		11.15	0.06	0	0		97.64
		61 vein	58.77	0	24.6		0.14	0	0	7		7.28	0.11	0	0.01		97.9
		62 vein	58.75	0	24.75		0.12	0.01	0.05	6.44		6.79	1.1	0	0.01		98.02
Surface Winze																	
	SW-14																
		44 vein	55.26	0	28.29	0.01	0.17	0	0	10.38	0	5.38	0.12	0	0		99.61
		45 vein	58.19	0	26.7	0	0.09	0	0.02	9.37	0	6.11	0.07	0	0		100.54
		46 vein	56.22	0	27.19	0	0.18	0.03	0.02	9	0	6.17	0.06	0	0		98.86
		47 vein	57.33	0.02	27.64	0.03	0.36	0.01	0.02	9.75	0	6.03	0.06	0	0		101.24
North Royal																	
	NR-18																
		78 chlor-ep-ab veins	70.3	0.03	20.37		0.04	0	0	1.44		9.92	0.06	0	0	0	102.16
		79 chlor-ep-ab veins	67.54	0	19.86		0.06	0	0	1.23		10.08	0.04	0	0	0	98.81
	NR-22																
		4 chlor-biot zone	60.67	0.02	24.54		0.44	0	0	6.45		7.05	0.06	0	0		99.23
		11 chlor-biot zone	59.15	0	24.62		0.31	0	0	7.14		6.89	0.05	0	0		98.16
	PRS-21																
		39 chlor-ep-ab veins	67.52	0	19.67		0.12	0.01	0	1.15		10.6	0.07	0	0.01		99.14
		42 chlor-ep-ab veins	66.36	0.03	19.82		0.12	0	0	1.08		10.95	0.06	0	0.01		98.42
		41 least-altered	59.17	0	24.32		0.1	0	0.02	6.53		7.62	0.06	0	0.01		97.82
		43 least-altered	60.31	0	24		0.15	0	0	5.85		7.94	0.07	0	0		98.31
		49 least-altered	61.89	0.02	23.15		0.06	0.01	0	4.8		8.82	0.07	0	0		98.81
	PRS-24																
		29 biot-chlor zone	61.06	0.03	23.58		0	0	0	5.74		8.11	0.07	0	0		98.58
		30 biot-chlor zone	61.01	0	23.32		0.21	0	0.02	5.57		8.37	0.06	0	0		98.55
		36 biot-chlor zone	58.58	0.03	24.85		0.75	0.01	0.03	6.95		7.4	0.1	0	0		98.69
	NR-25																
		54 biot-chlor zone	61.06	0	24.17		0.06	0	0	6.14		7.41	0.02	0	0		98.88
		55 biot-chlor zone	59.28	0	25.09		0.17	0	0.02	7.07		6.75	0.07	0	0		98.45
		56 biot-chlor zone	59.15	0	25.11		0.05	0	0	7.56		6.63	0.07	0	0		98.57
	NR-26																
		71 wallrock incl.	59.71	0	24.43		0.14	0	0	6.7		6.96	0.05	0	0.02		98.01
	NR-34																
		20 least-altered	57.23	0.03	25.7		0	0	0	8.13		6.16	0.05	0	0		97.3
		21 least-altered	58.43	0	25.32		0	0	0	7.5		6.48	0.07	0	0		97.8
		22 least-altered	58.15	0.02	25.56		0.01	0	0	7.72		6.61	0.05	0	0		98.12
		37 least-altered	57.51	0	26.15		0.24	0.01	0	8.33		5.88	0.06	0	0		98.18
Princess Royal																	
	PR-F																
		4 vein	60.67	0.03	24.15	0.04	0	0	0.02	5.88		8.24	0.07	0	0		99.09
		5 vein	61.23	0	24.02	0	0	0.03	0	5.64		8.32	0.1	0	0		99.33
		7 vein	65.87	0	20.26	0	0	0.04	0.02	1.47		10.96	0.1	0	0		98.71
		11 vein	60.57	0	23.77	0.01	0.05	0	0.02	5.64		8.37	0.1	0	0.02		98.54
Regent																	
	CN389157																
		43 vein	62.81	0	22.54	0	0.09	0	0	4.18		9.11	0.1	0	0		98.82
		44 vein	62.41	0.1	23.01	0.01	0.1	0.03	0	4.62		8.92	0.06	0	0.01		99.26
		50 vein	63.18	0	22.52	0	0.05	0	0.02	4.06		9.27	0.11	0	0		99.2
		51 vein	63.15	0	22.94	0	0.03	0	0	4.46		9.14	0.07	0	0		99.78
		54 vein	53.33	0.02	29.23	0	0.19	0	0.02	10.62		4.69	0.81	0	0.02		98.92
		55 vein	63.58	0	22.49	0	0	0.01	0	4.04		9.19	0.1	0	0.02		99.43
		59 vein	63.84	0	22.77	0	0.08	0	0	4.09		9.25	0.08	0	0		100.1
		60 vein	61.31	0	23.05	0	0	0.01	0	4.86		8.86	0.08	0	0		98.16
		61 vein	62.32	0	23.37	0	0.05	0	0.02	4.74		8.87	0.1	0	0.01		99.48
	S1113-A (tholeiite)																
		4 plag-cores	51.52	0.02	29.97		0.53	0	0.07	13.5		4.06	0.05	0	0.01		99.73
		5 plag-cores	53.31	0.02	28.15		0.63	0	0.12	11.81		4.87	0.02	0	0		98.93
		7 plag-cores	53.8	0.02	28.23		0.72	0	0.05	10.98		5.2	0.06	0	0		99.06
		3 plag-rims	46.12	0	32.75		0.21	0.01	0	17.8		1.74	0	0	0		98.63
		8 plag-rims	46.08	0.02	34.01		0.14	0	0	18.04		1.47	0.01	0	0.01		99.78
	AB293760 (HMT)																
		58 recrystallized	51.96	0.03	30.06	0	0.14	0.01	0	12.96	0.05	4.23	0.02	0	0.07		99.52
		60 recrystallized	48.93	0	30.67	0.03	0	0	0	13.78	0	3.49	0.02	0	0.13		97.04
	AB213763 (HMT)																
		51 recrystallized	55.71	0.02	25.7	0	0.01	0	0	7.53	0	7.1	0.06	0	0		96.12
		52 recrystallized	56.09	0.03	25.19	0	0.01	0.01	0.02	7.67	0.01	7.08	0.06	0	0.1		96.26
	AB213759 (HMT)																
		37 biot-chlor-amph	58.53	0	26.3	0	0.06	0	0	8.28	0	6.42	0.06	0	0		99.64
		38 biot-chlor-amph	58.64	0	25.72	0.03	0.03	0	0	7.95	0	6.98	0.02	0	0		99.36
	CN380911																
		1 least-altered	52.44	0	29.5	0.04	0.82	0.04	0.38	12.61	0.03	3.96	0.22	0	0		100.04
		2 least-altered	51.67	0	30.18	0	0.22	0	0.1	12.86	0.01	3.95	0.05	0	0		99.04
	AB213797																
		8 least-altered	67.35	0	22.14	0	0.18	0	0	3.15	0	9.69	0.05	0	0		102.55
		9 least-altered	61.1	0	25.41	0.01	0.23	0.01	0	7.16	0.08	7.56	0.06	0	0		101.62
Ajax																	
	AB372686 (HMT)																
		23 least-altered	59.56	0	26.34	0.03	0.3	0	0	8.09	0	7.17	0.02	0	0		101.5
Viking Decline																	
	RS-2a																
		8 vein selvedge	53.08	0	28.32		0.03	0	0	11.73		4.69	0.05	0	0.01		97.9
		9 vein selvedge	53.78	0	27.83		0.09	0	0	11.19		5.03	0.05	0	0		97.96
		12 vein selvedge	53.66	0	28.08		0.03	0	0	11.22		5.11	0.04	0	0.02		98.15
	RS-2b																
		22 kspar	62.66	0.02	17.48		0.12	0.05	0	0		0.18	16.41	0	0.02		96.93

	RS-3															
	4 amph-chlor	56.14	0.03	27.59		0	0	0	10.16		6.07	0.05	0	0.02	0	100.06
	7 amph-chlor	57.81	0	26.26		0.05	0	0.03	9.15		6.38	0.2	0	0.01	0	99.89
	RS-10															
	48 vein selvedge	59.82	0.03	25.09		0.06	0	0.02	7.29		7.58	0.11	0	0	0	100
	55 vein selvedge	58.19	0.03	25.53		0	0	0.05	7.72		7.1	0.08	0	0	0	98.7
Otary																
	OK-2															
	34 amph-biot zone	54.32	0	27.87		0.12	0.03	0.02	10.45		5.74	0.04	0	0		98.59
	48 amph-biot zone	57.27	0.03	25.56		0.22	0.04	0	8.62		6.83	0	0	0		98.57
	OK-4															
	15 vein	58.79	0	24.83		0.1	0	0	7.44		7.47	0.05	0	0		98.68
	21 vein	58.6	0	24.75		0.03	0	0	7.63		7.44	0.06	0	0.01		98.52
	OKu10															
	40 biot-amph zone	56.76	0	27.38		0.17	0	0	9.61		6.07	0.14	0	0	0.05	100.18
	OK-10															
	9 nm	63.07	0	21.67		0	0.03	0	3.95		9.22	0.06	0	0		98
	6 core, least-altered	54.3	0.05	27.06		0.69	0	0.08	10.42		5.54	0.12	0	0.01		98.27
	8 core, least-altered	52.22	0.05	27.74		0.67	0	0.13	12.45		4.48	0.11	0	0		97.85
	OK-11															
	26 recrystallized	60.14	0	23.3		0.04	0.01	0.02	6.49		7.95	0.06	0	0		98.01
	28 recrystallized	61.55	0	22.35		0.06	0.05	0	5.62		8.3	0.1	0	0		98.03
	OK-12															
	46 amph-biot zone	61.25	0.02	22.54		0.27	0	0.1	5.53		8.37	0.18	0	0.01		98.27
	47 amph-biot zone	59.26	0	24.56		0.19	0	0	7.43		7.51	0.06	0	0		99.01
Scotia																
	SC163-18															
	33 plag-cores	57.44	0.02	27.17	0	0.12	0	0.02	9.79	0	5.81	0.04	0	0		100.41
	35 plag-cores	56.8	0.03	27.1	0	0.13	0	0	9.63	0	5.69	0.04	0	0		99.41
	54 plag nms	60.95	0	24.62	0	0.21	0.03	0	7.22	0.04	7.16	0.06	0	0.01		100.3
	56 with act-zos	70.15	0.03	18.99	0	0.06	0.03	0	0.06	0.04	11.08	0.06	0	0		100.49
	58 with act-zos	69.68	0	18.99	0	0.12	0.03	0	0.14	0.05	11.28	0.06	0	0		100.34
	CN389171-e															
	24 microcline	64.61	0	17.93	0	0.03	0	0.02	0.07	0.03	0.4	15.92	0	0.03		99.03
	25 microcline	64.89	0	17.72	0	0.21	0	0.2	0	0	0.18	16.03	0	0.04		99.26
	CN389172d															
	19 biot-amph zone	54.36	0	28.95	0.18	0.17	0	0	11.84	0	4.73	0.02	0	0.01		100.25
	65 biot-amph zone	54.34	0	27.95	0	0.37	0	0.02	10.51	0	5.45	0.05	0	0		98.68
	69 biot-amph zone	58.85	0	26.04	0.06	0.06	0	0	8.27	0.05	6.7	0.01	0	0		100.03
	71 biot-amph zone	58.96	0	25.79	0	0.05	0	0	8.16	0	6.78	0.05	0	0.01		99.8

Appendix A5 Selected analyses of accessory hydrothermal alteration minerals

Mine	Sample	Mineral	SiO2	TiO2	Al2O3	Cr2O3	FeO	MnO	MgO	CaO	NiO	Na2O	K2O	F	Cl	P2O5	TOTAL
Junction																	
	JU-2																
		wallrock ilmenite	0	50.96	0	0.01	46.87	1.45	0.05	0.03		0	0	0	0		99.36
North Royal																	
	NR-14																
		wallrock sphene	30.59	36.18	0.96		0.45	0.04	0.02	28.66		0	0	0.18	0		97.08
		wallrock rutile	0	91.14	0		0.09	0.03	0.02	0.31		0	0.01	0	0		91.6
		wallrock rutile	0	92.28	0		0.05	0.04	0.02	0.52		0.03	0	0	0		92.94
	NR-18																
		metamorphic apatite	0	0.02	0		0.08	0	0	56.6		0	0	1.74	0.21	43.7	102.35
		metamorphic apatite	0	0.03	0.02		0.1	0.05	0	57.48		0	0	1.7	0.15	44.75	104.28
		metamorphic apatite	0	0	0		0.28	0.03	0.02	57.05		0	0.01	1.43	0.21	45.19	104.22
		metamorphic apatite	0	0	0		0.24	0.1	0.02	56.54		0	0	1.48	0.23	43.97	102.58
		metamorphic apatite	0	0	0.02		0.37	0.09	0.02	55.81		0	0	1.46	0.25	44.34	102.36
	NR-2 (Princess Royal Fault Zone)																
		hydrothermal ilmenite	0.09	46.92	0.02		47.28	2.39	0.07	0		0.01	0	0	0		96.78
		hydrothermal magnetite	0.19	0.42	0.04		93.75	0	0.02	0.01		0	0	0	0		94.43
	NR-4 (Princess Royal Fault Zone)																
		hydrothermal ilmenite	1.93	47.31	0.02		42.43	4.71	0.02	0		0	0	0	0		96.42
		hydrothermal ilmenite	1.28	48.14	0.02		41.45	6.46	0.03	0		0	0	0	0		97.38
	PRS-21																
		retrograde epidote	37.95	0.07	27.42		6.82	0.61	0.08	22.88		0	0	0	0		95.82
		retrograde epidote	38.06	0.07	27.11		7.33	0.34	0.07	23.27		0	0	0	0		96.24
	PRS-24																
		retrograde epidote	38.29	0.1	26.17		7.77	0.09	0	23.44		0.03	0	0	0.01		95.89
		retrograde epidote	37.93	0	25.81		8.39	0.05	0.02	23.49		0	0	0	0.01		95.69
	NR-34																
		wallrock rutile	0.02	91.04	0.02		0.13	0	0	0.9		0.01	0	0	0		92.12
		wallrock rutile	0	91.46	0		0.15	0	0	0.77		0	0.02	0	0		92.4
		wallrock ilmenite	0	47.79	0.02		42.93	2.09	0.02	0.01		0	0	0	0.01		92.87
Princess Royal																	
	PRF																
		retrograde sericite	45.89	0	33.8	0	1.6	0.04	0.93	0.13		0.26	10.41	0	0		93.06
Regent																	
	CN389157																
		vein ilmenite	0.02	52.26	0	0.01	42.3	5.55	0	0.08		0	0	0	0.01		100.22
		retrograde clinozoisite	37.74	0	26.02	0.01	3.43	0.18	2.17	23.04		0.07	0	0	0.01		92.66
	C-22																
		retrograde sericite	46.25	0.15	33.94	0	1.24	0	1.06	0.07		0.42	10.66	0	0.01		93.79
		retrograde sericite	45.61	0.18	34.12	0	1.05	0.01	1.04	0.06		0.4	10.73	0	0		93.19
		retrograde sericite	47.09	0.33	32.35	0	1.43	0	1.53	0		0.24	10.79	0	0		93.75
	S1113-A																
		retrograde epidote	37.91	0.03	24.2		11.26	0.13	0.02	24.3		0.03	0	0	0		97.88
		retrograde epidote	38.23	0.07	23.96		11.01	0	0.02	23.91		0.07	0	0	0.02		97.29
		retrograde epidote	38.68	0.07	27.15		8.05	0.1	0.38	23.23		0.22	0	0	0		97.88
		metamorphic ilmenite	0.02	50.49	0		44.81	2.96	0.08	0.18		0.01	0	0	0		98.55
		retrograde sphene	30.98	36.73	0.74		0.42	0.05	0	29.71		0	0.01	0.03	0		98.67
Viking Decline																	
	RS-2a																
		retrograde epidote	38.59	0	26.25		8.25	0.05	0	23.58		0.04	0	0	0.01		96.75
		retrograde epidote	38.36	0	24.88		10.18	0.03	0	23.53		0.03	0	0	0		97
		retrograde epidote	37.35	0	26.38		3.73	0.09	1.76	22.93		0.01	0	0	0		92.24
		retrograde epidote	38.12	0	25.77		8.62	0	0.02	23.58		0.03	0	0	0.01		96.14
	RS-2b																
		retrograde sericite	45.68	0	33.01		1.04	0	0.7	0.1		0.05	10.68	0	0.02		91.27
		retrograde sericite	47.47	0.03	34.43		0.81	0.03	0.6	0.07		0.12	10.2	0	0		93.75
		retrograde sericite	49.33	0	32.95		0.96	0	1.14	0.07		0.13	9.46	0	0		94.03
Okay																	
	OKu10																
		wallrock sphene	30.55	37.56	1.64		0.55	0.06	0	29.24		0	0	0	0	0	99.62
		wallrock sphene	30.49	37.03	2.15		0.55	0.05	0	30.24		0	0	0	0.01	0.05	100.57
	OK-10																
		metamorphic ilmenite	0	51.38	0.02		46.52	2.23	0.03	0.03		0.04	0	0	0		100.25
	OK-12																
		wallrock sphene	30.68	36.08	1.72		0.48	0.12	0	29.75		0.01	0	0	0		98.84
		wallrock sphene	30.76	36.86	1.74		0.62	0.04	0.02	29.19		0	0	0	0		99.23
	OK-13																
		wallrock sphene	30.66	36.96	1.32		0.63	0.04	0	29.23		0	0.02	0	0.01		98.87
	OK-14																
		wallrock ilmenite	0	51.28	0		39.32	8.59	0.05	0.21		0	0	0	0		99.45
	OK-26																
		coarse vein muscovite	44.91	0.65	32.01		2.3	0	2.04	0		0.28	10.74	0	0.01		92.93
		coarse vein muscovite	45.76	0.43	32.33		1.93	0	1.48	0.01		0.27	10.74	0	0.02		92.96
		coarse vein muscovite	45.05	0.45	32.5		2.26	0	1.69	0		0.26	10.85	0	0.02		93.07
		coarse vein muscovite	45.31	0.67	32.57		1.7	0.06	1.56	0.03		0.31	10.77	0	0.01		92.98
Scotia																	
	SC163-18																
		retrograde zoisite	39.49	0.05	29.42	0	5.03	0.14	0.03	23.9	0	0.01	0	0	0		98.06
		retrograde zoisite	39.13	0.05	28.98	0	5.42	0.22	0.05	23.8	0.01	0.03	0	0	0		97.69
		retrograde zoisite	40.05	0.03	28.61	0	5.26	0.08	0.02	23.9	0	0	0	0	0		97.94
		retrograde zoisite	39.83	0.02	29.34	0.01	4.26	0.06	0.2	23.88	0	0.01	0	0	0.01		97.61
		retrograde prehnite	44.88	0	24.17	0.07	0.18	0	0	26.98	0	0.03	0	0	0		96.31
		retrograde prehnite	44.24	0	23.32	0	0.9	0.05	0	27.14	0.05	0	0	0	0		95.69
		retrograde prehnite	44.71	0.02	23.73	0	0.42	0.04	0.02	26.89	0.01	0.04	0	0	0		95.87
	CN389171-e																
		clinopyroxene	53.55	0	0.36	0	12.45	0.4	10.91	23.65	0	0.12	0	0	0		101.43
		clinopyroxene	54.7	0.02	0.36	0.07	11.4	0.43	11.79	23.95	0.03	0.08	0	0	0		102.82
		clinopyroxene	54.77	0.05	0.34	0.06	11.12	0.45	11.66	23.73	0	0.07	0	0	0.02		102.27
		clinopyroxene	54.38	0.02	0.3	0.04	10.34	0.28	12.42	24.07	0.01	0.08	0	0	0		101.93
		clinopyroxene	54.66	0.07	0.47	0	8.74	0.36	13.43	23.84	0	0.07	0	0	0		101.63
		retrograde prehnite	44.58	0	23.92	0	0.3	0	0.02	26.58	0.05	0.03	0.01	0	0.01		95.49
		retrograde prehnite	44.26	0	24.3	0	0.15	0	0	26.29	0	0.03	0.02	0	0.02		95.06
		retrograde prehnite	44.52	0.03	24.02	0.03	0.42	0	0	26.33	0	0.04	0.04	0	0.02		95.44
		retrograde sericite	46.87	0.03	35.84	0	0.41	0.08	0.33	0.13	0	0.31	10	0	0.06		94.05

Appendix B

Whole-rock geochemical data

This appendix reports comprehensive whole-rock geochemical analyses of rock types not discussed in the thesis, but of peripheral interest to the petrogenesis and hydrothermal alteration of of lithologies within the Norseman Terrane. Analytical methods are as reported in Chapter 3.

Appendix B Whole-rock geochemical analyses of selected samples not reported in text

	Altered Porphyry			Pegmatites			Lamprophyre	Barren clinopyroxene veins					
Sample	PRS1177 -2	PRS1177 -6	PRS1177 -8	SCPEG -8	SC1484 -4	SC1484 -6	SC1484 -14	SC1484 -13	SC1484 -7	SC1484 -8	SCSE CGV	MOON -2	PRS1355
Depth m	220.78	251.44	269.05		74.1	172	261.9	250.2	173.3	227.25			
SiO2 %	70.3	76	74.1	75.5	74.3	49.2	35.3	46.3	38.6	54	64.9	59.1	60.2
TiO2 %	0.09	0.08	0.13	0.05	0.07	0.1	6.74	0.04	0.49	0.86	0.16	0.61	0.71
Al2O3 %	12	13.3	11.4	12.9	14.1	19.6	5.35	27.4	9.39	13.8	3.06	10.6	13.3
Fe2O3 %	1.25	1.39	3.09	0.81	0.66	2.97	15.6	0.62	7.91	8.44	10.1	8.22	7.43
MnO %	0.06	0.04	0.06	0.14	0.04	0.11	0.31	0.04	0.4	0.24	0.42	0.2	0.13
MgO %	0.53	0.83	2.28	0.27	0.38	1.87	13.4	0.62	5.27	2.81	4.02	4.68	4.7
CaO %	5.27	1.48	4.15	0.59	0.78	15.3	13.3	18.1	18.8	14.8	14.9	11.5	5.46
Na2O%	6.48	0.57	1.95	3.76	7.86	1.85	0.59	1.21	2.4	1.99	0.05	1.82	3.31
K2O %	0.15	3.47	0.93	3.84	1.1	1.96	0.94	2	1.77	0.63	0.03	0.45	2.27
P2O5 %	0.02	0.02	0.03	0.06	0.05	0.02	0.79	0.02	0.05	0.07	0.04	0.06	0.06
LOI %	4	2.31	2.23	0.65	0.65	6.85	5.55	3.93	14.3	2.08	1	3.15	2
Total	100.15	99.49	100.35	98.83	100.05	99.89	98.16	100.36	99.4	99.77	98.69	100.43	99.65
La	13.09	11.16	15.2	0.81	0.85	2.13	80.78	0.2	1.28	4.61	1.36	2.37	2.55
Ce	29.7	26.08	33.64	3.53	2.39	3.38	160.99	0.34	3.51	10.83	2.6	6.28	6.96
Pr	3.81	3.53	4.22	0.55	0.3	0.41	19.39	0.05	0.53	1.65	0.36	0.98	1.06
Nd	17.02	15.8	17.83	2.05	1.13	1.88	76.89	0.28	2.82	8.5	1.71	5.17	5.51
Sm	4.51	4.94	4.82	1.03	0.45	0.54	13.68	0.07	0.95	2.23	0.52	1.5	1.83
Eu	0.66	0.67	0.87	0.06	0.03	0.74	3.75	0.32	0.33	1.3	0.23	0.81	1.11
Gd	5.34	5.86	5.29	0.85	0.49	0.81	10.79	0.07	1.49	2.9	0.81	2.08	2.81
Tb	0.85	0.97	0.85	0.17	0.09	0.12	1.19	0.01	0.28	0.46	0.15	0.36	0.5
Dy	5.62	6.56	5.49	0.88	0.55	0.86	5.98	0.1	1.94	3	1.12	2.5	3.68
Ho	1.14	1.33	1.1	0.12	0.07	0.2	0.91	0.02	0.42	0.62	0.27	0.55	0.79
Er	3.53	3.84	3.32	0.32	0.22	0.64	2.14	0.07	1.21	1.8	0.88	1.67	2.42
Tm	0.54	0.61	0.49	0.06	0.04	0.11	0.25	0.01	0.19	0.26	0.14	0.24	0.36
Yb	3.48	3.96	3.2	0.52	0.3	0.99	1.27	0.07	1.18	1.64	1.08	1.7	2.4
Lu	0.52	0.57	0.47	0.08	0.04	0.21	0.18	0.01	0.19	0.25	0.2	0.25	0.36
Th	12.38	12.98	10.93	2.37	2.87	0.14	7.76	0.15	0.15	0.48	0.12	0.19	0.22
U	4.62	5.28	3.95	2.74	3.06	0.03	2.15	0.16	0.04	0.36	0.07	0.38	0.12
Cs	0.09	0.97	0.39	134.47	3.77	3.89	1.47	9.7	0.23	0.87	0.08	0.24	1.63
Tl	0.51	1.04	0.64	16.95	2.05	2.44	1.01	1.91	0.15	0.26	0.01	0.01	0.38
Rb	4.37	112.87	36.81	2216.1	308.98	261.64	46.93	293.65	40.51	40.14	2.05	8.94	70.03
Sr	70.47	37.62	77.51	4.3	18.1	107.07	567.45	144.42	21.85	61.5	35.14	46.48	79.16
Ba	113.21	541.75	237.96	16.04	34.37	257.54	816.32	322.9	91.8	83.06	17.47	34.73	256.52
Nb	8.49	9.42	7.59	42.01	43.31	1.58	120.34	0.14	1.25	6.44	0.93	1.53	2.32
Ta	0.97	1.1	0.88	9.7	16.84	1.25	7.44	0.01	0.15	0.57	0.22	0.16	0.27
Zr	98.18	92.43	92.68	14.00	11.00	5.84	405.16	1.27	28.00	48.00	9.82	35.00	48.00
Hf	4.24	4.27	3.75	1.06	0.58	0.17	10.08	0.07	0.55	0.76	0.28	0.9	1.11
Y	30.06	36.35	29.73	5.08	2.77	6.26	22.93	0.58	10.87	15.72	7.46	14.11	19.83
V	8.79	1.22	25.68	1.63	2.69	21.02	425.05	7.98	136.2	213.32	124.84	219.6	208.96
Sc	1.87	1.88	3.99	1.72	1.24	2.46	23.7	1.4	18.82	31.09	23.89	28.67	36.41
Cr	16	10	52	10	20	10	595	10	73	202	10	148	146
Co	2	1	15	2	2	8	78	6	30	33	26	39	46
Ni	3	2	24	1	7	12	419	2	71	85	29	85	100
Cu	7.3	3	4.3	2	9	2	172	2	88	67	7	48	75
Zn	18.7	26.5	27.9	106	8	16	126	6	54	96	194	56	94
Pb	9.23	14.52	9.64	57.03	13.05	8.59	7.67	2.77	1.3	3.08	1.56	7.53	2.73
Be	0.9	1.5	2	9.81	4.47	1.89	1.8	2.7	1.7	95.75	0.91	0.05	0.49
Mo	1.71	0.41	0.29	0.3	0.17	0.05	0.56	0.08	0.39	0.41	3.84	0.52	0.47
Bi	0.07	0.04	0.07	3.35	1.07	0.17	0.17	0.24	0.4	0.32	0.48	0.4	0.17
Cd	2	2	2	0.5	0.5	0.5	1	0.5	0.5	0.5	0.5	0.5	0.5
W	10	10	10	10	10	10	10	10	10	10	400	10	10
Ag	0.5	0.5	0.5	0.2	0.2	0.2	0.2	0.2	0.2	0.2	0.2	0.2	0.2
Au	1	1	1										
As	3	3	3										
Li	6	23	18	134.26	9.19	50.26	59.26	18.36	48.09	67.26	5.56	20.04	15.15
Mg#	27	34	39	22	33	35	43	46	36	22	26	33	35
Al2O3/TiO2	133.33	166.25	87.69	258.00	201.43	196.00	0.79	685.00	19.16	16.05	19.13	17.38	18.73
CaO/Al2O3	0.44	0.11	0.36	0.05	0.06	0.78	2.49	0.66	2.00	1.07	4.87	1.08	0.41
Total REE	90	86	97	11.03	6.95	13.02	378.19	1.62	16.32	40.05	11.43	26.46	32.34
(La/Yb)cn	2.48	1.86	3.13	1.56	2.83	2.15	63.61	2.86	1.08	2.81	1.26	1.39	1.06
(La/Sm)cn	1.78	1.39	1.94	0.79	1.89	3.94	5.9	2.86	1.35	2.07	2.62	1.58	1.39
(Gd/Yb)cn	1.24	1.20	1.34	1.63	1.63	0.82	8.5	1	1.26	1.77	0.75	1.22	1.17
Zr/Hf	23.2	21.6	24.7	13.2	19.0	34.4	40.2	18.1	50.9	63.2	35.1	38.9	43.2
Nb/Ta	8.8	8.6	8.6	4.3	2.6	1.3	16.2	14.0	8.3	11.3	4.2	9.6	8.6
Ti/Zr	5.5	5.2	8.4	21.4	38.1	102.6	99.7	188.8	104.9	107.4	97.7	104.5	88.7
Nb/Th	0.7	0.7	0.7	17.7	15.1	11.3	15.5	0.9	8.3	13.4	7.8	8.1	10.5
La/Nb	1.54	1.18	2.00	0.02	0.02	1.35	0.67	1.43	1.02	0.72	1.46	1.55	1.10
La/Th	1.06	0.86	1.39	0.34	0.30	15.21	10.41	1.33	8.53	9.60	11.33	12.47	11.59
Zr/La	7.5	8.3	6.1	17.3	12.9	2.7	5.0	6.4	21.9	10.4	7.2	14.8	18.8

Analytical methods as reported in Chapter 3. Depth refers to depth down drill core axis.

Appendix C

Sample locations

The conclusions reached in this study are in large part the result of 12 months of detailed field observation in underground, surface, and drill core exposure, and subsequent petrographic examination and analysis of over 300 thin sections. Space limitations preclude diagrams illustrating the location of all samples; such detailed documentation of sample location is provided in McCuaig (1989a) and McCuaig and McNaughton (1992). This appendix lists abbreviated locations and sample descriptions only for samples for which geochemical data has been presented in this thesis.

Appendix C1 Samples from DDH PRS1177 intersecting the Royal Tiara and Princess Royal veins

Geochemistry Sample	Polished Thin Section	Depth Down Drill Core (m)	Sample Description
PRS1177-1		211.1	m.g. basalt, weak fabric, east margin of PRFZ
PRS1177-2	NR-1	220.5	altered porphyry in PRFZ, intense fabric, quartz-biotite-carbonate veining
PRS1177-3	NR-2	229.5	intensely sheared basalt, quartz-carbonate-chlorite alteration
PRS1177-4	NR-3	238.5	intense fabric, biotite-chlorite-carbonate altered basalt
PRS1177-5	NR-4	250.3	intense fabric, biotite-carbonate-quartz altered basalt
PRS1177-6	NR-5	251.5	altered porphyry in PRFZ, intense fabric
PRS1177-7		268	intense fabric, biotite-chlorite altered basalt, quartz-cabonate veining
PRS1177-8		269	sheared porphyry in PRFZ
PRS1177-9	NR-6	272.7	strong fabric, carbonate-chlorite-biotite altered gabbro in PRFZ
PRS1177-10	NR-7	298	quartz-cb-chlor vein in PRFZ with chlorite alteration selvedge
PRS1177-11		329.4	chlorite altered HMT, weak fabric
PRS1177-12	NR-8	331.3	chlorite-biotite altered HMT
PRS1177-13	NR-9	344.4	chlorite-biotite altered HMT
PRS1177-14		350.9	chlorite-biotite altered HMT
PRS1177-15	NR-10	351.7	HMT in hangingwall of Royal Tiara vein
	NR-11		immediate hangingwall margin of Royal Tiara vein
	NR-12		immediate hangingwall margin of Royal Tiara vein
	NR-13		stylolitic lamination in Royal Tiara vein
	NR-19		footwall lamination in Royal Tiara vein
PRS1177-16	NR-14	352.5	HMT in immediate footwall of Royal Tiara vein
PRS1177-17	NR-20	353.5	chlorite-biotite altered HMT in footwall of Royal Tiara vein
PRS1177-18	NR-16	355.9	chlorite altered HMT
PRS1177-19		360.5	chlorite altered HMT
PRS1177-20	NR-17	361	chill margin of tholeiitic dyke, cuts HMT
PRS1177-21	NR-18	371.2	least-altered megacrystic Royal Dyke
	PRS-21	374.6	quartz-carbonate-epidote-albite veins in Royal Dyke
PRS1177-22	NR-22	378.6	chlorite ± biotite alteration in Royal Dyke
PRS1177-23	NR-23	378.9	same as PRS1177-22, with sulphide veinlets
PRS1177-24	PRS-24	383.5	biotite-chlorite alteration around quartz-carbonate-chlorite vein
PRS1177-25		384.9	intense biotite alteration in hootwall of Princess Royal vein
PRS1177-26		385.1	chlorite-biotite altered wallrock, Princess Royal vein
PRS1177-27	NR-26	386	banded chlorite-biotite alteration in hangingwall of Princess Royal vein
	NR-27		biotite-pyrite rich alteration
	NR-28		vein margin
PRS1177-28	NR-29	386.9	biotite-pyrite altered wallrock inclusion in Princess Royal vein
PRS1177-29	NR-30	387.6	biotite alteration in footwall of Princess Royal vein
PRS1177-30	NR-31	387.9	chlorite-biotite alteration in footwall of Princess Royal vein
PRS1177-31	NR-34	389.2	chlorite alteration in footwall of Princess Royal vein
PRS1177-32	NR-36	397.1	least-altered gabbro in footwall of Princess Royal vein
PRS1177-33	NR-35	390.8	chlorite-biotite alteration around quartz veinlet
PRS1177-34	NR-38	403.6	least-altered gabbro in footwall of Princess Royal vein
PRS1177-35	NR-37	446.4	least-altered HMT gabbro

Appendix C2 Samples from DDH S1113 intersecting the Mararoa vein

Geochemistry Sample	Polished Thin Section	Depth Down Drill Hole (m)	Sample Description
S1113-A		131.8	m.g. tholeiitic gabbro, massive
S1113-B	S13A	146.6	m.g. tholeiitic gabbro, massive
S1113-C		151.8	sheared gabbro, amphibole-plagioclase
S1113-D		152.1	sheared gabbro, amphibole plagioclase
S1113-E		152.6	sheared gabbro, amphibole-plagioclase
S1113-F		154.3	m.g. gabbro, thin quartz stringers
S1113-G	S13B	156.6	beginning of shear associated with Mararoa vein
S1113-H	S13C	157.4	c.g. gabbro with abundant pyrite
S1113-I		157.9	c.g. gabbro
S1113-J		159.1	sheared gabbro, amphibole alteration in quartz veinlets
S1113-K		159.9	sporadic biotite alteration begins in hangingwall of Mararoa vein
S1113-L	S13D	160.3	biotite-amphibole alteration
S1113-M	S13-10	160.9	biotite±amphibole alteration, immediate hangingwall of Mararoa vein
	S13-11a	161.1	biotite±amphibole alteration, immediate hangingwall of Mararoa vein
	S13-11b	161.1	partially retrogressed margin of Mararoa vein
	S13-11c	161.1	retrogressed (bleached) margin of Mararoa vein
	S13-13	162	sulphide lamination in Mararoa vein
	S13-12a	162.9	wallrock lamination, Mararoa vein
	S13-12b	162.9	wallrock lamination, Mararoa vein
	S13-14	163	footwall of Mararoa vein
	S13-15	163.1	footwall of Mararoa vein
S1113-N	S13E	163.1	amphibole-chlorite alteration in HMT, immediate footwall of Mararoa vein
S1113-O		163.7	biotite-chlorite altered HMT, footwall of Mararoa vein
S1113-P	S13F	164.9	biotite altered HMT
S1113-Q		166.1	biotite altered HMT
S1113-R		166.8	biotite-chlorite altered HMT
S1113-S		168.4	chlorite-amphibole altered HMT
S1113-T	S13G	169.1	HMT
S1113-U		169.7	sheared contact between HMT and tholeiitic gabbro
S1113-V		170.2	tholeiitic gabbro
S1113-W	S13H	180.2	chill margin of tholeiitic dyke
S1113-X		180.6	quartz-plagioclase alteration next to chill margin
S1113-Y	S13I	184.8	m.g. tholeiitic gabbro

Appendix C3 Samples from DDH S657 intersecting OK Main and O2 vein

Geochemistry Sample	Polished Thin Section	Depth Down Drill Hole (m)	Sample Description
S657-1	OK-1	397.4	f.g. least-altered basalt
S657-2		401.4	f.g. least-altered basalt
S657-3		401.8	amphibole±biotite alteration of basalt
S657-4	OK-2	402.7	amphibole-biotite alteration of basalt
S657-5b		403.1	biotite alteration
S657-5a	OK-3	403.2	retrogressed (bleached) vein margin, O2 vein
S657-6		405.4	biotite alteration
S657-7	OK-4	406.6	amphibole-carbonate veins
S657-8		407.1	amphibole-carbonate veins
	OK-5		immediate footwall of O2 vein, intense biotite alteration
S657-9	OK-6	407.5	biotite alteration of basalt
S657-10		408.7	biotite alteration of basalt
S657-11	OK-18	409.2	biotite-amphibole alteration of basalt
S657-12	OK-7	409.8	amphibole-biotite alteration of basalt
S657-13		415.4	amphibole-biotite alteration of basalt
S657-14		416.8	amphibole-biotite alteration of basalt
S657-15	OK-8	421.9	sulphide veinlets in basalt
S657-16		424.1	sulphide veinlets in basalt
S657-17		427.8	f.g. least-altered basalt, pillow rims preserved
S657-18	OK-18	449	f.g. least-altered basalt, pillow rims preserved
S657-19	OK-10	476.7	least-altered gabbro
S657-20		482.6	least-altered gabbro, 2m from Main vein shear zone
S657-21	OK-11	484.5	amphibole ±biotite altered gabbro
S657-22	OK-12	485.1	amphibole ±biotite altered gabbro
S657-23	OK-13	486.2	biotite alteration, immediate hangingwall of Main vein
S657-24	OK-14	486.7	biotite alteration, immediate footwall of Main vein
S657-25		487.8	amphibole ±biotite altered gabbro
S657-26	OK-15	489.2	1.5m wide fine-grained dyke (least-altered)
S657-27		490.5	least-altered gabbro
S657-28	OK-16	494.4	least-altered basalt
S657-29	OK-17	522	least-altered basalt

Appendix C4 Samples from DDH through the Scotia orebodies

Geochemistry Sample	Depth Down Drill Hole (m)	Sample Description
SC358-1	93.1	massive, least-altered, f.g. basalt
SC358-2	105.6	least-altered, massive, c.g. tholeiitic gabbro
SC358-3	108.8	c.g. tholeiitic gabbro, intense fabric
SC358-7	121.3	intense fabric, biotite-amphibole-plagioclase altered gabbro
SC358-11	123.6	c.g. HMT in immediate hangingwall of quartz vein
SC358-15	130.5	intensely sheared tholeiitic gabbro
SC358-24	143.3	biotite-amphibole-plagioclase alteration of gabbro
SC358-25	143.6	amphibole-plagioclase alteration of gabbro
SC358-27	144.1	biotite-amphibole-plagioclase alteration in f.g. basalt
SC358-28	144.6	amphibole-plagioclase ± biotite alteration of sheared basalt
SC358-29	144.7	quartz-carbonate-clinopyroxene veining (ore)
SC358-31	145.6	massive, least-altered basalt
SC358-33	124	quartz-clinopyroxene-carbonate vein
SC358-40	125	quartz-clinopyroxene-carbonate vein
SC358-54	126	quartz-amphibole vein
SC358-55	126	quartz-clinopyroxene-carbonate vein
SC358-78	144	quartz-amphibole vein
SC358-96	145	quartz-amphibole vein
SC358-99	145	quartz-amphibole vein
SC1484-1	43.7	clinopyroxene-garnet-pyrrhotite alteration in intensely sheared gabbro
SC1484-2	45.4	biotite-plagioclase-amphibole alteration of sheared gabbro
SC1484-3	45.8	amphibole-plagioclase ± biotite alteration of sheared gabbro
SC1484-4	74.1	zoned plagioclase-quartz-biotite pegmatite, 20 cm thick
SC1484-5	171.3	massive, least-altered m.g. basalt
SC1484-6	172	quartz-plagioclase-amphibole veining
SC1484-7	173.3	brittle microcline-carbonate-garnet veins
SC1484-8	227.25	clinopyroxene-garnet-carbonate vein
SC1484-10	244.6	massive, f.g. least-altered basalt
SC1484-13	250.2	quartz-plagioclase-clinopyroxene vein
SC1484-14	261.9	lamprophyre
Sc163-18	68	c.g. least-altered massive gabbro
SC163-62	52.1	late gypsum vein on brittle fracture
SC163-66	52.5	quartz-amphibole vein from ore zone
LE-23-1	110	strongly sheared gabbro, amphibole-plagioclase-quartz

Thin sections are labelled with identical sample numbers

Appendix C5 Surface, underground, and other drill core sample locations

Mine	Sample	Location	Sample description
Kalgoorlie Terrane			
Junction			
	JU-1		laminated quartz-molybdenum vein cut by later quartz-carbonate-albite-chlorite vein
	JU-2		quartz-chlorite-carbonate albite vein with biotite-rich vein selvedge
Higginsville			
	HIG-1	Poseidon South	laminated quartz vein with gn, asp, coarse gold
	HIG-2	Poseidon South	massive quartz vein with coarse gn
	CN389164	Poseidon South	biotite-plagioclase alteration adjacent to quartz vein
Norseman Terrane			
Surface Winze			
	SW-14	3/590 stp	massive quartz vein with biotite alteration halo, chlorite vein selvedges, coarse asp
	CN389173-C	3/590 stp	massive quartz vein with biotite alteration halo, chlorite vein selvedges, coarse asp
North Royal			
	NR-35	5/150 stp	strongly brittle-deformed quartz with abundant py, sp, gn, Au. Princess Royal vein
	NR-5/450	5/450 stp	massive quartz with gn, Princess Royal vein
	NRM-7	6 lvl, 450mS	massive quartz + wallrock breccia, Princess Royal vein
	NR-11	4 lvl, F shear	quartz-chlorite-carbonate selvedges to discontinuous quartz veins in F shear
	PR-F	4 lvl, F shear	quartz-chlorite-carbonate selvedges to discontinuous quartz veins in F shear
	RT 10/390	10/390 stp	Massive to laminated quartz with gn, Au, Royal Tiara vein
	PRS 1355	DDH PRS1355	brittle cpx-zoisite alteration in basalts
Regent			
	GSWA 99937	DDH S433, 81.3m	tholeiitic basalt
	GSWA 99787	DDH S169, 318m	tholeiitic basalt
	GSWA 99912	DDH C126, 1683'	tholeiitic basalt
	GSWA 99932	DDH S433, 166.7m	tholeiitic basalt
	GSWA 99955	DDH S156, 220.5m	tholeiitic basalt
	GSWA 99944	DDH S207, 282.7m	enriched tholeiitic basalt
	GSWA 99941	DDH S207, 330.6m	enriched tholeiitic basalt
	GSWA 99934	DDH S433, 130.0m	EHMT
	GSWA 99938	DDH S433, 61.3m	EHMT
	GSWA 109064	DDH S433, 135.1m	EHMT
	GSWA 109065	DDH S433, 130.1m	EHMT
	GSWA 109066	DDH S433, 129.7m	EHMT
	GSWA 109068	DDH S433, 62.2m	EHMT
	AB213755	14 lvl, 2083N, 295E	Butterfly Dyke 3m from Mararoa vein.
	AB213759	16lvl, 2065N, 372E	sheared, biotite-altered dyke adjacent to Mararoa basalt contact
	AB213760	16 lvl, 2072N, 374E	9m from AB213759, weak to moderately sheared Butterfly Dyke, weakly granophyric?
	AB213763	16 lvl, 2088N, 381E	undeformed, gabbroic Butterfly Dyke
	AB213797	16 lvl, 2053N, 368E	Mararoa basalt 3m from Butterfly Dyke contact.
	CN380911	DDH S222, 50.7m	massive basalt 15m from Butterfly Dyke
	AB372679	DDH S222 123.1m	Butterfly Dyke, gabbroic texture preserved, 10m from Mararoa vein
	AB372682	DDH S225 186.5m	chill margin of Butterfly Dyke
	AB372683	DDH S225 201.7m	Butterfly Dyke,gabbroic texture preserved
	AB372685	DDH AXU10-3 23.3m	sheared amphibole-chlorite altered Butterfly Dyke 7m from Mararoa vein
	AB372686	DDH AXU10-3 34.6m	cumulate zone of Butterfly Dyke
	AB372688	DDH AXU10-3 45.7m	gabbroic-textured Butterfly Dyke
	B-fault	16 lvl crosscut	folded quartz vein in HMT within B-fault
	16/70	16/70 stope	pillar with abundant visible gold in boudinaged Crown vein
	CN389157	16/70 stope	pillar with abundant visible gold in boudinaged Crown vein
	C-12	14 lvl	weakly laminated quartz, with gn, in vertical roll on Crown vein
	C-20	16lvl, B-fault	gn in boudinaged and folded quartz, Crown vein, within B-fault
	C-22	16 lvl	abundant brittle-deformed laminations in quartz in Crown vein
	M11/76	11/76 stp	gn , Au in boudinaged and weakly laminated Mararoa vein
	RM-1	29 lvl, S drv	galena on shear laminations in Mararoa vein
	RM-22	29 lvl, N drv	galena on shear laminations in Mararoa vein
	RM-71	25 lvl shaft	gn on laminations, boudinaged Mararoa vein
	RM-74	25 lvl shaft	gn on laminations, boudinaged Mararoa vein
	RM-99	11 lvl	galena in folded Mararoa vein, B-fault
	S3151-1	DDH S3151 126m	gn, sp, po on a sulphide lamination in quartz, Mt. Barker vein
	S3151-2	DDH S3151 126m	gn, sp, po on a sulphide lamination in quartz, Mt. Barker vein
	Moon-2		cpx alteration in shear zone immediately south of Jimberlana dyke
Ajax			

	AJ1	7 lvl, 1550mS	massive quartz with multiple gn, py generations, Norseman vein hosted in felsic porphyry
	AJ2	7 lvl, 1550mS	massive quartz with multiple gn, py generations, Norseman vein hosted in felsic porphyry
	AJ4	7 lvl, 1550mS	massive quartz with multiple gn, py generations, Norseman vein hosted in felsic porphyry
	AJ5	7 lvl, 1550mS	massive quartz with multiple gn, py generations, Norseman vein hosted in felsic porphyry
	AJ23	7 lvl, 900mS	coarse isolated gn and brittle-deformed gn in deformed Mararoa vein
	AJ34	7/656 stp	coarse gn with large Au nuggets, Norseman vein
	AJ56	10 lvl	Mararoa vein, E-fault, isolated gn in massive to weakly laminated quartz
	AJ58	10 lvl	brittle-deformed gn in quartz 5m from AJ 56
	AJ75	12 lvl	galena from laminated quartz, Mararoa/Valhalla vein intersection
Viking Decline			
	RS2	450W stp	plagioclase-amphibole selvedge to quartz vein, Royal Standard vein
	RS3	450W stp	plagioclase-amphibole-chlorite alteration of gabbro, 1m from Royal Standard vein
	RS10	450W stp	biotite-amphibole alteration adjacent to Royal Standard vein
	RS11	450W stp	gn isolated in massive quartz, Royal Standard vein
	RS12	450W stp	amphibole vein selvedge in weakly laminated quartz, Royal Standard vein
	RS13	450W stp	gn from sulphide-rich lamination in quartz, Royal Standard vein
Okay			
	OKD2	6 lvl	quartz veinlet crosscuts Main vein
	OK-L	6 lvl	gn from laminated quartz in Main vein, at O2/Main vein intersection
	OKM 3/585	3/585 stp	abundant visible gold, asp, gn in high-grade ore shoot on Main vein
	OK-26	5 lvl	c.g. muscovite at margin of massive + breccia quartz in Main vein
	CN275938	8 lvl	amphibole-biotite-asp alteration surrounding O2 vein
Scotia			
	CN380170	4/550 ramp	multiple quartz types (deformed, undeformed) with similar alteration assemlages
	SC3	4/550 ramp	multiple quartz types (deformed, undeformed) with similar alteration assemlages
	CN380171	7/440 crosscut	banded cpx-quartz-carbonate-amphibole-microcline vein
	CN380172	7/440 crosscut	biotite-amphibole-plagioclase alteration in host shear zone (altered gabbro)
	SC2	8/620 crosscut	massive quartz vein with banded cpx-carbonate-amphibole selvedges
	SC7/440N	7/440 crosscut	composite banded quartz-cpx-amphibole-carbonate-microcline vein
	SCPeg8	7/440 crosscut	zoned pegmatite crosscutts ore zone
	SCPV	7/440 crosscut	thin discontinuos cpx-amphibole-carbonate veins peripheral to ore zone
	SCSECGV	surface, SE of Scotia	quartz-cpx-amphibole-carbonate-garnet vein adjacent to late-tectonic granitoid

abbreviations: asp = arsenopyrite; cpx = clinopyroxene; gn = galena; lvl = level; po = pyrrhotite; py = pyrite; sp = sphalerite; stp = stope